Schaefer School of Engineering and Science
Department of Biomedical Engineering

1 Castle Point Terrace
Hoboken, NJ 07030
stevens.edu

The 50th Northeast Bioengineering Conference (NEBEC) – FULL PROGRAM

April 4th – 5th, 2024

Co-organized by:

Stevens Institute of Technology

New Jersey Institute of Technology

Sponsored by:

ENHANCER

Drexel University

NYU | Tandon

PARTNER

Carnegie Mellon University

Merck

OptiTrack

SUPPORTER

Fairfield University

mBrainTrain

New Jersey Institute of Technology

Noraxon

Rensselaer Polytechnic Institute

Sympfiny

University of Pittsburgh

STEVENS
INSTITUTE OF TECHNOLOGY

Conference Foreword

Welcome to the 50th Northeast Bioengineering Conference (NEBEC)!

This year's conference is being held on the campus of Stevens Institute of Technology, across the river from New York City. It is co-organized by the Departments of Biomedical Engineering at Stevens and New Jersey Institute of Technology (NJIT).

We are proud to bring together some of the best and brightest minds in the region to share their work in Bioengineering and Biomedical Engineering. Specific areas of discipline at this year's meeting include Cell and Tissue Engineering, Biomechanics, Medical Device Technology, Medical Imaging and Processing, Neuro-engineering, and Education. Scientific and design works are presented as oral talks and posters. We have renown keynote speakers in academia, medicine, and industry. We will culminate the conference with interactive discussed panels intended to foster greater career development for students and early-career faculty.

We look forward to seeing you and hope you have a great experience!

Stevens Organizers (Lead)

Jennifer Kang-Mieler, Conference Chair
Raviraj Nataraj, Program Chair
Sally Reiter
Rekha Manohar

NJIT Organizers (Support)

Amir Miri Ramsheh
Xianlin (Alex) Zhou
Alev Erdi
Bryan Pfister

STEVENS
INSTITUTE OF TECHNOLOGY

Conference Support Team

Stevens Events/Relations Personnel

Frances Salvo
Robert Gonzales
Mette Gomez

Stevens Ph. D. Student Volunteers

Sophie Dewil (lead)
Yu Shi (lead)
Sam Liu
John Battikha
Rana Ibrahim
Chaimae Gouya
Jiawen Chen
Zahava Hirsch
Aneri Patel

Faculty/Staff Support for Main Conference

Sally Shady
Peter Popolo
Becky Tucci
Antonia Zaferiou
Carrie Perlman
George McConnell
Yu Gan
Jinho Kim
Shang Wang
Hongjun Wang
Xiaojun Yu
William Querido
Max Roman
Ghazel Khayet
Elisa Kallioniemi
Jon Grasman
Kirsten Homeny

STEVENS
INSTITUTE OF TECHNOLOGY

Campus Map (Original 'CAMPUS MAP' link at website travel page: https://nebec.org/travel.html)

Main NEBEC 24 events take place at 1) UCC, 2) Howe, and 3) Gateway North/South.

STEVENS
INSTITUTE OF TECHNOLOGY

Table of Contents

DAY 1 = April 4, 2024 (Thursday) – Scientific Sessions
DAY 2 = April 5, 2024 (Friday) – Design and Career Development Sessions

AGENDA

DAY 1: Thursday, April 4		
Time	Segment	Location
7:30-8:30 AM	Check-In/Continental Breakfast	UCC, Lower-level Lobby; Pre-function Space
8:15-9:15 AM	**Scientific Poster Session 1**	**Howe Center 4th floor, Bissinger Room**
9:15-9:30 AM	Break	(Transition to UCC)
9:30-10:30 AM	Opening Remarks and Keynote Speaker 1 (Scientific)	UCC, Tech Flex Auditorium
10:30-11 AM	Coffee Break	Tech Flex Pre-function Space (Room flip for sessions)
11 AM-12 PM	**Scientific Podium Session 1** **Four Tracks:** **1) Biomech-Locomotion** **2) Cell/Tissue Eng** **3), Med Dev Tech** **4) Med Imag Proc**	**Four Locations (at UCC):** **1) Tech Flex A** **2) Tech Flex B** **3) Tech Flex C** **4) Gallery**
12-1 PM	Lunch	UCC, Pre-function Space
1-2 PM	**Scientific Podium Session 2** **Four Tracks:** **1) Biomech-Tiss** **2) Cell/Tissue Eng** **3) Med Dev Tech** **4) Med Imag Proc**	**Four Locations (at UCC):** **1) Tech Flex A** **2) Tech Flex B** **3) Tech Flex C** **4) Gallery**
2-2:15 PM	Coffee Break	
2:15-3:15 PM	**Scientific Podium Session 3** **Four Tracks:** **1) Biomech-Tiss, Loco** **2) Cell/Tissue Eng** **3) Cell/Tissue Eng** **4) Neuro-Eng**	**Four Locations (at UCC):** **1) Tech Flex A** **2) Tech Flex B** **3) Tech Flex C** **4) Gallery**
3:15-3:30 PM	Break	UCC, Pre-function Space
3:30-4:30 PM	**Scientific Poster Session 2**	**Howe Center 4th floor, Bissinger Room**
4:30-4:45 PM	Break	(Transition to UCC)
4:45-6:05 PM	**Faculty Innovator Spotlight Talks**	**UCC Tech Flex Auditorium**
6:05-8 PM	Social Networking Reception	UCC, Pre-function Space and Terrace

DAY 2: Friday, April 5		
Time	Segment	Location
7:30-8:30 AM	Check-In/Continental Breakfast	UCC, Lower-level Lobby; Pre-function Space
8:15-9:15 AM	**Senior Design Poster 1**	**Gateway North 103 & 204**
9:15-9:30 AM	Break	(Transition to UCC)
9:30-11:00 AM	**Keynote Speakers 2 & 3 (Medical, Industry)**	**UCC, Tech Flex B & C**
11:00-11:15 AM	Coffee Break	Tech Flex Pre-function Space
11:15 AM-12:15 PM	**Senior Design Poster 2**	**Gateway North 103 & 204**
12:15-1:30 PM	Lunch	UCC, Pre-function Space and Terrace (use Tech Flex A for seating as well)
1:30-3:30 PM	**Interactive Panels: Early-Career Faculty Development "Establishing Your Program"** **Two Tracks (back-to-back):** **A) Entrepreneurial opportunities** **B) Partners: Clinical & Industry**	**Gateway North 103**
1:30-3:30 PM	**Interactive Panels: Student (UG/G) Career Development "Planning Your Future"** **Two Tracks:** **A) Pathways: Medicine & Industry** **B) Graduate Student Strategies**	**Two Locations (UCC):** **A) Tech Flex Auditorium** **B) Gallery**
3:30-4 PM	Awards Recognitions (Young Scientist, Senior D, Faculty Innovators) and Closing Remarks	UCC, Tech Flex Auditorium

KEYNOTE PRESENTATION
(DAY 1, Thursday, April 4)

STEVENS
INSTITUTE OF TECHNOLOGY

We are pleased to welcome **Dr. Andrew Laine (Columbia University)** to deliver the Day 1 keynote at this year's NEBEC!

Harmonization and Airway Tree Subtyping on Large Cohorts of CT Images of the Lung for COPD Risk

Andrew F. Laine, D.Sc.

Percy K. and Vida L. W. Hudson Professor
Department of Biomedical Engineering
Professor of Radiology (Physics), Department of Radiology
Director, Heffner Biomedical Imaging Laboratory
Columbia University, New York, NY, USA

Email: LAINE@columbia.edu

Bio-Sketch:

Andrew F. Laine received his D.Sc. degree from Washington University (St. Louis) School of Engineering and Applied Science in Computer Science, in 1989 and BS degree from Cornell University (Ithaca, NY). He was a Professor in the Department of Computer and Information Sciences and Engineering at the University of Florida (Gainesville, FL) from 1990-1997. He joined the Department of Biomedical Engineering in 1997 and served as Vice Chair of the Department of Biomedical Engineering at Columbia University since 2003 – 2011, and Chair of the Department of Biomedical Engineering (2012 – 2017). He is currently Director of the Heffner Biomedical Imaging at Columbia University and the Percy K. and Vida L. W. Hudson Professor of Biomedical Engineering and Professor of Radiology (Physics).

He has served on the program committee for the IEEE-EMBS Workshop on Wavelet Applications in Medicine in 1994, 1998, 1999, and 2004. He was the founding chair of the SPIE conference on "Mathematical Imaging: Wavelet Application in Signal and Image Processing" and served as co-chair during the years 1993-2003. Dr. Laine has served as Chair of Technical Committee (TC-BIIP) on Biomedical Imaging and Image Processing for IEEE EMBS 2004-2009 and has been a member of the TC of IEEE Signal Processing Society, TC-BISP (Biomedical Imaging and Signal Processing) 2003-present. Professor Laine served on the IEEE ISBI (International Symposium on Biomedical Imaging) steering committee, 2006-2009 and 2009 – 2012. He was the Program Chair for the IEEE EMBS annual conference in 2006 held in New York City and served as Program Co-Chair for IEEE ISBI in 2008 (Paris, France). He served as Area Editor for IEEE Reviews in BME in Biomedical Imaging since 2007-2013. He was Program Chair for the EMBS annual conference for 2011 (Boston, MA). Professor Laine Chaired the Steering committee for IEEE ISBI, 2011-2013, and Chaired the Council of Societies for AIMBE (American Institute for Medical and Biological Engineers). He was the General Co-Chair for IEEE ISBI in 2022. Finally, he served as the IEEE EMBS Vice President of Publications 2008 – 2012 and was the President of IEEE EMBS (Engineering in Biology and Medicine Society) 2015 and 2016. He currently serves as the Chair of the Membership Committee for IAMBE (International Academy of Medical and Biological Engineers). He is a Fellow of IEEE, AIMBE and IFMBE.

Abstract:

Chronic obstructive pulmonary disease (COPD) defined by irreversible airflow limitation, is the 3rd leading cause of death globally and 4th in the United States. Smoking tobacco is a major extrinsic COPD risk factor, but despite six decades of declining smoking rates in many countries, the corresponding declines in COPD have been modest. Only a minority of lifetime smokers develop COPD, and up to 25% occurs in never smokers. While other factors have been linked to COPD much of the variation in COPD risk remains unexplained.

Airflow obstruction, or reduced airflow from the lungs, is determined in part by airway tree structure and lung volume, both of which can be imaged with high precision by high resolution computed tomographic (HRCT) scans. Emerging evidence by our group suggests that airway tree structure variation is common in the general population and is a major contributor to this unexplained COPD risk. By manual labeling of the airway tree structure, limited to one airway generation in just 2 of the 5 lung lobes (due to complexity of tree structure), we found that 26% of the general population has major airway branch variants that differ from the classical "textbook" structure, increase COPD risk, and have a strong and biologically plausible genetic basis. We further demonstrated that airway tree caliber variation (dysanapsis) measured on CT was a stronger predictor of COPD risk than all known risk factors including smoking. Yet there is no standardized approach to characterize the full scope airway tree variation, making the exact relationship between COPD and individual airway-structure features unclear.

This works applies the power of machine learning methods to the entire airway tree structure imaged on HRCT to build logically upon prior high-impact work to discover new COPD subphenotypes for risk stratification and biological pathways of intervention. Also, we apply sophisticated / rigorous mathematical clustering approaches to airway trees derived from over 18,000 computed tomography (CT) scans in three highly characterized cohorts – MESA Lung Study, SPIROMICS, COPDGene Study, in addition to CanCOLD – to discover and replicate novel and clinically significant airway tree subtypes and their genetic basis. By understanding airway tree structure subtypes from lung CT scans, we hope to advance our knowledge of disease susceptibility and improve personalized therapies, prognosis, and identify an underlying genetic basis to COPD risk.

SCIENTIFIC PODIUM SESSIONS (DAY 1, Thursday, April 4)

STEVENS
INSTITUTE OF TECHNOLOGY

SCIENTIFIC PODIUM SESSION 1 (11:00am - 12:00pm)

LOCATION:	UCC Tech Flex A	UCC Tech Flex B	UCC Tech Flex C	UCC Gallery
TRACK:	***Biomechanics - Locomotion***	***Cell/Tissue Eng. & Biomaterials***	***Medical Device and Technology***	***Medical Imaging & Processing***
START TIME	**SUBMITTING AUTHOR (*PRESENTER, if different*)**			
P1 (11:00)	Akbas, Kubra	Buckley, Christian	Bahabri, Razan	Dev, Isha
P2 (11:15)	Dewil, Sophie	Dogan, Elvan	Chen, Jiawen	Fang, Tianqi
P3 (11:30)	Jones, Rachel	Hu, Xiao	Iyasele, Patrick	Han, Huan
P4 (11:45)	Liu, Jun		Kumar, Suneel	HassanMazandarani, Azita
Track Chair (Institution):	*Alex Zhou (NJIT)*	*Amir Miri (NJIT)*	*Jon Grasman (NJIT)*	*Shang Wang (Stevens)*

Track 1: Biomechanics - Locomotion
P1: An Experimental Approach to Quantify Postural Stability in the Center of Mass State Space
P2: Error induction during rehabilitative training improves motor performance and increases EEG theta band power
P3: Analyzing the impact of passive exoskeleton assistance on lifting dynamics through musculoskeletal modeling
P4: Relationship between Peak Angular Momenta and Ball Speed in High School Baseball Pitchers

Track 2: Cell/Tissue Eng. & Biomaterials
P1: Porous, Perfusable Microtubular Networks for Improved Cell Viability in Volumetric Hydrogels
P2: Solute Diffusivity in Bioprinted GelMA Constructs: Implications for Biomimetic Tumor
P3: Ultrasound-Enhanced Silk-based Films and Nanofibers for Biomedical Applications

Track 3: Medical Device and Technology
P1: Integration of Wearable Sensors in Telerehabilitation to Monitor Health-Related Metrics to Predict Fitness Level
P2: Enhancing Intracellular Delivery of mRNA Therapeutics Using Mechanical Oscillation
P3: Efficacy of Rivaroxaban Anticoagulation During 10-day, In Vivo, Venovenous ECMO Support Using a Poly-Carboxybetaine Coated Artificial Lung
P4: Application of Polyelectrolyte Complex Dressing for Wound Healing

Track 4: Medical Imaging & Processing
P1: Machine Learning Analysis of Bone Submicron Composition: A Novel Approach to Identify Fragile Bones
P2: Three-Dimensional Velocimetry based on Optical Coherence Tomography for Assessing Transport of Preimplantation Embryo in the Mouse Oviduct In Vivo
P3: Assessing the Role of Oviduct Contraction in the Transport of Preimplantation Embryo through In Vivo Imaging in the Mouse Model
P4: Microplastics Assessment in Intact Tissue Phantoms with Infrared Spectroscopy

STEVENS
INSTITUTE OF TECHNOLOGY

SCIENTIFIC PODIUM SESSION 2 (1:00pm - 2:00pm)

LOCATION:	**UCC Tech Flex A**	**UCC Tech Flex B**	**UCC Tech Flex C**	**UCC Gallery**
TRACK:	***Biomechanics - Tissue***	***Cell/Tissue Eng. & Biomaterials***	***Medical Device and Technology***	***Medical Imaging & Processing***
START TIME	**SUBMITTING AUTHOR (*PRESENTER, if different*)**			
P1 (1:00)	Battikha, John	Li, Rui	Nasim, Umar	Mukhamedjanova, Aleese
P2 (1:15)	Luu, Ngoc	Liu, Lunan	Rajotte, Kiriaki	Shi, Yuan
P3 (1:30)	Ye, Jingnan	Lodge, Robert	Shin, Suji	Wootton, David
P4 (1:45)		Madhavarapu, Shreya	Starzynski, Sophia	
Track Chair (Institution)	*Carrie Perlman (Stevens)*	*Hongjun Wang (Stevens)*	*George McConnell (Stevens)*	*Yu Gan (Stevens)*

Track 1: Biomechanics – Tissue
P1: Alveolar Distribution of Nebulized Particles in Lung Injury Assessed by Confocal Microscopy
P2: Aging-Associated Decline in Vascular Mechanosensation: Implications of Piezo1 Signaling
P3: A novel experimental system to study collective cellular responses to patterned static stretching of surgical meshes

Track 2: Cell/Tissue Eng. & Biomaterials
P1: Deciphering CAR T-cell Biomechanics for Engineered Activation and Programed Immunotherapy
P2: Pancreatic Cancer Organoids-on-a-Chip for Tumor Microenvironment Modeling and Immunotherapy Study
P3: Liraglutide as a Treatment for Neuroinflammation Following Low-Level Blast Traumatic Brain Injury
P4: Novel Biomimetic 3D Printed Load-Sharing Scaffolds for Vascularized Bone Regeneration

Track 3: Medical Device and Technology
P1: Hemocompatibility Evaluation of an Oxygenator with a Computationally Optimized Fluid Path in an Ovine Model for 48 Hours without Systemic Anticoagulation
P2: Characterizing Charge Time of Wearable Devices using Qi Wireless Charging System
P3: Combined Use of Polycarboxybetaine Coatings with a Selective FXIIa Inhibitor to Create Potent Anticoagulation without Bleeding during ECLS
P4: Establishing a Normative Cerebral Blood Flow Database in a Non-Concussed Population

Track 4: Medical Imaging & Processing
P1: Time-Lapse Quantitative 3D Imaging of Outgrowth Formation from Ovarian Cancer Spheroid with Optical Coherence Tomography
P2: A Surgical Navigation Framework for Image-Guided Transoral Robotic Surgery
P3: High Through-Put Image-Based Modeling of Upper Airway Pressures Using Computational Fluid Dynamics

SCIENTIFIC PODIUM SESSION 3 (2:15pm - 3:15pm)

LOCATION:	**UCC Tech Flex A**	**UCC Tech Flex B**	**UCC Tech Flex C**	**UCC Gallery**
TRACK:	***Biomechanics – Tissue, Locomotion***	***Cell/Tissue Eng. & Biomaterials***	***Cell/Tissue Eng. & Biomaterials***	***Neuro-Engineering***
START TIME		**SUBMITTING AUTHOR (*PRESENTER, if different*)**		
P1 (2:15)	Singh, Charul	Mohammadi, Mohaddeseh	Patel, Aneri	Crockett, Anthony
P2 (2:30)	Sudesh, Reshma	Oruc, Doga	Spadavecchia, Felicia	Omidi, Saeed
P3 (2:45)	You, Zihang	Padilla, Cecilia	Truong, Thi	Shashikumar, Soham
P4 (3:00)			Tusnim, Jarin	Skog, Emily
Track Chair (Institution)	*William Querido (Temple)*	*Xiaojun Yu (Stevens)*	*Jinho Kim (Stevens)*	*Elisa Kallioniemi (NJIT)*

Track 1: Biomechanics – Tissue, Locomotion
P1: Scenario in which ARDS therapeutic has differential effects on inflammation and oxygenation
P2: Bone Tissue Water as a Biomarker to Predict Proximal Femur Stiffness
P3: Exploring Lower Limb Sagittal Angles for Enhanced Human Activity Recognition

Track 2: Cell/Tissue Eng. & Biomaterials
P1: Parafilm®-based low-cost rapid microfluidics for tumor cell sorting
P2: Investigating CHIR99021 as a Regulator of Adipogenesis in the Treatment of Myotendinous Junction Injuries
P3: Adapting and evaluating the advancing front model to design a biofabricated lung

Track 3: Cell/Tissue Eng. & Biomaterials
P1: Increasing paracellular permeability in Airway Epithelial for effective Drug Delivery
P2: Elucidating the Effects of Electrical Stimulation on Neural Cells for Tissue Regeneration Applications
P3: 3D Printed Hierarchical Scaffolds with Embedded Fibrous Membranes to Spatially Control Stem Cell Behavior
P4: Select NSAIDs Promote Peripheral Nerve Growth through PPARγ Activation

Track 4: Neuro-Engineering
P1: Persistent Post Concussive Symptoms with related Convergence Insufficiency patients within a longitudinal therapeutic intervention
P2: Detection of neuronal modulation by electromagnetic (EM) spectroscopy
P3: Understanding the Pathophysiology of Persistent Post Concussion Symptoms with Convergence Insufficiency
P4: Link between Neural Activity and Trial Aligned Respiration in Non-Human Primates

STEVENS
INSTITUTE OF TECHNOLOGY

FACULTY INNOVATOR SPOTLIGHT SESSION (4:45pm - 6:05pm)

START TIME	UCC Tech Flex Auditorium ***Biomechanics - Tissue***
P1 (4:50)	Gan, Yu
P2 (5:15)	Raimondo, Theresa
P3 (5:40)	Truong, David
MODERATOR (Institution)	*Raviraj Nataraj (Stevens)*

P1: Enhanced Coronary Imaging System: Leveraging Generative Artificial Intelligence for Adaptive Super-Resolution
P2: RNA-therapeutics for Cellular, Tissue, and Immune Engineering
P3: Human Genome Writing HLA-matched iPSCs for Off-the-shelf Smart Therapeutic Cells

SCIENTIFIC POSTER SESSIONS
(DAY 1, Thursday, April 4)

STEVENS
INSTITUTE OF TECHNOLOGY

SCIENTIFIC POSTER SESSION 1 (8:15am - 9:15am)

LOCATION: **Howe Center 4th floor, Bissinger Room**

BOARD#:	***1***	***2***	***3***	***4***
TRACK:	***Biomechanics***	***Biomechanics***	***Medical Device and Technology***	***Medical Device and Technology***
POSITION		**SUBMITTING AUTHOR (*PRESENTER, if different*)**		
A	Hernandez, Jobelle	Orins, Helen	Alruwaili, Fayez	Mohan, Stuti
B	Hirsch, Zahava	Patel, Ansh	Chow, Nicholas	Moss, Gabrielle
C	Hong, JiYeon (Ashley)	Ramanujam, Ranjini	Israel, Atara	Nuesi, Ciara
D	Kreis, Erin	Shamouil, Aaron	Kulkarni, Anushri	Rahman, Syeda

BOARD#:	***5***	***6***	***7***	***8***
TRACK:	***Medical Imaging & Processing***	***Cell/Tissue Eng. & Biomaterials***	***Cell/Tissue Eng. & Biomaterials***	***Cell/Tissue Eng. & Biomaterials***
POSITION		**SUBMITTING AUTHOR (*PRESENTER, if different*)**		
A	Abbott, Leslie	Abaci, Alperen	Buffone, Alexander (*Issa et al.*)	Dogan, Elvan (*Rishi Kuriakose*)
B	Di Pede, Rocco	Almeida, Bethany (*Rose Leader*)	Caron, Justin	Dunsmore, Madeline
C	Elgabori, Osama	Attia, Mohammed	Dalir, Laya	Fasciano, Samantha
D	Hou, Xinlong	Austin, Ann	Dodd-o, Joseph	Gharacheh, Hadis

BOARD#:	***9***	***10***	***11***	***12***
TRACK:	***Cell/Tissue Eng. & Biomaterials***	***Cell/Tissue Eng. & Biomaterials***	***BME Educ, Med. Dev. And Tech.***	***Faculty Innovators***
POSITION		**SUBMITTING AUTHOR (*PRESENTER, if different*)**		
A	Ibrahim, Rana *(Nicole Petrocelli)*	Mahon, Timothy	Mirza, Awais	Almeida, Bethany
B	Kozan, Natalie	Masters, Ethan (*Emily Labour*)	Govindaraju, Harshitha	Drazan, John
C	Lee, Nicholas	Meyer, Sadie	Rafi, Rifath	
D	Levovitz, Sarah	Miri, Amir K (*Luis Medina*)	Liao, Ruhuan	

Board 1: Biomechanics

A: Deep Learning Model's Estimation of Soleus Muscle Activation during Level Walking
B: Frontal Plane Balance Patterns of Older Adults During Pre-Planned and Late-Cued Turns
C: The Acute Compressive Strain Response of Osteoarthritic Cartilage: An In Vivo Study
D: Impact of a Cognitive Dual Task on Older Adult Motor Performance and Strategies

Board 2: Biomechanics

A: Marfan Syndrome Vascular Smooth Muscle Cells Show Increased Phenotypic Sensitivity to TGF-β1
B: Investigating Fracture Risks Associated with Corticotomies in Femoral Bones: A Finite Element Analysis and Mechanical Testing Approach
C: Fracture Mechanics of Blood Clots: Influence of Fibrin Structure on Rupture Resistance

D: Integration of Optical Coherence Tomography (OCT) and 3D Computational Fluid Dynamics (CFD) to Evaluate Right Coronary Artery (RCA) Hemodynamics

Board 3: Medical Device and Technology
A: A Haptic Virtual Reality Simulator for Robot-Assisted Femur Fracture Surgery
B: An investigation into to the current practices of monitoring extracorporeal membrane oxygenation
C: Dye Enhancement of an Antibody-Conjugated Nanosensor Platform
D: Aggregation morphology of magnetic beads within microfluidic droplets

Board 4: Medical Device and Technology
A: OculoMotor and Vestibular Endurance Screening (MoVES) Protocol Adult Concussion Data
B: The Sensitivity and Stability of Magnetic Nanoparticle – Based Aggregation Assays are Influenced by Surface Ligand Density and Electrolyte Concentration
C: Synthesis of Iron Nanoparticles Through Chemical Reduction
D: Design of a Single Walled Carbon Nanotube-Based Nanosensor for the Inflammatory Cytokine TNF-alpha

Board 5: Medical Imaging & Processing
A: Detection of Human Trust in AI Suggestions Using Brain Activity Data
B: Assessing the Viability of Near Infrared Spectroscopy to Evaluate Graft Maturation of Intraoral Bone Regeneration
C: Characterization of Scattering for Whole Blood Oximetry in Sub-Diffuse Regimes
D: A Comparative Study of Coronary OCT Image Registration

Board 6: Cell/Tissue Eng. & Biomaterials
A: Dense Cell Bioprinting within Hydrogels with Spatiotemporal Heterogeneity to Modulate Stem Cell Osteogenesis
B: Investigating the Effects of Stiffness and Viscoelasticity on Human Mesenchymal Stem Cell Immunomodulation
C: Taurine-Loaded Hydrogel Drug Delivery System for Sodium Iodate-Induced Dry Age-Related Macular Degeneration
D: How Photointitator Impacts Stem Cell Behavior in 3D Bioprinted Gelatin Mathacryloyl

Board 7: Cell/Tissue Eng. & Biomaterials
A: Precision editing of the Cancer Glycocalyx to Tune Mechanically Regulated Migration in Glioblastoma Multiforme
B: Investigation of Compressive Stress on Cancer Cell Migration
C: The Effect of Neuron-to-Neuron Forces on Neuronal Activity
D: Computational and Human Guided Approaches to Designing C5aR Antagonizing Cyclic Peptides

Board 8: Cell/Tissue Eng. & Biomaterials
A: Automated Cell Spheroid Positioning into Hydrogel-based Microfluidic Chips
B: Developing a Hypoxic Biosensor for Therapeutic Applications
C: Investigation of Cell Traction Force in Osteogenic Differentiation Using Microcontact Printing and Inhibiting Agents
D: Cell-Laden Composite Hydrogel Bioinks with Human Bone Allograft Particles to Enhance Stem Cell Osteogenesis

Board 9: Cell/Tissue Eng. & Biomaterials
A: Fabrication and characterization of Chitosan:Polystyrene Sulfonate Composite Scaffolds for Bone Regeneration
B: IGF-1- and IGFBP-5-Loaded Collagen Sponges for Skeletal Muscle Regeneration
C: Sacrificial Electrospun Dipeptide for Encapsulation of Cell Therapies
D: Deletion and Sequential Insertion of Large DNA in the Human Genome for Cell Therapy Applications

Board 10: Cell/Tissue Eng. & Biomaterials
A: Epigallocatechin-Gallate as a Novel Treatment for Joint Injury Repair
B: Prognosis of Prostate Cancer Metastasis Risk Through qPCR
C: Shape-Memory Actuated 3D Silk Wrinkled Surfaces Decrease Biofilm Formation on a Medical Device Model
D: A Multi-Layer Vocal Fold Microtissue to Study Fibrosis

Board 11: BME Educ, Med. Dev. And Tech.
A: Assessment of Strategies for False Discovery Rate Control and their Implications in Computational Biology
B: Computational Analysis of Cellular Dynamics in Microfluidics Using Advanced Hall Sensor Technology
C: Quantification of Cortical Activation During Vestibular Tasks: A Pilot fNIRS Study
D: Functional Near-Infrared Spectroscopy (fNIRS) Experiment Data Analysis Using ML Algorithm

Board 12: Faculty Innovators
A: Advanced Biomaterials Mimicking the Human Mesenchymal Stem Cell Microenvironment to Control Cell Behavior
B: A Community Situated Approach to Musculoskeletal Biomechanics Research

STEVENS
INSTITUTE OF TECHNOLOGY

SCIENTIFIC POSTER SESSION 2 (3:30pm - 4:30pm)

LOCATION: **Howe Center 4th floor, Bissinger Room**

BOARD#:	***1***	***2***	***3***	***4***
TRACK:	***Biomechanics***	***Cell/Tissue Eng. & Biomaterials***	***Medical Device and Technology***	***Medical Imaging & Processing***
POSITION		**SUBMITTING AUTHOR (*PRESENTER, if different*)**		
A	Shi, Yu	Griffith, Alexandra	Salimov, Amir	Mehmood, Sofia
B	Stahl, Jake	Gsell, Arielle	Shin, Christopher (*Tobias Meng-Saccoccio*)	Ryan, Amelia
C	Surendran, Tejus	Hanna, Marleen	Slupianek, Helena	Thaker, Shubh
D	Tohfafarosh, Mariya	Hindman, Zoe	Tahir, Muhammad Nabeel	Thumbavanam Arun, Nishanth

BOARD#:	***5***	***6***	***7***	***8***
TRACK:	***Neuro-Engineering***	***Cell/Tissue Eng. & Biomaterials***	***Cell/Tissue Eng. & Biomaterials***	***Cell/Tissue Eng. & Biomaterials***
POSITION		**SUBMITTING AUTHOR (*PRESENTER, if different*)**		
A	Apte, Vaidehi	Morel, Josuel	Patel, Siya	Roy, Abhishek
B	Casey, Odhrán	Owuor, Luiza	Paul, Nikhil	Shi, Fanghao
C	Das, Tulika	P R, Matangi	Pellegrini, Michael	Vasylaki, Anastasiia
D	Namdar, Negar	Patel, Dhruv	Pourmostafa, Aydasadat	West, Owen

BOARD#:	***9***	***10***	***11***	***12***
TRACK:	***Cell/Tissue Eng. & Biomaterials***	***Medical Imaging & Processing***	***Accommodation***	***Faculty Innovators***
POSITION		**SUBMITTING AUTHOR (*PRESENTER, if different*)**		
A	Whitman, Brycelyn	Vijay, Suruthikha	Guo, Yunhua	Miri, Amir K.
B	Yogeshwaran, Swaprakash	Yafai, Hanan		Tanyeri, Melikhan
C	Quartey, Brian	Johannan, Emily		Vega, Sebastian
D	Sarhaadei, Erfan	Saeedi-Hosseiny, Marzieh		Buffone, Alexander

Board 1: Biomechanics
A: Examining Modes of Augmented Sensory Feedback during Rehabilitative Training of Upper Extremity Function
B: Do Baseline Measurements Relate to Balance Behavior During Walking and Turning?
C: The Effects of Standing and Walking on Cartilage T2 Relaxation Time
D: Data Driven Prediction of Vertical Ground Reaction Forces in Stance Motions using a Custom Pressure Insole

Board 2: Cell/Tissue Eng. & Biomaterials
A: Investigating Combination Scaffolds of Self-Assembling Peptide Hydrogels for Root Canal Infections
B: Sequential Photopatterning of 8-arm PEG-Nor Hydrogels with Monothiolated Peptides
C: Synthetically derived antimicrobial peptides act as supportive agents for the regeneration of tissues in periodontitis dental wound healing

D: Identifying Optimal Scaffold Geometry for Enhanced Mechanical Strength and Porosity

Board 3: Medical Device and Technology
A: Universal Microfluidic Magnetic Connectors
B: Fluid Dynamics of the Three-Way Stopcock: Simulation and Experimental Validation
C: Testing the Sterilization Efficacy of 3D Printed Plastics Using E. Coli
D: An Automated Quality Estimation and Error Correction Tool for Fluorescence Images

Board 4: Medical Imaging & Processing
A: Imaging Tissue-Level Composition of Bone Biopsies with Submicron Resolution
B: Aptamer-Based Single-Walled Carbon Nanotube Sensors for Optical Detection of Interleukin-6
C: Geometric Validation of Deep Learning Segmentation-Based Numerical Mesh Generation of Aortic Valve from CT Images
D: Exploring the Efficacy of Coarse Labels for Machine Learning Algorithms for Tumor Segmentation

Board 5: Neuro-Engineering
A: Attenuating Mitochondrial Dysfunction Restores Endothelial Barrier Function & Integriy Post Traumatic Brain Injury
B: A Single-Cell RNA sequencing (scRNA-seq) Analysis of human Thalamic-like Organoids (hThO) derived from human Embryonic Stem Cells (hESCs), and their gene expression in comparison to ISH, Bulk and Single-Cell RNA data.
C: Role of Blood Brain Barrier Disruption and Neuroinflammation following Repeated Low-Level Blast Traumatic Brain Injury in Development of Post Injury Behavioral Deficits
D: Distinct TMS-EEG profiles reflect motor homunculus variability

Board 6: Cell/Tissue Eng. & Biomaterials
A: Antimicrobial Peptide In-silico Efficacy Assessment Using Molecular Dynamics
B: Characterizing Bacterial Response to Shape-Memory Actuated Silk Wrinkled Surface Topographies to Inform Strategies for Biofilm Prevention.
C: Evaluating the Effects of Calreticulin-Loaded Nanofibres on Diabetic Foot Ulcer Fibroblast Activity
D: Self-Assembled Chemokine and Neuropeptide Nanoparticles for Chronic Wound Healing After Spinal Cord Injury

Board 7: Cell/Tissue Eng. & Biomaterials
A: An Angiogenic and Myogenic Insulin-Like Growth Factor Receptor Targeted Therapeutic for Peripheral Artery Disease
B: Investigating Sintered Porous Polycaprolactone Scaffolds on Reduced Bone Production
C: Isolation and Characterization of Myogenic Proteins within Fertilized Egg Yolk
D: Real-time Monitoring of Biological Cells in a 3D Matrix

Board 8: Cell/Tissue Eng. & Biomaterials
A: Design of denovo self -assembling peptide hydrogels
B: Lymph node-on a Chip: Modeling Human Adaptive Immune Responses to Assess Vaccine Efficacy in Different Age Populations
C: Development and Optimization of Mesoscale Lipid Nanoparticles for Nucleic Acid Delivery to Renal Epithelial Cells
D: Self-assembling peptide hydrogels modulate Erk1/2 signaling in myoblast for tissue regenerative application

Board 9: Cell/Tissue Eng. & Biomaterials
A: Enhancing Functional Hepatocyte Cells for Developing a Human Brain-Liver-Gut Microphysiological System (MPS)
B: A 3D Bioprinted Vascular Model
C: Matrix-Bound Hyaluronan Molecular Weight as a Regulator of Dendritic Cell Immune Potency
D: Bioinspired gradient scaffold fabrication for treating segmental bone defects

Board 10: Medical Imaging & Processing
A: Understanding Protein Adsorption on High Flux Hemodialyzers: Insights from Infrared Spectroscopy and Imaging
B: Functionalized SWCNT-Aptamer Sensors for Selective Dopamine Detection: Exploring Selectivity and Sensitivity.
C: Periaqueductal Connectivity in SCI Induced Pain Using Resting State fMRI
D: Automated Femur Landmark Detection: Optimizing Surgical Alignment Evaluation

Board 11: Accommodation
A: Scaffold Surfaces Modified by Peptide-Loaded Polyanionic Microgels Resist Bacterial Colonization

Board 12: Faculty Innovators
A: High-throughput manufacturing of Hydrogel-Based Microfluidic Devices for Screening Applications
B: Development of a Microfluidic Viscoelastic Hemostatic Assay towards Point-of-care Testing of Coagulopathies
C: Design and Characterization of EPDA Transmembrane Receptors for Engineering Programmable Cell Behavior
D: Precise control of cellular motion to prevent chronic disease conditions.

SENIOR DESIGN POSTER SESSIONS (DAY 2, Friday, April 5)

***IMPORTANT NOTE**: for senior design posters, this conference recognizes **ALL student authors** listed on the abstracts as presenting authors. The session grids only list one corresponding and presenting author to streamline referencing for conference attendees seeking to review that work.*

STEVENS
INSTITUTE OF TECHNOLOGY

SENIOR DESIGN POSTER SESSION 1 (8:15am - 9:15am)

LOCATION: **Gateway North (Rooms 103 and 204)**

Gateway North (Room 103)

BOARD#:	***1***	***2***	***3***	***4***
TRACK:	***Biomechanics***	***BME Education***	***Cell/Tissue Eng. & Biomaterials***	***Medical Device and Technology***
POSITION	**SUBMITTING AUTHOR (*PRESENTER, if different*)**			
A	Cavella, Alyssa	Canencia, Marie	Bautista, Sophia	Ali, Hajer
B	Gibson, Margaret *(Brandon Sems)*	Criollo, Dennise (*Stephanie Anaya*)	Gazda, Connor	Androwis, Ghaith (*Chen et a*l.)
C	Mehl, Caitlin	Kannan, Kit		Baccaglini, Emily
D		Macken, Connor		Cavallero, Nicholas

BOARD#:	***5***	***6***
TRACK:	***Medical Device and Technology***	***Medical Device and Technology***
POSITION	**SUBMITTING AUTHOR (*PRESENTER, if different*)**	
A	Choe, Nathan (*Miskhat Habib*)	Dumas, Alexandra
B	Cilenti, Nicolette	Eisner, Annika *(Adiva Daniar)*
C	Crawford, Megan (*Crawford & Thampi*)	Eleh, Chiadika
D	Deren, Stephanie	

Gateway North (Room 204)

BOARD#:	***7***	***8***	***9***	***10***
TRACK:	***Medical Device and Technology***	***Medical Device and Technology***	***Medical Device and Technology***	***Medical Imaging & Processing***
POSITION	**SUBMITTING AUTHOR (*PRESENTER, if different*)**			
A	Forcellati, Nicholas	Gopal, Megha	Hugo, Hans Elijah (*Colton Pretzel*)	Androwis, Ghaith (*Dhuri et al.*)
B	Freudzon, Susan (*Emma Crowley*)	Grym, Gabriella (*Ethan Moyer*)	Kim, Sam	Caso, Elizabeth
C	Freudzon, Susan (*Ryan Baker*)	Hasan, Tasmia	Li, Nina	Kim, Carsi
D	Garcia, Janelle (*Andrew Dzikowki*)	Henderson, Brenna (*Colin Babick*)		

Board 1: Biomechanics
A: Universal Prosthetic Socket for Transfemoral Amputees in Underdeveloped Countries
B: Knee Extension Device for Post Operative Knee Flexion Contracture
C: Gait 2 Go: Gait Analysis, Anytime & Anywhere

Board 2: BME Education
A: Smart Seat Cushion for the Prevention for Pressure Ulcers in Wheelchair Users
B: An in vitro Mimic of Bacterial Contamination in the Operating Room

C: Mini-HART: Educational 3D-Printed Humanoid
D: Two-way thermoresponsive biliary stent

Board 3: Cell/Tissue Eng. & Biomaterials
A: Selective HIV DNA Enrichment Using Magnetic dCas9
B: Improving CRISPR Off-Target Detection Using Transposases

Board 4: Medical Device and Technology
A: ChromaScan Health - Color Strip Sensing Device
B: Developing an Inexpensive Device for Wheelchair Transfer for Persons with Mobility Impairments
C: EchoAware: An electronic vision aid with auditory feedback capabilities
D: BreatheEZ Respiratory Device (BERD)

Board 5: Medical Device and Technology
A: Lumbar Movement Prevention Device
B: TrueDose, an Adolescent Medication Adherence iOS Application
C: ParaVent: An Automatic Resuscitation Device
D: Pulse PairIt: Wireless Vital Monitoring for Neonates

Board 6: Medical Device and Technology
A: Erias: A Bluetooth Cardiac Monitoring System for Pediatric Inpatient Use
B: DRIPPY: A Gravity Bag Feeding Rate Modulator
C: See-Rynge: A Visually Accessible Liquid Measurement Device

Board 7: Medical Device and Technology
A: Development of Preeclampsia Wearable Detection Device
B: Affordable Cricothyrotomy Training Device
C: Realistic Ultrasound Phantom for Regional Anesthesia Training
D: WoundWatch: Chronic Wound Monitoring System

Board 8: Medical Device and Technology
A: TESee: A Transesophageal Echocardiogram (TEE) Visualization Simulator
B: Case-Based Reasoning to Aid in Clinical Decision Support of Traumatic Brain Injury
C: Advanced Optical Probe for Early Detection for Pediatric Hemorrhagic Shock
D: Triple C+: An Adaptive Neck Orthotic

Board 9: Medical Device and Technology
A: Humeral Rod with a Suture Tab
B: Wearable Device for Lee Silverman Voice Treatment-BIG Therapy Amplitude Training
C: Designing a 3-D Heart Model for In-Vitro Testing of Bioadhesive Cardiac Interventions

Board 10: Medical Imaging & Processing
A: Development of a Myoelectric Controlled Shoulder Orthotic for Persons with UE Impairment
B: Cardiopulmonary Resuscitation (CPR) Assistive Device For Cardiac Arrest (CA) Patients
C: A device to quantify non-nutritive infant sucking force

STEVENS
INSTITUTE OF TECHNOLOGY

SENIOR DESIGN POSTER SESSION 2 (11:15am - 12:15pm)

LOCATION: **Gateway North (Rooms 103 and 204)**

Gateway North (Room 103)

BOARD#:	***1***	***2***	***3***	***4***
TRACK:	***Biomechanics***	***Cell/Tissue Eng. & Biomaterials***	***Medical Imaging & Processing***	***Medical Device and Technology***
POSITION		**SUBMITTING AUTHOR (*PRESENTER, if different*)**		
A	Padykula, Monica	Khan, Aisha (*Arsian Hashmi*)	Rowey, Rachel	Lukens, Sera
B	Sheikh, Danyal	Le, Victoria (*Daniel Habboush*)	Roy, Ethan	Mavricos, Amanda (*Luke Zibbell*)
C	Teson, Hannah	O'Rourke, Feiyan	Zaatreh, Aya	McGoldrick, Tyler (*Jimin Jung*)
D	Warren, Alexa		Shevtsova, Alexandra (*Jack Tangstrom*)	Mishra, Aaveg

BOARD#:	***5***	***6***
TRACK:	***Medical Device and Technology***	***Medical Device and Technology***
POSITION	**SUBMITTING AUTHOR (*PRESENTER, if different*)**	
A	Narayan, Neha	Park, Stella
B	Ngo, Jonathan	Piccirillo, Annamarie
C	Noguera Saigua, Cesar (*Matthew Feroz*)	Rai, Isha
D	Ozcan, Evrim	Reilly, Noah

Gateway North (Room 204)

BOARD#:	***7***	***8***	***9***	***10***
TRACK:	***Medical Device and Technology***	***Medical Device and Technology***	***Medical Device and Technology***	***Medical Device and Technology***
POSITION		**SUBMITTING AUTHOR (*PRESENTER, if different*)**		
A	Sanchez, Eloy	Sullivan, Molly	Ward, Carly (*Elizabeth Su*)	Palahnuk, Grace
B	Song, Dahin	Terlevich, Karly	Wilken, Nicholas	Park, Juwon
C	Steneri, Matthew	Thomas, Malik	Willwerth, Andrew	Whitesel, Camilla
D	Stibler, Alexandra	Volpe, Nicholas	Zheng, Aunika (*Kosisochukwu Ugorji)*	

BOARD#:	***11***	***12***
TRACK:	***Accommodation***	***Accommodation***
POSITION		
A	Lescarbeau, Julia	Ho, Cassidy
B	Dougherty, Matthew (*Elyse Gathy*)	
C	Kowal, Emily	
D		

Board 1: Biomechanics
P1: Lower Extremity Joint Loading Deficits During Dynamic Single Limb Loading Tasks in Individuals Following Anterior Cruciate Ligament Reconstruction: A Retrospective Motion Analysis Study
P2: RhythmRehab: A Programmable Exoskeleton Glove for Personalized Hand Therapy
P3: Transtibial Amputee Prosthetic for Bionic Monofin
P4: Universal Hitch Attachments for Strollers

Board 2: Cell/Tissue Eng. & Biomaterials
P1: Electrical Stimulation Device
P2: A Hydrogel-Based Artificial Corneal Implant To Improve Outcomes of Patients With Corneal Blindness
P3: Development of Hydrogel-Based Artificial Meniscus with Self-healing Properties

Board 3: Medical Imaging & Processing
P1: Convolution Neural Network (CNN) for Nonpalpable Breast Lesion Localization
P2: Improved Test Fixture for Implantable Pulse Generator Magnetic Resonance Imaging Testing
P3: HeraHealth: Revolutionizing Postpartum Care through an Innovative Blood Loss Monitoring Application
P4: Inguinal Lymph Node Window Chamber with Channels

Board 4: Medical Device and Technology
P1: SmartRise Patient Lift
P2: PolypStop: Improved Hemoclip to Enhance Post-Polypectomy Procedure Outcomes
P3: VITAFLOW - Future of Heart Preservation
P4: Multi-Purpose Adaptor to Improve Hands-Free Storage for Patients with Retinitis Pigmentosa

Board 5: Medical Device and Technology
P1: Dilate: Enhancing Lactation with Adjustable Flange and Integrated Heating
P2: BiRed Imaging: Breast Cancer Screening Table
P3: Nomasound: Led Based Photoacoustic Device for Melanoma Screening
P4: A Novel Rapid Delivery Device For Intravenous Adenosine Administration

Board 6: Medical Device and Technology
P1: SOLaware: Personalized UV exposure quantification device for UV-sensitive population
P2: Modified Vacuum-Assisted Male External Catheter System
P3: Adaptable Acoustic Startle Response Device (AASRD)
P4: Plume Evacuation Device For Blepharoplasty

Board 7: Medical Device and Technology
P1: Assistive Cannulation Device for Home Hemodialysis
P2: Preventing and Detecting Nasogastric Tube Dislodgement in Infant Patients
P3: Lab-On-A-Chip Migration Assay for Scientific Research
P4: GripSense System: Quantifying Stroke-Related Hand Function

Board 8: Medical Device and Technology
P1: Portable Breathalyzer for Monitoring Diabetes
P2: WOVEN: Wearable Onesie for Vitals and Ease of Nursing
P3: PadIAD Incontinence Intervention
P4: Optoband: Demonstrating Feasibility of Optomyography for Active Prosthetics

Board 9: Medical Device and Technology
P1: Portable Impedance Breast Imaging Device (P.I.B.I.)
P2: Dual Linear Parallel Suture Sampler
P3: FlexFlow Novel 3 Way Stopcock Design
P4: ParkinPlay: Affordable and Accessible Monitoring of Parkinson's Symptoms Outside of the Clinic

Board 10: Medical Device and Technology
P1: AirEase BiPAP Mask
P2: Skin Tone Sensitive Pulse Oximeter
P3: The Lip and Palate Prosthetic Interface

Board 11: Accommodation
P1: Sustainable Prosthetic Socket Design
P2: Design of Balloon Dilator Pressure Testing Apparatus and Balloon Dilator Machine Testing
P3: Design and Fabrication of Microfluidic Chip Integration Platform

Board 12: Accommodation
P1: Novel ASO Treatment for Voltage-Gated Sodium Channel Nav 1.5 Metastasis in TNBC

KEYNOTE PRESENTATIONS
(DAY 2, Friday, April 5)

STEVENS
INSTITUTE OF TECHNOLOGY

We are pleased to welcome **Dr. Tamara Fountain (Rush University Medical Center)** to deliver the first Day 2 keynote at this year's NEBEC!

The Eyes Have It

Where Biomedical Meets Engineering

Tamara Fountain, M.D.

Rush University Medical Center Professor
Department of Ophthalmology
Director, Section of Oculoplastic and Reconstructive Surgery
Rush University, Chicago, Illinois, USA

Email: tfountainmd@gmail.com

Bio-Sketch:

Dr. Fountain is a professor of ophthalmology at Rush University Medical Center and section chair emeritus of oculofacial plastic surgery. She maintains a private practice near her home on Chicago's North Shore, a day's drive from where she grew up in Minneapolis, Minnesota.

Dr. Fountain graduated with a B.A. from Stanford University and an M.D. from Harvard Medical School. After completing residency in ophthalmology at Johns Hopkins' Wilmer Eye Institute, she returned to California for a fellowship in oculoplastic surgery at Doheny Eye Institute/University of Southern California.

Dr. Fountain was appointed to the board of directors of the American Board of Ophthalmology in 2022 and was President of the American Academy of Ophthalmology in 2021. She is Past-President of the American Society of Ophthalmic Plastic and Reconstructive Surgery (ASOPRS), where she has received the Robert Kennedy Presidential and Orkan Stasior Leadership Awards for service to the Society.

Dr. Fountain served 15 years with the Ophthalmic Mutual Insurance Company (OMIC), chairing the Audit, Strategic Planning, Risk Management and Insurance/Marketing committees before being elected Chair of the Board of Directors. She is past-president of the Illinois Society of Eye Physicians and Surgeons and has been involved in programming for the American Ophthalmological Society, Women in Ophthalmology and the Chicago Ophthalmological Society. She is a past Alumni Fund Chair for Harvard Medical School.

Outside medicine, Dr. Fountain is a news and podcast junkie and enjoys travel and speaking at conferences around the world. A long-time tennis, golf and bike enthusiast, she’s making room now for pickleball and doing her best to stay out of the kitchen.

Abstract:

Dr. Fountain will present how biomedical engineering intersects with ophthalmology. She will describe how biomedical engineering helps to develop new technologies and devices for ophthalmology. She will also talk about the difficulties and prospects for healthcare, including health inequality.

We are pleased to welcome **Joe Yacarinno (MTF Biologics)** to deliver the second Day 2 keynote at this year's NEBEC!

How Biomaterials Save and Heal Lives

Joe Yacarinno, M.B.A.

MTF Biologics
President and CEO
MTF Biologics, Edison, New Jersey, USA

Email: Joe_Yaccarino@mtf.org

Bio-Sketch:

Joe Yaccarino has served as the President and CEO of MTF Biologics since June 2018. He recently received the Leadership Award for large businesses in NJ's Top Workplaces and MTF has been named a Top Workplace for 5 years running. Joe joined MTF in 1997 as its first processing engineer, creating new spinal grafts, which led to significant growth for the organization. He later served as EVP of Processing Operations, overseeing departments including processing, distribution, engineering, spinal product development, logistics and supply chain.

A native of New Jersey, Joe received his Bachelor of Science in Mechanical Engineering from Stevens Institute of Technology in Hoboken, NJ, and a Master of Business Administration in Marketing/Finance from Pennsylvania State University in State College, PA. Prior to joining MTF Biologics, Yaccarino was a production engineering supervisor at Micro in Somerset, NJ.

Abstract:

This presentation will showcase how human donated tissues are an example of biomaterials that are used in healthcare. He will give an overview of MTF Biologics and how Biomedical Engineering has helped MTF become one of the biggest human tissue processors in the world. He will explain why Biomedical Engineers are essential in this and related industries and will share his views on what employers are seeking as they hire new graduates.

INTERACTIVE "CAREER DEVELOPMENT" PANELS - FOR FACULTY AND STUDENTS (DAY 2, Friday, April 5)

At this year's NEBEC, we are proud to innovate the traditional format with the introduction of "career development" discussion panels that have been strongly suggested to be of interest by chairs, faculty, industry, and students.

We have organized two sets of interactive panel discussions, one for early-career faculty (postdoctorates are welcome!) and one for undergraduate and graduate students.

For faculty panels (all in Gateway North), we have two tracks (themes) running back-to-back:

1. ***Track A (1:30pm - 2:30pm) = Opportunities to broaden impact and translate academic research through entrepreneurship and industry.***
    - Our two panelists for this track are **Jinho Kim (Stevens)** and **Pavita Howe (BioNJ)** who are asked to speak about this topic as they like but also in reference to NSF iCorps and BioNJ opps, respectively.
    - ***Bryan Pfister (NJIT)*** and ***Greg Townsend (Stevens)*** are co-moderating to facilitate discussions on this topic from perspective that are academic and corporate, respectively.

2. ***Track B (2:30pm - 3:30pm) = Building partnerships from academia to industry and clinicians.***
    - Our two panelists for this track are **Chris Schaber (Soligenix)** and **Bill Mieler (UIC)** who are asked to speak about this track topic as they like and from their perspectives for "advising" early-career faculty on how to effectively pursue such partnerships.
    - Bryan and Greg are still co-moderators for this second track within the same session.

For student panels, we have two tracks (themes) repeated and running in parallel:

1. ***Track A (1:30pm - 2:30pm and repeated 2:30pm - 3:30pm, in UCC Tech Flex Auditorium) = Strategies for bio-engineering students to pursue careers along medical/clinical or industrial.***
    - Our two panelists to speak on pathways for medical/clinical careers are **Tamara Fountain (Rush Univ**) and **Herman Morchel (Hackensack UMC)** who are asked to speak about this topic based on their personal experience as clinicians and what strategies or preparations they feel is most essential for bio-engineering students to consider if pursuing similar careers.
    - Our two panelists to speak on pathways for industry careers are **Moushmi Culver (Merck)** and **Janice Frontera (Merck)**. They are asked to speak about this topic (and provide advice) based on their personal experiences and perspectives working for a multinational company at the

forefront of large-scale medical science and technology and advice to students looking to advance along similar lines.

- ***Chris Wagner (TCNJ)*** is moderating to facilitate discussions on this topic with insights from an academia perspective.

2. ***Track B (1:30pm - 2:30pm and <u>repeated</u> 2:30pm - 3:30pm, in UCC Gallery) = The Stevens Graduate Biomedical Engineering Society*** *is presenting a forum to delve into essential considerations and strategies for those seeking to develop as a current or prospective graduate students (i.e., undergraduates welcome!). Topics include:*

    - How to pursue graduate study and develop a research partnership with your PI
    - Pursuing independent opportunities for support (e.g., fellowships)
    - Getting involved with professional societies

Jinho Kim, PhD

Assistant Professor
Department of Biomedical Engineering
Stevens Institute of Technology, New Jersey, NJ, USA

Email: jkim6@stevens.edu

Bio-Sketch:

Dr. Jinho Kim is an Assistant Professor of the Biomedical Engineering Department at Stevens Institute of Technology. Since his arrival at Stevens in 2018, Dr. Kim has been leading the Translational Lung Bioengineering Laboratory, which is dedicated to creating bioengineering solutions for clinical challenges, with initial focus on the diagnosis, treatment, and prevention of respiratory diseases. His contributions to the field have earned him prestigious recognitions, including the NSF CAREER Award in 2022 and the Best Abstract Award at the 2019 American Thoracic Society International Conference. His research has been supported by several funding agencies, including NSF, NIH, Cystic Fibrosis Foundation, American Thoracic Society, and New Jersey Health Foundation. Dr. Kim is devoted to converting research breakthroughs into clinical practices. He co-founded a startup with a former graduate student to develop a robotic biosensor for real-time tissue assessment during surgeries, aiming to improve the precision and outcomes of tumor removal. In addition, serving as the site PI for the NSF New York I-Corps Hub at Stevens, he aims to facilitate the commercialization of laboratory innovations developed at Stevens.

Christopher J. Schaber, PhD

Chairman, President and CEO of Soligenix, Inc.

Email: cschaber@soligenix.com

Bio-Sketch:

Christopher J. Schaber, PhD is a seasoned executive and entrepreneur with over 30 years of experience in the pharmaceutical and biotechnology industry. He has a proven track record of advancing novel therapies from discovery to approval, as well as securing funding and partnerships to support the growth and vision of the start-up companies he has co-founded and/or led. In his current position as Chairman, President and CEO of Soligenix, Inc., he leads a team of dedicated professionals who are committed to developing and commercializing products for rare diseases with high unmet medical need. Dr. Schaber is a recognized leader in the rare disease community, serving on the boards and councils of various organizations, such as the Alliance for Biosecurity, BioNJ, and National Organization for Rare Disorders (NORD). He is also an active advisor, mentor, and investor in the life sciences and technology sectors, supporting the growth and development of emerging companies and entrepreneurs. Dr. Schaber holds a PhD in Pharmaceutical Sciences, a MS in Pharmaceutics, and undergraduate degrees in Business, Economics and Chemistry.

Moushmi Culver, SVP

Head of Manufacturing Strategy, Business Development and Alliances
Manufacturing Leadership Development Program Executive Sponsor
Merck & Co. Inc

Email: moushmi_culver@merck.com

Bio-Sketch:

Moushmi Culver is Senior Vice President, Head of Manufacturing Strategy, Business Development, and Alliances for the Merck Manufacturing Division. She leads all business development, network strategy, third-party supply sales and global alliance management activities for the division, which includes evaluating acquisitions, divestitures, licensing opportunities and managing strategic business alliances. Additionally, she leads manufacturing strategy, portfolio management and manufacturing shared services. Moushmi joined Merck over 23 years ago in the Manufacturing Leadership Development Program (MLDP) and has held positions of increasing responsibility in Manufacturing, Global Procurement, and the Corporate Strategy Office. She is the Executive Sponsor of the MLDP and the Global Executive Sponsor of the Merck Asia Pacific Association (APA) Employee Business Resource Group.

Moushmi has received multiple recognitions for her leadership. She was included in the 2022 top 50 outstanding Asian Americans in Business, ranked #6 in the 2021 EMpower Top 100 Ethnic Minority Executives Role Model List by INvolve and Yahoo Finance, received the 2021 Trailblazer Award from WOCIP (Women of Color in Pharma), selected in the Deloitte Women to Watch Program from 2019-2021, the recipient of the Stevens Institute of Technology Young Alumni Achievement Award in 2015, selected to attend Fortune's Most Powerful Women of the Next Generation in 2015, and has received multiple leadership awards and recognition at Merck. She also serves on the Board of Advisors at the Schaefer School of Engineering and Science at Stevens Institute of Technology. Moushmi holds a B.E. in Chemical Engineering from Stevens Institute of Technology, Hoboken, NJ, and an M.B.A. from Lehigh University, Bethlehem, PA. Moushmi lives in NJ and is married with two sons.

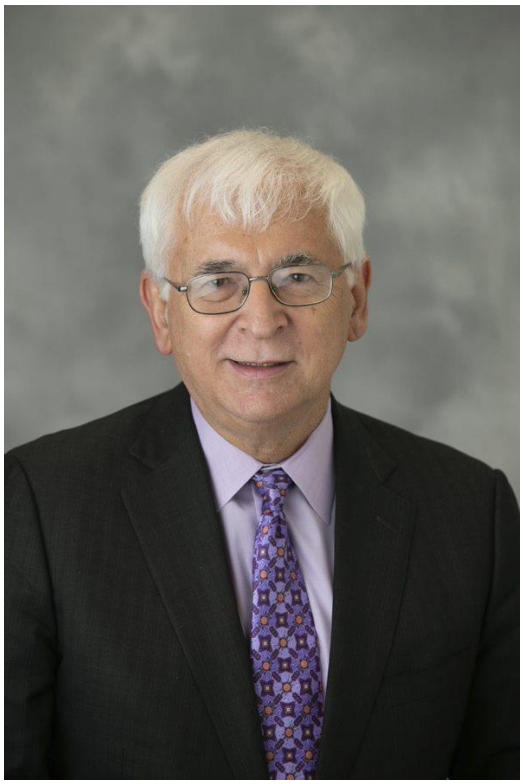

William F Mieler, MD

Cless Family Professor of Ophthalmology
Department of Ophthalmology & Visual Sciences
University of Illinois at Chicago (UIC), Chicago, IL, USA

Email: wmieler@uic.edu

Bio-Sketch:

William F Mieler, MD is the Cless Family Professor of Ophthalmology, in the Department of Ophthalmology & Visual Sciences at the University of Illinois at Chicago (UIC), Chicago, IL. He also serves as the Vice Chairman of Faculty Affairs, Director of Vitreoretinal Surgical Fellowship Training, and Director of Ocular Oncology Dr. Mieler received the UIC 2016 College of Medicine Faculty of the Year Award, and more recently, he received the UIC 2021 Distinguished Professor Award. His specialty areas include diseases and surgery of the retina and vitreous, along with ocular oncology.

Dr. Mieler received his Doctor of Medicine degree at the University of Wisconsin-Madison, Medical School (1979). After completion of his Internship at Mercy Hospital Medical Center in San Diego, CA (1980), he completed a three-year ophthalmology residency at the Bascom Palmer Eye Institute, University of Miami,

Miami, FL (1980-83). This was followed by a one-year vitreoretinal fellowship at the Eye Institute, Medical College of Wisconsin, Milwaukee, WI (1983-84). He then returned to the Bascom Palmer Eye Institute where he served as Chief Resident and Clinical Instructor (1984-85). Dr. Mieler then completed a second fellowship in Ocular Oncology, at Wills Eye Hospital, Thomas Jefferson University, Philadelphia, PA (1985).

In 1985, he joined the full-time faculty at the Medical College of Wisconsin, where he became Professor of Ophthalmology (1992) and was awarded the Jack A. and Elaine D. Klieger Chair in Ophthalmology (1998). Dr. Mieler then joined the faculty at the Baylor College of Medicine, in Houston, TX, as Professor of Ophthalmology (1999-2004). He then accepted the position of Professor and Chairman, Department of Ophthalmology, at the University of Chicago (2004-08), prior to his current position at the University of Illinois at Chicago (2008-present). He also briefly served as Interim Chair at UIC (2014).

Dr. Mieler has authored or co-authored 372 scientific papers, 118 book chapters, and 8 textbooks, including most recently The Retina Atlas, 2nd edition (2017), and Macular Surgery (2020), and Clinical Cases in Medical Retina (2024). Additionally, a 3rd edition of The Retina Atlas is planned for 2024. He has presented 28 named lectures. Dr Mieler is/has been the Principal Investigator or co-Investigator of more than 90 Scientific Grants and Collaborative Studies. He has served on the Editorial Board of Archives of Ophthalmology, RETINA, Current Eye Research, and the American Journal of Ophthalmology Case Reports, and currently serves on the Editorial Board of The Asia Pacific Journal of Ophthalmology. He also has served as a scientific reviewer for over 70 additional scientific journals.

He has served the American Board of Ophthalmology (ABO) as a Board Director (1998-2005), Chairman of the Board (2005), as Associate Executive Director (2006), and as Emeritus Director (2006-present). He also served on several committees with the American Board of Medical Specialties (ABMS). Dr. Mieler is also the past President of the Macula Society (2003-04), and he received the Gass Medal (2013). He has served on the Executive Committees of the Retina Society, and has been the Chair of the Fellow Grant Award Committee (2005-16). From the American Society of Retina Specialists (ASRS), he has received the Crystal Apple award (2005), and was named recipient of the Founders Award (2011). He is a past member of the Pan-American Board of Directors (2001-08), and he has chaired the PAAO Foundation Grants Committee (2006-11). In the American Ophthalmological Society (AOS), he has served as a member of the Council (2018-23), the Chair of the Council (2022-23), and is incoming President of the AOS (2025-26).

Dr. Mieler has served on the ARVO Board of Trustees (2010-16), representing the Retina section, and was President of ARVO (2014-15), along with being a member of numerous committees. He received the Distinguished Service Award from ARVO (2016).

From the American Academy of Ophthalmology (AAO), Dr Mieler received the Honor Award (1992), the Lifelong Education for the Ophthalmologist Award (2000), the Senior Honor Award (2001), the Life Achievement Honor Award (2011), and the Secretariat Award (2016). He served on the Ophthalmic Knowledge Assessment Program (OKAP committee (1991-98), and as Chair of the committee (1994-98) He also has served

as a member of the AAO Council (2001-08), the EyeNet Editorial Advisory Board (2003-07), and Chair of the Schepens Award (2007-10). Dr Mieler has also served the AAO as a Media Spokesman, as a member and chair of the CME Advisory Task Force, and as Associate Secretary for the AAO Subspecialty Day programs (2011-15). Most recently, he served on the AAO Board of Trustees (2017-20), and was a member of the Executive Committee on the Board of Trustees (2020).

Dr Mieler has been named as a Best Doctor in America (1995-2024), Top Doctor in Chicago (2006-24), America's Top Cancer Doctors in Chicago (2013-24), and Top Doctor in Cancer, Castle Connolly Medical (2008-2024).

Pavita Howe

Vice President, Innovation and Entrepreneurship at BioNJ

Email: phowe@bionj.org

Bio-Sketch:

As BioNJ's Vice President of Innovation and Entrepreneurship, Pavita supports the life sciences entrepreneurial community, expanding outreach and collaboration with investors, academia and industry partners. She spearheads the BioNJ BioPartnering Conference, facilitating funding and collaboration for entrepreneurs. Pavita also leads BioNJ's AI & Digital Health initiatives, providing opportunities for entrepreneurs to highlight their cutting-edge innovations in this space.Previously, she served as Director of Entrepreneurship Partnerships at Rutgers University, amplifying Rutgers' entrepreneurial ecosystem. Pavita's first entrepreneurial experience was with a California-based technology startup which was acquired. Having held marketing and leadership positions in multiple start-ups, Pavita has served as a mentor and advisor at TechLaunch NJ accelerator and the NJ Technology Council. Most recently, Pavita was appointed to the New Jersey-India Commission, and she serves as Chair of the Board at the New Jersey Bioscience Center incubator.

Herman Morchel, MD, PE

Board-Certified Attending Physician in Emergency Medicine
Hackensack University Medical Center, New Jersey, NJ, USA

Email: herman.morchel@hmhn.org

Bio-Sketch:

Dr Morchel holds a position as a Board-Certified Attending Physician in Emergency Medicine at Hackensack University Medical Center / Hackensack Meridian Health in Hackensack, New Jersey since completing a residency in Emergency Medicine at Newark Beth Israel Center in 2007 and graduating UMDNJ, now Rutgers New Jersey Medical School. He is founding core faculty of their Emergency Medicine Residency Program, founding Director of their Simulation Training facility, was Medical and Engineering Director of their Disaster Response Mobile Hospital program, and holds a position as an Associate Professor of Emergency Medicine at the Hackensack Meridian Health School of Medicine in Nutley, New Jersey. Prior to medical school Dr Morchel had over a 25-year career with ITT Corporation, now L3 Harris, in advanced electronics/computer systems engineering design and development including two US Patents. He is a licensed Professional Engineer in New Jersey. Master of Engineering - Electrical Stevens Institute of Technology, Hoboken, NJ in 1980, Bachelor of Science in Electrical Engineering from Newark College of Engineering, now New Jersey Institute of Technology in 1973. Dr Morchel also serves as a volunteer Professor of Biomedical Engineering at Stevens and also on the department's Academic Advisory Board.

Janice Frontera

Associate Director, Value Chain Management
Merck Manufacturing Division

Email: janice.frontera@merck.com

Bio-Sketch:

Janice Frontera is an Associate Director, Value Chain Management within the Merck Manufacturing Division where she is a Product Manager for pipeline programs. She is responsible for product strategies, integrated risk management, supply chain design, and continuous improvement of product supply chains. Janice also serves as the Chief of Staff to the Senior Vice President of Manufacturing Strategy, Business Development, and Alliances. She joined Merck in 2016 through the Manufacturing Leadership Development Program and has held roles of increasing responsibility in Technical Operations, Value Chain Management, and Global Engineering Solutions within the United States and Ireland. She is an active member of the Society of Women Engineers.

Janice holds a B.E. in Chemical Engineering, M.E. in Engineering Management, and Graduate Certificate in Project Management from Stevens Institute of Technology, Hoboken, NJ.

ABSTRACTS
(ALL PRESENTATIONS)

STEVENS
INSTITUTE OF TECHNOLOGY

An Experimental Approach to Quantify Postural Stability in the Center of Mass State Space

Kübra Akbaş[1], Neethan Ratnakumar[1], Rachel Jones[1], Jean-François Daneault[2], Carlotta Mummolo[3], and Xianlian Zhou[1].
[1]New Jersey Institute of Technology, [2]Rutgers University SHP, [3]Politecnico di Bari, Bari, Italy

Introduction: In clinical practice, the lack of reliable and objective balance and stability assessment metrics hinders the tracking of patient performance progression during rehabilitation. The assessment of bipedal balance plays a crucial role in understanding stability and falls in humans, while providing important information regarding rehabilitation outcomes to clinicians. To this end, analyzing balance through the body's Center of Mass (COM) state offers a holistic and comprehensible view of balance and stability. Building upon existing boundary-based stability criteria, a balance region (BR) can be constructed in the COM state space (COM position and velocity) by identifying the border of the COM state space within which the system can regain its balance by returning to equilibrium (static upright posture) [1]. Here, an experimental study of various balance exercises is presented to demonstrate the feasibility of empirically generating BRs and assessing balance.

Methods: 3D motion capture experiments were conducted in the BioDynamics Lab at NJIT to gauge the feasibility of empirically determining BRs. Data was collected from 22 healthy human subjects using marker-based optical motion capture and force plates. Each subject performed 5 sway exercises in the anteroposterior direction (10 reps each) without lifting their heels or toes: maximum voluntary sway, supported forward/backward leaning, and forward/backward leaning with a push. Maximum voluntary sway was performed by leaning maximally forward, then maximally backward, and returning to standing. In supported leaning trials, forward and backward directions were isolated into separate tasks; here, external support (researcher's hands) was provided while assuming position (Fig. 1, left), with no support during recovery. Similarly, pushing trials were also isolated and involved external support initially, but a push was applied at the maximum COM excursion and no support was given during recovery. A musculoskeletal model [2] was scaled for each subject using OpenSim 4.4 [3], and inverse kinematics (IK) were performed to calculate the COM state trajectories for each subject's activities and find their BR. External hand force was analytically estimated and removed for the supported and push trials. BRs were then compared with their Linear Inverted Pendulum (LIP) model limits [4], determined by subject height and foot size/Base of Support (BoS).

Results: All subjects' COM states in the BRs (without hand contact) generally stayed within the analytical LIP boundaries during all leaning exercises (Fig 1, right); though, some subjects could reach the edges of their BoS during the supported or pushing exercises. While supported leaning trials inform on the ability to recover from larger COM displacements, pushing trials shed light onto the ability to recover from perturbations and provide a range of feasible initial velocities that cannot be predicted by the LIP boundary. Subjects who were unable to reach the edges of their BoS, or analytical limits, were more conservative with their balancing. Using the BoS and LIP limits as references, the COM state trajectories from successful trials showed the subjects' ability to maintain their COM state within the analytical limits; this was expected since subjects were asked to maintain an ankle strategy.

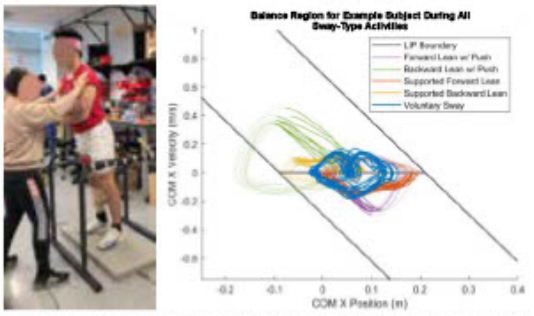

Figure 1. (left) Subject during supported forward leaning. (right) Experimental BR for one subject. LIP boundary is presented in black, and subject's BoS is also in black (ankle at x = 0). COM positions are w.r.t. the ankle position. Bold lines indicate balance recovery with no external hand contact, and lighter lines indicate the entire trial.

Conclusions: This series of experiments demonstrated a method of measuring postural stability using motion capture and using BRs to quantify balancing ability, which can help guide future clinical interventions using technology for motor rehabilitation. As opposed to the LIP and its analytical limits, the BR approach can address higher-order systems and various other balancing strategies beyond the ankle strategy. In future work, two other avenues for balance assessment can be explored: dynamic balance and recovery from platform perturbations.

References:

1. Mummolo C. et al. J Nonlinear Sci. 2017;27:1291-1323.
2. Hamner SR. et al. J Biomech. 2010;43(14):2709-2716.
3. Seth A. et al. PLoS Comp Biol 2018;14(7):e1006223.
4. Hof AL. et al. J Biomech. 2005;38(1):1-8.

Acknowledgements: We would like to thank Hans Elijah Hugo for his help in generating the IK data.

DEI: In balance rehabilitation, technologies can be expensive to integrate into clinics and cumbersome to use, preventing many patients from receiving necessary care. To this end, pursuing a low-cost, at-home balance system using wearables could be an avenue to address this need. Additionally, to make biomechanics a more accepting field—one that is cognizant of various personal barriers in higher education—we need to make outreach a priority. Initiatives like National Biomechanics Day are a great way to start this process; however, groups need to consider their lab culture and focus on how to make it a more inviting place more seriously.

wer

Error induction during rehabilitative training improves motor performance and increases EEG theta band power

Sophie Dewil[1], Yu Shi[1], Raviraj Nataraj[1]
[1]Department of Biomedical Engineering, Stevens Institute of Technology, Hoboken, NJ, USA

Introduction: After neurological traumas such as spinal cord injuries (SCI) or strokes, individuals undergo energy-consuming and time-intensive physical rehabilitation [1]. However, rehabilitation outcomes are often moderate, prompting the need for research to optimize the process [2]. Previous research has highlighted the beneficial role of errors in learning a cognitive task—allowing a person to re-evaluate their approach to a problem based on newly available information. As such, a person can more rapidly improve performance on a task than if they were experiencing no errors [3]. In this study, participants completed a series of reaching tasks in a virtual reality (VR) environment and received visuomotor rotation manipulations to induce errors during training. We then assess subsequent motor performance and changes in neurological patterns (theta band power) associated with error detection [4].

Methods: Neurotypical participants (n = 3) wore a 64-channel scalp-surface cap for EEG recording (*USBamp g.tec*). Marker-based motion capture (*Prime17W, Optitrack*) tracked the position and orientation of the participant's reaching hand (**Figure 1, left**). The marker data drove the motion of a virtual prosthetic arm in a custom environment (*Unity*) displayed to the participant on a large (40 in) flat-screen (*Roku Select Series HDTV*) placed directly in front of them. Participants were randomly assigned to one of two training groups: 1) *control* (no errors presented) and 2) *error* (errors presented in 30% of the trials). During training, participants reached toward target spheres (designated by color cues) positioned in one of 8 distinct directions (**Figure 1, right**) and received positive feedback upon successful reaches. Participants experienced an error when they observed the virtual hand moving at a visuomotor distortion (rotation) relative to their actual hand motion, leading to a failed reach. Before and after training, participants completed testing trials involving various directional reaches, including curves to the right and left. The primary motor measure of interest (i.e., reaching pathlength) was assessed and compared between trials before and after training to infer the impact of training.

Figure 1. Experimental setup showing performance of reaching task (left) and VR training environment (right)

Results: Motor performance improved (i.e., mean pathlengh was reduced) with the error-training group but worsened with the control group (**Figure 2, left**). In training trials, the EEG theta band was significantly higher in error trials than in control trials ($p = 0.0012$) (**Figure 2, right**).

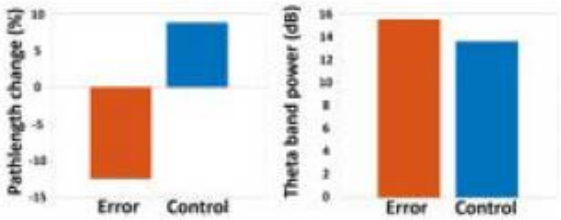

Figure 2. Percentage change in pathlength after training for error and control groups (left); theta band power in error vs. control trials (right)

Conclusions: Pathlength has been previously used as a reliable performance marker for efficient movement [5]. This study suggests that systematically introducing errors during training can support better motor performance outcomes [3]. We verified the neurological impact of introducing errors during training by observing significantly higher theta band power with error trials as expected [4]. In this study, we postulate that imposing errors encouraged participants to assume a heightened neural awareness to re-evaluate movement strategies during and after training. While this training construct has been well-validated in cognitive learning tasks [6], its use with motor training tasks has been limited [3]. Findings from this study motivate further consideration of inducing error-related neurological responses for supporting greater gains in motor function with rehabilitative training.

References:

1. Maclean N. et al., Soc. Sci. Med. 1982; 50:495-506
2. Spooren et al., JRM. 2009;41(7):497-505
3. Steib S. et al., Neurorehab. Neur. Repr. 2017; 31(8) 758–768
4. Dias C. et al, PeerJ. 2022; 10; e12627
5. Sanford S. et al., Front. Virtual Real. 2022; 3:943693
6. Falkenstein M.et al., Electroencephalogr. clin. neurophysiol. 1991; 78(6) 447-455

Acknowledgments: The authors acknowledge support from the Schaefer School of Engineering and Science at Stevens Institute of Technology, NSF CAREER award 2238880, and the Stevens Provost Doctoral Fellowship.

DEI: This research aims to improve rehabilitation techniques and functional outcomes for people with SCI. The proposed methods promise to minimize clinician burden in treating persons with a motor disability. Additionally, in recent years, non-Hispanic blacks accounted for 25% of spinal cord injuries, exceeding their 13% representation in the general population. Therefore, the approaches supported by this study can potentially benefit multiple underserved populations. Furthermore, we have involved STEM-underrepresented persons in the conduction of this research and in related educational activities.

STEVENS
INSTITUTE OF TECHNOLOGY

Analyzing the Impact of Passive Exoskeleton Assistance on Lifting Dynamics Through Musculoskeletal Modeling

Rachel Jones[1], PhD, Liying Zheng[2], PhD, Neethan Ratnakumar[1], Jaejin Hwang[3], PhD, and Xianlian Zhou[1], PhD.
[1]New Jersey Institute of Technology, [2]National Institute for Occupational Safety and Health, [3]Northern Illinois University

Introduction: Lifting and lowering tasks are an important part of daily life for workers from nurses to warehouse laborers. Over time, these tasks can cause pain or injuries to the spinal column resulting in chronic pain. Several companies have developed exoskeletons to assist workers and decrease fatigue. Quantification of the reduction of muscle torques in the workers will help regulation agencies formulate recommendations for industry standards for exoskeletons. Musculoskeletal (MSK) modeling allows us to quantify the kinematics, kinetics, and biomechanical performance of individuals performing work related tasks wearing exoskeletons. In this study, we used experimental data of lifting and lowering with and without an exoskeleton to compute muscle joint torques via a MSK modeling approach. The goal is to quantify the effects of the exoskeleton assistance on reducing back and lower limb joints during lifting tasks.

Methods: 8 subjects (5 male, 3 female) were asked to lift and lower a 20 lb box with and without wearing a passive back exoskeleton (Laevo V2.5, Delft, Netherlands). The lifting/lowering motion was recorded by a motion capture system (Optitrack, Natural Point, OR), and the ground reaction force (GRF) was measured with a force plate (AMTI, Watertown, MA). We adapted a full-body MSK model developed by Caruthers et al. [1] (194 muscles, 46 DOF), which includes knee joints designed for squatting motions and an articulated lumbar spine for evaluation of deep bending (the lumber range of motion was changed from 70° to 90° for this study). Inverse kinematics (IK) and inverse dynamics (ID) were performed on the scaled models to obtain joint angles and moments respectively for trials with and without the exoskeleton. The experimental data from one subject was trimmed to synchronize the motion between the two conditions (with and without exoskeleton), resulting in 5-second data samples of each for comparison. The total box lifting force was assumed to be the product of the weight of the box and its acceleration, which was equally distributed on two hands. The weight of the exoskeleton (2.9 kg) was added to the weight of the torso in the ID simulation involving the exoskeleton. According to testing [2], the assistance torque profile is directly correlated to the joint angle. This relationship was used to generate the assistance torque data during the lifting and lowering motion.

Results: From IK analysis of one subject, we found the peak joint angles were greater in the knee (16%) and lumbar (14.9%) while wearing the exoskeleton but decreased in the hip (-10%). The joint moments predicted from ID analysis, with and without exoskeleton assistance, are compared in Figure 1. The muscular loading for the exoskeleton condition showed lesser peak joint moments for the knee (-16.7%), and hip (-28.1%) than the non-exoskeleton condition. The change in lumbar moment was different between the lifting and lowering portions of the activity. The moment decreased (-19.5%) during lifting but increased (3.4%) during lowering.

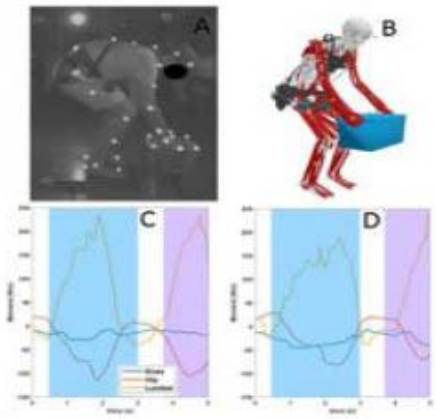

Figure 1: Joint moments from one subject for the knee (blue line), hip (red line), and lumbar (yellow line) during lifting(blue)/lowering(purple) activity with and without an exoskeleton. (A) Photo of experimental box lifting. (B) A snapshot of MSK model during simulation. (C) Moment produced by human without exoskeleton. (D) Moment produced by human while using exoskeleton.

Conclusions: We demonstrated the viability of a MSK modeling approach to assess the impact of passive exoskeleton assistance on lifting dynamics. Our comparative analysis revealed that moments generated by the human body are lower (ranging from -16.7% to -28.1%) when utilizing an exoskeleton compared to performing the same activity without it, particularly during the lifting phase. However, the improvement observed in the lifting phase did not extend to the lowering phase for the lumbar moment. An examination of joint angles showed increased ranges of motion in the lumbar and knees but reduced hip angles when utilizing an exoskeleton for the same task. The reduction in peak hip angle possibly indicates a limitation imposed by the exoskeleton itself. To further elucidate this pattern, additional subject data would be beneficial.

References:

1. Caruthers et al., J. Appl. Biomech.,2016;32(5):487-503.
2. Van Harmelen V. et al. Laevo White Paper. 2022.

Acknowledgements: Grant support from NIOSH (contract #: 75D30122P14469) is acknowledged.

DEI: This work can benefit and improve the healthcare of occupational workers that include many minorities.

DISCLAIMER: The findings and conclusions in this report are those of the authors and do not necessarily represent the official position of the National Institute for Occupational Safety and Health (NIOSH), Centers for Disease Control and Prevention (CDC). Mention of any companyor product does not constitute endorsement by NIOSH/CDC.

STEVENS
INSTITUTE OF TECHNOLOGY

Relationship between Peak Angular Momenta and Ball Speed in High School Baseball Pitchers

Jun Ming Liu[1], Christopher Knowlton[2], Nikhil Verma[2], Gregory Nicholson[2], Anthony Romeo[2], Antonia Zaferiou[1]
[1]Stevens Institute of Technology, [2]Rush University Medical Center

Introduction: Baseball pitching involves sequential rotations of the body segments from the ground-up to produce high ball release velocity.[1] The angular momentum (H) of all body segments combine to generate whole-body H, with some body segments contributing more than others. Each body segment's H is the sum of (1) its angular velocity multiplied by its moment of inertia, and (2) the cross-product of (a) a vector between the segment's center of mass (COM) and the body's COM and (b) the segment's COM linear momentum vector relative to the body's COM.[2] We hypothesized that maxima whole-body, torso, and pitching arm H about each global axis would positively associate with ball speed..

Methods: High school pitchers (n=21; male; mean (S.D.) age of 15.3 (1.0) years) volunteered for this study in accordance with the IRB. Participants self-reported an ability to pitch 75-mph fastballs. Participants pitched at least 5 fastballs on a practice mound at a regulation distance (18.44 m) with optical motion capture. H was defined in the global coordinate system with horizontal forward axis from mound to home plate, upward axis as global vertical, and leftward axis as cross product of upward and forward axes. For left-handed pitchers, H about forward and upward axes were reversed for easier comparisons with right-handed pitchers. H_{max} were computed from each limb segment and whole-body H.[2,3] Linear mixed models were used with ball speed as the outcome measure, each H_{max} as fixed effect and pitchers as random effect ($\alpha<0.05$).

Results: About the forward axis, ball speed positively associated with H_{max} for the torso ($p=0.02$) and pitching arm ($p=0.01$). About leftward axis, ball speed positively associated with H_{max} for the whole-body ($p<0.001$, **Fig. 1D**), torso ($p<0.001$, **Fig. 1E**), and pitching arm ($p=0.01$). About the upward axis, ball speed positively associated with H_{max} for the torso ($p=0.01$). All other associations were not significant.

Conclusions: Ball speed positively associated with torso H_{max}, pitching arm H_{max}, and whole-body H_{max} about specific global axes. Only whole-body H_{max} about the leftward axis was significantly associated with ball speed, and whole-body H_{max} was the largest about the leftward axis vs. the other axes. Therefore, this highlighted the importance of rotation generation in this direction. Torso H_{max} was a major contributor to whole-body H_{max} about leftward axis (**Fig. 1B**) and torso H_{max} occurred before ball release. Torso H_{max} decreased while the pitching arm H_{max} increased, indicating a transfer of momentum.

As a whole, this study highlights the importance of momentum generation in baseball pitching and may inform coaching practices that enhance momenta transfer towards the pitching arm.

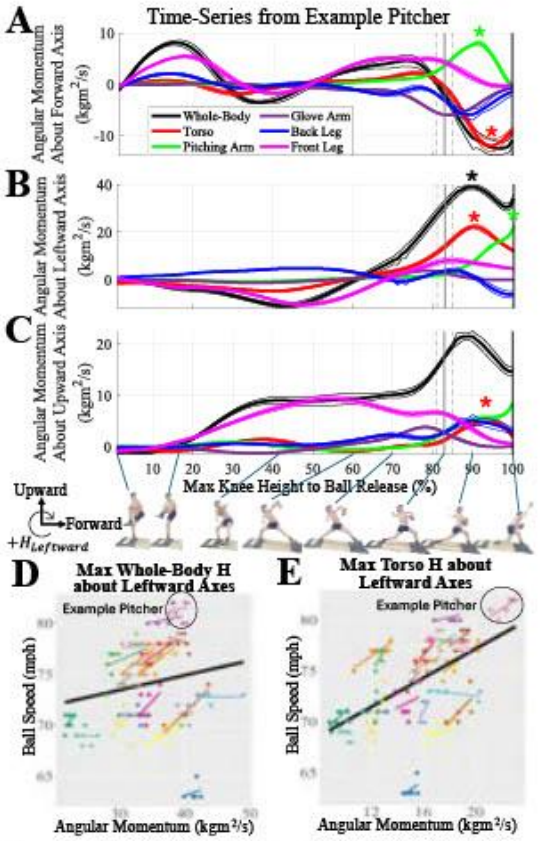

Figure 1. Time-series of whole-body and limb (*torso segment includes the head, trunk, and pelvis*) angular momentum about (**A**) forward, (**B**) leftward, and (**C**) upward axes from example pitcher (circled in D-E). *significant group trends between max H and pitch velocity. Group association plots (**D-E**) between ball speed and angular momentum variables with dots representing trials, color line as pitchers' trend lines and a black line as group trend line.

References:

1. Pappas AM et al. *Am. J. Sports Med.* 1985
2. de Leva P. *J. Biomechanics.* 1996
3. Herr H, Popovic M. *J. Experimental Biology.* 2008

Acknowledgements: This work was supported by a Major League Baseball research grant.

DEI: There are disparities in research, funding support, and coverage and visibility for women's baseball and softball when compared to men's baseball, and more can be done in terms of access to resources, facilities, and teams to enhance participation. Our lab had organized national biomechanics day events for and involving softball athletes. Events like this can spread awareness of STEM and biomechanics to athletes to promote future interests.

STEVENS
INSTITUTE OF TECHNOLOGY

Porous, Perfusable Microtubular Networks for Improved Cell Viability in Volumetric Hydrogels

Christian Buckley, Dr. Hongjun Wang
Stevens Institute of Technology, Department of Biomedical Engineering
Semcer Center for Healthcare Innovation

Introduction: Volumetric, cell-laden constructs for tissue regeneration suffer from inadequate vascularization, resulting in poor nutrient exchange to cells located in the center of the scaffold beyond the limits of oxygen diffusion[1]. To overcome this issue, 3D printing has been used to create large, perfusable channel structures that permit immediate nutrient delivery to cells throughout the scaffold. Common techniques often rely on soft hydrogels to directly print channel networks, or sacrificial template structures that leave behind hollow channels upon removal. However, these methods either lack long-term structural integrity or can damage cells from the process of template removal. In this work, a free-standing, porous, perfusable tubular network, based on the elastomer poly(1,8 octanediol-co-citrate) (POC), is developed and tested for its efficacy to sustain osteoblast viability in volumetric hydrogels.

Methods: 3D-printed sacrificial polyelectrolyte complex (PEC) templates were created according to procedures previously developed in our lab[2]. These PEC filaments were coated with POC prepolymer, created by heating citric acid and 1,8 octanediol to 160°C while stirring, and further polymerized at 100°C for 72 hours. Submersion in 3M potassium bromide caused the dissolution of PEC templates, leaving behind a free-standing POC tubular network. These networks were perfused with 0.1% (w/v) methylene blue solution to determine channel patency. To create pores in the POC channel walls, NaCl particulates (< 30 µm) were combined with the POC prepolymer during the coating procedure, and then soaked in deionized water overnight to remove the NaCl crystals. To test the efficacy of the tubular networks to improve cell viability, osteoblasts (hFOB 1.19) were embedded in 7% (w/v) gelatin methacrylate (GelMA) and cast around either solid-walled networks or porous-walled networks, and cell viability was compared to GelMA blocks without tubular networks as the control. The CellTiter-Glo 3D assay and Live/Dead staining were used to assess cell proliferation and viability.

Results: Stereomicroscope images show distinct differences in the structure throughout the coating and polymerization process, with the final POC networks having a glossy, opaque surface. Rapid perfusion of POC networks with methylene blue solution indicates complete PEC removal and patent channels. Scanning electron microscopy (SEM) images of the POC tubular networks revealed the presence of pores, roughly 19 µm in diameter, in the POC walls after salt leaching. Porous tubular networks increased the cross-wall fluid transport during methylene blue perfusion. It was found that both solid wall and porous wall networks increased cell proliferation by 365% and 563%, respectively, by day 7, when normalized to their day 0 values. In contrast, GelMA samples without tubular networks only increased by 188% by day 7. Live/Dead staining on day 7 showed marked differences between groups, and the percent viability was calculated to be 12%, 49%, and 63%, for control, solid wall, and porous wall groups, respectively. Porous wall samples contained significantly fewer dead cells than both other groups.

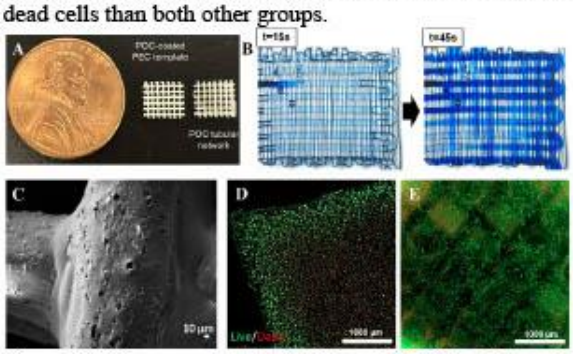

Figure 1. A) Images comparing POC-coated PEC templates and hollow POC tubular networks. B) Methylene blue perfusion of tubular networks. C) Porous POC tubular networks. D) Live/Dead image of hFOBs embedded in GelMA without tubular networks. E) Live/Dead image of hFOBs embedded in GelMA with porous tubular networks.

Conclusions: This study explores and validates the proof-of-concept development of free-standing, perfusable tubular networks that can be used for sustained viability of volumetric tissue-engineering constructs. Tubular networks with fully perfusable, patent channels of 100-400 µm in diameter were successfully created and salt leaching was employed to create pores that promote cross-wall fluid transport. *In vitro* studies with cell-laden hydrogels proved the efficacy of porous tubular networks to improve cell proliferation and viability over solid wall networks and hydrogels without POC tubular networks. Cells in both experimental groups maintained a healthy morphology compared to the densely necrotic core observed in the control hydrogels without tubular networks. This study provides a useful strategy for researchers to develop healthy, large-scale constructs for tissue regeneration, utilizing a facile, repeatable method for creating 3D vascular-like networks.

References:

1. Simunovic F. et al. Cells. 2021;10:1749
2. Wang H. et al. Bioactive Materials. 2022;17:261-275

Acknowledgements: The authors are thankful for the partial financial support by the National Science Foundation (NSF-GCR award number 2219014) and Army Medical Research and Material Command with award number W81XWH2211044.

DEI: The field of Bioengineering directly benefits from the inclusion of scientists from various and underrepresented backgrounds. This can be further promoted by funding programs to provide STEM education to economically-challenged regions, and improving access to quality healthcare for people of all backgrounds.

STEVENS
INSTITUTE OF TECHNOLOGY

Solute Diffusivity in Bioprinted GelMA Constructs: Implications for Biomimetic Tumor

Elvan Dogan[1], Anant Bhusal[2], Roshni Shukla[1], Amir K. Miri[1]
[1] Advanced Biofabrication Lab, Department of Biomedical Engineering, New Jersey Institute of Technology (NJIT), Newark, NJ, 07102.
[2] Department of Mechanical Engineering, Rowan University, Glassboro, NJ 08028.

Introduction: Light-assisted bioprinted gelatin methacryloyl (GelMA) constructs have created cell-laden microtissues and organoid models. GelMA is commonly infused with various cells, and its biophysical properties impact the cells in the bioprinted constructs. Controlling drug diffusion is a critical design criterion in GelMA constructs. Cell encapsulation, which occurs during photo-crosslinking, can affect the drug's diffusivity in GelMA, presenting a point of interest for biomimetic modeling of tumors. Predicting the drug particle diffusivity in 3D hydrogels and understanding how it is affected by various perfusion conditions has been a significant challenge. The findings of this study could assist bioengineers in developing more reliable drug transport models for cell-laden GelMA models [1].

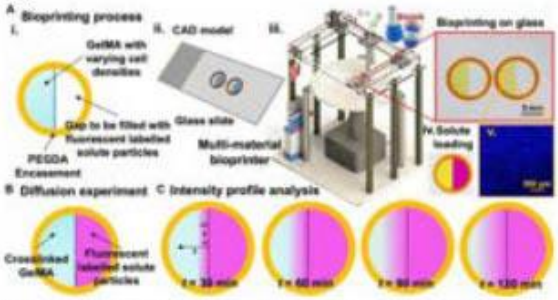

Figure 1. The experimental approach for measuring 1D concentration gradient through hydrogel samples within printed constructs with high control over size and shape [1].

Methods: The study involves preparing cell and bioink, measuring the degree of functionalization via NMR, bioprinting processes, mechanical testing for stiffness, diffusion experiments (**Fig. 1**) using Rhodamine-B (RhD-B, 81-88-9, Sigma Aldrich) for assessing solute movement through Fick's Second Law, release studies for understanding mass transport, viability assays for checking cell health, and statistical analysis to interpret the data. These steps collectively contribute to understanding how the GelMA bio ink's properties and cell encapsulation affect the diffusion and mechanical characteristics, which are critical for bioengineering applications like tissue engineering.

Results: We conducted experiments with GelMA containing 7% concentration, infused with cells at densities ranging from 1 to 10x10^6 cells/ml. When the cell density was at 5 x10^6 cell/ml, we observed a reduction of approximately 33% in the diffusion coefficient for GelMA with lower methacryloyl (MA) substitution (low MA) compared to GelMA without any cells. The diffusion coefficient increased by about 31% as cell density rose from 5 million to 10 x10^6 cells/ml, as demonstrated in **Fig. 2**. High cell concentrations can lead to a reduction in light penetration, reducing the extent of crosslinking in GelMA.

This phenomenon was similarly noted in GelMA with a higher level of methacryloyl substitution (high-MA). The impact of the MA content on the photo-crosslinking process was investigated by comparing the effects of cell density on the physical characteristics of 7% GelMA samples in both high- and low-MA scenarios. Experiments were performed using three different GelMA concentrations (5%, 7%, and 10%) with and without cells to observe the effects on the diffusion coefficient. The findings showed that the diffusion coefficient was greater at lower GelMA concentrations (**Fig. 2**) [1].

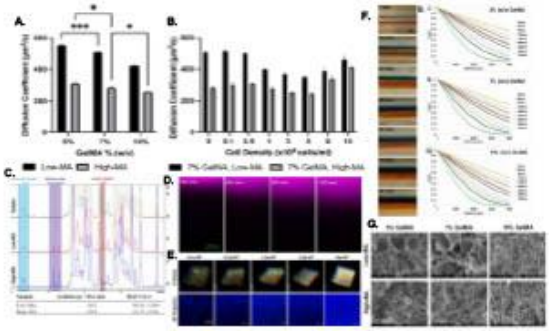

Figure 2. Comparative analysis of GelMA hydrogel solute transport properties. A. Apparent diffusion coefficients (μm^2/s) of RhD-B in GelMA (5, 7, and 10% w/v) with low and high MA degrees; B. Apparent diffusion coefficients (μm^2/s) of cell-laden GelMA 7% w/v. C. ^{1}H NMR spectra of gelatin and GelMA with different DoFs. D. RhD-B Diffusion through GelMA. E. Cell distribution of GelMA 7% w/v in 2D projection and volumetric cell distribution forms for selected cell densities (cells/ml). F. Sequential images of two straight channels perfused with buffer solutions, colored orange and blue. G. SEM imaging. All data are presented as the mean ± SD (n = 3). All conditions were significantly different (***$p \leq 0.001$) unless indicated [1].

Conclusions:
In this study, we examined how MA, mass concentration, and cell density influence solute transport in GelMA hydrogels used in bioprinting. Our findings reveal that higher cell densities significantly reduce diffusivity, particularly above 10^6 cells/ml. More than GelMA concentration, MA levels dictate the hydrogel network's uniformity, with high-MA samples showing little variation in diffusivity. Additionally, cell size and morphology also impact biotransport properties. These insights are crucial for designing cell scaffolds and drug delivery systems, and further research will focus on predictive models for GelMA's mechanical and diffusive behavior.

Acknowledgments: We thank NIH (R01DC018577) for the support. We acknowledge Ms. Christina Holshue (Rowan University) for contributing to this work.

References:
[1] Dogan E. et al. Front. bioeng. biotechnol. 2023; 11

Ultrasound-Enhanced Silk-based Films and Nanofibers for Biomedical Applications

Xiao Hu [a,b,*], Fang Wang [c]
[a] Department of Physics and Astronomy, [b] Department of Biological and Biomedical Sciences, Rowan University, Glassboro, NJ 08028, USA; [c] Center of Analysis and Testing, Nanjing Normal University, Nanjing, China (*Email: hu@rowan.edu)

Introduction: Recently developed ultrasound-assisted techniques have revolutionized the fabrication of protein-based films and nanofibers, offering a precise, non-invasive, and eco-friendly approach to structurally engineer biocompatible materials. This innovative method leverages cavitation to initiate free radical production, break chemical bonds, and swiftly alter material morphology, enhancing the efficiency, cleanliness, and versatility of processing natural polymers. Our research reveals that ultrasound can meticulously adjust protein structures during the solution assembly phase, allowing for the customization of biomaterial properties through variable manipulation. The resultant ultrasound-modified silk protein films exhibit enhanced thermal resistance, superior biocompatibility, increased breathability, and optimal mechanical resilience and flexibility. Moreover, the degradation rate and biological responses (such as cell growth and proliferation) of these silk proteins are finely adjustable via ultrasound settings. Further extending its application, this technology has been employed in the air-jet spinning of silk-soy protein nanofibers, resulting in biomaterials with adjustable characteristics and pronounced biocompatibility, ideal for uses in drug delivery and wound healing.

Methods: Comprehensive characterization of these ultrasound-enhanced protein materials was conducted using Fourier transform infrared spectroscopy (FTIR), X-ray diffraction (XRD), scanning electron microscopy (SEM), differential scanning calorimetry (DSC), thermogravimetric (TG) analysis, dynamic mechanical analysis (DMA), and assessments of gas permeability, water contact angle, enzymatic degradation, and cytotoxicity. FTIR analysis utilized a TENSOR 27 spectrophotometer (Bruker, Germany). Protein samples (~5 mg) underwent DSC heating in Al pans (Q100, TA Instruments, USA), or TG Analysis with a Hi-Res TGA 2950 (TA Instruments).

Results: Bombyx Mori silk fibroin films underwent ultrasonic treatments at varying intensities (100~800W) and durations (0~30min), elucidating the facilitation of silk molecule self-assembly and the enhancement of calcium ion interactions with silk molecular chains. This led to the formation of robust β-sheet crystals, increasing the water insolubility, mechanical strength, and flexibility of the films. Notably, increased ultrasonic intensity or duration amplified the β-sheet and α-helix structures, improved thermal stability, and allowed tunable enzymatic degradation rates, alongside enhanced hydrophilic swelling, breathability, and cell compatibility. Ultrasonic-assisted air-jet spinning was then implemented to fabricate soy-silk fibroin protein composite nanofiber membranes, demonstrating the method's superiority in cost, safety, and polymer variety. The study showcased that prolonged ultrasonic treatment time (30~180 min) resulted in nanofibers with smaller diameters and lower porosity, thereby enhancing their surface area and spinnability. Additionally, the increased treatment time fostered the transition from random coils to β-sheet conformations and elevated the thermal stability, hydrophilicity, water retention, and enzymatic degradation rate of the composites. These changes significantly bolstered cell adhesion and proliferation on the nanofiber surfaces, marking the soy-silk protein nanofibers as promising candidates for biomedical applications such as tissue regeneration and wound dressing.

Figure 1. Ultrasound treatment of silk proteins in solution can transform stacked β-sheet crystals into single-layer β-sheets or random coils, while stretching silk molecules into a more organized structure of intermolecular β-sheets and α-helixes. This process increases the silk's water insolubility, mechanical strength, and flexibility.

Conclusions: Through precise control over ultrasonic parameters, we can manipulate material properties to meet specific biomedical and environmental needs, showcasing the potential of ultrasound as a key innovator in biomaterial science. The findings offer promising prospects for advanced applications in tissue engineering and drug delivery, setting a new benchmark for the fabrication and enhancement of biomaterials.

References:

1. Hu X. et al. Protein-based composite materials. ***Materials Today*** 2012;15:208-215.
2. Cai B. et al. ***Ultrasonics sonochemistry*** 2021;79: 105800.
3. Yang F. et al. ***Ultrasonics Sonochemistry*** 2023;94: 106341.

Acknowledgements: X.H. is supported by Rowan University Seed Grants and NSF Future Manufacturing Program (CMMI-2037097).

DEI: Our field can address healthcare disparities by developing cost-effective protein-based medical products for wider accessibility. Additionally, enhancing STEM diversity can be achieved by fostering inclusive research environments and engaging in community outreach to support and inspire underrepresented groups in bioengineering.

STEVENS
INSTITUTE OF TECHNOLOGY

Integration of Wearable Sensors in Telerehabilitation to Monitor Health-Related Metrics to Predict Fitness Level

Doctoral Candidate: Razan S. Bahabri (Advisors: Dr. Christ Ruab)
Biomedical Engineering Department, School of Engineering, Catholic University of America.

Introduction: The utilization of sensors in telerehabilitation brings about a change by enabling the monitoring of a patient's movements and vital signs remotely and over time [1]. The integration of this technology not only enhances outcomes but also bridges the accessibility gap, ushering in a new era where wearable sensors become indispensable in shaping the landscape of telerehabilitation. These sensors offer precision and specificity, providing data for tailoring rehabilitation programs to suit individual needs. The combination of sensors and machine learning has emerged as tools in rehabilitation, offering healthcare professionals a detailed and comprehensive assessment of patients. Additionally, these sensors enable the analysis of fitness levels, showcasing their versatility in promoting well-being. This presentation discusses the utilization of "smart" garments embedded with physiological and inertial sensors for real-time data analysis for round-the-clock surveillance to improve the management of health-related metrics to predict fitness levels in the home setting.

Methods: The smart garment system consists of a microprocessor unit with communication (i.e. Bluetooth) and data acquisition capabilities enabling real-time, continuous collection of physiological and active information. It contains several sensors to collect physiologic and activity data to collect a holistic perspective at home. It includes monitoring of cardiac, respiratory, stress, and activity measures. Collected sensor data is wirelessly uploaded to a central server and/or cloud-based storage systems for continuous surveillance using machine learning and analysis. The smart garment has a sensor fusion algorithm to analyze the signals acquired from the smart garment.

This study aimed to use a wearable sensor system to discriminate the physiological reactions during submaximal exercise. Individuals across all activity levels engaged in the exercise sessions while wearing a sensor garment to obtain the cardiac, respiratory, electrodermal, electromyographic, and accelerometry data. The groups were differentiated using machine learning techniques, suggesting a sensor fusion algorithm for fitness evaluation.

	Rest	Ex1	Rest	Ex2	Rest	Ex3	Rest
ACC	0.074	0.349	0.117	0.125	0.031	0.339	0.079
EDA	1.409	3.419	2.246	1.277	2.604	4.6	1.329
HR	91.52	131.3	88.76	93.70	77.20	157.6	73.36
HRV	0.655	0.456	0.675	0.640	0.777	0.380	0.817
BR	21.05	35.55	19.89	35.08	23.94	40.88	30.58
BRV	1.097	0.913	1.052	0.670	1.067	0.774	0.878
EMG (Leg)	0.023	0.0295	0.0110	0.0439	0.0080	0.062	0.011
EMG (Arm)	0.031	0.0352	0.0302	0.0441	0.0273	0.056	0.027

Results:

Table1. Summary of physiologic monitoring by activity.

In this demonstration, we focus on the ECG and ACC signals to exemplify the responses during three distinct activities. As depicted, the heart rate (HR) demonstrates a direct correlation with physical exertion and movement, with heightened activity leading to increased heart rates, while periods of sedentary behavior correspond to lower HR levels. Table 1 further delineates this relationship by summarizing the extracted HR and breathing rate, activity rate and stress level information across different activity classes.

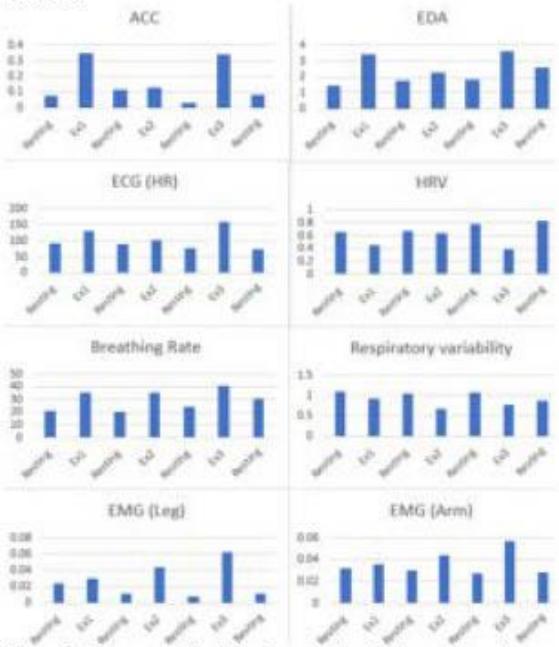

Figure 1. Summary of physiologic monitoring during resting and exercising.

Conclusion: In conclusion, integrating physiological and activity data offers valuable insights for health management. The smart garment continuously monitors ECG metrics like heart rate (HR), heart rate variability (HRV), and respiratory rate (RR), alongside electrodermal activity (EDA) and electromyography (EMG), combined with accelerometry (ACC). This comprehensive sensor array provides context for decision-making in health management. The next step is applying this analysis to broader health scenarios, revolutionizing monitoring by creating personalized profiles and interventions. Responsibly scaled, this technology could aid preventative medicine, promote independence, and shift healthcare towards proactive, community-centered care.

References:

[1] Posada-Quintero, H. F., & Chon, K. H. (2020). Innovations in electrodermal activity data collection and signal processing: A systematic review. *Sensors*, *20*(2), 479.

STEVENS
INSTITUTE OF TECHNOLOGY

Enhancing Intracellular Delivery of mRNA Therapeutics Using Mechanical Oscillation

Jiawen Chen[1], Aneri Patel[1], Mohammad Mir[1], Maria R. Hudock[2], Meghan R. Pinezich[2], Matthew Bacchetta[3,4], Gordana Vunjak-Novakovic[2], and Jinho Kim[1]

[1] Department of Biomedical Engineering, Stevens Institute of Technology, Hoboken, NJ, USA
[2] Department of Biomedical Engineering, Columbia University, New York, NY, USA
[3] Department of Cardiac Surgery, Vanderbilt University, Nashville, TN, USA
[4] Department of Biomedical Engineering, Vanderbilt University, Nashville, TN, USA

Introduction: Recent advancements in messenger RNA (mRNA) and lipid nanoparticle (LNP) technologies have opened up new possibilities for treating human diseases. However, a significant hurdle persists: the inefficient delivery of mRNA molecules into the cytoplasm of target cells, where the synthesis of therapeutic proteins is supposed to happen. Studies show that a substantial portion of the mRNA delivered using LNPs (nearly 98%) ends up trapped and eliminated through the endo-lysosomal pathway[1]. In response to this challenge, we present a paradigm-shifting approach that harnesses mechanical oscillation to prompt endosomal escape for enhanced intracellular mRNA delivery.

Methods: We formulated ionizable DLin-MC3-DMA (MC3) LNPs incorporated with fluorescent tracers (DiI). The LNPs were introduced into *in vitro*-cultured fallopian tube non-ciliated epithelial (FNE) cells. Subsequently, the cells were exposed to oscillation of 65 Hz for 5 min (Fig. 1). Downstream effects of the mechanical stimulation on endosomal escape were assessed by LysoTracker deep red (LT-Red) staining and calcein release assay. Furthermore, effects of the oscillation on intracellular mRNA delivery was studied by monitoring expression of GFP-encoding mRNA. Biosafety of this strategy was also evaluated using live/dead viability assay.

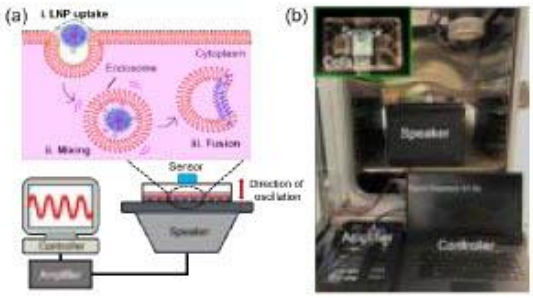

Figure 1. Schematic and the photo to show the setup for applying the oscillation on cells incubated with LNPs.

Results: LysoTracker staining revealed the application of oscillation resulted in a lower LysoTracker colocalization (Fig. 2A). Consitently, the results of calcein release assay showed a more diffused calcein signal in the cytoplasm of vibration-treated cells indicative of endosomal escape (Fig. 2B). Furthermore, in mRNA expression experiments, stronger GFP signals were detected in the treated cells (Fig. 2C). Cellular viability experimetns suggested no obvious alterations on cell viability caused by the mechanical stimulus (Fig. 2D).

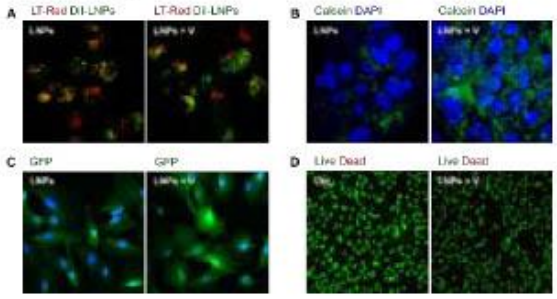

Figure 2. A. Colocalization of Lysotracker with DiI-labeled LNPs (DiI-LNPs). B. FNE cells incubated with LNP and calcien were treated without vibratrion (left) and with vibration (right). C. FNE cells incubated with LNP loaded with GFP-encoding mRNA were treated without vibratrion (left) and with vibration (right). D. Live/dead vibility assay.

Conclusions: Our research highlights the promise of the biomechanically facilitated mRNA delivery method. The results confirm the feasibility of mechanical oscillation in prompting endosomal escape of mRNA encapsulated in LNPs, and thus, improving mRNA expression. Additionally, *in vitro* cellular experiments also proved the safety of method. Thus, this breakthrough holds the potential for clinical applications in treating diseases requiring mRNA therapeutics.

References:

1. Yaru J. Adv Mater. 2024;36(4):2305300.

Acknowledgements: The authors would like to thank Dr. Tsengming (Alex) Chou for his assistance with imaging and Dr. Marcin Iwanicki for the FNE cells. The authors also acknowledge National Science Foundation (CAREER Award 2143620 to JK), New Jersey Health Foundation (PC 5-21 to JK), American Thoracic Society Foundation (Unrestricted Research Grant to JK), and National Institutes of Health (grants 2R01 HL120046, U01 HL134760 and P41 EB027062 to GVN) for funding support.

DEI: To support NEBEC's diversity initiative in Bioengineering, we propose targeted research for healthcare disparities, equitable access to services, and inclusive recruitment programs for underrepresented STEM individuals, fostering a more diverse and inclusive Bioengineering community.

STEVENS
INSTITUTE OF TECHNOLOGY

Efficacy of Rivaroxaban Anticoagulation During 10-day, In Vivo, Venovenous ECMO Support Using a Poly-Carboxybetaine Coated Artificial Lung

Patrick I. Iyasele, MS[1], Adel Akhavanmalayeri, MD[1], Umar Nasim, BS[1], Helen M. Scala, MS, RLATG[1], Yeahwa Hong, MD[1,2], Suji Shin, BA[1], Kelly R. Strong, BS[1], Keith E. Cook, PhD[1]
From [1]Biomedical Engineering, Carnegie Mellon University, Pittsburgh, PA USA

[2]Surgery, University of Pittsburgh Medical Center, Pittsburgh, PA USA

Introduction: Oral anticoagulation is needed for long-term, ambulatory extracorporeal membrane oxygenation (ECMO) to enable its application outside the ICU. Heparin is the standard ECMO anticoagulant, but it requires continuous intravenous delivery, and its anticoagulant effect must be monitored closely due to its short half-life and unpredictable dose-response relationship [1]. Rivaroxaban, a direct-acting, oral anticoagulant, is a possible replacement due to its flat dose-response and high oral bioavailability [2]. In this study, we evaluated the 10-day efficacy of the poly-carboxybetaine (PCB) coated Pulmonary Assist System (PAS) in an ovine model while administering rivaroxaban.

Methods: The PCB-coated PAS (PCB-PAS) was attached to a healthy sheep in a venovenous configuration with a dual-lumen cannula. The sheep was supported on the PCB-PAS for 10 days with 2 L/min of blood flow and 4 L/min sweep gas. The sheep was awake and freely able to sit and stand in a stanchion. A 1 hour infusion of 0.5 mg/kg dose of rivaroxaban (Xarelto) was administered intravenously every 6 hours to approximate a 10 mg oral dose in humans [3]. PCB-PAS function was measured by monitoring blood flow resistance and oxygen transfer. Anticoagulation efficacy was monitored with activated clotting time (ACT) and prothrombin time (PT) at rivaroxaban peak and trough plasma concentrations. The plasma free hemoglobin (pfHb), platelet count, and white blood cell count (WBC) were collected every 12 hours. At the end of the 10 days, device clot burden was measured by clot weight and gross imaging of the fiber bundle.

Results: One of six experiments has been completed. The blood flow resistance increased from 2.39 mmHg/(L/min) at baseline to 2.71 mmHg/(L/min) over 10 days (**Figure 1A**). The oxygen transfer of the PAS was consistent over course of the study (87.6 ± 10.7 mlO_2/min) (**Figure 1B**). The baseline plasma-free hemoglobin was 4.14±1.36 mg/dl. The pfHb was elevated with a peak of 49.0±3.91 mg/dl on day 3 due to cannula kinking. Once that was corrected, the pfHb decreased and remained stable for the remainder of the study at 10.8±6.9 mg/dl. The WBC did not increase from baseline (6.21±1.65 x 10^6 cells/ml), suggesting minimal systemic inflammation. The platelet count was 151 x 10^6 cells/ml at baseline, decreased by 53.6% (70±7.1 x 10^6 cells/ml) on day 1, and remained steady for the rest of the study at 69.4±26.6 x 10^6 cells/ml. The peak values for PT (40.0±6.3 s) and ACT (295.4±36.8 s) were consistent throughout the study, and the trough values for PT (13.2±1.4 s) and ACT (169.2±12.7 s) were 32% and 22% above baseline values for each parameter (Baseline PT=10 s, Baseline ACT= 138 s). The end clot weight was measured to be 75.38 grams. Gross imaging shows that most bulk clot formation was at the low velocity flow regions near the rear and sides of the outlet of the PCB-PAS.

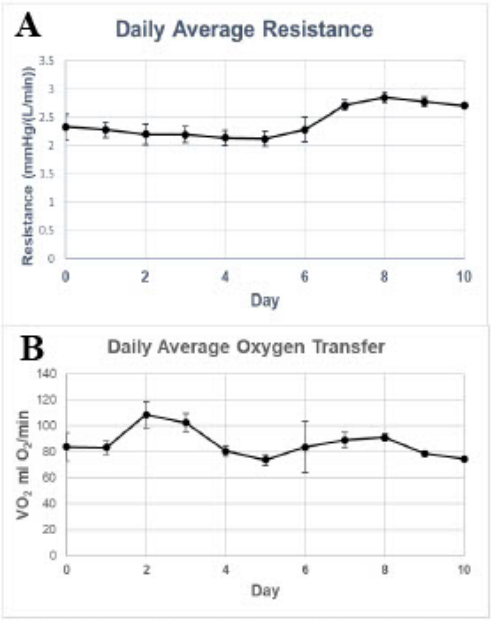

Figure 1. A. Daily average blood flow resistance in the PCB-PAS. Resistance increased from 2.39 mmHg/(L/min) to 2.71 mmHg/(L/min) over 10 days.
B. Daily average oxygen transfer of the PCB-PAS. Average of 87.6 ± 10.7 ml O_2/min.

Conclusions: This initial study demonstrates that rivaroxaban, when used with the PCB-PAS, can provide appropriate artificial surface anticoagulation. This result is promising for rivaroxaban to be a sufficient oral replacement for intravenous heparin during ECMO treatment. Future studies will refine test procedures and determine if this result is consistent.

References:

1. Cook BW. Semin Intervent Radiol. 2010 (4): 360-7
2. Eriksson, B.I. et al. Clin Pharmacokinet 48, 1–22 (2009)
3. Nasim, Umar ELSO Confer. Abstracts (34), 37 (2023)

Acknowledgments: Thank you to the CMU undergraduate students who helped conduct this study. This research was supported by the US Army CDMRP grant (W81XWH-22-1-0304).

DEI: As researchers to improve healthcare disparities, we should fund, lead, and support groups that support, promote, and develop diverse engineers, scientists, and entrepreneurs as they create culturally responsible and racially equitable innovations in healthcare, medicine, biotechnology, and allied fields.

STEVENS
INSTITUTE OF TECHNOLOGY

Application of Polyelectrolyte Complex Dressing for Wound Healing

Suneel Kumar, Priya Mistry, Rene Schloss, Francois Berthiaume, Noshir Langrana
Department of Biomedical Engineering, Rutgers, The State University of NJ

Introduction: Diabetic chronic wounds are decreasing the quality of life for millions as the number of diabetic patients is increasing worldwide. In terms of accelerating diabetic wound healing, chitosan has been proven to be effective as it has been shown to decrease inflammation, increase fibroblast proliferation, and contain hemostatic properties. Wound healing is a complex process requiring extensive communication between cells. Diabetic patient wounds are often characterized by excess inflammation and hyperglycemic conditions due to compromised insulin production/function thereby interrupting the physiological processes involved in wound healing. As a consequence, diabetic conditions can lead to chronic and non-healing skin wounds and in extreme cases causing osteomyelitis and amputation of the wound area. Current treatments of non-healing diabetic wounds include debridement, leaving the patient with large amounts of tissue removed, topical platelet-derived growth factor treatment, which has severe side effects including malignancy, and wound dressings in which effective remedies like bioengineered skin are costly and inaccessible. To overcome this problem, we developed a relatively low-cost polyelectrolyte complex (PEC) film dressing made of chitosan and polygalacturonic acid (PgA) and tested it for its ability to accelerate diabetic wound healing and related phenomena.

Methods: To prepare the chitosan and PgA solutions, 300 mg of chitosan including 1.5 mL of HCl and 300 mg of PgA including 1 mL of NaOH were added into 50 mL centrifuge tubes separately with 30 mL of water in each tube, and then vortexed briefly. After mixing overnight on a rotating nutator (37°C), the chitosan and PgA solutions were combined in a 60:40 volumetric ratio and sonicated for 3 min. The pH was recorded before and after the sonication of each solution. The mixture was then poured into a circular 37 mm radius dish to dry (41°C) for 32-36 h. To investigate the effects of Chi-PgA PEC films in vivo, 10 mm full-thickness wounds in diabetic mice were treated topically with fibrin gel and PEC film. Each mouse was photographed on days 0, 3, 7, and then weekly. Then mice were sacrificed, and tissue samples were collected for histological analysis. Images were analyzed using ImageJ.

Results: We found that PEC film dressings accelerate diabetic wound healing in mice. Initial optimization and characterization revealed the swelling behaviors of the PEC material, allowing for a robust manufacturing process. In vivo, testing showed that PEC films accelerated diabetic wound closure, such that on post-wounding 42-day, PEC-treated wounds had fully closed, while controls treated with fibrin gel were only 50 % closed. In addition, PEC films increased the number of hair follicles around the wound area and caused the skin to grow hair much more rapidly than gel control. These findings support the claim that PEC films can accelerate both wound healing and hair growth in mouse models of full-thickness diabetic wounds.

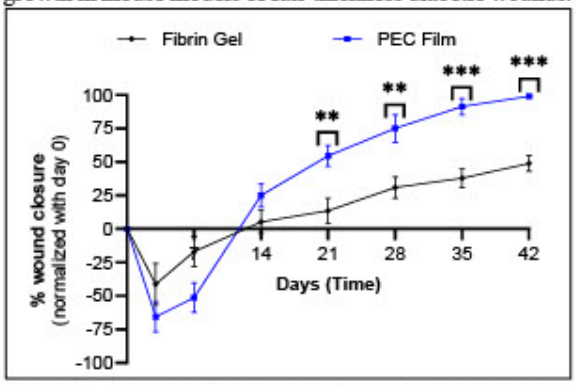

Figure 1. Effect of PEC film on diabetic wound healing. Wound closure dynamics of Fibrin Gel (thrombin & fibrin) control and PEC Film groups over 42 days. Data are represented as mean ± SEM (n = 6/group). Data are analyzed using repeated measures of two-way ANOVA followed by post hoc Tukey's HSD test. **$p < 0.01$ and ***$p < 0.001$.

Conclusions: Overall, the PEC film has been shown to accelerate diabetic wound healing in full-thickness wounds in a male mouse model and increase the number of hair follicles around the scar area, proving to be a promising treatment for chronic diabetic wounds. Future investigations should monitor hair growth in non-diabetic animal models, as well as in the absence of a wound. To assess the full potential of the PEC film, future testing should also include its drug delivery capabilities in vivo.

References:

1. Blakytny R. Diabet Med J Br Diabet Assoc. 2006; 23(6):594–608.
2. Lavery LA. Diabetes Res. Clin. Pract. 2009;83(3):347–352.
3. Mistry P. Biochem Biophys Res Commun. 2024: 696:149502.

Acknowledgments: This work was funded by Rutgers University TechAdvance grant (# AWD00004127). Rutgers University filed provisional patent using this work as "Langrana N, Kumar S, Berthiaume F, Schloss R, Mistry P, Kang HJ. (2023). Compositions and Methods for Wound Healing and Hair Growth using Polyelectrolyte Complex (PEC) Films. U.S. Provisional Patent Appl. No. 63/583,685."

DEI: To ensure the improvement of disparities in healthcare outcomes, testing treatments like the one described here should be done on a diverse set of samples. Also, ensuring new information to the healthcare industry is accessible such that underrepresented persons within STEM can participate.

STEVENS
INSTITUTE OF TECHNOLOGY

Machine Learning Analysis of Bone Submicron Composition: A Novel Approach to Identify Fragile Bones

Isha Dev[1], Sofia Mehmood[1], Nancy Pleshko[1], Iyad Obeid[2], William Querido[1*]
1. Department of Bioengineering, Temple University, Philadelphia PA. william.querido@temple.edu
2. Department of Electrical and Computer Engineering, College of Engineering, Temple University, Philadelphia PA.

Introduction: High-resolution compositional analysis of bone tissue is crucial to elucidate the origins of bone health impairments and understand the fundamental aspects of bone quality and strength [1]. A recent advancement in infrared spectroscopy and imaging, optical photothermal infrared (O-PTIR) spectroscopy, has provided a means to gather data with submicron resolution (500 nm) in thick samples [2]. In this study, our objective was to establish a new approach to evaluate bone health at the tissue level, by combining the novel application of O-PTIR spectroscopy and imaging to assess bone submicron composition and machine learning analysis to identify healthy and fragile bones based on their tissue-level spectral data.

Methods: We assessed cortical bone tissue composition in samples from control mice (wildtype, WT, n = 6) and from a genetic murine model that has impaired bone tissue quality, leading to greater bone fragility and risk of fractures (oim/oim, OIM, n = 7). Tibias embedded in blocks of poly(methyl methacrylate) (PMMA) were obtained from an IACUC-approved research study at the Hospital for Special Surgery (New York, NY). Minimal sample preparation involved cutting the initial block into 2-4 mm thick cross-sections at the mid-diaphysis. O-PTIR spectral data were acquired using the mIRage submicron infrared microscope (Photothermal Spectroscopy Corp., Santa Barbara, CA), via line scans across the cortical bone thickness and single-wavenumber imaging of the distribution of sample components at 500 nm spatial resolution. Support vector machine (SVM) using a radial basis function kernel was used in Python to identify healthy (WT) and fragile (OIM) bones based on spectral data.

Results: O-PTIR submicron spectral imaging of embedded bones showed the distributions of bone mineral and protein components and allowed a clear identification of tissue microporosity. Spectra acquired from WT and OIM cortical bone reflected the composition of the tissues, showing typical absorbance peaks arising from mineral and collagen (Fig. 1a). Principal components analysis (PCA) applied to the spectral data showed a clear separation of the spectra from healthy and fragile bones in the scores plot (Fig. 1b). Moreover, SVM analysis could identify spectra from healthy and fragile bones with strong predictive accuracy (Fig. 1c).

Conclusions: Our study demonstrates the application of O-PTIR spectroscopy and imaging in assessing bone tissue composition with submicron spatial resolution. Moreover, machine learning analysis highlights the potential of this approach to use tissue-level spectral data to identify fragile bones at risk of fracture. Further applications of O-PTIR spectroscopy and imaging combined with machine and deep learning analysis may offer an innovative approach to improve the clinical diagnosis and bone fragility diseases and assessment of risk of fractures.

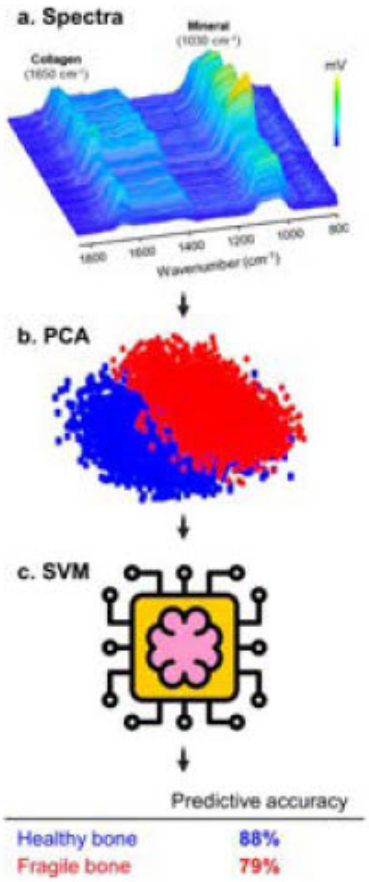

Fig. 1. Machine learning analysis can distinguish healthy and fragile bones based on their O-PTIR spectral data acquired at the submicron tissue level.

References: [1] Reznikov et al. Acta Biomaterialia. 2014; 10(9):3815. [2] Reiner et al. Appl Spectrosc. 2023; 77(11): 1311-1324.

Acknowledgements: NIH/NIAMS R21AR082129 and the Hospital for Special Surgery

DEI: We are committed to addressing healthcare disparities by innovating diagnostic strategies for skeletal diseases and fracture risk in a diverse population. We also aim to foster inclusivity by encouraging active participation and contributions from individuals underrepresented in STEM within the fields of bone and spectroscopy research.

Three-Dimensional Velocimetry based on Optical Coherence Tomography for Assessing Transport of Preimplantation Embryo in the Mouse Oviduct In Vivo

Tianqi Fang, Huan Han, Jingyu Sun, Aleese Mukhamedjanova, and Shang Wang.
Department of Biomedical Engineering, Stevens Institute of Technology, Hoboken, NJ 07030, USA.

Introduction: Optical coherence tomography (OCT) provides a unique imaging scale for 3D assessment of particle dynamics [1]. For relatively large particles, direct volumetric imaging and 3D tracking has been an easy and accurate approach to analyze the particle movement. However, with fast particle movement, the requirement of a high volumetric imaging rate often leads to low spatial sampling or small transverse field of view, due to the generally limited imaging speed of OCT. This is a technical hurdle particularly in using OCT to study the transport of preimplantation embryo in the oviduct (or fallopian tube) [2], where a large 3D image of the oviduct is needed to provide the context for analyzing the embryo dynamics. Here, we present a new 3D velocimetry method that relies on a single OCT volume with double B-scans at each B-scan location to quantify particle movements. In comparison with the existing OCT-based streak velocimetry techniques largely based on 2D imaging [1], this method produces 3D streaks, thus allowing for large-field-of-view, high-quality 3D OCT structural imaging at the same time as 3D velocity measurement.

Methods: OCT imaging consists of A-scan that is a depth profile (in Z). A fast transverse scan of the imaging beam (in X) generates a depth-resolved 2D image, as the B-scan, and a slow traverse scan (in Y) moves the B-scan to generate a volume. The new velocimetry method relies on the generation of a 3D particle streak during the acquisition of a single OCT volume that has dual B-scans at each B-scan location. The velocity quantification consists of two parts: a) velocities in X and Z measured by direct particle tracking within the X-Z plane, and b) velocity in Y measured based on the relative movement of particle with respect to the moving B-scan. The overall velocity of the particle, V, is then obtained based on the X, Y and Z velocity components, as $V=V_X+V_Y+V_Z$. For acquiring the single-volume, double-B-scan velocimetry data, the lab-built spectral domain OCT system was set with a B-scan moving speed of ~0.6 mm/s. Validation of the new method was performed with a flow phantom, and the comparison was made with results from traditional particle tracking across volumes. *In vivo* imaging experiments were performed to demonstrate the method for assessing the velocity of the preimplantation embryo movement in the mouse oviduct together with high-quality imaging of the surrounding tissue dynamics. Using this method, we also conducted a pilot investigation of the correlation between the oviduct contraction/relaxation and the embryo movement in the *in vivo* transport process. Data processing was performed using MATLAB. To present the 3D velocimetry result from *in vivo* imaging, the velocity direction was binarized for forward and backward movements and was color-coded. The brightness was linearly mapped to the speed values.

Results: The flow phantom experiment demonstrated that the design of the velocimetry method can be successfully implemented, and the results validated that the new method provides comparable measurements as the gold-standard approach. From the *in vivo* experiments, results indicate that this method can be utilized for *in vivo* assessment of the embryo movement within the native, dynamic oviduct environment. Figure 1 shows the *in vivo* 3D velocimetry results with the 3D OCT image of the mouse oviduct. The large field of view of the new method allowed for investigation into detailed dynamics, showing the unique feasibility to perform imaging analysis of the correlation between the oviduct activity and the embryo movement, which enables the study of the transport function of the oviduct.

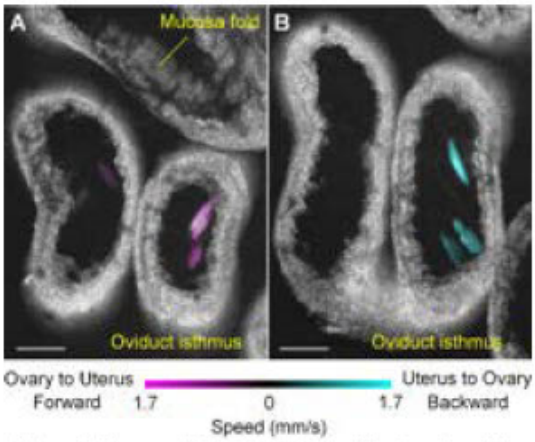

Figure 1. *In vivo* 3D OCT imaging of preimplantation embryo velocity together with the mouse oviduct isthmus structures. Scale bars: 200 μm.

Conclusions: We developed a novel 3D particle streak velocimetry method based on OCT, specifically for assessing the rapid movement of preimplantation embryos within the mouse oviduct *in vivo*. The method is validated and presented with both controlled *in vitro* experiment and *in vivo* mouse experiment. Results show distinctive capability of the method to provide embryo velocity together with the 3D dynamics of the oviduct over a large field of view, revealing pilot insights into the transport mechanism of the mammalian oviduct underlying the successful pregnancy.

References:

1. Zhou K C. et al. Biomed. Opt. Express.. 2016, 7(4): 1590-1603.
2. Wang S. et al. Cell Rep.. 2021, 36(2).

Acknowledgements: This work was supported by the National Institutes of Health (R21EB028409).

DEI: There has been a lack of study on the role of oviduct in pregnancy and associated female reproductive disorders, such as tubal ectopic pregnancy. Research in this area with technological development and biological investigations could help to improve the female reproductive health.

STEVENS
INSTITUTE OF TECHNOLOGY

Assessing the Role of Oviduct Contraction in the Transport of Preimplantation Embryo through In Vivo Imaging in the Mouse Model

Huan Han, Tianqi Fang, Aleese Mukhamedjanova, and Shang Wang.
Department of Biomedical Engineering, Stevens Institute of Technology, Hoboken, New Jersey 07030.

Introduction: The mammalian oviduct (or fallopian tube) is a tubular organ connecting the ovary and the uterus. It is essential for natural pregnancy, carrying out the transport of preimplantation embryo toward uterus for implantation. This tranpsort process has tranditionally been perceived as a simple, gradual movement of embryo primarily driven by the beat of motile cilia lining the epithelium of the ovdiuct lumen [1]. However, our recent work on the first high-resolution *in vivo* 3D time-lapse imaging in the mouse model showed complex dynamics of oocytes/embryos, suggesting multiple roles of the oviduct muscle contraction in the transport process [2]. Understanding the mechanism of the embryo tranport and the oviduct-embryo interactions during this process is critical to ecludicate the important biomechanical factors underlying a successful natural pregnancy and is also vital to uncover functional cause of associated female reproductive disorders, such as tubal ectopic pregnancy. In this work, we applied the *in vivo* imaging appraoch and developed quantitative methods to assess the role of oviduct contraction in generating the patterns of embryo movement and transporting the embryos toward pregnancy.

Methods: Our study focused on the stage of 1.5 days post conception of adult female mice, when the preimplantation embryos are expected to be in the isthmus of the oviduct. We employed a lab-built spectral-domain OCT system running at the central wavelength of 852 nm with an axial resolution of ~6 μm and a tranverse resolution of ~9 μm. The A-scan rate of the system was set as 100 kHz, and the volumetric imaging rate was up to 2 Hz. Imaging with OCT was conveniently combined with an *in vivo* intravital setup, where an intravital imaging window was implanted on the right dosal side of the mouse. The window was 3D printed, and the implantation of this window does not affect the normal physiology of the reproductive organs. This intravital window setup allows for pharmaceutical treatment of the oviduct. To investigate the role of oviduct contraction that is driven by the smooth muscle activities, we used prifinium bromide for topical treatment of the oviduct, which inbihited the oviduct contraction within minutes of administration. PBS was used for control. Time-lapse 3D imaging was performed, and 4D (3D+time) data were reconstructed and visualized with Imaris software (Oxford Instruments). The embryo movements were tracked (Fig. 1) and the parameters of movement were obtained for quantitative analysis with the oviduct contraction and relaxation.

Results: At 1.5 days post conception, preimplantation embryos were widely distributed throughout different regions of the oviduct isthmus. Specifically, their movements were not synchronized, suggesting the dynamics of fluids inside the isthmus is heterogeneous. The correlation between embryo movement and oviduct luminal area change indicated that the forward and backward long-distance movements of embryos appeared to be driven differently by the oviduct dynamics. In particular, the forward movement is correlated with peristaltic contraction waves from the lower ampulla to the upper isthmus. In contrast, the backward movement was found to be induced by the relaxation of the oviduct through a possible suction process. Without oviduct contraction, the embryos lost the bi-directional movement and stayed stationary, demonstrating that the smooth muscle activity drives the movements of preimplantation embryos in the isthmus.

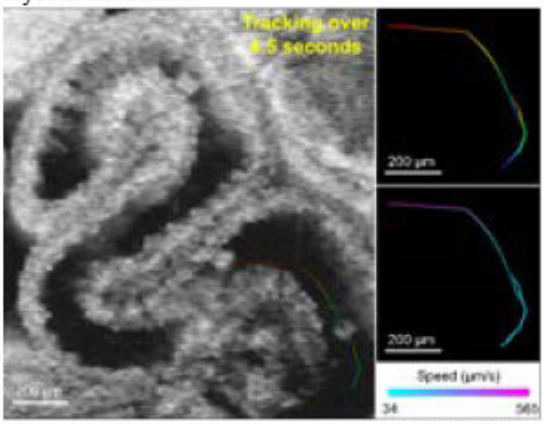

Figure 1. Tracking of embryo movement in 3D inside the mouse oviduct isthmus from *in vivo* OCT imaging.

Conclusions: We show the application of *in vivo* OCT imaging through an intravital window for assessing the process of preimplantation embryo transport in the mosue oviduct. Our results point to a previously unknown role of the smooth muscle in driving embryo movement in the isthmus and potentially delivering emrbyos towards the uterus. Our ongoing work further investigates how the oviduct contraction and relaxation create the heterogeneous fluid flow inside the oviduct and how an effective displacement of embryos towards the uterus is generated over a long duration. The insights are of significant value to elucidate the function of oviduct in mammalian reproduction.

References:

1. Li S., Winuthayanon W., J Endocrinol., 2017; 232(1): R1–R26.
2. Wang S., Larina, I. V., Cell Rep., 2021; 36(2): 09382.

DEI: There has been a lack of study on the function of the oviduct (or fallopian tube), largely due to the difficulty in imaging of its dynamics. Recent consensus acknowledged the significance to understand the role of oviduct in mammalian reproduction, which is critical for understanding the cause of female reproductive disorders and holds the promise to improve assisted reproductive technologies, such as *in vitro* fertilziation. This work presents a unique approach to study the oviductal function in natural pregnancy, contributing to the improvement of female reproductive health.

Microplastics Assessment in Intact Tissue Phantoms with Infrared Spectroscopy

Azita Hassan Mazandarani, William Querido, Nancy Pleshko.
Temple University

Introduction: Small plastic particles less than 5 mm are commonly referred to as microplastics (MPs) [1]. Given the prevalence of MPs in human tissues, the lack of knowledge surrounding their presence, and the potential negative impact of MPs on human health, further research on this contaminant is critical. When analyzing microplastics in tissue samples, the following procedures are typically involved: sample digestion, MP filtration and separation, MP detection, characterization, and quantification. Infrared (IR) spectroscopy is one technique utilized for MP detection, based on the ability to assess the molecular structure of materials and tissues. Nevertheless, the digestive process typically used may result in the loss of certain MPs and does not allow research into how the location of MPs within the tissue may impact health. The ultimate goal of our research is to use IR spectroscopy to detect and measure the amount and type of MPs in intact biological tissues. Towards this end, we are developing a protocol by characterizing, identifying, and quantifying MPs in tissue phantoms which contain specific amounts of MP particles.

Methods: Tissue phantoms were created using bovine gelatin that contained specified concentrations of common MP particles found in tissues, including polyethylene (PE, Cospheric LLC, Goleta, CA), polystyrene (PS, Cospheric LLC, Goleta, CA), polypropylene (PP, Polysciences, Inc., Warrington, PA), polyamides (PA, Goodfellow Corporation, Pittsburgh, PA), and microfibers, such as PTFE (Goodfellow Corporation, Pittsburgh, PA) [2]. Subsequently, the samples were cryosectioned into thin sections for evaluation by polarized light microscopy (Nikon Inc., Melville, NY) and infrared (IR) microscopic spectral imaging. This was done using the Perkin Elmer 400 Spotlight (PerkinElmer Inc., Shelton, CT) at 8 cm^{-1} resolution and 6.25- or 25-micron pixel resolution, and the optical photothermal infrared (O-PTIR, mIRage spectrometer, Photothermal Spectroscopy Corp., Santa Barbara, CA) with 2 cm^{-1} spatial resolution and 500 nm spatial resolution. Specific IR absorbance bands were identified to differentiate MPs from gelatin.

Results: We were able to detect MPs in tissue phantoms by polarized microscopy (Fig. 1). However, spectroscopic imaging is required to identify which MPs are present. Figure 2 shows a visible and spectral image of PP particles at 25 μ pixel resolution. The spectral image was created based on the infrared spectral signature of PP, using the absorbance peaks at 1452 cm^{-1}. Figure 3 shows a similar spectral image of PP from O-PTIR data. We can see that the O-PTIR image has better resolution, and smaller particles can be noted than in the Spotlight image.

Conclusions: Our results indicate that polarized microscopy is a highly effective technique in screening for MPs in tissue phantoms, based on their distinct pattern of birefringence. Further, we were able to detect and characterize particles using IR microscopic spectral imaging up to 500 nm. Future work will focus on refining this approach to quantify micro and nano plastic particles in tissue phantoms and biological tissues.

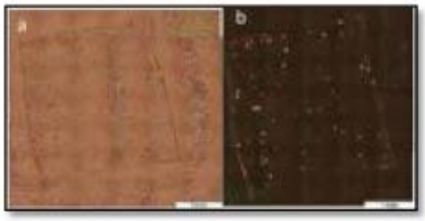

Figure 1. a. Microscopic visible image of tissue phantom containing PP MPs with 20x magnification. b. Polarized microscopic image of tissue phantom containing PP MPs with 20x magnification.

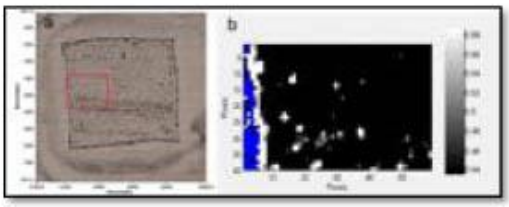

Figure 2. a. Visible image by Perkin Elmer 400 Spotlight. b. Hyperspectral image showing MPs in tissue phantom.

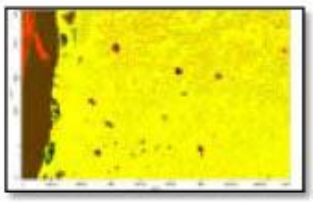

Figure 3.O-PTIR image showing PP particles in tissue phantom. Red color shows highest level of PP absorbance.

References:

1. Luo T. Environ. Pollut. 2019;255:113-122
2. Kutralam-Muniasamy G. Sci. Total Environ. 2023;856(2):159-164

DEI: Recent investigations have revealed that microplastics affect vulnerable communities more, which is elevating the risk of health outcomes. With this research, we can find a way for MP detection in tissues and find out how these can harm people's health. Consequently, it lowers the MP exposure for high-risk people.

STEVENS
INSTITUTE OF TECHNOLOGY

Alveolar Distribution of Nebulized Particles in Lung Injury Assessed by Confocal Microscopy

John Battikha*, Zahra Ansari*, Charul Singh, Carrie E. Perlman (* equal contributors)

Stevens Institute of Technology, Hoboken, NJ

Introduction: In pulmonary disease, nebulization enables direct drug delivery to the lungs. Delivery to injured regions is important but nebulized particle distribution in injured lungs has not been well characterized. Here, we use confocal microscopy to capture alveolar distribution with high spatial resolution. We compare images between and within lobes to identify heterogeneity, to determine if lung injury affects heterogeneity.

Methods: A prospective case-control study to assess nebulization distribution is conducted in Sprague-Dawley rats. We study n=4 healthy rats and n=4 rats (equal male/female) injured, 24 hrs before, by lipopolysaccharide instillation (0.75 mg/kg) in the trachea. First, we anesthetize a rat, perform a tracheotomy and cannulate the trachea, and connect the cannula to a mechanical ventilator (Inspira model 683, Harvard Apparatus, Holliston, MA). Then, we commence mechanical ventilation (6 ml/kg tidal volume, 4 cmH_2O positive end-expiratory pressure, 75/min respiratory rate, 20 min) and administer an intravenous paralytic (0.3 ml of 1 mg/ml pancuronium bromide, additional 0.1 ml on observation of breathing effort). After a 10 minute acclimation period, we nebulize fluorescein solution (5 mM in saline, 1 min on/1 min off power cycle; Aeroneb vibrating mesh nebulizer; 0.211 ± 0.028 ml delivered) in the last 10 min of ventilation. At the end of ventilation, we sacrifice the rat.

After nebulization, we close a stopcock at the tracheal entrance, excise the heart and lungs, connect, and open the tracheal stopcock to an air source, recruit the lungs with airway pressure of 30 cmH_2O, and then deflate to 10 cmH_2O. In each of six lung regions – upper, middle and lower regions on left and right side-costal surfaces – we image a bright sub-region and a dim-subregion at 20 µm subpleural depth by confocal microscopy (x20 water-immersion objective, 488/495-700 nm excitation/emission). All images are processed with ImageJ. In injured lungs, alveolar airspaces are often flooded with edema, which shows up in the images as a filled in green alveolus, while aerated alveoli are not filled in with green. In the bright sub-region images, we place a region of interest (ROI) atop the brightest septum of an aerated alveolus and quantify mean intensity within the bright sub-region ROI, I_B, as a measure of maximal nebulized particle deposition. In the dim sub-region images, we place a ROI atop a typical-intensity septum of an aerated alveolus and quantify mean ROI intensity within the typical ROI, I_D, as a measure of typical nebulized particle deposition. Then, we calculate an intralobar heterogeneity index, $H = (I_B - I_D)/[(I_B + I_D)/2]$. We compare average fluorescence intensity in each region and intralobar heterogeneity index between healthy and injured rats.

Results: From bright regions, across healthy and injured animals, there is greater deposition in upper regions ($p<0.001$) but no difference between left and right lungs or with injury (**Figure 1 A**). Heterogeneity between bright and dim regions does not differ with lung region but shows a trend ($p=0.097$) toward decreasing with lung injury (**Figure 1B**).

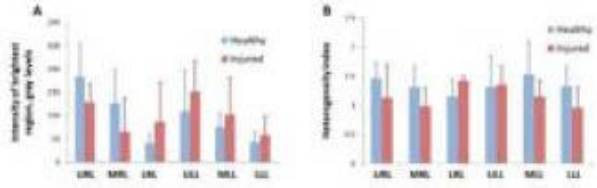

Figure 1: Heterogeneous distribution of fluorescent solution nebulized in vivo in rats and quantified by confocal microscopy. **A**: Fluorescence intensity along brightest septa in upper (U), middle (M) and lower (L) regions of left (L) and right (R) lung lobes. **B**: Heterogeneity index for same regions. Injury generated by intratracheal instillation of lipopolysaccharide.

Conclusion: While nebulization more effectively delivers aerosolized solution to alveoli in upper lung regions, nebulization is equally effective for alveolar delivery in healthy and injured lungs. Heterogeneity is present in all lung regions, with bright images being much brighter than dim images in all regions for both healthy and injured lungs. The decreased heterogeneity in injured lungs indicates that fluorescein deposition is more uniform, which may be due to the alveolar flooding homogenizing local fluorescence deposition.

Acknowledgements: ROI HL113577

DEI: Healthcare outcomes for patients with acute respiratory distress syndrome undergoing mechanical ventilation are bad even in high income countries, and can be increasingly disparaging in low-income countries where access to ventilators is limited. More research into making ventilators more affordable and more accessible can improve healthcare outcomes in these countries. In the academic community at Stevens Institute of Technology, participation of STEM-underrepresented persons in training can be improved by hiring diversified lab personnel.

STEVENS
INSTITUTE OF TECHNOLOGY

Aging-Associated Decline in Vascular Mechanosensation: Implications of Piezo1 Signaling

Ngoc Luu, Shuhao Zhang, Ria Kumar, Xiuxian Li, Weiqiang Chen
Biomedical Engineering Department, New York University, Brooklyn, NY

Introduction: Aging of the vasculature is associated with detrimental changes in properties of the vascular smooth muscle cells (VSMCs). VSMCs are crucial in regulating the contractility of vessel walls via mechanosensation, enabling the vessels to accommodate the rapidly changing mechanical perturbations from blood flow. VSMC mechanosensation depends on opening of tension-gated ion channels termed Piezo1 to trigger calcium (Ca^{2+}) influx that initiates cellular contraction. Yet, how aging alters Piezo1-mediated contractile dynamics remains unexplored. The objective of this study is to explore the distinct aging-associated mechanosensitive patterns of VSMCs, focusing on Piezo1-mediated signaling and cytoskeletal machinery.

Methods: The PDMS micropillars (height of 7μm, diameter of 2μm) were fabricated using standard photolithography and a double molding process. The tip of the pillars was functionalized with fibronectin to promote adhesion of mouse aortic VSMCs. Mechanical stress of approximately 100 pN was applied by ultrasound transducer onto a lipid microbubble bound to the cell membrane via Arg-Gly-Asp (RGD)-integrin linkage (**Fig 1A**). Expression of CSK markers and Piezo1 were assessed with immunofluorescence (IF) and quantitative reverse transcript polymerase chain reaction (RT-PCR). Ca^{2+} influx was monited by transfected VSMCs with Fluo4-AM Ca^{2+} indicator.

Results: Our measurements of VSMC traction force at the 'static' state using the micropillar array indicated that old VSMCs exerted a higher basal force than young cells, suggesting a shift to a more rigidified phenotype with aging (**Fig. 1B-C**). At the 'dynamic' level, the old cells exhibited impairment in their mechanoresponse to ultrasound stimulation, reflected by a delay in contractile response, a lower peak cellular force, and a longer time to reach homeostasis condition (**Fig. 1D**). We then implemented a framework to characterize VSMC mechanosensitivity based on a spatio-temporal decomposition of their force response into a frequency spectrum. The force response of the old cells showed a lower instantaneous frequency than that of the young cells, revealing a less robust and attenuated actomyosin machinery with aging (**Fig. 1E**). Aberrant aging-associated CSK functions were supported by IF results indicating alleviation of CSK contractile marker (α-actin) and upregulation of stiffening marker (γ-actin) in the old cells (**Fig. 1F-G**). Furthermore, our findings demonstrated that overexpression of Piezo1 channels in old VSMCs (**Fig. 1H**) mediated a prolonged Ca^{2+} influx upon activation by Yoda1 (a Piezo1 agonist) compared to a more transient Ca^{2+} response observed in the young cells. We further explore a potential 'mechano-medicine' strategy to restore healthy mechanosensation by silencing Piezo1 with siRNA transfection (**Fig. 1J**). Reducing Piezo1 overexpression in the old cells ameliorates their mechanosensitive functions, confirmed by a recovery in their force dynamics and instantaneous frequency upon ultrasound tweezers stimulation (**Fig. 1K, L**).

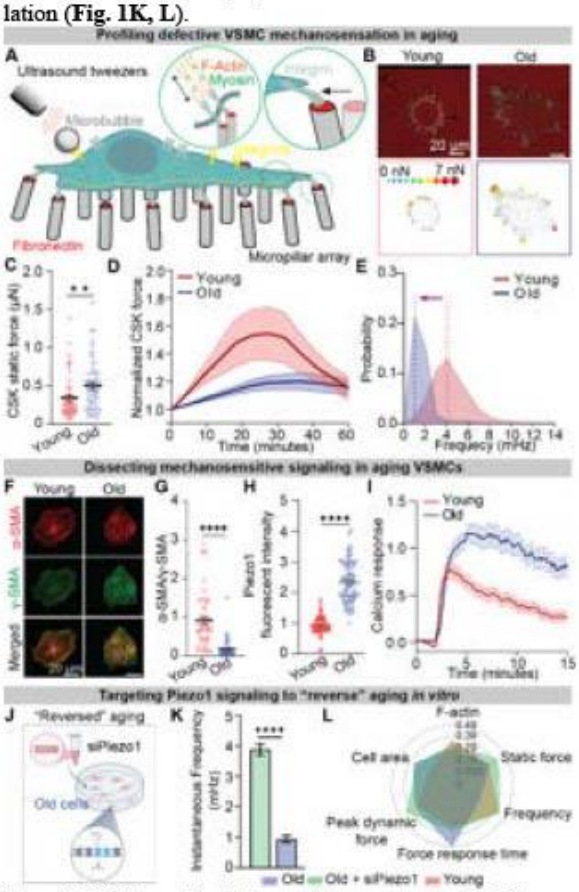

Figure 1. **A)** Schematic of ultrasound tweezer system. **B-C)** Traction force profile and quantification in young and old cells. **D)** Force dynamics of VSMCs to ultrasound tweezers stimulation. **E)** Frequency of VSMC force response. **F)** IF images and **G)** quantification of α-actin and γ-actin in VSMCs. **H)** IF quantification of Piezo1 expression. **I)** Piezo1-mediated Ca^{2+} influx in aging VSMCs. **J)** Piezo1-reversed aging *in vitro* model. **K-L)** Assessment of mechanosensitive functions of in reversed aging cells.

Conclusions: Our findings identified decline in mechanosensation as a new biophysical marker for vascular aging. Piezo1 mechanosensitive channel was revealed to be a key regulatory molecule and *a potential 'mechanomedicine' target for fitness restore vascular aging in VSMCs.*

Reference: Luu N. et al. Aging Cell. 2024; 23(1):e14036

Acknowledgements: This work was supported by the National Institute of Health (R35GM133646)

DEI: As mutations in Piezo1 are fairly frequent, our study is crucial for addressing disparities in vascular health outcomes across diverse populations and genders.

A novel experimental system to study collective cellular responses to patterned static stretching of surgical meshes

Jingnan Ye[1], Pamela A. Moalli[2], Yu-li Wang[1]
[1]Carnegie Mellon University, [2]University of Pittsburgh, Magee-Womens Research Institute

Introduction: External mechanical stimuli, such as substrate stiffness, compression, and stretching, have profound effects on cellular behavior. Stretching, being a ubiquitous physiological stimulation, has been demonstrated in many *in vitro* studies to alter cell orientation, migration, and differentiantion. These observations point to the possibility that nonuniform static stretching may play a role in pattern formation and morphogenesis through differential responses in cell migration, orientation, or contractility. In addition, *in vivo* studies implicate an impact of nonuniformly distributed strain on inducing patterned cell responses. For example, in sacrocolpopexy, a surgical intervention for alleviating symptoms of pelvic organ prolapse POP, nonuniform static stretching mediated by surgical mesh is associated with location-dependent variations in tissue stresses, with high stress areas leading to myofibroblast proliferation. These cells synthesize smooth muscle actin stress fibers and secrete copious amounts of collagen, leading to fibrosis and tissue contraction, the underlying cause of pain. Understanding the mechanism by which stress mediates impacts fibroblast behavior is critical in improving outcomes of POP surgery. In the present study, we have designed a device that imposes patterned static stretching on a fibroblast monolayer to investigate the impact on collective cell behavior.

Methods: To produce patterned static stretching, we employed a soft polydimethylsiloxane (PDMS) substrate embedded with Restorelle® POP mesh to function as the substrate. The device, fabricated using three-dimensional (3D) printing (Figure 1.A), served as both a cell culture chamber and the means for imposing static stretching via the embedded mesh. Six posts on one end of the chamber allowed anchorage of the substrate. Application of stretching forces was achieved via a movable stretching bar on the opposite side connected to the substrate via two pillars. Displacement of the stretching bar caused nonuniform stretching of the mesh with the largest strain located near the two pillars of the stretching bar and lower strain near the central region (Figure 1.A, right). The lowest and highest strains, calculated through the deformation of the mesh, were determined to be 3.6% and 18.9%, respectively. NIH3T3 fibroblasts seeded on the mesh-embedded PDMS substrate at a density of 500 cells/mm^2 were cultured without stretching for 24h. Cells were then subject to static tension for 72 hours and time-lapse recording was performed to follow the responses of migration, proliferation, and morphological changes as a function of location.

Results: Figure 1B depicts the orientation of NIH3T3 cells 24 hours post-stretching. Cells showed preferential alignment along the direction of stretching. Furthermore, polar histograms revealed variable extents of cell orientation corresponding to varying levels of strain. Strong alignment parallel to the direction of stretching was observed in regions of high strain (Figure 1.B, middle), while more random orientations took place in regions of low strain (Figure 1.B, right). In the absence of stress, cells exhibited random orientations (Figure 1.B, left). Time-lapse video in conjunction with particle image velocimetry (PIV) analysis further unveiled foci of contractile activities as cell density reached 4000 cells/mm^2 (Figure 1.C, left, middle). The number of contractile foci varied by location with areas of low tension exhibiting the highest density of contractile centers (Figure 1.C, right).

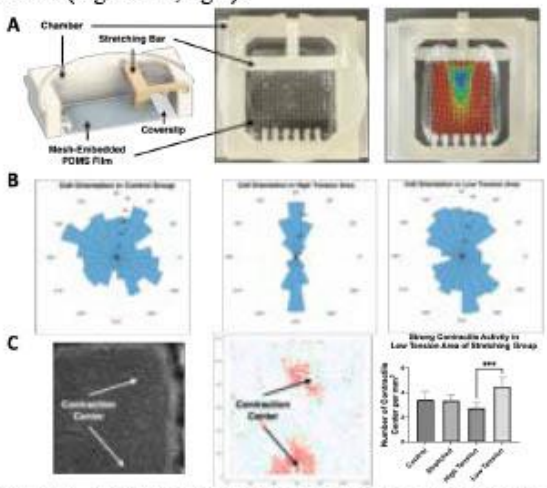

Figure 1. (A) Schematic (left) alongside images capturing the stretching device before (middle) and after (right) stretching. Heat map of simulated strain is superimposed, with red indicating the highest and blue representing the lowest strain. (B) Polar histogram illustrating cell orientation in the no tension group (left), high-tension region (middle), and the low-tension region (right). (C) Phase-contrast image (left), corresponding particle image velocimetry (PIV) analysis result (middle) of the same position, and the average number of contraction centers in different groups and areas (right).

Conclusions: Our novel apparatus demonstrates that fibroblast behavior in response to nonuniform static stretching is altered according to the amount of local strain. Nonuniform static stretching induced collective contractile activities, which led to the appearance of cell foci in a distribution reflecting the underlying strain pattern. These findings not only enhance our understading of collective cellular responses to nonuniform strain but also shed light on strategies for tissue engineering and improving the design of surgical materials for procedures like sacrocolpopexy, where the distribution of mechanical forces appear to play a role in clinical outcome.

Acknowledgements: We thank Haochen Nan and Allison Rojas for the help in developing the prototype of the stretching apparatus. This work is supported by NIH Grants R01HD083383 to Pamela A. Moalli and Yu-li Wang and R35GM136345 to Yu-li Wang.

STEVENS
INSTITUTE OF TECHNOLOGY

Deciphering CAR T-cell Biomechanics for Engineered Activation and Programed Immunotherapy

Rui Li[1], Ngoc Luu[1], Louis Hodgson[2], Weiqiang Chen[1]*.

1. Department of Biomedical Engineering, New York University, Brooklyn, NY, 11201 USA
2. Department of Molecular Pharmacology, Albert Einstein College of Medicine, Bronx, NY 10461, USA.

Introduction: Cytotoxic T-cell activation relies on tumor antigen recognition through immunoreceptors, with mechano-regulatory signals emerging as critical cooperative triggering pathways. In CAR T-cells, the ligation of tumor antigen and CAR rapidly initiate the T-cell activation, cooperated by the intense retrograde flow of cytoskeletons that transduce the force signals to develop a mature CAR T-cell synapse. However, a challenging question remains elusive is how the mechanics of synaptic force modulate CAR T-cells' activation and immune responses. Here, we aimed to decipher the mechanism and dynamics of mechanotransduction in CAR T-cells by developing a highly integrated micromechanical system to map the temporal and spatial mechanical dynamics of CD19-specific CAR T-cells during the antigen recognition, activation, and cytolytic killing process.

Methods: We fabricated force-measuring microfabricated pillar arrays (h=6μm, ⌀0.8μm) with a soft lithography technique and modified activating ligands recombinant Alexa 488-CD19, adhesive ligands ICAM-1, and poly-D-Lysine on the top of the pillars through stamping [1] (**Fig. 1A**). Then we seeded CD19 targeting CAR T-cells on the micropillar arrays, conducted time-lapse imaging for 30 min with a Nikon confocal microscopy and analyzed synaptic force dynamics with a customized software Cellogram and MATLAB algorism [2]. Furthermore, we quantify the CAR T-cell activation levels and cytoskeleton dynamics using RT-qPCR, IF staining, and Rac1 FRET biosensor. Finally, we correlate the activation and cytoskeleton dynamics to the synaptic force dynamics frequency to elaborate on the influences of biomechanics and the cytoskeleton machinery on CAR T-cell functions.

Results: Shortly after we seeded CAR T-cells, most T-cells exhibited a rapid spreading force and caused centrifugal pillar deflections(**Fig. 1A**). The generated synaptic force typically started at the center of the T-cell and reached peak value within seven minutes. Thereafter, the centrifugal spreading force gradually shifted to a centripetal contraction force with CAR T-cell activation progression with a fast-changing cycle of "protrusion-contraction" activities. Force measurement results demonstrated that CD19-activated CAR T-cells generally exerted a more vital synaptic force with an average peak force of 281.10 pN per pillar than moderate peak forces of 126.38 pN per pillar for the nonactivated CAR T-cells (**Fig. 1B**). Furthermore, we de-composited the synaptic force dynamics into the distribution of frequency of the force with Hilbert Huang transform and found that the characteristic frequency of activated CAR T-cells (16.2 mHz) is higher than that of the nonactivated cells (14.3 mHz) (**Fig. 1C**). Such characteristic frequency closely relates to the synaptic force magnitudes and activation status of CAR T-cells. After seeding the CAR T-cells on the CD19 functionalized substrates, we observed significant increases in T-cell activation surface markers CD25 and CD69 (**Fig. 1D**), indicating a successful activation of the CAR T-cells on the micropillar substrates. More importantly, we observed a positive correlation between the synaptic force magnitude and cytoskeleton activity levels during the activation process of CAR T-cells (**Fig. 1E**). Time-lapse FRET ratiometric imaging showed that the Rac1 activities were mostly centralized in the activated CAR T cells, while the Rac1 activity in nonactivated CAR T cells either evenly distributed throughout the whole cell or focused on the peripheral region of cells with weak Rac1 activity levels (**Fig. 1F**).

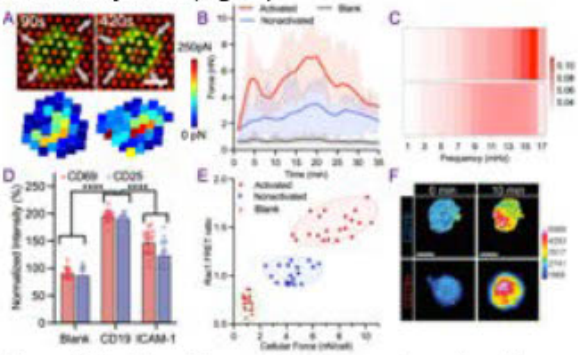

Figure 1. **A.** The scheme of force-measuring micropillar array. **B.** Synaptic force dynamics, **C.** frequency spectra, and **D.** activation levels of CAR T-cells. **E.** Correlation of peak synaptic force and Rac1 activity levels. **F.** Timelapse imaging of cytoskeleton dynamics in CAR T-cells.

Conclusions: Overall, the results of current biophysical experiments revealed a positive correlation between the robust dynamics of synaptic force exertion, the enhanced activation levels, and cytoskeleton dynamics in CAR T-cells, implying that robust cytoskeleton dynamics-driven biomechanics in IS accelerates the fulfillment of CAR T-cell activation. Meanwhile, the high characteristic frequency may serve as an ideal indicator of the robust cytolytic functions of the activated CAR T-cells which determine the ultimate clinical efficiency and outcomes of adoptive CAR T-cell immunotherapies.

References:

1. Luu, N. B. *et al.* Aging Cell. 10.1111/acel.14036
2. Qian W. *et al.* Nat. Commun. 13.1 (2022): 512.

Acknowledgements: This project was supported by the National Institute of Health (R35GM133646)

DEI: To improve disparities in healthcare outcomes, we should further address social determinants of healthcare to create solutions beyond the clinic. To broaden the participation of persons, early STEM education outreach is essential for bioengineering concepts and hands-on activities.

STEVENS
INSTITUTE OF TECHNOLOGY

Pancreatic cancer organoids-on-a-chip for tumor microenvironment modeling and immunotherapy study

Lunan Liu[1], Diane M. Simeone[2], Weiqiang Chen[1]
[1]Department of Mechanical and Aerospace Engineering, New York University,
[2]Department of Surgery, New York University Langone Health

Introduction: Pancreatic ductal adenocarcinoma (PDAC), the most common type of pancreatic cancer, responds poorly to conventional therapy and has had no major improvements in survival over the last several decades. The resistance to current therapy (e.g., immunotherapy) are largely attributed to the "immune cold" tumor microenvironment (TME). Novel immunotherapies like Chimeric antigen receptor (CAR) T-cell therapy had showed promising results in preclinical studies towards solid tumors like PDAC, yet their efficacy is limited in clinical trials. Therefore, to better recapitulate PDAC TME and assess new immunotherapies for filling the gap between preclinical and clinical results, there is a critical need of a humanized immuno-oncology model. Here, we proposed an PDAC organoids-on-a-chip model by integrating the patient-derived organoids (PDOs) on the microfluidic-based organ-on-a-chip. The proposed model can maintain the characteristics of original tumor by organoids and complement TME cues as well as conduct high precision spatiotemporal monitoring through organ-on-a-chip, therefore reconstitute the pathophysiology and heterogeneity of PDAC TME for immunotherapy testing.

Methods: The PDAC organoids-on-a-chip model (**Fig. 1a**) was engineered with 1) a central immunocompetent PDAC niche (center region) with PDAC PDOs, patient-derived cancer-associated fibroblasts (CAFs), PBMC-derived and induced tumor associated macrophages (TAMs) and endothelial cells, and 2) an adjacent vascular network (outer ring, green) for the transport of nutrients, drugs or lymphocytes like CAR T-cells (Promab Inc.). The patient samples were from the biobank in Dr. Simeone's lab. PDOs were cultured in PancreaCult™ Media (STEMCELL) before loading on the chip. The PDMS-based microfluidic chip was fabricated using standard soft lithography technique.

Results: We firstly demonstrated that tumor and niche cells (e.g., CAFs, TAMs) together shaped an immunosuppressive TME on chip. Comparing with the adjacent area or microenvironment with normal organoids, the PDAC niche showed a higher expression level of α-smooth muscle actin (α-SMA) on CAFs, a more extensive deposition of ECM components and the upregulation of inflammatory cytokines like IL-6 (**Fig. 1b-c**), indicating the desmoplasia and inflammation induced by CAFs in stromal niche. PDOs also induced TAMs inclined to be M2-like ($CD68^+CD163^+$) phenotype on chip (**Fig. 1d**). In turn niche contributed to the immunosuppression in PDAC TME: cytokine profiles showed the secretion of pro-tumor cytokines like IL-6, IL-13, MIP-1β and HGF were downregulated without niche cells (**Fig. 1e**). We also validated that the CCL18/VCAM-1 pathway between niche cells and PDOs would promote tumor progression. Next, we infused anti-MSLN CAR T-cells on chip for immunotherapy testing. The chip enabled the spatial-temporal monitoring of the migration and extravasation of CAR T-cells through vascular network (**Fig. 1f**). CAR T-cell then induced cytotoxicity marked by the upregulation of Granzyme B (**Fig. 1g**). Comparing with MOCK T-cells, CAR T-cells performed enhanced infiltration and proliferation (**Fig. 1h-i**)

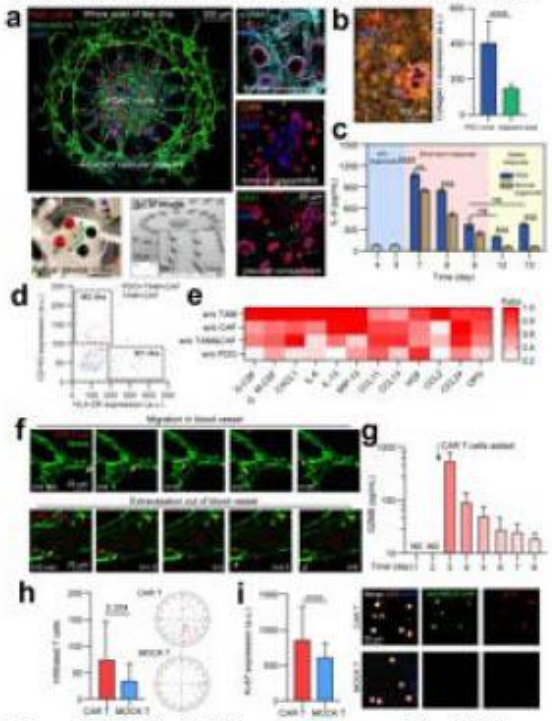

Figure 1. (**a**) The PDAC organoids-on-a-chip. (**b**) Excessive deposition of COL I in PDAC niche. (**c**) Continuous secretion of inflammatory cytokine IL-6. (**d**) TAMs were inclined to M2-like phenotype in in PDAC niche. (**e**) Cytokines profiles showed niche cells together contributed to immunosuppression. (**f**) Monitoring of CAR T-cells on chip. (**g**) GZMB indicated the cytotoxicity induced by CAR T-cells. (**h-i**) Enhanced infiltration (**h**) and proliferation (**i**) of CAR T-cells comparing with MOCK T-cells.

Conclusions: We developed a PDAC organoid-on-a-chip model which recapitulates the PDAC TME and is promising to serve as a platform for studying mechanisms of therapy resistance as well as testing novel immunotherapies like CAR T-cell therapy. We will further study barriers hindering the efficacy of CAR T-cell therapy like the lack of infiltration and the exhaustion of CAR T-cells. CAR T-cell products with different targeted antigens or armored CARs will be applied on chip for evaluation and screening.

DEI: Advanced *in vitro* platform like PDAC organoids-on-a-chip can serve as a tool for low-cost and high-speed therapy testing thus will greatly benefit the low-income groups.

STEVENS
INSTITUTE OF TECHNOLOGY

Liraglutide as a Treatment for Neuroinflammation Following Low-Level Blast Traumatic Brain Injury

Robert Lodge, Tulika Das
Faculty Advisors: Dr. Ying Li, Dr. Bryan Pfister
New Jersey Institute of Technology

Introduction: Blast TBIs are caused by the force of air pressure from explosions inflicting damage upon the brain. Individuals affected by war, civilians and soldiers alike, are exposed to high amounts of blasts. Soldiers who work with heavy artillery and civilians in active war zones experience the force of blasts. The repetitive blasts have a degenerative effect on brain structures responsible for auditory processing. Although earmuffs and earplugs protect the ears, they do not prevent the shockwave from affecting the brain. Liraglutide, a glucagon-like protein 1 receptor (GLP-1R) inhibitor, often used for patients with type 2 diabetes, has shown marked effects on the brain, most significantly evidenced in ameliorating traumatic brain injuries. The affected receptor plays a role in neuroinflammation, and by inhibiting its activation, liraglutide may reduce inflammation. The experiment described herein was conducted to test the question of whether subjects treated with liraglutide, when injured by a low-level blast, will exhibit less neuroinflammation than their untreated counterparts. Liraglutide is considered a successful treatment. Neuroinflammation is characterized by the increased activation of astrocytes and microglia, demonstrated by morphological changes. A reduction of inflammation in the treated group may enable preventative treatment to intercept the effects of mTBI-induced hearing loss before they start.

Methods: To test this hypothesis, chinchillas were chosen as subjects because their neurological hearing structures are similar to humans. Subsequently, the adult chinchillas were separated into cohorts and dosed with Liraglutide 7-14 days prior to or within 24 hours after blast exposure, with an additional naive group that was exposed with no injury or treatment. The brains of these chinchillas were perfused with PFA, removed, and stored in sucrose solution at 4℃. They were then embedded in OCT, frozen, sliced in a cryostat, and mounted on slides. The antibody markers IBA1 and GFAP were then used to stain the microglia and astrocytes of the tissue, respectively. The slides were then scanned using a fluorescence microscope. The appearance of more activated inflammatory markers in their ameboid state indicates heightened levels of inflammation and phagocytic activity.

ImageJ software was used to quantify the neuroinflammation by determining morphological differences in the inflammation markers. Specifically, the methods used to quantify the morphologies were skeleton analysis and fractal-lacunarity analysis (FracLac). Skeleton analysis simplifies the branching structures of the cells to single-pixel-width structures, allowing an automated count of the number of branches, number of junctions, and average branch length to be generated. This analytical technique was also performed on a cell-by-cell basis by analyzing several individual cells selected at random from samples to obtain more accurate morphological data. FracLac was also used to quantify the morphological complexity of the cells. The fractal dimension reveals the complexity of the cell's shape. Lacunarity is calculated by determining the perimeter of the cell and its density within a circle.

Results: The image analysis demonstrates an increase in the average number of microglia and astrocytes before versus after injury.

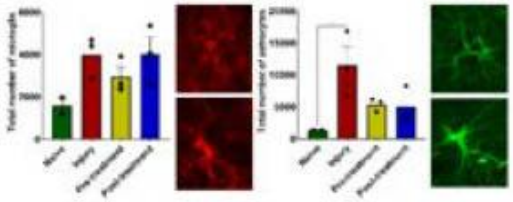

Figure 1. total number of microglia (left panel, Top: Resting microglia, Bottom: Activated microglia) and total number of astrocytes (right panel, Top: Native astrocytes, Bottom: Activated astrocytes) in AC at PID28.

The data exhibits a downward trend for inflammation when the chinchillas were treated prior to injury, but treatment after injury shows no significant decrease in microglia. However, there is a notable decrease in the number of astrocytes with both treatment times.

Conclusion: The decreased incidence of microglial activation corresponding to pre-treatment could indicate liraglutide's use as a preventative measure against low-level blast TBI. The decrease in astrocyte activation in both treatment groups demonstrates liraglutide's efficacy as a treatment method as well. This study underscores the importance of developing precise image analysis protocols to assess morphological differences in neuroinflammatory markers accurately. Overall, the study showed that the low-level blast did cause neuroinflammation in chinchillas, which tended to decrease with liraglutide treatment. These findings indicate that Liraglutide may be an effective treatment for such neuroinflammation.

References

1. Athauda, D. et al. (2016). Drug Discov Today, 21(5), 802-818.
2. Boscarino, J. A. et al. (2015). Mil Behav Health, 3(4), 244–254.

Acknowledgements Funding for this study was granted by the United States Department of Defense and conducted through the Center for Injury Biomechanics, Materials, and Medicine

DEI Equitable healthcare for veterans is an imperative effort, and the pursuit of curative measures for low-level blast TBIs sustained in combat poses to greatly improve soldiers' and veterans' quality of life by ameliorating the chronic hearing loss they may face. If liraglutide functions as a preventative measure against LLBTBIs, it would make treatment for the injury and thereby decrease the economic cost.

STEVENS
INSTITUTE OF TECHNOLOGY

Novel Biomimetic 3D Printed Load-Sharing Scaffolds for Vascularized Bone Regeneration

Shreya Madhavarapu, Barbara Perry, Dr. Charles J. Gatt Jr, Dr. Joseph W. Freeman
Rutgers, The State University of New Jersey

Introduction: Trauma, infection, tumor invasion and degenerative diseases can cause substantial bone loss, often resulting in large bone defects. Treatment involves the use of bone grafts, with approximately 2.2 million bone grafting procedures performed worldwide annually, making bone tissue the second most transplanted tissue.[1,2] While autografts and allografts are conventionally utilized as bone grafts, they pose drawbacks such as limited availability and potential disease transmission with allografts. Synthetic bone graft substitutes have emerged as recent alternatives, but they too exhibit shortcomings. Tissue engineered bone grafts offer promising alternatives, but their success hinges on addressing two crucial issues: inadequate cell infiltration throughout their structure and a lack of vasculature formation. To tackle these challenges, we have developed novel biomimetic 3D printed polylactic acid (PLA) scaffolds featuring distinct cortical and trabecular geometries. These scaffolds exhibit highly porous structures that facilitate the capillary inflow of blood and bone marrow. Moreover, they are mineralized and prevascularized, creating an environment conducive to stem cell differentiation into osteoblasts and vascular endothelial cells for the regeneration of both bone and its vasculature.

Methods: Scaffolds designed using Computer Assisted Design (CAD) software were fabricated with the Ultimaker 2+/S3 3D printers in transparent PLA. Scaffolds were subject to compression analysis and their mechanical properties compared to those of native bone. Their ability to promote capillary action was tested using fluids mimicking the viscosities of blood and bone marrow. Scaffolds were mineralized in concentrated simulated body fluid. Prevascularization was achieved by allowing vascular endothelial cells to grow within the cortical structure for 2 weeks followed by decellularization to leave behind a pro-angiogenic matrix. The osteogenic and angiogenic potential of the scaffolds was evaluated in vitro using human bone marrow mesenchymal stem cells (hMSCs). With approval from the Rutgers University Institutional Animal Care and Use Committee (IACUC), the scaffolds – both with and without autologous bone marrow were surgically implanted in adult female New Zealand white rabbits after creating a 15 mm critical-sized radial defect. Allografts served as controls. The regeneration of bone tissue was studied over the course of 20 weeks using X-Ray images acquired bi-weekly until the 10th week, followed by live CT imaging at 12-, 16- and 20-weeks post-surgery. At the end of the study, microCT images were acquired and histology was performed to monitor vascular development.

Results: The trabecular design displayed Ultimate Compressive Stress (UCS) and Compressive Modulus (CM) values of $9.55 \pm 0.45\ MPa$ and $325.13 \pm 21.89\ MPa$ respectively, which fall within the limits for trabecular bone (0.2-10MPa and 7-200MPa). The complete scaffold comprising both an inner trabecular and outer cortical section displayed a UCS of $39.83 \pm 2.07\ MPa$ and a CM of $603.37 \pm 24.79\ MPa$, these values are not as strong as those of native whole bone i.e., 200 MPa and 1 GPa respectively, but are superior to trabecular bone. Scaffold capillary action was observed over a range of viscosities. Mineral coating and prevascularized lumens promoted osteogenic and angiogenic differentiation of hMSCs respectively, in vitro, shown via levels of secreted osteocalcin, alkaline phosphatase and vascular endothelial growth factor. In vivo, scaffolds maintained their mechanical strength and structural integrity while promoting bone regeneration. Progressive bone regeneration was observed with the assistance of X-Ray images taken bi-weekly for the first 10 weeks, followed by live CT scans at 12, 16, and 20 weeks. CT imaging showed mature bone at later time points. Histology performed at the end of the study showed the presence of viable blood vessels within the regenerated tissue.

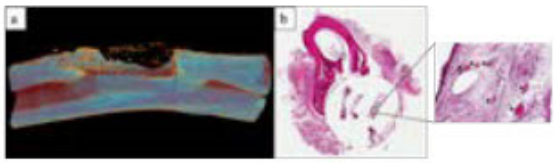

Figure 1. (a) MicroCT images after 20 weeks showing bone regeneration within the implant (b) H&E stained section showing the presence of blood vessels within regenerated bone.

Conclusions: We have developed load sharing scaffolds that mimic native bone architecture and facilitate the infiltration of bone marrow, reducing the need to add stem cells before in vivo implantation to enhance tissue regeneration. Rigorous assessments, in vitro and in vivo, showcased sustained mechanical stability and vascularized bone regeneration. These scaffolds hold substantial promise as bone graft alternatives or replacements for metallic trabecular mesh specifically tailored for load-sharing scenarios.

References:

1. Giannoudis PV. Injury. 2005;36(3):20-27
2. Roberts TT. Organogenesis. 8(4);114-124

Acknowledgements: This research was funded in part by the New Jersey Health Foundation (NJHF).

DEI: 1) 3D printing technology offers cost-effective bone graft alternatives. 2) Initiatives like outreach programs, mentorship, and inclusive research can address STEM underrepresentation and diverse healthcare needs, fostering broader participation.

STEVENS
INSTITUTE OF TECHNOLOGY

Hemocompatibility Evaluation of an Oxygenator with a Computationally Optimized Fluid Path in an Ovine Model for 48 Hours without Systemic Anticoagulation.

Umar Nasim, BS[1], Yeahwa Hong, MD[1,2], Adel Akhavanmalayeri, MD[1], Helen M. Scala, MS, RLATG[1], Suji Shin, BA[1], Patrick I. Iyasele, MS[1], Kelly R. Strong, BS[1], Abigail E. Gredell[1], Keith E. Cook, PhD[1]

From [1]Biomedical Engineering, Carnegie Mellon University, Pittsburgh, PA USA
[2]Surgery, University of Pittsburgh Medical Center, Pittsburgh, PA USA

Introduction: The only curative option for patients with severe chronic lung disease is lung transplantation.[1] The Pulmonary Assist System (PAS) is currently under development as an alternative destination therapy for these patients. The PAS is a wearable respiratory support system that includes a low-resistance gas exchanger (PAS-GE). The PAS-GE has a smaller surface area (0.9 m^2) and a computationally optimized blood flow path to minimize recirculation. The system also incorporates an antifouling poly-carboxy betaine (PCB) surface coating designed to minimize protein and platelet adhesion in the circuit.[2] In this study, we evaluated the hemocompatibility of the PAS-GE in a 48-hour ovine model with no systemic anticoagulation.

Methods: The PAS-GE (ART, Pittsburgh PA) was attached to a normal sheep in a venovenous configuration using either uncoated (UC) or PCB-coated (PCB) PAS-GE. Each sheep was supported on the PAS for 48 hours at 2 L/min of blood flow with a Pedimag centrifugal blood pump (Abbot, Chicago IL) and 4 L/min of oxygen sweep gas without maintenance anticoagulation. PAS-GE blood flow resistance was measured to evaluate occlusive clot formation. The oxygen transfer of the PAS-GE was evaluated using blood gas samples from the inlet and outlet of the device at 5 minutes, 2 hours, 4 hours, 8 hours, and every 8 hours following the initiation of support. Animal hematology was measured at baseline and each of the above time points. Plasma-free hemoglobin (pfHb), platelet count, and white blood cell (WBC) count were used as indicators of hemolysis, coagulation, and inflammation, respectively. After 48 hours of support, the clot weight in the device was measured after rinsing and drying the PAS-GE.

Results: A total of 5 experiments were performed with the UC (n=3) and PCB PAS-GE (n=2). The oxygen transfer was stable between baseline (UC: 78.3 ± 11.8 ml O2/min, PCB: 83.9 ± 14.9 ml O2/min) and endpoint (UC: 96.8 ± 19.9 ml O2/min, PCB: 99.2 ± 5.2 ml O2/min)(Figure 1A). The blood flow resistance of the UC and PCB PAS-GE did not vary appreciably from baseline (UC: 2.51 ± 0.71 mmHg/L/min, PCB: 2.42 ± 0.26 mmHg/L/min) over the study duration (Figure 1B). The baseline platelet count of the UC (178.8 ± 52.3 K/uL) and PCB (150.5 ± 43.13 K/uL) groups were comparable. However, the platelet count of the UC group dropped to 32.1 ± 9.5% of baseline after 8 hours and maintained this level to the end of the study (27.3 ± 13.4%). The PCB-coated PAS-GE preserved platelet count more effectively for the first 16 hours, but after 24 hours, the PCB group platelet counts were similar to those of the UC group. The low, stable pfHb and stable WBC counts observed in both groups indicate no significant hemolysis or inflammation. The clot weights of the UC and PCB PAS-GE groups were 68.7 ± 17.1 g and 48.4 ± 20.4 g, respectively.

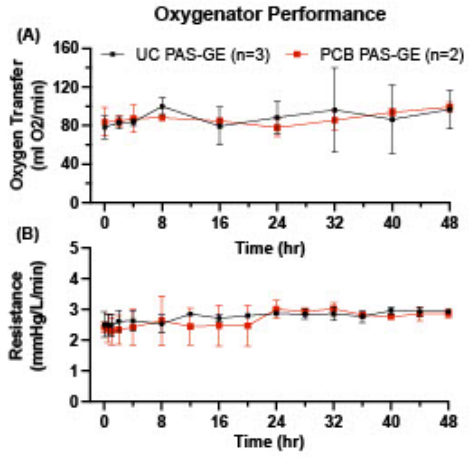

Figure 1. Summary of device performance, including (A) oxygen transfer and (B) blood flow resistance.

Conclusions: These results demonstrate that the design of the PAS-GE allows it to function for 48 hours without anticoagulation without any loss of function. The addition of the PCB coating appears to reduce platelet consumption and bulk clot formation, as indicated by the delay in platelet nadir and lower clot weight in these devices. Future work will also test a commercial oxygenator as a control.

References:

1. Quintel, M. et al. Anesth. 2020;132(5):1257-1276
2. Naito, N. et al. Biomaterials. 2021;272

Acknowledgments: This research was supported by the US Army CDMRP grant (W81XWH-21-1-0591).

DEI: Equitable distribution of organs for transplantation is a challenging and divisive issue. By offering an alternative therapy, we hope to increase access to care for all patients with severe chronic lung disease. In this field, we aim to fund and mentor all individuals who aim to develop these devices and implement them in an equitable and culturally conscious manner.

Characterizing Charge Time of Wearable Devices using Qi Wireless Charging System

Kiriaki Rajotte[1], Benjamin McDonald[2], Anson Wooding[2], Todd Farrell[2], Edward A. Clancy[1].
[1]Worcester Polytechnic Institute (WPI), Worcester, MA, USA. [2]Liberating Technologies, Inc., Holliston, MA, USA.

Introduction: When developing wireless, wearable biomedical sensors, some considerations that the designer(s) must make include the device's form factor, source of power, and usability. Wireless charging can be implemented to simplify the user experience and may easily integrate with existing chargers depending on the charging protocol selected. One challenge associated with the use of wireless charging in small form factor wearables is ensuring that the smaller receive (Rx) coil can reliably pair with the larger transmit (Tx) coils used in charging pads designed for devices such as smartphones.

In this work, the Qi wireless protocol was used to characterize the time required to charge a 105 mAh, lithium polymer battery for a small form factor (1–3 cm diameter and 1 cm thickness) wearable biomedical signal acquisition system. Two Rx coils of different shape and size were tested, and the material (representative of distinct device packaging options) placed between the Tx coil and Rx coil was varied to study its influence on battery charge time. For each measurement, the Rx and Tx coils were centered to ensure proper alignment.

Methods: As shown in Fig. 1, an Amazon Basics 15W Qi certified wireless charging pad was used to transmit power to the Texas Instruments (TI) wireless power receiver evaluation kit (BQ51050EVM-764). The kit features the BQ51050 Qi receiver with an integrated LiPoly battery charger; the output charge current was limited to 100 mA (set by the output circuit of the BQ51050EVM) to achieve a charge rate of 1C. To monitor the battery's charge, Adafruit's MAX17048 fuel gauge was selected. An Arduino Uno was used to read and log data from the fuel gauge. To discharge the battery, the HRTC C150 Balance (Dis)Charger was used.

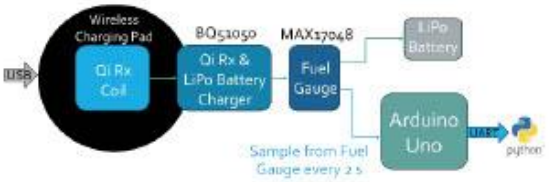

Figure 1. Block diagram of the experimental set-up

Two Rx coils from Würth Elektronik were tested: a large, rectangular coil (part number: 760308103215) measuring 48x32 mm and a smaller, round, 17 mm diameter coil (part number: 760308101220). Four different potential packaging materials were tested: 1) Rx coil directly placed on Tx pad separated by air, 2) Rx coil placed inside of the TI Rx evaluation kit's 2 mm thick enclosure, 3) Rx coil placed on 2 mm thick 3D printed ABS sample, and 4) Rx coil placed on 2 mm thick 3D printed PLA sample.

For each trial, the battery was initially discharged to under 10%. Then, the battery was connected to the output of the BQ51050EVM-764 and to the fuel gauge. The initial battery charge read by the fuel gauge was recorded. The Qi receiver set-up was placed on the Amazon Basics Qi transmitter pad, using the selected potential packaging options. The battery was left to charge until the percentage charge reached 95% or (due to transitioning to trickle charging) did not change for 15 minutes (whichever end condition was reached first).

Results: For each combination of coil and package option, five trials were completed. Table I shows the mean and standard deviation charging time for each combination. On average, 2.5–3 hrs. were required to charge the battery and the 17 mm diameter coil charged the battery faster than the larger antenna for each condition tested. When looking at the influence of the packaging options, placing the coil inside of the evaluation kit's enclosure led to the longest average charging times, while the 2 mm thick ABS material had the shortest average charge time for the two coils.

Table I: Summary of Results. Time, in hours to charge.

Coil Placement	48x32 mm Antenna	Ø 17 mm Antenna
Direct on TX pad	2.84 ± 0.10	2.68 ± 0.04
Inside of evaluation kit	2.95 ± 0.10	2.68 ± 0.22
On PLA	2.87 ± 0.12	2.53 ± 0.06
On ABS	2.71 ± 0.21	2.48 ± 0.36

Conclusions: This investigation determined Qi to be a feasible option for developing a wirelessly charged, biomedical sensor. The 105 mAh battery was found to charge from its initial charge point until it reached the stop criteria typically in under 3 hours for all trials with a minimum final charge of 88% achieved. Future work could look at the impact of smaller Rx coils or other Qi Rx circuits from different manufacturers. Additionally, there are other wireless charging protocols, such as NFC, that could be considered.

References:

1. Mirbozorgi SA. IET Power Elect. 2021;13(18):4183-4193.
2. Lyu H. IEEE Sensors Letters. 2019;3(3).
3. Kim J. Nature Reviews Bioengineering. 2023;1:631-647.

Acknowledgements: This work is supported by DoD STTR Contract W81XWH-22-C-0049. Any opinions, findings and conclusions or recommendations are those of the author(s) and do not necessarily reflect the views of the U.S. Army Medical Research and Development Command (USAMRDC).

DEI: Electrical engineering remains a male dominated field. To broaden participation for underrepresented groups in this field, early engagement with middle and high school students of different backgrounds through programs such as FIRST Robotics may help introduce and foster interest in this field while building student connections with practicing engineers. Building these connections prior to higher education may create future electrical engineers.

STEVENS
INSTITUTE OF TECHNOLOGY

Combined Use of Polycarboxybetaine Coatings with a Selective FXIIa Inhibitor to Create Potent Anticoagulation without Bleeding during ECLS

Suji Shin[1*], Yeahwa Hong[1*], Umar Nasim[1], Helen Scala[1], Adel Akhavanmalayeri[1], Chenjue Tang[2], Anna K. Iacocca[1], Alexander S. Potchernikov[1], Emily Lannen[1], Shaoyi Jiang[2], Keith E. Cook[1,]

From [1]Biomedical Engineering, Carnegie Mellon University, Pittsburgh, PA USA
[2]Meinig School of Biomedical Engineering, Cornell University, Ithaca, NY USA

*Co-first authorship

Introduction: Thrombosis causes rapid failure of artificial lungs. Heparin is the clinical standard anticoagulant used to combat thrombosis but causes bleeding complications. Four-hour studies have demonstrated that a polycarboxybetaine (PCB) surface coatings and a selective FXIIa inhibitor, FXII900, can provide improved anticoagulation without increasing bleeding risk[1]. However, these studies were performed in anesthetized rabbits. This study assessed if the same is true over a period of up to 72 hours in conscious rabbits.

Methods: ECLS circuits were constructed with custom-built miniature artificial lungs (mini-lungs), which are composed of polycarbonate housing and polymethylpentene (PMP) fibers to closely mimic clinically available oxygenators. The circuits were attached to rabbits in an arteriovenous configuration to allow complete ambulation of the animals. Rabbits were assigned to one of three experimental groups: 1) Heparin with an uncoated circuit (n=4; activated clotting time, ACT, of 200-240s), 2) heparin with a PCB coated circuit (n=3, ACT of 200-240s), and 3) FXII900 with a PCB coated circuit (n=4; ACT titrated to 800-1500s). Blood flow was maintained between 35-45 mL/min with a Hoffman clamp. After attachment, ACT and activated partial thromboplastin time (aPTT) were measured to evaluate the extent of anticoagulation. Mini-lung blood flow resistance was used as a measure of clot formation within the device. Mini-lungs were considered failed when their blood flow resistance was three times the baseline value for two hours or 10 times the baseline at any point.

Results: The failure time (hr) of the Heparin group was 3.31 ± 3.54, followed by Heparin+PCB at 22.0 ± 21.9, and FXII900+PCB at 25.0 ± 25.6. The average resistance (mmHg/mL/min) of the Heparin group was 1803 ± 134.8, while Heparin+PCB and FXII900+PCB groups were lower at 440.7 ± 57.00 and 216.1 ± 3.576, respectively. The average ACT (s) of the Heparin and Heparin+PCB groups were similar at 229.0 ± 23.53 and 237.0 ± 12.21, while FXII900+PCB group had an average ACT of 1064 ± 89.46. Heparin and Heparin+PCB groups showed similar average aPTT (s) of 22.6 ± 3.10 and 22.7 ± 0.80 over the duration of the experiment, whereas FXII900+PCB was 197 ± 64.6.

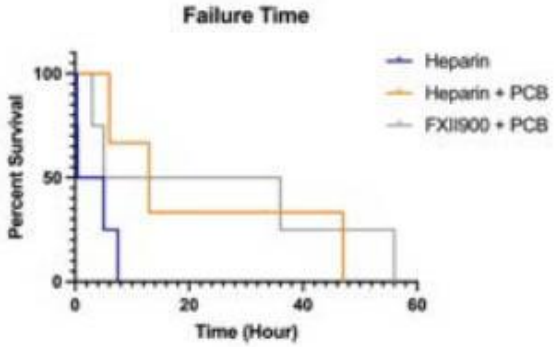

Figure 1. Kaplan-Meyer survival curve for device failure time

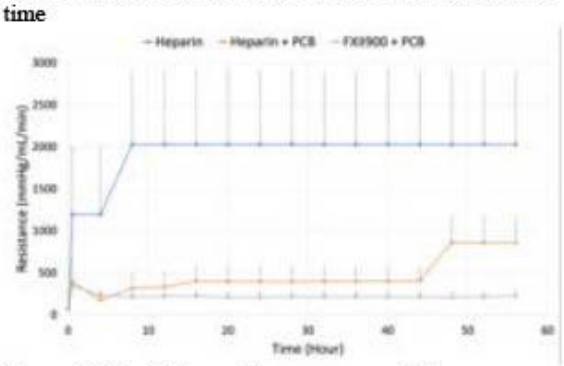

Figure 2. Blood flow resistance across mini-lungs

Conclusions: The preliminary results demonstrate that the PCB coating and FXII900 improved anticoagulation of the ECLS circuit leading to longer mean device failure time.

References:

1. Naito, N. et al. Biomaterials. 2021;272

Acknowledgments: This research was supported by the NIH R01HL157346-01A1. I would like to acknowledge and thank the members of Allegheny Singer Research Institute for their guidance and care of research animals.

DEI: Institutions should continue to establish mentorship programs, offer scholarships, and fundings targeted at underrepresented individuals to foster a DEI community.

STEVENS
INSTITUTE OF TECHNOLOGY

Establishing a Normative Cerebral Blood Flow Database in a Non-Concussed Population

Sophia Starzynski[1], Stephanie Iring-Sanchez[1], Mitchell M. Scheiman[3], Tara L Alvarez[1], Chang Yaramothu[2]
[1]Department of Biomedical Engineering, [2]School of Applied Engineering & Technology,
New Jersey Institute of Technology; [3]Pennsylvania College of Optometry, Salus University

Introduction: Traumatic brain injuries (TBI) resulting from an impact on the head are a significant health concern, particularly in sports-related concussions (1). The lack of understanding regarding concussion mechanisms has led to a gap in treatment guidelines, making research in sports medicine vital. This project aims to build a database of non-invasive physiological parameters that can be used in the future as a basis of comparison. The data is collected by stressing the oculomotor system and collecting cerebrovascular measures such as brain blood flow, blood pressure, heart rate, and respiration. By collecting pre-season baseline measures on athletes this project aims to determine if there is a correlation between cerebral blood flow and objective oculomotor measurements. Another aim is to determine if physiological measures differ based on sex, as this phenomenon has been alluded in previous literature.

Methods: Participants were recruited from the NCAA Division I athletic teams of the New Jersey Institute of Technology (NJIT) in Newark, NJ. Prior instances of brain injury, a medical screening questionnaire, and objective eye movements were collected after informed consent. Non-invasive techniques including ECG to measure heart rate, Finger plethysmography to measure blood pressure, transcranial Doppler to measure mid-cerebral blood velocity, duplex ultrasound to measure internal carotid flow, capnography to measure end-tidal CO2, and objective eye tracking in virtual reality headsets were utilized. These parameters were recorded simultaneously while the participant made various eye movements. The visual tasks included making eye movements such as horizontal and vertical saccades (side to side eye movements) and vergence jumps (eye movements in depth) during a specific amount of time. The eye movements tasks were repeated twice, where a visual endurance task of rapid repetitive eye movements was performed between the two tasks. Where the virtual reality headset tracked the eye movement to quantify peak velocity and accuracy. Group level analysis will investigate sex-based differences by stratifying data based on participants' sex at birth. By scrutinizing sex-related disparities, this research aims to identify potential variations in how males and females exhibit different physiological measures.

Results: The baseline study included 15 (9 males and 6 females) NCAA Division I athletes and students from NJIT. Average age was 18 ± 3 years. The mean mid-cerebral artery velocity during each of the tasks is shown in Figure 1. A general decrease in velocity is observed as the fatiguing visual tasks progressed.

Conclusions: The study established a foundation for physiological and oculomotor measures of young adult participants. The eye movements observed through the virtual reality headset and the collected cerebrovascular measures such as mid-cerebral blood velocity, blood pressure, ECG, and tidal CO2 waves show the stress placed on the oculomotor system reflected through the physiological changes.

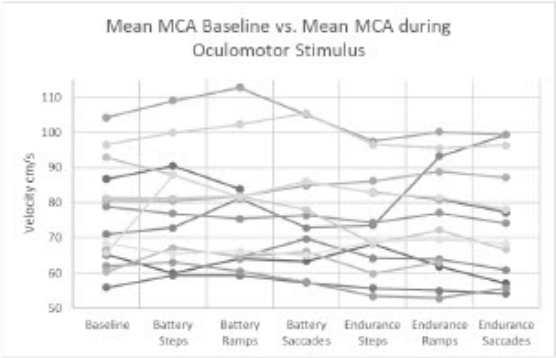

Figure 1. This graph shows the differences in the mean mid-cerebral artery velocity between baseline (at rest) and during different Oculomotor protocol moments.

Future work aims to collect post-concussion data from athletes who have suffered a head injury to determine the relationship between cerebral blood flow and oculomotor dysfunction by using internal carotid blood flow estimates of global blood flow during seated and supine position. Additionally, future studies should determine if there are gender based difference in physiological parameters. The ultimate goal is to determine the relationship between cerebral blood flow and oculomotor dysfunction in an attempt to establish carotid blood flow as a potential biomarker for concussion. A longitudinal comparison of injury data with the baseline should be conducted to assess recovery progress. The findings of this study can inform concussion management protocols for athletes.

References:

Stuss DT. J Neurol Neurosurg Psychitry.1989;52(6): 742-748.
Yaramothu C. Optom Vis Sci. 2021;98(6):636-643
Sankar, Sitara B Neurobiology of disease. 2019; 544-554.

Acknowledgments: This work is supported by NIH 1R01EY023261 to TLA

DEI: The field of bioengineering holds significant potential to address disparities in healthcare, such as creating affordable, user-friendly, and accessible solutions. Additionally have more data diversity, ensuring that research data collected on human participants are coming from a diverse and representative population, to reduce bias. Additionally, to broaden the participation of underrepresented groups in STEM, the field as a collective needs to put effort into outreach and education in these underrepresented areas.

STEVENS
INSTITUTE OF TECHNOLOGY

Time-Lapse Quantitative 3D Imaging of Outgrowth Formation from Ovarian Cancer Spheroid with Optical Coherence Tomography

Aleese Mukhamedjanova[1], Sadaf Farsinejad[2], Marcin Iwanicki[2], Shang Wang[1]
[1]Department of Biomedical Engineering, Stevens Institute of Technology, Hoboken, NJ 07030, USA
[2]Department of Chemistry and Chemical Biology, Stevens Institute of Technology, Hoboken, NJ 07030, USA

Introduction: Ovarian cancer (OC) was the cause of death for an estimated 12,180 women in the United States in 2022 [1]. 70% of OC patients present with synchronous metastases, and the 5-year survival rate for metastasized OC is only 29% [2]. This high occurrence rate may be facilitated by passive dissemination of OC cells through outgrowths extending and dissociating into the peritoneal cavity [3]. However, the mechanisms behind OC outgrowth formation have yet to be investigated. This pilot study employs optical coherence tomography (OCT) to establish a 3D quantitative imaging approach to reveal and study the process of outgrowth formation from OC spheroids, which addresses the technical need in further understanding OC metastasis.

Methods: Human high-grade serous ovarian adenocarcinoma HeyA8 cells were cultured in Gibco™ Dulbecco's Modified Eagle Medium/Nutrient Mixture F-12 (Thermo Fisher Scientific) supplemented with 5% (v/v) Gibco™ Fetal Bovine Serum (Thermo Fisher Scientific) and 1% (v/v) Gibco™ Penicillin-Streptomycin (Thermo Fisher Scientific). Spheroids were seeded using 150 and 1000 cells and reconstituted in 2% (v/v) Corning® Matrigel® Growth Factor Reduced Basement Membrane Matrix (Corning), which provides a physiologically relevant environment that supports morphological integrity and functional outgrowth. Three days after seeding, spheroids were transferred on top of 100% (v/v) Matrigel® and then maintained at 37°C with 5% CO_2 and 80% humidity for imaging.

We used a custom-built spectral-domain OCT system for OC imaging. The system employed a supercontinuum laser (SuperK EXTREME EXR-9 OCT laser, NKT Photonics) and had a central wavelength around 850 nm. The axial and transverse resolution were ~6 μm and ~9 μm, respectively. The A-scan rate was set as 100 kHz. Time-lapse volumetric OCT imaging was performed every 1 or 1.5 hours for about 20 hours. The 4D (3D+time) data were reconstructed with custom-developed program and visualized using the Imaris software (Oxford Instruments). The length of spheroid outgrowth was measured over time. Bright-field microscopic images were also taken of spheroids before and after OCT imaging to confirm the observations.

Results: The 150 cells-seeded (CS) spheroid (Fig. 1a) developed five outgrowths (Fig. 1b) with average length 172 μm and standard deviation 111 μm, suggesting outgrowths from the same spheroid can be heterogeneous. In contrast, the 1000 CS spheroid (Fig. 1c) developed three outgrowths (Fig. 1d) with average length 529 μm and standard deviation 110 μm, presenting a relatively faster growing rate. These suggest that primary OC tumor size could have an effect on the rate of outgrowth formation. Bright-field images of additional spheroids from the same 150 and 1000 CS batches are shown in Fig. 2 after outgrowth formation.

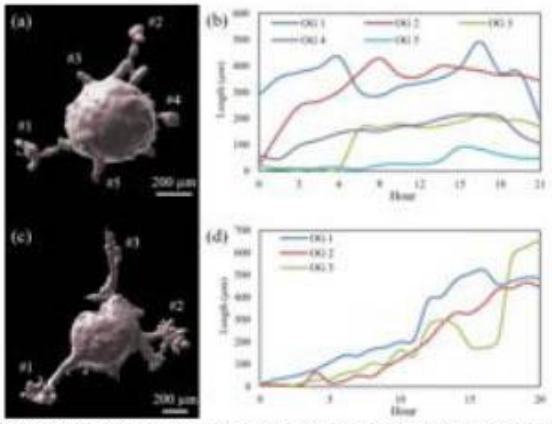

Figure 1. 3D surface reconstructions (a,c) and outgrowth lengths (b,d) of 150 CS (a,b) and 1000 CS (c,d) spheroids.

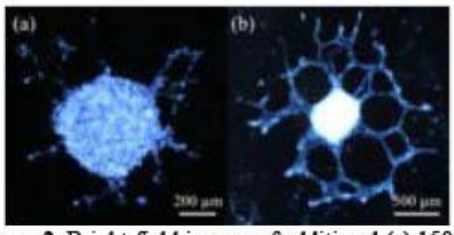

Figure 2. Bright-field images of additional (a) 150 CS and (b) 1000 CS spheroids post-outgrowth development.

Conclusions: With OC spheroid culture, OCT is useful for 4D imaging of spheroids and their outgrowths, providing a quantitative approach to assess phenotypic changes in OC growth and metastasis. From this pilot study, it appears that larger spheroids grow longer and more stable outgrowths at a faster rate, which interconnect to create web-like structures. This imaging approach is potentially useful to reveal tissue-level dynamics of OC dissemination into the peritoneal cavity.

References:

1. Siegel RL. CA Cancer J Clin. 2022;72(1):7-33
2. Wang Y. Front Surg. 2022;9
3. Alshehri S. Adv Biol. 2022;6(12)

Acknowledgements: This work was supported by the National Institutes of Health (R21CA256615). We thank Dr. Jingyu Sun for assistance in developing the protocol.

DEI: Racial disparities impact many aspects of reproductive and maternal health such as OC, maternal mortality, and preterm birth. These inequalities must be acknowledged when investigating mechanisms of reproductive pathologies and developing their interventions. It is similarly important to diversify the field to include relevant voices in reproductive biology research.

STEVENS
INSTITUTE OF TECHNOLOGY

A Surgical Navigation Framework for Image-Guided Transoral Robotic Surgery

Yuan Shi[1], Michael A. Kokko[1], Joseph A. Paydarfar[1, 2, 3], Ryan J. Halter[1, 3]
[1] Thayer School of Engineering, Dartmouth College, Hanover, NH; [2] Section of Otolaryngology, Audiology, and Maxillofacial Surgery, Department of Surgery, Dartmouth-Hitchcock Medical Center, Lebanon, NH; [3] Geisel School of Medicine, Dartmouth College, Hanover, NH

Introduction: Cancers of head and neck (oral cavity, pharynx, and larynx) are the 7th most common cancer in the world[1]. Transoral robotic surgery (TORS), usually performed with da Vinci Surgical Systems, is a minimally-invasive surgical alternative to traditional open surgery with improved oncologic and functional outcomes and reduced morbidity[2]. However, the lack of haptic feedback in TORS makes it challenging to assess the extent of tumor or identify critical structures, resulting in increased positive margin rates and neurovascular complications[3]. Surgical navigation with image guidance has shown success in reducing complications and improving dissection accuracy in non-TORS procedures[4], suggesting its potential in TORS to compensate for the sensory deficit. Previous work demonstrated the feasibility of intra-operative image guidance[5] and robotic instrument tracking in TORS[6], laying an essential foundation towards surgical navigation. This paper describes the development and evaluation of a surgical navigation framework to guide target localization in TORS.

Methods: *1. Instrument Tracking.* Custom adapters were designed to interface electromagnetic trackers (NDI, Waterloo, Ontario, CA) with robotic end effectors. Plus Server Launcher was used to broadcast tracking data to 3D Slicer through an OpenIGTLink connection. *2. Synchronized Visualization.* To enhance 3D intuition, we developed a pipeline to synchronize the CT-reconstructed 3D scene with stereo-endoscopic view of the surgical field by tracking the endoscope using an optical tracking system (NDI, Waterloo, Ontario, CA). Moreover, a heads-up display (HUD) was available to provide distance and angular offset between the instrument tip and target. Da Vinci Surgical System's TilePro feature (Intuitive Surgical, Sunnyvale, CA) enabled real-time display of the navigation view on surgeon's console. *3. Target Localization Study.* A simplified throat phantom was used to simulate the upper airway. Sixteen stainless steel beads were embedded as targets in right tonsil, left tonsil, and tongue base. An ear, nose, and throat (ENT) attending and four residents with various experience were asked to control a tracked instrument and place pins on embedded targets in two trials: (1) without navigation to mimic standard-of-care TORS, and (2) with navigation where real-time 3D guidance and HUD was available. Target localization error (TLE) was calculated as the Euclidean distance between each pair of pin tip and target.

Results: The TORS-experienced ENT attending (">10 times in the past year") achieved an average TLE of 4.60±3.29 mm in the non-navigation trial and reduced the error by 54% to 2.10 mm with navigation (p=0.0523) (Fig. 1). In both trials, the attending showed significantly better performance than other experience level groups. Residents with less TORS experience ("never" and "1-10 times in the past year") achieved significantly lower TLE in the navigation trial (p=0.0005 and 0.0000). The mean TLE and standard deviation were improved by 49% and 50% across all residents. All participants achieved TLEs below the 5 mm margin threshold with the assistance of navigation.

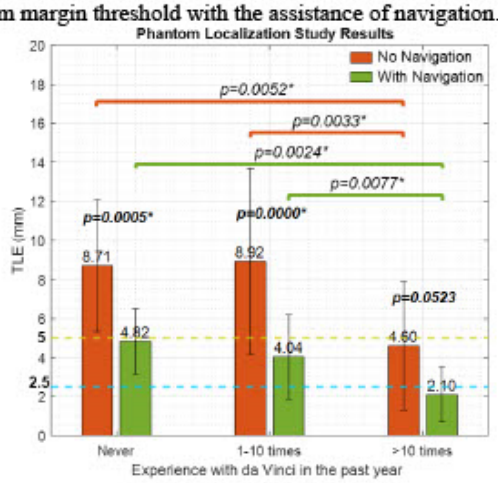

Figure 1. TLEs of different experience groups in non-navigation (red) and navigation (green) trials.

Conclusions: This work presented a real-time navigation framework for TORS that features robotic instrument tracking and a 3D guidance scene synchronized with endoscopic video to facilitate accurate localization. We successfully demonstrated the system efficacy in significantly reducing TLE when compared to the standard-of-care non-navigation approach ($p \leq 0.05$) in a multi-user phantom study. Future work includes improving performance of the navigation system and conducting target localization studies in ex-vivo animal tissues and cadaver specimens.

References:

1. Johnson DE, et al. Nat Rev Dis Primer. 2020;6(1):1-22.
2. Moore EJ, et al. Head Neck. 2018;40(4):747-755.
3. Zevallos JP, et al. Head Neck. 2016;38(3):402-409.
4. Stelter K, et al. Head Neck Surg. 2015;272(3):631-638.
5. Shi Y, et al. Proc. SPIE Med Imaging. 2021;11598.
6. Shi Y, et al. Proc. SPIE Med Imaging. 2022;12034.

Acknowledgements: This study was funded by National Cancer Institute (1R21CA246158-01A1). We would like to thank the study participants and Center for Surgical Innovation at Dartmouth Hitchcock Medical Center.

DEI: Our research has the potential to significantly reduce positive margin rates in TORS and provide patients from diverse backgrounds with more consistent and equitable healthcare outcomes. This growing field offers many mentorship and outreach opportunities for STEM-underrepresented persons and invites diverse perspectives to contribute to the growth of image-guided navigation technologies.

STEVENS
INSTITUTE OF TECHNOLOGY

High Through-Put Image-Based Modeling of Upper Airway Pressures Using Computational Fluid Dynamics

Jun Tao Cui, Kok Ren Choy, David Wootton, Sanghun Sin, Yubing Tong, Mark Wagshul, Jayaram Udupa, Raanan Arens
The Cooper Union, The Children's Hospital at Montefiore, Albert Einstein College of Medicine, University of Pennsylvania

Introduction: Obstructive sleep apnea syndrome (OSAS) is a prevalent condition characterized by repeated episodes of airway collapse during sleep, with negative long-term health effects. A better understanding of OSAS may improve diagnosis and treatment [1][2][3]. Previous papers used an image-based computational fluid dynamics (CFD) method to model the fluid mechanics in deforming upper airways. The method involved using CFD to simulate the flow in airway geometries obtained from dynamic MRI for frames in time [4][5]. However, only a small percentage of MRI frames could be processed, limited by the user inputs and long run times required of each simulation [6]. This is not ideal because OSAS patients exhibit different breathing behavior over the course of sleep, all of which should be considered to reveal a fuller picture of OSAS. We remedy the problems with the image-based CFD method with automation, and what we call *low-resolution CFD*.

Methods: This work used data from 5 OSAS patients. For each patient, data included upper airway geometry and flow rate for 960 frames in time over ~8 minutes. Airway geometries were segmented from dynamic MRI images using deep learning [7]. Low-resolution CFD that assumed steady flow and used coarse meshes modeled the flow in each frame (details in [8]). Coarse mesh settings were chosen from a mesh study that compared airway pressures resolved using low-resolution and gold standard CFD settings. Pressures were also estimated using engineering Bernoulli's equation, which included a loss from sudden area expansion. To represent pressure distributions, airway centerlines were calculated using the *Vascular Modeling Toolkit* [9], and average pressures were taken from sections along centerlines (Figure 1). Following the mesh study, meshing (*Altair HyperMesh 2022*) and CFD (*ANSYS Fluent 2022 R1*) were automated with Tcl and Python, to process 4800 frames from the 5 patients, on an engineering workstation (Lenovo, *AMD Ryzen Threadripper PRO 5975WX @ 3.59 GHz*) with 30 solver processes.

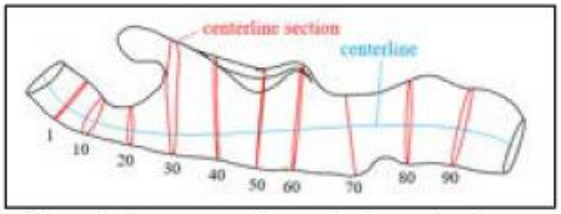

Figure 1. Airway geometry, centerline, and sections.

Results: Run times in the mesh study for low-resolution and gold standard CFD simulations were order(minutes) and order(weeks), respectively. Low-resolution CFD resolved pressures within ~7-18% of gold standard CFD, compared to the ~20-40% from engineering Bernoulli's equation (Figure 2). Of the 4800 frames, 3939 were processed at a rate of 1 frame per ~5 minutes. Frames were skipped due to airway geometries being unsuitable for meshing/CFD, and miscellaneous software bugs in the workflow.

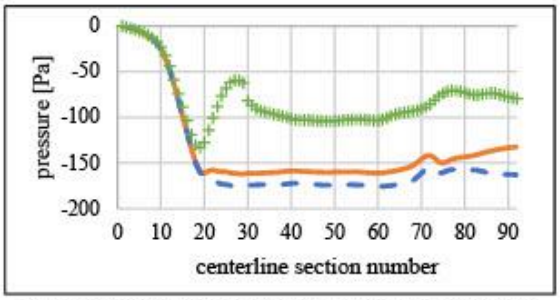

Figure 2. Centerline section pressures, low-resolution CFD (–), gold standard CFD (– –), and engineering Bernoulli's (+). Section numbers shown in Figure 1.

Conclusions: With accuracy tradeoffs, low-resolution CFD resolved the flow in ~4000 dynamic MRI frames in <1 month, a significant improvement from the years it would have taken higher resolution CFD to do the same on an affordable engineering workstation. More work is planned to optimize accuracy/speed tradeoffs for a wider range of airway constriction and flow rate. Our workflow allows for economical image-based CFD studies of OSAS from the new point of view of more resolution in time. The large datasets generated can be used to train neural networks for near real-time pressure profile estimates [8].

References:

1. Eckert DJ. JAppl Physiol. 2014;116(3):302-313.
2. Senaratna CV. et al. Sleep Med Rev. 2017;34:70-81.
3. Knauert M. et al. WJOHNS. 2015;1(1):17-27.
4. Wagshul ME. et al. MRM. 2013;70(6):1580-90
5. Persak SC. et al. JAppl Physiol. 2011;111(6):1819-27.
6. Choy K. et al. JAppl Physiol. 2021;131(2):532-543.
7. Xie L. et al. Medical Physics. 2022;49(1):324-342.
8. Cui JT. MS Thesis, The Cooper Union. 2023.
9. The Vascular Modeling Toolkit. vmtk.org.

Acknowledgements: The Cooper Union (Bioengineering Research Fellowship), NIH grant R01 HL130468.

DEI: OSAS is more likely to affect children from minority and lower socioeconomic status groups, and less likely to be treated. Healthcare disparities in OSAS may be reduced by (1) further research into environmental and economic factors that contribute to OSAS, (2) creation of outreach materials for public schools, (3) advocacy for increased healthcare access, and (4) reducing barriers to diagnosis and treatment such as cost and inconvenience. Our research may contribute to (4) by reducing cost and time required for advanced image-based diagnosis methods. Outreach initiatives that build on interests in computer games and graphics may broaden participation in the field of image-based diagnostics.

STEVENS
INSTITUTE OF TECHNOLOGY

Scenario in which ARDS therapeutic has differential effects on inflammation and oxygenation

Charul Singh, Carrie E. Perlman
Stevens Institute of Technology

Introduction: Acute respiratory distress syndrome is a life-threatening lung injury that is caused by inflammation in the lungs. Inflammation increases permeability of pulmonary capillaries, which leads to leakage of fluid and plasma proteins into alveolar air spaces and, consequently, reduced oxygenation. We previously found that sulforhodamine B (SRB), a non-toxic dye, lowers alveolar surface tension, T, and improves oxygenation in an excessive tidal volume, V_T, induced lung injury model (Wu, *J Appl. Physiol* 130: 1305, 2021). Here, we test the effect of SRB on oxygenation and inflammation in a two-hit, lung injury model that includes an inflammatory component thus is more clinically relevant.

Methods: To induce injury, at time t=0 hrs we anesthetize a Wistar-Han rat (male/female, n=12) and instill intratracheal lipopolysaccharide (LPS, 0.75 mg/kg). At t=24 hrs, we anesthetize again, perform a tracheotomy and mechanically ventilate with a 20-min injury period (excessive tidal volume, V_T: 50 ml/kg; positive end-expiratory pressure, PEEP: 0 cmH_2O; respiratory rate, RR: 75/min; fraction of inspired oxygen, F_IO_2: 1.0) and then a 4-hr support period (protective V_T: 6 ml/kg; PEEP: 4 cmH_2O; RR: 75/min; F_IO_2: initially 0.21, when peripheral arterial oxygen saturation, S_pO_2, decreases below 90%, increase F_IO_2 by 0.2). At the end of mechanical ventilation, we sacrifice. To test the effect of SRB, we study four groups: healthy unventilated control; untreated injury; prophylactic SRB (18.6 µg/kg IV at t=0 hrs coincident with LPS administration, estimate SRB is eliminated by ~ t=20 hrs); rescue SRB (185 ng/kg IV at t=24 hr at start of mechanical ventilation). We excise the lungs and collect bronchoalveolar lavage (BAL) fluid in which we quantify cytokines by ELISA.

Results: Compared with the healthy control group, in the untreated injury group final S_pO_2/F_IO_2 is reduced, indicating impaired oxygenation, and BAL cytokine levels are elevated, indicating inflammation (Figure). Prophylactic SRB does not affect inflammation but improves oxygenation. Rescue SRB limits inflammation but does not affect oxygenation.

Conclusions: By lowering T, SRB presumably limits ventilation induced lung injury (Wu, 2021) and, in turn, inflammation/BAL cytokines, edema liquid accumulation and impairment of oxygenation. However, only rescue not prophylactic SRB limits BAL cytokines in our model. We note, with the LPS dose we administer, cytokine levels have been shown to peak within hours and resolve by 24 hrs (Barnett-Vanes, *PLOS ONE* 11:e0142520, 2016). And we suspect that the prophylactic IV SRB has been eliminated by 24 hrs. Thus, the elevated cytokines in the prophylactic SRB group are likely caused by the mechanical ventilation, which administration of pre-ventilation rescue SRB is able to prevent. However LPS/ inflammation induced edema should not resolve in the time course of our experiments. Prophylacitc SRB is able to limit edema formation thus limit impairment of oxygenation. Rescue SRB is administered after marked edema accumulation thus not able to improve oxygenation. Going forward, we aim to administer rescue SRB at an intermediate time point and redose as necessary to maintain protection through the end of the experiment. That said, here we identify an interesting situation in which inflammation and oxygenation do not correlate.

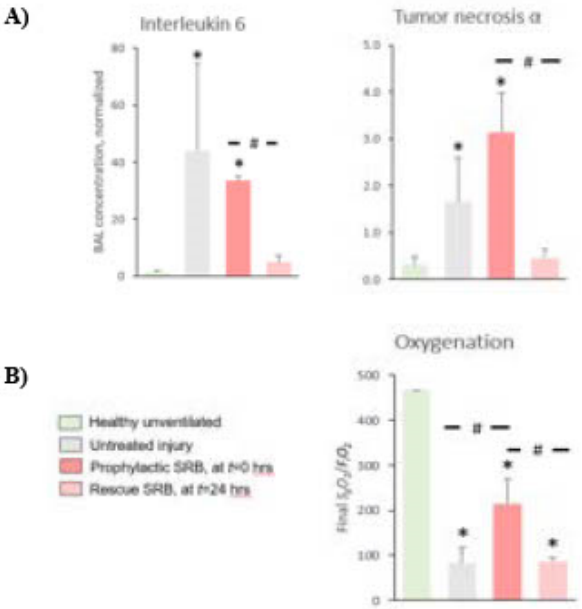

Figure: A) Cytokine levels in bronchoalveolar lavage (BAL) fluid normalized by level of interleukin 1β, which does not vary between groups. **B)** Final ratio of peripheral arterial oxygen saturation to fraction of inspired oxygen, S_pO_2/F_IO_2. Statistics: n=3/group, *p<0.05 vs. healthy unventilated group, #p<0.05 between indicated groups.

Acknowledgement: RO1 HL 113577

DEI: The current treatment for acute respiratory distress syndrome is mechanical ventilation (MV), Mechanical ventilation has a high mortality rate and is not always available in low income countries. Sulforhodamine B has the potential to reduce the need for MV as well as the mortality rate when MV is required. Thus SRB could improve the treatment of respiratory distress in low income countries.

STEVENS
INSTITUTE OF TECHNOLOGY

Bone Tissue Water as a Biomarker to Predict Proximal Femur Stiffness

Reshma Sudhesh[1], Michael W. Hast[2], Chamith S. Rajapakse[2,3], Nancy Pleshko[1], William Querido[1*]
[1]Department of Bioengineering, Temple University, Philadelphia, PA. *william.querido@temple.edu
[2]Department of Orthopaedic Surgery, University of Pennsylvania, Philadelphia, PA
[3]Department of Radiology, University of Pennsylvania, Philadelphia, PA

Introduction: The hallmark of osteoporosis is impaired bone mechanical strength, with hip fractures being one of its most debilitating threats. While bone mineral density (BMD) is the primary bone property used for the diagnosis of osteoporosis and the prediction of hip fracture risk, it is well recognized that assessment of BMD alone is a poor predictor of bone mechanics, missing nearly half of the women at high risk of hip fractures [1]. Bone mechanical function is determined by a combination of factors, including the extent of tissue-level hydration, which we have explored in this study. Water molecules in bone are present in different locations—generally defined as loosely or tightly bound to collagen or mineral. The term "loosely bound" refers to water present at the surface and interface of collagen fibrils and mineral crystals (physical adsorption), which can be removed through lyophilization. "Tightly bound" water is trapped within the collagen triple helix or the mineral crystal lattice (chemical adsorption), requiring high-temperature conditions for removal. The goal of this study is to investigate the relationship between stiffness and total and tightly bound bone water in the proximal femur of human cadaver bones.

Methods: Whole femurs from twelve donors were obtained from the National Disease Research Interchange. Stiffness at the proximal femur was assessed by testing under loading conditions simulating a sideways fall onto the hip at the Penn Center for Musculoskeletal Disorders Biomechanics Core. The water content of cortical and trabecular tissues was quantified in hydrated and lyophilized femoral neck cross-sections by near-infrared (NIR) spectroscopy, using a LabSpec 4 spectrometer (ASD, Longmont, CO) with a fiber optic probe. Spectral analysis was carried out to quantify peak intensity ratios that reflect total water content (hydrated samples; 5300/5800 cm^{-1}) and tightly bound water content (lyophilized samples; 5300/5800 cm^{-1}) [2]. Partial least squares (PLS) regression models were obtained by combining multiple tissue properties as explanatory variables to predict proximal femur stiffness. The methods are illustrated in Fig. 1.

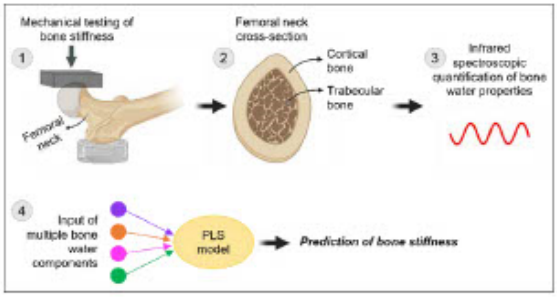

Figure 1. Methods and experimental approaches.

Results: Correlation analysis revealed a statistically significant negative relationship between bone stiffness and both total (r = -0.63) and tightly bound (r = -0.55) cortical and trabecular water content, respectively. Interestingly, we found markedly stronger models (R^2 = 0.80–0.92) by applying PLS regression to predict stiffness based on combinations of bone water properties, with the strongest model found when including water parameters from both total and tightly-bound, in cortical and trabecular (Fig. 2).

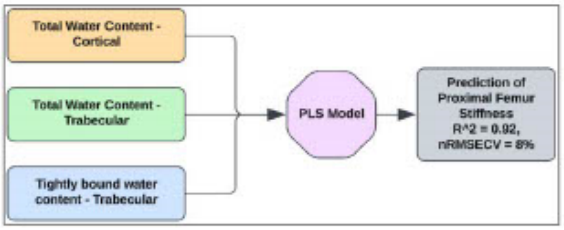

Figure 2. Strongest PLS model. nRMSECV: normalized root mean squared error of cross-validation.

Conclusions: Our findings highlight the role of bone water in proximal femur stiffness, indicating that lower tissue water content correlates with greater bone stiffness. This study sheds light on the potential of bone water as a critical biomarker for proximal femur mechanical function and, by extension, overall bone health. Future studies will focus on investigating how bone tissue composition and its relationship to bone strength differ in females and males, aiming to improve sex-specific fracture risk assessment to guide the prevention and treatment of skeletal diseases.

References:

1. Friedman AW. J Clin Rheumatol. 2006;12(2):70-77.
2. Querido W, Kandel S, Pleshko N. Molecules. 2021;26(4):922

Acknowledgments: Pennsylvania Department of Health PA Cure; Biomechanics Core at the Penn Center for Musculoskeletal Disorders (NIH/NIAMS P30AR069619)

DEI: We are committed to addressing healthcare disparities by innovating diagnostic strategies for skeletal diseases and fracture risk in a diverse population. We also aim to foster inclusivity by encouraging active participation and contributions from individuals underrepresented in STEM within the fields of bone and spectroscopy research.

STEVENS
INSTITUTE OF TECHNOLOGY

Exploring Lower Limb Sagittal Angles for Enhanced Human Activity Recognition

Zihang You, Neethan Ratnakumar, Xianlian Zhou.
Department of Biomedical Engineering, New Jersey Institute of Technology, Newark, NJ, USA.

Introduction: Goniometers, adept at measuring joint angles in both the sagittal and frontal planes, are particularly relevant for activities like walking and squatting. In Human Activity Recognition (HAR), considering the use of lower limb joint angles and velocity alone merits consideration to streamline sensor usage in assistive devices. The work of Camargo et al. [1] revealed that the sagittal and frontal angles provided by goniometers can enhance the accuracy of HAR. Movements such as walking and squatting primarily occur in the sagittal plane for key joints (hip, knee, and ankle). This specificity suggests a promising avenue for HAR: focusing on sagittal angles might suffice for assessing activities dominated by lower extremity movements, using either single or multiple goniometers. Moreover, the need for additional sensors such as Inertial Measurement Units (IMUs) to capture joint angular velocity can be circumvented. By deriving angular velocity with central differential method from the angle data collected by goniometers, we propose a novel approach to enhance HAR accuracy. This method leverages artificially generated joint angular velocities, utilizing only sagittal plane goniometers, thereby streamlining the process and potentially improving the effectiveness of HAR methodologies.

Methods: We used a comprehensive open-source dataset of lower extremity biomechanics [2], which include sagittal plane time series data from three goniometers on the right side of the body (at hip, knee and ankle) for 21 subjects, to recognize six activities, including standing, level ground walking, and the ascending and descending of stairs and ramps. Central difference method was used to generate corresponding angular velocities. We focused on using three neural network (NN) models: long short-term memory (LSTM), convolutional neural network-LSTM (CNN-LSTM) and multilayer perceptron (MLP) for HAR, all with direct input of time series windows (sampled at 200 Hz) instead of extracted features. LSTMs were chosen given their ability to learn and retain long-term dependencies in sequential data. The sliding window length was set at 50ms with an overlap of 50% with the intent for fast prediction. Each subject's data was divided into training and test sets with a ratio of 7:3 and the models were trained for each subject individually.

Results: We tested the performance of all possible combinations of the three goniometers, including just one goniometer, any combination of two goniometers, and all three goniometers. The mean classification accuracy and standard deviation averaged for all 21 subjects were recorded in Figure 1. When using only the time series of the angles provided by the goniometers, the HAR accuracy with 2 goniometers on one side of the body can reach between 80% to 85%, and up to 95% when 3 goniometers were applied. When using only a single goniometer, the accuracy is much lower, with a range from 50% to 65%. It was substantiated through rm-ANOVA analysis that increasing the number of goniometers significantly improves the HAR accuracy (all $p<0.05$), suggesting that the HAR accuracy rate is influenced by the number of input data channels. Nevertheless, for tests with single and two goniometers, the choices of the goniometers, as tested by a post-hoc paired t-test, have no significant impact on the HAR accuracy ($p>0.083$). After derived angular velocity is added into the dataset, the increase of HAR accuracy is significant to all three NN models (paired t-test, all $p<0.05$). The performance improvement of LSTM by adding angular velocity is the largest (close to 10%), followed by CNN-LSTM, and MLP is the least.

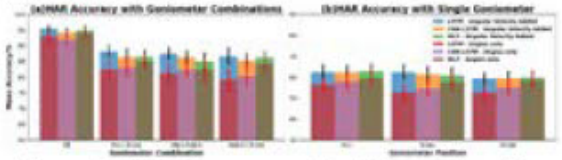

Figure 1. (a) HAR accuracy with all three goniometers and combinations of any two goniometers. (b) HAR accuracy with a single goniometer. Results with and without derived angular velocities are compared.

Conclusions: This work uses a publicly available dataset and tests the performance of three NN models for HAR with data collected from multiple goniometers mounted on a single side of the human lower limbs. Our results demonstrate that, with time series of the sagittal angles and a sliding window as short as 50ms, it is feasible to use 3 goniometers on one side of the human lower extremities to achieve over 90% HAR accuracy. After adding angular velocity as part of the data set, the accuracy of HAR can be improved significantly. For any combination of two goniometers, the accuracy of HAR can approach 90%, while the accuracy rate can exceed 95% when using three goniometers. We plan to further investigate the effects of sliding window length and overlap rate on the goniometer based HAR accuracy, in order to obtain lower latency in real-time applications such as the control of human exoskeletons or higher accuracy in health monitor that is less time critical. For wearable robots or exoskeleton applications, high HAR accuracy achieved by goniometer measures can potentially be replicated with exoskeleton joint encoders that measure both joint angle and velocities.

References:

1. J. Camargo et al. IEEE Transactions on Biomedical Engineering. 2021;68(5):1569-1578
2. J. Camargo et al. Journal of Biomechanics. 2021; vol. 119, p. 110320

DEI: By incorporating precise HARin the development of lower limb exoskeleton control techniques, our field can enhance rehabilitation for patients with conditions like muscle atrophy and spinal cord injuries, addressing healthcare disparities.

STEVENS
INSTITUTE OF TECHNOLOGY

Parafilm®-based low-cost rapid microfluidics for tumor cell sorting

M111

Mohoddeseh Mohammadi[1], Zhenglong Li [2], Swaprakash Yogeshwaran[1], Sagnik Basuray[2], Amir K Miri[1].
Department of Biomedical Engineering, New Jersey Institute of Technology (NJIT), Newark, NJ; Department of Chemical and Materials Engineering, NJIT, Newark, NJ

Introduction: Parafilm®-based Microfluidics technologies enable affordable, customizable, and high-throughput platforms suitable for individual lab use. Parafilm® is disposable, eliminating the need for complex cleaning and sterilization while microfluidic platforms allow to scale down biological processes and require very low volumes of reagents and cells. Here we describe a novel low-cost microfluidic cell sorter that operates in continuous flow at high sorting rates. The spiral inertial microfluidic device can achieve label-free, constant separation of cell mixtures with high throughput and efficiency. The device utilizes hydrodynamic forces acting on cells within a laminar flow, coupled with rotational drag due to the curvilinear microchannel geometry. A mixture of cells can be sorted directly from bulk media without encapsulation, contrasting agents, fluorescent tags, or labeling. We have successfully directed MSCs (Mesenchymal Stem Cells) and MDA-MB-231 (breast cancer cells) using the low-cost ($0.50) microfluidic chip. Cell sorting on microchips provides numerous advantages over conventional methods by reducing the size of necessary equipment, eliminating potentially biohazardous aerosols, and simplifying the complex protocols commonly associated with cell sorting. Additionally, microchip devices are well suited for parallelization, enabling complete lab-on-a-chip devices for cellular isolation, analysis, and experimental processing.

Methods: A Parafilm®-based microfluidic device, encompassing a tri-layer architecture, was utilized to investigate breast cancer cell dynamics (MDA-MB-231, Oct4-GFP tagged) under inertia. This device was designed with a first layer featuring a spiral configuration, a central layer with a single aperture, and a basal layer adopting a trident configuration. Silica glass slides were adopted as substrates for the microfluidic device as they were easy to assemble, and more reliable than flexible substrates. The Parafilm® sheets were adopted to prepare microchannel patterns and used as middle bonding layers in the hybrid "glass + double-sided tape + Parafilm® + double-sided tape + glass" systems. The device's entry point, located at the spiral first layer, facilitates the high-throughput and efficient stratification of cellular mixtures. The intermediate layer is an impermeable foundation for the upper and lower layers, preventing fluid leakage. The terminal layer functions as the egress for the size-based segregation of cells (Fig 1A.). This allows for precise manipulation and analysis of cell populations within a controlled microfluidic environment. The channel size was in the range of 100 to 1000 micrometers (Fig 1B.). The channels were infused with fluorescent Rhodamine Dye (Fig 1C.) and fluorescently tagged breast cancer cells (Fig 1D.) to visualize the microchannels in the different layers.

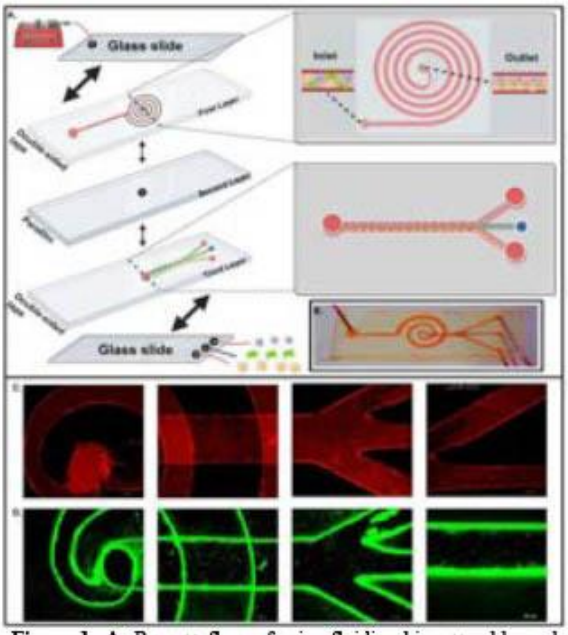

Figure 1. A. Process flow of microfluidic chip assembly and fabrication. **B.** Microfluidic setup with tubing connections and flow. **C.** Fluorescent microscopic imaging of microchannels infused with Rhodamine dye. **D.** Visualization of cancer cells in the spiral and trident-shaped microchannels.

Results: In this study, we chose a laser cutter over a plotter cutter for fabricating microchannels in Parafilm® sheets and double-sided tapes. The precision offered by the laser cutter is crucial as the dimensions of the channels directly impact the volumes of samples and reagents needed for assays. The three layers of the low-cost microchip were tightly sealed and the inlet and outlets were connected to tubes to complete the microfluidic setup. The infusion of fluorescent dye showed well-formed spiral patterns and continuous flow capabilities (50ul/min to 500ul/min). The presence of cells in channels provided proof-of-concept capabilities.

Conclusions: This research validated the practical application of a low-cost microfluidic chip using Parafilm® sheets and double-sided tape. The findings substantiate the feasibility and accuracy of employing laser cutting technology for detailed microfabrication tasks, highlighting its potential for economical and precise microscale patterning.

References:
1. Wanti A. et al. Science. 2018;6(26):972-1018
2. Li, Zhenglong, et al. Sensors and Actuators B: Chemical 404 (2024): 135212.

Acknowledgments: We acknowledge the support from NSF (2243506).

STEVENS
INSTITUTE OF TECHNOLOGY

Investigating CHIR99021 as a Regulator of Adipogenesis in the Treatment of Myotendinous Junction Injuries

Doga Oruc, Joseph W. Freeman.
Department of Biomedical Engineering, Rutgers, The State University of New Jersey, Piscataway, NJ.

Introduction: Severe myotendinous junction (MTJ) injuries exhibit fatty accumulation within and around the muscle, disrupting MTJ structure and compromising functionality. As a result, surgical suturing methods present longer rehabilitation times and a greater risk of re-injury [1,2]. This intramuscular fat accumulation is regulated by the WNT/β-catenin-dependent pathway. When a WNT molecule is absent, β-catenin levels decrease due to GSK3β-dependent phosphorylation, leading to an increase in proliferator-activated receptor gamma (PPARγ) expression.

This study investigates the effect of CHIR99021, a GSK3β inhibitor, on adipogenic differentiation of bone marrow-derived human mesenchymal stem cells (hMSCs) as a treatment for fat accumulation after MTJ repair. The administration of CHIR99021 indirectly suppresses PPARγ expression, thereby inhibiting the formation of lipid droplets in vitro. Based on our preliminary findings, we hypothesize that cytocompatible CHIR99021-loaded polymeric scaffolds can support muscle regeneration while limiting fatty infiltration of MTJ.

Methods: hMSCs were seeded at a density of 15,000 cells/cm^2 in growth medium (GM) (MEM α, nucleosides, no ascorbic acid, 10% FBS, 1% P/S) and switched to adipogenic differentiation medium (ADM) (GM supplemented with 0.1 µM dexamethasone, 1 µg/mL insulin, 0.2 mM indomethacin, 0.45 mM IBMX) with or without CHIR99021 [3]. CHIR99021 concentrations in ADM were adjusted to 0.5 µM, 1.0 µM, and 1.5 µM. Rosiglitazone was added to the adipogenic medium at a final concentration of 1 µM before use. Presto Blue Assay and LIVE/DEAD Viability/Cytotoxicity Kit were utilized to assess cell viability. Live and dead cell counts were obtained using Celigo Image Cytometer. Cells were fixed in 4% PFA and stained with Oil Red O to measure lipid formation as a sign of adipocyte differentiation. Lipid formation was quantified by assessing the absorbance of Oil Red O at 515 nm.

Results: The results obtained from Presto Blue and Live/Dead assays, collected at day 7 and day 14, (Figure 1) suggest that CHIR99021 does not negatively alter cellular metabolic activity or viability at the concentrations in this study. Administration of CHIR99021 in adipogenic cultures inhibited lipid formation, Figure 2. Cells cultured solely in ADM exhibit significantly higher lipid droplet formation compared to cells cultured with CHIR.

Conclusions: Our preliminary studies have demonstrated that CHIR99021 administration can inhibit lipid formation in adipogenic cultures of hMSCs without inducing cell death at administered concentrations. Our current focus is to examine the impact of CHIR99021 on adipose-derived human stem cells to demonstrate its ability to inhibit lipid formation in cells with a higher predisposition to adipogenic differentiation.

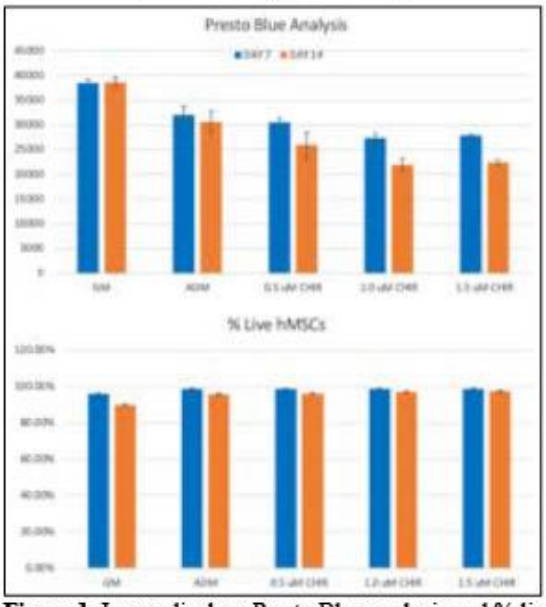

Figure 1. Image displays Presto Blue analysis and % live hMSCs cell counts from Live/Dead quantification.

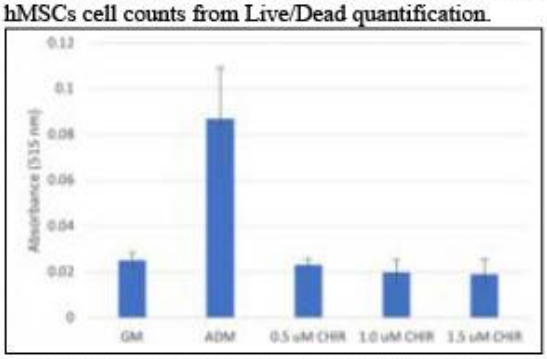

Figure 2. Image displays the quantification of Oil Red O. staining, two weeks after induction of differentiation.

The CHIR99021 concentrations from these studies will be integrated into scaffolds for MTJ repair. To our knowledge, this is the first attempt to limit fat buildup in the MTJ using scaffold-based approaches.

References:

1. Barton, E.R. et al. J. Orthop. Res. 2005; 23:259-265.
2. Maffulli N. et al. Transl Med UniSa. 2014; 12:14-18.
3. Fink T. et al. Methods in Molecular Biology. 2011; 698.

DEI: Eliminating fat accumulation in muscle after repair reduces rehabilitation time, making this treatment available to people from various economic backgrounds. This study includes training opportunities for STEM-underrepresented persons.

STEVENS
INSTITUTE OF TECHNOLOGY

Adapting and evaluating the advancing front model to design a biofabricated lung

Cecilia Padilla B.S.[1], Kelly R. Strong B.S.[1], Tracy Wan[1], Xi Ren Ph.D[1]., Keith E. Cook, Ph.D[1].
From [1]Biomedical Engineering Department, Carnegie Mellon University, Pittsburgh, PA, USA.

Introduction: Chronic obstructive pulmonary disease (COPD), the fourth leading cause of death in the US, is characterized by a gradual decline in respiratory function often coupled with life-threatening exacerbations. Currently, there are no restorative treatments for COPD other than lung transplantation. However, lung transplants are rare and not widely available to COPD patients. A biofabricated lung is being designed as a means of permanent respiratory support for patients with chronic lung disease. This lung is composed of type I collagen (COL I) parallel plates seeded with naturally anticoagulant endothelial cells on the blood side and epithelial cells on the air side to improve barrier function. However, an accurate oxygen transfer model is needed to design a compact biofabricated lung that transfers gas efficiently. Previously, Ukita et al. used an advancing front model to predict oxygen transfer (VO_2) in polydimethylsiloxane (PDMS) microchannel lungs.[1] Here, the model has been adapted, evaluated to predict the oxygen transfer of COL I channels, and subsequently used to design biofabricated lungs.

Methods: To evaluate the advancing front model, two groups of COL I channels (Corning, NY, USA) were cast with varying surface areas (see **Table 1**). To assess VO_2, the inner lumen of the COL I channels was perfused with 0.5 and 1.1 mL/min of citrated bovine blood (Lampire Biological Laboratories, Bucks County, PA) conditioned to AAMI venous blood conditions. Simultaneously, 100% oxygen with a flow rate equal to 2x the blood flow rate was provided over the outside of the channel. To calculate the experimental VO_2, inlet and outlet blood samples were taken and analyzed for PO_2, pH, and hemoglobin concentration with a blood gas analyzer (ABL800 FLEX, Radiometer, Brea, CA, USA). The theoretical VO_2 for each channel was calculated using the methods of Ukita et al. with the measured inlet PO_2, pH, and hemoglobin; membrane oxygen solubility equal to that of water; and a least squares determination of the COL I oxygen diffusivity. The resulting oxygen diffusivity, D, was compared to published values, and the experimental and theoretical outlet saturations were compared. Lastly, the optimized model was used to create a family of rat-scale biofabricated lung designs with a blood flow of 38.03 mL/min, 40% O_2 sweep gas, VO_2 of 2.2 mL O_2/min, wall shear stress of 15 dynes/cm^2, and wall thicknesses of 10, 20, and 40 µm.

Experimental Groups for Oxygen Transfer Studies

Group	Target lumen height (µm)	Actual lumen height (µm)	Membrane thickness (µm)	Effective length (cm)
Base case (N=6)	150	411.6 ± 101.8	25.8 ± 5.3	3
Increased surface area (N=3)	150	411.6 ± 101.8	25.8 ± 5.3	6

Table 1. Experimental groups for oxygen transfer studies

Results: The optimized COL I membrane D should be within the expected range $0.66\times10^{-5} \leq D \leq 3.85\times10^{-5}$ cm^2/s based on the literature. However, the optimized D was outside of this range. Thus, the model used $3.85\text{x}10^{-5}$ cm^2/s. As seen on Figure 1, the theoretical and predicted VO_2 values align well. The average percent error for the base group predictions was 14.2%, while the average percent error of the large surface area predictions was 8.7%. The priming volumes and number of COL I channels of the family of rat-scale biofabricated lungs with VO_2 of 2.2 mL O_2/min are shown in **Fig. 2**.

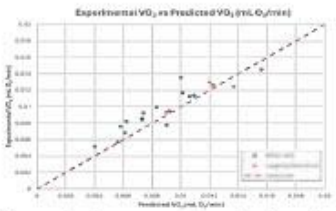

Figure 1. *Experimental vs. Predicted VO_2.* Base case is shown in dark blue while large surface area group in orange.

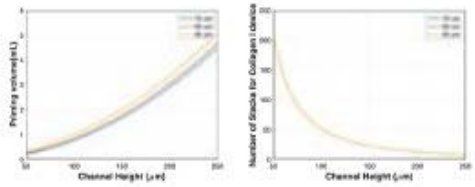

Figure 2. *Sample design curves for a rat-scale lung with a 2.2 mL/min VO2 with varying membrane thicknesses*

Conclusions: The advancing front model can be adapted to model the oxygen transfer of a COL I channel. The validated model is a great asset to efficiently design a biofabricated lung that meets performance requirements and is feasible to manufacture. It is important to note that it is challenging to maintain a uniform lumen height throughout the COL I channels due to the flexible nature of COL I. Thus, discrepancies between the model and experimental results can be attributed to the variability in channel height. Future studies will focus on completing data acquisition for channels with varying surface area, wall thicknesses, and lumen heights. In addition, the lumen height of the channels will be further assessed by perfusing a blood mimicking solution. The computational model will be revised as needed.

References:

1. Ukita R. ASAIO Journal. 2020; 66(9): 1054-1062.

Acknowledgements: This project is funded through Carnegie Mellon University's Bioengineered Organs Initiative, CMU Tobacco Settlement Funds, and the NSF Graduate Research Fellowship.

DEI: Institutions should continue to support and fund programs geared towards improving and fostering a DEI community in graduate school, such as the GEM fellowship.

STEVENS
INSTITUTE OF TECHNOLOGY

Increasing paracellular permeability in Airway Epithelial for effective Drug Delivery

Aneri Patel[1], Jiawen Chen[1], Mohammad Mir[1], Maria R. Hudock[2], Meghan R. Pinezich[2], Matthew Bacchetta[3,4], Gordana Vunjak-Novakovic[2], and Jinho Kim[1]

[1] Department of Biomedical Engineering, Stevens Institute of Technology, Hoboken, NJ, USA
[2] Department of Biomedical Engineering, Columbia University, New York, NY, USA
[3] Department of Cardiac Surgery, Vanderbilt University, Nashville, TN, USA
[4] Department of Biomedical Engineering, Vanderbilt University, Nashville, TN, USA

Introduction: Tight junctions (TJ) are vital for cell-cell adhesion and control substance movement between cells. From the dynamic protein structure of TJ, ZO-1 (zonula occludens-1) is crucial for TJ formation and maintenance. Researchers aim to use ZO-1's functionality to develop drug delivery systems that temporarily open these barriers, enhancing drug absorption and targeted delivery. Despite exploring various methods and molecules, challenges such as low efficacy and high toxicity hinder the practical application of these systems in pharmaceutical therapy.

Methods: To address this, we developed a clinical approach wielding the combined forces of osmotic pressure and mechanical stress **(Fig 1A)**. Isolated rat airway tissue was immersed in a hypertonic NaCl solution, simultaneously receiving low-frequency vibrations – a technique already clinically used **(Fig 1B)**. The treatment's effects were evaluated by observing the structure of ZO-1 proteins and assessing electrical properties using bioimpedance. Additionally, to evaluate the efficiency of particle incorporation through the modulated TJ, we employed dextran, a well-characterized macromolecule, as a permeability tracer.

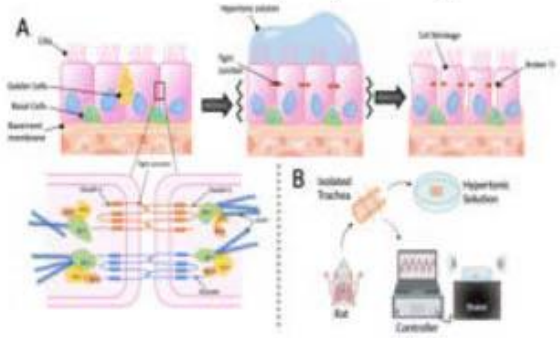

Figure 1. **A** Schematic representation of effect of hypertonic solution and mechanical stress on epithelial tight junction. **B** Experimental set-up of the treatment.

Results: As treatment intensity escalated, the impact on TJ became increasingly evident. ZO-1 protein structures, pristine in the control group, displayed progressive disruption with higher treatment intensity and longer exposure times **(Fig 2A)**. This structural disturbance aligns with bioimpedance data, indicating a significant reduction in tissue resistance as increased permeability allows for enhanced electrolyte movement **(Fig 2B)**. Dextran incorporation validated the increased permeability induced by the combined vibration and osmotic pressure treatment, suggesting its potential for delivery of the needed drug to the target cells **(Fig 2C)**.

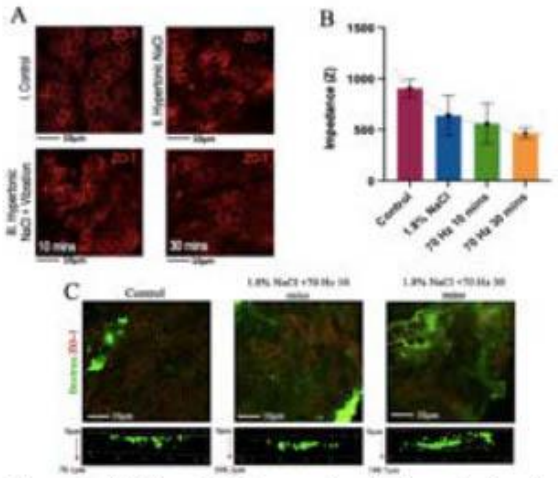

Figure 2. **A** Effect of the hypertonic solution and vibration at 10 mins (left) and 30 mins (right) on ZO-1 Proteins. **B** The electrical properties of the samples diminish as the permeability increases. **C** Dextran incubated after treatment.

Conclusions: Our refined combination of osmotic pressure and mechanical stress introduces an innovative approach to unlocking the potential of TJ in drug delivery. Prioritizing both efficacy and safety paves the way for personalized, targeted therapies to reach their full potential.

References:

1.Hogman M. et al. ERS journal. 2002; 20: 1444 -1448

Acknowledgements: The authors would like to acknowledge National Science Foundation (CAREER Award 2143620 to JK), New Jersey Health Foundation (PC 5-21 to JK), American Thoracic Society Foundation (Unrestricted Research Grant to JK), and National Institutes of Health (grants 2R01 HL120046, U01 HL134760 and P41 EB027062 to GVN) for funding support.

DEI: In furtherance of NEBEC's diversity initiative in Bioengineering, we focus on developing affordable diagnostic tools and treatments tailored to underserved communities. We aim to boost diversity by implementing targeted outreach programs and mentorship to STEM underrepresented individuals.

STEVENS
INSTITUTE OF TECHNOLOGY

Effects of Electrical Stimulation on Neural Cells for Tissue Regeneration Applications

Felicia Spadavecchia, Dr. Hongjun Wang
Department of Chemistry and Chemical Biology, Semcer Center for Healthcare Innovation, Stevens Institute of Technology

Introduction: Peripheral nerve injuries (PNIs) represent a significant medical challenge, with severe cases affecting 44 individuals per 1 million annually and incurring an average cost of $48,000 per patient. Existing treatments, such as neurorrhaphy, nerve conduits, and autografting, offer limited success; even autografts, considered as the gold standard, have a success rate of only 40%. Electrical stimulation (ES) has emerged as a promising intervention to enhance nerve regeneration, yet its mechanistic contributions remain unclear. Understanding the mechanism is critical to develop innovative treatments for PNIs. The role of calcium as an intracellular messenger was a particular focus, given its essential function in muscle contraction, hormone secretion, synaptic transmission, and gene transcription directly connected to neurite outgrowth[1]. Voltage-gated calcium channels (VGCCs), which open in response to electrical membrane potential changes, were hypothesized to be activated by ES, thus allowing for calcium influx and subsequent activation of intracellular signaling pathways and gene transcription within the nucleus. Furthermore, this study introduces a newly designed autoclavable device equipped with integrated electrodes for standard tissue culture dishes, enabling controllable delivery of ES to cells.

Materials and Methods: Rat pheochromocytoma cells (PC12) were cultured *in vitro* and seeded at a density of 5,000 cells/well in a 96-well plate. Cells were exposed to 50ng/mL nerve growth factor for neuronal differentiation and then electrically stimulated using parallel electrodes in each well for 1 hour daily using direct current (DC) from an external power source. An electrical stimulation device designed and produced in-house was used to deliver ES directly to the cells. The effects of ES on PC12 cells were evaluated *via* real-time imaging with a calcium probe to measure cytoplasmic calcium concentrations and immunofluorescent staining to quantify neurite outgrowth. Briefly, after 2 days of culture, cells were exposed to fluorescent calcium probe, Fluo-8AM, incubated for 30 min, then given 100mVcm^{-1} DC electrical stimulation while simultaneously undergoing real-time imaging with EVOS M7000 fluorescent microscope. After 6 consecutive days of ES *in vitro*, cells were fixed and stained for β3Tubulin and DAPI immunofluorescently. Images were recorded using 80i Nikon epifluorescent microscope and neurite lengths were quantified using NeuronJ, a plugin on *FIJI/ImageJ*.

Results: Although not significant, the results show a trend in the calcium concentration between groups as observed in Figure 1a. Notably, increased intracellular calcium levels were observed, supporting the hypothesis that ES-induced electric potential changes trigger VGCCs to facilitate calcium entry and activate downstream regenerative processes. Calcium influx through VGCCs can influence the growth cone dynamics and guide neurite outgrowth, which is a critical step in the regeneration of damaged nerves[2]. Further tests must be conducted to validate the results. Most importantly, the designed device (Figure 1b) ensures sterility and functionality, allowing for repeated use in biological experiments without compromising the culture environment. Our results indicate that ES through this new device enhanced neurite outgrowth, as illustrated in Figure 1d.

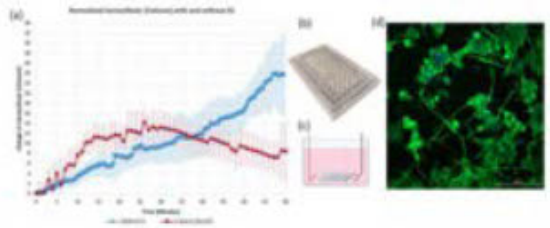

Figure 1. (a) Graph comparing intracellular calcium concentration with 100mV/cm ES compared to no ES. (b) 3D printed 96-well plate lid with electrodes for ES delivery. (c) Illustration of the electric field delivered from the electrodes onto the cells. (d) Representative immunofluorescence image of neurites stained with β3Tubulin (green) and DAPI (blue) in response to ES.

Conclusions: Initial investigations suggest that electrical stimulation mediates neuronal cells by altering membrane potential, which in turn triggers the opening of voltage-gated calcium channels, facilitating calcium entry into the cell. While the present results did not achieve statistical significance, there is a clear trend on the occurrence of calcium influx as observed in Figure 1a. Ongoing studies are conducted to reinforce these findings by increasing the sample size. Identifying the underlying intracellular mechanism in response to ES would be revolutionary in the field, opening doors to novel drug targets ultimately ending with the goal of promoting peripheral nerve regeneration. Most importantly, the convenience and efficacy of this new ES delivery device may revolutionize in vitro cellular research by providing a seamless, user-friendly interface for ES treatment in tissue culture. This device is pivotal for studies in nerve regeneration and repair.

References:

1. Merz, K., Herold, S. & Lie, D. C. EU J Neurosci **33**, 1078–1086 (2011).
2. Kamijo, S. et al. J Neurosci 38, 5551–5566 (2018).

Acknowledgement: This study was financially supported by the Army Medical Research and Material Command with award number W81XWH2211044.

DEI: The outcomes of this research have the potential to influence areas of high crime rates globally as this treatment can potentially save thousands of dollars in rehabilitation of PNIs. This research combines electrical engineering, tissue engineering, and biology, offering a wide breadth of options can that be accessible to a variety of underrepresented persons in the field.

STEVENS
INSTITUTE OF TECHNOLOGY

3D Printed Hierarchical Scaffolds with Embedded Fibrous Membranes to Spatially Control Stem Cell Behavior

Thi Ngoc Hang Truong[1] and Murat Guvendiren[1,2]
[1]Otto H. York Department of Chemical and Materials Engineering, New Jersey Institute of Technology
[2]Department of Biomedical Engineering, New Jersey Institute of Technology

Introduction: Extrusion-based 3D printing of biodegradable polymers have been commonly used to fabricate tissue engineering scaffolds with large pores (~500 mm). In addition to low cell retention (or seeding efficiency), these scaffolds do not allow spatially control distribution of seeded cells, which is particulary crucial for interface tissue engineering. To address these issues, we present a hydbrid 3D printing approach integrating airbrushed fibrous gelatin methacrylate (GelMA) hydrogel membranes into 3D printed polycaprolactone (PCL) scaffolds. Seeded stem distribution within the 3D scaffolds were controlled by adjusting the fiber density of the members. GelMA membranes were used to deliver biological cues control stem cell differentiation spatially. This is a promising platform to enable spatial control of cell distritbution and cellular behavior towards creating 3D scaffolds for tissue interfaces such as osteochonral tissue.

Methods: Scaffolds were fabricated by melt extrusion 3D printing of PCL pellets (Mw = 55,000 g/mol, Scientific Polymer) at 180°C. Airbrushing solution was prepared by dissolving either PCL (Mw = 80,000 g/mol, Scientific Polymer) in chloroform or GelMA in Acetic acid solution (90%, v/v). The concentration of solution, applied pressure, and airbrushing time were varied to optimize airbrushing parameters. For cell studies, hMSC (passage 5, Lonza) were cultured on the scaffolds which were coated with fibronectin solution (Invitrogen). Scaffolds were collected at culture day 1, 4, and 7 and stained for F-actin (Alexa FluorTM 488 phalloidin) and cell nuclei (DAPI).

Results: PCL/PCL hydrid scaffolds were fabricated by airbrushing fibrous PCL membrane layer on top of 2 layers of 3D printed PCL scaffold, and this process was repeated as needed to develop a large-scale scaffold. Design of Experiments (DoE) was used to optimize the airbrushing conditions to control fiber density to create permissive and inhibitory membranes (Fig. 1A). When cells were seeded on the top, fluorescent images (crosssectional view) confirmed cell penetration for through the membrane for low-density permissive membranes whereas high-density membranes inhibited cell penetration (Fig. 1B). To investigate our ability to control stem cell distribution within our scaffolds, we fabricated two sets of scaffolds composed of three membranes (low, high and low *(LHL)*; or low, low, low *(LLL)*) placed equally distanced from the surface of the scaffold after each 2-print layers. The scaffods were first seeded with green-labelled cells from top. The scaffold was then turned upside down and seeded with red-labelled cells. Fluorescent images (Fig.1C) and quantitative analysis (not shown) showed that the *LHL* membranes led to biphasic distribution of the green- and red- labelled cells (high density membrane inhibiting mixing of the cells) whereas *LLL* membranes led to gradual mixing of the cells.

Although PCL membranes allowed spatial control of seeded cell distribution, they were not suitable for delivering biological cues. To achive this, we developed gelatin (Gel) and gelatin methacrylate (GelMA) fibrous membranes. We were able to control the fiber density by adjusting airbrushing parameters. Fig. 1D shows optical (top) and SEM (bottom) images of the GelMA fibrous membranes. Here, membranes were crosslinked with glutaraldehyde and methacrylates were used for attaching peptides with cysteine moieties such as integrin binding RGD peptide.

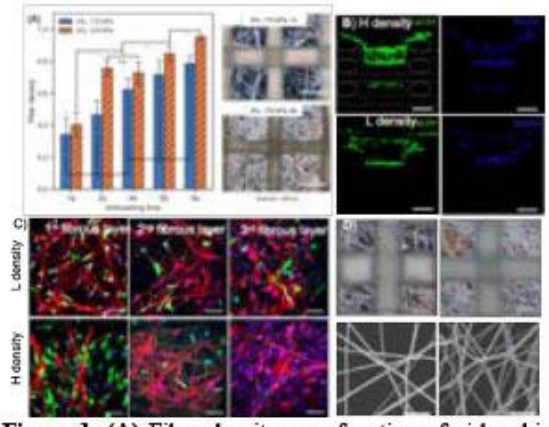

Figure 1. (A) Fiber density as a function of airbrushing time, and optical images showing the distinct fiber densities, scale bars are 500 µm. (B) Cross-sectional two-photon microscopy images showing F-actin (green) and cell nuclei (blue) within the scaffolds with low-density and high-density fibers on Day 1, scale bars are 300 µm. (C) Confocal images showing the distribution of hMSC (labeled with green or red probes) in three different fiber membrane layers scaffolds on Day 7, scale bars are 100 µm. (D) Optical images and SEM images showing the fiber of GelMA with different densities.

Conclusions and Ongoing Work: We successfully developed PCL/PCL hybrid scaffolds to control seeded stem cell distribution within the scaffolds. Cellular penetration within 3D printed scaffolds was controlled with the fibrous membranes. We demonstrated the fabrication of hybrid PCL/GelMA scaffolds with controlled GelMA membrane fiber density. We are currently applying this scaffold to spatially deliver osteogenic (bone) differentiation factors to control stem cell differentiation.

References: 1. Liaw-CY. et al. AIChEJ. 2021;67(12).

Acknowledgements: We acknowledge the funding from NSF CAREER- 204479

STEVENS
INSTITUTE OF TECHNOLOGY

Select NSAIDs Promote Peripheral Nerve Growth through PPARγ Activation

Jarin Tusnim, Karl Chelala, Jonathan M. Grasman.
Department of Biomedical Engineering, New Jersey Institute of Technology, Newark, NJ, USA.

Introduction: Peripheral nerve injury (PNI) is prevalent, with 20 million recorded cases annually in the US (1). The gold standard for peripheral nerve repair (PNR) is autologous nerve transplantation, but these methods are limited by the generation of an additional surgical site, donor-site morbidity, and neuroma formation at the site of harvest. Appropriately targeted drug compounds have the potential to influence axonal growth, however, the rate of failure in drug discovery is high (2). Therefore, we propose to repurpose commonly used nonsteroidal anti-inflammatory drugs (NSAIDs) to assess their role in PNR, which should facilitate an easier transition into the clinic. We have developed an ***in vitro*** hollow channel collagen gel model that successfully supports neuronal network formation (3). We previously tested ibuprofen, indomethacin, and suramin in our model as a proof of concept study to screen potential compounds to study PNR, and identified that ibuprofen and indomethacin significantly increased axonal length while suramin, which is a neurotoxin, inhibited axonal growth. In the present study, our goal is to investigate the underlying mechanism of axonal growth by NSAIDs to identify a common target for developing therapeutics to treat PNI. Ibuprofen and indomethacin share similar structural features with other peroxisome proliferator-activated receptor gamma (PPARγ) agonists, and ibuprofen has been shown to enhance axonal growth via PPARγ in the central nervous system (4). Therefore, we hypothesize that ibuprofen and indomethacin will significantly enhance axonal growth for PNR via activation of PPARγ in neurons independent of their primary function of reducing cyclooxygenase (COX).

Methods: Using polydimethylsiloxane (PDMS) molds and needles, hollow channels within collagen gels were fabricated as we previously described (3). DRGs isolated from E16 rat embryos were seeded inside hollow channels and incubated with medium supplemented with optimized drug solutions or controls for 5 days. After incubation, the constructs were fixed, immunostained, and both average and maximum axonal lengths were quantified using ImageJ.

Results: To identify whether ibuprofen and indomethacin enhance axonal growth by activating PPARγ, we seeded DRGs in presence of these drugs along with a known PPARγ antagonist, GW9662, or a known PPARγ agonist, GW1929. Representative images show axons growing from explants seeded inside the channel (Fig 1 A-D), notably in presence of indomethacin axons appear longer (Fig 1B). When constructs were cultured with GW9662, we observed noticeably shorter axonal growth (Fig 1C). Interestingly, the addition of GW9662 to indomethacin cultures inhibited the axonal growth-enhancing effect of indomethacin (Fig 1D). Quantitative analysis involved measuring the average and maximum length of every axon from each explant. These results revealed that indomethacin and GW1929 significantly enhanced axonal growth compared to all other groups (Fig 1E). The presence of GW9662 significantly decreased axonal growth in all conditions. Our current research involves investigating the role of NSAIDs in neuronal function as well as silencing PPARγ to confirm our proposed mechanism that NSAIDs work as PPARγ agonists in PNR.

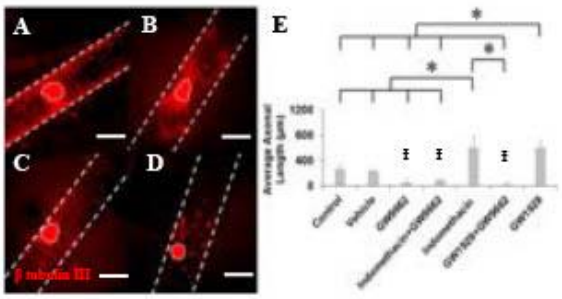

Figure 1. Representative images of axonal growth from DRGs inside hollow channels with (A) Control(no drug), (B) Indomethacin, (C) GW9662, (D) Indomethacin + GW9662. Scale: 500 μm, dotted lines denote explant bodies and hatched line represents the channels. (E) Quantification of average axonal length. * indicates statistical significance between groups and ǂ indicates statistical significance with control and vehicle by one-way ANOVA with post hoc Tukey test ($p<0.05$). Sample size N= 9.

Conclusions: We determined that NSAIDs, ibuprofen and indomethacin, enhance axonal growth by activating PPARγ. While positive outcomes in terms of axonal growth are highly promising, evaluating the impact of the drugs on neuronal function through techniques like calcium imaging will add depth to the understanding of its potential therapeutic role in nerve regeneration. Thus, our future work will aim to test the effect of these NSAIDs on neuronal function using calcium imaging to treat PNI.

References:

1. L.Fernendez et al. JHS. 2018;43 (4): 368-373
2. Takebe et al Clin Transl Sci. 2018; 11(6): 597–606.
3. Grasman et al. Adv Funct Mater. 2018; (48): 1803822
4. Dill et al. J. Neurosci. 2010; 30 (3): 963-972

DEI: Drug repurposing of NSAIDs makes PNI treatment more affordable and accessible to all, reducing economic disparities. This opens participatory opportunities to involve diverse scientists, clinicians, patient advocates, and trainees across the translational pipeline. Our laboratory invites individuals from underrepresented groups to participate in research to boost awareness and promote inclusion.

STEVENS
INSTITUTE OF TECHNOLOGY

Persistent Post Concussive Symptoms with related Convergence Insufficiency patients within a longitudinal therapeutic intervention

Anthony Crockett[1], Farzin Hajebrahimi PhD[1], Mitchell Scheiman OD PhD[1,2,4] Arlene Goodman MD[3], Melissa Noble MSW[1], Christina Master MD[4], Kate Rowd MS[4], Rebecca Baro OTD OTR/L[2], Josie A. Bachman OTD OTR/L[2], Suril Gohel PhD[5], Tara L. Alvarez PhD[1,2]
[1]New Jersey Institute of Technology, [2]Salus University, [3]Somerset Pediatric Group, [4]Children's Hospital of Philadelphia [5]Rutgers University

Introduction: Convergence insufficiency (CI) is a binocular vision dysfunction where the eyes fail to successfully maintain single and clear vision at near. Patients with CI, experience symptoms such as doubled and blurry vision, eye fatigue, and headaches. These symptoms make daily living tasks such as reading or using a computer challenging. Importantly, CI is a prevalent factor among patients with mild traumatic brain injury (mTBI) with persistent post-concussion symptoms (PPCS) and is known as PPCS-CI [1]. Previous research on the effectiveness of the Office-Based Vergence and Accommodation Therapy (OBVAT) has shown that patients with CI will benefit from OBVAT [2]. However, whether PPCS-CI patients will benefit from immediate OBVAT or will the symptoms subside due to a natural recovery is not clear. Additionally, no consensus is reported on the dosage of OBVAT after concussion is available. Therefore, the current research studied how patients with PPCS-CI are impacted from concussion, what the difference between the effectiveness of the OBVAT in immediate intervention and natural recovery is, and which dosage of OBVAT (12 sessions of OBVAT compared to 16 sessions) is recommended for PPCS-CI patients to alleviate their CI-related symptoms.

Methods: Patients were diagnosed with PPCS by a concussion specialist (co-author AG or CM), and diagnosed as PPCS-CI by an optometrist (co-author MS). Patients with PPCS-CI were randomly allocated to immediately receive 12 sessions of OBVAT (immediate group) or to receive no OBVAT for 6 weeks (natural recovery group). Patients in the immediate group received 4 additional sessions of OBVAT and patients in the natural recovery group received 16 OBVAT sessions after the 6 weeks of natural recovery. Every patient's CI-related symptoms were investigated using the Convergence Insufficiency Symptom Survey (CISS) [3,4]. This survey is a validated outcome measure in the treatment of the CI and a score of 16 points or higher is the criterion used to classify patients as CI. CISS was investigated for every subject regarding the time before injury (preinjury), after injury (baseline), after 12 sessions of OBVAT in the immediate group or 6 weeks of natural recovery in the natural recovery group (outcome 1), and after 2 weeks of additional 4 sessions of OBVAT in the immediate group or 16 sessions of OBVAT in the natural recovery group (outcome 2).

Results: Patients in both groups were relatively similar before injury and at the baseline (Figure 1). Patients in the immediate group showed substantial decrease in the symptoms after 12 sessions of the OBVAT. Although symptoms decreased further after receiving four additional OBVAT sessions, the change was not substantial (Figure 1). Patients in the natural recovery group continued to have symptoms during their waiting period for 6 weeks. However, their symptoms subsided after receiving 16 sessions of OBVAT at the end of natural recovery period (Figure 1).

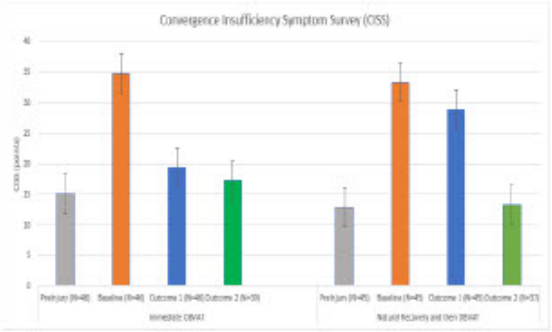

Figure 1. Changes in the CISS scores, before and after concussion, and after receiving immediate OBVAT compared to natural recovery.

Conclusions: The results of the current study show that patients with PPCS-CI will experience CI-related symptoms after experiencing a concussion, compared to their preinjury assessment with lower symptoms. While both groups can benefit from OBVAT, patients in the natural recovery will continue to suffer from CI-related symptoms during the waiting period in the natural recovery. Notably, patients will benefit from immediate OBVAT soon after the concussion. The results of the current research show that patients with OBVAT will benefit from the immediate OBVAT, and even shorter dosage of the OBVAT will also be beneficial for the patients. In conclusion, patients with PPCI-CI benefit from immediate OBVAT even with smaller dosage of 12 OBVAT sessions.

References:

1. Scheiman MTL *et. al.*, Clin Pediatr, 2016
2. Alvarez, TL *et. al.*, Optometry and vision science, 2020
3. Borsting E *et. al.*, Optometry & Vision Science, 2003.
4. Rouse M.W. *et. al.*, Ophthalmic and Physiological Optics, 2004

Acknowledgements: This research was supported by NIH EYR01EY023261 to TLA.

DEI: Concussion impacts males and females and may lead to personalized therapeutic interventions.

STEVENS
INSTITUTE OF TECHNOLOGY

Detection of neuronal modulation by impedance spectroscopy

S. Omidi[1], G. Fabi[3], X. Wang[3], J. C. M. Hwang[3], Y. Berdichevsky[1,2].
[1]Deptartment of Bioengineering, [2]Deptartment of Electrical and Computer Engineering, Lehigh University, Bethlehem, PA;
[3]Deptartment of Materials Science and Engineering, Cornell University, Ithaca, NY

Introduction: Examination of dielectric properties of cells and tissues at radio- and micro-wave frequencies led to identification of relaxation processes occurring in different frequency ranges. These processes have been correlated with physiological mechanisms linked with cell disease states, enabling development of novel, label-free diagnostics, such as microwave-based stroke detection. However, spectroscopy in the megahertz and gigahertz range has not, up to now, been used to examine activity-related processes in neurons. Several physiological processes occurring in active neurons, such as synaptic vesicle cycling and changes in ionic concentrations and water content, may potentially cause changes in dielectric properties in this frequency range. Ability to detect these processes in brain tissues in a label-free manner, with high time resolution, may lead to improved understanding of neuronal function and mechanisms of neuromodulation. Here, we examined whether activity-dependent changes in neuronal properties can be detected using wideband spectroscopy.

Methods: We developed a microfabricated array of eight gold-titanium grounded coplanar waveguides (GCPWs) on a glass waver. A polydimethylsiloxane (PDMS) well was mounted on top of the exposed portion of the array. We then placed 3D spheroids of rat cortical cells into the PDMS wells (one well per array chip) and allowed the spheroids to attach to the waveguides over the course of 2-3 days. Spheroids expressed channelrhodopsin-2 (ChR2) for optogenetic activation, and red fluorescent calcium indicator jRGECO1a. We then placed spheroid-containing arrays on an inverted microscope with a patterned light stimulator that allowed us to modulate activity of neurons in the spheroids. The waveguides were connected to a vector network analyzer with a bandwidth of 9 KHz to 9 GHz. Transmission and reflection spectra were taken twice per second while activity of neurons was modulated.

Results: We found that a correlation between transmission of electromagnetic waves in the gigahertz range through the waveguides and modulated activity in the spheroid. Figure 1 shows a the ΔF/F trace of neural activity, blue lines show the optical modulation periods, and the heatmap corresponds the magnitude of transmittion ($|\Delta S| = |S| - |S_{baseline}|$) for 0.07 to 9 GHz. We also found that disinhibition of the spheroids with bicuculine resulted in increased amplitude of neuronal activity and changes in megahertz and gigahertz transmission. The time domain analysis led us to find that the temporal changes in transmission during neural modulation has an exponential behavior until reach a stable maximum, and then decay with an undershoot after modulation is finished to recover to the rest state.

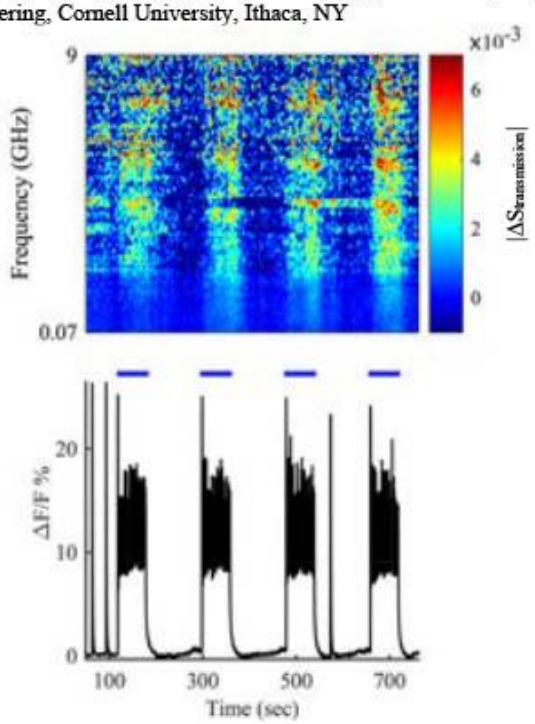

Figure 1. A ΔF/F trace of neuro actvivity with optical modulation as blue lines on top it. The heatmap show the transmission changes in time and frequecnty domain. Time asix for both are same.

Conclusions: We were able to successfully modulate the neural activity using optogenetic for an in-vitro 3D neural spheroid model. Our electromagnetic measurements led to understand the changes in transmission in frequency and time domain during neuromodulation. This study demonstrates first evidence that activity-associated changes in neuronal dielectric properties can be detected at this frequency range.

Acknowledgements: This study has been supported by the Air Force Office of Scientific Research (AFOSR).

STEVENS
INSTITUTE OF TECHNOLOGY

Understanding the Pathophysiology of Persistent Post Concussion Symptoms with Convergence Insufficiency

Soham Shashikumar[1], Christopher Morris M.S. [1], Sophia Starzynski[1], Mitchell Scheiman OD PhD[2], Arlene Goodman MD[3], Melissa Noble MSW[1], Stephanie Iring-Sanchez PhD[1], Tara L Alvarez PhD[1]
[1]New Jersey Institute of Technology, [2]Salus University, [3]Somerset Pediatric Group

Introduction: Convergence insufficiency (CI) is a vision dysfunction where the eyes struggle to maintain binocular vision while performing activities at near like reading. Symptoms include blurry and double vision, eyestrain, and headaches making tasks like reading or using a computer difficult. About half of the traumatic brain injury (TBI) patients with persistent post-concussion symptoms (PPCS) are diagnosed with CI [1]. Current literature on PPCS-CI is focused on optometric testing, lacking insights into the pathophysiological changes affecting multiple brain regions. Therefore, this study investigated cerebrovascular differences following OBVAT in concussed subjects, as well as positional differences in physiology, aiming to establish a better physiological profile for PPCS-CI.

Methods: Participants were clinically diagnosed as having a concussion by a concussion specialist (co-author AG) and diagnosed as having CI by an optometrist (co-author MS). PPCS-CI participants completed eye movement tasks were completed in a virtual reality headset while physiological recordings were taken in LabChart. The main outcome measurements include internal carotid cerebral blood flow, mid-cerebral artery blood flow velocity, heart rate, blood pressure and respiration. Internal carotid and mid-cerebral artery measurements were also taken using a TCD doppler. Physiological measurements were segregated based upon rest versus disparity vergence eye movement tasks and analyzed in LabChart. Doppler recordings were analyzed in MAUI and compiled with LabChart physiology data in MATLAB to calculate carotid cerebral blood flow and mid-cerebral artery velocity. Within a randomized clinical trial, measures were compared at baseline upon entering study and after completing 16 one-hour sessions of office based vergence and accommodative therapy (OBVAT).

Results: In analyzing sex differences in middle-cerebral artery velocity (MCAv), male participants with PPCS-CI demonstrated an elevated baseline values compared to females. MCAv was increased in men overall to a greater extent than women (see Figure 1).

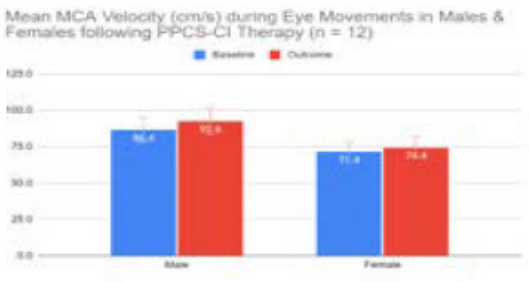

***Figure 1**. Mean MCA velocity (cm/s) in concussed males (n=4) and females (n=8) before and after OBVAT indicates a greater increase in males than females.*

Comparing carotid cerebral blood flow (CBF) for both patients in the seated and supine position showed an increase in the seated position following OBVAT and a decrease in the supine position (see Figure 2).

***Figure 2.** Percent change in mean carotid CBF before and after OBVAT, both in the seated and supine positions. Carotid CBF increased in the seated position and decreased in the supine following OBVAT (n =3).*

Conclusions: Following OBVAT, male participants entered a compensatory state to accommodate the recovery process. Female participants likely begin compensating earlier and return to a baseline MCAv value following OBVAT. Carotid CBF is known to increase following concussions as a compensatory mechanism, but interestingly, it was shown to remain elevated in the seated position. There is a greater CBF demand in the supine position, so CBF reduction and thereby recovery may be delayed in the seated position. While pilot data hold promise, more patients need to be studied to determine whether the results observed here generalize to a larger population. Further analysis could also consider disparities in physiological recovery following immediate versus delayed OBVAT.

References:

1. Master, T.L Scheiman M *et. al* Clin Pediatr 2016;55(3):260-7.
2. Alvarez TL, et al. Vision Research 2021;185:58-67.

Acknowledgements: This research was supported by NIH EYR01EY023261 to TLA.

DEI: Concussion impacts males and females. Our research is studying whether an anatomical sex difference impacts physiological recovery of PPCS-CI. This can lead to more personalized treatment and more effective patient prognoses, as compared to using a generalized treatment approach for males and females.

STEVENS
INSTITUTE OF TECHNOLOGY

Link between Neural Activity and Trial Aligned Respiration in Non-Human Primates

Emily Skog[1], Deepa Issar[1], Madison Grigg[1], Matthew Smith[1,2], and Jana Kainerstorfer[1,2]
[1]*Biomedical Engineering Department, Carnegie Mellon University, 5000 Forbes Avenue, Pittsburgh, PA 15213*
[2]*Neuroscience Institute, Carnegie Mellon University, 5000 Forbes Avenue, Pittsburgh, PA 15213*

Introduction: The interaction between our brain and body is defined as interoception, and it refers to how we internalize systemic changes, such as in breathing or heart rate[1]. Interoception has a significant impact on how we interact with our environment and makes it possible for us to calibrate and adjust our body to perform optimally. For instance, it has been demonstrated that exhaling while shooting a bow and arrow increases the likelihood of making a precise shot[2,3]. From this example, we are aware that behavior and respiration are related, but we do not yet understand the neural mechanisms that underlie this association. By studying changes in respiration and neural activity occurring over time in non-human primates (NHP), we have been able to identify a series of different respiration features that align to behavior, coupled to increased neural activity at inhalation. This work provides us with the ability to draw inferences on human interoception thanks to the similarity of brain and behavior between humans and NHPs.

Methods: We trained 1 NHP to perform a fixation task, where the animal holds its gaze at the center of the screen until a target appeared, after which they were required to saccade to the target to receive a reward. Some of these trials included a full field checkerboard stimulus in the beginning of the trial, while others only a grey background. Simultaneously, we measured neural activity from V4 using a 96-electrode Blackrock "Utah" array (Salt Lake City, UT) and respiration using a custom thermal probe (Fig. 1A). From the array we collected neuronal spiking activity and then correlated this to different respiration features that were extracted from the respiration trace. These features included inhalation/exhalation onset, respiration depth and duration, which were all identified with Matlab's in-built function "findpeaks." Then we aligned all these different features to the subject's fixation behavior.

Results: Our approach permitted us to analyze not only the relationship of respiration patterns in a task, but also how it links to cortical activity. We found an alignment of inhalation onset to saccade (Fig 1B). More precisely, the probability to inhale was highest at the beginning of the trial and decreased as it approached saccade. Respiration depth, like inhalation, decreased as it approached the time of saccade (Fig. 1B). There was an increase of neuronal spiking rate aligned to inhalation and appeared regardless of whether the checkerboard visual stimulus was present (Fig. 1C).

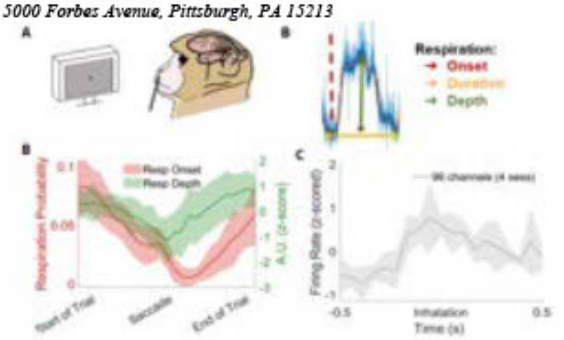

Figure 1. NHP performing fixation task while measuring respiration and neural activity (A). Respiration Features (B). Trial Aligned Respiration Features (C) and firing rate increase across 96 channels at inhalation (D).

Conclusions:

From this work, we concluded that there was trial-aligned respiration entrainment, indicating a potential preparatory response in the subject, specifically in anticipation of saccades and rewards. Additionally, the increase in neural firing rate at inhalation suggests that there may be an underlying relationship between breathing and the activity in visual cortex, which is in agreement with past studies in rodent and feline models[4,5,6]. These results allow us to deepen our understanding as to how systemic changes influence our response to certain tasks. Nevertheless, the current fixation task does not elicit a strong enough behavioral response that might help us learn how respiration patterns change with different trial outcomes (correct/incorrect). Future work will focus on applying tasks with a higher cognitive load to prompt clear behavior differences.

References:

1. Craig A. Curr. Opin. Neurobiol. 2003;13(4):500–505.
2. Patel K. Int. j. phys. educ. sports health. 2021;8(2):109–110.
3. Migliaccio G.M. et al. Sports. 2023;11(5):103.
4. Basha D. al. Sci Rep; 2023;13(8529).
5. Biskamp J. et al. Sci Rep. 2017;7(1).
6. González J. et al. ELife. 2023;12.

Acknowledgements: This works was partially supported by:

-NIH T32 EB029365

DEI: In the field of neural engineering, it is crucial for the field to give top priority to research targeted at creating neurotechnologies that affect various communities in order to address healthcare disparities. Also, adopting inclusive policies in academic and professional settings is essential so people from all backgrounds have equal opportunities to make significant contributions to the complex subject of neural engineering.

STEVENS
INSTITUTE OF TECHNOLOGY

Enhanced Coronary Imaging System: Leveraging Generative Artificial Intelligence for Adaptive Super-Resolution

Yu Gan
Department of Biomedical Engineering, Stevens Institute of Technology

Biographical Summary of Applicant: I'm currently an Assistant Professor in the BME department at Stevens Institute of Technology. I earned my Ph.D. from Columbia University and pursued postdoctoral research there. In 2018, I established the Intelligent Imaging and Image Processing (I^3P) Laboratory, focusing on artificial intelligence (AI) techniques for analyzing biological samples from optical coherence tomography (OCT) images. Previously, I served as an Assistant Professor at the University of Alabama from 2018 to 2021. My research has been instrumental in developing OCT image processing tools for registration, classification, and fiber orientation analysis, with applications spanning cardiology, oncology, and reproductive studies.

Clinical Impact and Significance of Research Problem: Coronary artery disease (CAD) is a leading cause of death in the United States, accounting for 1 in 7 fatalities. Percutaneous coronary intervention (PCI), a treatment for CAD, commands a market worth over $2.8 billion annually in the U.S., with approximately 1,000,000 procedures performed yearly. During PCI, precise vessel characterization is crucial for informed clinical decisions. Intravascular optical coherence tomography (IVOCT) has emerged as an ideal coronary imaging system for assessing plaques, ensuring stent deployment success, and evaluating vascular response to intervention. However, current IVOCT spatial resolution is limited to the cellular level, hindering visualization of sub-cellular features vital for assessing stent coverage and plaque composition, such as fibrin and cholesterol crystals. Such image resolution is constrained by the imaging speed required by a typical pullback procedure. Addressing this limitation is essential for enhancing interventional procedures. This project aims to explore innovative generative AI methods for achieving effective super-resolution visualization of coronary images, enabling detailed plaque characterization and improving clinical outcomes.

Innovative Programmatic Approach of Applicant: The proposed research introduces a novel concept of object-adaptive super-resolution in coronary imaging, offering computational tools to tackle algorithmic design challenges through advanced techniques in robust learning, network uncertainty, and multi-scale generative learning. At a systemic level, this concept overcomes the resolution versus imaging speed tradeoff by selectively enhancing regions of interest (ROI) in low-resolution images. The framework intelligently links object information to enhance super-resolution efficiency, combining object detection and super-resolution adaptively to avoid unnecessary processing in non-critical areas. At the algorithmic level, the research addresses multiple key questions: robust ROI identification, preparation of a unified, multi-scale generative network capable of flexible super-resolution, and efficient ROI enhancement by arbitrary scale factors.

Key Findings of Applicant to Date: We have made significant progress in showcasing the effectiveness of adaptive zoom-in super-resolution. We devised a robust object detection framework to detect the ROI from human coronary images[1]. Within each ROI, we developed a unified, multi-scale super-resolution neural network[2] (Fig. 1). Importantly, the total imaging and processing cost in Fig. 1d is significantly lower than that of capturing high-resolution images in Fig. 1a, highlighting the potential of software-based methods to maintain both speed and resolution simultaneously. Additionally, we enhanced this network by incorporating frequency components to improve super-resolution performance[3]. Furthermore, we recently developed a cross-platform super-resolution technology, increasing resolution from 7 μm to 2 μm[4]. These advancements highlights the potential of applying AI-based approaches to reveal crucial cellular structures in coronary imaging to aid in CAD diagnosis.

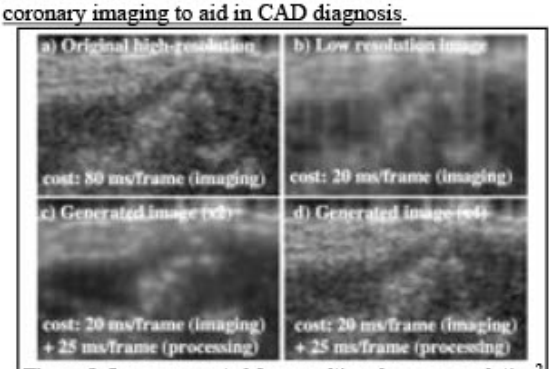

Figure 1. Image generated from multi-scale super resolution[2]

Future Goals: This study aims to transition into translational research, aligning with my overarching objective of enhancing clinical imaging-based diagnoses and interventions through the creation of generative AI-driven super-resolution techniques. Additionally, I plan to leverage my connections within the educational community in Alabama, particularly the resources available at historically black colleges and universities (HBCU), along with the resources developed in this study, to reduce the current disparity of biomedical participation in the Deep South region. I will integrate various research tools into the format of remote education and undergraduate research training. This holistic approach will bridge the gap between AI advancements and biomedical engineering, nurturing the next generation of researchers from underrepresented groups.

Acknowledgements: This study is supported by NSF (CAREER-2239810, CRII-2222739), NIH (R21HD104164), and USDA/NIFA (Data Science-2022-67021-36866).

References:

1. Liu H. et al. J Biomed Opt. 2023; 28(3).
2. Li X. et al. IEEE Trans Biomed Eng. 2022; 69(12).
3. Li X. et al. Biomed Opt Express. 2023;14(10).
4. Li X. et al. IEEE ISBI, 2024. Accepted

STEVENS
INSTITUTE OF TECHNOLOGY

RNA-therapeutics for Cellular, Tissue, and Immune Engineering

Theresa M. Raimondo, Ph.D.
Brown University

Biographical Summary of Applicant: I am an Assistant Professor of Engineering, in the School of Engineering, with a secondary appointment in the Division of Biology and Medicine at the Warren Aplert School of Medicine at Brown University. I am also a member of the Cancer Therapeutics Program, at the Legorreta Cancer Center at Brown. The overarching goal of my research program is to develop nanomedicine technologies for targeted therapeutic delivery, with a specific emphasis on RNA delivery to immune cells. I completed my PhD under the mentorship of Dr. David Mooney at Harvard University. My doctoral research focused on the development of protein decorated-gold nanoparticles for macrophage and T cell modulation in skeletal muscle. By promoting regenerative macrophage polarization and regulatory T cell recruitment we improved muscle strength following acute injury[1] and in advanced muscular dystrophy[2]. I received postdoctoral training with Dr. Daniel Anderson and Dr. Robert Langer at MIT. My postdoctoral work centered around the design of lipid nanoparticles (LNPs) for RNA-based cancer immunotherapy. By silencing immune checkpoints in a range of innate immune cells, we observed adaptive immune responses, and increased survival in murine models of peritoneal metastasized cancer. My faculty appointment started Jan. 1, 2024.

My vision is to develop RNA-therapeutics for immune modulation, in the contexts of functional tissue regeneration and cancer immunotherapy. My training and experience in bioengineering and clinical collaboration uniquely position me to lead multidisciplinary projects ranging RNA design, LNP optimization, and preclinical testing.

Clinical Impact and Significance of Research Problem: Completion of the human genome sequencing twenty years ago, and substantial advancements in next-generation sequencing since then, have elucidated the genetic roots of many diseases including cancer, chronic inflammatory diseases, and degenerative dystrophies. Thus far, this knowledge has been well adapted for diagnostic use, but its translation to therapeutic interventions is just beginning to be realized. Nucleic acid-based therapeutics are promising because, unlike small molecules and protein-based drugs, they can sequence-specifically target any gene of interest. *In vitro* transcribed (IVT) mRNA has emerged as a key component of modern vaccination and cancer immunotherapy. Chemical modifications to RNA have been observed to control its stability, translation efficiency, and modulate immune responses.[3]

LNPs play a critical role in RNA-therapeutics by allowing efficient RNA encapsulation and protection from degradation *in vivo*, aiding transfection and endosomal escape, and targeting delivery.[4,5] Recent data suggest that immune responses to IVT mRNA modifications depend on LNP formulation. [6] Thus there is a critical need to study the role of RNA modifications in conjunction with LNP formulation. RNA-LNPs have the potential to treat a wide range of diseases, from protein replacement to gene editing and cancer immunotherapy, however a deeper understanding of the interplay between LNP formulation, RNA modification, and immune response, will be essential.

Innovative Programmatic Approach of Applicant: Our research is innovative in concept and in experimental approach.

Conceptually, we explore the therapeutic potential of innate immune cells in diverse tissues and pathologies. My research was among the first to demonstrate that macrophage modulation promotes the regeneration of functional tissue in chronic dystrophy. In cancer immunotherapy, our work capitalized on efficient LNP delivery to innate phagocytic cells, macrophages, to effect an adaptive immune response.

Experimentally, our work incorporates RNA modification as a novel immunotherapeutic design parameter. By high-throughput screening of RNA with LNP formulation parameters we seek to both (i) improve our understanding of the role of RNA modification in RNA translation and immune activation and (ii) use this understanding to optimize therapeutic applications.

As a biomedical engineer, situated on the Brown medical school campus, our research benefits from collaboration with clinical, RNA, regenerative and cancer experts.

Key Findings of Applicant to Date:

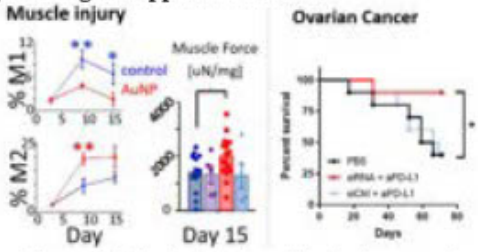

Figure 1: Doctoral and postdoctoral research

Future Goals: My research goals are to (i) use engineering optimization and statistical approaches to optimize LNP and RNA design and for therapeutic applications, (ii) use RNA/LNPs as a tool to increase our fundamental understanding of immune cells in diverse pathologies and tissue regeneration, and (iii) to apply these mythologies and understanding to the design of novel therapeutics.

I am also passionate about mentorship, and the stewardship of my trainees to independence. I am coteaching a capstone design class, and am proud that many of my students are presenting here at NEBEC. I seek to create a lab and classroom environment welcoming to underrepresented students, particularly women, and have been active in advisory groups.

References:
1. Raimondo et al PNAS 2018 115(42):10648-53
2. Raimondo et al Sci Adv 2021: 7(6)
3. Freund et al Genes 2019: 10(2)
4. Hou et al Nat Rev 2021: 6(2)
5. Cheng et al. Nat Nantech 2020: 15(4)
6. Melamed et al. J Cont Rel 2022: 341

STEVENS
INSTITUTE OF TECHNOLOGY

Title of Abstract: Human Genome Writing HLA-matched iPSCs for Off-the-shelf Smart Therapeutic Cells

David M. Truong, PhD
New York University Tandon School of Engineering, Department of Biomedical Engineering.

Biographical Summary of Applicant: Dr. Truong is a tenure-track Asst Professor of Biomedical Engineering and started his lab Sept 2021. He received a B.S. from UC San Diego, a PhD from UT Austin, and postdoctoral training in synthetic biology at NYU Langone Health. His research expertise spans cell therapies, genome engineering, stem cells, and regenerative medicine. His early work was on embryogenesis of the kidney, and his doctoral work was on programmable gene editing tools from transposons called mobile group II introns. As an F32 fellow, he engineered yeast to wrap their genomes with human chromatin instead of their own[1]. He led a team to humanize and engineer 2 megabases of the mouse immune system. After winning an SBIR award to build "off-the-shelf" human iPSCs, he led the genome engineering team at the startup Neochromosome Inc, later acquired by Opentrons Robotics. He started his lab at NYU to continue developing the patent-pending "REWRITE" method[2] to engineer +100kb regions of the human genome and continue off-the-shelf immune-compatible iPSCs. He was awarded an NIH Director's New Innovator Award (DP2) from NIAID on "Programmable Dendritic Cells" for cancer therapy.

Clinical Impact and Significance of Research Problem: Cell therapies like CAR-T have revolutionized standard of care but have high costs due to using patient-derived cells. Human iPSCs could provide an unlimited resource of differentiated cells but must be "HLA-matched" to prevent immune-mediated rejection. Genetic engineering could be a solution, but there are no methods to engineer the 6 megabase polymorphic HLA-locus in human iPSCs. Technologies to "rewrite" large sections of the human genome could provide these "personalized" iPSCs for cheaper, safer, more effective universal cellular therapies. Moreover, HLA-engineered iPSCs could be used to make patient-matched "smart" dendritic cells (DC) and macrophages (MΦ), which are both motile cells that can enter solid tumors or bypass the blood-brain-barrier. Moreover, there are limited approaches for making highly pure scalable amounts of DCs and MΦs from iPSCs. Overcoming these challenges would enable a new paradigm of modular and upgradable cell therapies for solid tumors and neurodegeneration.

Innovative Programmatic Approach of Applicant: Dr. Truong is pioneering mammalian synthetic biology to the clinic by merging advances in human genome writing, universal iPS cells, synthetic genetic circuits, and transdifferentiation. These could provide a new generation of patient independent smart DCs and MΦs, that could be continuously "updated" with new genetic features as fields advance. This has already led to collaborations in solid tumors using CAR-DCs with Ned Landau (NYU SoM). The use of smart MΦs to enter the brain as a "trojan horse" has led to CAR-Aβ-MΦs with Martin Sadowski, who leads the NYU Alzheimer's Clinical Trials program.

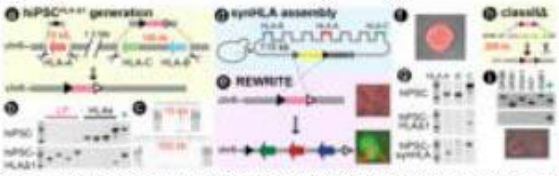

Fig 1. HLA-engineered hiPSCs. REWRITE enables HLA-locus engineering as an off-the-shelf source of HLA-matched hiPSCs. **(a)** CRISPR-based biallelic deletion of HLA-A (10 kb) and HLA-C → HLA-B (100 kb) in PGP1. **(b)** PCR-gel verifying mod1-LP integration, and loss of class-I HLA loci in blank-hiPSC. **(c)** IGV views verifying biallelic deletion via WGS against hg38. **(d, e)** Yeast recombineering of synthetic HLA locus (synHLA) of 115 kb retaining native gene regulation. **(f)** Embryoid body assay. **(g)** PCR verification of integration of synHLA. **(h)** Biallelic deletion of 209 kb class II HLA locus in NCRM2. **(i)** PCR verification of missing locus (top) NCRM2, (bottom) deletion line.

Key Findings of Applicant to Date: We genetically engineered two separate hiPSC lines (PGP1-male and NCRM2-female) with large bi-allelic deletions of class-I (100 kb and 10 kb) and class-II HLA loci (209 kb) using CRISPR, and now contain the REWRITE module1-LP (**Fig 1**). We verified the cells genetic integrity via whole-genome sequencing and PCR analysis, and pluripotency by RT-qPCR, embryoid body assays, and endothelial cell differentiation. We generated human synthetic HLAs (synHLA) using yeast recombineering, with full native regulatory regions, and enable us to match any persons HLAs. We verified the genome integration of both 35- and 115-kb synHLAs and obtain as many as 80 distinct clones.

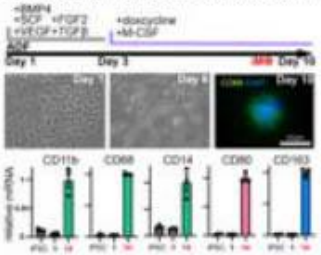

Fig 2. iMΦ transdifferentiation from hiPSCs. Condition 1 (dox+MCSF) for 6 days showed low MΦ markers. Xeno-free, fully defined condition 14 (top: 6 factors) produced 1.8 iMΦ per 1 iPSC in 10 days. Green- unpolarized. Red- M1 markers. Blue – M2 markers. ***DC data not shown***

We developed a rapid and scalable trans-differentiation method of hiPSCs to MΦs (**Fig 2**) and DCs (*not shown*) within 10 days using a genetically integrated doxycycline-inducible gene circuit. The MΦ use forced expression of transcription factors Spi1/Cebpα, whereas DCs use Spi1/Irf8/Batf3. We found both require a brief mesoderm induction with cytokines for 3 days, before a rapid dox-induced conversion within 7 additional days. We compared to a directed differentiation method and calculated our approach is >20x more efficient and 2x faster.

Future Goals: HLA-engineered iPSC-derived cell therapies will provide cheaper therapies for all people, especially for ethnically diverse individuals with rare HLAs.

References:

1. Truong & Boeke. ***Cell.*** 2017;171:1508-1519.
2. Truong. US Patent. 2023; US20230295668A1

Acknowledgements: This work to DMT was funded by NIAID awards DP2 AI154417 and R43 AI148008 and an NYU Mega-Grants seed award.

STEVENS
INSTITUTE OF TECHNOLOGY

Deep Learning Model's Estimation of Soleus Muscle Activation during Level Walking

Jobelle B. Hernandez, Oliver Gu, Aymen Elassa, Mariam Sharobim, Samira Santana, and Jongsang Son
New Jersey Institute of Technology

Introduction: Meaningful insight into musculoskeletal or cardiovascular issues can be gained from a combination of qualitative clinical judgement and quantitative movement analysis of electromyogram (EMG) data. However, there are limitations to the qualitative diagnosis of musculoskeletal gait abnormalities due to the subjectiveness of physician observation. On the other hand, the collection and subsequent analysis of quantitative data such as EMG is less convenient.[1] Thus, more efficient and simplified methods of quantitative data collection and analysis are needed. Accordingly, this proof-of-concept study aims to demonstrate the feasibility of using a deep learning model to estimate soleus muscle activation patterns (MAP) from lower limb joint angles during walking. This proposed model will be a reliable and objective tool to assess patients as it provides unbiased data analysis. Addressing the gap of accessible quantitive data collection and analysis will better inform clincians about patients' conditions.[1]

Methods: The joint angle and EMG data of 24 healthy, adult-aged (18+) individuals with no self-reported locomotor disorders or other health issues (i.e., cause irregular motor performance) from a public dataset published by Lencioni *et al.* are used to train a long short-term memory model to estimate the soleus MAP from 12 joint angles during walking at different speeds.[2] The angles used are the flexion, adduction, and rotation of the pelvis, hip, knee, and ankle. The EMG data is processed into MAP data through a series of steps (resampling, rectification, smoothing, and normalization). The data is split into 3 sets: 80% of the subjects are allocated for training, 10% for validation, and 10% for testing. Model performance is evaluated using root-mean-square error (RMSE) and coefficient of determination (R^2) between the predicted and actual MAP. The model training and data analysis described above were conducted in MATLAB (The MathWorks, Inc., Natick, MA).

Results: The proposed model showed an average RMSE of ~0.10 and R^2 of 0.85, based on 31 trials. Figure 1 displays a sample of 4 trials in which the measured and predicted MAP are plotted. The bottom left plot displays the trial with the lowest RMSE of 0.06. The plots in the top row have an RMSE of 0.10, reflecting the overall average. The bottom right plot displays the trial with the highest RMSE of ~0.18 (1 of 4 outliers). Outliers are values 1.5 times the interquartile range above the third quartile or below the first quartile. The maximum RMSE value that is not an outlier is ~0.13. The RMSE range (excluding outliers) is 0.06 to 0.13, with a median value of 0.09.

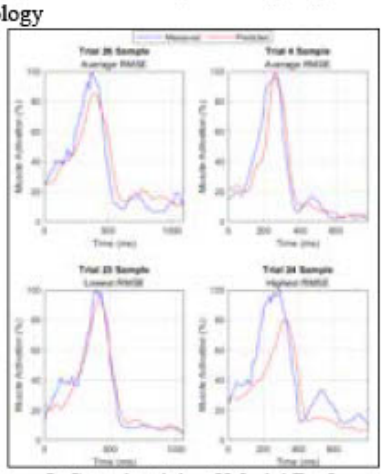

Figure 1. Sample trials of Model Performance

Conclusions: The accuracy shown in average performance (Trials 4 and 26 in Figure 1) demonstrates the feasibility of using a deep learning model to estimate soleus MAP from lower-limb joint angles during walking. The range (excluding the outliers) and median RMSE also supports the model's reliability as a prediction tool. But, the outliers show the network needs to be further generalized. Future studies are also required to optimize the model's performance using fewer input angles.

References:

1. Simon, Sheldon R. "Quantification of human motion: gait analysis-benefits and limitations to its application to clinical problems." Journal of biomechanics, (vol. 37,12 (2004): 1869-80. doi:10.1016/j.jbiomech.2004.02.047
2. T. Lencioni, I. *et al*, "Human kinematic, kinetic and EMG data during different walking and stair ascending and descending tasks," Scientific Data, 2019 (Vol. 6 Issue 1)

Acknowledgements: We would like to express our gratitude to Dr. Joel Schesser, Dr. Alev Erdi, and Dr. George Collins for the helpful discussions during the project's initial stages.

DEI: The BME field can improve through telehealth expansion and diversity promotion initiatives. A result of inequal healthcare access is outcome discrepancies. One solution is minimizing the costs and location of care through telehealth. The reach and usefulness can be expanded through tools such as simplified mobile applications. The participation of STEM-underrepresented persons in the BME field can be addressed through promoting inclusive teaching styles, and creating more pre-college programs that include an introduction to the research field and opportunities to work in a research lab.

STEVENS
INSTITUTE OF TECHNOLOGY

Frontal Plane Balance Patterns of Older Adults During Pre-Planned and Late-Cued Turns

Zahava Hirsch[1], Mitchell Tillman[1], Jun Liu[1], Allison Clark[1], Antonia Zaferiou[1]
[1]Stevens Institute of Technology, Biomedical Engineering Dept., Hoboken, NJ USA

Introduction: Up to half of walking steps are turns [1] and for older adults, a fall during a turn is eight times more likely to result in a hip fracture [2]. The purpose of this ongoing study is to understand how older adults maintain balance while walking and turning. We looked at two measures of balance: whole-body frontal plane angular momentum (Hf), which can convey mediolateral balance regulation information [3]; and lateral distance (LD), which describes if the center of mass (COM) remains within the base of support [4]. Based on findings from young adults [5], we hypothesized that during pre-planned and late-cued turns vs. straight line gait, older adults will: 1) have larger Hf range, and 2) have smaller LD minima.

Methods: This study included four healthy older adults (2 female; age 68 ± 1.9 years; mass 78.8 ± 8.8 kg; height 1.70 ± .02 m). Participants passed cognitive and balance assessment tests and did not fall in the prior 6 months. Baseline measurements were collected, including the miniBEST, Dynamic Gait Index (DGI), Montreal Cognitive Assessment Test (MOCA), and Fall Efficacy Scale (FES). A 13-segment kinematic model [6] was built using optical motion capture data (250 fps; OptiTrack, USA). A taped T-shaped walkway was used, including a 10 m straight-way with a 90° turn in the center. Three tasks were performed 12-14 times in an order of increased challenge. First, participants walked straight for 10 m. Next, they performed 90° pre-planned left turns. Finally, they performed 90° late-cued left turns visually cued by a display at the end of the 5 m aisle (50% turn trials). Hf about the COM was normalized to a dimensionless form [3]. LD was calculated as the distance from the COM to the closest lateral edge of the base of support (mediolateral defined by the pelvic frontal plane). LD is positive when the COM is medial to the lateral edges of the feet and negative if the COM is lateral of the lateral edge of the foot. Hf and LD ranges were found during the turn phase (defined by a pelvis rotation threshold) or steady-state straight-line gait. A percentile bootstrap statistical test was used to compare measurements within-participant across the three tasks performed.

Results: Participants 1 & 4 had significantly larger Hf ranges during turns vs. straight-line gait (**Fig. 1A**). It is notable that the Hf range of Participant 3 was significantly *smaller* during late-cued turns, which could be a protective strategy. Though there was no hypothesis about baseline factors, Participant 3 also had the smallest MoCA and DGI score, and the largest FES score, indicating a potential relationship between standard baseline measurements and older adult balance strategies (**Fig. 1C**). All participants had significantly smaller LD minima in pre-planned turns vs. straight-line gait; but only Participants 1 & 2 had significantly smaller LD minima during late-cued turns vs. straight-line gait (**Fig. 1B**). Though there was no hypothesis related to gait speed, the average gait speed was progressively slower from straight-line to pre-planned to late-cued turns, which may provide context for these initial findings. This is an ongoing study that we will expand to include more participants, including fall-prone older adults. We plan to explore both within and across-participant trends, including gait speed and turn strategies as covariates or moderators.

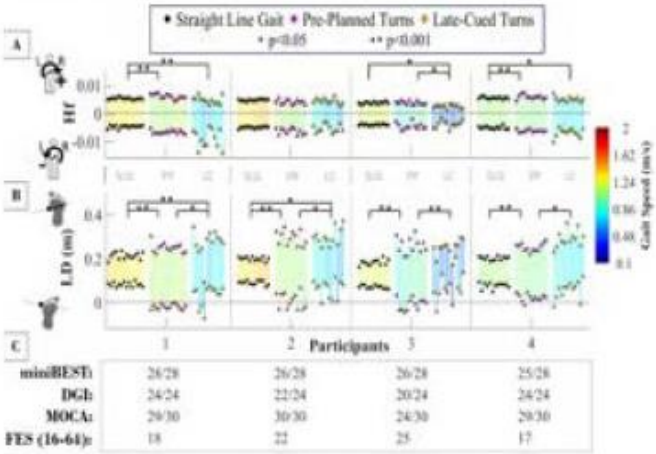

Figure 1. Min, max, and range **(A)** Hf and **(B)** LD for all trials and participants during straight-line gait, pre-planned, and late-cued turns. Gait Speed indicated by the colors of the range bars. Significance bars: Hf based on range, LD based on minima. **(C)** Baseline measures for all participants.

Conclusions: While more participants are needed to understand group trends, none in this study progressively significantly increased their Hf ranges from straight-line gait to pre-planned to late-cued turns, a group trend we previously found in young adults [5]. These findings suggest that healthy older adults may regulate their frontal plane balance during turning using strategies that are person-specific and may differ from healthy young adults [5]. Using these initial findings, we expect that as the study expands, we may find divergent strategies in the extent to which older adult participants control their angular momentum and COM positioning during turns. Overall, this research advances our understanding of how balance strategies during turns may change with age and may inform more focused therapies to improve balance in older adults.

References: [1] Glaister (2007), *Gait & Posture*. 25; [2] Nevitt & Cummings (1994), *Osteoporosis Int*. 4; [3] Vistamehr et al. (2021). *J Biomech*. 128; [4] Dixon et al (2016). *Clin. Biomech*. 32; [5] Tillman et al. (2021). *J Biomech*. 141; [6] de Leva (1996). *J Biomech*. 29.

Acknowledgements: We acknowledge the financial support from NSF Award #1944207.

DEI: We incorporate a participant-centered research approach to ensure that our findings contribute to the development of accessible and beneficial interventions for all older adults, regardless of background or circumstances.

STEVENS
INSTITUTE OF TECHNOLOGY

The Acute Compressive Strain Response of Osteoarthritic Cartilage: An In Vivo Study

JiYeon Ashley Hong, (1), Daniel K. White (2), Axel C. Moore (1).
[1] Department of Biomedical Engineering, Carnegie Mellon University
[2]Department of Physical Therapy, University of Delaware

Introduction: Articular cartilage is a specialized connective tissue that functions as a biological bearing, supporting load and enabling low friction joint articulation. Previous studies have shown that acute in vivo loading of cartilage leads to compressive strain, while static unloading leads to strain recovery (passive recovery). Recently, in a young asymptomatic cohort, we showed that walking, a loaded dynamic activity, was also capable of strain recovery. Surprisingly, the recovery rate during activity was more than 3 times faster than passive recovery. We refer to this novel recovery mode as active recovery. In this study we aimed to determine if active recovery is conserved in symptomatic osteoarthritis (OA). Since, OA cartilage is known to be softer, contain less proteoglycan content, and have a damaged collagen network, we hypothesize that the OA cohort will exhibit larger compressive strains and slower recovery.

Methods: The study consisted of eight symptomatic OA participants, who met the following criteria defined by the National Institute for Health and Care Excellence (UK): age 45+, activity related knee pain, and no morning knee stiffness. All participants completd a Knee Injury and Osteoarthritis Outcome Score (KOOS) questionnaire for pain and symptoms, where 0 is extreme pain and dysfunction, and 100 is no pain or impact on daily life. The KOOS pain score ranged from 50 to 89 with the average being 69. The group performed a fixed series of tasks as seen in **Fig 1**. The order of the tasks was as follows: 1) stand for 30 minutes (to induce cartilage strain), 2) walk for 10 minutes (for potential active strain recovery), 3) stand for 30 mintues (to induce strain), and 4) lie supine for 50 mintues (for passive strain recovery. Following each task, the affected knee of each participant was scanned with a 3T magnetic resonance scanner using a saggital plane Proton Density Turbo Spin Echo (PD-TSE) sequence. The resulting voxel size was 0.34 x 0.34 x 1.5 mm. The scan duration was 3:43 min.

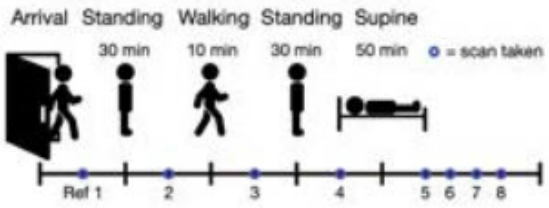

Figure 1. Task and imaging timeline.

Results: In the OA group, the mean strain in the medial and lateral compartments following standing for 30 minutes = -11.8% and -7.9% strain, walking for 10 minutes = -12.1% and -5.7% strain, and lying supine for 50 minutes = -7.7 and -7.1% strain. When compared to our prior work in an asympotomatic cohort, OA led to significantly ($p < 0.0003$, Kruskal-Wallis) increased compressive strain across all conditions and greater variance between individuals. Due to the large variance and small cohort size we did not detect significant effects of task on the compressive strain in OA. Despite this several important trends can be observed. First, the OA cohort exhibited increased strain between the first and second period of standing (-9.8% vs -13.0% strain, mean of both compartments), which is not consistent with the healthy cohort, see **Fig 2**. Second, walking for OA participants did not always lead to strain recovery, which is particularly evident in the medial compartment where on average, walking increased the compressive strain from the first stand (-11.8% strain) to walk (-12.1% strain). Third, the passive recovery rates between the medial and lateral compartment appear to have mostly a linear recovery response, which is in agreement with the asymptomatic cohort, but the rate of recovery differs from the asymptoatic cohort (0.08%/min, mean of both compartments) and between OA compartments (0.11%/min medial and 0.0325%/min lateral).

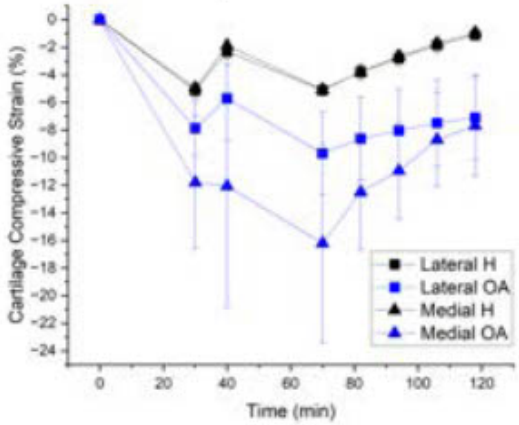

Figure 2. Mean compressive strain in an osteoarthritic (OA) and asymptomatic cohort (H) as a function of task.

Conclusions: This study shows that although walking is a form of active recovery for asymptomatic participants, this may not be true for those with OA. Depending on the severity of the OA, walking may actually add strain to the cartilage. Our future work will correlate the severity of OA (KOOS scores) to each participant's task specific compressive strain response. We hypothesize that more serve OA will correlated with higher strains and reduced recovery rates.

DEI: The Bioengineering community should strive to include a greater diversity of participants in research studies. This would allow greater insight into differences that may arise among different demographics, informing treatment, and reducing disparities in healthcare outomes.

STEVENS
INSTITUTE OF TECHNOLOGY

Impact of a Cognitive Dual Task on Older Adult Motor Performance and Strategies

Erin Kreis, Mitchell Tillman, Jun Ming Liu, Zahava Hirsch, Antonia Zaferiou.
Stevens Institute of Technology.

Introduction: Falls are the leading cause of fatalities and nonfatal injuries among older adults, impacting over fourteen million older adults annually [1]. The impact of falls can extend beyond physical harm, threatening a person's independence and overall quality of life. Situations involving the simultaneous execution of a motor and cognitive task may lead to falls. These dual task scenarios arise in everyday life (e.g., walking while talking) and pose a significant threat to older adults due to aging-related physical and cognitive changes.

The current body of literature regarding dual tasks has focused on straight-line gait [2]; however, motor tasks involving postural controls and transfers, such as turns, are also common movements. The Timed Up and Go (TUG) test is a validated mobility assessment that combines multiple everyday movements, including straight-line gait, turns, and sit-to-stand tasks. A significant decrease in gait speed or cognitive performance when a dual task (DT) is introduced has been associated with higher fall risk [2]. We hypothesized that the TUG performed with a DT would be associated with decreased motor performance (e.g., increased completion time) and altered movement strategies (e.g., more, shorter steps) vs. the TUG without the DT.

Methods: Older adults (n=8, mean age 70.9 ± 6.0 years) volunteered to participate in this research, in accordance with the IRB. The TUG consists of standing up from a chair, walking three meters forward, making a 180° turn, walking three meters back, and returning to a seated position in the chair. Each older adult performed the TUG twice: once without any additional cognitive load, followed by once with a serial subtraction dual task. A physical therapist administered the test.

Optical motion capture (Optitrack) was used to measure movement and a data processing program (MATLAB) was used to compute measures of interest. Measures of interest included: (1) the completion time of the test, measured by the Physical Therapist, (2) the number of steps used, (3) the step length, and (4) the step duration. Measures 2-4 required heel strike events, which were determined using motion capture software to observe the beginning of the foot's rotation in the sagittal plane after the heel contacted the ground. Heel strike times were confirmed with a video review. A two-tailed paired sign test was used to evaluate the direction of difference between TUG and DT for the measures of interest (α=0.05).

Results: Between the TUG and DT trials, there was an increase in completion time (p=0.0078) and total steps (p=0.0156) (**Figure 1**). Associations between task type and median step length (p=0.0703) and median step duration (p=0.2891) were not significant (**Figure 1**).

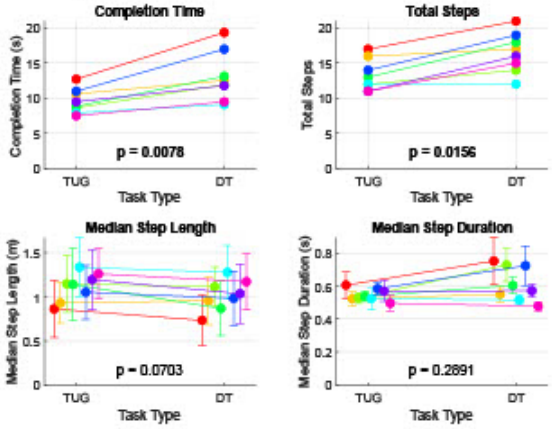

Figure 1. Comparison of Timed Up and Go (TUG) and Dual Task TUG (DT) across outcome measures. Each participant's data are distinct colors; group p-values are included.

Conclusions: Our finding that total steps and completion time increased with the addition of the DT is consistent with our hypothesis and with the results of previous studies [2]. Though not significant in this small cohort, **Figure 1** shows that median step length decreased with the addition of a DT for most older adults. This trend may be significant with a greater sample size.

The TUG test with a DT replicates complex daily scenarios that may pose additional fall risk for older adults. Future research that focuses on how the addition of a DT impacts kinematics and specific phases of the TUG test could expand our understanding of how DT impacts a variety of motions, leading to the development of more specific and effective DT training interventions.

References:

1. Kakara R. et al. CDC. 2023;72(35):938–943
2. Bayot M. et al. NCCN. 2020;50(6):401-440

Acknowledgements: This study uses existing data from a larger ongoing study (NSF Award#1944207).

DEI: Studies show that dual tasks affect older adults differently than young adults, emphasizing the need for age-inclusive studies to develop effective interventions for health outcomes like reducing fall risk. I founded a walking community, SilverStrides, to connect older adults with a shared interest in healthy aging. Concurrently, our lab has been organizing "Mindful Movement" sessions where we gather monthly to explore different movement practices. We will invite the SilverStrides community and a physical therapist to future sessions, which could include dual task training. Engaging with older adults through community events like these can help reduce ageism in research and spread knowledge of bioengineering to local communities.

STEVENS
INSTITUTE OF TECHNOLOGY

Marfan Syndrome Vascular Smooth Muscle Cells Show Increased Phenotypic Sensitivity to TGF-β1

Helen Orins[1], Robert J. Wiener[1], Kevin D. Costa[1]
[1]Cardiovascular Research Institute,
Icahn School of Medicine at Mount Sinai, New York, NY

Introduction: Marfan Syndrome (MFS) is a genetic condition linked to vascular aneurysms, primarily in the ascending aorta, caused by a mutation in the fibrillin 1 (*fbn1*) gene[1]. This gene mutation disrupts the regulation of transforming growth factor-β1 (TGF-β1), which impacts cell survival and phenotype[1]. The role of TGF-β1 in MFS aneurysm development remains unclear. Aortic smooth muscle cells (ASMCs) can shift between contractile and synthetic phenotypes: contractile cells are less migratory, proliferative, and are stiffer, whereas synthetic cells are more proliferative and migratory[2]. TGF-β1 regulates this shift, but its impact on MFS phenotype progression is uncertain. Our study, using ASMCs derived from human-induced pluripotent stem cells (iPSCs), investigates whether TGF-β1 significantly influences ASMC phenotypes in MFS, aims to determine if **(1)** MFS ASMCs are inherently more synthetic than healthy ASMCs and **(2)** if TGF-β1 affects the phenotype switch in MFS ASMCs.

Methods: Healthy and MFS iPSCs were differentiated into two region-specific ASMC lineages until they reached maturity, which is detailed elsewhere[3]: neural crest-derived ascending aorta ASMCs (aASMCs) and paraxial mesoderm-derived descending aorta ASMCs (dASMCs). Differences in iPSC-derived ASMC migration were determined by a scratch migration assay[4] in the presence of untreated control, 2 ng/mL TGF-β1, or 20 ng/mL TGF-β1. Migration over 24 hours was assessed using ImageJ by measuring the injury area as ASMCs invaded into the scratched field of view. In separate experiments, ASMC stiffness in response to untreated control, 2ng/mL TGF-β1, or 20ng/mL TGF-β1 was determined by nano-indentation with a biological atomic force microscope (AFM), using a pyramidal cantilever tip that was advanced until it made contact with a cell and reached a deflection of 20 nm. Each cell was indented in a 4x4 array of 16 indentations covering a 5x5-μm square region of the cell midway between the nucleus and periphery. Each indentation was then analyzed using Hertz contact theory to determine the apparent elastic modulus, and the median value was used to represent the stiffness of the cell. Total exposure time to TGF-β1 for all experiments was 48 hours.

Results: When treated with TGF-β1 for 48 hours, MFS aASMCs exhibited a dose-dependent increase in cell stiffness as compared to their healthy counterparts (Fig. 1). There was a significant increase in cell stiffness (p=0.0452) between untreated control and 20 ng/mL of TGF-β1. However, MFS dASMCs become significantly softer (p=0.0034) when treated with TGF-β1, whereas healthy dASMCs did not (Fig. 1). Additionally, when treated with TGF-β1 healthy aASMCs exhibited a strong decrease in cell migration, whereas MFS aASMCs, did not. This demonstrated that healthy ascending ASMCs were more responsive to TGF-β1 as compared to their diseased counterparts. Our results suggest that through the involvement of TGF-β1, iPSC-derived Marfan dASMCs could work in a similar process by migrating faster at higher dosages of TGF-β1. Although a faster rate of wound closure was not present in Marfan aASMCs, the drive in the opposite direction could indicate an altered sensitivity to TGF-β1 in ascending ASMCs compared to descending. This may not confirm that migration is a driver of aneurysm progression in MFS, but it does demonstrate an involvement of the synthetic phenotype in the disease. These differences in the two lineages indicate that more needs to be explored in determining the effect of TGF-β1 on ASMC phenotypes in MFS.

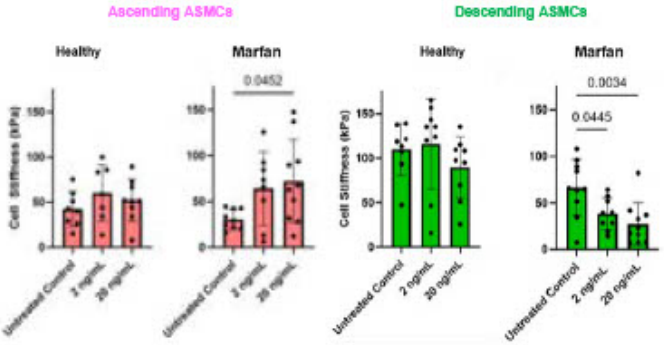

Figure 1: TGF-β1 effects on ASMC stiffness by AFM.

Conclusions: The difference in migration was evident between MFS dASMCs treatment groups, which reflects its role in influencing the synthetic phenotype of MFS ASMCs. Our results demonstrate that mature iPSC-derived MFS dASMCs exhibit significantly faster migration and significantly lower cell stiffness at a higher dosage of TGF-β1 (20 ng/mL) vs. the untreated control. Together, these results corroborate that TGF-β1 induces a synthetic phenotype by increasing migration and decreasing cell stiffness in MFS dASMCs. However, ascending Marfan ASMCs confirm an altered sensitivity to TGF-β1, which indicates the existence of the phenotype switch continuum that needs to be further explored.

References:

1. Granata, et al., *Nat Genet*, 2017.
2. Crosas-Molist, et al., *Arterioscler Thromb Vasc Biol*, 2015.
3. Cheung, et al., *Nature Protocols*, 2014.
4. Liang, et al., *Nature Protocols*, 2007.
5. Zhou, et al., *Cardiovasc Res*, 2017.
6. Gerthoffer. *Circ Res*, 2007.

Acknowledgements: Funding from NIH: S10RR027609

DEI: The Graduate School at Icahn School of Medicine at Mount Sinai (ISMMS) addresses healthcare disparities by providing affordable technologies for underserved populations, focusing on diagnosing cardiovascular disease in marginalized communities. In STEM, ISMMS engages underrepresented groups, fostering diversity and innovation.

STEVENS
INSTITUTE OF TECHNOLOGY

Investigating Fracture Risks Associated with Corticotomies in Femoral Bones: A Finite Element Analysis and Mechanical Testing Approach

Ansh Patel[1], Alexa Warren[1], Sierra Finn[1], Alison Blumstein[2], Evan Derector[2], Dr. Gutowski[2], Dr. Erik Brewer[1]
Rowan University[1], Cooper University[2]

Background: In surgical interventions, bone structures may need alterations, including procedures like corticotomies, which are vital for reaching the inner bone canal during surgical examinations of bone abnormalities. However, it is unknown how these changes are affect the bone's structural integrity, particularly for patients at higher risk for fractures, including those with osteoporosis. Despite the widespread application of these methods in orthopedic practice, there is an absence of standardized protocols for handling potential complications after surgery. Analytical approaches, like Finite Element Analysis (FEA) and mechanical assessments, provide avenues for investigating these potential hazards.

Hypothesis: Our investigation hypothesizes that corticotomies, because of their stress-inducing properties, might weaken the femoral bone and raise the chances of postoperative fractures. This study intends to evaluate the impact of various surgical factors, including the configuration, dimensions, and location of corticotomy, on the risk of fractures with cortical and osteoporotic bone and assess the necessity of preventive measures in situations with elevated risks.

Methods: This investigation unfolds in two phases. Phase one employs FEA on a rendered femur model, reconstructed from a quantitative CT scan of an adult male sourced through an open-source library. Force fectors were applied to recreate two potential failure models: (1) axially on the femoral head to simulate loading during running, and (2) laterally on the greater trochanter to simulate a sideways fall. Diverse configurations of cortical defects were examined to gauge their effect on bone strength. Phase two involves mechanical testing on thirty synthetic composite bone models. Surgical alterations, mirroring those performed in clinical settings, are enacted, followed by axial compression and lateral bending tests to assess mechanical behavior under varying loading conditions.

Results: The preliminary outcomes of our investigation indicate a noteworthy correlation between the size of cortical defects and local stresses. Through finite element analysis we have seen a noteable decrease in the the max von mises failure when there is a surgical defect on the femur. For a healthy femur bone with a fracture on the distal medial shaft we find a max von mises failure of 1.16E+08 (n/m^2) when a 1000N fracture force was applied. In comparison for a healthy femur with a 2mm circular defect with a fracture on the distal medial shaft of the femur showed an average of 1.09+08 (n/m^2) when a 1000N fracture force was applied.

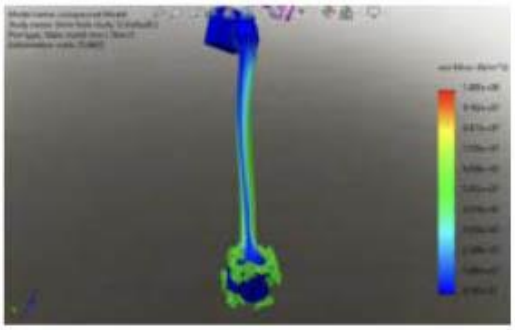

Figure 1. Finite element analysis on femur model with 2mm hole in proximal femur area shows increased von Mises stress along the femoral shaft

Conclusion:
Moving forward, our research aims to explore the biomechanical effects of lateral falls, anticipating discovering similar stress distrubution patterns that we have seen in our axial finite element analysis tests. Subsequent to this, the second phase entails conducting mechanical evaluations on synthetic bone models with surgically induced modifications, analyzing their reactions to assorted stressors. Preliminary observations hint at the impact of specific surgical configurations on fracture risk. This study seeks to offer valuable insights into the biomechanical repercussions of corticotomies, assisting orthopedic surgeons in postoperative care decisions and contributing to the establishment of standardized guidelines for preventative measures. Additionally, this research advances the utilization of FEA in orthopedic studies, opening the door to future inquiries into long-term consequences.

STEVENS
INSTITUTE OF TECHNOLOGY

Fracture Mechanics of Blood Clots: Influence of Fibrin Structure on Rupture Resistance

Ranjini K. Ramanujam[1*], Farkhad Maksudov[2], Rebecca A. Risman[1], Rustem I. Litvinov[3], John W. Weisel[3], John L. Bassani[3], Valeri Barsegov[2], Prashant K. Purohit[3], Valerie Tutwiler[1]

*Presenting author – 599 Taylor road, Piscataway, NJ 08854; Ph:2024607079; Email: rk931@rutgers.edu
[1]Rutgers University; [2]University of Massachusetts Lowell; [3]University of Pennsylvania

Introduction: Thrombosis, including common conditions such as stroke, myocardial infarction, etc. is a leading cause of morbidity and mortality. A complication of thrombosis is embolization, wherein a portion of the clot ruptures and becomes lodged in downstream vessels, thereby cutting off blood supply and increasing the mortality rate. Fibrin is a highly extensible polymer that provides the main structural and mechanical stability to blood clots[1,2]. The structural scaffold must be able to withstand the highly dynamic intra- and extravascular forces that occur *in vivo*. Previous studies have shown that altering the concentration of coagulation activators (thrombin or tissue factor (TF)) has a significant impact on the structure of the fibrin clot[3]. Furthermore, fibrin network structure is altered in hypercoagulable states, affecting the mechanical response of blood clots under dynamic conditions[3], but rupture properties are mostly unknown. Toughness, which corresponds to the ability to resist rupture, is independent of viscoelastic properties.. In this study, we aimed to assess the role of fibrin structure modulated with different TF concentrations on the rupture resistance of blood clots.

Methods: We performed single-edge notch fracture tests to examine fibrin rupture under a constant strain rate (Figure 1A) with varying TF concentrations using a Biomomentum mechanical tester. Using these data, we assessed fracture toughness of clots. We assessed viscoelastic mechanics using rheology. We utilized confocal and scanning electron microscopy to quantify the fibrin network structure under varying TF concentrations, both before (Figure 1B) and during the rupture process.

Results: Our results revealed that increased TF concentration resulted in increased fibrin density (16-23 fiber pixels/total voxel (%), $p<0.0001$) (Figure 1C), and thinner (150-75 nm, $p<0.0001$) (Figure 1D), shorter (16-7 µm, $p<0.0001$) fibrin fibers with a reduction in pore size (6.5-3.0 µm, $p<0.0001$). Increasing TF concentration yielded a non-monotonic distribution of fracture toughness with a maximum of 7 N/m at 75pM TF concentration (Figure 1E) while the low TF concentration samples showed the highest stiffness (not shown). Low (30pM) and high (600pM) TF concentrations showed a significantly lower toughness when compared to 75pM samples ($p<0.0001$ and $p<0.01$ respectively). Correlation analysis revealed no dependence of toughness on initial crack lengths across all TF concentrations studied ($p>0.05$), demonstrating that toughness is a well-defined material parameter. We show that fibrin diameter and network density underlie a complex role in influencing the rupture resistance of blood clots, resulting in a nonmonotonic relationship between TF and toughness, and revealing that fibrin structural changes significantly impact rupture resistance.

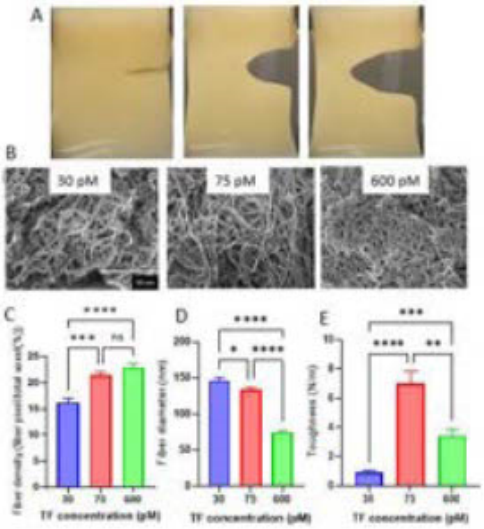

Figure 1 A): Crack propagation in stretched plasma clot. Corresponding images were taken at 0%, 10% and 35% strain (left to right). B) SEM images of clots formed with 30, 75 and 600 pM TF (left to right) scale bar-50um C) Fibrin density D) Fiber diameter E) Fracture toughness as a function of TF concentration.

Conclusions: Variations in fibrin density, fiber diameter, and fiber length give rise to a complex influence of fibrin structure on rupture. The differences in mechanical responses point to the importance of studying the structure-function relationships of fibrin networks, which may be predictive of the tendency for embolization.

References: 1. Litvinov R.I., Matrix Biology 60 (2017): 110-123. 2. Tutwiler V, Acta Biomater.(2021) ;131:355-369. 3. Kattula, S., Arteriosclerosis, thrombosis, and vascular biology, (2017), 37(3), e13-e21.

Acknowledgements: This work was supported by the NIH grant R01HL148227 (J.W.W), R01-HL135254 (J.W.W.), R00HL148646 (V.T.)

DEI: By leveraging diverse perspectives and expertise in fields of biology, computation and mechanics, we can address healthcare disparities through targeted interventions and broaden participation in STEM fields, fostering inclusivity and equity in scientific research.

STEVENS
INSTITUTE OF TECHNOLOGY

Integration of Optical Coherence Tomography (OCT) and 3D Computational Fluid Dynamics (CFD) to Evaluate Right Coronary Artery (RCA) Hemodynamics

Aaron Shamouil, Mohammad Mir, Robert Gordanier, Xueshen Li, Yu Gan, Jinho Kim
Department of Biomedical Engineering, Stevens Institute of Technology, Hoboken, NJ

Introduction: Coronary artery disease is a heart condition characterized by atherosclerosis, which involves the gradual buildup of calcified regions in the coronary artery, leading to arterial stiffening and narrowing. The right coronary artery (RCA) supplies blood to the right ventricle and when affected by atherosclerosis has an increased risk for arterial rupturing [1]. Optical Coherence Tomography (OCT) is a high-resolution imaging modality that has revealed the extent and composition of calcification within coronary layers (intima, media, adventitia) through deep learning algorithms [2]. Furthermore, 3D Computational Fluid Dynamics (CFD) modeling offers valuable analysis for hemodynamic properties. However, limitations exist in understanding the hemodynamic implications of atherosclerosis from OCT images. Therefore, this study aims to integrate OCT imaging with 3D CFD modeling to assess the impact of different calcification levels on pressure distribution, blood flow velocity, and stress applied on the RCA wall. This analysis aims to provide insight on the relationship between atherosclerosis progression and potential therapeutic interventions to enhance clinical decision-making.

Methods: To acquire the parameters of the RCA model, OCT imaging was performed on five RCA samples that were acquired from the School of Medicine at the University of Alabama at Birmingham. A straight incision was applied along the surface of the RCA to flatten the sample. A benchtop OCT system from Thorlabs (Newton, NJ) with an axial resolution of 3 μm was used to determine measurements for wall thickness and radii of the RCA utilizing a built-in measurement tool. For each sample, three imaging volumes were considered and the thickness values of 75 B-scans were recorded. COMSOL (Burlington, MA) CFD software was utilized to simulate the hemodynamic properties of the RCA. Calcification levels of 0% (None), 25% (Mild), 50% (Moderate), and 75% (Severe) were considered. The laminar flow of the RCA was recorded by using the Navier Stokes Equation. A high mean pressure of 126.11mmHg was applied at the inlet and 125.09mmHg to the outlet of the RCA.

Results: From OCT imaging, the samples had an average inner diameter of 3.64 ± 0.21 mm, wall thickness of 0.696 ± 0.0571 mm, and an outer diameter of 5.04 ± 0.114 mm that were used to create the RCA 3D model. Figure 1A provides an example of how OCT imaging was used to determine the thickness of the RCA wall by summing the three layers. In the CFD model, the percentage of calcification was applied to the inner diameter of the RCA. Figure 1B represents the simulation results that compare the pressure and blood flow velocity distributions across different levels of calcification. Within the normal RCA (0% calcification), there is a uniform pressure distribution and blood flow velocity due to minimal vascular resistances acting against the blood flow (Figure 1B). However, in calcified RCAs as the percent calcification increased, the pressure patterns became more concentrated at the calcified regions and dispersed more towards the inlet and outlet regions (Figure 1C-E). Moreover, the velocity profiles showed a maximum velocity at the center of the calcification regions due to a decrease in the inner diameter of the artery. Additionally, the maximum stress applied to the RCA wall was within the calcified region, in which the stress became more pronounced as percentage of calcification increased (Figure 1F). Therefore, analyzing patterns associated with pressure distribution, blood flow velocity, and stress applied on the RCA wall may help with predicting vulnerable sites for plaque development and providing insight on possible RCA ruptures, when monitoring patients with atherosclerosis [3]. In terms of limitations of this study, there were simplifications considered when modeling the geometry of the RCA and when applying boundary conditions for the blood flow dynamics.

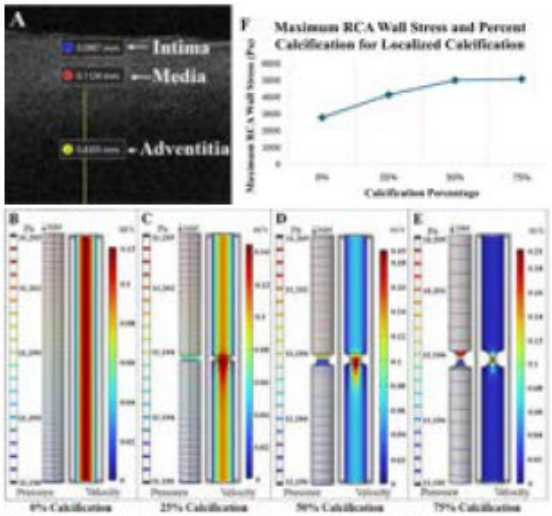

Figure 1: OCT Imaging Protocol and CFD Simulation Results. *(A) OCT measurement tool for RCA thickness. (B-E) Surface pressure and blood flow velocity results for 0%, 25%, 50%, and 75% calcification respectively. (F) Localized calcification results for maximum RCA wall stress.*

Conclusions: In this study, OCT imaging was integrated with 3D CFD modeling to assess the impact of diverse calcification levels on pressure distribution, blood flow velocity, and mechanical stress within the RCA. This integration enhanced our understanding of the hemodynamic implications of varied calcification levels associated with atherosclerosis. Additional efforts will be directed towards enhancing the precision of the CFD models by incorporating detailed anatomical parameters for more accurate results.

References:

1. Liu, Y. et al. Front Cardiovasc Med (2022) 9
2. Liu, H. et al. J Biomed Opt (2023) 28 (3)
3. Poznyak, A. et al. Front Cardiovasc Med (2022) 9

A Haptic Virtual Reality Simulator for Robot-Assisted Femur Fracture Surgery

Fayez Alruwaili[1], David W. Halim-Banoub[2], Jessica Rodgers[1], Adam Dalkilic[1], Christopher Haydel[3], Javad Parvizi[4], Iulian I. Iordachita[5], Mohammad H. Abedin-Nasab[1,*]
[1]Rowan University, [2]Rowan-Virtua School of Osteopathic Medicine, [3]Virtua Health, [4]Rothman Orthopedic Institute, [5]Johns Hopkins University.

Introduction: Surgical standards and training are achieved through numerous hours of practice and failure using imitated models under the supervision of a limited number of highly specialized surgeons [1]. This can be very time-consuming and costly for future specialized surgeons to attain the experience needed for operational proficiency. Virtual Reality (VR) simulators allow residents and skilled surgeons alike to learn new complex surgical procedures when they best fit their schedules and grant them the opportunity to perfect their skills through failure with low risk [2]. This more flexible training regimen has been translated to surgical evaluation improvements such as shortened surgical times, greater tool manipulability, and greater accuracy in the operating room [3]. Motivated by these remarks, we aim to develop the Robossis Surgical Simulator (RSS) to provide the surgeon(s) and operating staff with the required skills to operate the Robossis system.

Methods: We design and develop the RSS to inherit the Robossis system surgical environment as previously completed in a cadaver experiment [4]. Further, the RSS is developed to immerse the users in a 3D environment utilizing the Meta Quest VR headset and experience haptic feedback via the Sigma.7 haptic controller (HC). We use the Sigma.7 HC as the interface between the user input trajectories and speed into the RSS environment for manipulating the Robossis surgical robot (RSR). A motion control algorithm was developed to scale the user input trajectories to a maximum linear and angular velocity to represent conditions similar to the real world. Additionally, we developed the kinematic representation of the RSR and HC to resemble the real-world physical systems. We compute the inverse kinematics to drive the RSR and HC joints so that each robot's end-effector is manipulated to the desired location and orientation. Further, we extended the implementation of the separating axis theorem to retrieve the collision between the distal and proximal bone segment and, hence, determine the required haptic feedback that restricts the bone-bone collision.

Results: The RSS environment was created to immerse the trained users in a realistic operating room environment for femur fracture surgery using the Robossis system (**Fig. 1**). To interact with the environment, the HC Sigma-7 was used to manipulate the distal bone segment to the desired translational and rotational directions. Validation and simulation testing were conducted to determine the deviation of the RSR from the motion of the user's hand via the HC. The results show that the user's hand motion was accurately translated to the RSR movement, with a maximum deviation for translation (~ 5 mm) and rotation (~ 0.6 deg). Additionally, the integration of haptic feedback into the RSS provides users with the virtual representation and collision of the bone segments during the training. Thus, realistic behavior is experienced during training on the simulator.

Figure 1. Robossis-assisted femur fracture surgery environment was designed to include (1) a haptic controller, (2) a surgeon workstation, (3) the Robossis surgical robot, (4) a cadaver patient, (5) a C-arm X-ray machine, and (6) real-time visual rendering of the location of the bone is displayed as 2D fluoroscopic imaging. The Robossis surgical robot is attached to the distal bone segment using surgical rods (7). The environment was created to immerse the trained users in a similar operating room environment for femur fracture surgery using the Robossis system.

Conclusions: In this study, we developed a haptic-enhanced VR simulator designed explicitly for the Robossis system femur fracture procedure. This advancement in training not only enhances the learning curve but also promises to elevate the standard of medical education and patient care.

References:

1. M. P. Rogers. et al. Surgery. 2021;169(5):1250–1252.
2. A. J. Lungu, et al. Expert Rev Med Devices, 2021;18(1):47–62.
3. M. P. Fried et al., Ot—He and Ne Su, 2010;142(2):202–207.
4. M. S. S. et al., IEEE Robot Autom Lett, 2023. 8 (5), 2438-2445

Acknowledgements: This work is funded by the National Science Foundation (NSF) under grants 2141099, and 2226489, and by the New Jersey Health Foundation (NJHF) under grant PC 62-21.

DEI: The RSS training enhances accessibility in surgical education and healthcare by offering immersive, customizable learning experiences that reach diverse and underrepresented groups. It promotes access to high-quality training and healthcare insights, breaking geographical and socio-economic barriers and fostering a more inclusive and equitable field.

STEVENS
INSTITUTE OF TECHNOLOGY

An investigation into to the current practices of monitoring extracorporeal membrane oxygenation

Nicholas Chow, Shiffoni Sukhlal, Alisa Permessur, George Pittas, Dr. Wei Yin, and Dr. Jon Longtin
Stony Brook University

Introduction: Extracorporeal membrane oxygenation (ECMO) serves as a critical life support system for individuals facing cardiac or respiratory failure. Various manufacturers produce these systems, each featuring three key components: a mechanical pump, an oxygenator, and tubing. Together, these components emulate the functions of the heart, lungs, and blood vessels externally. Given its invasive nature, intra-device thrombus formation poses a significant concern, with the potential to impair gas exchange and potentially leading to the migration of blood clots into the body, thereby exacerbating complications [1]. In clinical practice, perfusionists meticulously monitor both the patient and the ECMO system, regulating blood and gas flow, and assessing the need for oxygenator or system replacement as necessary. To counter thrombus formation, clinicians often administer blood-thinners like heparin, albeit with the inherent risk of internal hemorrhage. Hematology labs play a crucial role in monitoring patients, albeit at the expense of time [2]. Despite its complexity, the monitoring of ECMO systems lacks standardization. This study delves into the complications associated with blood clotting in ECMO systems, exploring its mechanisms and how clinicians respond to such occurrences.

Methods: Participation in the NSF I-Corps Gotham Innovation Gambit in Fall 2023 facilitated engagement with various stakeholders, including clinicians closely involved with ECMO. Each interview adhered to predefined inclusion criteria and a set of questions aimed at eliciting insights into interviewees' clinical practices regarding ECMO and prevalent challenges. Analysis of their responses revealed trends across different roles. Clotting within the oxygenator of ECMO systems is a well-documented issue recognized by ECMO practitioners. However, the intricate fluid mechanics in this component remain poorly understood. To address this knowledge gap, a highly simplified 3D model of the Maquet Quadrox oxygenator's blood flow path was developed using AutoCAD, refined with Netfabb, and simulated using Comsol for computational fluid dynamics (CFD) modeling. By simulating expected parameters within the oxygenator, relationships between pressure, flow, velocity, permeability, and porosity could be observed.. Furthermore, an IRB-approved, de-identified database of ECMO patients was analyzed using Microsoft Access and original Matlab code. The focus was on longitudinal changes and significant clinical decisions based on quantifiable parameters. The analysis also examined how these parameters evolved following such decisions, if at all.

Results: 45 interviews were conducted via I-Corps; 20 participants held clinical titles like perfusionist, nurse, or respiratory therapist. Others included researchers, engineers, technicians, sales personnel, and more, that were familiar with ECMO systems but unable to offer insights on patient risks. Among the 20 clinicians interviewed, 75% acknowledged clotting as a significant ECMO system issue, while 12.5% considered it an insignificant occurrence.

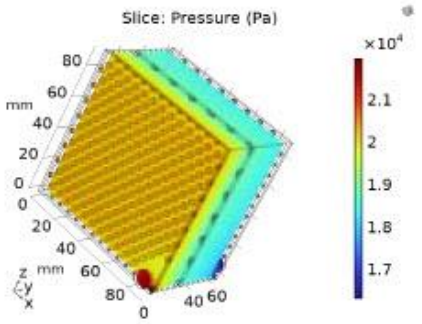

Figure 1. Sample pressure gradient plot across XZ-Plane slices of Maquet Quadrox oxygenator interior.

Across 9 patients, the average oxygenator inlet and outlet pressures were found to be 223.89 mmHg and 179.44 mmHg respectively (29849 Pa and 23923 Pa), with an average flow rate of 5.08 L/min (8.47e-5 m^3/s).

Conclusions: The interviews revealed current issues in the ECMO system, emphasizing clotting's impact on patient outcomes. Further interviews with relevant clinicians are necessary to understand trends across different patient profiles such as neonates and pediatrics. Automating the current CFD model protocol could expedite results generation. There is ongoing effort to interpret model results and simulate scenarios that would replicate patient data. While the patient database is vital for assessing ECMO parameters and trends, additional clinical context is needed to grasp the correlation between quantifiable factors and key decisions as the data from patient to patient varies greatly.

References:

1. Staessens S, et al. J Thromb Haemost. 2022;20(9):2058-2069.
2. Mossadegh C. Nursing Care and ECMO. 2016:45-70.

Acknowledgements: We thank Dr. Jonathan Schwartz for providing the ECMO patient database, as well as the NSF I-Corps Program and all the interviewees for the opportunity to learn more about ECMO.

DEI: 1) By understanding the ECMO device across different populations (neonates, children, and adults), it may be possible to suggest improvements for the care that patients receive during clot-related events, thus improving healthcare disparities. 2) Our diverse group, including underrepresented individuals in STEM, prioritizes community outreach, data analysis, and collaboration within and beyond our network. We aim to persist in our research and utilize minority-driven resources for success.

STEVENS
INSTITUTE OF TECHNOLOGY

Dye Enhancement of an Antibody-Conjugated Nanosensor Platform

Atara R. Israel, Ryan M. Williams, PhD
The City College of New York, CUNY, New York, NY, USA

Introduction: Single walled carbon nanotubes (SWCNTs) have the innate ability to fluoresce in the near infrared (NIR) region. What is unique about SWCNT fluorescence is its stability; the fluorescence emission exhibits no photobleaching or blinking in its signal, and measurements can be repeated as necessary over extended periods of time[1]. The NIR region specifically allows for SWCNTs to be implemented for in vivo use as a sensor since it is within the biological tissue transparency window. This allows for detection of biomarkers for specific diseases. Interleukin 6 (IL-6) is a pro-inflammatory cytokine that is present in diseased states, including cancers, COVID-19, and cardiovascular diseases. Detection of these biomarkers using SWCNTs is evaluated by changes in the optical band gap when interfaced with its complimentary antigen[2]. We are working to create an antibody conjugated SWCNT based nanosensor for detection of IL-6 as well as other inflammatory cytokines to be used in point of care settings for early disease diagnosis. To enhance the fluorescence signal seen, we have also introduced organic dyes, which interact with valence electrons on the SWCNT's surface, altering the intensity of the signal as well as shifting the center wavelength[3].

Methods: SWCNTs (HiPCo, NanoIntegris Technologies, Inc.; Quebec, Canada) were functionalized with single stranded DNA (ssDNA sequence) Integrated DNA Technologies; Iowa, USA) via probe-tip sonication (Fisher Scientific; New Hampshire, USA), followed by ultracentrifugation and filtration, along with characterization via absorption spectroscopy. To determine which ssDNA sequence would elicit the most interaction with different dyes, 12 ssDNA sequences were tested against 8 dyes. SWCNTs at a concentration of 1 mg/L were mixed with 1 µM of dye, and fluorescence activity was measured over a 3-hour timeframe using a high-throughput NIR plate reader spectrophotometer (ClaIR, Photon Etc.; Montreal, Canada) as well as shorter time intervals. Once compatible dye-ssDNA combinations were determined, antibody conjugated SWCNT based sensors were made by functionalizing SWCNTs with the selected ssDNA sequence containing a 3`-amine group. The antibody of choice was conjugated to the SWCNT surface via activation of the carboxylic acid ends on the antibody to join with the amine group on the SWCNT surface. The nanosensor was then left to dialyze for 48 hours and characterized using dynamic light scattering and zeta potential measurements to ensure conjugation. The complimentary antigen, along with dye was added to the nanosensor, and fluorescence measurements were measured over 3 hours, followed by evaluation of intensity and center wavelength changes.

Results: Dye-ssDNA compatibility tests showed center wavelength shifts up to 12 nm, and intensity either greatly increasing or being diminished completely. This was confirmed with what was seen in experiments using the spectral probe, where the interaction between the dye and SWCNT surface takes effect instantaneously and is stable. Translating these results to antibody-conjugated nanosensor experiments, we initially noted unsuccessful conjugation of the sensor complex with pre-selected ssDNA-dye combinations. Revision using a known ssDNA sequence for nanosensor formation showed increased center wavelength shifting from presence of dye (5 nm) to no dye present (-0.6 nm) after the addition of IL-6 antigen (Figure 1), enhancing the signal observed during nanosensor interaction with its complimentary antigen.

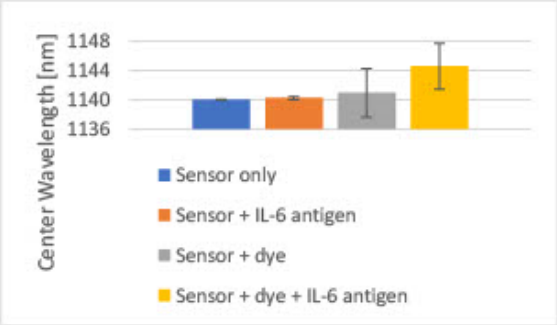

Figure 1. Center wavelength of nanosensor 5 minutes after addition of IL-6 antigen.

Conclusions: From these experiments, we can conclude that dye interactions with SWCNT surface are beneficial in amplifying its fluorescence activity and can serve as a promising tool to be used in further recognizing nanosensor-protein interactions that may be difficult to detect, especially under biological conditions where other proteins can compete for interactions with the surface of the nanosensor. Future directions of this research include in vivo implementation using methylcellulose hydrogels as a carrier for the nanosensor and validate analyte detection via this method. Further investigation can also be conducted on optimal pairings of ssDNA and antibodies to determine which pairings will result in successful conjugation.

References:

1. Ackermann J. et al. Angew. Chem. Int. Ed. 2022
2. Williams RM. et al. Sci Adv. 2018
3. Zheng Y. et al. ACS Nano. 2020 (14;12148-12158)

Acknowledgements: NIH Grant R35GM142833

DEI: Nanomedicine can help improve health disparities by creating more accessible, lost cost methods of diagnostic tools to allow for early detection of diseases and cancers via continuous cytokine detection and monitoring. Diversity in STEM can be improved by creating educational and informative programs for underserved communities to spark their interests in a field they may have not been exposed to before.

STEVENS
INSTITUTE OF TECHNOLOGY

Aggregation morphology of magnetic beads within microfluidic droplets

Anushri Kulkarni, Evan Lammertse, Ashiful Islam, Dr. Eric Brouzes.
Stony Brook University Biomedical Engineering Department.

Introduction: Magnetic beads are ubiquitous in biochemical processes to purify molecules of interest and enable workflow automation. Microfluidic droplets, a recent technology, miniaturizes reactors to perform those processes at high throughput (1,000's / s) and in tiny volumes (nanoliter range, 10^{-9} L). They can be easily manipulated but lack an efficient purification module. To address this gap, we designed a purification module where beads were clustered on one side of droplets before splitting[1]. However, the module is low throughput compared to other droplet manipulations. We aim to understand the aggregation dynamics of magnetic beads in flowing droplets to improve the module design. In flowing droplets, magnetic beads are subjected to two opposite forces: the aggregative magnetic forces and the dispersive viscous forces. We seek to describe this aggregation morphology as a function of the Mason number (Mn) by varying the droplet velocity.

Methods: Microfluidic devices were manufactured in PDMS by soft-lithography[2]. Droplets (0.2 nl) containing 350 magnetic beads (1 πm, Dynambeads Oligo-dT_{25} Invitrogen) were re-injected into a long straight 50 πm wide and 50 πm deep channel with a channel: droplets ratio of 1:2.5. Snapshot data collection: Images were collected at the midpoint of a magnet (N52, K&J Magnetics) placed where field lines are parallel to the channel and captured with a CCD camera. The morphology of magnetic aggregates were extracted by manual contouring. ImageJ was used to compute aggregate quantity, size, shape, and position. Dynamic data collection: Initial short sequences were obtained with a high-speed camera (Q-MIZE HD, V2).

Results: We first looked at the number of aggregates as a function of velocity (the magnetic force is maintained constant across experiments) using the snapshot images. We observed that the number of magnetic aggregates increases in a non-linear fashion with the droplet velocity (**Fig. 1**). There are four distinct phases 1) a plateau until 1 mm/s, 2) an abrupt jump in the number of aggregates, 3) a linear increase with a modest slope between 1 mm/s and 7 mm/s, and 4) an accelerated rate for velocities larger than 7 mm/s.

To understand those transitions, we started looking at the aggregates dynamics using realtime images. Figure 2 shows the aggregation of short bundles to a larger aggregate through a jigsaw-puzzle-like mechanism. The fragments recirculate in the droplet and slide along the larger aggregate until they lock at its extremity, remarkably, in a specific beveled shape.

While these data were obtained with a high-speed camera during a short period, we re-engineered a stage to enable droplet tracking over a long distance to accumulate statistically significant data. We will also couple those observations to high resolution map of droplet recirculation flow[3].

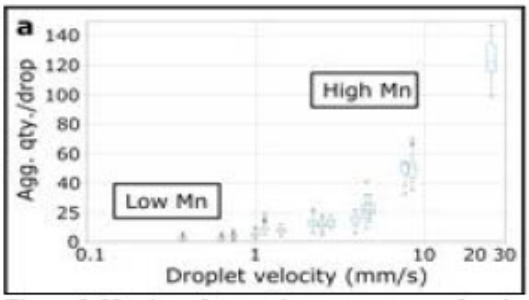

Figure 1. Number of magnetic aggregates as a function of droplet velocity (Mn: Mason Number).

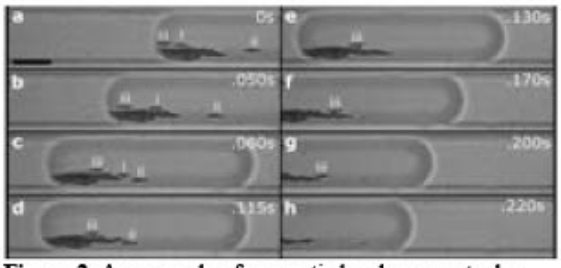

Figure 2. An example of magnetic bead aggregate dynamics (Scale bar = 20 πm).

Conclusions: Magnetic beads within low velocity droplets (low Mn) assemble into large aggregates at low counts, while those within high velocity droplets (high Mn) assemble into smaller aggregates but higher in count. Our data show a non-linear relationship between the number of magnetic aggregates with the Mason number (droplet velocity here). We are currently collecting dynamic data to study how these droplets behave in real time and elucidate the different regimes observed. This work will fill a considerable gap in our knowledge as dynamic aspects of magnetic bead aggregation have been overlooked outside the case of rotating magnetic fields.

References:

1. Brouzes et al. *Lab Chip*. **2015**, 15, 908.
2. Duffy, D.C., J.C. McDonald, O.J.A. Schueller, and G.M. Whitesides, *Anal. Chem.* **1998,** *70,*4974-4984.
3. Lammertse et al. *Microsystems and Nanoenginering*. **2022**, 8:72.

Acknowledgements: NSF CBET (No. 1705578).

DEI: Our work has direct applications within areas such as low-cost diagnostics. Understanding the behavior of magnetic beads within microfluidic droplets can allow for faster and more accurate point-of-care solutions, which can help address healthcare inequities.

STEVENS
INSTITUTE OF TECHNOLOGY

OculoMotor and Vestibular Endurance Screening (MoVES) Protocol Adult Concussion Data

Stuti Mohan[1], Jacqueline Theis[2], OD, FAAO, Chang Yaramothu[1], PhD, FAAO
[1]School of Applied Engineering & Technology, New Jersey Institute of Technology
[2]Virginia Neuro-Optometry Group

Introduction: A concussion, or mild traumatic brain injury (mTBI), is an umbrella diagnosis given for a variety of potential phenotypes: cognitive problems, oculomotor dysfunction, affective disturbances, cervical spine disorders, headaches, and cardiovascular and vestibular anomalies.[1] Many anatomical systems are negatively affected after an mTBI, notably the oculomotor system. Prior work led to the development of a diagnostic protocol and tool: the MoVES (oculomotor and vestibular endurance screening) protocol using the OculoMotor Assessment Tool (OMAT).[2]

The MoVES protocol and OMAT were used to establish a normative eye movement database for healthy participants with no prior self-reported history of concussions. The resulting normative database will be used to compare patient populations that may demonstrate oculomotor dysfunction due to a traumatic brain injury, such as a concussion.

Currently, clinicians at the Virginia Neuro-Optometry group are collecting data from adult concussion patients, an understudied population, undergoing rehabilitation. The data collection process involves a comprehensive assessment of oculomotor function in adult concussion patients during their initial clinic visit, as well as multiple periodic visits until the patient is completely recovered and symptom-free.

This project evaluates whether the data collected at the Virginia Neuro-Optometry Group via the MoVES protocol can provide evidence supporting the protocol's effectiveness in identifying concussed adults and filling in the gap of literature in the assessment of the understudied population of adult concussion patients.

Methods: Patients referred to the Virginia Neuro-Optometry clinic following a concussion diagnosis, aged 18 to 65 years old, were recruited for this study. The participants were assessed using the MoVES protocol during their initial baseline visit and their movements and resulting provoked symptoms for the following tests were recorded: 1) horizontal saccades, 2) vertical saccades, 3) vergence jumps, 4) horizontal vestibular-ocular reflex, 5) vertical vestibular-ocular reflex, 6) near point of convergence, and 7) near point of accommodation. The participants were instructed to alternate visual fixation between targets provided by the OculoMotor Assessment Tool (OMAT, Gulden Ophthalmics, Elkins Park, PA, USA, product number 18009) as rapidly as possible without overshooting or undershooting the target for one minute of the first five assessments. The OMAT was used adjunctively to standardize eye movement magnitudes for the MoVES protocol. The operator counted the number of eye movements or head rotations using the OMAT companion smartphone application, which recorded the repetitions in 15-second intervals. Traditional clinical protocols for assessing accommodations and convergence amplitudes were followed for the last two assessments using the OMAT.

Results: A total of 40 (85% female at birth) participants were recruited for this study with a mean age of 38 ± 13.2 years. A trend of decreasing average number of movements was observed in all assessments in each subsequent 15-second interval: HS (23.9, 21.3, 18.3, 16.6), VS (23.0, 17.4, 14.6, 12.3), VJ (15.0, 12.2, 10.7, 10.1), HVOR (24.4, 20.1, 17.7, 13.1), VVOR (24.5, 18.6, 17.6, 14.1). An average of the symptoms provoked after each test was calculated: Baseline (4.1), HS (6.0), VS (6.8), VJ (6.9), HVOR (7.8), VVOR (8.6), AA (5.4), NPC (8.6). Three NPC trials were attempted with an average break of 11.3 ± 8.8 cm and recovery of 18.7 ± 12.4 cm for trial 1, break of 12.1 ± 8.8 cm and recovery of 20.8 ± 12.8 cm for trial 2, break of 12.6 ± 9.1 cm and recovery of 21.0 ± 10.6 cm for trial 3.

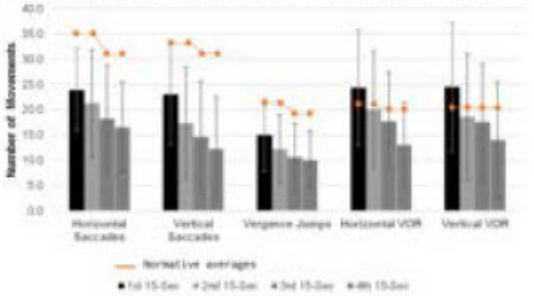

Figure 1. Group-Level Means for the five timed MoVES assessments

Conclusions: Compared to the normative (non-concussed) cohort,[2] the number of movements performed by this cohort was lower on average and decreased with each subsequent interval. The data support the efficacy of the MoVES protocol in identifying concussions in adults, which quantifies eye movements, head rotations, and accompanying symptoms. These quantitative and endurance-based measurements may aid in informing concussion diagnosis, quantifying symptomology, and tracking recovery.

References:

1. CratonT. Brain Sci. 2017 Sep; 7(9): 119.
2. YaramothuC. Optom Vis Sci. 2021Jun1;98(6): 636–643.

Acknowledgments: Funding for the research was provided by NJIT Faculty Startup Funds

DEI: Develop outreach programs that 1) educate diverse communities about concussions, their symptoms, and the importance of seeking timely medical attention and 2) foster mentorship initiatives for STEM-underrepresented persons to provide guidance and support throughout their academic and professional journeys

STEVENS
INSTITUTE OF TECHNOLOGY

The Sensitivity and Stability of Magnetic Nanoparticle – Based Aggregation Assays are Influenced by Surface Ligand Density and Electrolyte Concentration

Gabrielle Rose Moss[1], Christian Knopke[2], Solomon G. Diamond[1,2]
[1] Thayer School of Engineering, Dartmouth College, Hanover, New Hampshire, USA
[2] Lodestone Biomedical LLC, Lebanon, New Hampshire, USA

Introduction: We have developed a magnetic nanoparticle (MNP)-based aggregation assay for *in vitro* applications. Our aggregation assay is a model system consisting of biotinylated MNPs that target streptavidin. A 1 kHz AC magnetic field with 20 mT field strength, conveys the MNP harmonic response at 3 kHz. We are interested in studying how changes in functionalized MNP (fMNP) zeta potential, due to electrolyte concentration changes, affect fMNP aggregation when in the presence of their target.

According to the DLVO theory[1], colloidal stability of fMNPs in solution is determined by the polarity of the sum of the repulsive electrostatic double layer force, which is dependent on surface charge density and electrolyte concentration, and the attractive van der Waals force acting upon similarly charged fMNPs. A positive sum suggests stability, whereas a negative sum suggests instability and hence aggregation. Our work can aid in the progression of aggregation assay-based technologies[2] by demonstrating (1) that receptor density can be used to tune the dynamic range (a biosensor's measurable concentration range) and sensitivity of aggregation assays, and (2) that changes in nanoparticle zeta potential and electrolyte concentration can cause changes in aggregation and subsequent loss of biosensing efficacy.

Methods: Amine functionalized 25 nm magnetite (SHA 25) particles (Ocean Nanotech, San Diego, CA, USA) were functionalized with the following amounts of PEG_4-biotin (Thermo Fisher Scientific, USA) via NHS chemistry: 15 PEG_4-biotin per MNP and 6,650 PEG_4-biotin per MNP. Once functionlized, the fMNPs were exposed to streptavidin (Rockland Immunochemicals, USA) serial dilutions in either 1x phosphate buffered saline (PBS) or deionized (DI) water.

Results: Streptavidin induced fMNP aggregation causes an increase in fMNP 3rd harmonic phase (figure 1). We estimate that fMNP biotin density is 2 times the streptavidin:fMNP ratio at which the maximum 3rd harmonic phase occurs. Our fMNPs' receptor densitites were 9.62 and 141.56 biotins/MNP. fMNP streptavidin sensitivity increased as biotin density decreased. The 9.62 biotins/MNP fMNPs had a dynamic range from 0 to 149 nM streptavidin, while the 141.56 biotins/MNP fMNPs had a dynamic range from 522 to 1,368 nM streptavidin.

Streptavidin induced fMNP aggregation is dependent on the diluent's electrolyte concentration (figure 1). In PBS the fMNPs formed aggregates with streptavidin, however in DI water the fMNPs did not form aggregates with streptavidin. The zeta potential of the 9.62 and 141.56 biotins/MNP fMNPs were obtained in PBS and DI water. In PBS the 9.62 biotins/MNP fMNPs had a zeta potential of -6.29 ± 1.35 mV, in DI water it was 13.95 ± 2.07 mV. In PBS the 141.56 biotins/MNP fMNPs had a zeta potential of -3.60 ± 3.61 mV, in DI water it was 23.23 ± 2.60 mV. Both fMNP types have higher zeta potentials in DI water (hence increased stability), compared to PBS. According to the DLVO theory, if an fMNP has a high surface charge density and is in a low salt environment, like DI water, particle interactions are repulsive and dominated by the electrostatic double layer force[1]. This insight from the DLVO theory explains the lack of fMNP aggregation in DI water.

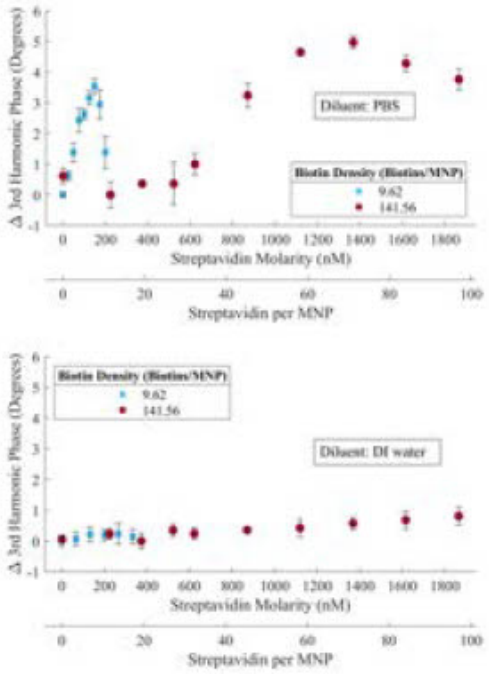

Figure 1. fMNP 3rd harmonic phase as a function of streptavidin in PBS (top) and DI water (bottom). The data shows that the assay's sensitivity increases as receptor density decreases, and the assay's output is electrolyte concentration dependent.

Conclusions: Our work shows that (1) the sensitivity and dynamic range of aggregation assays can be tuned with receptor density and (2) zeta potential and electrolyte dependent changes in fMNP aggregation lead to multiple assay readouts for a constant amount of target, indicating efficacy loss. For further contributions, we are interested in the effects of theragnostic relevant ligands, such as methoxyl PEG (mPEG), on fMNP aggregation.

References: [1] G. Trefalt, and M. Borkovec, "Overview of DLVO Theory," (2014).
[2] M. Sabela, S. Balme, M. Bechelany, J. Janot, and K. Bisetty, "A Review of Gold and Silver Nanoparticle-Based Colorimetric Sensing Assays," Adv Eng Mater **19**(12), 1700270 (2017).

STEVENS
INSTITUTE OF TECHNOLOGY

Synthesis of Iron Nanoparticles Through Chemical Reduction

Ciara Nuesi[1], Chathura Wijethunga, Melissa E. King[2]
[1]Department of Civil Engineering, [2]Department of Chemistry and Biomolecular Science
Clarkson University

Introduction: Nanoparticles (NPs) have had many influences in the biomedical and engineering fields. NPs vast properties can be applied to biosensors, drug delivery, magnetic resonance imaging, and environmental remediation. This research focuses on the synthesis of iron NPs and the effect of varying parameters on the characteristics of NPs. Refining NPs can help optimize the field of nanotechnology and areas of biomedical science.

Methods: Iron nanoparticles were synthesized with N_2 bubbled ultra-pure water (9.5 mL), iron (III) nitrate nonahydrate ($Fe(NO_3)_3$, 250 µL – 10 mM), Nitric Acid (HNO_3, 25 - 100 µL 1M), Trisodium Citrate (TSC) ($Na_3C_6H_5O_7$, 250 µL – 10 mM, and 5 mL – 1 mM), Sodium Borohydride ($NaBH_4$, 500µL $NaBH_4$ 100mM and 500µL $NaBH_4$ 500 mM). After 3 hours, the contents were centrifuged at 7200 rpm for 5 minutes. Subsequently, a Scanning Electron Microscope (SEM) produced the nanoparticle images.

Results: Each set consisted of 9.5 mL of N_2 bubbled ultra-pure water, a variation in the TSC, Fe(NO3)3, HNO3, and NaBH4 concentration.

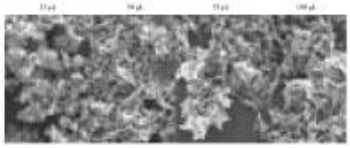

Figure 1 SEM images of 250-10mM µL TSC and 25-100 µL of HNO_3. A-C) 25 µL HNO_3, D-E) 50 µL HNO_3, G-H) 75 µL HNO_3. Scale bar 100 nm.

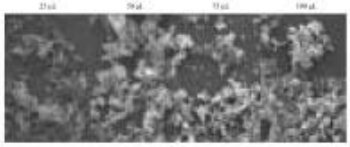

Figure 2 SEM images of 5mL-1mM TSC, 500µL-500 mM $NaBH_4$, and 25-100 µL of HNO_3. A-C) 25 µL HNO_3, D-E) 50 µL HNO_3, G-H) 75 µL HNO_3. Scale bar 100 nm.

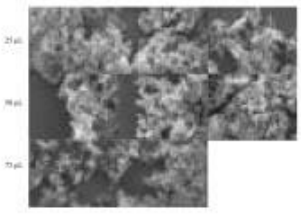

Figure 3 SEM images of 5mL-10mM TSC, 500µL-500 mM $NaBH_4$. A-C) 25 µL HNO_3, D-E) 50 µL HNO_3, G-H) 75 µL HNO_3. Scale bar 100 nm.

Initial results afforded agglomerated metal clusters rather than discrete nanoparticles (Figure 1). Combinatorial synthetic processes over the course of these studies showed the effects of varying HNO_3, TSC, and $NaBH_4$. **Figures 1, 2, and 3** illustrate the effect of varying HNO_3, TSC, and $NaBH_4$ via analysis of SEM micrographs. A comparison of the obtained results shows that the increase of TSC (**Figure 2**) results in more dispersed particles rather than agglomerates. Further increase of growth solution concentrations of TSC (**Figure 3**) resulted in more uniform discrete nanoparticles. These findings are interesting because a critical point or limit exists within the synthesis.

Conclusions: In conclusion, a working synthesis through chemical reduction was successful. The formation of NPs relied on HNO_3 as a stabilizing agent. HNO_3 interacts with NP surfaces and prevents rust, oxidation, and aggregation of particles. Reducing agents like $NaBH_4$ and TSC aided in controlling the characteristics of NPs. However, greater concentrations of TSC lead to more uniform particles and greater morphological control. Future works should include the exploration of attaining homogeneous control of the morphology of the NPs. Enhancing morphology to be homogenous can benefit predictability and optimize specific characteristics for certain applications. Future directions should also include achieving greater monodispersity in particles. Uniformity ensures consistency and reliability.

References: 1. Prashant L. S. Synthesis of Iron Oxide Nanoparticles Green Process Synth 2018; 7: 1–11
2. Chiara T. Iron Oxide Nanoparticles as Drug Delivery Pharmaceuticals (Basel). 2021 May; 14(5): 405.

Acknowledgments:
Clarkson University BOREALIS Scholars Program.

DEI: 1) Nanoparticle research has advanced vastly through numerous fields. Nanoparticles' unique characteristics can be implemented into various medical practices and medicines. It can be tailored to specific needs and address concerns in underrepresented communities. 2) Broadening participation among STEM-underrepresented persons can be initiated by creating outreach programs to display the diverse opportunities of nanoparticle research.

STEVENS
INSTITUTE OF TECHNOLOGY

Design of a Single Walled Carbon Nanotube-Based Nanosensor for the Inflammatory Cytokine TNF-alpha

Syeda Rahman, Ryan Williams.
The City College of New York

Introduction: In recent years, single-walled carbon nanotubes (SWCNT) have gained considerable attention for serving as building blocks for biosensors due to their unique optical properties. Semiconducting SWCNTs are fluorescent in the near-infrared range (NIR, 900–1600 nm) due to their optical band-gap between valence and conduction band.[1] Different structures of SWCNT, called chiralities, exhibit unique absorbance and emission bands. Optical nanosensors are advantageous over electrochemical biosensors because of their biocompatibility, photostability and potential for continuous monitoring of analytes. Due to its high surface to volume ratio, SWCNT sensors are very sensitive to their local chemical environment.[2] We are working to build highly specific aptamer-based nanosensors that fluoresce in the NIR region to detect disease biomarkers such as inflammatory cytokines. Aptamers are short DNA sequences that act as a recognition unit for the analyte. TNF-alpha is a proinflammatory cytokine involved in a diverse range of functions, including cell signaling, apoptosis, necrosis, resistance to infection and cancer. It plays a critical regulatory role in enhancing dysregulated immune responses in degenerative diseases.[2] We designed a TNF-alpha aptamer based SWCNT sensor that responds to the addition of TNF-alpha protein by changes in fluorescence intensity.

Methods: HiPCO- SWCNT (NanoIntegris Technologies) were sonicated in a 1:2 ratio with a TNF-alpha specific aptamer (IDT) to solubilize and functionalize the nanotubes. The resulting suspension was ultracentrifuged (Beckman Coulter; California, USA) to remove impurities and aggregates. The top 75% of the centrifuged suspension was filtered through a 100kDa Amicon centrifugal filter to remove excess DNA. The resulting nanosensors were characterized with a V-730 UV-Visible absorption spectrophotometer (Jasco Inc.). To test the sensor's response to its target, 250 nM TNF-alpha protein was added to 0.5 mg/L SWCNT-aptamer in 1X PBS. For 3 hours following antigen addition, repeated nIR fluorescence measurements were taken with a MiniTracer NIR spectrophotometer (Applied NanoFluorescence; Texas, USA.) at an excitation wavelength of 638 nm. We took fluorescence spectra before adding the protein indicated as (-1 min) and immediately after adding the protein (0 min) followed by continuous time points. We further tested our sensors in a more complex environment, sensor with the addition of 10% fetal bovine serum (FBS). All chiralities were analyzed for center wavelength shift and fluorescence intensity changes to determine any interaction between the nanosensor and the protein.

Results: We found that the fluorescence intensity of the SWCNT decreases over time with addition of 250 nM TNF-alpha protein in buffer condition. The intensity of the sensor exposed to the TNF-alpha protein dropped 50% from the initial timepoint. In serum conditions, the changes in intensity were less observable. This difference in results from buffer to serum conditions could attributed to the interference of serum proteins on the nanotube surface. To mitigate this issue, we assessed various passivation agents like poly-l-lysine (PLK) and bovine serum albumin (BSA) to block non-specific protein binding of the serum. The passivation did not have an impact on fluorescence modulation of the sensor at 50x mass ratio to SWCNT.

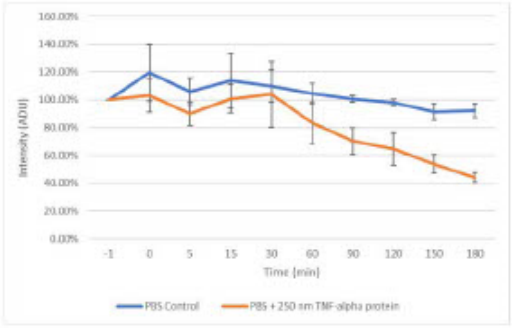

Figure 1.(7,5) Peak Normalized Intensity

Conclusions: Aptamer-based SWCNT nanosensors hold great promise for the future of point of care devices, early detection of specific biomarkers and other sensing applications. Future directions of our sensors include screening various passivation agents with 70-100x mass ratio of SWCNT in conditioned media to detect proteins of interest with selectivity and specificity. We will use LPS induced macrophage cell media expressing TNF-alpha in large quantity to evaluate the sensitivity and selectivity of our sensor. To validate our sensor in a complex biological environment, conditioned cell media treated with LPS will be used. TNF-alpha siRNA PLGA-PEG will be used to knock down TNF-alpha expression in cells as a negative control. The quantification of the amount of the TNF-alpha protein will be done with an immunosorbent assay (ELISA). We hope to create a nano sensor construct that can determine and quantify low levels of biomarkers of interest with more accuracy than currently available immunoassays.

References

1.Ackermann J Angew.Chem.Int.Ed.2022,61,e202112372(1-5)
2. S. Kruss et al. / Advanced Drug Delivery Reviews 65 (2013) 1933–1950
3. Orava E.W. ACS Chem Biol. 2013, 8, 170-178

Acknowledgements: This work was supported by NIH R35GM148233.

DEI: The field of Biomedical Science can improve tremendously in terms of overcoming disparities in healthcare outcomes by engineering accessible and cost effective testing devices to diagnose disease markers before late stage progression. STEM outreach programs are a great way to increase diversity and inclusion in the field. Programs that educate students and pique their interest in STEM could be a great way to start.

Detection of Human Trust in AI Suggestions Using Brain Activity Data

Leslie Abbott, Ruhuan Liao, Danushka Bandara
Fairfield University

Introduction: The purpose of this research is to utilize data collected from an fNIRS system to investigate and understand human trust in an AI agent. By processing and analyzing the fNIRS data, the aim is to uncover patterns of neural activation and cognitive processes underlying trust and the implications for designing trustworthy AI systems.

Methods: Participants were selected from both the undergraduate and graduate student body at a university in the northeast (n=18). Utilizing a Hitachi ETG-4000 fNIRS device operating at a sampling rate of 10 Hz, the data acquisition involved optodes arranged in a cap with a probe configuration, symmetrically placed on the participants' forehead area. This setup facilitated the capture of oxygenated and deoxygenated hemoglobin levels in the frontal cortex. Participants underwent a series of tests with increasing instances of stress, being asked whether they were able to trust a computer-generated response to a question or not. Their confidence level in the given answer was also inquired and recorded.

The collected data undergoes preprocessing, which includes parsing timestamp files to determine data segment boundaries and partitioning the data accordingly. Data analysis entails computing mean values for each channel and data entry, examining central tendencies to detect neural activation and cognitive patterns, and performing statistical analyses to assess differences across experimental conditions or participant groups. Interpretation involves deriving insights into cognitive processes and question responses, linking findings to existing literature and theoretical Frameworks.

Results: The significance of the differences in hemoglobin concentration between the trust and mistrust condition was tested using the Welch Test. Any channel that produced a significant difference was noted, possibly indicating that this neural channel plays a role in task performance. In the initial analysis, two channels were noted to produce significant results across all subjects: a visual diagram of the differences in these channels is provided below. The implications of this study include better understanding of the mechanics of trust in the human brain and design of more trustworthy AI systems.

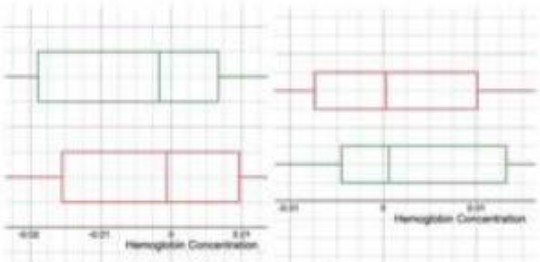

Figure 1 and 2: Statistically Significant Differences in Hemoglobin Concentration in Channels 9 (left) and 10 (right).
The mistrust condition is shown in red and the trust condition is shown in green.

Conclusions: Thus far in the experiment, there have been two neural channels that exhibit statistically significant results in hemoglobin concentration; a visual representation of these differences is provided above. Channel 9 exhibited a p-value of 0.02428 and Channel 10 exhibited a p-value of 0.021245. Using the collected data, different neural channels can be tested according to their significance level to determine which channels are confirmed to be involved in the human trust in AI suggestion condition

References:

1. Bandara, D., Grant, T., Hirshfield, L. *et al.* Identification of Potential Task Shedding Events Using Brain Activity Data. *Augment Hum Res* 5, 15 (2020). https://doi.org/10.1007/s41133-020-00034-y

Acknowledgements: Fairfield University laboratories are used as the site of data collection in this experiment.

DEI: This data can be utilized in the trust conditions of a diverse range of people. Further testing can be done to show how diversity may affect the probability that the participant is going to accept the AI generated response. This can further be applied to how diversity as a whole experiences variance in trust when involved in medical equipment, such as the Hitachi ETG-4000, and how discrepancies in quality of healthcare may lead to lesser trust for certain diversities.

STEVENS
INSTITUTE OF TECHNOLOGY

Assessing the Viability of Near Infrared Spectroscopy to Evaluate Graft Maturation of Intraoral Bone Regeneration

Rocco Di Pede[1], Amanda Spurri[1], Dr. William Querido[1], Dr. David Semeniuk[2], Dr. Nancy Pleshko[1].
[1] Temple University College of Engineering, [2] Temple University Kornberg School of Dentistry.

Introduction: Bone grafting in implant dentistry is necessary in patients with significant bone resorption because it allows for the replacement of missing teeth with a dental implant. Normally, a volume of bone graft substitute is placed in the area of deficiency and is then stabilized by an overlying collagen membrane. Over the course of many months, blood vessels infiltrate the graft material, begin to resorb the graft material, and replace it with native bone. However, due to the variability in patient healing, the degree of maturation of the graft is difficult to assess. This makes it challenging to determine when the graft is mature enough to move forward with dental implant placement. The current clinical standard involves the use of radiographic imaging; however, this does not give sufficient information about tissue quality. This has led to interest in visible near infrared (VNIR) spectroscopy as a possible approach. VNIR works by using light absorbance to assess the composition of tissues and materials. The goal for this project is to determine if non-invasive VNIR can accurately assess and differentiate models of bone graph maturation.

Methods: Overall approach: Multiple tissue configurations were assessed to determine if VNIR spectroscopy is a feasible method for differentiation of healing stages of intraoral bone tissue healing. Figure 1 explains the compositions of the different configurations used. They are in successive order of representative bone maturation and healing.

Name in Project	Composition
GingivaOnXenograft	Gingiva atop xenograft
GingivaOnMix	Gingiva on a mixture of 50% bone shavings and 50% xenograft
GingivaOnBoneShavings	Gingiva on a mixture of 85% bone shavings and 15% xenograft
GingivaOnRawBone	Gingiva on intact mandibular bone

Figure 1. Configuration Table

Samples: Tissues (gingiva, bone shavings, mandible) were collected from a juvenile porcine jaw. The gingiva was cut to 1.25mm + 0.42[2], the average thickness of human gingiva Spectra collection: an ASD Labspec 4 (Malvern Panalytical, Boulder, Colorado) was coupled with a fiber optic probe for data collection. A Spectralon background was used for reference data collection. Ten spectra were collected per configuration. Spectra were collected at 50 coadded scans with a 2 mm spacer to ensure consistent probe distance from sample. Data Analysis: Spectra were evaluated using the Unscrambler (CAMO Software AS, Norway). A principal component analysis (PCA) was completed over the range 28571cm^{-1} to 4000cm^{-1} to assess whether the spectra from the maturation models could be differentiated.

Results: From the four different configurations, the averages of the 10 scans each were taken and plotted as raw spectra (Figure 2). Specific peaks and overall spectral contours were compared to one another to investigate differences present. For example, spectra of the gingiva on top of the solid mandibular (raw) bone had overall lower intensity compared to the other configurations. Differences in quality of spectra were observed with the granulated tissues. Using the scores plot of the PCA, distinct trends were seen. These trends demonstrated a grouping of each configuration that was distinct from each other (Figure 3). Also, these groupings demonstrated relative distinctive positions to one another.

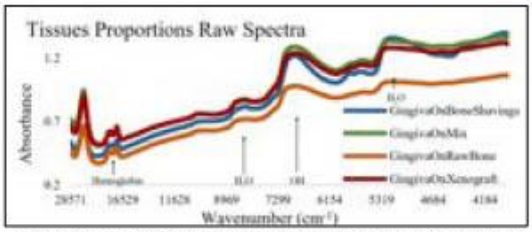

Figure 2. The Spectra of Different Tissue Proportions

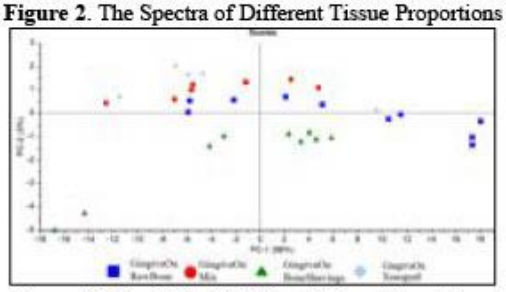

Figure 3. The PCA of Different Tissue Proportions

Conclusions: The data presented gives a promising proof of concept for the ability of VNIR spectroscopy to differentiate between different proportions of native bone and bone graft substitutes. The data found on the PC-2 of the PCA plots demonstrates the ability for VNIR data to give a progressive gradient of tissue composition, noting the configuration groupings in an order of bone maturation. For future research, the introduction of a clinical membrane, blood, and a singular, more accurate, substitute for native bone beneath the gingival tissue will be investigated.

References:

1. Jensen SS. et al. Clin. Oral Impl. Res. 2007;752-60
2. Goaslind GD. et al. J Periodontol. 1977;48(12):768-71

Acknowledgements: Thanks to Straumann Group (Peter Merian-Weg 12, 4002 Basel, Switzerland) for donating the Xenograft used in this research.

DEI: This research aims to improve economic disparities in healthcare by providing a more accessible alternative to X-ray imaging. If NIR spectroscopy is found to be an accurate substitute for assessing intraoral bone maturation, a more affordable, more mobile, and easily operated form of tissue imaging would be an option for dental clinics in low resource areas that might not have access to X-ray imaging. This would lead to an improvement in patient care in underprivileged areas.

STEVENS
INSTITUTE OF TECHNOLOGY

Characterization of Scattering for Whole Blood Oximetry in Sub-Diffuse Regimes

Osama Elgabori[1], William B. Scammon[1], Kelly R. Strong[1], Keith Cook[1], Jana M. Kainerstorfer[1,2]
[1]Department of Biomedical Engineering, Carnegie Mellon University; [2]Neuroscience Institute, Carnegie Mellon University

Introduction: Extracorporeal membrane oxygenation (ECMO), a life support system, is unsuitable for permanent respiratory support due to high thrombogenicity and bulkiness[1]. Pulmonary assistant systems (PAS), wearable devices with an axial flow pump and compact gas exchanger, aim to overcome these challenges. However, for long-term use of these devices, incorporating feedback on blood oxygenation is essential. We are developing an optical sensor that measures light attenuation through the blood-filled tubes of these devices to quantify blood oxygenation and monitor device performance over time. The tissue optical properties, the absorption and scattering coefficients (μ_a, μ_s), enable assessment of tissue function and morphology[2]. If tissue is only absorbing, the Beer Lambert law (BBL) can be used to quantify absorption. In highly scattering tissues, the diffusion equation can be used to describe light transport. However, whole blood, being neither a diffuse medium nor only absorbing, requires evaluating optical properties in the sub-diffuse regime. Literature has suggested that the BLL can be used when adding a scattering correction term based on Mie theory[3]. Here we present results of applying this model to broadband transmission measurements made on whole blood samples.

Methods: We collected broadband optical transmission data on bovine blood samples placed into a cuvette for determination of the total attenuation coefficient μ_t with a spectrometer (Ocean Optics). For each blood sample, the spectrometer collected data for 60 scans and 3 measurements were made per sample. We constructed a circuit containing a centrifugal blood pump, an oxygenator, and a 400-ml soft bag reservoir to adjust the blood oxygen saturation. At test points, samples were drawn from the circuit to measure oxygen saturation and hemoglobin concentration using a blood gas analyzer (BGA, Radiometer ABL 825 Flex). We applied least squares fitting of a literature-derived model to our data within the wavelength range of 640-860 nm. We fit three parameters (SO_2, a, b) in the equation: $\mu_t(\lambda) = \mu_a(\lambda) + \mu_s(\lambda) = \epsilon^{\lambda}_{HBO_2} C_{HBT} SO_2 + \epsilon^{\lambda}_{HHB} C_{HBT}(1 - SO_2) + a(\frac{\lambda}{\lambda_0})^{-b}$, where μ_t is the total attenuation coefficient, C_{HBT} is the total hemoglobin concentration, SO_2 is the oxygen saturation, $\epsilon^{\lambda}_{HBO_2}$ and ϵ^{λ}_{HHB} are respectively the molar extinction coefficients of oxy-and deoxy-hemoglobin from literature, and a and b are the scaling factor and scattering power respectively that empirically describe scattering.

Results: Figure 1 displays data on the total attenuation coefficient and scattering parameters across varying oxygen saturations (51.9-93.4%) for whole blood with a hemoglobin concentration of 7.8 g/dL. The model fits closely with measured data, showing strong agreement (R^2 >0.9). As expected, the total attenuation coefficient spectra of whole blood mirror hemoglobin's spectral characteristics. Additionally, the scattering coefficient of whole blood (1a) remains insensitive to oxygenation, with minimal changes in scaling factor a and scattering power b with saturation.

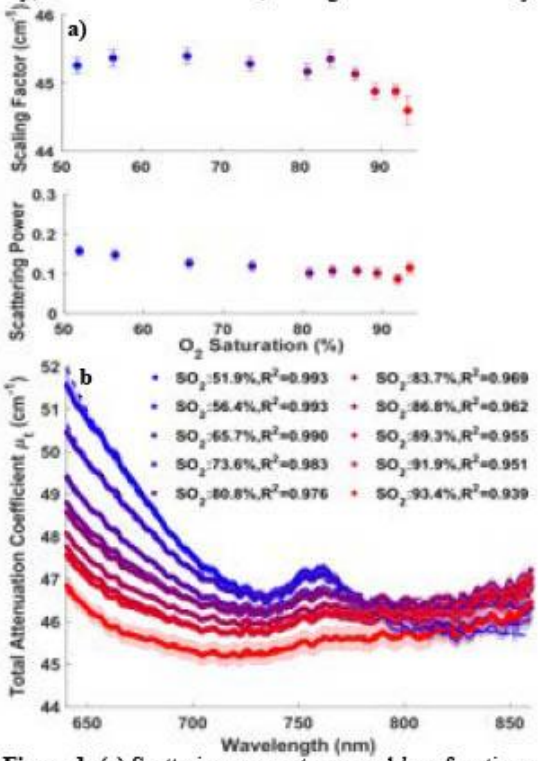

Figure 1. (a) Scattering parameters a and b as functions of oxygen saturation. (b) Measured total attenuation coefficient (solid) at various oxygen saturation and the model fits (dashed). Error bars are the standard deviation of the mean.

Conclusions: The results support the model assumptions that scattering and absorption can be treated independently and that scattering in whole blood is constant and insensitive to oxygen saturation. For application to whole blood oximetry, it is necessary to determine the degree to which changes in hematocrit influence the scattering coefficient. In summary, these results presented here warrant further study of whole blood light scattering, particularly for applications in which absolute quantification of physiological parameters by oximetry would be useful.

References:

[1]T. A. R. Seemungal et al. 2000. [Online].
[2]S. L. Jacques. *Physics in Medicine and Biology*, vol. 58, no. 14. pp. 5007–5008, 2013
[3]N. Bosschaart et al. *Lasers Med Sci*, vol. 29, no. 2, pp. 453–479, 2014.

Acknowledgements: Funding was received from CDMRP grant W81XWH-22-1-0304 and GEM.

DEI: The biophotnics field is striving to improve healthcare disparities through research that aims to identify and remove racial bias in widely used technologies, such as pulse oximeters.

STEVENS
INSTITUTE OF TECHNOLOGY

A Comparative Study of Coronary OCT Image Registration

Xinlong Hou, Mahdi Babaei, Yu Gan
Department of Biomedical Engineering, Stevens Institute of Technology, Hoboken, NJ

Introduction: Images from Optical Coherence Tomography (OCT) are essential for the diagnosis and treatment of plaques in the coronary. With the help of these finely detailed, high-resolution cross-sectional images, early identification, accurate monitoring, and customized treatment planning are made possible by their insights into the microstructures. In such a circumstance, image registration is essential for tracking progression and facilitating comparative analysis. Typical image registration consists of similarity metrics, optimizers, and interpolators. According to the types of interpolators, it's divided into rigid and non-rigid registrations, which respectively transform image matrices globally and locally. In this study, we explored and compared three image registration methods, i.e., Affine [1], B-Spline [2], and Displacement Field [3] methods aligning low-resolution images (moving images) to high-resolution coronary OCT images (fixed images), and evaluated their performance and suitable use cases.

Methods: In the initial image preprocessing stage, we normalized images to grayscale within the range of 0 to 255. Subsequently, an image registration model was constructed in the following sequences: similarity metrics, optimizers, and interpolators. Similarity metrics contain mean square and correlation, which assess the similarity of point matrices in moving and fixed images. While correlation focuses on structural similarities, mean square calculates similarity at the pixel level. Optimizers fine-tune interpolator parameters to achieve optimal performance, with Gradient Descent typically employed as the optimizer. Interpolators act as interpreters of images, representing features of subdivisions through methods like transformation matrices and polynomial functions. We provided three interpolators in this article. The Affine interpolators [1] deform moving pictures via Euler translation, $\boldsymbol{y} = \boldsymbol{A}\boldsymbol{x} + \boldsymbol{B}$, where $\boldsymbol{x}$ and $\boldsymbol{y}$ are pixel intensity matrices of moving and registered images. $\boldsymbol{A}$ and $\boldsymbol{B}$ are translation vectors and their variation will result in the rotation, shift, and zoom of moving images. The B-Spline interpolators [2] use a combination of polynomial bands to express structural elements. Polynomial bands are polynomial function curves that pass through and end with control points selected from pixel metrics. The control points in moving images will refer to points in fixed images and move to the same corresponding positions, further changing their relevant polynomial curves. The bands will segment both images, and the segmentation results will be used to evaluate the parameters of polynomial functions and control points. The Displacement Field [3] interpolators segment images by directly extracting boundary matrices from images. These boundaries will be treated as membranes, and pixels of moving images will move in or out of these membranes to match the fixed images. For these pixels, the moving directions and distances are independent, and their moving vectors form the Displacement Fields. Executing the fields will move pixels accordingly, and vectors will be tuned during optimization.

Results: These three types of interpolators are implemented. We conducted a comparative study on human coronary OCT images (N = 40) acquired from our previous super-resolution work [4]. A representative result of such comparisons is shown in Fig. 1. We selected the Gradient Descent optimizer and the Mean Square similarity matrix to focus on pixel-wise matching performance. Through iterations of calculating similarity, applying transformations, and optimizing parameters, the moving images progressively resembled the fixed images. In Figure 1, fixed and moving images are the high-resolution and low-resolution images of the same objects. We aligned the moving images to the fixed images and get the registered images. The overlaid images are fusion of fixed images and registered images in the fourth column. Figure 1a shows the results of Affine registration; Figure1b displays the results of B-Spline registration; Figure1c shows the results of Displacement Field registration. Their peak signal-to-noise ratio (PSNR) and mean structural similarity index measure (MSSIM) results are also reported.

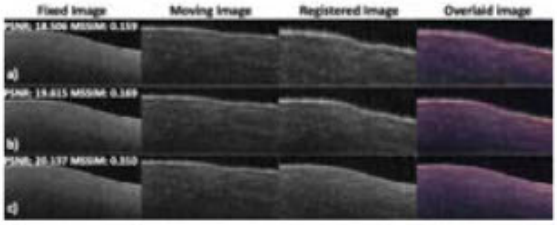

Figure 1 Registration results. (a) Affine registration; (b) B-Spline registration; (c) Displacement Field registration.

Conclusions: Rigid image registration applies linear and global transformations to images while maintaining the shape and relative positions of points. It's suitable for scenarios where the overall structures of the objects in the images remain unchanged. Non-rigid image registration allows for non-linear changes in shape and local deformations on images, which is straightforwardly shown in 1b and 1c. The higher PSNR and MSSIM values in 1b and 1c prove non-rigid methods are more versatile and suitable for aligning images with local structural differences. Besides, Displacement Field registration gets the highest MSSIM value attributed to its pixel-wise tuning of moving vectors. Except for the obvious boundary in the images, other portions lack features supporting polynomial bands for B-Spline registration, which negatively affect its performance and can be observed by the overall lightness distribution in its registered image.

References:

1. Block, A. A. J. Inst. Telev. Eng. Japan, 1974;28(4).
2. Vandemeulebroucke, J. ICCR, 2007; .
3. Pitiot, A. Medical image analysis, 2008;12(1).
4. Li X. et al. IEEE ISBI, 2024. Accepted.

STEVENS
INSTITUTE OF TECHNOLOGY

Dense Cell Bioprinting within Hydrogels with Spatiotemporal Heterogeneity to Modulate Stem Cell Osteogenesis

Alperen Abaci[1] and Murat Guvendiren[1,2].
[1]Otto H. York Department of Chemical and Materials Engineering, New Jersey Institute of Technology
[2]Department of Biomedical Engineering, New Jersey Institute of Technology

Introduction: Three-dimensional (3D) bioprinting is an advanced technology that has a strong potential to address tissue and organ shortage for transplantation. Successful fabrication of a functional tissue requires bioprinting strategies that can replicate the biological and structural features of native tissue. While the advances in embedded printing approaches allow fabrication of architecturally and biologically complex structures, support baths used in these approaches generally lack the relevant bioactivity and heterogeneity in their formulations. In this study, we developed a method to create dense cellular structures where cell-only bioinks could be deposited into photocurable support matrices. Developed approach can utilize multiple cell types or functional hydrogels to create highly heterogeneous and complex structures that could potentially be used to fabricate functional tissue models, as well as tissue interfaces, with relevant biochemical and physical complexities.

Methods: *Bioprinting:* Support matrix inks were prepared with 5 or 10 w/v% methacrylated hyaluronic acid (MeHA, functional support) in PBS containing 0.05% (w/v) photoinitiator, LAP (lithium phenyl-2,4,6-trimethylbenzoylphosphinate). Cell-only bioinks were prepared by collecting respective cell type (NIH 3T3s), human umbilical vein endothelial cells (HUVECs) or human mesenchymal stem cells (hMSCs) into a 50-mL centrifuge tube and loading into 3 mL syringe.

Osteogenic differentiation studies: hMSCs (passage 4, Lonza) embedded within MeHA (5 or 10 w/v%) with and without tricalcium phosphate (TCP, 1 w/v%) or bone morphogenetic protein-2 (BMP-2, 100 ng/mL) functionalization were used for differentiation studies. Samples were cultured for 28 days in growth media and then 14 days in osteogenic induction media. Osteogenic differentiation of hMSCs were characterized through Alkaline Phosphatase (ALP) activity and Alizarin Red staining (ARS).

Results: In our developed method, a support matrix was printed in a layer-by-layer manner with a commercially available photocurable hydrogel, MeHA, instead of using a bulk support bath. Each layer was partially crosslinked by a brief blue light exposure to provide sufficient mechanical strength to support the following layers. At the desired layer, a secondary ink (hydrogel, cell-laden hydrogel, and cell-only bioink) could be printed within the viscous, uncured solution layer prior to partial crosslinking. After deposition of the secondary ink, more layers can be printed and the whole structure can be fully cured by exposing the structure to blue light for 75 s. With the developed method, it was possible to fabricate structures with multiple cell aggregate layers (Figure 1Ai) or cell-laden hydrogel layers (Figure 1Aii), which can be composed of different cell lines. and also embed dense cell aggregates into functional supports printed as a matrix embedded in another mechanical support to improve structural integrity (Figure 1Aiii). These results clearly show that, using the developed approach, dense cellular structures with high material and biological heterogeneity can be fabricated. To show the potential of the developed method and importance of matrix functionalization, hMSCs embedded in multiphasic MeHA matrix (Figure 1Aiv) (5-10% MeHA, 10% MeHA w/ and w/o TCP, and 10 % MeHA w/ and w/o BMP-2 functionalization matrix couples) was used for *in vitro* bone regeneration. When bioprinted dense structures with hMSCs embedded in 5% MeHA (Figures 1Bi&Ci), w/ BMP-2 (Figures 1Bii&Cii), and w/ TCP (Figures 1Biii&Ciii) regions showed higher amount of alkaline phosphatase (ALP) activity and calcium deposition, indicating spatial control of osteogenesis in a continuous cell strand through functionalization of support matrices with mechanical and biochemical cues, that could be further expanded to other tissue applications.

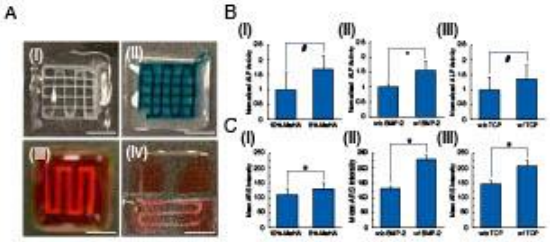

Figure 1. A) Representative images showing (i) multiple cell aggregate and (ii) cell-laden hydrogel layers in a functional support matrix, (iii) cell aggregates embedded in a functional matrix (red) embedded in another support matrix (clear), and (iv) continuous cell aggregates embedded in a heterogeneous matrix. Scale bars for camera pictures: 5 mm and confocal image: 200 μm. B) Normalized ALP activity and C) mean alizarin red staining intensity of embedded hMSCs cultured in biphasic matrix for 14 days in osteogenic induction media.

Conclusions: We developed a novel embedded bioprinting method that allows fabrication of highly complex and heterogeneous dense cellular structures. It was possible to functionalize commercially available photocurable hydrogel support matrices with mechanical and biochemical cues and create structures for *in vitro* bone regeneration. With the developed method multiple relevant functional hydrogels could be utilized along with multiple cell types to create living functional tissues and tissue interfaces that resembles complexity of respective native tissues.

Conflict of Interest: New Jersey Institute of Technology has a financial interest in the bioprinting approach reported in this manuscript and has already issued a patent for the technology described in this paper (U.S. Patent 11,806,444).

Acknowledgements: We acknowledge the funding from NSF/DMR - CAREER 2044479.

STEVENS
INSTITUTE OF TECHNOLOGY

Investigating the Effects of Stiffness and Viscoelasticity on Human Mesenchymal Stem Cell Immunomodulation

Rose Leader,[1] Sara Olsen,[2] Bethany Almeida, Ph.D.[2]
[1]Department of Mechanical and Aerospace Engineering, [2]Department of Chemical and Biomolecular Engineering,
Clarkson University, Potsdam, NY 13699

Introduction: Chronic, non-healing wounds are a growing financial and medical burden, costing $20B in 2022.[1] Human mesenchymal stem cells (hMSCs) are an attractive therapy for chronic, non-healing wounds due to their immunomodulatory behavior.[2] However, hMSCs have low viability, poor engraftment, and a risk of eliciting an immune response, thereby reducing therapeutic potential.[3] Additionally, variability in donor, age, and tissue source results in hMSC heterogeneity.[4] Substrate stiffness has been shown to modulate hMSC differentiation, but its effects on hMSC immunomodulation remain largely unknown.[5] Thus, we seek to elucidate the synergistic effects of substrate stiffness and viscoelasticity on hMSC immunomodulatory behavior.

Methods: PAAm gels were fabricated following published literature.[6] Three gel compositions, a soft gel with a Young's modulus (E) of ~1.16 kPa, a medium gel with a Young's modulus of ~4.47 kPa, and a stiff gel with a Young's modulus of ~19.7 kPa, were fabricated. To impart viscoelastic properties, linear polyacrylamide was mixed with the acrylamide and bis-acrylamide prior to gelation.[7] Young's modulus was characterized using dynamic mechanical analysis (DMA; DMA850, TA Instruments, New Castle, DE). Viscoelasticity, defined as shear stress-mediated storage and loss moduli, G' and G'', was characterized using a rheometer (AR2000, TA Instruments, New Castle, DE). The PAAm gels were coated in fibronectin (Sigma, Billerica, MA) to aid cell attachment and bone marrow-derived hMSCs (Lonza, Hopkinton, MA) were seeded at 5,000 cells/cm^2. Viability was assessed using a live/dead assay (Fisher Scientific, Hampton, NH), and cellular morphology was characterized by fluorescently staining F-actin using Alexa Fluor 488 Phalloidin (Fisher Scientific, Hampton, NH) and nuclei using DAPI (Sigma, Billerica, MA) and imaging on a Ti2E inverted microscope (Nikon, Tokyo, Japan).

Results: The Young's modulus of the gels were 1.44 ± 0.11, 1.15 ± 0.08 4.13 ± 0.51, 4.99 ± 0.34, 9.50 ± 0.99, and 20.1 ± 0.94 kPa for soft without and with linear polyacrylamide, medium without and with linear polyacrylamide, and stiff without and with linear polyacrylamide, respectively. Interestingly, the stiff gel showed an increase in Young's modulus when linear polyacrylamide was added. We hypothesize that this is due to the increase in acrylamide monomer concentration for the stiff gel vs the soft and medium gels (i.e., 4% acrylamide and 0.06% bis-acrylamide, 5% acrylamide and 0.15% bis-acrylamide, and 8% acrylamide and 0.26% bis-acrylamide for the soft, medium, and stiff gels, respectively). Thus, given the additional acrylamide concentration for the stiff gels, there is a greater chance for the linear polyacrylamide to crosslink at its terminal ends, decreasing the dissipative effects and increasing stiffness. Live/Dead assay confirmed the viability of the hMSCs on these gels (Fig1A). It is notable that there are fewer cells on the soft and stiff gels in comparison with the medium gels, likely due to decreased focal adhesion formation on these gels. In addition, morphology staining demonstrated that cells on soft gels were rounder and smaller than those on the medium and stiff gels (Fig1B).

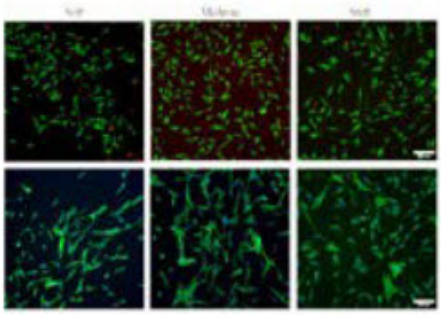

Figure 1. Viability (top) and morphology (bottom) of hMSCs cultured on non-viscoelastic soft (left), medium (middle), and stiff (right) PAAm gels. Top: Live cells = green, dead cells = red, scale = 200 µm; Bottom: F-actin = green, nuclei = blue, scale = 200 µm.

Conclusions: Differences in hMSC morphology are known to affect hMSC behavior. The preliminary data confirms the potential for variations in immunomodulatory potential as a result of differences in hMSC interactions with the different PAAm gels. Current work is focused on quantifying viscoelastic properties, investigating focal adhesion formation and morphology changes over time, and quantifying immunomodulatory potential over time by investigating the production of immunomodulatory cytokines by hMSCs cultured on these gels.

References: 1. Sen C. Adv Wound Care. 2023;12(12):657-670; 2. Keshavarz R. Bioeng. & Trans. Med. 2023; 9(1):e10598; 3. Im G. Int J Mol Sci. 2019;20(19):4835; 4. Chen S. Colloids Surf B Biointerfaces. 2016;140:574-582; 5. Wang S. Adv Healthc Mater. 2020;10(3):2001244; 6. Tse J. Cur. Prot. in Cell Bio. 2010;47(1):10.16.1-10.16.16; 7. Pogoda K. Bio-protocol 2021;11(16):e4131.

Acknowledgments: We acknowledge funding from NSF #2138587. RL acknowledges funding from NIH ESTEEMED #R25EB033080. We acknowledge support from Hubert Bilan with DMA and Rheology.

DEI: Chronic, non-healing wounds are well known to disproportionately affect minority populations. This work will advance the development of hMSC therapies for these wounds. RL is a first-year undergraduate student who is an inaugural member of Clarkson's NIH ESTEEMED grant.

STEVENS
INSTITUTE OF TECHNOLOGY

Taurine-Loaded Hydrogel Drug Delivery System for Sodium Iodate-Induced Dry Age-Related Macular Degeneration

Mohammed Attia,[1] Tonja Pavlovic,[2] Maria Mihalatos,[2] Marcin Iwanicki,[2] and Jennifer Kang-Mieler[1]
[1]Department of Biomedical Engineering, [2]Department of Chemistry and Chemical Biology at Stevens Institute of Technology

Introduction: Over 19.8 million Americans aged 40 and older have age-related macular degeneration (AMD). There are two types: dry AMD and wet AMD, where ~80% of AMD cases are dry AMD. Early pathogenesis of AMD involves lipid and protein accumulation that leads to drusen. Coupled with oxidative stress, changes in the photoreceptors and retinal pigment epithelium (RPE) progress over time.[1] An oral taurine supplement may be a viable early treatment option, but a high dose of taurine and an extended treatment duration may be needed to achieve a therapeutic level.[2,3] This will be challenging with oral supplements. To address this need, we developed a taurine-drug delivery system (taurine-DDS). This study tested the feasibility of taurine therapy in *in vitro* and *in vivo*.

Methods: Taurine and sodium iodate were purchased from Thermo Fisher Scientific (Waltham, MA). Poly(ethylene glycol)-co-(L-lactic acid) diacrylate (PEG-PLLA-DA) was purchased from Akina (West Lafayette, IN). N-Isopropylacrylamide (NIPAAm), N-tert-Butylacrylamide (NtBAAm), N,N,N,N-Tetramethylethylenediamine (TEMED), and Ammonium Persulfate (APS) were purchased from Sigma-Aldrich (St. Louis, MO). Taurine ELISA was purchased from Cell BioLabs(San Diego, CA).

Biodegradable thermoresponsive hydrogels (PEG-PLLA-DA/NIPAAm) were synthesized by free radical polymerization. Hydrogel precursors contain 2 mM PEG-PLLA-DA, 350 mM NIPAAm, 50 mM NtBAAm, 13 mM APS, and 320 mM Taurine in 1xPBS (pH 7.4), then the polymerization initiated with 200 mM TEMED (pH 7.4) and was placed on ice for 30 minutes. Taurine-hydrogel DDSs were collected and washed with DI water. Taurine ELISA was utilized to quantify the release of taurine at 0.5, 2, 6, 24, 48, 96, and 144 hours.

hTERT RPE-1 cells (ATCC, CRL-4000) were grown *in vitro* using DMEM/F-12 medium formulation (Gibco) with 5% FBS (Cytiva). RPE cells were supplemented *in vitro* with either 2mM of taurine alone or 2 mM of taurine and 2 mM of sodium iodate.

Sodium iodate ($NaIO_3$) rat model (preclinical AMD model) was established by a single intravenous injection of 6% $NaIO_3$ at 80mg/kg.[4] Fundus imaging and spectral-domain optical coherence tomography (SD-OCT) were acquired using Spectralis (Heidelberg Engineering, Germany) to assess the disease progress.

Results: Taurine-DDS was successfully synthesized with an encapsulation efficiency of 16%. The release profile exhibited continuous taurine release over two days with a cumulative release of 50.3mM (Figure 1.A). *In vitro* treatment of RPE cells with sodium iodate resulted in significant cell death (over 75% cells dead), but when supplemented with taurine, cell death by sodium iodate was significantly reduced to less than 25% (Figure 1.B and 1.C). Ophthalmic examinations showed that retinal degeneration in the $NaIO_3$ rat model started on day 7 and progressed to severe degeneration by day 14 (Figure 1.D). A sodium iodate rat model for dry AMD was successfully established. Fundus images post-$NaIO_3$ injection display significant retinal damage, marked by small dark spots around the optic nerve, indicating ONL degeneration, correlated by OCT images showing ONL undulations.

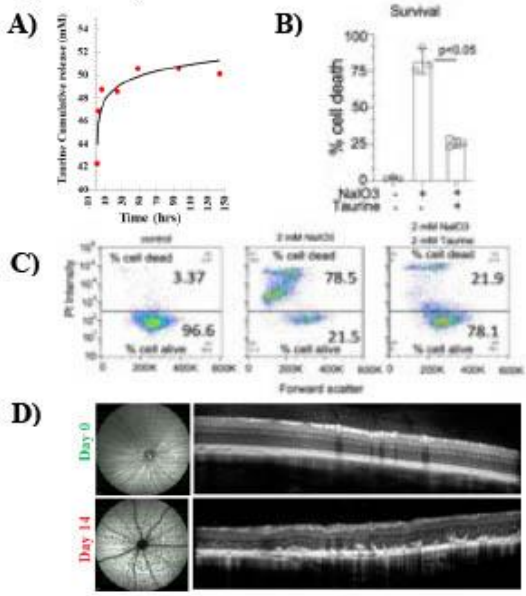

Figure 1. **A)** Taurine release profile, **B, C)** Flow cytometry analysis of propidium iodide signal inferring cell death, and **D)** Fundus images and OCT for $NaIO_3$ rat model.

Conclusions: In this study, taurine was effectively incorporated and released from a biodegradable, thermoresponsive hydrogel DDS to potentially treat dry AMD, which can be administered intravitreously through a 27-gauge needle at room temperature. In vitro studies indicate taurine's ability to protect RPE cells from AMD-inducing agent $NaIO_3$. This dry AMD model will be utilized to evaluate the treatment effectiveness of the proposed taurine-DDS in future studies.

References:

1. Rein et al. JAMA Ophth. 2019;140(12):1202-1208.
2. Preising et al., FASEB J. 2019 Oct;33(10):11507-11527.
3. Centeno et al., bioRxiv 2023.02.24.529893
4. Anderson et al. Experimental Eye Research. 2024;239:109772.

DEI: Our work aims to develop Taurine-loaded hydrogel DDS for the treatment of retinal degenerative diseases like AMD that could potentially bridge gaps in healthcare outcomes. Our study's interdisciplinary approach, encompassing bioengineering and ophthalmology, creates opportunities for the participation of diverse STEM individuals.

STEVENS
INSTITUTE OF TECHNOLOGY

How Photointitator Impacts Stem Cell Behavior in 3D Bioprinted Gelatin Mathacryloyl

Ann Austin[1]*, Elvan Dogan[1]*, Amir K Miri[1,2]
[1] Department of Biomedical Engineering, New Jersey Institute of Technology, Newark, NJ 07102
[2] Department of Mechanical and Industrial Engineering, New Jersey Institute of Technology, Newark, NJ 07102
* *Equal Contributions*

Introduction: Light-based hydrogel crosslinking represents a novel and efficient technique for achieving rapid and precise 3D bioprinted structures [1]. The application in tissue engineering presents difficulties because of the toxic nature of the photoinitiators (PI) [2]. This study investigates the generation of reactive oxygen species (ROS) in mesenchymal stem cells (MSCs) encapsulated in GelMA hydrogels, crosslinked with three distinct PIs: Eosin Y, Lithium phenyl-2,4,6- trimethyl-benzoyl-phosphinate (LAP) and Irgacure. This work aims to compare the effects of these PIs on cellular oxidative stress, a critical factor influencing cell viability and function in tissue engineering applications.

Methods: Different concentrations of Photoinitiators (0.01 to 1% w/v), such as LAP and Irgacure 2959 in 5% GelMA [3], were used to form cylindrical-shaped samples. Each group of hydrogels was crosslinked for 2.5 mins under 365 nm for a light power of 10 mW/cm^2 using a commercial UV crosslinker (VWR, Radnor, PA) to study swelling and degradation. The hydrogels were also subjected to compression and rheology tests to identify storage, viscosity, and compressive modulus. Bioink was prepared with Bone-marrow derived human Mesenchymal Stem Cells (PT-2501, Lonza, Walkersville, MD) that were used for Live Dead assay (Thermo Scientific, Waltham, MA) and CCK-8 (Sigma Aldrich, St. Louis, MO) assay.

Results: The hydrogels with higher concentrations of PI showed increased elastic modulus than the lower concentration of PI for both LAP and Irgacure 2959. The hydrogel with higher PI concentration resulted in lower degradation and swelling than the hydrogel with lower PI concentration for LAP and Irgacure 2959. CCK-8 assays and Live Dead Assay showed increased proliferation of MSC cells for the lower concentration of PI than the hydrogels with a higher concentration of PI. At Day 1, the swelling ratios were relatively similar across all LAP concentrations. However, as time progressed, distinct trends emerged. By Day 5, the samples with 0.05% LAP exhibited the highest swelling ratios, indicating a strong correlation between LAP concentration and swelling behavior. The samples with lower concentrations of LAP, particularly those with 0.01% and 0.03% w/v, showed a lesser degree of swelling. The samples with the lowest photoinitiator concentration displayed the highest mass loss, suggesting a less cross-linked network that was more susceptible to enzymatic cleavage. Conversely, hydrogels with the highest photoinitiator concentration maintained a greater percentage of their mass over the five days, indicative of a more densely cross-linked matrix providing resistance to collagenase activity. The data indicated that the concentration of the photoinitiator influenced cell viability within the GelMA hydrogels. Samples with the lowest photoinitiator concentration showed the highest cell viability, which suggests that a less cross-linked network may be more conducive to cell growth and proliferation. This could be due to the increased nutrient and waste transport within the hydrogel matrix, essential for cell survival and proliferation. MSC cell morphology exhibits greater attachment and a more branched distribution in GelMA with lower PI ratios. At the same time, MSCs display a round and compact morphology in GelMA with higher PI concentrations. These results indicate a possible influence on stem cell fate due to the varying concentrations of PI in GelMA.

Conclusions: The effect of photoinitiators is evident in 5% GelMA hydrogels, where the swelling, degradation, elastic modulus, and cell proliferation were drastically affected due to the concentration of the PI. This knowledge can close the gap that is present in tissue engineering. Further, we will investigate the effect of PI concentration on ROS generation and stem cell fate through RT-qPCR.

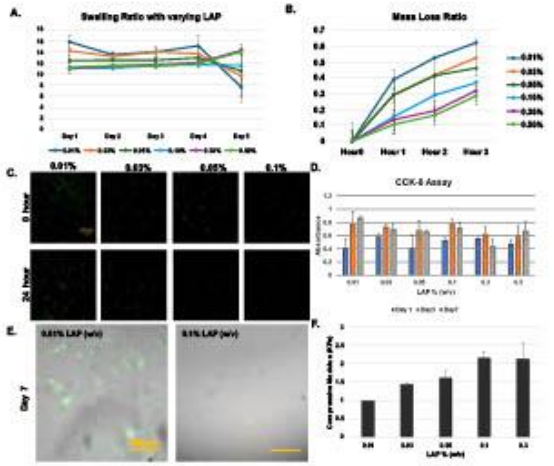

Figure 1. A. Swelling data; B. Degradation profiles; C.-D. Viability of MSCs encapsulated in 5% GelMA (w/v) with varying LAP masses; E. MSC morphology was encapsulated in GelMA with varying LAP concentrations at Day 7; F. Compressive modulus with varying PI.

References:

[1] E. Dogan, Frontiers in Bioengineering and Biotechnology 11 (2023).
[2] H. G. Hosseinabadi, ACS Biomaterials Science & Engineering 8 (2022).
[3] W. Schuurman, Macromol Biosci 13(5) (2013).

Acknowledgments: We acknowledge the receipt of funding from NIH (R01DC018577, T34GM145521).

STEVENS
INSTITUTE OF TECHNOLOGY

Precision editing of the Cancer Glycocalyx to Tune Mechanically Regulated Migration in Glioblastoma Multiforme

Issa Funsho Habeeb[1,3], Juan J Ramirez[1], Aman Mittal[1], and Alexander Buffone, Jr, Ph.D.[1,2,3]
[1]Department of Biomedical Engineering, [2]Otto H. York Department of Chemical and Materials Engineering,
New Jersey Institute of Technology, Newark, NJ, USA

Introduction: Glioblastoma multiforme (GBM) is one of the most aggressive cancer type that affect the brain and is characterized by a bulky presence of sugar glycocalyx, to mechanically tension its membrane and fuel aggression. This glycocalyx is a potent mechanosensor that transmit mechanical and chemical environmental cues as well as all signals that must navigate this barrier to reach the cell. Any changes to the composition of this sugar layer would in turn impact the harmonius interaction between the cell its environment. In more than 95% of cancer cells, specific glycocalyx signatures including increased thickness with bulky side chains have been demonstrated to cause increased proliferation, migration, invasion, and immune evasion. So far, treatment options to prevent GBM metastasis or increase immune recognition have been ineffective as most patients do not survive 8 months post-diagnosis. In a bid to extent the length of survival in patients, modification of the glycocalyx remain a promising therapeutic target worthy of pertubation. GBMs expresses a complex mixture of glycoproteins, glycolipids, and mucins, and insight into the specific glycan that is homing the critical functional end group sugar(s) to mediate mechanical forces on it membrane is needed to effectively edit it. To this end, we hypothesize that CRISPR-Cas9 mediated editing of either the chain initiating enzymes of N-linked glycans (MGAT1), O-linked glycans (COSMC), or glycolipids (UGCG) can edit the glycocalyx in such a way that it disrupts the aggressive ability of GBMs to migrate, signal, and evade immune recognition.

Materials and Methods: CRISPR plasmids with gRNA sequences against human *COSMC*, *UGCG* and *MGAT1* in the pSpCas9(BB)-2A-Puro (PX459) V2.0 vector were generated and COSMC-KO (U87-COSMC-KO), MGAT1-KO (U87-MGAT1-KO) and UGCG-KO (U87-UGCG-KO) single KO cell lines were created by chemically transfecting the WT U87s with these vectors using lipofectamine 3000™ reagent. To characterize the KOs, the region surrounding the CRISPR target site was amplified from genomic DNA and specific deletions confirmed. Approximately 6 weeks after transfection, morphological changes were quantified by microscopy with firmly adherent, spindle like cells being more aggressive and mesenchymal GBMs and loosely attached, more rounded cells being pro-neural and less aggressive. Then we fashioned polyacrylamide gels at a range of stiffnesses (400-60,000 Pa) conjugated with Fibronectin and monitored if the knockouts migrate differently than the controls and if the stiffness effects the migration of the GBMs. Next, we checked to see if the signaling (FAK) is altered in any of the GBM knockouts through use of FAK tyrosine specific activated antibodies (and western blotting) on both the wild type and mutants to check changes in migration profiles and response to mechanical cues.

Results: Microscopic observation (**Figure 1**) showed a trend towards a more pro-neural phenotype, as expected, in each of U87-COSMC-KO, and U-87-UGCG-KO and U87-MGAT1-KO. What is more surprising is that U87-COSMC-KO and U-87-UGCG-KO showed the most robust trend as they were detached, less aggressive, and had the most recognizable pro-neural phenotype. This phenotype is seen more often in healthy cells, an observation that is expected to correlate with a glycocalyx content and size upon quantification.

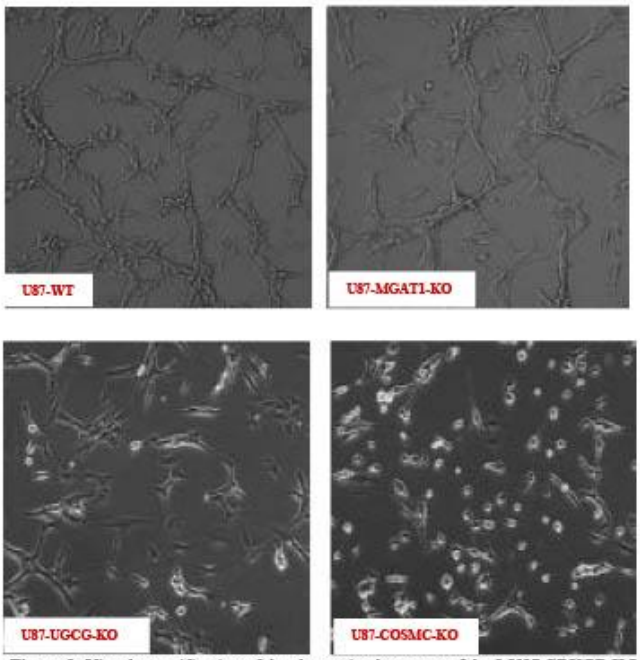

Figure 1: Visual quantification of the change in phenotype of the 3 U87 CRISPR KOs. While the U-87-MGAT1 KOs resemble the mesenchymal morphology of the U87 WT cells, the U87-COSMC-KO and U87-UGCG KOs adopt a loosely adhered, circular morphology like healthy pro-neural cells.

Conclusions, and Discussions: COSMC and UGCG appear to be the most critical sugars responsible for GBM aggression. However our ongoing experiments are quantifying the changes in surface topography and glycocalyx architecture as well as signaling and migration associated with the phenotypic changes seen in the U87-COSMC-KO and U-87-UGCG-KO with the hope of identifying mucin or glycolipids as key players in GBM aggression. We plan to inject each of the KOs in mice to study tumor development and survival. Finally, we will check for immune and drug susceptibility for each KOs. This could ultimately lead to new potential therapies that increases immune recognition and in improved patient prognosis in GBM.

Acknowlegement: This work was funded by Center for Engineering Mechano Biology (CEMB) CMMI: 15-48571 subaward 570440, NJIT Faculty Seed Grant, and New Jersey Health Foundation (NJHF), Grant number: PC:26-24, to ABJ and the cellular motion lab.

STEVENS
INSTITUTE OF TECHNOLOGY

Investigation of Compressive Stress on Cancer Cell Migration

Justin Caron, Dr. Shue Wang
University of New Haven

Introduction: Uncontrolled growth of cancer cells in solid breast cancer generates mechanical compression that may drive the cancer cells into a more invasive phenotype, but little is know how compressive stress affects key cellular behaviors and regulatory mechanisms. Cancer cells spread by growing within a localized space or going through metastasis. The conditions of the tumor and the human body will impact in which way the cancer cells will spread. Under specific conditions the cells may be driven towards an invasive phenotype. [1] Understanding these conditions can help develop ways to predict or manipulate cancer metastasis. Compressive stress is one such condition that can lead to metastasis. At specific compress stresses the cell migration may increase without causing significant increases to cell death. Here, we investigated how compressive stress affects breast cancer cells MDA-MB-231 cells migration.

Methods: MBA-MD-231 cancer cells were cultured in RPMI with 10% Fetal Bovine Serum (FBS) and 1% Penicillin-streptomycin-Glutamine. These cells were washed using 1x PBS and the medium was changed every two days. Cells were incubated in a humidified incubator with 5% CO at 37°C. At 80-90% confluency the cells were passage into four wells in a six well dish. Each well was prepared with 2*10^5 cells. After culturing for 48 hours, agarose gel and weights were added to two of the four wells. The weights were left for two days before imaging was performed. The cells were stained with Hoechst and PI. Three 200 pascal trials and a single 300 pascals trial. Images were taken using a Leica DMi1 inverted microscope and Zoe Fluorescent Cell imaging system. of both the trans well membrane as well as the well plate beneath each membrane. The presence of cells beneath the porous membrane would indicate that the cells were driven towards an invasive phenotype.

Results: We first evaluated the live/dead cells numbers using PI/Hoechst assay. Images were taken with a specific interest in the concentration of dead and living cells and the presence of cell beneath the trans well membrane. In both the 200 and 300 pascals compressive stress increased cell proliferation was found in the experimental wells. Both also showed little to no increase in dead cells compared to the control wells. Under 300-pascal compressive stress, there are more cells were observed in the lower well beneath the trans well membrane.

Under 200 pascals, the cells didn't show significant difference regarding cell viability and cell proliferation, compared to control group. Although Figure 1 is an illustration of the experimental setup.

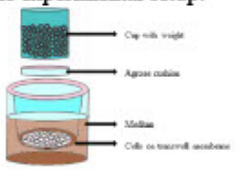

Figure 1: Experimental Setup

Figure 2 includes images from below the membrane from the third trial. The experimental trial has more growth cellular growth than the control. This indicates an increase in cellular migration and an invasive phenotype.

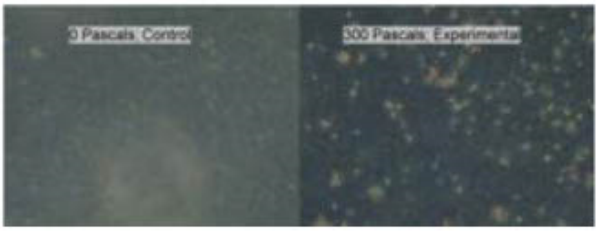

Figure 2: Trial 3, below trans well membrane.

Conclusion: The application of compressive stress to the cancer cells caused an increase in cell growth and caused cells to grow through the porous membrane without increasing cell death significantly if at all. The growth through the membrane indicates that the correct conditions were met for the cells to develop into invasive phenotypes and attempt to go through metastasis. Future research into this topic could focus on one of several topics. Additional experiments should be conducted to further study the fundamental mechanism underlying compressive stress caused cell behavior changes. , Another area of research could be attempting to manipulate the specific growth of cancer cells using compressive stress and investigate its effects on cell migration.

Acknowledgements: The authors would like to acknowledge the support from NSF CMMI program (Award number: 2143151).

Reference:

1. Tse JT, Me Comp Inv Pheno. 2011;109(3)911-916

DEI: This research provides an opportunity to undergraduate students to pursue careers in the biomedical engineering field.

STEVENS
INSTITUTE OF TECHNOLOGY

The Effect of Neuron-to-Neuron Forces on Neuronal Activity

Laya Dalir[1], Yevgeny Berdichevsky[1,2]
Departement of Bioengineering, Lehigh University, Bethlehem, PA, USA
Departement of Bioengineering, Department of Electrical and Computer Engineering, Lehigh University, Bethlehem, PA, USA

Introduction: Cells are attracted to each other by mechanical forces mediated by cell adhesion molecules and cytoskeletal tension. We have previously shown that these forces are present in rat cortical neurons and neurons derived from human induced pluripotent stem cells. Neuron-to-neuron attraction causes tissue contraction in dissociated neuronal aggregates. Neurons at the edge of aggregates which were experiencing disbalanced contractile forces also had more baseline and dynamic Ca2+ activity. We hypothesized that an imbalance in cell attraction forces in the brain tissue after trauma may result in tissue contraction and hyperexcitability and may contribute to post-traumatic epileptogenesis. Overall, our research aims to explore the relationship between trauma-induced imbalance in contractile forces and neuronal activity. Understanding the underlying mechanisms of this phenomenon can help identify strategies to mechanically relax the tissue and prevent the onset of epilepsy.

Methods: we used organotypic hippocampal culture model to determine whether contractile forces exist in ex vivo tissue, and whether they influence epileptogenesis. First, organotypic hippocampal slices were embedded in fluorescent-bead containing Matrigel to observe whether cells in the slice exerted contractile forces. Then, we cultured slices on substrate printed with patterns of cell-substrate adhesion molecule poly-D-lysine (PDL) to control contraction. Cultures were transfected with jRGeco1a for optical recording of Ca2+ activity.

Results: In slices cultured with Matrigel, after 48 hours, significant movement of beads toward the slice occurred, confirming that cells in the slice exerted contractile forces. In slices cultured on patterns of PDL coating, we observed that tissue contraction was accelerated in slice sub-regions located over PDL-free regions. The effect of contraction varied depending on the force direction (along or perpendicular to the apical-basal axis). Contraction along the apical-basal axis in the CA3 region led to decreased seizure Ca^{2+} dynamics figure (1). On the other hand, when neurons in CA3 were subjected to contraction in transverse direction had increased non-seizure Ca^{2+} activity figure (2).

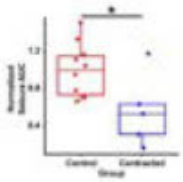

Figure 1. Normalized seizure Ca2+ activity area under the curve subjected to force along apical-basal axis in the CA3

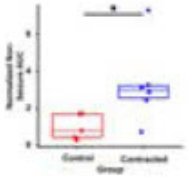

Figure 2. Normalized non-seizure Ca2+ activity area under the curve subjected to force transverse to apical-basal axis in the CA3

Conclusions: Neuron-neuron forces can cause tissue contraction and pull the extracellular matrix. In organotypic ex-vivo tissue, an imbalance of cell adhesion forces leads to accelerated localized tissue contraction. The effect of contraction on activity varies in different regions of the slice.

References:

[1] Hasan, Md Fayad, and Yevgeny Berdichevsky. "Neuron and astrocyte aggregation and sorting in three-dimensional neuronal constructs." Communications Biology 4.1 (2021): 587.

[2] Webster, Kyria M., et al. "Infammation in epileptogenesis after traumatic brain injury. " Journal of neuroinfammation 14 (2017): 1-17.

[3] Heer, Natalie C., and Adam C. Martin. "Tension, contraction and tissue morphogenesis." Development 144.23 (2017): 4249-4260.

[4] Ikoma, Yoko, Daichi Sasaki, and Ko Matsui. "Local brain environment changes associated with epileptogenesis." Brain 146.2 (2023): 576-586.

STEVENS
INSTITUTE OF TECHNOLOGY

Computational and Human Guided Approaches to Designing C5aR Antagonizing Cyclic Peptides

Joseph Dodd-o[1], Abdul-Lateef FNU[1], Owen West[1], Vivek Kumar[1,2,3].
[1]Department of Biomedical Engineering, New Jersey Institute of Technology; [2]Department of Endodontics, Rutgers School of Dental Medicine; [3]Department of Chemical Engineering, New Jersey Institute of Technology.

Introduction: In periodontitis, initial infection leads to chronic inflammation of the subgingival space. This inflammation is partially mediated by the Complement 5a Receptor (C5aR) Pathway, which is constantly activated by free Complement 5a[1]. Untreated, this leads to dysregulation of angiogenesis in the dental pulp and maintenance of the tooth apical root structure[2]. To address the pathological C5aR activation, cyclic peptide antagonists have been designed. The design, synthesis, and characterization of the peptides is described herein.

Methods: The Rosetta molecular modeling suite[3] was used to design 8AA cyclic sequences. Briefly, the PMX53 ligand was cleaned from the structure of C5aR complexed with PMX53 (PDB ID: 6C1R) [1]. A peptide stub was positioned within the binding pocket, and the Rosetta PackRotamersMover [4] was employed to randomly mutate the sequence for increased binding affinity. The structure of the cyclic peptide was predicted using the Generalized Kinematic Closure Mover [5] and iterated repeatably using RosettaScripts. A custom Python script evaluated the propensity of the top scoring peptides to conform to the lowest scoring energy structure. The peptides were synthesized with Solid Phase Peptide Synthesis chemistry with FMOC protecting groups and trichlorotrityl resin. The peptides were cleaved using a 20% hexaflouroisoproponol (HFIP) solution in dichloromethane. The peptides were separated from the resin in solution using a fritted column and rotovap to remove the cleavage cocktail. Cyclization was performed using HBTU-HOBt solution, and the peptides were purified using high performance liquid chromatography [6].

Results: 3000 peptides sequences were generated using the RosettaScripts protocol above. Of these, 10 were selected for further evaluation. P_{NEAR} metrics were generated for the top 10 peptides. 5 peptides with the highest P_{NEAR} values were selected for synthesis. Initial purity values are approximately 90%.

DEI: The development of new technology in biomedical engineering will only be efficacious in improving healthcare outcome disparities if the resulting tissue engineered products are accessible. Acellular materials that do not require special storage or preemptive cell culture before implantation will make new tissue engineered products more accessible in a variety of healthcare settings.

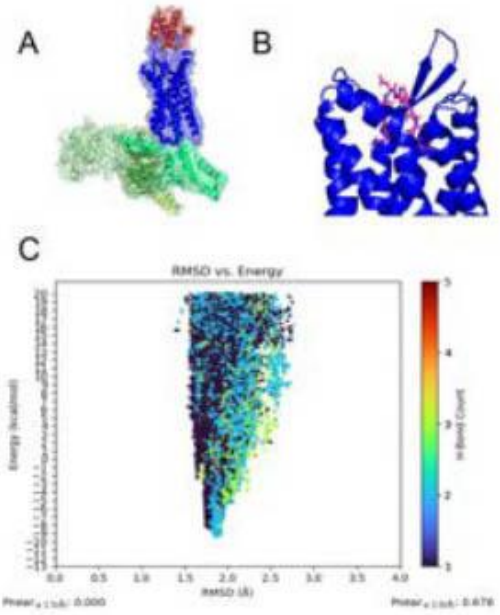

Figure 1. (A) Complement 5a Receptor (PDB ID: 7Y65) [7] (B) The binding pocket with a C5aR candidate (C) Evaluating the number of hydrogen bonds, energy, and RMSD of the different cyclic peptide conformations relative to the best scoring ligated conformation.

Conclusions: This represents a comprehensive approach to human-guided in-silico design of cyclic peptide antagonists. The peptides described will be tested using in vitro and in vivo models of C5aR activation and complemented by a machine learning approach to generate new sequences.

References:

1. Liu H. et al. Nat Struct Mol Bio. 2018; 6: 472-481
2. Abe T. et al. J Immunol. 2012; 189(11): 5442-5448
3. Kaufmann K. et al. Biochemistry. 2010; 49:2987-2998.
4. Fleishman S. et al. PLoS ONE. 2011; 6(6): e20161
5. Bhardwaj G. et al. Nature. 2016; 538: 329-335
6. Krumberger M. et al. J Org Chem. 2023; 88: 2214-2220

Acknowledgements: This study was supported by NIH NIDCR R01DE031812

STEVENS
INSTITUTE OF TECHNOLOGY

Automated Cell Spheroid Positioning into Hydrogel-based Microfluidic Chips

Elvan Dogan[1], Rishi Kuriakose[1], Amir K. Miri[1]
[1] Advanced Biofabrication Lab, Department of Biomedical Engineering, New Jersey Institute of Technology, Newark, NJ 07102.

Introduction: Bioprinting has emerged as a transformative technology, enabling the fabrication of complex, three-dimensional (3D) structures that closely mimic native biological tissues. It has been used to model tumor microenvironment (TME), a complex system of multiple cell types in the native extracellular matrix (ECM) [1]. In this perspective, integrating cellular components, such as tumor spheroids, into bioprinted constructs with high precision and reproducibility has remained a significant challenge. Tumor spheroids, as cell clusters, serve as pivotal models for studying tumor behavior, cancer progression, and drug efficacy due to their resemblance to native tumors regarding cellular heterogeneity and microenvironmental cues. Recognizing the need for precise spatial control of tumor spheroids within bioprinted matrices, our research introduces a novel adaptation to the conventional extrusion- and inkjet-based bioprinting platforms.

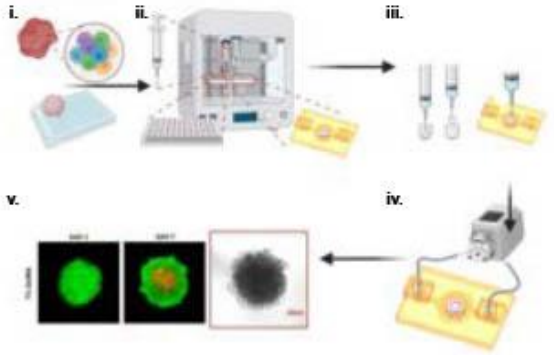

Figure 1. Schematic representation of bioprinting and screening process of tumor spheroid-on-a-chip platform. The cell spheroids are HT1080 cell line: organotypic spheroid formation (i), spheroid positioning in hydrogel chip through modified bioprinter (ii), positioning of toroid into Pluronic F-127-GelMA printed hydrogel chip construct (iii), active perfusion using a peristaltic pump (iv), and drug screening applications on STS spheroids (v).

Methods: About 15,000 soft tissue sarcoma (HT1080) spheroids were formed in ultra-low attachment 96-well plates for three days. Low methacrylate gelatin methacryloyl (GelMA) was synthesized, and GelMA precursor (7% w/v) was prepared with DPBS and pre-warmed at 50°C with constant stirring. After approximately an hour, the solution was clear and homogeneous. Once fully dissolved, a final concentration of 0.5% w/v 2-hydroxy-1-(4-(hydroxyethyl) phenyl)-2-methyl-1-propanone was used as the photoinitiator of the crosslinking process. Pluronic F127 was used for sacrificial printing to obtain perfusable channels. We optimized our photoinitiator concentration based on the viability test and compressive modulus with varying PI concentrations (0.1-1% w/v). Vacuum pressure was selected based on previously published data [2].

Results: This innovative approach advances the capabilities of extrusion-based bioprinting in constructing more complex and physiologically relevant 3D models and opens new avenues for in-depth studies of TME and the screening of anticancer therapeutics. We positioned spheroids in a diameter of 834.32 ± 17.82 µm with 233.26 ± 21.52 µm planar accuracy. By enabling the precise co-localization of tumor spheroids within bio-printed tissues, our method offers a significant leap forward in the simulation of tumor-stroma interactions and the evaluation of targeted drug delivery strategies, paving the way for more accurate preclinical models in cancer research. We showed that tumor spheroids were undamaged and viable after positioning.

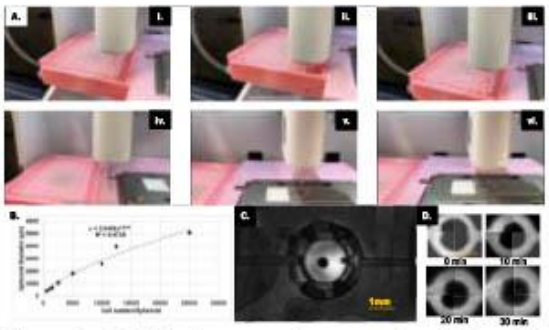

Figure 2. A. Positioning steps of a tumor spheroid into a bioprinted GelMA chip: the nozzle descends towards the spheroid (i), negative pressure is applied to aspirate the spheroid into the nozzle (ii), the nozzle ascends with the spheroid (iii), the spheroid is moved to the desired location within the bio-printed hydrogel chip (iv-v), negative pressure is released to deposit the spheroid at the target location (vi); B. Spheroid diameters per cell number; C. Spheroid positioned chip; D. Diffusivity of RhD-B through active perfusion for 30 min.

Conclusions: We have engineered a vacuum-based nozzle system to manipulate and position tumor spheroids within a bioprinted GelMA chip. This modification is pivotal, as it allows for the exact placement of spheroids into predetermined locations within the hydrogel matrix, thereby facilitating controlled studies on tumor behavior and drug delivery dynamics [3]. The integration of this system is guided by customized G-code programming, which enables the automated and precise manipulation of spheroids, enhancing the reproducibility and scalability of tumor model fabrication.

Acknowledgments: We thank federal agencies for the support (NSF-2243506 and NIH-R01DC018577).

References:

[1] Dogan E. et al. Adv Nanobiomed Res. 2021; 1(11).
[2] Ayan B. et al. Science Advances. 2020;6 (10).
[3] Dogan E. et al. Biofabrication, (submitted)

STEVENS
INSTITUTE OF TECHNOLOGY

Developing a Hypoxic Biosensor for Therapeutic Applications

Madeline Dunsmore, Leah Davis, Mary Staehle Ph.D.
Rowan University Department of Biomedical Engineering

Introduction: Hypoxia's significant impact on cellular functions including metabolism, gene expression, protein synthesis, and overall cell behavior positions it as a pivotal factor in the progression of several major causes of mortality, including cancer, cardiac, kidney, and reproductive diseases. For example, the hypoxic tumor microenvironment has been associated with cancer progression and placental hypoxia has been a key driver in pathological manifestations of preeclampsia.[1,2] The hypoxic environment in these conditions has the potential to be harnessed as a target for therapeutics. Hypoxia-inducible factors (HIFs) are proteins present in most cells that mediate the hypoxic response. It is known that HIF-1α and HIF-2α exhibit different cellular responses based on acute and chronic conditions, respectively.[3] HIF-1α has been utilized for different therapeutics and cancer treatments, but despite HIF-2α's growing prevalence in chronic hypoxic conditions, is poorly understood and underutilized. Probing the mechanisms of both HIF-1α and HIF-2α offers the potential to utilize their unique dynamics to modulate cellular responses. We propose the creation of a novel hypoxic biosensor that leverages the spatiotemporal dynamics of HIF-1α and HIF-2α for potential diagnosis and treatment purposes.

Methods: Our biosensor consists of the active domain of a kinase linked to half a leucine zipper; the substrate of the kinase linked to both the cognate half of the zipper and split mNeonGreen; and the SH2 domain of the phosphorylated substrate linked to the cognate of mNeonGreen. Truncated oxygen-degradation domains (ODDs) of HIF-1α and HIF-2α were cloned into the substrate portion of the biosensor. Activation of the biosensor initiates an orthogonal phosphorylation cascade that constitutes a split fluorescent protein. HEK-293T cells were transfected using chemical transient transfection and subjected to normoxic (21%) and hypoxic (1%) conditions for 16 hours. Flow cytometry was used to measure the Mean Fluorescent Intensity (MFI) of mNeonGreen as an indicator of expression. Paired two sample t-tests for means were performed for both the HIF-1α and HIF-2α sample groups.

Results: Biosensors containing truncated versions of the HIF-1α ODD or the HIF-2α ODD were developed. Both biosensors showed an increase in expression levels in hypoxic conditions compared to normoxic conditions (Figures 1 and 2). HIF-2α performed extremely well, exhibiting an 11.82-fold change in expression, signifying a high level of activation in chronic hypoxic conditions. HIF-1α also showed activation, but not to the same degree as HIF-2α, showing a 2.74-fold change. Thus, while HIF-1α expression levels did increase in the hypoxic environment, the biosensor was more successfully activated using HIF-2α.

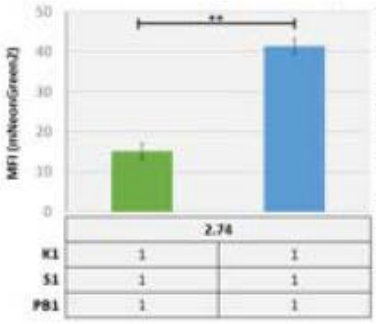

Figure 1. HIF-1α Truncated ODD

Comparison of expression in normoxic(green) and hypoxic(blue) conditions for truncated HIF-1α ODD. (** indicates $p<0.01$.)

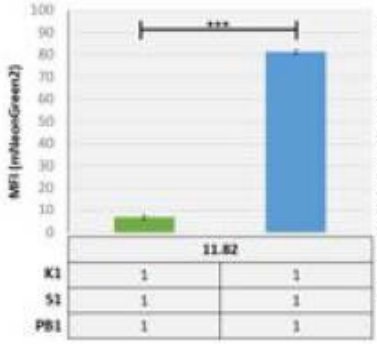

Figure 2. HIF-2α Truncated ODD

Comparison of expression in normoxic (green) and hypoxic (blue) conditions for truncated HIF-2α ODD. (*** indicates $p<0.001$)

Conclusions: The importance of HIF-2α in regulating the hypoxic response is evident in HIF-2α's stronger performance compared to HIF-1α. From these results, the potential to harness HIF-2α's activation in these environments is promising. While expression levels still increased in HIF-1α, HIF-2α is a better candidate in the 1% oxygen condition. It has been hypothesized that there is a certain level of oxygen where regulation of the hypoxic response shifts from HIF-1α to HIF-2α, which can be important in targeting different levels of hypoxia appropriate to the conditions of interest.[4] We will examine this in further experiments. Regardless, the current work suggests that the dynamics of both HIF-1α and HIF-2α should be considered for future research and therapeutic applications.

References:

1. Chen P.S. et al. Path. Implications of hypoxia. Journal of Biomedical Science. 2020:1-19
2. Tal R. The role of hypoxia. Biology of Reproduction. 2012;87(6), 134-1
3. Loboda A. et al. HIF-1 and HIF-2 transcription factors. Molecules and cells. 2010;29:435-432
4. Saxena K. et al. Acute vs chronic vs cyclic hypoxia. Biomolecules. 2019;9(8), 339

DEI: Immunoengineering has the potential to improve disparities in healthcare outcomes by offering an approach to personalized medicine. This work advances the fundamental principles involved in immunotherapeutic development.

STEVENS
INSTITUTE OF TECHNOLOGY

Investigation of Cell Traction Force in Osteogenic Differentiation Using Microcontact Printing and Inhibiting Agents

Samantha Fasciano[1], Shue Wang[2]
[1]Department of Cellular and Molecular Biology, College of Arts and Science, University of New Haven, West Haven, CT, 06516
[2]Department of Chemistry, Chemical Engineering, and Biomedical Engineering, Tagliatela College of Engineering, University of New Haven, West Haven, CT, 06516

Introduction: Human mesenchymal stem cells (hMSCs) are self-renewing, multi-potent cells that offer a promising option in cell-based therapies. Cell traction forces have been found to play a role in cellular characteristics including cell shape, cell motility, and extracellular matrix reorganization. The role of cell traction forces during osteogenic differentiation is not fully elucidated due to the inability of cell culture techniques to effectively display cell patterning.

Methods: Microcontact printing was used to encourage cell growth in a designated shape and size. This was done using an elastomeric stamp made of Polydimethylsiloxane (PDMS) that transferred hMSCs onto a PDMS substrate. Osteogenic differentiation was induced and osteogenic differentiation was measured by alkaline phosphatase (ALP) activity. Cell traction forces were reduced using the addition of Rho-associated protein kinase inhibitor Y27632 and Calyculin A to hMSCs. Osteogenic differentiation was measured by analyzing ALP activity.

Results: Physical confinement was created with microfabricated structures to investigate the effects of geometric control on hMSC osteogenic differentiation. The results indicated that hMSCs at the edge of geometrically confined microstructures have a higher osteogenic differentiation rate compared to inner cells, with increased ALP activity and enhanced calcium deposition. When cell traction forces were reduced using Y27632 and Calyculin A, increased osteogenic differentiation was observed.

Figure 1: Image of the resulting hMSC cells grown using microcontact printing. The cells were cultured in hMSC basal media for a total of 5 days.

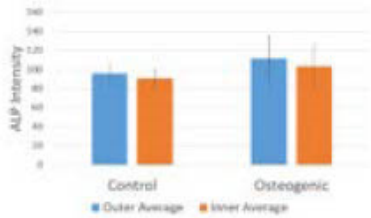

Figure 2: Increased ALP intensity observed at the outer edges of the confined microstructures.

a. b.

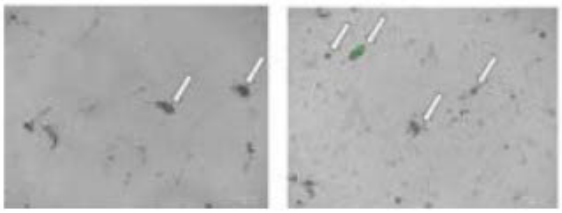

Figure 3: hMSCs stained with ALP five days after osteogenic induction in the absence (a) and presence (b) of rho-associated kinase inhibitor Y27632.

Conclusion: In summary, the effects of geometry guidance and the reduction of cell traction forces during hMSCs differentiation were studied. The results indicate traction force plays an important role during osteogenic differentiation. These findings will provide new insights to improve cell-based therapies and organ repair techniques. Further studies will focus on the addition of nanoparticles in examining the hMSC differentiation rate.

Acknowledgement: The authors would like to acknowledge the support from NSF CMMI program (Award number: 2143151). S. F. is supported by Provost's Fellowship at the University of New Haven.

STEVENS
INSTITUTE OF TECHNOLOGY

Cell-Laden Composite Hydrogel Bioinks with Human Bone Allograft Particles to Enhance Stem Cell Osteogenesis

Hadis Gharacheh[1] and Murat Guvendiren[1,2]
[1]Otto H. York Department of Chemical and Materials Engineering, New Jersey Institute of Technology
[2]Department of Biomedical Engineering, New Jersey Institute of Technology

Introduction: Limitations of the gold standard autograft for treating bone defects, such as availability of large enough bone tissue and complications in the harvesting site such as infection, pain, and bleeding, have led to search for alternative treatment options[1]. Allograft bone has recently gained significant interest due to its inherent osteoconductive and osteoinductive characteristics. Here, we developed a novel bone-mimetic bioink composed of methacrylated alginate (MeALG) hydrogel filled with human bone allograft particles to enhance adult human mesenchymal stem cell (hMSC) osteogenesis[2] (Fig 1A).

Methods: *Rheology:* The rheological behavior of the ink was examined by measuring the viscosity with respect to shear rate (0.01 to 1000 s^{-1}) and strain sweep (0.5-300% at 1 Hz) for the evolution of the elastic modulus (G') and viscous modulus (G"). *Mechanical characterization:* Compression test was performed to calculate the Young's modulus (*E*) of hydrogels (a disk with 14 mm in diameter and 2 mm in height) that were equilibrated in PBS. Hydrogels were prepared following the bioprinting protocol. *Bioprinting:* Bioinks were prepared from 3% (w/v) methacrylated alginate (MeAlg) with/without 1% (w/v) human bone particlesin PBS containing 0.1% (w/v) photoinitiator (LAP). HMSCs (passage 4, Lonza) were encapsulated in ink (3 million cells/mL) for bioprinting the scaffolds. The grid scaffold (2mm x 2mm) composed of 4-layers (150-µm layer height and 500-µm offset between struts) was used for culture studies (Fig 1A). Extrusion-based BioX (CellINK) bioprinter was used in this study (with print pressures of 150-200 kPa and speed of 20-30 mm/s). Each layer was partially crosslinked for 15 s (405 nm, 2 mW/cm^2) to allow self-supporting layers, followed by 1 min light exposure at the end of the bioprinting procedure. *In-vitro studies:* Cell viability studies were performed on 3D bioprinted scaffolds using Live/Dead staining kit (Invitrogen) at 1-28 day culture. Alkaline phosphatase (ALP) activity and alizarin red (AR) assay, as well as osteocalcin (OC) immunostaining were performed to evaluate the osteogenic differentiation of the hMSCs. For this purpose, 3D bioprinted scaffolds were cultured in growth media for one day, followed by culturing in osteogenic differentiation media for 28 days.

Results: In this study, human allograft bone particle containing composite bioinks were developed to bioprint cell-laden composite hydrogel scaffolds for bone tissue engineering. The zero-shear viscosity (at shear rate ~0.01 s^{-1}) of the neat (*N*) MeALG bioink significantly increased with the addition of bone particles for composite (*C*) bioinks, such that the viscosity value increased from ~7 (*N*) to ~30 Pa·s (*C*) (Fig 1B). Both inks showed shear thinning behavior allowing bioprinting of the inks. The % swelling of the *N* hydrogels decreased for *C* bioinks (84% as compared to 72% for neat hydrogels) (Fig 1C), and *E* increased from 21±6.2 kPa (*N*) to 51±7.1 kPa (*C*) (Fig 1D). In vitro studies (up to 28 days) confirmed high cell viability (~90%) for hMSCs within 3D bioprinted *N* and *C* scaffolds (Fig 1E). When cultured within bioprinted *C* scaffolds, hMSCs showed significantly higher ALP activity (such as 48× at day 28 and 9× at day 7) (Fig 1F) and AR activity (1.2x at day 21) (Fig 1G) in osteogenic differentiation media (OM) compared to *N* scaffolds. In addition, majority of the hMSCs (~95%) stained positive for OC within *C* scaffolds as compared to *N* scaffolds (~70%) (Data not shown).

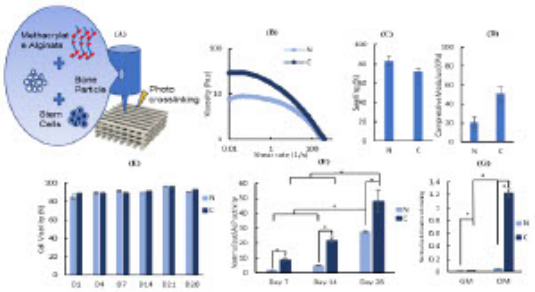

Figure 1. (A) Bioprinting approach. **(B)** Change in viscosity with shear rate for the neat (*N*) and composite (*C*) inks. **(C)** Percent swelling and **(D)** elastic modulus of the scaffolds. **(E)** Percent cell viability with culture day for hMSCs within bioprinted *N* and *C* scaffolds. **(F)** Normalized ALP activity (with respect to day 1) for culture day 7-28 in osteogenic media (OM), and **(G)** AR expression at day 21 in growth (GM) and OC. * indicates $p<0.05$ for n = 3 samples per group.

Conclusions: We report a novel photocurable composite bioink composed of methacrylated alginate with human bone allograft particles for 3D bioprinting of bone scaffolds. Incorporation of bone particles led to a decrease in swelling and an increase in stiffness of the composite hydrogels as compared to neat hydrogels. In vitro culture studies revealed high cell viability (~90%) for hMSCs when bioprinted within *N* and *C* bioinks. Differentiation studies confirmed significantly high ALP activity, calcium deposition and OC expression for hMSCs within bioprinted *C* hydrogels as compared to *N* hydrogels. Overall, our results confirm that our composite bioinks have a significant potential to create scaffolds for bone tissue engineering.

Acknowledgements: This study is partially supported by MTF Biologics Junior Investigator Award and NSF CAREER Award (2044479).

References:

1. Gharacheh, H., Guvendiren, M. Three-dimensional bioprinting vascularized bone tissue. *MRS Bulletin* 48, 668–675 (2023). https://doi.org/10.1557/s43577-023-00547-y
2. Gharacheh, H.; Guvendiren, M. Cell-Laden Composite Hydrogel Bioinks with Human Bone Allograft Particles to Enhance Stem Cell Osteogenesis. *Polymers* 2022, *14*, 3788.

STEVENS
INSTITUTE OF TECHNOLOGY

Fabrication and characterization of Chitosan:Polystyrene Sulfonate Composite Scaffolds for Bone Regeneration

Rana Ibrahim, Nicole Petrocelli, Matangi PR, Hongjun Wang
Department of Biomedical Engineering and Semcer Center for Healthcare Innovation, Stevens Institute of Technology

Introduction:

Regenerating a large bone defect remains a big clinical challenge, often requiring bone grafts to facilitate regeneration. In search of an effective graft, Chitosan (CS) and beta-glycerophosphate (β-GP) have both been used in bone tissue engineering in consideration of their favorable osteogenic properties individually or in combination [1]. However, due to the weak crosslinking capacity of β-GP, the CS-β-GP composite hydrogels lack stability and mechanical strength, fully degrading within 12 weeks [1]. Meanwhile, these hydrogels only have a compressive modulus between 0.5 and 7 kPa, significantly lower than bone [5-20 GPa] [2]. In this regard, by adding Polystyrene sulfonate (PSS) to a complex with chitosan, we are expecting the new composite scaffold will significantly show increased mechanical strength and reduced degradation rate through the stabilizing effects of electrostatic interaction with a long-chain polymer. Also, it is believed that adding PSS will increase the mineralization of the CS-PSS scaffolds as a result of the negatively charged sulfonate groups.

Materials and Methods:

Scaffolds composed of CS and PSS are made by mixing CS and PSS solutions at different ratios (1:0.5, 1:0.7, 1:1, 1:1.4, and 1:2 CS to PSS) to form precipitates. The precipitates were collected and further treated with .25M NaOH for 15 minutes to form a hydrogel before neutralizing and freeze-drying for 24 hours.

A compressive test was performed on the freeze-dried scaffolds (n=18) with the Chatillon MTS using a crosshead rate of 2 mm/min. The compressive modulus was determined using the slope of the linear region of the stress-strain curve.

A degradation study was conducted to determine the effect of PSS on the degradation rate. Samples (n=3 per time point) were incubated in phosphate-buffered saline (PBS, pH 7.4) under shaking at 37℃ for up to 12 weeks. The weight of the dried samples harvested weekly was recorded to determine the remaining weight percentage.

To determine the porosity, the as-prepared scaffolds were examined with both scanning electron microscopy(SEM) and micro CT to assess the 2D surfaces and 3D structure.

To determine the effect of PSS on mineralization, the weighed scaffolds (n=4) were incubated in 1.5X simulated body fluid (SBF, pH 7.4) for two weeks under shaking at 37℃. The solution was changed every 2 to 3 days. After the 2-week incubation, samples were washed with deionized water and freeze-dried before weighing to determine the weight loss or gain. Additionally, 3 of the 4 samples underwent microCT examination to determine the volume % and distribution of the deposited minerals. A sham control(n=4) soaked in PBS only under the same conditions was included to compare the weight change.

Results and Discussion:

While all scaffolds comprising CS and PSS demonstrate high porosity (75-90%) and interconnectivity (<15% of pores are closed), the 1:1 ratio of CS to PSS is more appropriate for bone regeneration based on the following results. Increasing PSS improved the mechanical properties of the composite scaffold; however, the improvement reached a plateau after the 1 to 1 ratio. Although the presence of PSS significantly reduced the degradation rate compared to literature-reported values of CS-β-GP, increasing the amount of PSS in the composite scaffold increased the degradation rate because of the rapid absorption of water enabled by PSS. It is also noted that the presence of PSS significantly increases the mineralization capabilities of the composite scaffolds, but the benefit dwindles after the 1 to 1 ratio.

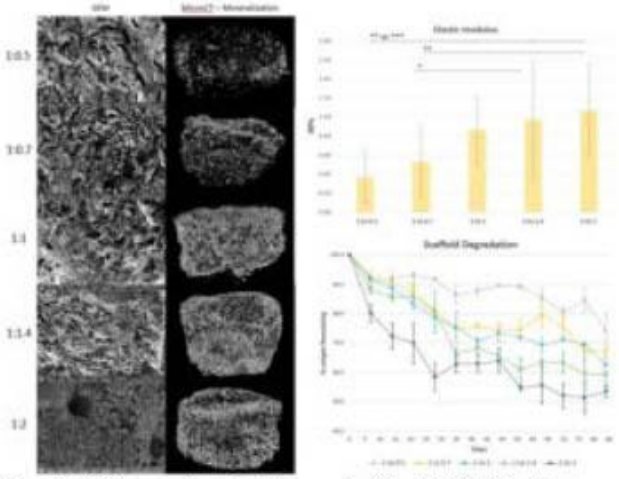

Figure 1: SEM images demonstrate the porosity of the CS:PSS ratios, The MicroCT images show the mineral deposition on the various CS:PSS samples after 2 weeks incubation in simulated body fluid. The elastic modulus increases significantly with increasing PSS formulations (* $p<0.05$, ** $p<0.01$, *** $p<0.001$). Increasing PSS concentrations lead to an increased degradation rate; after 12 weeks, samples retain 75 to 50% of their mass depending on the amount of PSS added.

Conclusion:

The combination of CS and PSS have demonstrated to be effective to improve both the mechanical properties and mineralization capabilities which will be favorable for bone tissue regeneration. These initial results suggest that it may provide a supportive environment for bone regeneration. Therefore, this scaffold material paves the way for developing innovative biomaterials that promote bone regeneration. Further studies are needed to demonstrate the effect of this scaffold on the attachment, proliferation, and differentiation of bone-forming cells.

References:

1.Saravanan, S., Vimalraj, S., Thanikaivelan, P., Banudevi, S., & Manivasagam, G. 2019; 121, 38–54.
2. Panyamao, P., Ruksiriwanich, W., Sirisa-ard, P. & Charumanee, S, 2020; 12, 2514

STEVENS
INSTITUTE OF TECHNOLOGY

IGF-1- and IGFBP-5-Loaded Collagen Sponges for Skeletal Muscle Regeneration

Natalie G. Kozan, Sean Caswell, Jonathan M. Grasman.
New Jersey Institute of Technology, Newark, New Jersey

Introduction: Volumetric muscle loss (VML) is a condition in which skeletal muscle mass is lost due to trauma to the muscle. This condition is marked by lack of muscle regeneration and thus a permanent loss of muscle functionality.[1] The current treatment for VML is autologous tissue transfer, which often results in graft failure and is limited by reduced muscular function post-surgery.[2] Tissue engineering seeks to develop implantable scaffolds to regenerate the muscle and restore functionality. Current scaffolds, however, are limited in their regenerative capabilities, often due to lack of sufficient satellite cell recruitment and subsequent growth and myofiber formation.[1] The addition of insulin-like growth factor-1 (IGF-1) to the scaffold should overcome this limitation, since IGF-1 enhances both the proliferation and differentiation of myoblasts[3]. Additionally, the complex formed between IGF-1 and an IGF-binding protein (IGFBP-5) has been shown to enhance myoblast differentiation[4]. We will therefore add both IGF-1 and IGFBP-5 to our scaffold and test its ability to enhance the proliferation and differentiation of myoblasts.

Methods: Type I collagen was polymerized into hydrogels within cylindrical PTFE molds, and frozen to generate anisotropic porous sponges, as we described previously.[1] Sponges were crosslinked with 12.9 mM EDC, 10.4 mM NHS, and 34 mM heparin. IGFBP-5 was then incubated on the sponges overnight at 4°C, followed an overnight incubation of IGF-1 (37°C and 5% CO_2) to facilitate growth factor loading. Sponges were made into 6 different groups: 1) heparin/IGFBP-5/IGF-1, 2) heparin/IGF-1, 3) heparin, 4) IGFBP-5/IGF-1, 5) IGF-1, and 6) none (control). Conditioned myoblast growth medium from each sponge was collected every 24 hours, replaced with fresh medium, and added directly to cells pre-plated in a 96-well plate. The CCK8 cell metabolism assay was conducted at days 0 and 3 to quantify cell proliferation. To determine whether released IGF-1 would enhance differentiation, conditioned differentiation medium was similarly collected. After 7 days of culture, cells were fixed and immunostained against myosin and counterstained with DAPI and phalloidin. The fusion index was calculated to quantify myoblast differentiation. Statistical analysis was conducted using one-way ANOVA with Tukey's post-hoc analysis ($p<0.05$).

Results: To quantify cell proliferation, we conducted CCK8 testing and found an increase in cell proliferation between days 0 to 3 for all groups (Fig 1A). However, sponges containing heparin showed qualitatively lower absorbance values than sponges without heparin at day 3, suggesting that these sponges support lower levels of proliferation. To quantify differentiation at day 7, sponges containing heparin have significantly higher fusion indices than sponges without heparin, suggesting that heparin-loaded sponges induce greater amounts of myofiber differentiation than heparin un-loaded sponges.

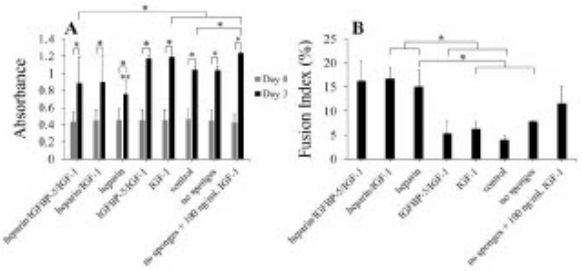

Figure 1. Analysis of (A) cell metabolism shows an increase in proliferation from day 0-3. Analysis of (B) fusion index on day 7 shows more differentiation in heparin-loaded sponges. * denotes significance ($p<0.05$) between indicated groups. ** denotes significance from all other groups on day 3. Error bars show standard error of the mean.

Conclusions: The increase in absorbance values from day 0 to day 3 show that all of the sponges tested induce myoblast growth, confirming their *in vitro* biocompatility. While collagen sponges containing heparin supported less proliferation than other groups, they instead facilitated the most differentiation. This supports our hypothesis that heparin-loaded sponges will be most beneficial for muscle regeneration, as they support the most myofiber formation. Heparin-loaded sponges with IGF-1/IGFBP-5 elevated myoblast proliferation levels, and as such may be advantageous for implantation to promote skeletal muscle tissue regeneration. Future work includes implanting sponges into a murine model of VML to test their *in vivo* efficacy.

References:

1. Kozan, NG et al. J. Fuct. Biomater. 2023; 11:p.1245897.
2. Mulbauer, GD et al. Discoveries (Craiova). 2019; 7(1):e90.
3. Yang, SY et al. FEBS Lett. 2002;522(1-3):p.156-60.
4. Duan, C et al. Gen Comp Endocrinol. 2010;167(3):p.344-51.

Acknowledgements: The authors would like to thank Milan Patel, Sydnee Sicherer, Jarin Tusnim, and Satyaj Awasthi for their contributions to this work, as well as funding from the NIH (R21-AR079708 and KL2-TR003018) and startup funds from NJIT.

DEI: This research seeks to develop a more easily accessible treatment for VML by developing a scaffold which can be administered as an off-the-shelf product in clinics and reduce the need for expensive surgery and post-operative care. In our lab, we routinely involve undergraduate students from various fields and socioeconomic or cultural backgrounds in research training, thus expanding the accessibility of research to anyone interested in science.

STEVENS
INSTITUTE OF TECHNOLOGY

Sacrificial
Electrospun Dipeptide for Encapsulation of Cell Therapies

Nicholas Lee, Yu-li Wang.
Carnegie Mellon University.

Introduction: Cell based therapies are promising approaches with both academic and industry interest due to the broad range of disease applications, but the advances in stem cell research and genetic engineering that make the field so attractive are held back by biomaterial and engineering challenges. Hydrogel microencapsulation approaches excel at immunoisolation and suppressing fibrotic response, but is difficult to scale into safe, retrievable treatments. Current polymer macroencapsulation devices that address retrievability struggle to balance transport with protection and prevent thick fibrotic capsule formation [1]. The objective of this study is to develop a 3D printable hydrogel material with controlled submicron porosity to increase the rate of transport across an immunoprotective barrier while also enabling increased flexibility in device design. Here, we present a UV crosslinked hydrogel embedded with easily removable nanofibronic porogens. The improved transport properties, in conjunction with light-induced polymerization, should be compatible with 3D printing to obtain a wide range of sizes and shapes for the versatility of artificial organ designs.

Methods: Several types of porogens were tested to produce nano-microporous hydrogels including calcium carbonate nanoparticles, two types of ionic surfactants, and electrospun alginate. The final molecule selected for further testing was Fmoc-diphenylalanine (Fmoc-FF), a pH sensitive dipeptide capable of self assembly. Solutions of Fmoc-FF nanofibers were electrospun directly into a solution of dilute HCl to form nano to micro scale fibers. The fibers were collected then suspended into a solution of acrylamide monomer, bisacrylamide (crosslinker), and LAP (photoinitiator). The fibers were dissolved and removed from polymerized gels by incubating the gels in a basic buffer. The gels were also placed into a custom electrophoresis device to drive out remaining peptide molecules. Gel total and macro porosity were measured gravimetrically. Preliminary evaluation of gel porosity performed was through comparison of electrophoresis of BSA. Diffusion of low molecular weight dextran was measured using a custom diffusion cell. Oxygen permeability was measured using a dissolved oxygen probe by mounting gels directly on the probe end. Molecular weight cut off was also investigated by imaging penetration of fluorescent dextrans (MW 3-70kDa) into gels mounted in a custom fluidic chip.

Results: Electrospun fibers incorporated with rhodamine dye were imaged in polymerized gel with confocal microscopy and measured to be about 450 nm in diameter on average. From the gravimetric data, removal of the fibers from polyacrylamide gel results in 50% added macroporosity. Preliminary BSA electrophoresis testing showed that the protein band in gel prepared with Fmoc-FF porogens travels up to 2.7 times further than the control using the same conditions. The effective diffusion coefficient measured from diffusion cell experiments of 3kDa dextran of gel prepared with Fmoc-FF porogens was 80% greater than that of the control gels. The oxygen permeability of porous gels was 67% greater than control gels. Dextran penetration testing showed that only 3kDa dextran could enter control gels, while dextrans up to 40kDa could enter gels that were prepared with porogens but 70kDa dextran was still excluded.

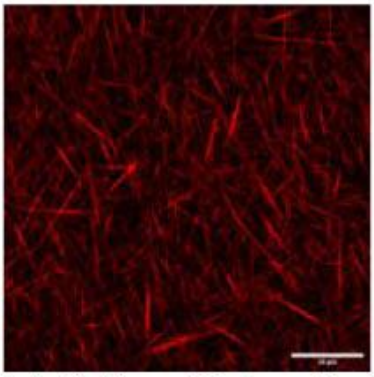

Figure 1. Confocal image of electrospun fibers in PAA using a 63x objective lens. 20 um scale bar.

Conclusions: The approach presented here allows for the preparation of a dispersion of peptide nanofibers that are stable in polyacrylamide matrices and can be easily dissolved and removed. The resulting highly porous hydrogels have significantly improved transport of oxygen and small molecules while still excluding molecules larger than 70kDa. Further, the improved transport properties, in conjunction with light-induced polymerization, is compatible with 3D printing to obtain a wide range of sizes and shapes for the versatility of artificial organ designs. Future studies will apply 3D printing to produce cell culture chambers to explore the effect of our highly porous gel on spheroid viability.

References:

1. Dang H. et al. J Cell Mol Med.2022; 26:(4756-4767)

Acknowledgements: NIH R35 49848.1.1090633

DEI: On top of the already high demand for organ transplants, there are racial disparities in those that receive organ transplants. Providing alternative solutions can broaden access and level out the disparities. To broaden STEM to underrepresented persons, universities should work directly with highschools to design and offer tissue engineering programs where students can perform simple experiments in university teaching labs and speak to researchers.

STEVENS
INSTITUTE OF TECHNOLOGY

Deletion and Sequential Insertion of Large DNA in the Human Genome for Cell Therapy Applications

Sarah Levovitz, Minjoo Kim, Susanna Jaramillo, Serena Generoso, Sumanth Dara, Tomoki Yanagi, David M. Truong
New York University Department of Biomedical Engineering

Introduction: Deleting and inserting large amounts of DNA into the genome is a topic of major interest in synthetic biology. The ability to engineer large portions of the human genome can open doors to new innovations related to cell-based therapeutics. For example, deletion and insertion of MHC genes in iPSCs would allow for the production of immune-matched stem cells that can be differentiated into immune cell types useful for cell therapy. Here, we present a method called REWRITE for sequentially inserting large fragments of DNA into the human genome. Coupled with large-scale deletions, this will allow us to re-engineer portions of the human genome. We are also creating a bank of refactored native HLA haplotypes that can be delivered into iPSCs for the purpose of creating off-the-shelf cell therapies.

Methods: Synthetic HLA plasmids are engineered via yeast recombineering. PCR, next-generation sequencing, and Sanger sequencing (Azenta) are used to confirm the correct assembly of HLA haplotypes. Human iPSCs (PGP1 cell line) are nucleofected with a linearized landing pad and a CRISPR plasmid (pX459 backbone) to insert a cassette for sequential DNA insertion into the desired region of the genome. Resistance genes present in the cassettes allow for chemical selection to be performed to screen for correct integrations. Fluorescence imaging and PCR are used to confirm proper CRISPR editing of the cells, as well as qPCR for verifying the pluripotent potential of engineered cells. Subsequent insertions of DNA into the landing pad cassette are also performed via nucleofection and similar PCR screenings. Large genomic deletions are performed via CRISPR-Cas9 using two guide RNAs that flank the region to be deleted, and a landing pad is inserted into the deleted genomic locus.

Results: The REWRITE system uses RMCE to replace a landing pad cassette containing blasticidin resistance and mScarlet genes with a cassette containing puromycin resistance and mNeonGreen on a delivery plasmid. Orthogonal lox sites flanking both cassettes allow for RMCE to occur. To test this system, two plasmids, named Zero1 and FlpOut, were delivered into a landing pad inserted into the Rogi1 safe harbor region of the genome. Chemical selection, fluorescence imaging, and PCR were used to confirm the replacement of the blasticidin resistance and mScarlet genes in the landing pad cassette. The FlpOut plasmid contains an FRT site which, along with the FRT site on the landing pad, allows for the cassette to be removed from the genome, leaving only the payload DNA delivery. The Zero1 plasmid introduces a new lox site into the genome, and sequential insertion of Zero2 into Zero1 cells swaps out the PuroR and mNeonGreen for BlastR and mScarlet again. Restriction cloning was used to create a series of Zero1 and Zero2 plasmids with various lox sites to test which is the most efficient for sequential deliveries. Using the FlpOut plasmid backbone, full synthetic HLA plasmids were engineered by Neochromose, Inc., and miniature versions of the HLA plasmid containing only the HLA genes and regulatory regions were engineered via yeast recombineering in the lab (Figure 1). These plasmids have repositioned HLA-A to be in between B and C to aid in delivery and also to examine the feasibility of rearranging genes in the human genome. Genomic HLA A, B, and C genes were deleted via CRISPR-Cas9, and a landing pad was inserted into the region of HLA B and C deletion (Figure 1). PCR confirmed the absence of HLA genes and the presence of landing pad junctions.

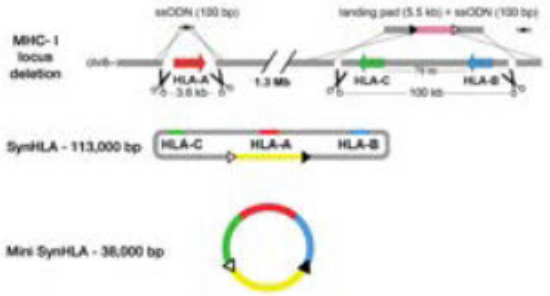

Figure 1. Process of deleting HLA Class I from the genome, assembling a full synthetic HLA plasmid and a miniature synthetic HLA plasmid

Conclusions: Using the REWRITE system, we were able to successfully integrate a landing pad into a desired portion of the human genome and sequentially insert payload plasmids into the landing pad locus. FlpOut, Zero1, and Zero2 plasmids can all be engineered to contain large DNA payloads, and along with a series of novel lox sites, will allow for sequential delivery of large fragments of DNA into the genome, with the aim of inserting 1 Mb of DNA. Deleting the HLA Class I locus and replacing it with a landing pad confirmed our ability to delete large amounts of DNA from the human genome using this method. Using these HLA blank cells, we can deliver our engineered synthetic HLA and minisynHLA plasmids to create a bank of iPSCs with common HLA haplotypes that can be used for off-the-shelf cell therapy applications. Making custom-engineered HLA haplotypes will enable us to include rare HLA types that match individuals who may be underrepresented and would typically have difficulty finding matching donors.

Acknowledgements: We thank the people at Neochromosome for their work on the REWRITE system and in making the HLA matched plasmids and HLA deleted iPSC cell lines. We thank the NIAID for their support through a DP2 and SBIR award. DMT was previously an employee of Neochromosome Inc/Opentrons Robotics and owns stock in the company. The results of this work are subject to a pending patent

STEVENS
INSTITUTE OF TECHNOLOGY

Epigallocatechin-Gallate as a Novel Treatment for Joint Injury Repair

Timothy Mahon, Mary Pat Reiter, Joseph W. Freeman, PhD.
Department of Biomedical Engineering, Rutgers University, Piscataway, NJ 08854, USA.

Introduction: Traumatic joint injuries and genetic disorders that affect connective tissue often result in chronic joint instability. Ehlers-Danlos Syndrome (EDS) is one such genetic disorder where a defect in α1(I) chains of collagen triple helices result in loosely packed collagen with decreased mechanical strength that causes tissues to become easily injured. Strains and sprains are common injuries that result in joint laxity, which can lead to recurrent injury and dislocations without surgical intervention and repair. Polyphenols, such as epigallocatechin-3-gallate (EGCG), have potential to generate a wound healing response due to interactions between their hydroxyl groups and connective tissues. These interactions can strengthen the mechanical properties of ligaments and tendons. We propose the use of EGCG to strengthen injured joints. The delivery of EGCG to strained or sprained soft tissue will crosslink the tissue, resulting in increased mechanical strength of the joint. EGCG could also be used prior to strenuous activity to increase tissue strength to prevent against tissue damage.

Methods: *Cell Culture & Treatment*: rat-derived patellar tendon fibroblasts (rPTF) were cultured in alpha-MEM (10% FBS, 1% pen/strep). Cells were plated and allowed to recover overnight before a 1-hour treatment with EGCG.
Cell Viability Analysis: Absorbance of PrestoBlue (ThermoFisher) was used to measure cell proliferation, 24h, 72h, and 7 days post treatment with EGCG. Experimental samples were treated with a serial dilution of EGCG at concentrations ranging between 0.6% - $6x10^{-6}$%.
Collagen Production Analysis: Cells were fixed using 4% formalin after assessment of viability. The cell samples were then stained with SiriusRed dye and imaged. The dye was then extracted from the samples and absorbance readings were taken to determine collagen content.
Tensile Testing: Rat tail tendons were isolated from 200-220 g Sprague Dawley rats. Experimental groups were exposed to 0.06% (wt/v) EGCG. Tendons were evaluated with an Instron 5800 (Norwood, MA) with an extension function of 0.1 mm/s after a preload of 0.1 N.

Results: rPTF cells were treated with a range of EGCG concentrations. It was determined via PrestoBlue analysis that high concentrations (0.6% & 0.06% EGCG) significantly reduced cell viability, whereas cell viability at lower concentrations of EGCG did not significantly differ from control groups. Collagen production followed the same trend as cell viability, with samples treated with high concentrations (0.6% & 0.06% EGCG) producing less collagen. Collagen production in samples treated with lower concentrations of EGCG did not significantly differ from controls.

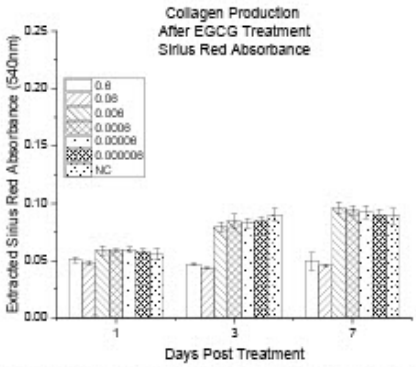

Figure 1. Collagen production in cell samples treated with varying concentrations of EGCG or untreated.

Tendons treated with EGCG were found to have increased mechanical strength as determined by measurement of Elastic Modulus and Ultimate Tensile Strength.

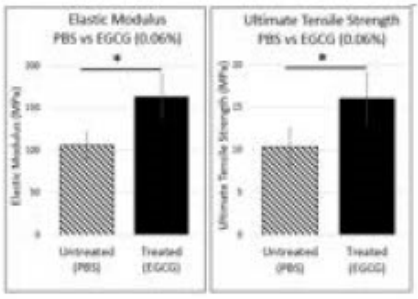

Figure 2. Elastic Modulus and Ultimate Tensile Strength (UTS) respectively comparing control tendons soaked only in PBS and tendons soaked in EGCG treated PBS.

Conclusions: It was determined that EGCG will interact with collagenous tissues, thereby increasing their mechanical strength. The data also shows that at high concentrations, EGCG is cytotoxic, which will have to be considered when delivered *in vivo*. At non-cytotoxic concentrations, EGCG did not result in any change in collagen production, meaning the cells retained their normal activity. Future studies will investigate possible delivery systems and the ability of EGCG to prevent tissue failure.

References:

1. McMasters J, et al. AAPS J. 2015;17(5):1117-25.
2. Burkel B, et al. Phys Rev E. 2018;98(5).
3. Paderi, J. E, et al. Biomacromolecules 9(9): 2562-2566.

Acknowledgements: This project is supported by NSF grant CBET-2207577.

STEVENS
INSTITUTE OF TECHNOLOGY

Prognosis of Prostate Cancer Metastasis Risk Through qPCR

Anthony Watt[1], Emily Labour[1], Ethan Masters[1], Dr. Leszek Kotula[2]
Syracuse University Department of Biomedical and Chemical Engineering[1], SUNY Upstate Medical University Department of Urology[2]

Introduction: Prostate cancer is a disease afflicting more than 190,000 men in the United States [1]. Although curable in early stages, stage IV prostate cancer patients have only a 32% relative survival rate 5 years after diagnosis [2]. Our research focuses on optimizing the detection of a novel cancer biomarker– an isoform of the protein Abelson interactor 1 (ABI1), a signal transduction protein associated with increased cell movement and proliferation that is produced by the prostate [3]. In healthy prostate epithelial cells, ABI1 RNA undergoes splicing to form a protein product excluding exon 4 (delta exon 4, Del4), whereas inclusion of exon 4 results in tumors more prone to metastasis (wild type, WT) [4]. The early and accurate detection of the exon-4-containing ABI1 isoform will allow for a better diagnosis of disease severity for patients. We aim to optimize qPCR conditions for ABI1 detection by developing and optimizing the thermocycling conditions for novel probes. Previous internal data suggests that the existing fluorescent probes used in TaqMan qPCR assays for ABI1 isoform detection cannot specifically anneal either ABI1 transcript during amplification. Ultimately, we hope to create a protocol that can be applied directly to patient samples.

Methods: Preliminary qPCR has been run on purified and concentrated cDNA samples of reverse-transcribed WT and Del4 ABI1 mRNA using the TaqMan fluorescence system and CFX Connect Real-Time PCR Detection System. Concentrated sample was diluted with DI water to test the minimum detectable concentration of cDNA. If these probes anneal specifically, results should show early threshold detection of cDNA correctly matched with a corresponding probe. The cycle threshold (CT) indicates the cycle level at which sufficient fluorescence is emitted through probe annealing on a sample to be detected. Smaller CT values indicate greater expression, as it takes fewer replication cycles to achieve detection. The resulting CT values from the qPCR run conducted at 60°C, the existing protocol conditions, and 70°C, the expected annealing temperature given probe sequence, in triplicate were graphed to visualize detection trends.

Results: Fluorescence threshold values were graphed comparing how each probe anneals to each sample at different annealing temperatures. The results indicate that the WT probe suboptimally distinguishes between cDNA sequences with high concentrations of cDNA regardless of 60°C or 70°C cycling conditions, while the Del4 probe does not distinguish between sequences. The 70°C experiment shows large variation and little trend in amplification level between sample/probe conditions. The current Del4 probe is not specifically annealing to the Del4 cDNA at either 60°C or 70°C. The WT probe is annealing without significant specificity at 70°C cycling conditions.

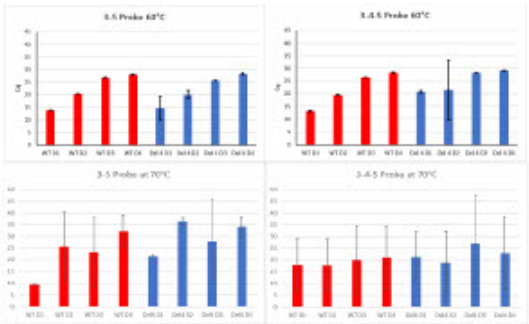

Figure 1. 3-5 refers to Del4, 3-4-5 refers to WT. D1-4 indicates the mass of cDNA sample used per 20 µL reaction. D1: 1 ng, D2: 10 pg, D3: 100 fg, D4: 1 fg

Conclusions: Based on the current results, running this protocol with true patient samples, as opposed to purified cDNA, would be inadequate for accurate prognosis. Future experiments with more precise temperature adjustments will be conducted to verify the impact of temperature on the specificity of the existing probes. Nonspecific annealing may be caused by sequence similarities resulting in probe attachment to both WT and Del4. The 3' end of exon 3 has the same four bases as the 3' end of exon 4, meaning the difference between the 3–5 bridge and 4-5 sequence is limited to the remaining 11 base pairs that make up exon 4. Novel probes have been designed in an attempt to improve specificity by destandardizing the amplified region of the primer sets. Since existing primers amplify the same regions of each sample, producing a segment of ABI1 between exons 3 and 5, there is the possibility that adjusting forward and reverse primer regions to amplify different portions of cDNA to specify exon-4 containing or lacking sample may improve results.

References:

1. Siegel R. L. et al. CA. 2020;70(1):7-30
2. Siegel D. A. et al. MMWR. 2020;69(41):1473-1480
3. Chen Z. et al. Nature. 2010;468(7323):533–538
4. Kotula L. et al. JCO. 2022;40(6):172-172
5. Lowder D. et al. Cancer Lett. 2022;10(531):71-82

Acknowledgements: The authors thank the Syracuse University SOURCE Office for funding, Kevin Lin for his lab training, Xiang Li for the project foundation, and Dr. Douglas Yung for his support and guidance.

DEI: In the United States, Black men are 1.76 times more likely to be diagnosed and 2.14 times more likely to die from prostate cancer compared to White men. Black men are also more likely to have a more advanced stage of prostate cancer at the time of diagnosis [5]. These statistics must be considered when selecting cell lines for testing to ensure universal applicability of prognostic techniques.

STEVENS
INSTITUTE OF TECHNOLOGY

Shape-Memory Actuated 3D Silk Wrinkled Surfaces Decrease Biofilm Formation on a Medical Device Model

Sadie Meyer, Elizabeth Oguntade, Luiza Owuor, Mary Beth Monroe, James H. Henderson.
Department of Biomedical & Chemical Engineering, BioInspired Institute, Syracuse University, Syracuse, NY 13244.

Introduction: Bacterial biofilm formation on the surfaces of indwelling medical devices, such as catheters, often results in pathogenic infections that can lead to increased patient morbidity and mortality.[1] Among recognized antifouling surface topographies, surface wrinkle patterns have exhibited notable antimicrobial characteristics.[2] Biopolymer films, such as silk fibroin (SF) has been previously demonstrated to achieve wrinkling, but there has been little investigation of biopolymer wrinkling for antifouling surfaces. Critical questions include (1) the extent to which biopolymer wrinkling can be translated to a 3D material platform that can mimic the enivornments of biofilm associated infections related to indwelling implants and (2) the effects of structure on microbial attachment and colonization. Since SF has been widely employed in the biotechnology field due to its intrinsic antifouling performance,[3] we coated a silk film onto the surface of thermo-responsive shape memory polymers (SMPs) to trigger silk wrinkle topographies when exposed to heat. For the specific application of mimicking indwelling catheters, we 3D printed SMP single lumen cylindrical tubes, in which we intend for the heat-actuated contraction of the SMP to be capable of inducing the silk wrinkled topographies to prevent biofilm formation.

Methods: Programming via Printing (PvP),[4] an advanced manufacturing technique we recently developed, was utilized to simultaneously fabricate and program the tensile strain (15%) in SMP substrates. This single 3D printing process allows for the customizability of programmed strain through manipulation of printing parameters such as nozzle temperature. The SMP filament used in this printing process was fabricated through extrusion (3Devo composer 450) of semicrystalline thermoplastic polyurethane pellets (MM-4530, SMP Technologies, Inc.). Programmed cylinders were printed as concentric fibers in a layer-by-layer manner for shape memory circumeferential contraction. Following fabrication, the substrates were dip-coated in 2% w/v SF solution and then post-treated in methanol to induce secondary structural changes in the silk network and minimize water solubility. Silk wrinkle formation was achieved by heating the SMP in an isothermal oven above its glass transition temperature (45 °C) to enable heat-induced contraction of the SMP. Atomic force microscopy was used to capture images of the silk wrinkles and determine the wrinkle wavelengths and amplitudes. Lastly, the silk wrinkled surfaces were incubated with *S. aureus* or *E.coli* in Lysogeny broth for 24 h. Then, samples were fixed, dehydrated, and dried prior to insepection of microbial adhesion and colonization with scanning electron microscopy. Statistical analysis was performed via one-way ANOVA followed by Holm Sidak's multiple comparisons test.

Results: For both *S. aureus* and *E. coli* bacteria strains, the wrinkled surface groups on the 3D structures displayed lower biofilm coverage compared to their respective controls, the uncoated SMPs and the unwrinkled silk coated SMPs (**Figure**). The control samples, lacking any surface modifications, qualitatively showed high biofilm coverage. In the unwrinkled, silk-coated SMP substrate there was a slight reduction in biofilm coverage compared to uncoated SMPs.

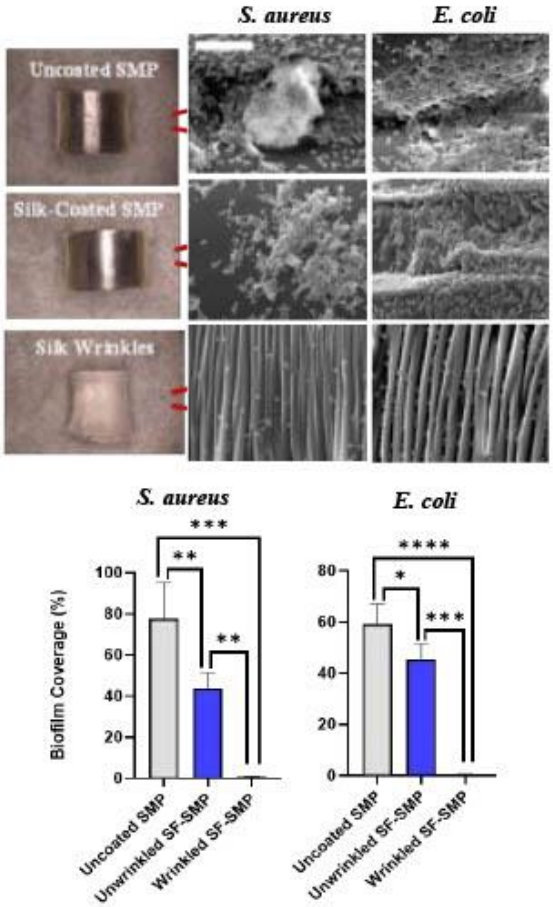

Figure. Qualitative and quantitative characterization of *S.aureus* & *E.coli* biofilm coverage following 24 hr incubation. Scale bar of 5 µm applies to all SEM images. Significance reported as *p<0.05, **p<0.01, ***p<0.001, ****p<0.0001.

Conclusions: These results demonstrate the feasibility of introducing biopolymer wrinkling on the surface of 3D architectures that can mimic the enivornments of biofilm associated infections related to indwelling implants and medical devices. The 3D wrinkled surfaces significantly decreased biofilm coverage compared to the uncoated and unwrinkled silk-coated surfaces. Ultimately, these findings provide a potential strategy for biopolymer wrinkled topographies to be studied in 3D material systems for use as antibiofouling surfaces for biofilm prevention.

References: [1] Jia Z. *Focus on Bact Biofilm, IntechOpen.* 2022. [2] Nguyen et al., *Polymers*, 2020. [3] Tullii et al., *ACS Appl. Mater. Interfaces*, 2019. [4] Pieri et al., Advanced Materials Technologies, 2023.

STEVENS
INSTITUTE OF TECHNOLOGY

A Multi-Layer Vocal Fold Microtissue to Study Fibrosis

Luis M. Medina[1], Elvan Dogan[1], Ryan Branski[2], Amir K Miri[1]
[1]Department of Biomedical Engineering, New Jersey Institute of Technology (NJIT), Newark, NJ 07102; [2]Otolaryngology-Head and Neck Surgery, NYU Grossman School of Medicine, New York, NY 10016

Introduction: To understand vocal fold (VF) disorders and their underlying mechanisms, *in vitro* models that replicate the biophysical characteristics of VF tissue are necessary. The VF tissue is a multilayered structure with a vocalis muscle and a soft, avascular lamina propria. Any alteration in the biophysical properties of extracellular matrix (ECM) during voice disorders affects phonation parameters. This increase in stiffening of the VF lamina propria is known as fibrosis. Fibrosis can be characterized as an altered state of extracellular metabolism via cells, where fibroblasts are differentiated into a more metabolically active myofibroblast. Due to the complex nature of fibrosis, an increased cellular metabolism of fibroblasts leads to elevated levels of disorganized collagen that alters the structure, size, shape, and organization of the ECM. The current methods use removed larynges or bioreactor models. They require greater repeatability and control over microscale phenomena. A constructed biomimetic VF model that enables microscale cell response research is required. We demonstrated the use of hydrogel engineering and 3D printing to create a microfluidic-based model of the VF tissue. A gelatin scaffold and a hyaluronic acid glycosaminoglycan were used to mimic VF.

Methods: We presented a hydrogel-based microfluidic model with two main layers developed in our laboratory. The first layer comprises HA in the form of hyaluronic acid methacrylate (HAMA) and a well-engineered version of gelatin called gelatin methacrylate (GelMA). The second layer will consist of acellular polyethylene glycol diacrylate (PEGDA; Sigma), with a constant concentration of 35% v/v, designed to mimic muscle structure. To create GelMA at the following mass concentrations: 2.5%, 5%, 7.5%, and 10% w/v, we adhered to our normal procedure. Using HAMA at different mass concentrations—0%, 0.5%, 1%, and 2% w/v—we will combine them with our GelMA mass concentrations mentioned previously. The photoinitiator used was Irgacure (0.5% w/v, Sigma). Next, we looked at how stiffness affected the behavior of VF fibroblasts in a static environment. To explore VF scarring, we employed an immortalized VF fibroblast cell line (HVOX) as the cell model. We employed immunostaining of cells to verify the production of αSMA and collagen I, the key fibrotic markers in VF cells.

Results: Using our lab's previously established multilayer platform with an average layer height of 200um (Figure 1C), we showed biocompatibility with our hydrogels in a layerwise format through live/dead staining after 5 days (Figures 1A and 1B). We tuned our models with the mechanical properties of our hybrid hydrogels through storage modulus and elastic modulus (Figures 1E and 1G). From this data, we can tune our system to values associated with the VF lamina propria. We showed the stability of our hydrogel scaffolds via swelling ratio and degradation rates up to two weeks, in which we also evaluated worse-case scenarios using lyophilized hydrogels (Figure 1F). We evaluated the cell biocompatibility of our scaffolds using a quantitative assay over one week to assess cell proliferation at various cell densities. The model showed high cell proliferation in the lamina propria for all groups. We then showed how stiffer gel led to more generation of α-SMA and collagen I proteins in the ECM model, known as fibrotic models within our system.

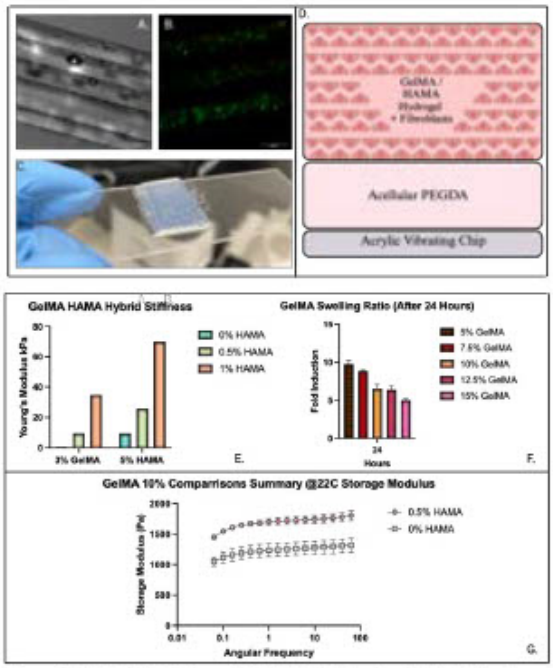

Figure 1. (A-C) Multi-layered GelMA hydrogel with fibroblasts encapsulated phase contrast, live/dead fluorescence, and gel image. (D) Breakdown of the model, acellular PEGDA, and vibrational chip represented. (E-G) Mechanical characterization of tunable gels, elastic modulus, swelling, and storage modulus.

Conclusions: The results pave the way for more biological analysis of the model. We aim to optimize our material systems to create a biomimetic environment while maintaining our microfluidic device stable for the long term and future work. The next step is to include immune-response cells in the model to include the impact of macrophages in the development of scarring and evaluate how vibration changes cellular markers within the gels.

References

1. Thibeault SL. Et Al. J Voice. 2002;16:96–104
2. Tang SS. Et Al J Voice. Sep;31(5):520-527
3. Solon J et Al Biophys J. 2007 Dec 15;93 (12) 4453-61

Acknowledgments: We acknowledge the support from NIH (R21DC18818).

STEVENS
INSTITUTE OF TECHNOLOGY

Assessment of Strategies for False Discovery Rate Control and their Implications in Computational Biology

Awais Mirza[1], Fatir Qureshi[2,3], Halil Arici[2,3], and Juergen Hahn[2,3,4].
[1]Department of Biology, Georgetown University, Washington, DC, United States
[21]Department of Biomedical Engineering, Rensselaer Polytechnic Institute, Troy, NY, United States
[3]Center for Biotechnology and Interdisciplinary Studies, Rensselaer Polytechnic Institute, Troy, NY, United States
[4]Department of Chemical and Biological Engineering, Rensselaer Polytechnic Institute, Troy, NY, United States

Introduction: The analysis of measurements from metabolomics, transcriptomics, epigenetics, or metagenomics, often requires hundreds or even thousands of hypothesis tests which concurrently compare two or more groups. Multiple hypothesis testing becomes essential under those circumstances to control the overall rate of false discoveries. Commonly employed techniques for correcting the multiple hypothesis testing problem include the Bonferroni method, the Benjamini-Hochberg (BH) procedure, and the Storey-Tibshirani approach [1]. However, each method comes with its own set of limitations. The Bonferroni method utilizes a conservative readjustment of significant p-values based on the total number of hypotheses tested, regardless of dependency and sample size. The handling of dependencies among hypothesis tests is also one of the principal limitations of the Benjamini-Hochberg test, potentially leading to increased false discoveries in correlated data sets. While some studies have demonstrated the use of a leave-n-out approach within the Storey-Tibshirani procedure, a comprehensive comparison against alternative techniques is lacking [2]. This work aims to fill this gap by systematically comparing these methods under different assumptions to evaluate their performance under distinct conditions.

Methods: This study employed MATLAB (MathWorks, Natick, MA) to create synthetic datasets simulating biological data across various conditions. A custom function was developed to generate simulated data for comparing two subsets, either drawn from the same population or alternative populations. The generative function enabled users to adjust parameters such as the simulated data distribution type, number of variables, standard deviation and mean range, maximum allowable effect size, sample size, and proportion of correlated samples. The datasets, generated through this function's modulation, underwent univariate hypothesis testing. The p-values then underwent testing using the Benjamini-Hochberg, Bonferroni, and leave-n-out methods. The accuracy of the predicted relationships between groups was evaluated across all multiple hypothesis testing correction methods, utilizing an adjusted p-value of 0.05 and FDR rate of 0.10. To investigate the impact of specific parameters, a chosen variable in the equation was isolated and manipulated, while other factors were held constant.

A preliminary analysis was performed using generated normally distributed data, evaluating the proportion of significant findings ranging from 0.01 to 0.50, the number of hypotheses tested ranging from 10 to 10,000, and the sample size ranging from 5 to 1000. Initial introduction of correlation was made only for the proportion of significant findings. A total of 100 iterations were conducted to assess possible alterations in false discovery rates, utilizing the central limit theorem to determine the average performance across conditions. For the initial analysis, a leave-1-out approach was utilized.

Results: The number of hypotheses tested had limited impact on the accuracy of the leave-n-out approach, while the Bonferroni method had the greatest decrease in accuracy. The proportion of significant findings emerged as a pivotal factor influencing accuracy across all methods, but to varying degrees (r=0.-79, r=0.-76, r=-0.64 for Bonferroni, BH, and leave-1-out, respectively). Notably, in cases with high correlation or proportion of significant findings, the leave-n-out approach consistently outperformed others. However, when BH and Bonferroni assumptions held true, these techniques consistently surpassed the accuracy of the leave-n-out approach. However, this is not surprising as these methods were specifically designed for these cases.

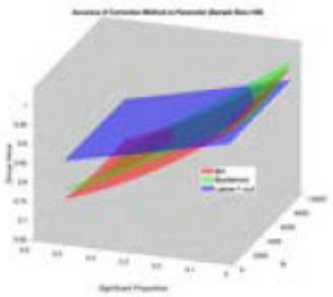

Figure 1. Comparison of accuracy, number of hypothesis tests, and proportion of dignificant findings across methods with an ample size of 100

Conclusions: The findings highlight the efficacy of employing a leave-n-out approach under specific conditions, notably in data sets with high correlations or a large proportion of significant findings. This insight offers valuable considerations for the optimal application of multiple hypothesis testing techniques across diverse statistical scenarios. Future endeavors will expand the analysis protocol to enhance optimization under additional conditions and include comparisons with various real-world datasets. Such extensions aim to provide practical guidance for researchers in choosing the most appropriate technique tailored to their specific data, ensuring informed decision-making in statistical analyses.

References:

1. Korthauer K, et al. Genome Biol. 2019; 20, 118
2. Vargason T, et al. Res Autism Spectr Disord. 2018;50:60-72.

STEVENS
INSTITUTE OF TECHNOLOGY

Computational Analysis of a Biochip for Monitoring Cellular Dynamics Using Advanced Hall Sensor Technology

Harshitha Govindaraju, Umer Hassan.
Rutgers, The State University of New Jersey.

Introduction: This research presents a computational model for on-chip diagnostic sensing, significantly advancing our understanding of cellular responses to magnetic stimuli. Utilizing an integrated system of Circular Halbach Magnetic Arrays and Hall Effect sensors[1], our model explores the interaction dynamics between magneticnanoparticles and cells at the microscale. These nanoparticles, previously used as selective tagging agents, are key in detecting and quantifying cellular uptake due to their chemical coatings, which enable specific reactions indicative of sample characteristics and biomarker levels. This innovative approach enables precise quantification of cellular uptake of magnetic particles, establishing a direct correlation with specific biomarkers. Such advancements in technology are vital for the progression of precision medicine, offering substantial improvements in targeted prognosis and personalized healthcare.[2] This model sets a new standard in biomedical sensor technology, improving the accuracy and efficiency of diagnostics and health condition monitoring.

Methods: Our research utilized the computational capabilities of COMSOL Multiphysics® to simulate a Halbach array, crafted to generate a uniform magnetic field within the XY plane. The focus was a Hall Effect sensor, strategically positioned at the array's center, orthogonal to magnetic field lines on the XZ plane. This sensor was tasked with detecting changes induced by a simulated magnetic bead, 1µm in diameter, hovering over a semiconductor plate (5µm x 5µm x 0.5µm) within a microfluidic chamber that has an inlet and outlet. The plate's properties included an electrical conductivity of 1.04e3 S/m and a Hall coefficient of 1.25e-3 m³/C. Our primary model equation, $J = \sigma (E - \sigma RH (EXB))$, was pivotal in assessing interactions between the electric field (E), magnetic field (B), and resultant current density (J). As the magnetic bead, mimicking an industry-standard functionalized magnetic bioparticle, moved along the +z direction, distinct Hall voltage peaks were observed, corresponding to its trajectory. Additionally, to mimic a realistic cell matrix, we substituted the standard maghemite material for a cell-like matrix in our simulations that was non-magnetic, thus adjusting the material properties. This change allowed us to accurately record the Hall voltage responses, reflecting the particle's impact on the cell-like environment. This methodology enabled a detailed study of the Hall voltage peaks in response to the movement of the magnetic particle, providing insights into the interactions between magnetic particles and non-magnetic cellular structures. This approach is essential for understanding cellular level quantifyable properties to enable the on-chip diagnostic systems.

Results: The computational model successfully generated bell-shaped Hall voltage peaks when a functionalized magnetic bioparticle crossed the sensor, contrasting with the flat response from the non-magnetic cell matrix (Figure 1). This highlights the platform's capacity for detecting magnetic influences of particles, facilitating precise cellular uptake quantification research by monitoring the voltage peaks induced by magnetic nanoparticles (MNPs). These voltage peaks are indicative of MNPs' magnetizability inside the cells, offering significant insights for cellular engineering and therapy.

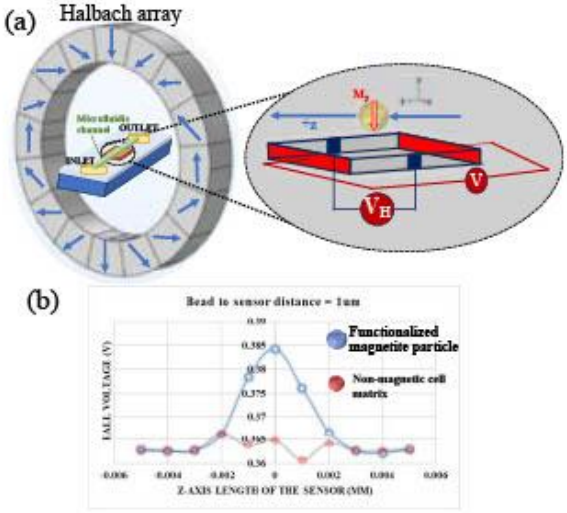

Figure 1. (a)Halbach Array Enabled Hall-effect Biosensing. (b) Voltage response

Conclusions: Our computational model marks a significant advancement in tracking and quantifying cellular interactions with magnetic nanoparticles in real-time. This breakthrough, utilizing precise Hall Effect sensor technology, has substantial implications in diagnostic medicine and personalized healthcare. By accurately distinguishing magnetic particle behavior within cellular environments, our approach paves the way for innovative diagnostic tools and targeted therapies, enhancing our understanding of cellular mechanisms and setting a new standard in magnetic nanoparticle technology for medical research.

References:

1. Govindaraju, H., et al., Elsevier J. 2024. (*In review*)
2. Mocanu-Dobranici, A. E., Costache, M., Dinescu, S., Int. J. Mol. Sci. 2023;24(3):2028.

Acknowledgements: Authors would like to acknowledge the funding support from NSF Award # 2053149, and Rutgers, The State University of New Jersey.

DEI:1) Utilizing our computational model for affordable, precise diagnostics can help reduce healthcare disparities. 2) Encouraging diversity in our research team will foster inclusivity and innovation in biomedical engineering.

STEVENS
INSTITUTE OF TECHNOLOGY

Quantification of Cortical Activation During Vestibular Tasks: A Pilot fNIRS Study

Rifath Hasan Rafi[1], Chang Yaramothu, PhD[2]
[1]Department of Biomedical Engineering, [2]School of Applied Engineering & Technology,
New Jersey Institute of Technology.

Introduction: Approximately 42 million people worldwide suffer from mild traumatic brain injury (mTBI)[1], also known as concussion. Evidence from previous studies demonstrates oculomotor and vestibular manifestations following concussion[2]. This study aims to establish cortical baseline data using functional near-infrared spectroscopy (fNIRS), enabling future comparisons with concussed individuals, and subsequently helping establish biomarkers for concussion. This study explores the interplay between the vestibular and oculomotor systems in healthy controls. We utilized fNIRS for its non-invasive nature, access to superficial cortical regions, suitability for true-to-life settings, temporal resolution, portability, and motion compatibility. Six non-concussed participants, aged 22 to 27 years, underwent monitoring of oxygenated concentration in the parietal-temporal region—a region associated with activation during balance tasks[3].

Methods: Cortical activation data was gathered using a custom head cap, a fNIRS system, and a Neural Navigator Stereotactic camera system. The head cap allowed easy insertion and removal of optodes. An optimal source-detector (SD) configuration was crucial to maximize channels with minimal optodes. The finalized design provided 15 channels in each hemisphere, facilitating the study of functional brain activity in the region of interest, shown in Figure 1. To ensure precise optode placement, the Neural Navigator Stereotactic camera system was utilized. We used a standard rest/task paradigm using a block design. Subjects were positioned 3 feet away from an eye-level target. Tasks were categorized into four subsections (Eyes closed, Saccades, Horizontal and Vertical VOR), with a minute gap at the end of each. Each subsection included 10 rest/task blocks, concluding with a task block. 'Rest' phases (Eyes open standing still) lasted 20 seconds, and 'task' phases lasted 30 seconds. Experimental timing and triggers were managed with E-Prime 3.0 software, with start and end times marked on analog triggers for fNIRS data sets. The cerebral blood flow changes were quantified at 25 Hz and saved in a *.nirs format for offline analysis. The raw fNIRS data were analyzed using MATLAB toolbox Homer2. Optical intensity was converted into optical density signal and then oxygenated (HbO) and deoxygenated (HbR) hemodynamic concentrations for each source-detector channel were computed.

Results: While performing the VOR tasks, the HbO response was most pronounced in specific channels: left hemisphere channels 10 and 11 and right hemisphere channels 25 and 26. The hemodynamic response function (Fig 2) indicated a higher concentration of HbO during the task phase. Task data was compared with rest data, revealing that performing the vestibular task necessitates increased oxygenation in the specified brain regions, aligning with previous literature.

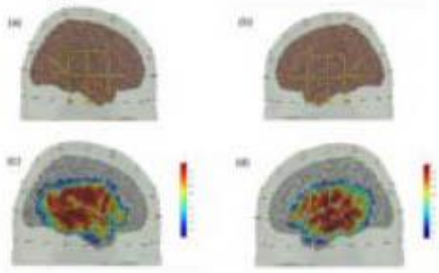

Figure 1. Optode Configuration and sensitivity map in right hemisphere (a &c) and left hemisphere (b & d).

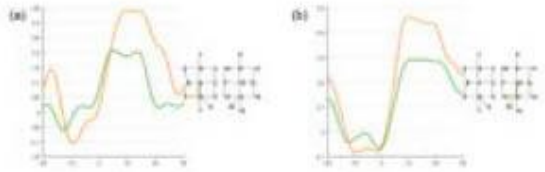

Figure 2. HbO HRF for channels 10 (a, yellow) and 11 (a, green) in the left hemisphere and for channels 25 (b, yellow) and 26 (b, green) in the right hemisphere.

Conclusions Our fNIRS investigation into balance tasks during eye movements has offered insights into the neural dynamics related to the vestibular and oculomotor systems. Future endeavors will involve expanding the participant pool to 30 individuals, aiming to validate and generalize our current findings to a larger population. Establishing this expanded dataset will serve as a baseline for comparative analysis, particularly in exploring potential impairments in the vestibular and oculomotor systems among patients with mild traumatic brain injuries.

References:

1. Gardner RC, Yaffe K. Epidemiology of mild traumatic brain injury and neurodegenerative disease. Mol Cell Neurosci. 2015;66(Pt B):75-80.
2. McCrory P, Meeuwisse WH, et al. Consensus statement on concussion in sport: the 4th International Conference on Concussion in Sport held in Zurich, Nov 2012.
3. Karim H, Fuhrman SI, Sparto P, et al. Functional brain imaging of multi-sensory vestibular processing during computerized dynamic posturography Neuroimage. 2013;

Acknowledgements: Study was funded by the NJIT Faculty Startup Package.

DEI: This study aims to (1) identify concussion biomarkers with fNIRS for improved early detection and (2) enhance inclusivity by including participants from diverse age groups, genders, and cultural backgrounds, thereby increasing the applicability of the findings.

Functional Near-Infrared Spectroscopy (fNIRS) Experiment Data Analysis Using ML Algorithm

Ruhuan Liao, Leslie Abbott
Research advisor: Dr. Danushka Bandara
Fairfield University

Introduction: The purpose of this research is to utilize data collected from participants with the fNIRS device to classify human trust using brain activity data collected during specific tasks or activities. Participants were selected from Fairfield University's undergraduate and graduate student population (n=18), where the fNIRS data collection was conducted. The fNIRS device was used to measure the oxygenated and deoxygenated hemoglobin levels in the frontal cortex of each participant. Before collecting data, calibration of the fNIRS device was performed to ensure accurate probe readings and to minimize the influence of ambient light, which could potentially lead to data inaccuracies. By developing a machine learning algorithm using the calculated feature values for the oxygenated and deoxygenated channels as input features to train and test the processed fNIRS data, the aim is to understand how the brain activity works and uncover patterns of neural activation using analyzed data to train a machine learning model to predict accuracy.

Methods: In this research, we utilized a NIRx NIRSport2 fNIRS device operating at a sampling rate of 10 Hz to capture brain activity data. The device outputs raw light intensity signals which are then processed to obtain blood oxygen concentrations. These are further filtered using a third-order zero-phase Butterworth filter (filter range between 0.01 Hz and 0.5 Hz). During the experiment, these individual participants underwent a series of tests designed to induce differing levels of stress. They were prompted to determine whether they trust a computer-generated response to a question or not, while also indicating their confidence level in the provided answer, which is then recorded. The filtered hemoglobin level data then undergoes preprocessing, which includes parsing timestamp files using Python scripts to determine the time range for data segment boundaries and extracting the relevant time series for each trial. The data analysis entails computing mean, standard deviation, kurtosis, min, and max values as feature values for each hemoglobin channel for each trial. Several machine learning methods were tested on the resulting dataset to assess the binary trust classification performance. Interpretation of the models involves examining the feature coefficients of each channel column to obtain the feature importance values.

In conducting binary classification tasks, the workflow begins with logistic regression without undersampling, followed by logistic regression with undersampling, random forest, and gradient boosting. Model training includes Z-score normalization using the standard scaler technique specifically for logistic regression. Further analysis involves assessing model accuracy, visualizing feature coefficients, and analyzing confusion matrices and ROC curves to evaluate performance.

Results: Our analysis uncovered a relationship between hemoglobin levels and binary trust values. Using a leave one subject out method, we calculated the classification performance of our model. These findings highlight the potential of fNIRS-derived data and machine learning techniques in analyzing trust within the brain.

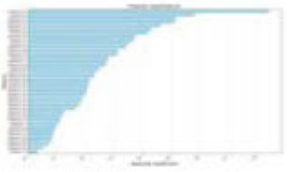

Figure 1. Feature Importance
Uses the coefficient of the features to display feature importance in the collected dataset.

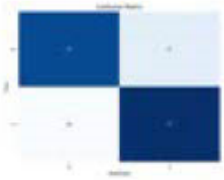

Figure 2. Confusion Matrix
Uses the confusion matrix to illustrate the distribution of true positives, true negatives, false positives, and false negatives, offering insights into the model's performance across the trust and mistrust classes in the dataset.

Conclusions: The logistic regression model achieved an accuracy of 0.760 without undersampling and 0.723 with undersampling. Meanwhile, the random forest model demonstrated a slightly higher accuracy of 0.749, while gradient boosting achieved an accuracy of 0.790 on the dataset. These results indicate a reasonable predictive capacity of the models.

References:

1. Bandara, D., Grant, T., Hirshfield, L. et al. Identification of Potential Task Shedding Events Using Brain Activity Data. Augment Hum Res 5, 15 (2020). https://doi.org/10.1007/s41133-020-00034-y (https://doi.org/10.1007/s41133-020-00034-y)

Acknowledgment: This work was funded by NASA CT Space Grant award (DB)

DEI: 1)This research provides an opportunity to study trust in human-AI interactions. The result could contribute to the development of more trustworthy AI systems, helping to bridge gaps in equitable access and acceptance of such systems. 2)This research has provided opportunities for women in STEM, while also bringing a diverse perspective for addressing complex challenges in bioengineering.

STEVENS
INSTITUTE OF TECHNOLOGY

Advanced Biomaterials Mimicking the Human Mesenchymal Stem Cell Microenvironment to Control Cell Behavior

Bethany Almeida
Department of Chemical and Biomolecular Engineering, Clarkson University, Potsdam, NY 13699, USA

Biographical Summary of Applicant: Dr. Bethany Almeida is a tenure-track Assistant Professor at Clarkson University. Previously, Dr. Almeida was an ASEE Postdoctoral Research Fellow at the US Naval Research Laboratory. Dr. Almeida received her Ph.D. in Biomedical Engineering from Brown University and a dual B.S. in Biomedical Engineering and Professional Writing from WPI. Dr. Almeida has received numerous awards, including a 2018 Graduate Collegiate Competition Finalist for the SWE We-Local Conference, a 2020 BMES Career Development Award, a 2020 Rising Stars in Engineering in Health Award, and the 2022 Clarkson University Nominee for the Pew Biomedical Scholars Program, among others.

Clinical Impact and Significance of Research Problem: Human mesenchymal stem cells (hMSCs) have significant therapeutic potential, yet limitations such as heterogeneity and innate differences between in vitro and in vivo culture conditions impede their clinical use. Thus, there is a need to improve therapeutic outcomes. The cell microenvironment consists of biochemical cues (e.g., growth factors) and biophysical cues (e.g., matrix stiffness) and is known to influence hMSC behavior. Biomaterials can be engineered such that their physicochemical properties mimic the cell microenvironment, thereby controlling cell behavior. The Almeida Lab's long-term vision is to elucidate the interrelationship between the hMSC microenvironment and hMSC behavior using biomaterials and apply this knowledge to develop clinically translatable hMSC-biomaterial therapies. While the effects of biochemical cues on hMSC behavior are relatively well-understood[1], the effects of biophysical cues is an active research area. The literature has shown that matrix stiffness[2] and geometric shape[3] can control hMSC osteogenesis and adipogenesis via mechanosensitive pathways. However, the mechanisms behind hMSC chondrogenesis and immunomodulatory behavior remain largely unknown. Thus, the major questions of the Almeida Lab's research program are: 1. What are the molecular and genetic mechanisms by which the cellular microenvironment influences hMSC differentiation and immunomodulation?; 2. How can advanced engineering tools be used to systematically design biomaterials to elucidate these mechanisms and control hMSC behavior?

Innovative Programmatic Approach of Applicant: The Almeida Lab applies concepts from organic chemistry, materials science, engineering, and stem cell biology to design biomaterials mimicking the hMSC microenvironment. Such work includes the design of advanced polymeric nanoparticles laden with bioactive small molecules[4], elucidating the mechanisms by which stiffness and viscoelasticity affect hMSC immunomodulatory behavior using highly tunable polyacrylamide gels[5], and designing hydrogels for wound healing and cartilage tissue engineering using naturally-derived polymers covalently conjugated using novel click chemistry approaches[6,7]. This research program has broad therapeutic relevance and will lead to a paradigm shift in how biomaterials are designed for hMSC therapies.

Key Findings of Applicant to Date: The literature predominantly focuses on the effects of biomaterials on cells. Early studies[3,8] by Dr. Almeida were among the first to demonstrate that cell culture conditions induce dynamic changes to biomaterial properties, subsequently altering the intended effect on cell behavior (Figure 1A-B). In addition, Dr. Almeida's previous work[7] showed the feasibility of novel bioorthogonal click chemistry for hMSC culture (Figure 1C). Current work in the lab uses bioorthogonal click chemistry to develop advanced biomaterials capable of controlling hMSC behavior with known effects of the cells on the material and the material on the cells.

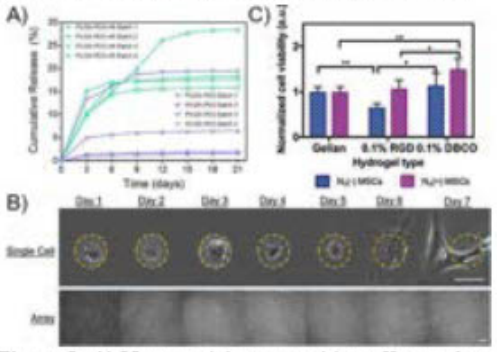

Figure 1. A) Nanoparticle composition affects release profiles[4]. B) Gold thickness affects hMSC pattern stability[8]; top/bottom = 62/200 µm. C) hMSCs clicked to non-adhesive hydrogels show improved viability[7]; *p<0.05.

Future Goals: This research can improve disparities in healthcare outcomes by targeting diseases with no cures (e.g., Osteoarthritis and diabetic foot ulcers) that disproportionately affect minority populations. Dr. Almeida seeks to become a leader in biomaterials, pioneering new technologies and answering fundamental scientific questions towards clinically relevant hMSC-biomaterial therapies. Dr. Almeida's mission is to train the next generation of bioengineers, particularly those from underrepresented populations, such as herself. To do this, Dr. Almeida currently serves on the National BMES Diversity Committee and as a mentor for Clarkson's NIH ESTEEMED program.

References:

1. Pittenger MF. Science. 1999;284(5411):143-147; 2. Engler AJ. Cell. 2006;126(4):677-689; 3. Kilian KA. Proc Natl Acad Sci. 2010;107(11):4872-4877; 4. Almeida B. Ann Biomed Eng. 2020;48(7):2090-2102; 5. Tse JR. Curr Protoc Cell Biol. 2010; 6. Battigelli A. Bioconj Chem. 2022;33(2):263-271; 7. Battigelli A. Chem Commun. 2020;56(55):7661-7664; 8. Almeida B. J Biomed Res A. 2017;105(2):464-474.

Acknowledgements: I acknowledge the contributions of all lab members and funding by the NSF (#2138587).

STEVENS
INSTITUTE OF TECHNOLOGY

A Community Situated Approach to Musculoskeletal Biomechanics Research

John F. Drazan
Department of Electrical and Biomedical Engineering, School of Engineering and Computing, Fairfield University

John Drazan is an assistant professor of Biomedical Engineering at Fairfield University. Dr. Drazan completed his undergraduate degree in Physics at SUNY Geneseo, where he was a 4-year varsity athlete in basketball. He completed his PhD in Biomedical Engineering at the Rensselaer Polytechnic Institute where he was an NSF-GK12 Fellow. He was a NIH IRACDA Postdoctoral Fellow at the University of Pennsylvania within the McKay Orthopedic Research Laboratory. For his work combining community engagement and biomechanics, Dr. Drazan received the 2020 Early Career Award for Public Engagement from the American Association for the Advancement of Science.

Clinical Impact and Significance of Research Problem: Muscle structure, particularly the length and orientation (pennation angle) of the muscle fascicles that compose it, is an important mediator of muscle function. These structure-function relationships of musculoskeletal (MSK) tissues change throughout the lifespan – responding differently to biomechanical factors based on age, sex, and genetic make-up. Ideally, these properties would be studied using longitudinal designs in humans, however, these approaches are often not implemented on large scales due to many barriers; effectively limiting the potential societal and scientific benefits. One such barrier is the location of the laboratories where this research takes place. These are typically located in elite venues like universities and hospitals, which are both geographically and culturally removed from the general population, resulting in widespread use of convenience samples in predominantly cross-sectional studies. Just as MSK studies suffer from convenience sampling, informal STEM opportunities such as robotics clubs are often geographically and culturally distant from populations of youth who are under-represented in STEM careers. As there is significant overlap in demographics of those under-represented in research studies and those under-represented in STEM careers, there is a need to develop new approaches in both MSK research and STEM outreach to bridge this divide between science and society for the benefit of all.

Innovative Programmatic Approach of Applicant: The purpose the Community Situated Biomechanics Lab (CSBL) is to address this problem of convenience sampling in both MSK research and STEM educational outreach by demonstrating a novel research paradigm that broadens research and educational opportunities through community-situated engagement. This research has three interlocking goals: 1) The development and deployment of novel STEM outreach approaches through youth sports to build close ties with the community. 2) The development of low-cost, mobile devices to measure MSK structure and function outside of the laboratory. 3) The deployment of MSK research tools within these communities as a part of STEM educational outreach to transform the collection novel MSK data sets into valuable service to the community.

Key Findings of Applicant to Date: Our research in using youth sports as a venue for STEM engagement has demonstrated that, in contrast to STEM intensive programs such as robotics clubs, youth sports provide a distinct population of youth who are not self-selected based on a preexisting interest/identity in STEM. These programs generate a statistically significant increase in STEM interest and identity among youth participants, with higher efficacy correlated to higher basketball interest. This community-situated approach to STEM engagement through sports has been deployed to engage over 30,000 youth across the US through a close partnership with 4th Family Inc., a black-led nonprofit based out of Albany, NY. Other partners include the National Basketball Association, SC Johnson, and Microsoft (Fig 1. A). We have developed novel approaches to measure musculoskeletal function in the community for both joint level kinetics and whole-body kinematics (Fig 1. B). We have also developed and validated mobile approaches to measure musculoskeletal tissue structure using ultrasound. We used these methodologies to measure muscle structure and function relationships within the plantar flexors to study the effect of natural variation in muscle structure on joint-level muscle function (Fig 1. C).

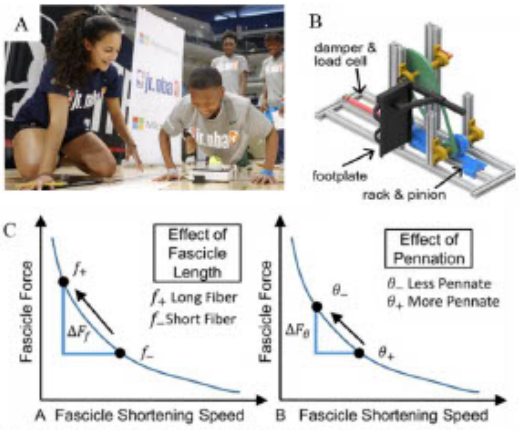

Figure 1. A) Deployment of the CSBL at the 2022 NBA Rookie Combine with 80 Chicago-based youth. B) Mobile Isokinetic Dynamometer. C) Representation of research findings linking muscle structure to muscle function at the joint level in humans.

Future Goals: We have developed new MSK research devices to measure muscle structure and function outside of the laboratory and built a robust network within youth sports in Bridgeport and beyond. We plan to incorporate these devices into our outreach programs in Bridgeport to longitudinally study how changes to muscle structure during growth effects joint level function in typically-developing adolescent athletes while introducing hundreds of youth to STEM careers as a broader impact of our work.

Acknowledgements: The work was funded through a gift from an anonymous donor through the Sapere Aude Fund.

STEVENS
INSTITUTE OF TECHNOLOGY

Examining Modes of Augmented Sensory Feedback during Rehabilitative Training of Upper Extremity Function

Yu Shi[1], Mingxiao Liu[1,2], Sophie Dewil[1], Noam Harel[2], Raviraj Nataraj[1],
[1]Stevens Institute of Technology, [2]James J. Peters VA Medical Center

Introduction: Currently, physical therapy remains the primary rehabilitation method for spinal cord injury (SCI) [1]. The repetitive nature of traditional therapy can lead to boredom and diminish functional gains. Emerging therapies integrate advanced technologies like virtual reality (VR) and wearable devices to engage and motivate participants through immersive, gamified experiences. However, the improved effectiveness of VR motor rehabilitation is notably reduced when controlling for training dosage. Augmented sensory feedback (ASF), which entails providing persons with additional information about motor performance through sensory cues, can be readily supplied in VR. Although proven to enhance motor learning [2], it is not typically used in rehabilitation since its impact on task performance is uncertain. In this study, we examine how various modes of ASF can improve task performance after providing real-time visual and audio cues for spatial orientation, aiding in self-correction during training.

Methods: Fifteen neurotypical participants were recruited for this study, approved by the Stevens Institutional Review Board. We designed and implemented a myoelectric control task in VR (*Unity*) for participants to move a robot arm and contact designated targets. Participants exerted semi-isometric muscular efforts with their dominant upper extremity placed in a position-adjustable support brace. Skin-surface sensors (*Delsys Trigno*) recorded electromyography (EMG) signals from fourteen muscle groups used as inputs to a regression support vector machine (*Matlab*) that detected command intention, with variable speed control, to move the robot end-effector in two dimensions (forward-backward, left-right). Participants also wore a 64-channel electroencephalography (EEG) cap (g.tec USBamp) to record brain activity and other physiological sensors for electrodermal activity and electrocardiogram (*Shimmer3 GSR*). Participants underwent three blocks of trials (pre-training, training, post-training) while receiving one of four modes of ASF: no ASF, visual, haptic (vibration), or multimodal (visual + haptic). Visual and haptic ASF encoded guidance information about the straight-line direction participants should follow to minimize end-effector motions in pursuing designated targets.

Results: Figure 1 shows the percentage changes in the primary motor performance metrics (i.e., task completion time, motion pathlength) after training with each of the four ASF modes. Training with ASF reduced completion time and motion pathlength compared to the control case of no ASF. Notably, there was a significant ($p<0.05$) reduction in these performance metrics after visual ASF compared to no ASF. As expected, ASF significantly increased EEG activity, given the increased sensory stimulation, and was highest with multimodal ASF. However, electrodermal activity, an indicator of emotional arousal and engagement, was highest for visual ASF.

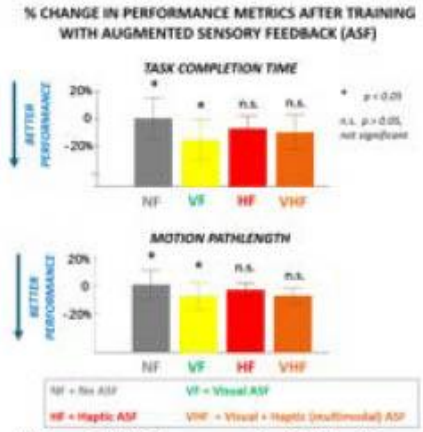

Figure 1. Performance after ASF training

Conclusions: Augmented sensory feedback with physical training can enhance the performance of a rehabilitation task significantly. For this study's task, visual ASF produced the best results. While multimodal feedback can accelerate the crossing of neural thresholds that improve motor learning in specific contexts [3], additional haptic cueing was distractive for this task. Visual ASF cues supported this visually driven task [4], facilitating increased engagement as indicated by higher electrodermal activity. The increased engagement may have, in turn, produced the observed increase in performance. Alternatively, using haptic cues alone or combined with visual cues may result in a higher cognitive load less conducive to performing this task. This study demonstrates participants are sensitive to how sensory cues are provided to guide performance. Such findings suggest the opportunity to optimize rehabilitation outcomes by personalizing the delivery of sensory-driven guidance cues.

References:

[1] R. M. Hakim, et al. *Disability and Rehabilitation: Assistive Technology*, vol. 12, no. 8, Nov. 2017.
[2] S. Prasad, et al. *Asian Spine J*, vol. 12, no. 5, Oct. 2018.
[3] A. R. Seitz and H. R. Dinse, *Current Opinion in Neurobiology*, vol. 17, no. 2, Apr. 2007.
[4] Sanford, Sean, et al. Frontiers in Virtual Reality 3 (2022): 943693.

Acknowledgements: NSF career award 2238880 and Charles V. Schaefer, Jr. School of Engineering and Science, Stevens Institute of Technology, provided funds to support the fundamental development of this research.

DEI: We enhance the diversity represented with our datasets by recruiting participants of varying ages, genders, and backgrounds. Furthermore, we involve persons with a disability and STEM-underrepresented pre-college students in educational programs supporting this project's research initiatives for movement rehabilitation.

STEVENS
INSTITUTE OF TECHNOLOGY

Do Baseline Measurements Relate to Balance Behavior During Walking and Turning?

Jake Stahl[1,2], Zahava Hirsch[1], Antonia Zaferiou[1]
Department of Biomedical Engineering, Stevens Institute of Technology, Hoboken, NJ
Department of Biomedical Engineering, Case Western Reserve University, Cleveland, OH

Introduction: Falls are multifactorial and a major health concern for older adults. A long-term goal is to better understand how person-specific factors relate to balance and walking behaviors related to fall-risk. The purpose of the study was to initially investigate the relationships between how older adults move during turning and walking vs. clinical baseline tests.

Methods: Nine participants aged 65 and older, who had not fallen in the past six months, volunteered to participate in this study in accordance with the IRB. Participants completed a series of clinical balance, strength, and cognitive exams, to create a baseline profile to compare to their movement measures. The baseline tests included the Fall Efficacy Scale–International (FES-I), Mini-Balance Evaluation Systems Test (miniBEST), Montreal Cognitive Assessment (MOCA), among others. Biomechanical measurements were captured by optical motion capture and included gait speed, lateral distance (a measure of balance), foot clearance, and stride length. The participants performed at least 10 trials walking straight down a 10 m path and 10 trials turning halfway down this path. To investigate associations, Pearson's correlations were computed between each baseline and movement variable, where p-value < 0.05 was considered statistically significant.

Results: The data comparison results revealed limited instances where the correlation between biomechanical measurements and the baseline tests reached statistical significance (**Table 1**). When comparing cognitive and perception baseline tests to biomechanical measurements, only the turn trials of SL vs. FES-I had statistical significance and agreed with the hypothesis that there would be a negative correlation. This comparison had a Pearson's correlation p-value of 0.043. The strength baseline tests had no statistical correlation to the biomechanical measurements, with the closest Pearson's correlation p-value being 0.222 for the turn trial GS vs. hip flexion strength trials. The clinical balance comparisons had the most statistically significant results, with the miniBEST having a Pearson's correlation p-value of less than 0.05 for three of the four biomechanical measurements. GS and SL agreed with the hypothesized correlation for straight and turn trials, while min LD agreed with just the turn trials. GS vs. miniBEST and SL vs. miniBEST both hypothesized a negative correlation, and min LD vs. miniBEST hypothesized a positive correlation. Finally, the composite baseline calculation, which had an equation of ((FES-I - 64)/(16 - 64)) + (MOCA/30) + AVERAGE((DGI/24), (miniBEST/28)) had no statistical significant correlation but comparisons with both GS and SL had turn trial data with a calculated p-value greater than 0.05 but less than 0.1. This p-value range was also seen for the GS vs. MOCA turn trials in the cognitive and perception baseline tests.

Table 1: Pearson's correlation results with statistically significant differences bolded.

Baseline Measures	Biomechanical Measures	Straight-Line Gait	90-degree Turn Trials
FES-I	GS	R^2=.017 p=.740	R^2=.121 p=.358
	Min LD	R^2=.039 p=.610	R^2=.186 p=.246
	SL	R^2=.182 p=.252	**R^2=.463 p=.043**
MOCA	GS	R^2=.110 p=.382	R^2=.375 p=.079
	Min LD	R^2=.079 p=.464	R^2=.024 p=.691
	SL	R^2=9.72e-5 p=.980	R^2=.018 p=.732
mini-BEST	GS	**R^2=.597 p=.015**	**R^2=.610 p=.013**
	Min LD	R^2=.011 p=.792	**R^2=.544 p=.023**
	SL	**R^2=.686 p=.006**	**R^2=.587 p=.016**
DGI	GS	R^2=.051 p=.557	R^2=.334 p=.103
	Min LD	R^2=.022 p=.703	R^2=.161 p=.285
	SL	R^2=.099 p=.410	R^2=.260 p=.161

DGI= Dynamic Gait Index; GS= gait speed; min LD= minimum lateral distance; SL= step length

Conclusions: This study initially explored relationships between baseline and biomechanical measurements in older adults performing straight-line gait and turns. There were a few data instances with significant associations between baseline tests and gait measures. In the future, larger sample sizes will be helpful to compare with non-linear analyses. Future research will expand the studies from healthy older adults to those with lower scores on baseline exams to explore a larger variety of scores and biomechanical measures. Another observation from this study is that out of the comparisons that returned significant, most of them (4/6) occurred during turn trials.

References:

1. Delbaere K. Age Ageing. 2010;39:210-216.
2. Ciolek C.H. Gucc Geriatr Phys Ther. 2020

Acknowledgements: National Science Foundation, REU/RET Site Grant #2050921 and Career #1944207.

DEI: Biomedical engineers can improve disparities in healthcare outcomes by remaining engaged in different diverse communities to understand the unique healthcare needs of the community. We can improve in broadening the participation of underrepresented persons in STEM by providing additional outreach programs to create opportunities for those persons to get involved at a younger age.

The Effects of Standing and Walking on Cartilage T2 Relaxation Time

Tejus Surendran (1), Daniel K. White (2), Axel C. Moore (1)

1. Carnegie Mellon University
2. University of Delaware

Introduction: Articular cartilage is the connective tissue that covers the ends of long bones located within diarthrodial joints. Its primary functions are to enable low friction articulation while providing a surface capable of bearing loads that can often exceed a person's body weight. Due to its poroelastic nature, loading the articular cartilage causes fluid exudation and deformation. Our previous research demonstrated that walking could restore the deformation induced by standing. Due to the relationship between cartilage deformation and fluid content it is likely that the composition of cartilage (e.g., hydration) changes during different daily activities. To assess this in vivo, we quantified T2 relaxation time, which has been associated with cartilage composition, for different daily tasks (standing, walking, lying supine). We hypothesize that tasks associated with increased cartilage deformation (standing), will lead to a reduction in T2 relaxation time, while tasks associated with recovery (walking and lying supine) will restore T2 relaxation time.

Methods: Following IRB approval, we selected four participants without knee symptoms to participate in this study. The participants were asked to perform 4 separate tasks across 8 distinct time points. The tasks included: static loading (standing for 30 mins), active loading (walking for 10 mins) and static unloading (lying supine for 50 mins). A 3T magnetic resonance (MR) scanner along with a 15 channel Tx/Rx knee coil were used to acquire MR images of the articular cartilage in the knee. The scan sequence used was a T2-weighted multi-slice multi-echo with a time of echo (TE) = 12.5, 25, … 75 ms and time of repetition = 4480 ms. To improve boundary identification, images were up sampled using spline interpolation from a 0.5 x 0.5 x 3 mm to 0.25 x 0.25 x 1.5 mm voxel. Image stacks were then registered via a 6 degree of freedom rigid transformation. T2 relaxation time was calculated using a mono-exponential decay function ($S(TE) = S_0 * e^{-TE/T2}$) fit to each voxel, where S_0 is the initial signal intensity at time 0 and TE is the time of echo, **Fig 1A**. In agreement with prior work, T2 relaxation times exceeding 100 ms and R^2 values below 70% were removed from analysis (1). We identified three contiguous slices that exhibited articular cartilage contact within the medial and lateral compartments. On these selected slices, we computed the average T2 relaxation time by marking the identical point of interest across all three aligned slices and then calculating the mean T2 relaxation time within a 3-pixel or 0.75 mm radius circle.

Results: The effect of task on the individual and mean T2 relaxation time in the medial compartment is shown in **Fig 1B**. A Kruskal-Wallis test detected a significant effect of task ($p = 0.042$). A post-hoc analysis was conducted using Dunnett's test and revealed a significant difference between walking and baseline ($p = 0.039$). T2 relaxation times after both standing tasks (49.0 ms and 50.3 ms) were similar to baseline (51.2 ms), while lying down for 50 min increased the T2 relaxation time (57.0 ms, $p = 0.089$).

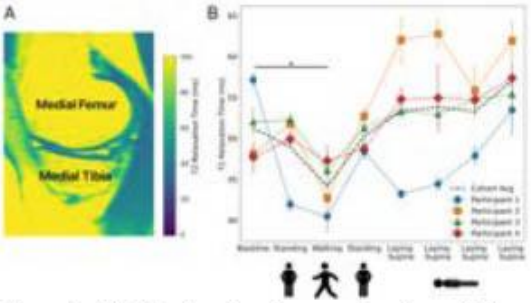

Figure 1. (A) T2 relaxation time map for the medial compartment, and (B) the effect of task on T2 relaxation time. Asterisk (*) indicates a significant difference with respect to baseline, $p < 0.05$.

Conclusions: While task has a significant effect on T2 relaxation time, only walking was statistically significant difference from baseline. This result is interesting as it is counter to our hypothesis. We expected walking to cause a recovery in T2 relaxation time, instead it appears to cause a reduction in T2 relaxation time. In addition, we hypothesized that standing, and activity that induces cartilage deformation, would reduce T2 relaxation time. Instead, we found very similar T2 relaxation times between baseline and both standing periods. There are two notable limitations to our study. First, this was a small sample size using only 4 participants. Given this it is surprising we still detected a significant effect of task. Second, the T2 scan takes 6:04 min to acquire, and it occurs after a 3:43 min proton-density turbo spin echo scan. This delay in scanning potentially allows for significant recovery of the articular cartilage during the scan sequence, which may diminish the detectable changes in T2 relaxation time. In future work we will analyze the lateral compartment of our current study cohort as well as expand the participant population and eventually include participants suffering from osteoarthritis.

References:

1. Gatti AA. J. Biomech. 2017;53:171-177.

DEI:

Diversifying and expanding our current participant population offers a significant opportunity to enhance the generalizability of our findings, thereby amplifying the impact of this work.

STEVENS
INSTITUTE OF TECHNOLOGY

Data Driven Prediction of Vertical Ground Reaction Forces in Stance Motions using a Custom Pressure Insole

Mariya Tohfafarosh, Neethan Ratnakumar, Rachel Jones, Zihang You, Xianlian Zhou.
New Jersey Institute of Technology.

Introduction: Measuring vertical ground reaction forces (vGRF) is vital in biomechanics for analyzing and understanding human movements, and in rehabilitation or training with real-time feedback. However, traditional GRF measurement devices such as force plates are expensive, immobile, and often limited to indoor lab settings. Pressure insoles, on the other hand, are lightweight, wearable, and can be used at home or outdoor settings. In recent years, several commercial pressure insoles have been introduced to analyze or monitor plantar pressure distribution during activities [1]. However, the inability to directly access data from proprietary products or the need for extra hardware/software that further delays data transmission limits their possible integration into assistive devices such as prostheses or exoskeletons for enhanced control. In this study we present a portable, wireless, and affordable insole system and provide preliminary evidence for the ability of our custom-made insoles to accurately predict vGRF during stance motions (motions during which the feet continuously remain on the ground) which have significance in balance quantification and rehabilitation training [2].

Methods: A pair of custom pressure insoles (Fig. 1A) was built using a flexible 8-FSR pressure mat (ZNX-01, Leanstar Electronic Technology Co., ltd, China.) as the base. Each FSR has an effective diameter of 20 mm. The voltage changes across each FSR were recorded using an Arduino Nano and transmitted with transceiver module (nRF24L01). One subject (M, 32 yrs. and 92 kg) was asked to perform a set of static stance activities (standing, standing on the right leg (Stand_R), swaying anteroposterioraly (Sway_AP), swaying mediolaterally (Sway_ML), and squatting) in three different sessions while wearing the insoles (see Fig. 1B) and standing on force plates (AMTI, MA, USA). The force plate and right insole individual sensor readings were synchronized, recorded and postprocessed. A range of different regression models (Linear regression (LR), K-nearest-neighbor (KNN) (n=5) and Random Forest (RF) (estimators=100)) were fit for each different activity and the performance of the models was compared by calculating the root mean squared error (RMSE) and coefficient of determination (R^2). This was performed by training models on data from two out of the three trials while keeping the third one entirely for testing. Lastly, generic models were also fitted with data from all activities across two trials and the same three methods and then tested on the third in a similar manner.

Results: Fig. 1C shows the mean RMSE values for the activity specific models obtained through leave-one-out cross validation. The LR model exhibited the lowest error, except for the case of standing. The largest errors were observed for the squatting and Sway_ML activities with errors ranging up to a maximum of 75 N. In Fig. 1D, the best performing model (RF) was employed to predict the time history of vGRF for the squat activity, yielding a R^2 = 0.2(±0.39) and RMSE = 63.75(±22.6) N. For testing involving generic models, the KNN model performed the best with an R^2 of 0.95(±0.004) and RMSE of 51.81(±2.60) N, whereas the LR showed the least accuracy, with an R^2 of 0.90(±0.0007) and RMSE of 77.51(±5.32) N.

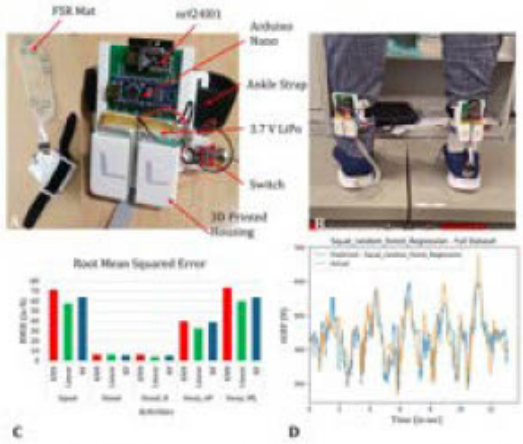

Figure 1. (A) Components of the pressure insole system. (B) A subject standing on the force plates while wearing the pressure insoles (C) The RMSE (in Newtons) for different activities over different trials. (D) Squat activity specific RF regression performance on second trial.

Conclusions: We demonstrated preliminary evidence for the feasibility of using our custom-made pressure insoles to estimate vGRF for stance motions. For the activity specific evaluations LR gave the best results, whereas in the generic model trial KNN and RF regression showed better results. This could be due to LR excelling in simple, activity-specific tasks, while KNN and RF excel in complex, generic models for their adaptability and robustness. The results need to be confirmed with a larger number of subjects. Additionally, exploring the potential application of these insoles in dynamic contexts, such as during walking activities, is needed. The developed insole system could be used in real-time feedback, control of assistive devices, or other biomechanical applications after further testing.

References:

1. Renganathan, G. et al. *Ad Pro Desg Hlth*. 2022;115-141.
2. Price, F. T. *Miami University, Master's Thesis*, 2018

DEI: This study contributes to DEI by developing a custom pressure insole intended to enhance accessibility in biomechanical assessments for diverse populations, including those with mobility challenges.

STEVENS
INSTITUTE OF TECHNOLOGY

Investigating Combination Scaffolds of Self-Assembling Peptide Hydrogels for Root Canal Infections

Alexandra Griffith[1], Josuel Morel[1], Joseph Dodd-o[1], Bobak Shadpoor[1], Corey Heffernan[1], Emi Shimizu[2,3], Carla Cugini[2], Vivek Kumar[1,3,4].

[1]Department of Biomedical Engineering, New Jersey Institute of Technology; [2]Department of Oral Biology, Rutgers School of Dental Medicine; [3]Department of Endodontics, Rutgers School of Dental Medicine; [4]Department of Chemical Engineering, New Jersey Institute of Technology.

Introduction: Root canal treatment is necessary when the dental pulp inside the tooth becomes infected. The current standard treatment removes all living tissue inside the tooth and replaces it with an inert thermoplastic, leaving behind a dead tooth prone to reinfection and failure. Alternative filling materials can act as scaffolds for new tissue ingrowth after root canal treatment. Our group has shown successful root canal revascularization with an angiogenic self-assembling peptide hydrogel (SAPH) termed SLan [1]. However, this injectable SAPH does not address infection. Therefore, we propose to create a scaffold for root canal regeneration using a combination two other SAPHs, one with ideal mechanical properties (SAP1) and another with potent antimicrobial properties (AMP6) [2]. Ideal combination scaffolds will retain the thixotropy of SAP1 for injectability and bolus retention as well as antimicrobial efficacy against relevant endodontic pathogens.

Methods: Mechanical characterization of the combination peptide hydrogels will be investigated with atomic force microscopy, rheometry, and circular dichroism. AFM will be used to analyze fiber formation. Rheometric analysis will be used to assess the shear recovery of the combination constructs. Circular dichroism will be used to verify beta sheet formation which is the mode of self-assembly. Additionally, we will evaluate the efficacy of the constructs against the dental pathogen *Streptococcus mutans* as a model organism for its ability to form robust biofilms in vitro and its role in the etiology of root canal infections. Investigations of differences in minimum inhibitory concentrations and minimum bactericidal concentrations of various constructs as well as their ability to destroy preformed biofilms will assist in determining the most efficacious combination and concentration for *in vivo* work.

Results: AFM images seen in Figure 1 have demonstrated that the addition of AMP6 to SAP1 causes attenuation in fiber length and density, with SAP1 alone showing the strongest fiber network. Circular dichroism results indicate beta sheet formation is optimal in SAP1 and lessens when AMP6 is added. Rheometric analysis showed a nonlinear reduction in mechanical stiffness of SAP1:AMP6 constructs as the AMP6 concentration increased which was measured as the storage modulus at <10% amplitude.

Results of antimicrobial efficacy assays of the peptides alone and in combination showed an approximately two-fold decrease in MBC values of AMP6 with the addition of SAP1 in a one-to-one ratio when *Streptococcus mutans* was grown in the presence of the peptide constructs. However, pre-formed biofilms of *S. mutans* that were then exposed to various peptide constructs showed more biofilm biomass destruction when AMP6 was used in combination with SAP1 as seen in Figure 1D.

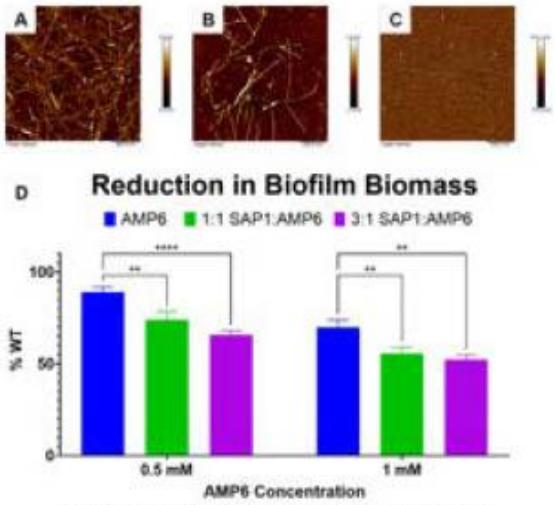

Figure 1. AFM images of (A) SAP1, (B) 1:1 SAP1:AMP6, and (C) AMP6. (D) Destruction of preformed biofilms of *S. mutans* by AMP6 alone as well as 1:1 and 3:1 ratios of SAP1:AMP6 normalized to PBS control (100%WT).

Conclusions: The AFM and CD results together indicate that supramolecular self-assembly of the hydrogel is increased with increasing amounts of SAP1. Overall, combinations of SAP1 and AMP6 create a construct with superior mechanical properties compared to AMP6 alone while also remaining efficacious against the dental pathogen *Streptococcus mutans*, both in preventing growth and in destroying preformed biofilms. Future work will explore the use of these peptide combinations as regenerative scaffolding capable of abrogating endodontic infection.

References:

1. Siddiqui Z. Acta Biomater. 2021; 126:109-118.
2. Sarkar B. et al. ACS Biomater Sci Eng. 2019; 5(9):4657-4670

Acknowledgements: This study was supported by NIH NIDCR R01DE031812

DEI: The development of new technology in biomedical engineering will only be efficacious in improving healthcare outcome disparities if the resulting tissue engineered products are accessible. Acellular materials that do not require special storage or preemptive cell culture before implantation will make new tissue engineered products more accessible in a variety of healthcare settings.

STEVENS
INSTITUTE OF TECHNOLOGY

Sequential Photopatterning of 8-arm PEG-Nor Hydrogels with Monothiolated Peptides.

Arielle Gsell[1,2], Umu S. Jalloh[1], Kirstene A. Gultian[1], James MacAulay[1], Abigail Madden[1], Jillian Smith[1], Luke Siri[1], Sebastián L. Vega[1,3].
[1]Rowan University, Department of Biomedical Engineering, Glassboro, NJ, USA
[2]NIH Undergraduate Research Training Initiative for Student Enhancement Fellowship
[3]Cooper Medical School of Rowan University, Department of Orthopaedic Surgery, Camden, NJ, USA.

Introduction: Despite advancements in chemical and physical stimuli-responsive strategies, many hydrogels formed are monolithic and oversimplify the characteristics of the native extracellular matrix. However, by using light-mediated click chemistry reactions, synthetic hydrogels can be modified by targeting available reactive handles on the macromer after the base hydrogel network is established. Photopatterning base hydrogels with crosslinkers or bioactive molecules provides an in-situ approach to modify the microenvironment with spatiotemporal control. This work examines the formation of 8-arm PEG-Nor macromers and di-thiolated dithiothreitol (DTT) crosslinkers into biocompatible hydrogels amenable to sequential photopatterning with mono-thiolated peptides.

Methods: Hydrogel formation was the result of a thiol-ene click chemistry reaction between 8-arm norbornene-modified PEG (PEG-Nor, JenKem Technology Plano, TX) and di-thiolated crosslinkers (dithiothreitol, DTT) in the presence of a photoinitiator and ultraviolet light. Compression testing was performed one day after gel formation to determine the elastic moduli of hydrogels formed. Secondary reactions were conducted by immersing base hydrogels in solutions containing either DTT (2 mM), mono-thiolated RGD (cRGD, 2 mM), or mono-thiolated 5(6)-carboxyfluorescein (cGFP, 0.10 mM) solutions, followed by UV irradiation. Vertical stripes were patterned onto base PEG-Nor hydrogels by first soaking the base hydrogel in a cRhodamine or cGFP (100 µM) PBS solution containing 0.05 wt% I-2959 for 10 minutes. A striped photomask (100 µm stripe thickness, 100 µm stripe spacing) was then placed atop the soaked hydrogel followed by UV light (5 mW/cm^2, 1 minute). A Nikon A1 confocal microscope was used to acquire representative images.

Results: The elastic moduli of base hydrogels were controlled by varying the concentration of DTT in the hydrogel solution at a constant PEG-Nor weight percent. The elastic modulus increased in a crosslinker concentration-dependent manner to obtain the range of 3.32 kPa to 29.66 kPa observed across the formed hydrogel compositions (Figure 1A). Following PEG-Nor hydrogel formation, a secondary photopolymerization reaction was performed to either increase hydrogel stiffness or to incorporate thiolated peptides in situ. Secondary hydrogel modifications were evaluated on initial gel compositions of 5 wt% PEG-Nor with DTT concentrations of 5 and 7 mM. Hydrogels functionalized with cRGD and cGFP resulted in non-significant changes in elastic modulus compared to base hydrogels. In contrast, using DTT as a secondary reaction molecule resulted in a significant increase in elastic modulus for 5 mM ($p = 0.0001$) and 7 mM ($p = 0.0263$) PEG-Nor hydrogels (Figure 1B). Representative confocal images of PEG-Nor hydrogel photopatterning demonstrate secondary thiol-norbornene reactions using either cRhodamine or cGFP (Figure 1C). Additionally, the sequential photopatterning of cRhodamine and cGFP resulted in multiple peptides being covalently bound in distinct patterns (Figure 1D).

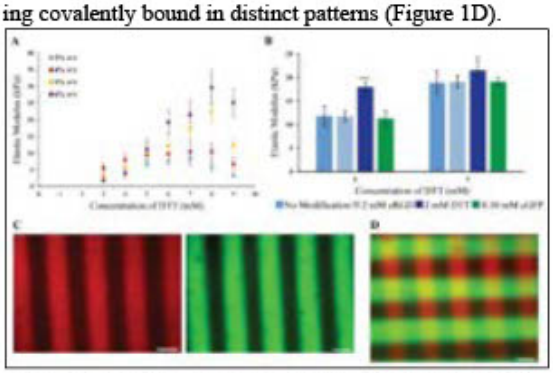

Figure 1. PEG-Nor Hydrogel Mechanical Characterization and Photopatterning. Bar graphs represent the mean and error bars represent standard deviation, * $p < 0.05$, *** $p < 0.001$. Scale bars: = 100 µm.

Conclusions: This study leverages thiol-norbornene click chemistry to form synthetic 8-arm PEG-Nor hydrogels and modify them using photopatterning. By varying PEG-Nor macromer and DTT crosslinker concentration, base hydrogels with a wide range of elastic moduli values can be synthesized. The pendant norbornenes on these hydrogels can then be used to spatially tether mono-thiolated peptides via subsequent light-mediated thiol-norbornene reactions using photomasks. This study demonstrated that thiolated fluorescent peptides and thiolated RGD can be covalently bound to PEG-Nor hydrogels, and the same scheme can also be applied to other peptides. Thus, the presented method of sequential photopatterning presented allows for the modification of synthetic hydrogels to closer mimic tissue ECM.

Acknowledgements: Research reported in this publication was supported by the National Institute Of General Medical Sciences of the National Institutes of Health (NIH) under Award Number T34GM136492. The content is solely the responsibility of the authors and does not necessarily represent the official views of the NIH.

DEI: This study reports a simple technique to create fully synthetic hydrogels with tunable mechanical and biochemical properties. All of the materials used are commercially available and thus scientists with limited resources from diverse backgrounds can create PEG-Nor hydrogels and use this platform for a range of biomedical applications.

STEVENS
INSTITUTE OF TECHNOLOGY

Synthetically derived antimicrobial peptides act as supportive agents for the regeneration of tissues in periodontitis dental wound healing

Marleen Hanna[2], Abhishek Roy[1], Laura L. Osorno[1], Alexandra Griffith[1], Corey Heffernan[1], Emi Shimizu[2], Carla Cugini[2], George Kotsakis[2] Vivek Kumar[1].
[1]Biomedical Engineering Department, New Jersey Institute of Technology, Newark, NJ; [2]Rutgers School of Dental Medicine, Newark, NJ.

Introduction: The diverse structural adaptations in self-assembling peptides present numerous functional opportunities as the field of dentistry progresses with technological and bioengineering advancements. Administered as an efficient antimicrobial injectable hydrogel, these peptides hold the potential to treat gum disease. Periodontitis, a condition that significantly harms the gums, leads to the destruction of soft and hard tissue around the teeth. Antimicrobial peptides play a crucial role in defending against invasive pathogens by regulating the innate immune response within host cells. With the use of advanced technology, specifically CT imaging, and analysis, one can detect the prominence of the induced infection before and after the treatment with the self-assembling peptides. Narrowing down the length, width, and other parameters of the infected gum, through analysis of live scans, will quantify the accuracy of the self-assembling peptides as a treatment for periodontal disease. Exploring periodontitis through the effects of synthesized self-assembling peptides revealed through CT imaging will benefit the future of the transformative dental field by engineering an antimicrobial injectable hydrogel.

Methods: This *in vivo* study, approved by the Rutgers-NJIT IACUC committee, specifically targets two Female Wistar rats (200-233 g) that were used due to their analogous molar anatomy compared to that of a human molar. In the study, the peptides were examined through the conditions of induced periodontal infection and plaque. The animals underwent surgery to induce infectious microbes causing periodontal inflammation around the tooth structure around the first molar of the left maxilla. The left side molars of the mandible were used as controls (intact teeth). The periodontitis models underwent a ligature periodontitis surgery as a small suture, was securely wrapped around the tooth as its method of plaque induction. The animal's living conditions consisted of food consumption and saliva production causing the surrounding area of the tooth to accumulate plaque and infection surrounding the gums, underneath the gums, and the outer tooth structure as a whole. The second set of surgery, the treatment with peptides, was completed after confirmation of periodontitis (28 days after induced infection). The periodontal pocket was filled with 2 µL of the self-assembling peptides. VivoQuant was utilized to measure the infected distance (between the base of the crown and the alveolar bone. Fig 1). Data was normalized to the infection distance at 28 days (peak of infection).

Results: Figure 1A illustrates the CT scan used for analysis of infection distance of the first molar post-initial infection. Figure 1B shows a reduction in values when comparing this data to measurements taken from the scan 26 and 39 days after treatment with the peptides (orange bars). Specifically, we observed a 17% distance reduction from day 28 after infection to day 36 post-treatment. This decrease in values indicates closer proximity between the upper and lower bone structures compared to the infectious period, indicating the peptides' efficacy in promoting bone growth while reducing infection sites near the apical canals.

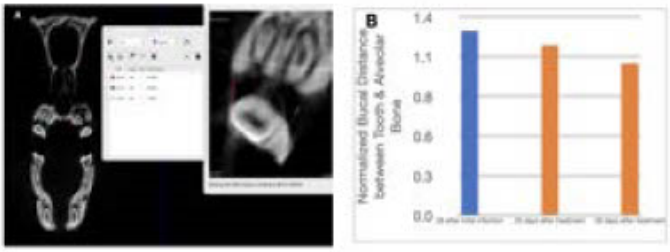

Figure 1. (A) Visual of CT Scan around the first molar, showing infection space as well as distance measurements. (B) Graph showing a decrease in buccal distance between the tooth and the alveolar bone, indicating healing.

Conclusions: The cationic antimicrobial peptide hydrogels are composed of a peptide nanostructure that reduces the bone resorption caused by bacterial infection; it completes a successful performance, through the characteristic temperature and pH-responsive factors. In this prospective study, once the animals underwent treatment, several observations and scans demonstrated that the plaque and infection declined. We focused on the buccal side, as it showed a decrease of the infected distance (between tooth and alveolar bone), a sign of healing.

References:

1. Tang G. et al. Front Bioeng Biotechnol. 2020 Sep 17; 8:587658.
2. Lee S. et al. Int J Mol Sci. 2019 Nov 21; 20(23):5850

DEI: These peptides represent a significant advancement in gum disease treatment, complementing established methods and contributing to the overall enhancement of dental care. Bioengineering underscores the diverse applications available to individuals from underrepresented backgrounds in STEM disciplines, enriching the field with varied academic expertise.

STEVENS
INSTITUTE OF TECHNOLOGY

Identifying Optimal Scaffold Geometry for Enhanced Mechanical Strength and Porosity

Zoe Hindman*, Maria Cipriano, Ella Santoro, Helen Lee, Rana Ibrahim
Stevens Institute of Technology

Introduction: Scaffolds are essential in tissue engineering where they repair damaged or lost bone by providing structural support for cellular proliferation. The scaffold geometry is essential to consider in designing the scaffold structure as it impacts cell adhesion, proliferation, and distribution by affecting the access to cell recruitment, vascularization, nutrients, and oxygen [1]. The shapes and dimensions of the scaffold pores contribute to the mechanical strength, which must closely match the properties of bone to be viable in the human body. Triangular pores have high mechanical properties and can equally distribute forces while hexagonal cells have the largest area where the outer periphery lengths of these cells are equal allowing the highest tissue amplification on channel faces [2]. This study determines if a 5-layer bone scaffold with an outer region of triangular pores and an inner region of hexagonal pores would provide porous conditions for cellular proliferation and the proper mechanical properties to be placed in the femur.

Methods: First, prepared cortical and trabecular bone was mechanically tested and analyzed using Excel to obtain the mechanical properties of each, necessary in the design of the scaffold. Several design sketches were made and a final scaffold design measuring 24 mm in diameter by 10 mm in height, per design specifications, was constructed in Solidworks. Theoretical load forces experienced by the femur were calculated and an FEA analysis was done to test the mechanical load the scaffold could withstand. Design modifications were made based on the FEA results and a final scaffold was printed in PLA using the MakerBot Replicator. The parameters of the MakerBot Replicator were set to a travel speed of 115 mm/s, an extrusion speed of 30 mm/s, an extrusion temperature of 215 °C, and an infill of 20% was chosen. Printed scaffold dimensions were recorded, and the scaffold was mechanically tested using the Instron 5965. Instron 5965 data was obtained, and the mechanical properties of the scaffold were calculated.

Results: The scaffold consisted of 5 layers; each 2 mm thick. An outer region, 2.5 mm in diameter, was made to mimic cortical bone and contained 24 triangular pores, 1.5 mm in height, spaced 0.5 mm apart. An inner region, simulating trabecular bone, contained 5 rings of hexagonal pores ranging from 0.55 mm to 0.70 mm in size. The printed scaffold dimensions were confirmed by a calibration measuring tool and read 23.45 mm in diameter and 10.11 mm in height. The scaffold was observed under a microscope and the Sartorius TE64 Weighing Scale measured the mass of the scaffold at 3.37 g. The percent porosity was calculated to be 38.25%. The scaffold reached the Instron 5965 stop parameter of 3 kN without displacing more than 5 mm. No visible cracks or structural changes were observed under the microscope after testing was performed. The modulus of the scaffold was calculated to be 241.92 MPa and the compressive strength was 6.942 MPa. While the modulus of the scaffold is far less than the modulus of cortical bone, 2363 MPa, had the Instron 5965 continued applying a force past 3 kN, the modulus of the scaffold would likely be a more accurate representation of what forces the scaffold could endure. Based on the free body diagram analysis conducted before mechanically testing the scaffold, for an average person weighing 200 lbs. the femur would experience 2.5 times this weight, which is close to 2.3 kN, far below the force the scaffold was mechanically tested at.

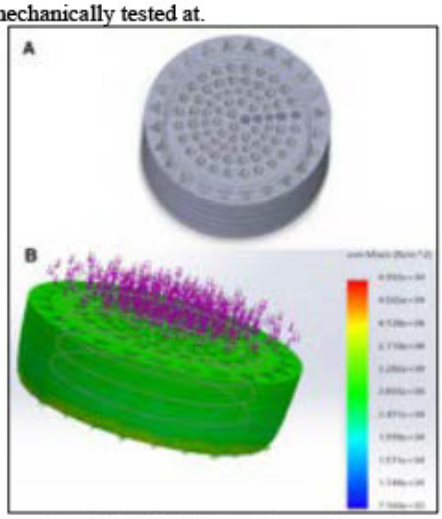

Figure 1. A) Full SolidWorks Assembly of Scaffold
B) Stress Analysis of full SolidWorks Assembly

Conclusions: Based on the scaffold design and geometry, its high mechanical strength would allow it to withstand the forces typically experienced by the femur. Further testing would need to be conducted to determine if the scaffold could endure fast, high impact forces, such as those experienced by an athlete. With an advanced printer able to produce intricate designs more accurately than the MakerBot Replicator, the scaffold design could be made more complex to improve the percent porosity. Biocompatibility testing would need to be conducted to determine the scaffold efficiency and cellular proliferation capabilities. An alternate material such as polyurethane can be used to improve the mechanical strength, fatigue resistance, and increase biocompatibility. Overall, the geometric design of the scaffold proved to be mechanically compatible with the femur bone, however alterations to scaffold material and the manufacturing process could lead to improved biocompatibility and scaffold porosity.

References:

1. T. Wu *Materials* 2017, 10, 1187.
2. K. Hayashi *ACS Nano* 2022, 16 (8), 11755–11768.

DEI: Bioengineering can improve disparities and broaden participation in STEM through educational programs across all grades starting in primary school. Funding STEM programs in diverse, underrepresented areas exposes students to a variety of careers in the STEM field and provides them opprotinuties for further career development.

STEVENS
INSTITUTE OF TECHNOLOGY

Universal Microfluidic Magnetic Connectors

Amir Salimov, Maria Alvarez-Amador, Eric Brouzes
Stony Brook University

Introduction: Polydimethylsiloxane (PDMS) is the material of choice for rapid prototyping in laboratories because it's simple to use and doesn't require large investments. PDMS elasticity also provides a simple sealing solution with injection tubing. However, PDMS manufacturing at high volume is prohibitive. Thermoplastics, the industry standard for microfluidics, has recently ventured into rapid prototyping[1]. Nevertheless, there is no simple solution to connect injection tubing to thermoplastic devices[2]. Current solutions are costly and mostly single use. We've combined PDMS sealing with magnetic clamping to create versatile, reusable connectors for high injection pressures across various solid materials. We simply pour PDMS in magnetic ring, the overflow ensures the sealing between the connector and the device (**Figure 1A**). Our testing assessed the connectors' capacity to withstand injection pressures and examined the correlation between sealing pressure and magnetic clamping pressure. These easy-to-manufacture, cost-effective, and reusable connectors effectively bridge a critical gap in the current toolkit for thermoplastic rapid prototyping.

Methods:

Magnetic Connectors- R636(1/2" OD x 1/8" ID x 1/8" thick) and R844-N52(3/8" OD x 3/16" ID x 3/8" thick) magnetic rings were purchased from K&J Magnetics. PDMS (Sylgard 184 Silicone Elastomer Kit) was mixed at a 10:1 (polymer:crosslinker) weight ratio and poured into the rings[3]. The assembly was cured at 65°C in an oven for 2 hours. The PDMS insert was punched with a biopsy tool. PEEK tubing (0.254 mm ID, 0.787 mm OD, Zeus) was inserted through the hole, and its extremity was cut clean but not flush to allow easy alignment with the port.

Devices- 1mm-thick flat pieces of the chosen material were drilled to create a series of 1mm ports. One side of the ports was plugged with pressure-sensitive adhesive (PSA) tape. The materials used included cyclic olefin copolymer (COC), polycarbonate(PC), PSA tape, and polymethyl methacrylate (PMMA). Glass was tested without injection ports.

Results: To determine the sealing pressure, we increased the injection pressure was increased until leakage. We observed the port for leakage using an inverted microscope equipped with a 10X objective and CCD camera. Fifteen trials were performed per thermoplastic material using the 1/2" OD ring, with all materials consistently showing sealing pressure ranges of 35-46 psi. Attention was directed towards the 3/8" ring due to its ease of manipulation during tests. For the 3/8" OD ring, five magnetic connectors were tested. All the materials exhibited resilience to high pressures, ranging from 46-60 psi (**Figure 1B**). Our setup allowed for a maximum measurement of 60 psi, but it's probable that the actual ranges exceeded this limit.

The 3/8" provides a higher sealing pressure despite having a lower magnetic force than the 1/2" OD magnetic connectors. To explain this result, we hypothesized that the sealing pressure relates to the magnetic clamping pressure, which is the pullup force divided by the area of the magnet.

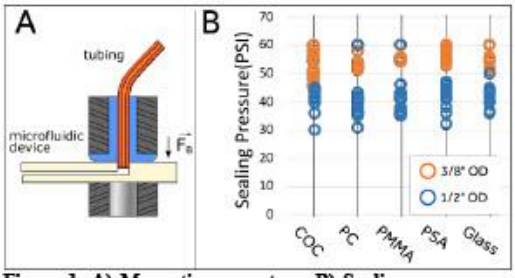

Figure 1. A) Magnetic connectors, B) Sealing pressure vs diverse materials for the 3/8" and ½" OD magnetic connectors.

Using five 3/8" magnetic pairs and a COC injection device, the pullup force was modulated by inserting COC shims to vary the inter-magnet distance. The pullup force values were tabulated from the K&J Magnetics website. **Figure 2** shows a linear correlation between the clamping and sealing pressures. We showed the same behavior for the ½" magnetic connectors (not shown).

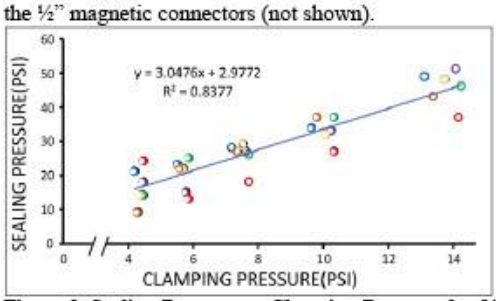

Figure 2. Sealing Pressure vs Clamping Pressure for 3/8" OD magnetic connectors with COC.

Conclusions: We've developed reusable magnetic connectors and demonstrated their effectiveness with various materials under high injection pressures. The 3/8" OD magnetic connectors have proven to be the optimal choice, withstanding high pressures and being easy to manipulate. Across COC, glass, polycarbonate, PMMA, and PSA, the 3/8"OD connectors consistently maintain sealing pressure over 46 psi. Additionally, we establish a linear correlation between clamping and sealing pressures. These magnetic connectors efficiently accommodate both hydrophobic and hydrophilic materials, addressing a gap in the rapid prototyping of microfluidic devices.

References:

1. A. Shakeri et al. Materials(Basel). 2022;15(18):6478
2. J. Atencia et al. Lab on a Chip. 2010;10(2):246-249
3. P.L. Quan et al. Analyst. 2024;149(1):100-107

DEI: Our magnetic connector facilitates the development of affordable educational tools for introducing microfluidics in underserved communities, supporting workshops, internships, and programs in regions with limited resources.

STEVENS
INSTITUTE OF TECHNOLOGY

Fluid Dynamics of the Three-Way Stopcock: Simulation and Experimental Validation

Christopher J. Shin[1], Tobias Meng-Saccoccio[1], Evrim E. Ozcan[1], Venkatsai Bellala[1], Albert Q. Wu[1], Paul Ogan[1], Patrick Lee, PharmD[2], Sakina Sojar, MD[2]
[1]School of Engineering, Brown University, Providence, RI, [2]Department of Emergency Medicine, Warren Alpert Medical School of Brown University, Providence, RI

Introduction: Supraventricular tachycardia (SVT) is an irregularly fast heart rhythm that accounts for approximately 150,000 emergency department visits annually, with over $3 billion spent on its management [1]. Adenosine is the first-line drug used in acute cases of SVT and is administered intravenously via a three-way stopcock followed by a saline flush.

The three-way stopcock presents difficulties in usage and accuracy. The standard methods of drug administration using the stopcock requires two clinical providers to either simultaneously push both syringes or sequentially push down each syringe while adjusting the channels in between to prevent backflow. The lack of quantitative data in clinical literature comparing efficacy across the two standard delivery methods has contributed to ambiguity in informing standards of care.

We tested the efficacy of both simultaneous and stepwise delivery, examining their respective fluid velocity and drug concentration profiles during a 1 second delivery time using finite element analysis and particle image velocimetry (PIV) scale modeling to evaluate which method is more rapid and delivers more total drug.

Methods: We used the finite element analysis software COMSOL Multiphysics (COMSOL Inc., Stockholm, Sweden) to perform *in silico* simulations. We used a standard kappa-epsilon turbulence model to compute flow patterns within the 3D mesh of the stopcock for both stepwise and simultaneous flush. We assigned each inlet of the stopcock a normal velocity function of $v = 0.164sin(\pi t)$ m/s to model a sinusoidal function that attains a velocity of 0.164 m/s, corresponding to the velocity observed in a standard syringe during a 1-second delivery time, which aligns with the duration of adenosine administration via intravenous fast push [2]. Adenosine delivery was modeled using the dilute chemical species transport equation with diffusion coefficient $D_{AB} = 10^{-9}$ m^2/s, the standard diffusive value for small molecules [3]. To evaluate mass of adenosine delivered through the outlet, the surface integral of adenosine concentration was computed every 0.1 seconds. Cumulative dosing over time was calculated by the area under the curve.

For the simultaneous flush simulation, both adenosine and saline were administered for the full 1 second. For stepwise flush simulation, adenosine was administered for the first 0.5 seconds and saline for the next 0.5 seconds. A no-backflow condition was implemented in both to prevent saline from entering the adenosine channel.

For PIV experiments in progress, we printed the standard stopcock model at four times its original size using transparent resin. By adjusting the water to glycerin ratio and the inflow pumps' rotational frequencies, we set the Reynolds number of the system identical to the COMSOL model. We used a lab grade laser with a high-frame rate camera to visualize fluid flow.

Results: Distribution of residual drug loss at the final timestep $t = 1.0$ seconds indicates that adenosine is sequestered in the channel leading to the stopcock for both administration methods (Figure 1). Additionally, the simultaneous flush loses a noticeable amount of adenosine along the upper length of the stopcock outlet due to the shear flow of saline, while the stepwise flow avoids this fate (Figure 1). Cumulative adenosine delivery data supports that stepwise delivery is more effective at administering adenosine quicker and with less loss; however, neither method achieves more than 65% efficacy (Figure 2).

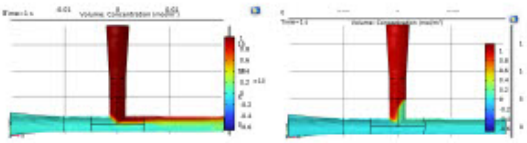

Figure 1. Distribution of residual adenosine at time 1.0 seconds for simultaneous (left) and stepwise (right) administration.

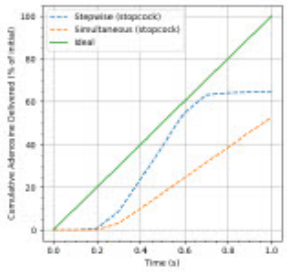

Figure 2. Cumulative adenosine delivery over time.

Conclusions: Simulation data supports that the stepwise method of adenosine delivery is more efficient than simultaneous administration. Evidence also suggests that further design innovation is needed to reduce residual drug loss in the upper channel of the three-way stopcock.

References: [1] Milestone Pharmaceuticals (2022), US SEC Form 10-K. 2. [2] Faulds D et al.. *Drugs*. 1991;41:596-624. [3] Truskey GA et al. *Transport Phenomena in Biological Systems* (2004).

Acknowledgements: This study was funded by the Rothberg Catalyzer Fund and Hazeltine Grant, Brown University. The authors would like to thank Professors Anubhav Tripathi, Lindsay Schneider, Marissa Gray, Theresa Raimondo, Daniel Harris, Roberto Zenit, and Zachary Saleeba for their support.

DEI: In the emergency department, racial and ethnic minorities experience disparities in wait time and clinical outcomes. We strongly encourage the representation of STEM-underrepresented persons in emergency medicine and engineering through educational programs and broader community outreach.

STEVENS
INSTITUTE OF TECHNOLOGY

Testing the Sterilization Efficacy of 3D Printed Plastics Using *E. Coli*

Helena Slupianek, Joseph P. Licata, Jonathan A. Gerstenhaber, Yah-el Har-el, and Peter I. Lelkes
Temple University, Department of Bioengineering

Introduction: Additive manufacturing (3D printing) continues to play a central role in medical technology and research worlds and has emerged as an increasingly efficient method for designing and prototyping devices[1]. There are several types of printers and materials available, with key characteristics including physiologically relevant mechanical properties and surface porosity[2]. The printed object must be able to undergo sterilization to reduce the risk of contamination.

As 3D printed objects are progressively more common for *in-vitro* use, there is an unmet need for establishing biocompatibility of these objects. The materials should be cytocompatible, and the objects must not be altered in shape during traditional sterilization methods, which should penetrate the material surface successfully. The goal of this study was to determine if 3D printed materials can successfully undergo traditional sterilization techniques so that all bacteria on and within the object area are destroyed.

Methods: The materials used throughout this study include polylactic acid (PLA) and Nylon-12 (N12), E. coli bacteria, LB powder, and DMEM. To conduct the experiment, a 5 mL vial of E. coli bacteria was obtained and 20 20mm x 20mm x 8mm squares with a "shelf-like" construction through the middle were 3D printed; 10 were printed in PLA, 10 in Nylon-12. These materials were chosen due to their ability to withstand structural change under the conditions needed for typical sterilization methods.

For 18 total trials, 50 mL conical tubes were used to contain the 3D printed object (besides the "no plastic" control), 250uL of E. coli solution, and 20mL of sterilized liquid LB solution, respectively. The tubes were left in a 37˚C incubator for 3 hours to allow for bacteria to grow/proliferate. Thereafter, seven rounds of testing for the respective 3D printed materials were conducted to determine the most effective method of sterilization. Three sets were conducted in duplicate, the first run having the object in a "dry" pipette box with no other material, while the second had the objects placed in salt for structural support. Two controls were also included, one with "no sterilization" method applied, and one with only the LB solution and "no plastic". At the end of the tests, the objects were removed, placed into new 50 mL conical tubes, and submerged in 20 mL of DMEM overnight to allow for the appearance of any remaining bacteria to occur.

Thereafter, 1 mL of each trial DMEM solution was collected and placed onto a petri dish. The dishes were observed under a microscope, with images being taken to determine the yes/no presence of E. coli bacteria.

Results: Both the 'no sterilization' and 'no plastic' controls demonstrated the presence of bacteria, while all seven tested trials did not. Combined with previous data confirming the structural stability of PLA and Nylon-12 upon sterilization, and lack of cytotoxicity, both materials are effective for medical study.

Figure 1. Phase contrast microscope analysis; L-to-R: "No plastic" Control; PLA: Salt, Autoclave; "No sterilization" Control N12

CONDITIONS	PLA	NYLON-12
Autoclave (121•C, 15 Mins)	N	N
Autoclave (121•C, 15 Mins), Salt	N	N
Dry Oven (75•C), 30 Mins	N	N
Dry Oven (75•C), Salt, 30 Mins	N	N
Dry Oven (75•C), 60 Mins	N	N
Dry Oven (75•C), Salt, 60 Mins	N	N
Ethanol Soak (24 Hrs)	N	N
No Sterilization	Y	Y
No Plastic	Y	Y

Table 1: Bacteria presence per trial (Y/N)

Conclusions: The 3D printed materials tested here (PLA, Nylon 12) can be sterilized using traditional sterilization methods. There was no difference between the various trials or the types of material. In combination with cytotoxicity testing and structural analysis, we conclude that PLA and Nylon-12 can be used for 3D printing of objects with increasingly complex geometries. Future studies include testing of multiple strains of bacteria, and of the viability of cells seeded onto the sterilized 3D printed materials for diverse biomedical applications (e.g. bioreactors).

References:

1. Told, R., Ujfalusi, Z., Pentek, A., Kerenyi, M., Banfai, K., Vizi, A., ... & Maroti, P. (2022). A state-of-the-art guide to the sterilization of thermoplastic polymers and resin materials used in the additive manufacturing of medical devices. Materials & Design, 223, 111119.Wanti A. et al. Science. 2018;6(26):972-1018.
2. Jackson, R. J., Patrick, P. S., Page, K., Powell, M. J., Lythgoe, M. F., Miodownik, M. A., ... & Bear, J. C. (2018). Chemically treated 3D printed polymer scaffolds for biomineral formation. ACS omega, 3(4), 4342-4351.

Acknowledgements: Thank you to Temple University and the members of the i-CTERM Lab for their support.

DEI: Through expanding the use of 3D printed materials in medical and research applications, there will be increased access to this technology. The process of 3D printing is easily manageable, with most material including PLA and Nylon-12 being relatively inexpensive. Additive manufacturing also allows for more customization and personal design, producing less waste material.

An Automated Quality Estimation and Error Correction Tool for Fluorescence Images

Muhammad Nabeel Tahir, Muhammad Ahsan Sami, and Umer Hassan.
Rutgers the State University of New Jersey.

Introduction: Fluorescence microscopy has become a crucial component of bioscience including cell biology, life science, and pathology. From investigating the cellular processes to highlighting and imaging the complex cellular or protein structures fluorescence microscopy provides a wide set of tools. In a typical fluorescence microscopy setup, a bioparticle is tagged with a fluorophore at one end, and an antigen at the other end. The tagged bioparticles bind the target molecules or cells and help in the detection, quantification, and analysis of the target species. Although the process is very sophisticated it still introduces process and instrument noise into the image making interpretation difficult. Moreover, manual processing is required to analyze the fluorescence microscopic images either obtained from a benchtop microscope or smartphone-based fluorescent microscope (SFM) poses a significant challenge. In this study, we present an automated tool for the estimation and analysis of the quality of fluorescence images through the application of classical image processing techniques.

Methods: The images of fluorescent particles of sizes (8.3, 2, 1, and 0.8 µm) and Human Leukocytes tagged with nuclear stain were collected using a custom-designed SFM developed by our team in previous studies [1]. Three independent parameters (Bioparticle intensity, vicinity noise, and background noise) were estimated using ImageJ an open-source software These values were used to calculate the signal difference to noise ratio SDNR as (intensity- vicinity noise)/(background noise) and contrast to noise ratio CNR as (intensity- vicinity noise)/(background noise* vicinity noise). The tool has been divided into two sub-processes. In the first process, initially, the features associated with each particle were detected using the fast feature detection algorithm. The resultant features were passed through a pipeline of feature selection, association, particle intensity, vicinity intensity, background noise estimation, and finally the particle selection. The estimates of particle intensity, vicinity intensity, and background noise were employed to calculate and report the SDNR and CNR values for a particular image [1]. In the second stage classical image processing techniques were employed to reduce the background and vicinity noise segments. More specifically, Average and Gaussian filters with varying kernel sizes and hyperparameters were applied and results were studied. A final algorithm with a kernel size of 21x21 was generated to effectively estimate the quality and reduce the error in the fluorescent image [2]. Figure 1 shows the image data collection, feature detection, and algorithm flow chart.

Results: The SDNR and CNR values along with the particle intensity, vicinity intensity, and background noise values obtained from the ImageJ and developed tool with and without error correction were used to generate the correlation curves for fluorescent particles and human leukocyte images. It was observed that the developed tool generated a correlation coefficient of R^2>0.96 on all the datasets compared to the ImageJ results. With the application of error correction filters a 10-25% increase in SDNR and a 30-50% increase in CNR values was observed as it reduces the background and vicinity noise.

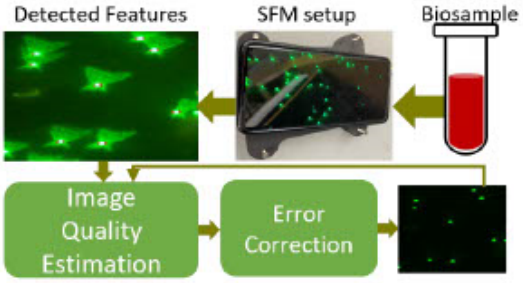

Figure 1. The flow chart shows the data collection, feature detection, image quality estimation, error correction, resultant filtered image, and final estimate loop.

Conclusions: The study presents an algorithm that automates the quality estimation in fluorescence images and implements error correction techniques to further improve the quality of the image as reported by the selected parameters. The quality estimation step not only reduces manual labor but improves the estimate of parameters SDNR and CNR. The error correction step further enhances the quality of the image by reducing the background noise improving the overall estimate of the parameters. Combining the two sub-processes results in a sophisticated algorithm that at the same time estimates and improves the quality of fluorescence images thus providing a suitable alternative to the existing state-of-the-art software. In the future, we aim to enhance the capabilities of the algorithm by introducing complex image enhancement techniques and particle detection algorithms.

References:

1. M. A. Sami, et.al, "AQAFI: a bioanalytical method for automated KPIs quantification of fluorescent images of human leukocytes and micro–nano particles," The Analyst, p. 10.1039.D3AN01166F, 2023, doi: 10.1039/D3AN01166F.
2. M. A. Sami, et.al, "Enhancing Biomarker Detection and Imaging Performance of Smartphone Fluorescence Microscopy by Integrating Computational Processing Techniques,"(Submitted).

Acknowledgments: The authors would like to acknowledge the support from NSF (Award # 2002511 and 2315376). The authors also acknowledged the funding support from Rutgers University under the Exploratory Research Seed Grant.

STEVENS
INSTITUTE OF TECHNOLOGY

Imaging Tissue-Level Composition of Bone Biopsies with Submicron Resolution

Sofia Mehmood[1], Yana Bronfman[2], Edward DiCarlo[2], Nancy Pleshko[1], and William Querido[1*]
1. Department of Bioengineering, College of Engineering, Temple University, Philadelphia PA. *william.querido@temple.edu
2. Department of Pathology and Laboratory Medicine, Hospital for Special Surgery, New York NY

Introduction: Osteoporosis is a degenerative bone disease that affects millions of people worldwide [1]. Conventional analysis of bone biopsies to improve the diagnosis of osteoporosis and subsequent fracture risk assessment does not take into account properties of bone mineral and collagen at the submicron scale—the building blocks of bone structural integrity [2]. This represents a critical gap in understanding how tissue-level compositional properties of bone underly the poor bone quality associated with osteoporosis, which may be instrumental in informing the development of better therapies and treatment plans. Here, our goal is to establish the application of the recently developed technique optical photothermal infrared (O-PTIR) spectroscopy to assess the submicron-scale composition of human bone biopsies from subjects with osteoporosis, aiming to establish a new approach to gain insights into disease development and progression in clinical samples.

Methods: Human iliac crest biopsies embedded in standard blocks of polymethyl methacrylate (PMMA) were acquired from the Hospital for Special Surgery (New York, NY). Each block was ~22 mm thick and had an exposed bone surface in one face. Standard assessment of bone tissue structure was carried out micro computed tomography (microCT), and scanning electron microscopy (SEM). 3D modeling of a sample holder for the O-PTIR microscope was done using SolidWorks. O-PTIR data from cortical and trabecular tissues were collected at 500 nm spatial resolution using the mIRage Sub-Micron IR Spectrometer (Photothermal Spectroscopy Corp), both as point spectra and single-wavenumber images at specific peaks of interest, including the phosphate (mineral), amide I (collagen), and PMMA peaks [3]. The images were analyzed using ratio mapping and RGB overlays using PTIR Studio. Spectra were analyzed using.

Results: MicroCT, and SEM images (Fig 1a-b) of the bone biopsies show a range of tissue structural properties across subjects, with varying bone area and volume, trabecular architecture, and cortical thickness and porosity. For O-PTIR analysis, the first outcome to be achieved was the development of a custom sample holder to fit the thick bone biopsy blocks into the O-PTIR microscope stage, which was carried out by 3D modeling and printing (Fig 1c). Inspection of the bone surface using the visible mode of the microscope allowed clear identification of cortical and trabecular bone to select the regions of interest for O-PTIR spectral data collection. The spectra were typical, comprising bands of mineral (phosphate, carbonate) and collagen (amides, CH), with bands of PMMA (acrylate) seen only on the edges of the tissue and within tissue porosity. O-PTIR imaging of osteons and trabecula at 500 nm spatial resolution (Fig 1d-e) enabled the visualization of bone tissue-level composition in individual lamella and around osteocyte lacunae and Haversian canals. Moreover, thousands of point spectra could be collected at cortical and trabecular bones, with quantitative analysis of peak ratios revealing overall trends in tissue-level compositional properties across subjects, including in mineral content, mineral crystallinity, carbonate content, and collagen integrity.

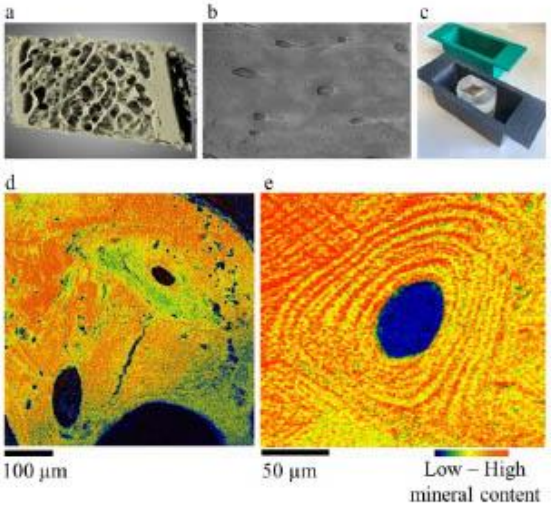

Figure 1. Analysis of bone biopsy. (a) microCT, (b) SEM, (c) 3D printed custom sample holder to fit biopsy block into O-PTIR microscope, (d-e) O-PTIR imaging bone composition at 500 nm spatial resolution

Conclusions: We show that O-PTIR spectroscopy and imaging is an effective method to analyze the submicron tissue composition of human bone biopsies embedded in standard thick PMMA blocks. This approach brings a significant advantage to the field when compared to conventional Fourier transform infrared (FTIR) spectroscopy [3], as it can inform on submicron tissue-level composition without the need for cumbersome thin-sectioning of calcified tissue. Additionally, the method is non-destructive, preserving the clinical samples for further analysis. Future directions will involve implementing a machine learning approach to delve into the relationship between O-PTIR-derived tissue compositional properties and structural properties of bone obtained by microCT and SEM, aiming to provide new insights into compositional factors underlying poor tissue integrity and health.

References: [1] Curtis et al. Bone. 2017. [2] Reznikov et al. Acta Biomaterialia. 2014. [3] Querido et al. Molecules. 2021.

Acknowledgements: NIH/NIAMS R21AR082129.

DEI: We are committed to addressing healthcare disparities by innovating diagnostic strategies for skeletal diseases and fracture risk in a diverse population. We also aim to foster inclusivity by encouraging active participation and contributions from individuals underrepresented in STEM within the fields of bone and spectroscopy research.

STEVENS
INSTITUTE OF TECHNOLOGY

Aptamer-Based Single-Walled Carbon Nanotube Sensors for Optical Detection of Interleukin-6

Amelia Ryan, Ryan Williams
City College of New York

Introduction: The inflammatory cytokine interleukin-6 (IL-6) plays a critical role in the pathogenesis and progression of neurodegenerative diseases, autoimmune diseases, cancer, and other inflammatory conditions. As a known diagnostic biomarker and therapeutic target, efficient and accessible detection of IL-6 is of clinical interest. Single-walled carbon nanotubes (SWCNTs) are versatile NIR fluorescent materials that can be functionalized to detect a variety of targets. In rational nanosensor design, a molecular recognition probe with known affinity for the intended target – such as an antibody or DNA aptamer – is utilized to lend specificity to the sensor. Aptamers may hold advantages over antibodies for sensor applications due to their smaller size, more flexible structures, high stability, easy chemical customization, and low cost. Our objective in this work is to develop an aptamer-based SWCNT sensor to rapidly detect IL-6 with high sensitivity and specificity. The nanosensor should be stable and responsive in a variety of conditions, easy to assemble, and relatively inexpensive.

Methods: DNA sequences tested include: a 31-nt aptamer [1], a 15-nt aptamer [1], $(GT)_{15}$, a 61-nt sequence of $(GT)_{15}$ + 31-nt aptamer, and a cyanine-5 (Cy5) tagged version of the 31-nt aptamer (Integrated DNA Technologies; Coralville, IA). HiPCO-prepared SWCNT (NanoIntegris Technologies; Boisbriand, QC) and DNA were suspended in PBS via sonication. The sonicated suspension was collected and filtered with a 100 kDa Amicon centrifugal filter to remove free DNA. The resulting suspension was characterized with a V-730 UV-visible absorption spectrophotometer (Jasco Inc; Easton, MD). Varying concentrations of IL-6 protein (Invitrogen; Waltham, MA) from 0.1 to 400 nM were added to nanosensors suspended in PBS (with the addition of 10% fetal bovine serum for serum conditions only). Fluorescence spectra were acquired with a MiniTracer spectrophotometer (Applied NanoFluorescence; Houston, TX) every 30 minutes for 3 hours following antigen addition. Continuous fluorescence measurements were performed with a custom NIR probe (Photon etc; Montreal, QC) to evaluate kinetic sensor response. Modulations of fluorescence were analyzed in MATLAB. To test if IL-6 displaces aptamer from the SWCNT surface, SWCNT-Aptamer+Cy5 was incubated overnight with 250 nM IL-6. Samples were filtered to separate displaced DNA from Visible absorbance of the washout was measured with a microplate reader (BioTek; Winooski, VT).

Results: Of the DNA sequences tested, the 31-nt aptamer showed the greatest response to 250 nM IL-6 protein – SWCNT fluorescence quenched to 55% in buffer conditions (Fig. 1) and quenched to 70% in serum conditions. This DNA sequence was therefore chosen as the main candidate for further testing. The resulting nanosensor demonstrated detection of IL-6 at concentrations as low as 10 nM. With increasing concentration of IL-6, SWCNT showed a more dramatic reduction in fluorescence intensity, quenching to 40% response to 400 nM of IL-6. Continuous NIR measurement of SWCNT showed a decrease in fluorescence intensity within seconds of IL-6 addition, indicating a near-immediate nanosensor response. There was no evidence of DNA displacement from SWCNT-Apamter+Cy5 after overnight incubation with 250 nM IL-6.

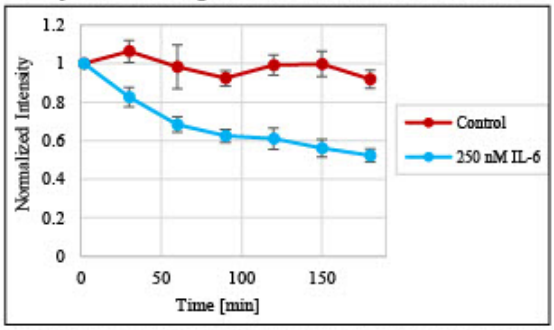

Figure 1: *Fluorescence intensity of SWCNT-Aptamer in response to 250 nM IL-6 protein in PBS over 3 hours*

Conclusions: In this work, we have developed a novel nanosensor for the rapid detection of IL-6 based on SWCNTs and an analyte-specific DNA aptamer. After screening multiple SWCNT-DNA constructs, we identified the DNA sequence that provided the highest sensitivity to IL-6. SWCNTs functionalized with this aptamer showed sensitivity and specificity for IL-6 in both buffer and serum conditions. Fluorescence modulation was dependent on IL-6 concentration, with a limit of detection at 10 nM, demonstrating the sensor's ability to identify and quantify the presence of IL-6 *in vitro*. We investigated the mechanism of the nanosensor and concluded IL-6 does not displace the aptamer from the SWCNT surface, indicating stability of the nanosensor construct. Future work may include sensor-deployment in cell culture models or *in vivo*. Rapid, inexpensive, minimally invasive detection of IL-6 as an inflammatory disease biomarker holds promise for early diagnosis, observation of disease progression, and evaluation of response to therapy.

References: 1. Spiridonova VA. Moscow University Physics Bulletin. 2016; 71:135-138.

Acknowledgements: NIH Graduate Research Training Initiative for Student Enhancement (G-RISE, Grant #T32GM136499) and NIH R35GM148233.

DEI: The field of optical biomedical sensors holds the potential to improve disparities in healthcare outcomes by providing methods of rapid, user-friendly, and inexpensive biomarker detection. Optical nanosensors may therefore increase the accessibility of diagnostic technologies among underserved populations. Participation of underrepresented groups in this field may be improved through conscious hiring practices as well as increased visibility and representation of successful individuals from these groups in publications, scientific meetings, and social media.

STEVENS
INSTITUTE OF TECHNOLOGY

Geometric Validation of Deep Learning Segmentation-Based Numerical Mesh Generation of Aortic Valve from CT Images

Shubh Thaker, Salwa Anam, Brandon Kovarovic, Danny Bluestein
Stony Brook University

Introduction: Deep learning (DL) are increasingly being utilized in cardiac device research, particularly in transcatheter aortic valve replacement (TAVR) development. Required traditional computational models like computational fluid dynamics and finite element analysis are clinically limited due to computational complexity and expertise requirements. One complexity is the generation of accurate numerical meshes necessary for simulations which can take much time to create through the traditional method of manual segmentation [1]. Pak and colleagues developed an automated approach to generate numerical meshes from cardiac CT scans in 0.13 seconds using a deformation-based DL algorithm [2]. The aim of this study is to validate their generations for TAVR-related computational studies through geometric comparisons of DL-based meshes and expertly-created manually generated meshes.

Methods: Patient CT scans of cardiac region were obtained from an ongoing study at Stony Brook University (n = 3). DL-based meshes were generated utilizing DeepCarve, a package based with the deformation-based method integrated within it, on 3D Slicer (Kitware Inc, Clinton Park, NY). Manually generated models served as the ground truth and were created through manual segmentation methods utilizing Simpleware ScanIP (Synopsys, Sunnyvale, CA). Models were standardized but cutting them to the same height, remeshing for standard point density, and were aligned with respect to the sinotubular junctions. 50-point centerlines of both models were extracted and compared by measuring distances between corresponding points and Procrustes analysis, yielding a Procrustes distance (PD). MATLAB (Mathworks, Natick, MA) was used to create slices along the vertical axis of the centerline points to compare areas between model types. The Chamfer (CD) and Hausdorff distances (HD) were also calculated to measure similarity. Principal Component Analysis (PCA) was used to analyze variance of whole point clouds and the annulus point clouds. Statistical analysis was conducted using Z-tests and student's T-test.

Results: There were noticeable geometric differences between both model types in all patients, especially the annulus. For patient 1, a PD of 0.9712 and a significant pairwise distance average of 27.9847 ($p < 0.005$) was measured. DL-based model significantly underestimated areas compared to the ground truth ($p < 0.005$). Whole body PCA resulted in PC1 accounting for 47% of the variance, which was primarily influenced by variations in the X and Z directions (loading values at -0.6082 and 0.6765 respectively). Variances of the annulus were dominated in the same directions. The CD and HD for patient 1 were 3.118 and 7.5847 mm, respectively. For patient 2, the PD was 6 and there was significant pairwise distance between corresponding points at 8.4702 ($p < 0.005$). Unlike patient 1, there was not a significant difference in the areas. Like patient 1, there was great influence of variances in the X and Z directions (-0.6415 and -0.6705, respectively) of 50% of the overall variance. The annular PCA demonstrated a similar trend. The CD and HD of 8.8654 and 13.9312 mm, respectively. For patient 3, the centerline comparisons yielded a PD of 3.22 and a significant pairwise distance average of 30.7282 ($p < 0.005$). Manually generated models significantly differed from DL-based models ($p < 0.005$) that underestimated the areas. 48% of total body variance was explained by variance in the X and Z directions (-0.7021 and 0.7077, respectively). Annular PCA showed a similar trend. The CD and HD were 6.0352 and 11.2970 mm, respectively.

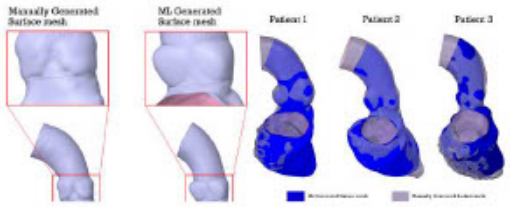

Figure 1 A. Visual differences of Patient 2 before height cut. B. Manually generated surfaces overlayed on DL-based meshes for three patients.

Conclusions: Visually, the manually generated models consistently show a larger annulus compared to their DL-based counterpart, possibly a result of restricted template deformation at this region in the DL-based generation. Significant average distances between corresponding centerline points suggest dissimilarities in curvature for all three models. For patients 2 and 3, there was a large Procrustes distance, suggesting that curvatures may differ. DL-based models of patients 1 and 3 significantly underestimated areas of slices associated with the centerline points of the models, suggesting that there may be underestimation issues in future models. Furthermore, heightened variance in X and Z directions may relate to a combination of curvature and slice dimension differences, hinting at further geometric differences between model types. Large Chamfer and Hausdorff distances relative to the overall dimensions of the models indicate dissimilarity for all three patients. These findings raise concerns about the viability of this DL method in TAVR studies.

References:

1. Anam et Al. J Cardiovasc. Transl. Res. 2022;1-11
2. Pak et Al. IEEE Trans. Med. Imaging 2023;43:203-215.

Acknowledgements: No acknowledgements

DEI: Advances in this field reduce expertise and time needed, thus allowing more medical personnel to administer personalized medicine.

STEVENS
INSTITUTE OF TECHNOLOGY

Exploring the Efficacy of Coarse Labels for Machine Learning Algorithms for Tumor Segmentation

Nishanth Arun, John Galeotti.
Carnegie Mellon University, 5000 Forbes Ave, Pittsburgh PA 15213

Introduction: In this study, we explore the intricate relationship between annotation precision and segmentation accuracy within the realm of medical image analysis. The high demand and subsequent dearth of precise expert annotations for large segmentation datasets has historically impeded research development in this area. Prior work in this area has largely focused on weakly supervised and semi supervised learning approaches as a result of the perceived need for expert annotated data[1]. Although several studies exist that leverage other algorithmic methods to deal with sparsity or absolute quality of labels[2], we wish to answer the fundamental question of determining if rough annotations are viable for performing tumor segmentation in medical imaging through a series of comprehensive experiments. To address this challenge, we evaluate the trade-offs between annotation detail and segmentation performance on tumor segmentation datasets, shedding light on alternative strategies for dataset preparation. We introduce an innovative approach that employs coarse annotations of varying degrees of precision, created using splines, to investigate their efficacy compared to expert-level supervision annotations and to test the hypothesis that coarse annotation offer a cost-effective solution to the hurdle of annotation for tumor segmentation.

Methods: We use two popular publicly available datasets, the Liver Tumor Segmentation Benchmark dataset[3], consisting of 130 contrast-enhanced abdominal CT scans from various clinical sites around the world for primary experimentation, and the Breast Ultrasound Imaging dataset[4], consisting of 780 scans of breast ultrasound images among women between 25 and 75 years old for external validation. These two datasets were chosen to demonstrate the efficacy of coarse labels across modalities and anatomies. We use a novel spline-based approximation technique on the expert-annotated labels by (a) selecting N uniform points along the tumor boundary and (b) fitting a b-spline[5] to these points. The choice of N gives us added flexibility over the coarseness of the resulting labels. We use a UNet[6] model, as it is a very popular choice for segmentation tasks. We use an 80-10-10 split of the dataset into training, validation and testing sets respectively and use Binary Crossentropy loss with the Adam optimizer. To perform the experiment, we approximate portions of the dataset with a 5-point spline and train the UNet on this partially approximated dataset to see how performance degrades with an increasing proportion of coarse annotations.

Results: Figure 1 shows the segmentation performance using dice scores of the model trained with varying proportions of the dataset 'corrupted' with coarse labels. We find that training on a dataset where 75% of the labels have been approximated with a 5-point spline still leads to only a 3.2% reduction in capturing the tumor in the LiTS dataset. Moreover, we find that a model train with fully coarse labels had a 83.6% tumor detection rate on the LiTS dataset and 81.62% on the BUSI dataset (not shown in graph), demonstrating an ability to learn effective tumor representations in the absence of finer tumor features

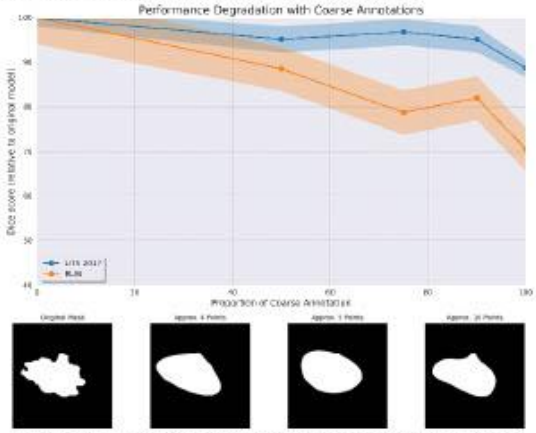

Figure 1. (top) Dice score degradation with labels corrupted by a 5-point spline on LiTS (liver tumor segmentation) and BUSI (breast tumor segmentation) datasets as a percentage of baseline model performance and (bottom) Visualization of coarse labels generated with different number of boundary points on the BUSI dataset

Conclusions: In this study, we explore and demonstrate the viability of a more cost-effective form of annotation, potentially reducing expert annotation burden by eliminating the need to provide fine annotations and accelerating the development and deployment of deep learning models in clinical setting. We also study the feasibility of leveraging large volumes of coarsely annotated data and find that having fine annotations on only 25% of the data still leads to remarkably similar performance as having fine annotations on 100% of the data. Additionally, we note that if the goal of the task is to detect tumor location for clinical reference, there is virtually no drop in detection efficacy under a fully coarse annotation regime.

References:

1. Zhang, AI Review. 2020;53:4529-4288 .
2. Tajbaksh, Med Img Analysis. 2020;63
3. Bilic P, Arxiv, 2019; 1901.04056
4. Al-Dhabyani W, Data in Brief, 2020; 28:104863
5. Unser M, IEEE TSP, 1993;43,821-833
6. Ronneberger, Springer, 2015;234-241

Acknowledgements: This work was supported by the Mayo Clinic - CMU Transforming Transplant Initiative

DEI: Machine Learning models for medical imaging often suffer from bias stemming from the lack of diverse data. Proper care must be taken to train AI on inclusive data. Additionally, ML initiatives could include partnerships with educational institutions serving diverse populations to integrate real-world bioengineering projects into their curriculum

STEVENS
INSTITUTE OF TECHNOLOGY

Attenuating Mitochondrial Dysfunction Restores Endothelial Barrier Function & Integriy Post Traumatic Brain Injury

Vaidehi Apte[1], Rene Schloss, PhD[1], Martin L. Yarmush MD/PhD[1]
[1]Rutgers University, The State University of New Jersey Biomedical Engineering

Introduction: Traumatic brain injuries (TBIs) are life threatening and pose serious long-term consequences. Patients often experience neurological symptoms such as headaches, seizures, impaired motor skills, and an increased likelihood of developing neurodegenerative diseases later in life. The blood brain barrier breakdown is a major initiator of the secondary traumatic brain injury cascade, associated with oxidative stress, reactive oxygen species (ROS), and inflammation of the endothelial layer of the blood brain barrier (BBB). Increased metabolic rate of the injured endothelial cells results in increased ROS generation by the mitochondria, overloading the antioxidant recovery mechanisms, and ultimately contributing to the state of oxidative stress at the BBB, leading to its eventual breakdown. BBB breakdown enables toxic and inflammatory molecules to pass into the neural microenvironment, contributing to the neuroinflammatory cascade responsible for patients' symptoms [1-2]. Currently, no treatment exists to intervene earlier in the neuroinflammatory cascade post TBI to repair and restore the integrity of the blood brain barrier and offer functional recovery. As hypermetabolism and mitochondrial dysfunction in the endothelial cells of the BBB post-TBI are a key contributor to BBB breakdown, we hypothesize that attenuating mitochondrial dysfunction will restore the endothelial barrier function and integrity.

Methods:

Cell Culture: Human umbilical vascular endothelial cells (HUVECs) were maintained in tissue culture flasks at 37°C and 5% CO_2 in HUVEC maintenance media. HUVEc maintenance media is Large Vessel Growth Media supplemented with 2ng/mL fetal bovine serum (FBS), 1000ng/mL hydrocortisone, 10ng/mL hEGF, 3ng/mL bFGF, 10000 ng/mL heparin, and 1% penicillin/streptomycin. Media was changed every 48-72 hrs.

Barrier Integrity Assessment: Endothelial barrier integrity was assessed by trans-endothelial electrical resistance (TEER) measurements using an EVOM2 voltmeeter (Wold Precission Instruments) permanufacturers instructions.

Mitochondrial Assays: Mitochondira were labeled for live-imaging using MitoTracker Deep Red (ThermoFisher Scientific, M22426). Cells were stained with 100nM MitoTracker for 60 mins and counterstained with 0.2uL/mL of Hoechst 33342 at the same time. The cells were washed 2x with PBS after staining. Images were obtained using an Olympus IX81 microscope and Slidebook software (Olympus) using the 20x objective. Mitochondrial membrane potential was assessed using JC-1 dye (ThermoFisher Scienific, T3168). Cells were stained with 2ug/mL of JC-1 dye diluted in Large Vessel Growth Media for 30 mins at 37°C and 5% CO_2, after which the cells were left to equilibriate in fresh Large Vessel Growth Media at 37°C and 5% CO_2.

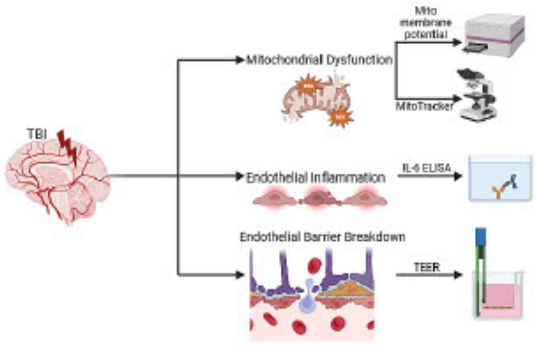

Figure 1. *In vitro* endothelial barrier model design and analysis approach

Results: Using the approaches described in *Figure 1*, we present the development of an *in vitro* model of LPS induced endothelial barrier breakdown to model the breakdown of the endothelial barrier post-TBI. We also present that mitochondria specific drugs 5-(N-Ethyl-N-isopropyl)-Amiloride (EIPA) and LY344864, restore the function and integrity of an LPS-stressed *in vitro* endothelial barrier. These mitochondria specific drugs also attenuate endothelial IL-6 secretion. We also confirm the ability of EIPA to preserve the mitochondrial membrane potential and the ability of LY344864 to promote mitochondrial biogenesis.

Conclusions: We demonstrate that resolving mitochondrial dysfunction restores endothelial barrier integrity and function. These results indicate that a mitochondria specific treatment may be able to restore the endothelial barrier of the BBB post-TBI.

References:

1. Kuriakose, M. Scientific Reports. 2019; 9:7717
2. Daneman, R. CSH Perpect. In Bio. 2015; 7(1): a20412

Acknowledgements: Research reported here was supported by the National Institute of General Medical Sciences of the National Institutes of Health under award number T32 GM008339. Images created with BioRender.com.

DEI: The field of bioengineering can improve disparities in healthcare outcomes by developing accessible technologies, and collaborating with organizations and researchers to address challenges in low resource environments.

STEVENS
INSTITUTE OF TECHNOLOGY

A Single-Cell RNA sequencing (scRNA-seq) Analysis of human Thalamic-like Organoids (hThO) derived from human Embryonic Stem Cells (hESCs), and their gene expression in comparison to ISH, Bulk and Single-Cell RNA data.

Odhrán Casey[1], Prabir Patra[2], Peiqiao Wu[1].
[1]Department of Biomedical Engineering, School of Engineering, University of Bridgeport
[2]Department of Biomedical Engineering, College of Engineering & Computer Sciences, Marshall University.

Introduction: Methods to replicate structures of the human brain through the generation of organoids have been explored extensively. In this study, we compared the gene expression data of human Thalamic-like Organoids (hThO) and human Embryonic Stem Cells (hESCs) generated in vitro to that of current human and mouse brain data, that are accessed through the Neuroscience Multi-Omic Data (NEMO) Portal, and both human and mouse brain data being accessed through the Allen Brain Atlas (ABA). Validating ThO's similarities to the thalamus and broader brain structures is a vital step in allowing researchers to use these organoids in future studies with full confidence that they truly represent that of in vivo thalamus structure, function, and gene expression. Single-Cell RNA sequencing (scRNA-seq) analysis was performed to reveal the expression of known Thalamic markers in our data, in addition to structure similarity mapping to existing bulk-RNA sequencing data derived from the human brain.

Methods: Study on data from human thalamic organoids from Early (day 34) and Late (day 89) time points, human thalamus from Carneige Stage (CS) 19 to Gestation Week 18, human diencephalon from CS12, human and mouse developmental brain from Post Conception Week (PCW) 8-24 and Embryonic Day 11 (E11) to Embryonic Day 18 (E18). Statistical Packaes from R (v4.3.1) programming language were used for the analysis of each of our datasets. scRNA-seq analysis and integration done using R package Seurat (v5.0.1), comparison to BrainSpan data using package Voxhunt (v1.0.1), data manipulation using Dplyr (v1.1.4), data visualization using ggplot2 (v3.4.4) and cell clustering done using umap (v0.2.10.0).

Results: On analysis of the hThO data we found strong expression of thalamic marker genes *OTX2*, *TCF7L2*, *PAX6* and *CDH2* at both timepoints (Early and Late). Their average expression in our cells reached a maximum normalized and scaled value of 2.5, 4, 4 and 3 respectively. Integrative analysis took place between our Late timepoint cells along with CS19, CS22 and GW18 and Thalamus datasets from the NEMO portal. This integrated dataset was clustered and visualized, showing 24 distinct clusters within our data. Upon further analysis of our Early timepoint cells, comparison to Bulk-RNA BrainSpan data revealed a strong similarity between these cells and the Dorsal Thalamus (DTH) at Post Conception Week (PCW) 8 (Similarity Score ≈ 0.60) and 12 (Similarity Score ≈ 0.65) respectively. When analyzed further, we see a strong similarity to Diencephalic structures, namely prosomeres 1, 2 and 3 (pretectum, thalamus and prethalamus) at Embryonic stages 11 and 13 (E11 and E13). Similarity were as follows for each section during each Embryonic Day; E11 ≈ 2,2,1; E13 ≈ 1.5, 2, 1. We also saw strong comparison between the early cells and the Mediodorsal (MD) Nucleus in PCW16 (Score ≈ 0.55). The same results are true for the late timepoint cells, which show the same similarity to DTH structure at PCW8 (Score ≈ 0.65) (**Fig1**).

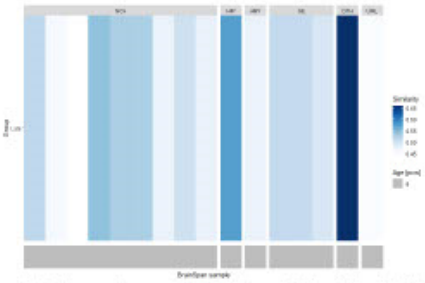

Figure 1. Comparison of Late Time Point (day 89) hThO expression to Bulk-RNA sequencing BrainSpan data. Structures PCW8 -NCx: neocortex; HIP: hippocampus (hippocampal formation) ; AMY: amygdaloid complex; GE: ganglionic eminence; DTH: dorsal thalamus; URL: upper (rostral) rhombic lip.

Conclusions: Our study suggests that there is a close similarity between human Thalamic Organoids and Diencephalic and Dorsal Thalamic structures. We believe that these Bioinformatics Analysis have the potential to understand neurodegenerative diseases and/or neurodegenerative disorders pertaining to the Thalamus.

References:

1. Y. Xiang. et al., Cell Stem Cell. 2019; 24(3): 487–497.e7.
2. JS Fleck et al., Cell Stem Cell. 2021; 28(6): 1148-1159.e8
3. A. Bhaduri et al., Nature. 2021; 598: 200-204
4. Allen Institute for Brain Science (2004). Allen Mouse Brain Atlas, BrainSpan.

Acknowledgements: We sincerely acknowledge Ridvan Kiral for his contribution in directing us to the appropriate papers which contain useful datasets and methods for our study.

DEI: In support of this year's NEBEC initiative to promote greater diversity, equity, and inclusion in Bioengineering, our Bioinformatics study in this work is very diverse and includes people of all sectors and it represents the broader community for the inclusion of STEM underrepresented people.

STEVENS
INSTITUTE OF TECHNOLOGY

Role of Blood Brain Barrier Disruption and Neuroinflammation following Repeated Low-Level Blast Traumatic Brain Injury in Development of Post Injury Behavioral Deficits

Tulika Das, Dr. Ying Li, Dr. Bryan Pfister
New Jersey Institute of Technology, Newark, NJ

Introduction: Members of the military and civilian law enforcement can experience repeated low-level blast exposures due to increased use of heavy weaponry including large caliber rifles and explosives. In humans, low-level blasts (rLLB) are often not associated with overt symptoms, however, can lead to cognitive impairments and attention deficits over time. Recent models are suggesting the cumulative effect of rLLB may cause neurological deficits that develop over months. The mechanisms of repeated blast TBI on neuro-pathophysiological deficits remains poorly understood. Under normal condition, blood brain barrier (BBB) highly selectively permeable and does not allow foreign bodies to enter central nervous system (CNS). In TBI including blast TBI (bTBI) pathology, acute BBB breakdown and monocyte infiltration have been well documented following the injury. Monocytes gets activated by in response to damaged brain tissue and matured into macrophages which then functionally and morphologically indistinguishable from microglia, the resident macrophage of the central nervous system. Taken together, activation of both peripheral and resident macrophages exacerbates neuroinflammation, a major mechanism in both acute and chronic pathology of bTBI which can ultimately lead to loss of neurons. A previously published study from our lab showed acute and chronic anxiety like symptoms and short-term memory impairments in mice exposed to single moderate blast (180 kPa) in parallel with activation of both resident microglia and infiltrated monocytes. Here we hypothesized that repeated exposures to low-level blast overpressure causes breakdown of BBB, inducing inflammation, cognitive deficits, and anxiety like behavior. To determine the potential therapy Poloxamer-188 (P188), a membrane resealing agent with anti-inflammatory property, was used as a potential treatment to minimize the neurocognitive deficits of induced by rLLB.

Methods: Adult double-transgenic CX3CR1GFP/+: CCR2RFP/+ mice in which resident microglia are labeled with GFP and peripheral monocytes with RFP, were exposed to 70 kPa blast over pressure (BOP) three successive times with one- minute intervals. Sham animals were placed in the shock tube, but no blast wave was delivered. Animals were divided in 4 groups: Sham, rLLB injured, Vehicle treated (injury+ saline) and P188 treated (blast+P188). Open Field Test (OFT) and Elevated Plus Maze (EPM) test were performed to determine animal's anxiety level acutely (post injury week or PIW 1) and chronically (PIW 4). Anxiety like behavior was determined by calculating the time spent in center zone (OFT) and closed arms in the maze (EPM) were analyzed by ANYMaze software. Novel object recognition (NOR) test was used to evaluate the ability of the rat to differentiate between a novel and familiar object. The total time spent exploring each of the two objects was measured using ANYMaze. At the completion of behavioral tests, animals were anesthetized with 10:1 ketamine and xylazine (10 mg/kg) via intraperitoneal injection and perfused transcardially with phosphate-buffered saline (PBS, pH 7.0) followed by 4% paraformaldehyde (PFA). The brain was harvested, postfixed in 4% paraformaldehyde for 48 hours, followed storage in 30% sucrose solution. Cryostat frozen sectioning of ultra-thin sections (20 μm) of hippocampus (HC) were prepared and mounted on glass slides to visualize RFP/GFP labeled cells under the fluorescence microscope. Image analysis was performed using ImageJ software. Statistical analysis was performed using Graph Pad Prism 8.0.1 and values were expressed as mean ± SEM. One-way ANOVA with Tukey's Honest Significance post-hoc test and Student t-tests were used in this project.

Results: Animals exposed to rLLB displayed acute and chronic anxiety-like symptoms, depression like behavior and short-term memory impairments. At 1 month post injury, in open field test (OFT), number of entries to the center zone as well as the time spent in center zone was significantly higher in sham group when compared with the rLLB injured group. With P188 treatment, number of entries to the center zone and total time spent in the center zone significantly went up when compared with the vehicle treated animals. For EPM, number of entries and total time spent in the open arm are significantly higher for sham animals when compared with the rLLB injured animals. This deficits in injured animals were improved with P188 treatment where the animals treated with P188 spent significantly more time and number of entries to the open arm when compared with the vehicle treated animals. For NOR, rLLB injured mice had lower discrimination index when compared with the rLLB injured group (sham 0.71 ± 0.07, rLLB 0.51 ± 0.07) and this DI showed improvement when treated with P188 (P188 0.71 ± 0.04, vehicle 0.54 ± 0.05). The total number of GFP-labeled microglia per unit area in hippocampus at 1 day after the injury was significantly higher ($p < 0.05$) in the injured group. This change was persisted through 7 days post injury ($p < 0.05$).

Conclusions: This study established persistent behavior deficits as an effect of rLLB in mice. rLLB injury induces acute and chronic neurobehavioral changes while P188 treatment showed improvement of these behavioral deficits suggesting that rLLB could cause BBB damage and be responsible for neurobehavioral changes. The changes observed in the behaviors are supported by the biochemical changes. Taken together, these data indicate that even if the blast pressure level is very low, repeated exposures to low-level blasts can induce neurological changes which is comparable to the consequences of moderate blast injury.

References:

1. Murugan M et al., Brain Behav Immun. 2020 Aug;88:340-352
2. Rama Rao et al., J Neurotrauma. 2018 Sep 1;35(17):2077-2090.

STEVENS
INSTITUTE OF TECHNOLOGY

Distinct TMS-EEG profiles reflect motor homunculus variability

Negar Namdar[1], Jukka Saari[2], Sara Määttä[2], Laura Säisänen[2,3,4], Jelena Hyppönen[2], Päivi Koskenkorva[5], Elisa Kallioniemi[1]
[1]Department of Biomedical Engineering, New Jersey Institute of Technology, New Jersey, USA
[2]Department of Clinical Neurophysiology, Kuopio University Hospital, Finland
[3]Department of Applied Physics, Faculty of Forestry and Natural Sciences, University of Eastern Finland, Finland
[4]Department of Clinical Neurophysiology, Clinical Medicine, Faculty of Health Sciences, University of Eastern Finland, Finland
[5]Department of Clinical Radiology, Kuopio University Hospital, Finland

Introduction:

Transcranial magnetic stimulation (TMS) is a non-invasive brain stimulation technique. When electroencephalography (EEG) is used concurrently with TMS, the resulting TMS-evoked EEG potentials (TEPs) offer a means to assess the excitability, connectivity, and oscillatory patterns within the targeted cortical region .So far, most motor cortex studies have focused on the hand area for two main reasons: Its low stimulation intensity, which results from its proximity to the scalp, and its easily detectable hand knob structure .The reason for the limited research on other motor areas, such as the leg, arises from its deeper location in the homunculus, the challenge of targeting individual muscles, and the differences in the corticospinal tract of the upper and lower limbs .On the other hand, the challenges in evaluating the cortical face and tongue representations arise from directly stimulating peripheral facial nerve fibers due to the spread of the TMS-induced electric field Consequently, TEPs have been mainly studied in the hand area, with no research available evaluating the TEPs across the homunculus. In this study, we recorded and assessed TEPs in the hand, leg, and face areas to characterize them.

Methods: Eighteen healthy volunteers (11 females, 7 males, age 46.5±17.3 years) participated in the study. First, the cortical representation areas for the right leg (tibialis anterior), hand (first dorsal interosseous), and face (mentalis) were mapped, and the resting motor threshold (rMT) of these areas was measured as the percentage of maximum stimulator output (%MSO). After that, 150 TEPs from each region were measured using single TMS pulses with a stimulation intensity of 90% rMT. TEPs were recorded with a 60-channel electrode system. The TEPs were averaged over subjects in each stimulated area in three different ROIs: left M1 (9 electrodes), right M1 (9 electrodes), and Cz (1 electrode). Artifacts in the data were removed with independent component analysis. Differences between the TEPs between different muscle groups were evaluated with a two-sample t-test ($p < 0.05$, uncorrected) calculated every 1ms.

Results: In the TEPs of the right motor area there were peaks at 16, 27, 34, 54, 80, 100, 102, 112, 117, 155, 164, 168, 180, and 182ms after the TMS for the face area; at 19, 35, 51, 64, 76, 80, 88, 98, 109, 137, 147, 162, 171, and 196ms for the leg; and at 21, 31, 53, 86, 117, 126, 132, 178, 190, and 195ms for the hand area. The TEPs differed between face and leg in the time windows 15-22ms, 178-201ms, between face and hand in windows 15-23ms, 137-156ms, and between leg and hand in windows 33-41ms, 73-99ms, 179-182ms.

In the TEPs of the left motor area, there were peaks at 21, 35, 142, 145, 154, and 199ms after TMS for the face area; at 17, 31, 47, 82, 90, 107, 114, 138, 158, 162, 169, 178, and 182ms for the leg and at 34, 84, 129, and 170ms, for the hand area. The TEPs differed between face and leg in the time windows 36-53ms, 192-206ms, between face and hand in the windows 73-83ms, 198-233ms, and between leg and hand in the window 37-55ms.

Lastly, the TEP results from the Cz electrode show peaks at 31, 56, 78, 92, and 182ms for the face area; at 32, 50, 57, 76, 137, and 181ms for the leg, and at 30, 50, 63, 72, 157, and 165ms for the hand area. The TEPs differed between face and leg in the time windows 73-79ms, 115-143ms, 164-195ms, and between leg and hand in the windows 29-36ms, 67-94ms, 120-150ms.

Conclusions:
TEPs of the hand, face, and leg areas are different.

DEI: Measuring EEG signals from people who have braids is challenging, as the EEG electrodes cannot make a good connection to the scalp through the braid. Poor connection will lead to poor quality of data. This means the data from these individuals has to be excluded from the study. To solve this issue, there have been suggested ways, such as tailoring a specific type of electrode or having a specific type of braid compatible with the EEG electrode layout. However, there are challenges, such as not having consistent data with the conventional electrodes due to different electrode locations, sizes and other features and the practicality of the compatible braid models. as solution to this we may need to consider for this problem is using adaptive data processing methods to interpret the data coming from these individuals differently to consider the electrode differences.

STEVENS
INSTITUTE OF TECHNOLOGY

Antimicrobial Peptide In-silico Efficacy Assessment Using Molecular Dynamics

Josuel Morel[1], Alexandra Griffith[1], Joseph Dodd-o[1], Carla Cugini PhD [3], Vivek Kumar PhD [1,2,4]

[1]Department of Biomedical Engineering, New Jersey Institute of Technology; [2]Department of Endodontics, Rutgers School of Dental Medicine, [3]Department of Oral Biology, Rutgers School of Dental Medicine; [4]Department of Chemical Engineering, New Jersey Institute of Technology

Introduction: Antibiotic resistance has become an issue of great concern to the medical community and society. We have shown that antimicrobial peptides (AMPs) can potentially solve this issue due to their nonspecific charge-based mechanical mode of action.[1] Due to the proposed mechanical mode of action of these AMPs, it is difficult for pathogens to gain resistance compared to traditional antibiotics. Here, we have studied two peptides. One has been termed our structural self-assembling peptide (SAP), and the other is our AMP. While both peptides have been shown to self-assemble, [1] our structural peptide has not shown antimicrobial efficacy in-vitro due to its less charged active domain compared to our AMP. While having more positively charged residues on each end makes our AMP a more effective antimicrobial agent, it makes the peptide less capable of self-assembling into organized beta-sheets, which has been shown to improve antimicrobial efficacy.[2] In order to aid in the design of these self-assembling AMPs, we have decided to investigate the mode of action of these peptides via coarse-grained molecular dynamics (CG-MD) simulations against multiple pathogenic cell membrane types over the course of five microsecond simulation times. We hypothesized that the increased charge of the AMP active domain would allow it to destabilize these pathogenic membranes more effectively than our SAP, as the proposed mechanical mode of action is charge-based.

Methods: We have performed five-microsecond simulations against multiple pathogenic membrane types to understand these peptides' efficacy against different pathogens. We have performed simulations against representative Gram-positive and Gram-negative bacterial membranes. [1,3-4] All simulations were carried out using GROMACS software. All peptide models were created in Pymol atomistically and converted to CG representation using the Martinize2 script. Elastic bonds were used to ensure that the peptides maintained their beta-sheet conformation throughout the simulations, per previous circular dichroism data.[1] Once the CG version of the peptide was made, the membrane was built and solvated via the Insane.py script. After the minimization, equilibration, and production runs, the simulations were analyzed visually via animations and quantitatively via trajectory calculations within GROMACS.

Results: Our results consist of animations, which give a more qualitative understanding of the destabilization of the membrane, and trajectory calculations, which give a more quantitative understanding of where the phospholipids are most tightly packed throughout the simulation. These density calculations are reported as an average calculation of the density of the membrane's phospholipids over the entire simulation box with respect to the lipid membrane. These average density calculations are then compared to that of a control membrane where no peptide is present. This is done to account for natural fluctuations in the membrane that can occur when no antimicrobial is present. Displayed in **Figure 1** are images of the simulations done against a representative gram-negative cell membrane.

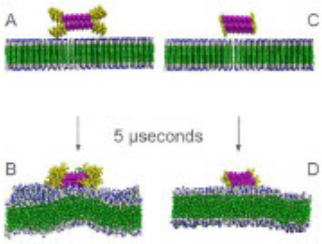

Figure 1: (A, C) Pre-Simulation images of AMP and SAP above representative Gram-negative bacterial membranes. Assembly domains are depicted in magenta. Active domains are depicted in yellow. Lipids are depicted in green with white phosphate and blue amine groups. (B, D) Post-simulation images of AMP and SAP simulations, respectively.

Conclusions: Through the completion of these CG-MD simulations, it has been found that the AMP creates stronger membrane destabilization against these representative pathogenic cell membranes compared to our SAP. The density calculations made from the resulting trajectories of these simulations have shown that significant membrane distortion is present when the membrane is exposed to the AMP. This knowledge can aid in the potential creation of a combined SAP-AMP therapeutic to aid in treating antimicrobial-resistant pathogens.

References

1. Sarkar B. ACS Biomaterials, 2019;5(9), 4657–4670.
2. Beter M. Molecular Pharmaceutics, 2017;14 (11), 3660-36683.
3. Chakraborty, A. ACS Omega, 2021;6(1), 388-400.
4. Shahi, G. FEMS Yeast Research, 2020; 20(6).

Acknowledgments: This study was supported by NIH NIDCR R01DE031812.

DEI: As described herein, we have created a nonspecific antimicrobial potentially capable of killing more Gram-positive and Gram-negative pathogenic species than standard antibiotics. By making this treatment easy to access in its future use, we can aid in combating disparities in healthcare outcomes by making treatment available to traditionally disadvantaged groups. Due to the interdisciplinary work of this field of computational biomedical engineering, it is very important to maintain a diverse team of researchers who are experts in fields including computer science, biology, and engineering.

STEVENS
INSTITUTE OF TECHNOLOGY

Characterizing Bacterial Response to Shape-Memory Actuated Silk Wrinkled Surface Topographies to Inform Strategies for Biofilm Prevention

Luiza Owuor, Elizabeth Oguntade, Changling Du, Mary Beth Monroe, James H. Henderson
Biomedical and Chemical Engineering, Bioinspired Institute, Syracuse University, Syracuse, NY 13244

Introduction: Biofilms contribute to up to 80% of microbial infections.[1] Wrinkle patterns have demonstrated promise as antifouling surfaces.[2] Biopolymer films, such as silk fibroin (SF), have been previously employed to achieve wrinkling,[3] but there has been little study of biopolymer wrinkling for antifouling surfaces. A critical outstanding question is the extent to which the wavelength and amplitude of biopolymer wrinkles affect bacterial attachment to prevent biofilm formation. To address this question, here we investigated the effect of wrinkle wavelength and amplitude on bacterial adhesion and colonization using tunable, on-demand SF wrinkled surface topographies on thermo-responsive shape memory polymer (SMP) substrates.

Method: Semicrystalline thermoplastic polyurethane pellets (MM-4520, SMP Technologies, Inc.) with a glass transition temperature (T_g) of 45 °C were extruded (3Devo Composer 450) to prepare SMP filament for 3D printing. Filament was loaded into a 3D printer, and our recently developed technique known as Programming via Printing (PvP)[4] was used to simultaneously fabricate and program strain (20%) in the SMP. Specific printing parameters of fiber orientation, speed, and temperature identified by preliminary experiments were held constant to fabricate samples with a programmed strain magnitude of 20% strain via printing Programmed SMP squares were printed with fibers aligned layer-by-layer to enable shape memory-based uniaxial contraction. The substrates were dip-coated in varying SF concentrations (1%, 2%, 3%) and then treated in 70% methanol to induce secondary structural changes in the silk network and prevent dissolution of SF in aqueous solution. To induce silk wrinkle formation, the substrates were heated in an isothermal oven above the T_g of the SMP, which enabled the silk film to buckle into a wrinkled state. Wrinkle wavelength and amplitude were determined from images captured by atomic force microscopy. Lastly, the wrinkled samples were exposed to two biofilm-causing agents, *S. aureus* and *E. coli*, in Lysogeny broth for 24 h. Thereafter, samples were fixed, dehydrated, and dried before observation of microbial adhesion and colonization by scanning electron microscopy (SEM). Statistical analysis was performed via one-way ANOVA followed by Holm Sidak's multiple comparisons test between groups for comparisons involving more than two groups.

Results: Upon shape recovery, the SF film buckled and formed wrinkles on the SMP surface. With increasing SF concentration, the wrinkle wavelength increased from 0.8 to 7.2 µm and the amplitude increased from 220 to 1481 nm. Following exposure to microbes, all silk wrinkled surfaces had significantly reduced bacterial adhesion and biofilm formation (**Figure**) compared to the uncoated SMP and flat SF-SMP.

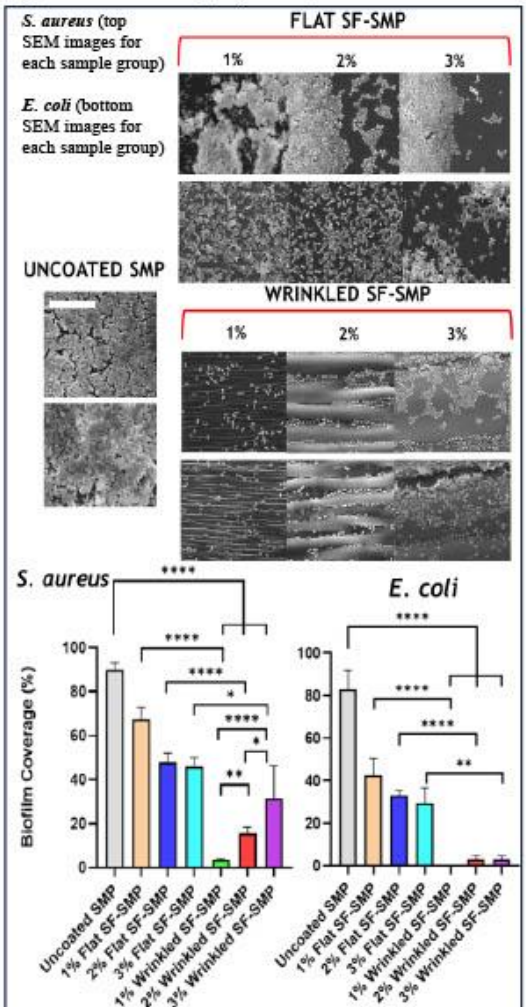

Figure: Qualitative and quantitative characterization of *S. aureus* and *E. coli* biofilm coverage. Scale bar of 5 µm applies to all SEM images. Significance reported as *p< 0.05, **p< 0.01, ***p<0.001, ****p<0.0001.

Conclusions: We successfully created an array of tuneable silk wrinkle wavelengths and amplitudes to study microbial attachment and biofilm formation. We found that smaller wavelengths and amplitudes prevented biofilm formation. Based on previous work,[5,6] we can speculate that smaller length scale topography could minimize bacterial attachment due to a reduction in contact area. To conclude, our overall findings suggest the potential for SF wrinkled topographies to be studied for use as antimicrobial surfaces for biofilm prevention.

References: [1] Li, X et al., Coatings, 2021, 11 (3), 294, [2] Nguyen et al, Polymers, 2020, 38 (5), 558–571. [3] Wang et al., PNAS, 2019, 116 (43), 21361–21368. [4] Pieri et al., Advanced Materials Technologies,2023. [5] Epstein et al., New Journal of Physics, 2013. [6] Scardino et al., *Biofouling*, 2008.

STEVENS
INSTITUTE OF TECHNOLOGY

Evaluating the Effects of Calreticulin-Loaded Nanofibres on Diabetic Foot Ulcer Fibroblast Activity

Bowen Luo, Matangi P R, Dr. Leslie. I. Gold, Dr. Hongjun Wang
Department of Biomedical Engineering, Semcer Center for Healthcare Innovation, Stevens Institute of Technology

Introduction: Diabetic foot ulcers (DFUs) are deep, unhealed, and open wounds in the feet resulting from hyperglycemia-induced cell damage. 19% to 34% of all diabetic patients are susceptible to DFUs, and it is the leading cause of non-traumatic amputation worldwide [1]. Currently available treatments for DFUs are met with limited success as they are not designed for the diabetic microenvironment. Calreticulin (CALR), a ubiquitous chaperone protein when loaded within nanofibre (NF) matrices demonstrated a sustained protein release profile that aided in improved proliferation and migration of healthy fibroblasts and keratinocytes. The NFs not only preserve the bioactivity of CALR but also protect it from enzymatic degradation [2]. This study elaborates on the usage of CALR-NFs for wound care and expands it to a diabetic setting to test the response of diabetic fibroblast activity on CALR-NFs. It is based on the hypothesis that CALR-NFs can modulate the behavior of diabetic fibroblasts and induce them to switch to a healing phenotype to advance diabetic wound repair.

Materials and methods: Polycaprolactone (PCL) - collagen type I (Col1) polymer solution (3:1 ratio) was mixed with 90 µg/mL CALR at a ratio of 7:3 and electrospun under optimized conditions (17kV, 17 cm, 0.6 mL/hr.) to get the CALR-NFs. NFs without CALR were used as the control.

Patient-derived diabetic foot ulcer fibroblasts (DFUs) and normal foot fibroblasts (NFFs) were cultured in low glucose Dulbecco's Modified Eagle medium supplemented with 10% fetal bovine serum and HEPES, at 37 ° C and 7.5 % CO_2.

The cells were seeded on the NF samples and fibroblast activity was assessed by measuring the cell proliferation and viability (days 1, 2, and 3), and migration (72 hrs). Cell metabolic activities were quantified using the Alamar blue assay and the migration was determined by allowing the cells to migrate across a 0.9 mm wound gap. % gap closure was measured by staining the cells with 0.1 % methylene blue after 72 hrs. The response of the diabetic cells and normal cells on the CALR-NFs was compared to the CALR-free NFs to analyze the efficacy of the CALR-NFs for diabetic wound care.

Results: DFUs and NFFs exhibited enhanced cell metabolism when cultured on CALR-NFs (Fig. 1). On day 2 and day 3, DFUs and NFFs cultured on CALR-NFs demonstrated a statistically significant increase in cell metabolic activity compared to the control group cultured on CALR-free NFs (Two-Way ANOVA, $p < 0.0001$).

DFUs and NFFs also showed increased cell motility and wound-healing capacity when cultured on CALR-NFs, evidenced by a greater number of cells filling the initial gap area (Fig. 2).

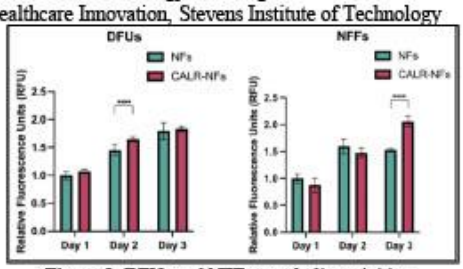

Figure 1. DFUs and NFFs metabolic activities.

Fig. 2 presents brightfield images of wound-gap closure assays, where DFUs and NFFs were allowed to migrate and proliferate on NFs and CALR-NFs for 72 hours. The initial gap is approximated in red.

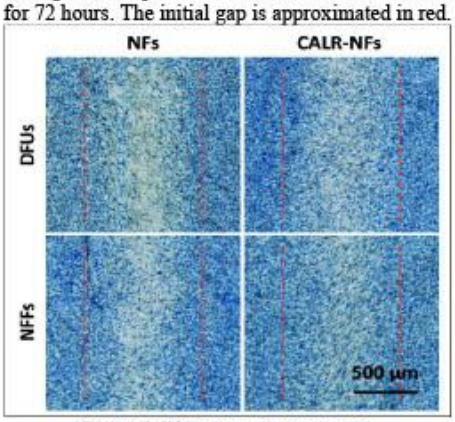

Figure 2. Wound-gap closure assays.

Conclusion: DFUs are typically characterized by impaired metabolic activity and reduced motility. This study provides the first experimental evidence that CALR can enhance the metabolic and migratory activity of patient-derived DFUs, thereby improving the wound healing process. Due to the limited accessibility of DFU cells, the current data were collected from a small sample size, consisting of one diabetic foot ulcer patient and one healthy individual. To strengthen our conclusions, future studies will include multiple DFUs and NFFs groups from different patients and healthy individuals to minimize individual variations. In addition, we will explore and focus on studying the cell signaling pathways that contribute to these effects, elucidating the behind cell mechanisms.

References:

1. McDermott K, Fang M, Boulton AJM, Selvin E, Hicks CW. Etiology, Epidemiology, and Disparities in the Burden of Diabetic Foot Ulcers. *Diabetes Care*. 2023;46(1):209-221.
2. Stack ME, Mishra S, Parimala Chelvi Ratnamani M, Wang H, Gold LI, Wang H. Biomimetic Extracellular Matrix Nanofibers Electrospun with Calreticulin Promote Synergistic Activity for Tissue Regeneration. *ACS Appl Mater Interfaces*. 2022;14(46):51683-51696.

STEVENS
INSTITUTE OF TECHNOLOGY

Self-assembled Chemokine and Neuropeptide Nanoparticles for Chronic Wound Healing After Spinal Cord Injury

Dhruv Patel, Suneel Kumar, Dnyaneshwari Rananavare, Greeshma Manjunath, Shashank Madhavan, Francois Berthiaume
Department of Biomedical Engineering, Rutgers, The State University of New Jersey, Piscataway, NJ08854

Introduction: Spinal cord injury (SCI) patients face prolonged periods of bed rest as rehabilitation can take weeks to years depending upon the type of injury. As a result, SCI patients are susceptible to chronic secondary complications, such as pressure wounds (PWs). About one-third of injured patients develop PWs during their initial hospitalization while >40% are readmitted due to the presence of PWs. PWs can impact social, psychological, and physical well-being while also affecting overall quality of life. They can take months to heal as PWs developed following SCI result in delayed wound healing due to a decrease in immune cell response at the wound site. We hypothesize that modulating the immune cells around the wound site via exogenous application of self-assembled chemokine (MCP-1) and neuropeptide (α-MSH) fused with elastin-like polypeptides (ELP) nanoparticles promotes wound healing after SCI.

Methods: Recombinant MCP-1 and α-MSH were cloned in front of elastin cassette V40C2 in the cloning vector pET25b+ using the protocol developed by members of our lab. As per the published protocol, plasmids were transformed into *Escherichia coli*, cultured overnight at 37°C, purified using centrifugation, and characterized using SDS-PAGE and Western Blot. Purified nanoparticles were tested for their size, in an in vitro system of migration for their biological activity, and later using an animal model of pressure wounds after complete SCI. 10-week-old Balb/C male mice were used to induce complete SCI and full-thickness wounds below the SCI site. Mice were divided into 6 treatment groups: Control, ELP, MCP-1, MCP-ELP, α-MSH, and MSH-ELP. 100 ng of each nanoparticle treatment was administered topically on each wound every day for the first 7 days. On days 3 and 7, mice from each group were sacrificed and wound site tissue samples were excised to characterize the acute phase of wound healing. The rest of the mice were sacrificed on day 26 after complete wound healing to identify long-term wound healing properties. Tissue samples were stained for H&E, Trichrome, and F40/80. Images were captured using an ECHO Revolution microscope and analyzed using ImageJ (NIH) software.

Results: We developed pure, low-cost MCP-ELP and MSH-ELP self-assembled nanoparticles which induced comparable biological activity as compared to native proteins. A transwell migration assay was conducted to evaluate the biological activity of these nanoparticles using THP-1 monocytes. We found that THP-1 cell migration as a chemotactic response was significantly better in the case of native (MCP and α-MSH) and nanoparticles (MCP-ELP and MSH-ELP) compared to the ELP and Control groups. However, MSH-ELP induced better migration as compared to all other groups and its native form ($p<0.001$). Immunohistological studies at different time points (days 3, 7, and 26) showed successful migratory effects of macrophages to the wound sites in a time-dependent manner. Wound healing was enhanced overall compared to the control group by continuously applying up to 7 days of these nanoparticles (MCP-ELP and MSH-ELP).

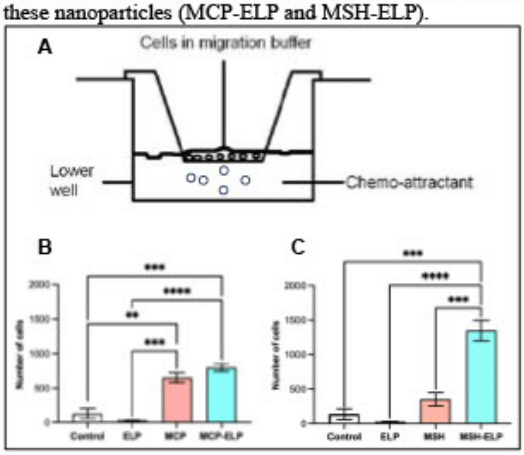

Figure 1: Effect of MCP-ELP and MSH-ELP nanoparticles on THP-1 cell migration (A-C) assay as a chemotactic response. Data is presented as mean ± SEM (n=9). Data was analyzed using one-way ANOVA followed by Tukey's HSD test. **p<0.001, ***p<0.0002, ****p<0.0001. Control-only media without nanoparticles/protein.

Conclusions: We successfully developed and purified the fusion nanoparticles (MCP-ELP and MSH-ELP) using inverse transition cycling which is an easy and cost-effective process. In vitro studies suggested enhanced chemotactic response. Animal studies suggested successful recruitment of macrophages to wound sites and thereby enhanced wound healing after SCI.

References:

1. Lala D. Arch Phys Med Rehabil. 2014;95:2312-2319.
2. Kumar S. J. Neurotrauma, 2018;35:815-824.
3. Marbourg JM. J Neurotrauma. 2017;34:1149-1155.
4. Kang HJ. J Controlled Release. 2021;333:176-187.

Acknowledgements: This work was funded by Rutgers Busch Biomedical Grant 2021 (Suneel Kumar). The authors thank Rick Cohen from Biomedical Engineering, Rutgers University for his technical support.

DEI: The work conducted in our lab is committed to offering care to patients of diverse demographics and backgrounds. We persistently challenge ourselves in researching and developing accessible, low-cost therapies for prevalent healthcare issues. We are dedicated to extending our welcome to anyone interested in joining us

STEVENS
INSTITUTE OF TECHNOLOGY

An Angiogenic and Myogenic Self-Assembling Peptide Hydrogel Therapeutic for Peripheral Artery Disease

Siya Patel[1], Abhishek Roy[1], Gelavizh Gharati[1], Krish Poudel[1], Vivek A. Kumar[1].
[1]Department of Biomedical Engineering, New Jersey Institute of Technology, Newark, NJ.

Introduction: Peripheral Artery Disease (PAD) is depicted by decreased perfusion in the lower extremities caused by constriction or blockage of arteries to the leg. This condition is related to atherosclerosis, or the buildup of plaque in the arteries.[1] PAD can cause severe ischemia and result in cardiac conditions such as myocardial infarctions or a need for amputation of the whole limb. Current therapeutics for PAD include stents and angioplasty which remove blockage in large arteries but do not address decreased blood flow in smaller blood vessels, or microvascularization.[2] The objective of this study is to address this gap in treatment by observing the angiogenic and myogenic nature of a self-assembling peptide hydrogel (SAPH). The effects of the SAPH are tested using a Critical Limb Ischemia (CLI) animal model and through an in vitro tube formation assay which measures the angiogenic potential of the peptide hydrogel.

Methods: The peptide was prepared through solid phase peptide synthesis in a Liberty Blue Solid Phase peptide synthesizer using Fmoc chemistry and the hydrogel was prepared in 1xPBS. In the tube formation assay, human umbilical vein endothelial cells (HUVECs) were combined with conditioned media and stained with calcein AM. Quantitative analysis of the nodes and tube formation was conducted for the SAPH and compared to a Suramin negative control. CLI was induced in BALB/c mice through an initial surgery involving unilaterally ligating the femoral artery. The SAPH was prepared at 10 mg/mL and was compared to a PBS control. Both treatments were injected intramuscularly (IM) in the gastrocnemius muscle and the quadriceps of the ischemic limb. The animals were monitored over a 28-day study period. Laser Doppler Perfusion Imaging was performed to analyze the blood reperfusion and a behavioral treadmill test was conducted on Exer 3/6 treadmill every 7 days of the study period.

Results: In a previous study, hydrogels have shown angiogenic properties through a hind limb ischemia (HLI) model.[3] A previous study was conducted with an angiogenic SAPH termed Slanc, which mimics vascular endothelial growth factor (VEGF). This study introduces a CLI model, a more aggressive model compared to HLI, to study the potential of revascularization and evaluation of motor function in a mouse model that has severely decreased perfusion to the limb.

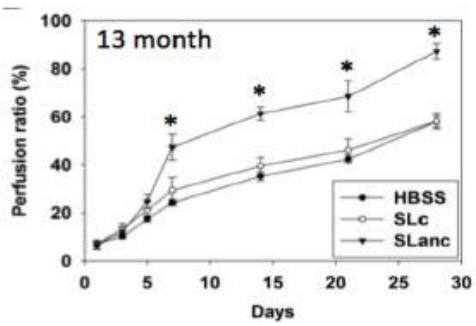

Figure 1. Comparison of the perfusion rate in a C57BL/6 mouse of an angiogenic peptide hydrogel (Slanc) compared to control (HBSS) [3]

Conclusions: We introduced a SAPH with a potential angiogenic and myogenic response to promote revascularization and functional limb utilization in an CLI model. We aim to increase the efficacy of the SAPH in the future through computational modeling and modifying the bioactive mimic.

References:

1. Shamaki, G.R. Curr Probl Cardiol, 2022. **47**(11): p. 101082.
2. White, C.J, Circulation, 2007. **116**(19): p. 2203-15.
3. Kumar, V.A., Biomaterials, 2016. **98**: p. 113-9.

Acknowledgements: NIDCR R01DE031812 (PI), NIDCR R01DE029321 (Co-I), NINDS R61NS127271 (Co-I), NIAMS R21AR077835 (MPI), NIAMS R01AR080895 (Co-I), NJIT URI

DEI: PAD plagues patients (>200M) with substantial financial burden (~$11,000 annually/patient) and health consequences. There is a clear need for an alternative, minimally invasive solution that is cheaper and more widely available to rectify such a health disparity. Our SAPH can rectify these existing disparities as they have a lower production cost due to the "off-the-shelf" nature of the product.

STEVENS
INSTITUTE OF TECHNOLOGY

Investigating Sintered Porous Polycaprolactone Scaffolds on Reduced Bone Production

Nikhil Paul, Joseph Freeman, Kristen Labazzo.
Rutgers, The State University of New Jersey

Introduction: Bone tissue scaffolds are frequently examined to repair skeletal trauma through cell and tissue development in 3D matrices. The body naturally features gradients in pore size within the human skeleton, and as such, researchers have investigated its effect upon bone cell differentiation (1). The current study employed a pore-size gradient using a combination of scaffold fabrication processes to observe the effects of pore size on cell viability, mobility, and differentiation (1). This was accomplished by introducing salt into multiple layers of electrospun scaffolds, which were then sintered together. SEM imaging was used to verify the structure, and the scaffolds were examined for their effects on cell viability and differentiation. Data may be used to create scaffolds to limit tissue development to prevent excess tissue growth after trauma or amputation.

Methods: PCL solutions were made and electrospun according to our previous work. Four types of scaffolds were fabricated based on salt size. The salt sizes ranged from a lack of salt pores to diameters of 100-300 µm, 300-500 µm, and 500-700 µm, crystal sizes were separated by sieve. Mats were then sintered together in an oven at 68 °C to produce triple-layered scaffolds of similar pore size, with an additional group composed of all three types of pore sized mats. The scaffolds were then tested for cytocompatibility using a viability assay on mouse calvarial osteoblasts, and for differentiation using an ELISA for osteocalcin.

Results: The results displayed good cell viability overall. Cell viability/metabolic activity increased after Day 7 in the scaffold groups, Figure 1. Trends in osteocalcin ELISA showed links between increasing pore size and increased concentrations., Figure 2. Unfortunately, these trends were not statistically significant due to large standard deviations. Similarities in viability data imply that this data is not due to a decreased number of adhered cells on scaffolds. Linking ELISA data and DNA later can validate the data.

Confocal microscopy was used to measure cell motility in the scaffolds. Trends were seen in average motility relative to pore size, but there was a lack of statistical significance due to relatively large standard deviations.

Conclusions: The present study showed a clear capability of the fabricated scaffolds to support cell viability, while also inhibiting differentiation. In future work, other parameters can be varied to examine the potential for increased cell migration, decreased bone cell differentiation, and enhanced degradation rates.

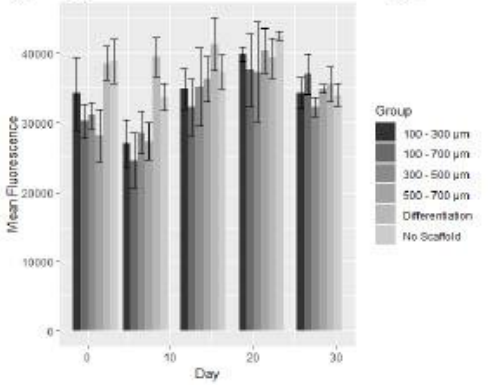

Figure 1: Cell viability measurements taken over the course of a month.

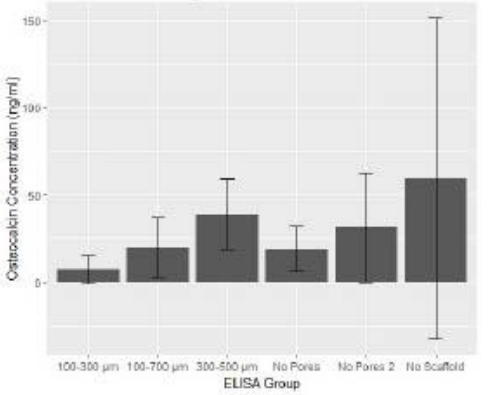

Figure 2: Osteocalcin concentrations per group collected on Day 21.

References:

1. Di Luca, Andrea, et al. *Scientific reports* 6.1 (2016): 1-13.

Acknowledgements: Rutgers Busch Biomedical Award

DEI: Using degradable scaffolds to limit cell movement and differentiation could limit heterotopic ossification or jagged bone growth after amputation which keeps overall costs down, making it affordable for a wide range of socioeconomic groups.

STEVENS
INSTITUTE OF TECHNOLOGY

Isolation and Characterization of Myogenic Proteins within Fertilized Egg Yolk

Michael Pellegrini, Don Angibou, Augustine George, N'Dea Wheeler, Lin Mai, Kirsten Barboza, Joseph Freeman PhD
Rutgers University New Brunswick, Biomedical Engineering

Introduction: Sarcopenia, or muscle wasting, is a condition that effects various populations such as: the elderly, cancer patients with cachexia, and various forms of muscular dystrophy[1]. The process of muscle wasting is caused by an increase in muscle catabolism, the breakdown of lean muscle mass, and a decrease in hypertrophy, the increase in size of existing muscle tissue through increased translation of muscle proteins or through the fusion of satellite cells[2]. One solution to the muscle loss is through a nutritional approach by ensuring that both the quality and quantity of ingested protein combats muscle catabolism. Egg yolk is considered a nutrient rich food that contains lipids and proteins that are beneficial to muscle hypertrophy. Discovery of myogenic compounds in egg yolk could lead to low cost, nutrient-based interventions for muscle wasting that would be economically attainable to all communities. We hypothesize that enrichment of bioactive egg yolk derived molecules will result in increased differentiation of myoblasts *in vitro* when used as an additive to culture media. Furthermore, we aim to identify such molecules through repetitive fractionation and tandem mass spectrometry.

Materials and Methods: Fertilized egg yolks were processed through centrifugation and addition of sodium alginate creating the following fractions: Granule, Lipid, and Aqueous. Fractions derived from granule portion were further separated using centrifugation and size exclusion chromatography (SEC) to produce subfractions. Fractions and subfractions were then analyzed for protein concentration and molecular weight through BCA assay and SDS PAGE. C2C12-MLC luciferase reporter cells were then differentiated in culture media supplemented with: Granule, Lipid, and Aqueous fractions. Similarly, cells were later cultured in differentiation media containing the subfractions from the granule fraction. Spent media collected from the cultured cells was then assayed for luciferase expression. Additionally, cells were stained for Actin and nuclei to visualize myotube formation. Pro-differentiation subfractions were processed using Liquid Chromatography-Tandem Mass Spectrometry (LC-MS/MS) to determine the peptide/protein composition by comparison of the resultant spectra to the database of proteins for *gallus-gallus domesticus*.

Results and Discussion: Luciferase Studies (figure 1A) indicate that the cell line is responding appropriately to the positive control, Insulin like Growth Factor-1 (IGF-1) with a significant increase in expression compared to the null control, 1% FBS media (labeled 1%). Three experimental groups show increased differentiation compared to the differentiation media control: both concentrations of the granule fraction additives and the low concentration of the lipidic fraction ($p<0.05$, Tukey post-hoc test). Images show the presence of myotubes in all groups (figure 1B). Further fractionation of the granule group by size using centrifugation and SEC yielded subfractions that show varying levels of differentiation with the lighter 2 subfractions (7k and S) showing significantly increased differentiation compared to the media control. SEC conducted on these two subfractions resulted in 8 peaks and 7 peaks in the 7K and S subfractions respectively determined by absorbance at 280 nm. Using these sub-subfractions as additives to cell culture media further selected for the subset of proteins responsible for increased differentiation. Comparison of these subfractions to a null subfraction in terms of their profiles on LC/MS-MS shows increased levels of several proteins of interest: Albumin, Gelsolin, Lysozyme C, Ovalbumin, and Phosvitin.

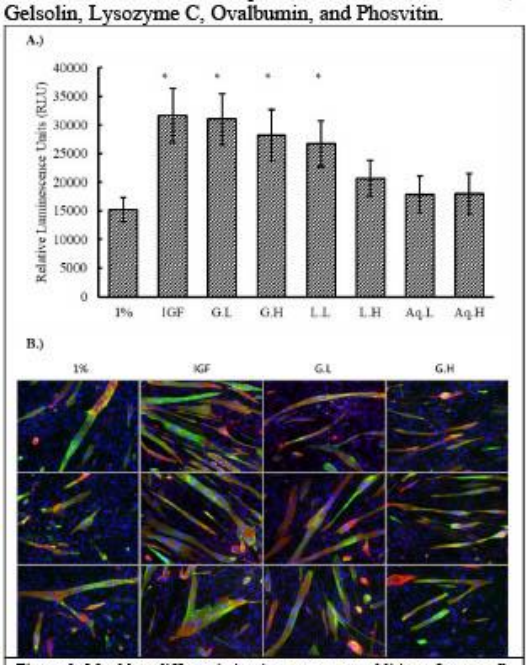

Figure 1: Myoblast differentiation in response to addition of egg yolk fractions to the media. **A)** Quantification of luciferase concentration in collected media G, L and Aq denote Granule, Lipid, and Aqueous fractions respectively. L and H represent the final concentration of each fraction in the cell culture media, 100 and 500 ng/ml respectively. **B)** Flourescence microscope images of myoblasts organized by group. Green: Actin, Blue: DNA, Red:Myosin Heavy Chain

Conclusions: There is a need to find myogenic compounds to combat sarcopenia. Compounds present the Granule fraction of fertilized egg yolk have a positive effect on muscle cell differentiation in vitro and therefore fertilized egg yolk provides a possible source for novel compounds to treat muscle loss. We have identified several subfractions within the granule fraction that promote differentiation of myoblasts and matched them to known proteins from the chick genome.

Acknowledgements: Funding Provided by MYOS Corp, Cedar Knolls NJ

References:

1. Morley J. E. et. al. JAMDA 2010 11(6) 391-396
2. Schiaffino S. et. Al. FEBS J. 2013 280(17) 4294-4314

STEVENS
INSTITUTE OF TECHNOLOGY

Real-time Monitoring of Biological Cells in a 3D Matrix

Ayda Pourmostafa[1], Anant Bahusual[2], Niranjan H. Menon[3], Sagnik Basuray[3], Amir K Miri[1]

[1] Biofabrication Lab, Department of Biomedical Engineering, New Jersey Institute of Technology (NJIT), Newark, NJ; [2] Department of Mechanical Engineering, Rowan University, Glassboro, NJ; [3] Department of Chemical and Materials Engineering, NJIT, Newark, NJ.

Introduction: Developing real-time analysis techniques for monitoring 3D organoid models will improve understanding of biological processes during tumor cancer progression. [1]. Current analysis techniques for 3D cell models rely on endpoint assays and fluorescent microscopy. Integrating the *in situ* monitoring method increases/improves the time resolution and continuous readouts [2]. Electrochemical impedance spectroscopy (EIS) has been applied as a label-free method for single-cell analysis and monitoring biological barriers developed in 2D cell structures. 3D bioelectronics based on biocompatible electroconductive polymers allow the application of real-time monitoring methods to understand cell-cell and cell-extracellular matrix (ECM) interactions. We propose using PEDOT:PSS, a tunable biocompatible conductive polymer, as an electrode-based material model for screening cellular environments. This will enable better integration with organoid models for personalized medicine. We can use durable and biocompatible hydrogel-based electrodes to monitor cell response under different conditions.

Methods: We optimized a protocol to create conductive inks to print inside the hydrogel-based microfluidic platform to help with real-time monitoring of cell behavior [3]. Doping particles of PEDOT:PSS into polyethylene-glycol-diacrylate (PEGDA) was optimized. The conductivity was measured using the four-probe method at different concentrations of conductive particles in the ink. The cyclic voltammetry performance of the conductive hydrogel was assessed within the -1 to 1-volt potential range in a buffer solution containing 1 mM [Fe(CN)6]3-/4- and 0.1 M KCl. Conductive hydrogel coated the electrodes. EIS was conducted in a dynamic range of 0.001-1 MHz, with an amplitude of 50 mV and 8-point averaging for different concentrations. In bioelectronics applications of conductive hydrogels, impedance biosensors were used for live cell sensing at GelMA concentrations similar to those *in vivo* ECM. We analyzed EIS data for 5, 10 and 15% GelMA to measure physical changes during swelling.

Results: Four-point conductivity measurement data indicated that the lowest value at 0.5% w/v and the highest at 5% w/v showed no predictable change in conductivity when varying the number of layers in the light-assisted 3D printing process (Fig. 1A). As expected, doping PEDOT:PSS in PEGDA showed lower impedance magnitude in (100-10000Hz) frequency, which shows the permittivity of the material, which changes by an increase in porosity (Fig. 1B). Increasing the PEDOT:PSS concentration exhibited a greater current response than Au electrodes, which shows an increase in charge interface between electrolyte and hydrogel electrodes (Fig. 1.C). The EIS results showed a decrease in impedance during swelling for GelMA within 24h (Fig. 1.D). EIS measurements related to PEGDA swelling did not show significant differences between 1h and 24h. The decrease in impedance value, associated with swelling, correlated with increased pore size of the hydrogel, indicating a higher ionic composition in the hydrogel's microstructure. Lower GelMA concentration exhibited a larger decrease in impedance; this aligns with our previous research, where we demonstrated that lower GelMA concentration results in increased porosity [4].

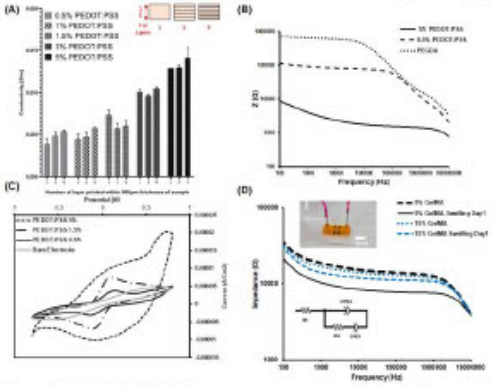

Figure 1. A) Conductivity measurement for different layer selections of conductive ink (PEDOT: PSS) in 3D printed samples, B) Impedance properties of Au bare electrode and our conductive ink, C) CV curve of the bare electrode and our conductive ink, D) Bode plot spectra of different gelatin-based ink concentrations during swelling.

Conclusions: We developed a bioelectronic platform that offers exceptional versatility for monitoring multiple biological parameters of 3D cell organoid models. The observed increase in impedance with cell density and change in ECM microscopic architecture has implications for the sensing of biological components. The correlation between cell density and impedance suggests that this system could be used as an online monitoring system during the remodeling of the 3D organoid models to analyze cell-associated ECM changes' responses to physical and electrical stimuli [5].

References: 582-590.; [1] A. Bhusal., et al. ACS appl bio mater,9 (2022): 4480-4492 [2] S, Achilleas, et al. Materials Horizons 10.9 (2023): 3589-3600. [3] D. Heo., et al, Mater Sci Eng C, 99 (2019): . [4] E. Dogan., et al. Front. Bioeng. Biotechnol. 11 (2023): 1193970. [5] L.Gong., et al. Small 17.21 (2021): 2007500.

Acknowledgments: A.K.M acknowledges NSF and NIH for this research. A.P. and A.B. have equal contributions to this work.

STEVENS
INSTITUTE OF TECHNOLOGY

Design of denovo self -assembling peptide hydrogels

Abhishek Roy, Joseph Dodd-o, Bobak Shadpoor, Vivek Kumar.
New Jersey Institute of Technology

Introduction: Self-assembling peptide hydrogels (SAPHs) have the unique characteristic of tunability, biocompatibility and versatility in different biomedical applications. These three-dimensional gels formed due to hydrogen bonding, electrostatic interactions and hydrophobic interactions form antiparallel β-sheets, which can be observed by various analytical tests such as circular dichroism (CD) and Fourier transform infrared spectroscopy (FTIR). These peptides (named New Candidate 1, 2, 3) consist of a sequence of amino acids which allows control over the gelation kinetics, mechanical characteristics and also biofunctionalization via attachment of a mimic domain from a larger growth factor help in various tissue regeneration and drug delivery applications. This proposed material based approach involving a new self-assembling peptide backbone which has been utilized over the past decade have shown promising results in angiogenic, neurogenic, and dentinogenic scaffold-based signaling

Methods: Peptide was synthesized using solid-phase peptide synthesis, and its purity and identity were confirmed via HPLC and MS. The structural characteristics of the peptide were determined using FTIR, CD, SEM and AFM. The bulk rheological testing was tested on the hydrogel samples at different concentrations. A CCK8 metabolic assay was performed where human umbelical vascular endothelial cells were cultured with peptide hydrogels at various concentration incubated in EBM2 supplemented with 2% FBS, with full media as a control. We have currently determined *in vivo* biocompatibility in a rodent model along with cellular infiltration and blood vessel on one of the candidates and are evaluation for the other sequences.

Results: The peptides containing fibrillizing domains, forms nanofibers which crosslink in three dimensions to form a hydrogel at 10mg/ml in phosphate buffer, like previous SAP platforms.[1, 2]. CD analysis confirms a combination of a β-sheeted content by 195nm peak and 215nm trough , further confirmed by FT-IR with a 1615 Amide I and 1530 Amide II peak. SEM imaging of critical point dried hydrogels reveals a porous sponge-like structure. Cytocompatibility on HUVECs at 8 hr condition media was confirmed via no statistical difference among the groups when compared to a full media control. The hydrogels were injected subcutaneously in a Wistar rat model where there was no signs of systemic or adverse side effects or tumorigenicity. There was infiltration of cells and development of collagen deposition around the bolus of one of the candidates.

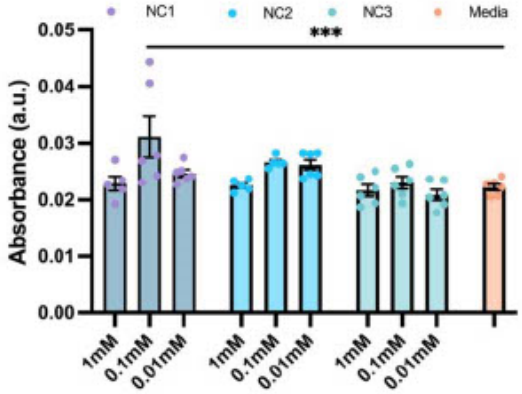

Figure 1. Cytocompatibility evaluation of the various constructs with HUVECs with CCK8

Conclusions: The self-assembling peptide hydrogel forms into antiparallel β-sheet secondary structure with a ECM mimetic.The shear recovery and thinning properties of similar hydrogels indicate that they can be syringe aspirated and injected. The cytocompatibility and the biocompatibility of the gel is proved via CCK8 assay(HUVECs) and subcutaneous implants(Wistar rats).

References:

1. Siddiqui, Z., et al., *Angiogenic hydrogels for dental pulp revascularization.* Acta Biomater, 2021. **126**: p. 109-118.
2. Roy, A., et al., *Self-Assembling Peptides with Insulin Like Growth Factor Mimicry.* ACS Appl Mater Interfaces, 2024. **16**(1): p. 364-375.

Acknowledgements: NIDCR R01DE031812(PI)| NIDCR R01DE029321 (Co-I)| NINDS R61NS127271(Co-I) | NIAMS R21AR077835 (MPI) | NIAMS R01AR080895 (Co-I)

DEI: Formulation of new peptide hydrogel from a manufacturing perspective, are attractive for cell-free synthesis, eliminating some of the inherent challenges associated with cell dependent synthesis in process variability and scalability. While there is a lot of scope and interest in the field, the only requirement in synthesizing and evaluating these peptide sequences is dedication and hardwork. This field can provide a wide range of involvement among the researcher around the world as well as the personnel who are interested in research also.

STEVENS
INSTITUTE OF TECHNOLOGY

Lymph node-on a Chip: Modeling Human Adaptive Immune Responses to Assess Vaccine Efficacy in Different Age Populations

Fanghao Shi, Weiqiang Chen
Tandon School of Engineering, New York University, Brooklyn, NY

Introduction: Lymph nodes (LN) are important hubs of adaptive immunity. Post-vaccination, dendritic cells (DCs) carry vaccine antigens to LN, where DCs induce $CD4^+$ T cell activation, naïve B cell differentiation into plasma cells and memory B cells, sustaining long-term immune responses (**Fig. 1 a**). However, aging alters LN niches, highlighting the need for research on adaptive immunity to improve vaccination strategies. Here, we developed a 'Lymph Node-on-a-Chip' system that simulates human LN structure and function, allowing for the study of adaptive immune responses and the evaluation of vaccines across different ages. This model aids in understanding how variations in the LN niche impact immunity, crucial for tailoring effective vaccines for diverse populations.

Methods: Our microfluidic LN-on-a-chip, crafted via soft lithography (**Fig. 1b**), incorporates PBMC-derived immune cells (T cells, B cells, DCs) from various donors (STEMCELL Technologies), replicating human LN architecture. T cells, fibroblastic reticular cells (FRCs), and HUVECs are placed in the paracortex, with B cells and follicular dendritic cells (FDCs) in the B follicle area. The FDC cell line (YK6) was isolated from discarded human tonsils as described in [1]. The biomimetic ECM hydrogel will be a mixture of fibrin (Sigma) and Matrigel (Corning). With the human seasonal influenza vaccine (ATCC BEI), we study adaptive immune responses on chip—antigen presentation, T cell activation, germinal center develop-ment, and antibody production—to develop a functional in-dex assessing vaccine efficacy across age groups.

Results: After seeding T cells, FRCs, and HUVEC into paracortical area, B cells and FDCs into B cell follicular area in the LN chip, we observed the formation of 3D blood vessels (HEVs) in the paracortical area on 7 day (**Fig. 1c**). Concurrently, we detected an increase in the concentrations of CCL19 and CCL21 in the culture medium. Im-munostaining revealed that the FRC stromal reticulum sup-ports vascular integrity and T cell attachment (**Fig. 1d**). Upon introducing ovalbumin (OVA) as an antigen stimu-lus, T cell migration along the FRC network significantly accelerated (Fig. 1e). Further experiments with the human seasonal influenza virus vaccine to trigger adaptive im-mune responses resulted in an enhanced differentiation of naïve B cells into $CD138^+$ plasma cells, alongside the emergence of germinal center-like structures (**Fig. 1f**). Subsequently, we loaded PBMC-derived immune cells from young (≤ 60 years) and elderly (> 60 years) donors. After vaccine antigen stimulation, the proportion of $CD138^+$ plasma cells in the young group was significantly higher than that in the elderly group (**Fig. 1g**), alongside significantly greater total IgG secretion in the young group's culture medium (**Fig. 1h**). This indicates that PBMC-derived immune cells from individuals of different ages exhibit varying abilities to respond to vaccine antigens. These findings suggest that the immune response to vaccine antigens varies with age, with younger individuals displaying a more robust adaptive immune response in our LN chip model.

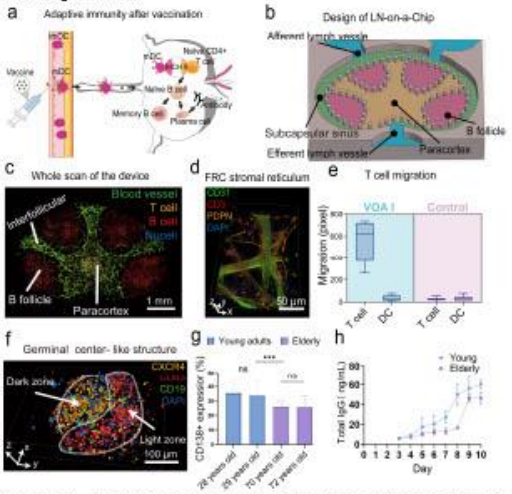

Figure 1. **a)** Scheme of immune function of human lymph nodes. **b)** Design, **c)** whole scan of LN chip. **d)** $CD3^+$ T cells, $CD31^+$ HUVECs, and $PDPN^+$ FRCs in the paracortex. **e)** Effects of OVA I-induced mDCs and imDCs (control) on T cell migration in the paracortex. **f)** Immunostaining image of germinal center-like structure formed in the B cell follicles upon vaccine antigen stimulation. **g)** $CD138^+$ plasma cells, **h)** total IgG secretion affected by human seasonal influenza virus vaccines in different ages on chip.

Conclusions: Overall, the current experimental results validate our model's ability to simulate the complex immune responses and stromal niches of LN in vitro. Our model's simulation of key adaptive immune responses (including T cell migration, B cell differentiation, and antibody secretion) within the LN demonstrates that delayed or attenuated adaptive immune responses in older populations are a significant factor contributing to the reduced vaccine efficacy.

References:

1. Rebecca Caeser, et al. ***Nat Commun***, 10, 4543 (2019).

Acknowledgements: This work was supported by the National Institute of Health (R35GM133646) and the Cancer Center Support Grant (P30CA016087) at the Laura and Isaac Perlmutter Cancer Center.

DEI: We prioritize DEI by studying how changes in the LN niche impact LN immune function in different populations (e.g., age, health status, race, gender, etc.), ensuring our "lymph node-on-a-chip" model advances inclusive vaccine research and development strategies.

STEVENS
INSTITUTE OF TECHNOLOGY

Development and Optimization of Mesoscale Lipid Nanoparticles for Nucleic Acid Delivery to Renal Epithelial Cells

Anastasiia Vasylaki[1], Ryan Williams[1].
[1] Department of Biomedical Engineering, The City College of New York.

Introduction: Increasing prevalence of acute and chronic kidney diseases poses a major problem in healthcare (*1*, *2*). Due to limited treatment options (*3*, *4*), there is a need for novel therapeutics that would efficiently accumulate in the kidneys and exert sufficient therapeutic effect. Selective targeting of the proximal tubular epithelial cells in the kidneys has been demonstrated with nanoparticles in the mesoscale size range (300 – 400 nm) (*5*, *6*). This drug delivery platform has the potential to improve therapeutic efficacy through increased accumulation of kidney therapeutics at the disease site, as well as reduced off-target effects. Moreover, nanocarriers enable delivery of biological molecules, which hold promise as the next-generation treatments. With the development of nucleic acid therapeutics, lipid nanoparticles have proven to be efficient carriers for easily degradable biological cargo (*7*). However, kidney targeting of mesoscale nanoparticles has thus far only been demonstrated with polymeric carriers. Hence, the purpose of this work was to develop a lipid-based mesoscale nanoparticle formulation, which can later be applied for targeted delivery of nucleic acids for kidney disease treatment.

Methods: Mesoscale lipid nanoparticles (MLNP) with siRNA cargo have been formulated with an ionizable lipid, a phospholipid, cholesterol, and a PEGylated lipid. Nanoparticles were prepared using the nanoprecipitation method. Briefly, varied amounts of lipids were dissolved in ethanol and added dropwise to the aqueous phase containing siRNA, NaCl, and sodium acetate buffer (pH=5.2) under magnetic stirring. After nanoparticle formation, the buffer was changed to PBS by overnight dialysis to neutralize the ionizable lipid charge. Modifications of the formulation composition and process parameters have been applied to optimize the nanoparticle size. MLNP size and polydispersity index were characterized via dynamic light scattering and zeta potential via electrophoretic light scattering. siRNA encapsulation efficiency was measured using a fluorescence-based RNA-quantitation assay. MTT assay has been applied to test the MLNP cytotoxicity.

Results: Five formulation modifications have been tested to obtain siRNA-loaded lipid nanoparticles with a size in the mesoscale range (Fig. 1). While all modifications resulted in an increase of nanoparticle size, MLNP with a size >300 nm have been produced through a combination of increased total lipid concentration, modification of lipid molar ratio, increased ion concentration, and modification of mixing parameters. To achieve the stable PEGylation required for kidney targeting (*5*), the lipid composition of MLNPs has also been optimized. MTT assay has demonstrated that treatment with the MLNP formulations encapsulating non-targeting siRNA and IL-6 siRNA has no effect on the viability of renal epithelial cells. Thus, the developed formulation is non-cytotoxic to renal epithelial cells and is suitable for further experimentation.

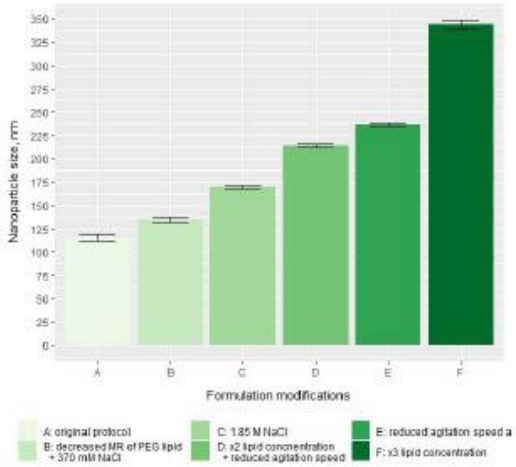

Figure 1. Lipid nanoparticle size as a result of various formulation modifications.

Conclusions: In the current work, we have developed a formulation of mesoscale lipid nanoparticles that has been optimized for targeted nucleic acid delivery to the renal epithelial cells. The MLNP formulation has demonstrated preliminary indications of safety, and additional *in vitro* and *in vivo* studies will be carried out to establish the efficacy of nucleic acid delivery to the renal cells.

References:

1. United States Renal Data System, "2022 USRDS Annual Data Report: Epidemiology of kidney disease in the United States" (National Institutes of Health, National Institute of Diabetes and Digestive and Kidney Diseases, Bethesda, MD, 2022).
2. Li P. K. T. et al. Kidney International. 2013. 83, 372–376.
3. Chen T. K. et al. JAMA. 2019. 322, 1294–1304.
4. Levey A. S. et al. Ann Intern Med. 2017. 167, ITC66–ITC80.
5. Williams R. M. et al. Nano Lett. 2015. 15, 2358–2364.
6. Williams R. M. et al. Hypertension. 2018. 71, 87–94.
7. Hou X. et al. Nat Rev Mater. 2021. 6, 1078–1094.

Acknowledgements: CCNY-MSK Partnership U54CA132378

DEI: Disparities in healthcare outcomes in kidney disease treatment could be improved by thorough consideration of genetic contributions to disease progression for patients with various racial and ethnic backgrounds and development of tailored therapeutics. Participation of STEM-underrepresented persons in the field could be increased through stronger community outreach initiatives.

STEVENS
INSTITUTE OF TECHNOLOGY

Self-assembling peptide hydrogels modulate Erk1/2 signaling in myoblasts for tissue regenerative application

Owen West, Abhishek Roy, Joseph Dodd-O, Corey Heffernan, Vivek Kumar.
Department of Biomedical Engineering, New Jersey Institute of Technology, Newark, NJ, 07102

Introduction: Peripheral Artery Disease (PAD) and diabetic wounds are clinically impactful maladies which require sufficient improvement of site-specific tissue regeneration to observe improved patient outcomes [1,2]. Self-assembling peptide hydrogels (SAPHs) are a notable biomaterial platform that is being studied to develop an off-the-shelf, injectable, localized, tissue regenerative therapeutic [1]. Advancements in SAPH design have produced growth-factor mimetic peptide sequences capable of increasing the resulting cell signaling when injected into the site of interest. The SAPHs studied here are K1 (a generic, non-bioactive, amphiphilic self-assembling peptide), SLIGF (K1 conjugated to IGF-1c, a mimic of Insulin-like Growth Factor), and SLan (K1 conjugated to QK, a mimic of Vascular-Endothelial Growth Factor-165). The sequences and corresponding receptor affinities are displayed in Fig 1A. We hypothesize that the growth-factor mimetic SAPHs will demonstrate tissue regenerative capabilities in a variety of applications, but specifically in the context of improving myogenesis and vascularization in the lower extremities. Preliminary signaling ability was assessed via a Western blot interrogating the relative phosphorylation of p44-42 MAPK (Erk1/2).

Peptide	Domain		Receptor Affinity
	Self-Assembling	Bioactive	
K1	KSLSLSLSLSLSLK	N/A	N/A
SLIGF	KSLSLSLSLSLSLK	GYGSSSRRAPQT	IGF-1R
SLan	KSLSLSLSLSLSLK	KLTWQELYQLKYKGI	VEGFR2

Figure 1. Peptide self-assembling domains, bioactive conjugates, and receptor affinity.

Methods: We designed and synthesized these tissue-regenerative hydrogels, incorporating both self-assembling and bioactive domains. After incubating ~90% confluent C2C12 myoblasts with peptides and control for 10 minutes, cell lysate was collected and electrophoresed. Upregulated Erk1/2 signaling was confirmed by calculating the ratio between total and phosphorylated Erk1/2 band intensity.

Results: We noticed only basal activity in myoblasts treated with the non-bioactive hydrogel K1. However, there is a marked increase in Erk1/2 pathway activation upon addition of either IGF-1R or VEGFR2 agonist domains.

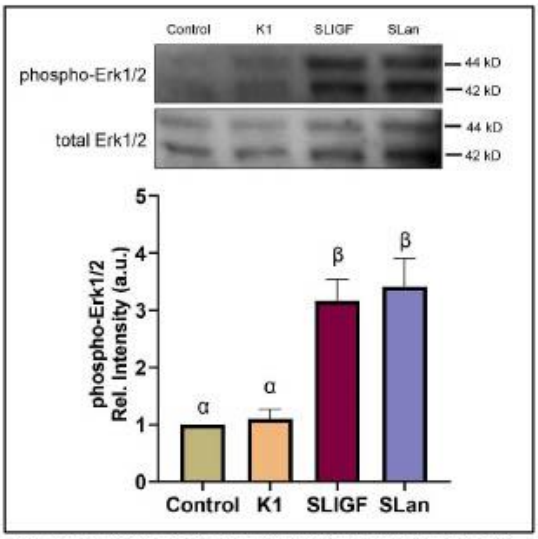

Figure 2. Upregulation of ERK1/2-related signaling in myoblasts. a) Representative Western blot showing bioactive-domain dependent increase in myoblast ERK1/2 signaling. b) Quantitation of n=2 blots. Different Greek letters indicate statistical significance (*$p < 0.05$).

Conclusions: We conclude that the conjugation of these short bioactive domains to SAPHs upregulates the proangiogenic and promyogenic Erk1/2 signaling pathway. The growth-factor mimetic peptides SLIGF and SLan, while still harboring the injectable scaffold characteristics of K1, show preliminary emergence of a "two-pronged" therapeutic ability. This is very promising in the context of future tissue-regenerative clinical application.

References:

1. Xiang, T *Adv. Healthc. Mater.* 13 (2024) 2301885
2. Golledge, J *Clin. Ther.* 45 (2023) 1077-1086

Acknowledgements: **NIDCR R01**DE031812 (PI) | **NIDCR R01**DE029321 (Co-I) | **NINDS R61**NS127271 (Co-I) | **NIAMS R21**AR077835 (MPI) | **NIAMS R01**AR080895 (Co-I)

DEI: Dr. Vivek Kumar and the KumarLab are strong proponents of undergraduate research programming and believe that continued support of undergraduate research involvement positively contributes to minority representation in STEM.

STEVENS
INSTITUTE OF TECHNOLOGY

Enhancing Functional Hepatocyte Cells for Developing a Human Brain-Liver-Gut Microphysiological System (MPS)

B. Whitman, R. Hinshaw, E. Cekanaviciute, C. Juran, M. Trapecar, E. Blaber
Rensselaer Polytechnic Institute

Introduction: In regenerative medicine, Microphysiological Systems (MPS) aim to revolutionize organ replication in vitro.[1,2] Here we focus on development of liver organoids, involving precise differentiation of human induced pluripotent stem cells (hiPSCs) to recapitulate liver funciton.[3] Crucial liver functions include drug metabolism and systemic metabolic homeostasis.[4] This work explores iPSC differentiation into hepatocytes, highlighting methodologies, key markers, and implications for liver physiology. We will explore the broader application of integrating these hepatocytes within MPSs to incorporate brain and gut components to emulate intricate multi-organ interactions in a controlled in vitro environment. MPSs offer a versatile tool for understanding human responses to stressors. This interdisciplinary approach promises transformative advancements in disease modeling, drug discovery, and personalized medicine in a concise manner.

Methods: Cell Culture and Hepatocyte Differentiation: iPSCs cultured on Matrigel-coated plates in mTeSR™ plus medium underwent passaging every 4-6 days using ReLeSR. Hepatocyte differentiation followed a stepwise protocol: iPSCs cultured in mTeSR™ plus medium until 80-90% confluency were induced into definitive endoderm using RPMI 1640 medium supplemented with 100 ng/mL Activin A and 2% B27 Supplement without insulin for 5 days. Subsequently, RPMI 1640 medium supplemented with 20 ng/mL BMP4, 10 ng/mL FGF2, and 2% B27 Supplement with insulin for 5 days promoted hepatic specification. Hepatoblast formation occurred via treatment with 20 ng/mL hepatocyte growth factor (HGF) and 2% B27 Supplement with insulin in RPMI 1640 for an additional 5 days. Finally, maturation and functionalization of hepatoblasts occurred in Hepatic Culture medium supplemented with 20 ng/mL oncostatin M for 5-10 days.

Characterization of Differentiated Cells: Cells were fixed and immunofluorescence stained for hepatocyte-specific markers, including alpha-fetoprotein (AFP) and albumin, using specific antibodies. Total RNA was extracted from both iPSCs and differentiated cells using a commercially available kit. Gene expression of hepatic markers (e.g., ALB) was assessed by quantitative reverse transcription-polymerase chain reaction (qRT-PCR). Hepatocyte functionality was evaluated by measuring albumin secretion and determining lipid accumulation by Oil Red O staining.

Results: The differentiation of iPSCs into hepatocytes yielded promising results, demonstrating the successful transition through distinct developmental stages. Immunofluorescence staining confirmed the acquisition of hepatocyte-specific markers, including alpha-fetoprotein (AFP) and albumin, underscoring the effectiveness of the differentiation protocol (Figure 1). Gene expression analysis via quantitative reverse transcription-polymerase chain reaction (qRT-PCR) revealed a significant upregulation of key hepatic markers, such as ALB, in the differentiated cells compared to undifferentiated iPSCs. Functional assays demonstrated enhanced hepatocyte functionality, as evidenced by albumin secretion compared to undifferentiated iPSCs. These findings collectively affirm the successful differentiation of iPSCs into functional hepatocytes, laying the groundwork for subsequent studies involving the integration of the long-term liver system with the brain and gut for comprehensive investigations into multi-organ interactions.

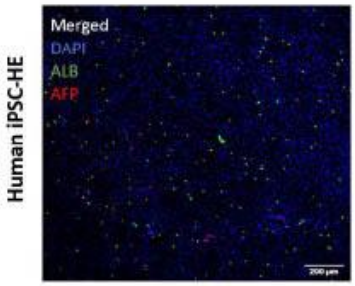

Figure 1. Fluorescence images of iPSCs cells stained to visualize the expression of alpha-fetoprotein (AFP) and albumin (ALB), indicating successful hepatocyte differentiation.

Conclusions: In this work we have successfully differentiated induced pluripotent stem cells (iPSCs) into hepatocytes, demonstrated by acquiring hepatocyte-specific markers and enhanced functionality, a significant step in our work developing long lived MPS organoids. Robust hepatic marker expression highlights clinical potential for use of iPSC-derived hepatocytes in drug development. Future work aims to refine differentiation protocols, integrate hepatocytes into 3D tissue models, and explore co-culture behavior with brain and gut organoids. These efforts enhance our understanding of multi-organ interactions, paving the way for innovative approaches in personalized medicine.

References:

(1) Marx, U. *PMC*. **2016.**
(2) Malik, M. *Front. Cell Dev. Biol.* **2021**.
(3) Takebe, T. *Nat. Protoc.* **2014**.
(4) Rhyu, J. *World J. Hepatol.* **2021**.

Acknowledgements: Grant Number: 80ARC023CA007/PO4200814457). We also appreciate the contributions of individuals in the Blaber's lab whose involvement significantly enriched this project.

DEI: In support of NEBEC's diversity initiative, MPSs show promise. They offer accurate disease models for diverse populations, improving the inclusivity of healthcare strategies. MPSs create opportunities for STEM-underrepresented individuals, fostering engagement and training. By incorporating diverse perspectives, MPS technology broadens participation and addresses health challenges in underrepresented communities, promoting equity in Bioengineering.

STEVENS
INSTITUTE OF TECHNOLOGY

A 3D Bioprinted Vascular Model

Swaprakash Yogeshwaran, Elvan Dogan, Daniel Ehab Gendy, Amir K Miri
Department of Biomedical Engineering, Newark College of Engineering, New Jersey Institute of Technology, Newark, NJ

Introduction: A blood vessel is organized into concentric layers with endothelial cells (ECs) organized in the core (tunica intima) and smooth muscle cells (SMCs) as the shell (tunica media). Some challenges with 3D bioprinted vascularized models have been the need for an abundant cell source and appropriate culture flow conditions. The major limitations observed in using vascular cells, such as umbilical vascular endothelial cells, are the quantity and proliferative potential of cells and their attachment to the inner wall. MSCs, as an alternate source, are among the most promising and suitable stem cell types for vascular tissue engineering. Physiological levels of shear stress have been known to promote the Endothelial differentiation of MSCs with alignment in the flow direction. Coaxial nozzle extrusion allows for the creation of a stiff wall for cell attachment. We have developed a novel 3D bioprinted double-layer vasculature model embedded in hydrogels.

Methods: Human bone-marrow-derived mesenchymal stem cells (hMSCs, Lonza Inc.) with fluorescent tags were seeded at a high cell concentration (5-10 M cells/ml) in a two-layer tube in gelatin methacryloyl (GelMA). The cell-laden structures were embedded in a gel construct and subjected to physiological levels of flow-induced shear stress (1-15 dyn/cm2) using appropriate cell culture media supplemented with VEGF (Lonza, 50ng/ml) for seven days. The effects of varying levels of flow-induced shear stress on MSC alignment and morphology were assessed using live/dead assay. We assessed the extent of endothelial differentiation by measuring specific biomarkers using immunostaining experiments and RT-PCR.

Results: The FRESH (Freeform Reversible Embedding of Suspended Hydrogels) method was adapted for GelMA as a support matrix for the co-axial extrusion of collagen-alginate double-layer microchannel fabrication (Fig 1A). The granular support matrix was then photocrosslinked to maintain tubing connections for our microfluidic chip models. The cell-laden alginate bioink was extruded as the shell, while the core comprised collagen (3-10 mg/ml). Collagen systems were effective in creating a lumen structure compared to other hydrogel systems, and combining the core-shell method using MSCs allowed for the creation of thick vascular linings. The MSCs were also more viable under flow conditions with elongation and alignment in the flow direction (Fig 1B). Phenotype expression assessment was done for stem cell surface markers (CD29 and CD44) and endothelial markers (Fig 1C), including platelet-endothelial cell adhesion molecule-1 (PECAM-1; CD31) and VE-cadherin (cell-cell junctions). The PCR result showed a decrease in the stemness markers underflow, while an increase in the endothelial markers was observed after seven days of flow-induced shear stress.

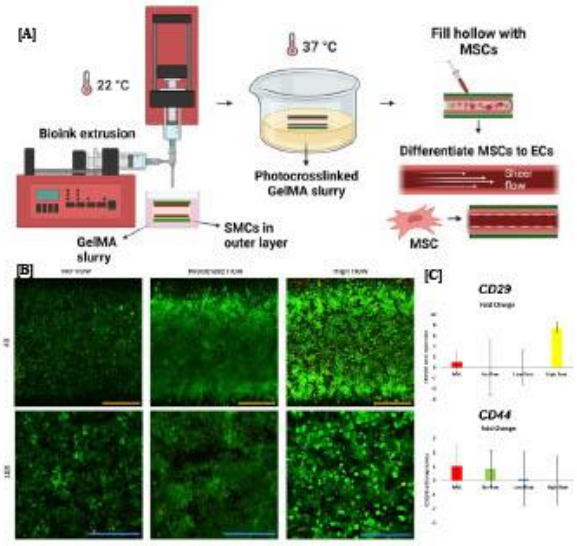

Figure 1. (A) Co-axial extrusion of collagen-alginate double layer channels for MSC seeding using FRESH bioprinting (B) Shear stress effects on MSC alignment and viability. Live/Dead (Calcein-AM) staining Live cells are represented in green, and dead cells in red. (C) RT-PCR for selected genes under flow and no-flow conditions. Scale bars: Orange- 1000 µm, Blue- 500 µm.

Conclusions: The FRESH method was optimized to make collagen channels embedded in granular GelMA structures using a multi-material bioprinter (BIOMAKER 3D, SunP Biotech, NJ), which led to the formation of hollow tubular structures at predefined shapes (300-800 um in diameter and 200-500 um in thickness). The optimization process also involved a large cell-seeding density and cell adhesion in the collagen-GelMA core-shell structures. The effect of varying levels of shear stress within physiological ranges was studied. The results showed that the cells were adhesive and proliferative under flow conditions. The MSCs were aligned and elongated in the flow direction and were more viable than static conditions. The RT-PCR data for selected genes showed that the MSCs could express endothelial markers under flow conditions, with increased biomarker expression under appropriate physiological conditions.

References:
1. Thomas J. Hinton et al. Sci. Adv.1,e1500758(2015).
2. Shiwarski DJ. et al. APL Bioeng. 2021 Feb 16;5(1):010904.
3. Reiprich, S. et al. Int journal of mol sciences, 22(6), 3123.

Acknowledgments: We acknowledge the support from NSF (2243506).

STEVENS
INSTITUTE OF TECHNOLOGY

Matrix-Bound Hyaluronan Molecular Weight as a Regulator of Dendritic Cell Immune Potency

Brian Chesney Quartey[1,3], Jiranuwat Sapudom[1], Mei ElGindi[1], Aseel Alatoom[1,2], Jeremy Teo[1,2,3]
[1] Division of Engineering, New York University Abu Dhabi, Abu Dhabi, UAE., [2] Department of Mechanical Engineering, Tandon School of Engineering, New York University, USA., [3] Department of Biomedical Engineering, Tandon School of Engineering, New York University, USA.

Introduction: Dendritic cells(DC) are a type of immune cell and are vital as they serve as the key intermediates between the innate and adaptive immune response(1). They are highly specialized for antigen presentation and hence able to scavenge tissues, recognize foreign antigens, process them and efficiently present them to T and B lymphocytes to activate the adaptive immune response. Increasing evidence suggests that the immune potency of dendritic cells are regulated by various biological factors, particularly the various components in the extracellular matrix. Among these different extracellular matrix molecules, is hyaluronan (HA), a glycosaminoglycan which has been shown to exhibit immunoregulatory properties. What makes HA interesting is that its immunoregulation is dependent on the molecular weight of the glycosaminoglycan(2). Under normal physiological conditions HA is synthesized by cells such as fibroblasts in high molecular weight forms. However, during certain pathological conditions such as in inflamed tissues, wound or cancer tissues, these high molecular weight HA may be broken down into smaller molecular weight fragments(. The impact of these different molecular weights of HA on DCs is not well understood. In this work we investigate how matrix-bound HA of different molecular weights impact cytokine binding properties of matrices, as well as how they impact DC differentiation and immune functions

Methods: To investigate DCs in defined biosystems, different molecular weights(MW) of HA (low molecular weight HA (LMW-HA;8-15kDa), medium molecular weight HA (MMW-HA; 500-750kDa), and high molecular weight HA (HMW-HA; 1250-1500kDa)) were immobilized onto 3D collagen matrices, maintaining similar microstructure and HA levels. Surface marker expression and cytokine secretion profiles of DCs in both mature and immature states were analyzed. immature DC antigen uptake capacity as well as migratory capacity of DCs were also analyzed to understand how HA MW impact DC immune potency.

Results: We found that MW of HA impacts the cytokine binding capabilities of matrices, indicating that HA MW may contribute to regulation of bioavailability of cytokines in tissues. Further, our results show that LMW-HA enhances immature DC differentiation and antigen uptake, while MMW-HA and HMW-HA increase cytokine secretion in mature DCs. The effect on DC phenotype and cytokine secretion by different MWs of HA is independent of CD44. However, blocking the CD44 receptor reveals its potential role in regulating acute inflammation through increased secretion of CCL2, CXCL8, and IL-6. Additionally, MMW- and HMW-HA matrices reduce migratory capacity of DCs, dependent on CD44.

Conclusions: Based on our findings, we propose a physiological model, suggesting that LMW-HA present in tissues during inflammation, injury and cancer, enhance immature dendritic cell functions by increasing their antigen uptake and migratory capacity(Figure 1). Upon maturation, DCs move towards lymphatic and nearby tissues containing MMW and HMW HA, where their functions are enhanced and motility is diminished. Overall, the fundamental knowledge obtained from this study provides insights into MW-dependent effects of matrix-bound HA on DCs, opening avenues for the design of DC-modulating materials to enhance DC-based therapy.

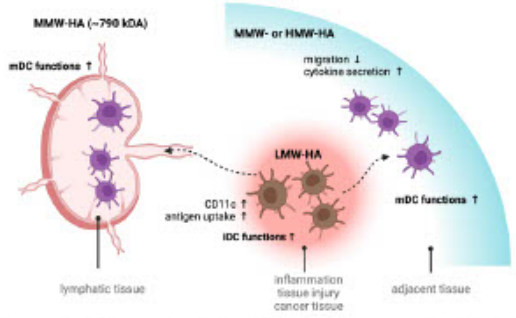

Figure 1: Schematic illustration of the proposed HA MW-dependent effect on DC immune potency. Image created with Biorender.

Acknowledgements: The authors acknowledge the support from the New York University Abu Dhabi (NYUAD) Faculty Research Fund (AD266). The authors would also like to acknowledge support from the NYUAD core technology platform.

References:

1. M. Y. Zanna et al. Int. J. Mol. Sci. 2021, 22, 8044
2. S. Garantziotis et al. Matrix Biol. 2019, 78–79, 1.
3. J. Sapudom et al. Biomater. Sci. 2020, 8, 1405.

DEI: To address healthcare disparities, Immunoengineering researchers can engage in community-based research, develop culturally sensitive technologies, and prioritize accessibility of innovations to marginalized populations. To broaden participation of STEM-underrepresented individuals, the field should implement outreach programs, offer scholarships, create inclusive academic environments, and establish mentorship initiatives for underpresented minorities.

STEVENS
INSTITUTE OF TECHNOLOGY

Bioinspired gradient scaffold fabrication for treating segmental bone defects

Erfan Sarhaadei, Qin Song, Jiaying Wang, Xiaojun Yu.
Biomedical Engineering department, Stevens Institute of Technology

Introduction: Human body is uncapable of healing so called above the critical size bone defects (5cm in case of femur or tibial bone). Annually, there are half a million patient with a cost of 2.5 billion US dollars. The gold standard to treat such defects is to use autografts which are normally bone taken from iliac crest at a cost of second surgery. Autografts are limited and lead to donor-site morbidity. Therefore, bone tissue engineering (BTE) became a method to compensate for these shortcomings. Many scaffolds have been designed for BTE applications, however, autografts could not be replaced by the new methods. There is need for improving the scaffolds designs and the best way to do it is to stick to bioinspiration method, meaning that trying to replicate the human body design. Hence, I tried to fabricate a bioinspired scaffold with gradient porosity which is detectable in long bones. It is especially designed for whole segmental bone defect (i.e., a whole 5cm length). Later I added electrospun fibers (aligned and random) in between the layers so that cells will be entangled between the nano-fibers.

Methods: we used 3D printing system (FlashForge Adventurer 4 Pro) to print strips of PLA with different ranges of pore sizes, and thicknesses. The strips were heated up to 60°C and rolled-up when it is soft under the heat. We were waiting for that to cool down and once it reached room temperature, we started to putting small amount of solvent on the outermost edge of the strip to close down the strip. In the case of strips with electrospun fibers, I attached the strips on the top of rotating drum and let the drum rotate at an specific speed while electrospinning system is attached to the drum and it is running simultaneously. This way aligned fibers were easily deposited on the top of the strips and later strips were rolled-up with extreme care. To analyze the morphology and structure of scaffolds, photos were taken from each scaffold group in different conditions including open strip and rolled up. We have used Revolve – Discover Echo microscope (Model: RVL2-K2), Confocal microscope (Olympus IX83) and Camera connected microscope (Nikon TS 100) to take images from open strips of scaffolds in microscope scales. General measurements were also conducted by using a caliper. By rolling up the strips, there are some gaps left between the strips. The porosity of the scaffolds was measured both in open strip by mathematics (based on volumetric measurements) as well as in Archimedes principal. The Young's modulus of each group (N = 3) was evaluated by Universal Testing Systems produced by Instron co. in compression condition. The load cell was 5kN, the loading speed was 0.5mm/min and the data were collected every 50 ms.

Results: structure and morphology of scaffolds were captured by normal photo-shooting camera. We found that all the scaffolds had a dimension of 10mm in height and 6.2mm in diameter in cylindrical style. The rest of the morphological analyses were handled by microscopes (e.g., Echo, camera connected and confocal microscope). Technically we can provide two types of photos for microscope images; first open strip style with no fibers, second open strip with fibers deposited on strips. We also found that by increasing the pore size, the porosity is also inclining. In case of the thinnest scaffold, although we had small gap size (in between the layers), the number of strip layer increased and that is the reason why we saw high porosity in comparison to all other groups except for group with highest porosity. According to the results, by increasing the pore size, Young's modulus decreases. Another important parameter is the strip thickness; by decreasing the strip thickness, indeed Young's modulus also plummeted as as the impact is obvious on thinnest scaffold group (0.15mm of thickness in design) and scaffold with highest porosity (0.2mm of thickness in design). Based on the results of porosity measurement and Young's modulus, we can determine that scaffolds with circular pores (1.21mm^2) with very large pores, acceptable porosity (54%) and close to bone Young's modulus (0.472 GPa) is an optimal candidate for further study (e.g., cell study). Cancellous bone porosity is between 75% to 85% and its Young's modulus has an average of 0.35GPa. Because of nutrition/waste exchange, it is very important to have acceptable porosity and that is why scaffolds with circular pores (Radius: 0.62mm) is a good candidate for bone regeneration. According to studies, a pore size ranging from 0.2mm to 1.2mm is optimal for bone regeneration. Gradient scaffold with small pores in the middle is also another good candidate since its Young's modulus is close to bone (0.455GPa) and its porosity is also acceptable (47.3%).

Figure 1. outermost structural view of scaffolds

Conclusions: the results from this study would be applicable for treating above the critical size bone defects, especially segmental bone defects since the design is representative of bone structure with gradient porosity. Many polymers such PLA using currently for designing these scaffolds would result in residues in blood or they are not bioabsorbable. It would be great if we could use bioabsorbable materials with similar mechanical properties.

Acknowledgements:

DEI: 1) It is essential to have communities similar to USA, participate more into healthcare system by paying more taxes, therefore, healthcare would be cheaper and affordable for people. 2) It is required to teach and include people with uncommon ethnicities to be within the western culture so that they would be more willing to participate in conferences and other communities of their field.

STEVENS
INSTITUTE OF TECHNOLOGY

Understanding Protein Adsorption on High Flux Hemodialyzers: Insights from Infrared Spectroscopy and Imaging

Suruthikha Vijay[1,2], Azita HassanMazandarani[2], Nancy Pleshko[2], Rouzbeh Tehrani[1], William Querido[2]
[1] Department of Civil and Environmental, [2] Bioengineering, College of Engineering, Temple University

Introduction: Chronic kidney disease affects more than 1 in 7 US adults every year and can ultimately lead to kidney failure or end stage kidney disease. The main treatment at that point is a kidney transplant, but if there are issues with transplantation, or while individuals are waiting for the transplant, hemodialysis is used. Hemodialysis is a procedure where an external machine aids in the removal of waste products from the blood and maintains healthy levels of essential minerals and proteins. Dialysis occurs by running both blood and dialysate, a cleaning solution, against each other in a dialyzer. The dialysate will pull waste materials out of the blood. The actual exchange occurs in hollow fibers present in the dialyzer. One main issue with dialysis is the inefficient retention or removal of certain proteins. In particular, it is important that patients retain healthy levels of albumin while effectively removing beta 2 microglobulin (B2M) [1]. This research investigates the possibility of using infrared spectroscopy and imaging [2] as a tool to visualize and understand the interactions between proteins and the dialyzer fibers.

Methods: Samples of unused Fresenius Optiflux dialyzer fibers (pure fibers), fibers that had come into contact with porcine blood simulating hemodialysis (used fibers), and pure bovine serum albumin (BSA) were collected and lyophilized. Bulk analysis was carried out by attenuated total reflection (ATR) Fourier transform infrared (FTIR) spectroscopy using an iS5 spectrometer (Thermo Scientific) with a resolution of 4 cm^{-1} and 32 scans. For FTIR imaging, the fiber samples were embedded in optimal cutting medium (OCT) and cross-sections were obtained via cryosectioning. Hyperspectral images were obtained using a Spotlight 400 (PerkinElmer) microscope with a resolution of 8 cm^{-1}, 2 scans, and pixel size of 6.25 micrometers. Spectral data were processed using the Unscrambler X and ISys software.

Results: ATR-FTIR spectra showed spectral differences between pure and used dialyzer fibers based on the presence or absence of specific absorbance bands. The primary band identifying the dialyzer fiber was seen at 1584 cm^{-1}, arising from the benzene ring in the polysulfone fiber membrane. In the used fiber, the spectra showed an additional band at 1660 cm^{-1}, which arises from the amide I (C=O) bonds in proteins and was typical in the spectra of BSA. In addition, a method for embedding these samples and obtaining cross-sections has been established and utilized in order to obtain FTIR images. Imaging the distribution of the protein content relative to the dialyzer fiber (1660/1584 peak intensity ratio) further showed that the proteins adsorbed to the used fibers were primarily located on the internal side of the hollow fibers (Fig. 1). Moreover, quantitative comparison of the FTIR image data showed that the protein content was significantly higher in the used fibers ($p < 0.05$, t-test).

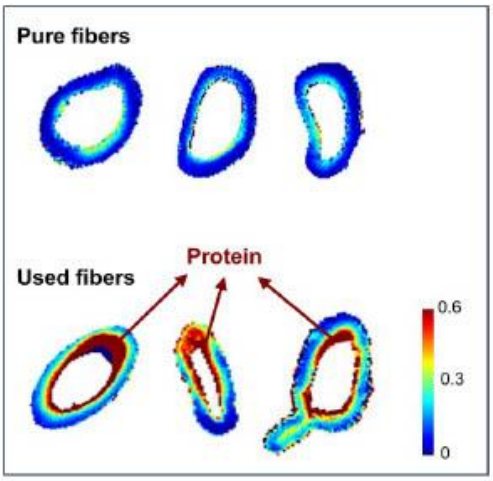

Figure 1. FTIR spectral images of the relative protein content (1660/1584 peak intensity ratios) in pure and used dialyzer fibers.

Conclusions: FTIR spectroscopy and imaging are promising approaches for understanding protein adsorption on high flux hemodialyzers. Our results show that upon use for hemodialysis, proteins are adsorbed to dialyzer fibers, primarily to the internal side closest to the fiber lumen in which blood flows through. Future work will focus on using spectroscopy and imaging to identify and distinguish the absorption of albumin and/or B2M to the fibers, as well as to better understand the distribution of these proteins across the fiber wall. This study and future studies can pave the way for developing new techniques to study the effectiveness of various nanomaterials in the efficient retention of essential proteins and electrolytes or the removal of waste products from the blood.

References:

1. Kalantar-Zadeh et al. Int J Nephrol Renovasc Dis. 2021
2. Querido et al. Molecules. 2021.

DEI: African Americans are currently three times more likely to have kidney failure than White Americans while Hispanics are 1.3 times. Innovative research into optimizing the effectiveness of hemodialysis may improve disparities in healthcare outcomes by advancing the development of personalized options for dialyzers.

STEVENS
INSTITUTE OF TECHNOLOGY

Functionalized SWCNT-Aptamer Sensors for Selective Dopamine Detection: Exploring Selectivity and Sensitivity.

Hanan Yafai, Ryan M. Williams.
Department of Biomedical Engineering, The City College of New York, New York, NY 10031

Introduction: Neurotransmitters function as critical chemical messengers, facilitating communication among neurons in the brain and nervous system.[3] Dopamine (DA), a crucial catecholamine neurotransmitter, regulates movement, cognition, and emotions.[3] Dysregulated DA levels are linked to neuropsychiatric disorders, highlighting the need for precise monitoring to enable early detection. Existing methods are invasive, time-consuming, and inaccurate, prompting exploration of novel approaches. This study investigates single-walled carbon nanotubes (SWCNTs) as building blocks for DA sensors. SWCNT-based nanosensors offer advantages like near-infrared (nIR) fluorescence, photostability, and sensitivity. We explore SWCNT-aptamer sensors, where aptamers (short single-stranded DNA molecules obtained through selection process known as SELEX) are functionalized around SWCNTs to enhance DA selectivity. Addressing the limitations of traditional methods lacking spatial, temporal, or chemical resolution, SWCNT-Aptamer sensors aim to present a solution with high spatial and temporal precision. We employed a literature-selected aptamer with high DA affinity, optimized its compatibility with SWCNTs, and characterized and analyzed the conjugated sensor's response to DA.

Methods: For sensor and control preparation, a DA aptamer and (GT)10 control were prepared by suspending 0.5 mg HiPCO SWCNTs (NanoIntegris, Boisbriand, Quebec, Canada) and both DA aptamer and (GT)10 single-stranded DNA (10 g/L, Integrated DNA Technologies, Coralville, IA, USA) in a 2:1 oligonucleotide-to-SWCNT mass ratio in 1X PBS solution. The solution was probe-tip sonicated then ultracentrifuged to remove impurities and residual catalyst (58,000 × g, 1 hr, 4 °C) in an Optima MAX-XP (Beckman Coulter, Indianapolis, IN, USA). To eliminate unbound DNA, the remaining solution was filtered through a 100 kDa molecular weight cutoff filter (Millipore Sigma, St. Louis, MO, USA). Remaining (GT)10-SWCNTs in the filter were resuspended in 1X PBS (100-200 µL). The final solution was characterized by absorbance spectroscopy using a V-730 UV-VIS spectrophotometer (JASCO, Easton, MD, USA) to determine concentration. Fluorescence response of DA Aptamer and (GT)10-SWCNT sensors to dopamine was analyzed using the NS MiniTracer NIR spectrometer (Applied NanoFluorescence, TX, USA). Fluorescence peaks were assigned to SWCNT chiralities based on literature data. MATLAB was used for pseudo-Voigt model fitting to determine the center wavelength and intensity of the (7,5) E11 chirality peak.[4]

Results: Our findings affirm the efficacy of our sensor in detecting dopamine. The (GT)10-SWCNT sensor exhibited sensitivity to dopamine, with varying levels. Notably, at time point 0, the Aptamer+dopamine group displayed a higher initial intensity increase (352%), while the GT10+dopamine group exhibited a lower initial intensity (257%). A sustained intensity decrease was observed in both groups over time after the 30-minute mark until reaching baseline.

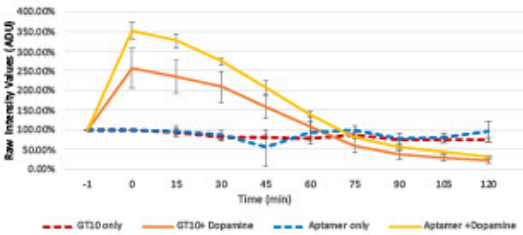

Figure 1. SWCNT (7,5) Normalized Fluorescence Intensity

Conclusions: The observed rapid fluorescence increase in the DA aptamer group upon initial dopamine binding suggests specific interactions. However, limited binding sites or faster dissociation may account for the subsequent intensity decrease over time, ultimately reaching baseline. In contrast, the GT10 sequence, with a potentially slower initial binding, may facilitate continuous dopamine interaction or accumulation, resulting in a more prolonged intensity increase. The next steps involve assessing the aptamer's ability to discriminate dopamine against other catecholamines like norepinephrine and epinephrine offering valuable insights into its specificity. Additionally, exploring the sensor's response across a wider dopamine concentration range will elucidate its sensitivity and dynamic range, aiding in optimization for various physiological contexts. SWCNT- Aptamer based sensors hold significant promise for dopamine detection, although further research is needed to refine aptamer selection and sensor optimization to achieve high specificity.

References

1. Polo E, Kruss S. Anal Bioanal Chem. 2015; November 19. [https://doi.org/10.1007/s00216-015-9160-x]
2. Zhao T, Wang JW, Zhang HS, Zheng X, Chen YP, Tang H, Jiang JH. Development of Dual-Nanopore Biosensors for Detection of Intracellular Dopamine and Dopamine Efflux from Single PC12 Cell. November 4, 2022. [https://doi.org/10.1021/acs.anachem.2c04050]
3. Hyman SE. Curr Biol. 2005;15(5):R154-R158. [https://doi.org/10.1016/j.cub.2005.02.037]
4. Cohen Z, Parveen S, Williams RM. ECS J Solid State Sci Technol. 2022;11(10). [https://doi.org/10.1149/2162-8777/ac9929]

Acknowledgements: This work was supported by NIH Grant R35148233.

DEI: Future research efforts in neurotransmitter sensing biotechnologies must prioritize affordability and accessibility to bridge healthcare disparities and ensure equitable access to this potentially life-changing technology for all individuals, regardless of their socioeconomic background. To diversify the STEM workforce, we must actively engage underrepresented groups through outreach programs and create inclusive research environments that welcome and retain talent from all backgrounds.

Periaqueductal Connectivity in SCI Induced Pain Using Resting State fMRI

Emily Johannan, Omid Shoraka, Shreya Mandloi, Angela Gallagher, Daniel Mattera, Sara Thalheimer, Hsiangkuo Yuan, Dr. James Evans, Dr. Joshua Heller, Feroze B Mohamed, Dr. Ashwini Sharan, Dr. James Harrop, Laura Krisa, Dr. Mahdi Alizadeh
(Jefferson Integrated Magnetic Resonance Imaging Center (JIMRIC); Thomas Jefferson University, Philadelphia)

Introduction: PAG, or periaqueductal gray is a region of gray matter known to play a critical role in the descending pain modulation system. Despite knowledge on PAG's role in pain modulation, little is known about its functional connectivity. This study aimed to determine how functional connectivity patterns differed in spinal cord injury (SCI) patients compared to HCs. Studying areas of functional connectivity would provide deeper anatomical and physiological understanding of PAG, as well provide information on the PAG's role in the development and prolongation of pain in patients with chronic pain.

Methods: Resting state fMRI scans were performed on 10 HC and 10 patients with SCI induced neuropathic pain using 3T Philips Ingenia scanner with a dedicated 32 channels head coil. Of the 10 SCI patients, 7 experienced medium to severe pain levels, and 3 experienced mild to no pain. Seed-to-voxel analysis was performed with PAG as the seed region. A voxel threshold p value set of .05 was used, with the results corrected for multiple comparison using fdr with the significance level set at .05. Age and gender were used as confounding variables.

Results: The location and size of clusters are shown for HC vs SCI patients with pain for Figure 1 and for SCI patients with pain vs those without in Figure 2. Significant clusters (areas) synchronized with PAG Blood-oxygen-level-dependent (BOLD) signal time series when comparing HC vs SCI patients with pain, and SCI patients with pain versus no pain were analyzed. We observed various significant areas among those developed pain versus those without including thalamus, cingulate and frontal lobe.

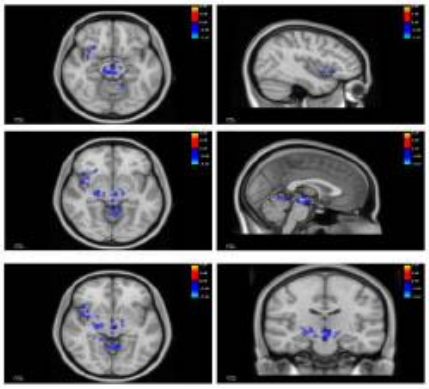

Figure 1. 2. Sections indicate regions containing clusters with negative FC (cold) in SCI patients with pain vs HC group

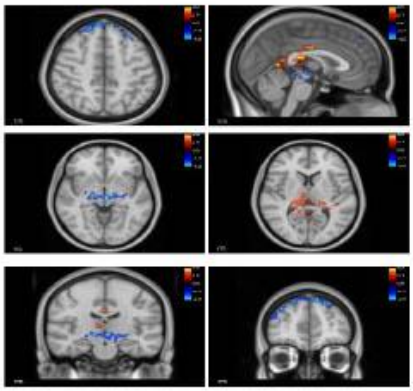

Figure 2. Sections indicate regions containing clusters with positive FC (hot) and negative FC (cold) in SCI patients with pain vs those without

Conclusions: Clusters present in several regions in both the HC and SCI group indicate altered PAG functional connectivity. Establishing these differences in functional connectivity elucidates a deeper understanding of how dysfunction in the interaction between these regions can contribute to the pathology of chronic pain. The PAG acts as a functional interface, and deeper understanding of its interactions in patients with spinal cord injuries will require continued research. Further studies will be needed to provide understanding on the significance of these differences and if they are specific to SCI induced neuropathic pain.

References:

1. Benarroch EE. et al. Neurology. 2012;78(3):210-7
2. Heinricher MM. et al. ScienceDirect Topics. 2008
3. Heminton KS. et al. J Neurophysiol. 2015;114(4):2080-3
4. Kong J. et al. Behav Brain Res. 2010;211(2):215-9.
5. Yu R. et al. 2014;6:100-8 NeuroImage Clin.
6. Cheriyan J. et al. J Neurosci. 2018;38(20):4829-4839
7. Huynh V. et al. 2021;42(12):3733-3749

DEI: Ongoing disparities within the field of imaging require professionals to prioritize recruiting a diverse pool of subjects to ensure comprehensice and representative healthcare, and to share experiences with current youth to expose them to possible career paths.

STEVENS
INSTITUTE OF TECHNOLOGY

Automated Femur Landmark Detection: Optimizing Surgical Alignment Evaluation

Marzieh S. Saeedi-Hosseiny[1], Aziza L. Jadallah[2], Mohammad H. Abedin-Nasab[3].
1. Electrical and Computer Engineering Department, Rowan University, 2. Virtua Health College of Medicine and Life Sciences, Rowan University, 3. Biomedical Engineering Department, Rowan University

Introduction: Surgical intervention is often required for femur fractures due to trauma, necessitating precise femur alignment amid significant muscular forces [1,2]. However, the current orthopedic approach relies on manual alignment, leading to additional soft tissue damage and frequently inaccurate positioning [3,4]. Moreover, the dependence on two-dimensional X-ray images limits surgeons' ability to accurately visualize the femur's position during surgery, contributing to intraoperative planning and alignment challenges. To tackle these constraints, we propose employing a U-Net model to identify crucial femur landmarks using X-ray images. These identified landmarks serve as pivotal elements for evaluating anatomical alignment intraoperatively and furnishing the necessary data to guide any surgical robot in manipulating the bone fragments to attain precise alignment [5,6]. This approach enhances surgical precision, addressing the limitations of manual alignment and X-ray visualization.

Methods: A neural network was trained to identify specific femur landmarks in fluoroscopy, utilizing the FracAtlas dataset [7] for training. FracAtlas is a publicly available dataset containing over 4000 high-quality anonymized X-ray images and annotations of both fractured and intact upper and lower extremities. Ground truth two-dimensional segmentation masks, established by a domain expert, provided the foundation for our study. The authors selected leg and hip X-ray images for annotation, categorizing them based on X-ray view (frontal or lateral) and bone area (hip and knee). Subsequently, the images were uploaded to the Computer Vision Annotated Tool (Intel, USA), where a domain expert created ground truth segmentation masks. Segmentation labels were based on anatomical landmarks including the femoral neck axis, epicondylar axis, femoral shaft, and condylar axis. These landmarks were selected for their utility in calculating femoral length and rotation to improve intraoperative alignment assessment. Uniquely, we identified the epicondylar axis on frontal X-rays, which is traditionally assessed using 3D imaging modalities [8]. Leveraging the created dataset, we tailored a U-Net model with a MobileNetV2 backbone to extract crucial features. The model was then trained to autonomously segment the specified femur landmarks with high precision. Evaluation of our model's performance was carried out using dice score and intersection over union (IoU) metrics.

Results: In this study, 560 anterior-posterior (AP) X-ray images focusing on the hip and knee region were annotated with ground truth segmentation labels and anatomical landmarks according to our specific approach. Utilizing this dataset, the U-Net model underwent training, yielding mean dice coefficients and intersection over union (IoU) scores for the simultaneous segmentation of the femur shaft, neck, epicondylar, and condylar axes. The achieved scores were 0.87 and 0.85, respectively. Furthermore, a novel method leveraging these bone axes was introduced to measure alignment.

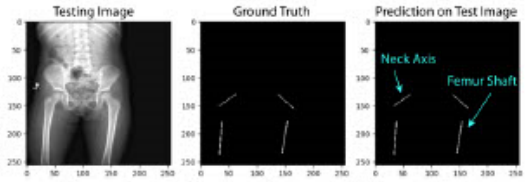

Figure 1. The landmark segmentation results.

Conclusions: We address a critical gap in the literature by focusing on femur landmark segmentation, specifically in the hip and knee areas, essential for assessing correct alignment during femur fracture surgery. Our investigation represents a focused effort to achieve this segmentation task, utilizing a well-established U-Net model with a MobileNetV2 backbone. This methodology enables accurate and automated segmentation of femur landmarks, offering potential improvements in intraoperative alignment assessment. Moreover, the segmented landmarks hold promise in guiding surgical robots for automatic alignment and facilitating manual surgeries by providing essential measurement tools for assessing femur alignment intraoperatively.

References:

1. Jaarsma RL, *JOT*. 2004;18(7):403-409.
2. Gosling T, et al. *MBEC*. 2005;43(1):115-120.
3. Oszwald M, et al. *J. Orthop. Res.* 2008;26(12):1656-1659.
4. Hawi N, et al. *Technol Health Care*. 2012;20(1):65-71.
5. Saeedi-Hosseiny MS, et al. *EMBC*. 2021:3301-3304. doi:10.1109/EMBC46164.2021.9630866
6. Saeedi-Hosseiny MS, et al. *IEEE RA-L*. 2023;8(5):2438-2445. doi:10.1109/LRA.2023.3251198
7. Abedeen I, et al *Sci Data*. 2023;10(1):521. doi:10.1038/s41597-023-02432-4
8. Scorcelletti M, et al. *J Anat*. 2020;237(5):811-826. doi:10.1111/joa.13249

Acknowledgments: This work was supported in part by the National Science Foundation (NSF) under Grants 2141099 and 2226489.

DEI: By addressing the limitations of femur alignment assessment, this work contributes to improving access to high-quality healthcare for diverse populations, particularly in remote or rural areas. This work promotes interdisciplinary collaboration and inclusivity in STEM through innovative femur landmark segmentation methods, encouraging participation from underrepresented individuals in medical technology development.

STEVENS
INSTITUTE OF TECHNOLOGY

Scaffold Surfaces Modified by Peptide-Loaded Polyanionic Microgels Resist Bacterial Colonization

Yunhua Guo,[1] Zhuozhuo Yin,[2] Christian Buckley,[2] Hongjun Wang,[2] Matthew Libera,[1*] Ryan Isber,[3,4] Esther (Hayeon) Kim, [3,4] Nicole Gill, [3,4] David G. Davies,[3,4] Cláudia N. H. Marques,[3,4] and Karin Sauer [3,4,*]

[1] Dept of Chemical Engineering & Materials Science, Stevens Institute of Technology, Hoboken, New Jersey, USA. [2] Dept of Biomedical Engineering, Stevens Institute of Technology, Hoboken, New Jersey, USA. [3] Department of Biological Sciences, Binghamton University, Binghamton, New York, USA. [4] Binghamton Biofilm Research Center, Binghamton University, Binghamton, New York, USA

Introduction: Tissue engineering typically uses a temporary scaffold to define the tissue structure while providing instructive cues to drive the recruitment, proliferation, migration, and differentiation of tissue cells. The development of temporary scaffolds for tissue engineering has thus far concentrated almost exclusively on their healing properties. There has been little focus on the competing problem of scaffold-associated infection. However, resorbable tissue-engineering scaffolds are just as susceptible to infection as their permanent non-resorbable counterparts, such as hip and knee prostheses, among many others. Anticipating the compelling challenges that scaffold infection can introduce, we are exploring how to modify the surfaces of resorbable scaffolds in a manner that preserves their important healing properties and simultaneously inhibits bacterial colonization.

Materials & Methods: 3-D printed PCL filament scaffolds (~100 µm diameter and ~300 inter-fiber distance) were primed by poly(allyl amine) (PAH). Poly(acrylic acid) (PAA) microgels (~10 µm diameter) were then electrostatically deposited onto the PCL surfaces. The microgels were then loaded with cationic Sub5 antimicrobial peptide (AMP) *via* complexation. In parallel we have developed *in vitro* methods to contaminate a biomaterial surface by a burst exposure to bacteria. Bacteria (*P. aeruginosa* and *S. aureus*) were diluted to the desired CFU concentration and then incubated with the scaffolds to mimic hematogenous contamination (Sub5-loaded; non Sub5-loaded, control) for two hours in a CO_2 incubator. The scaffolds were then plated to determine the rate of bacterial attachment.

Results and Discussion: As shown in **Fig. 1**, Sub5-loaded PAA microgels were successfully deposited onto the PCL surface. In our initial experiments, unmodified PCL surfaces immersed in DMEM medium supplemented with 10% fetal bovine serum under a 5% CO_2 atmosphere at 37 °C, were inoculated with 10^1-10^4 CFU. After 1 h, *P. aeruginosa* showed significantly increased attachment

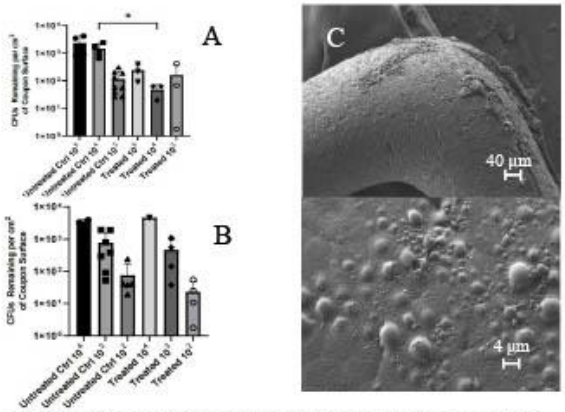

Fig.1 (A) S. aureus survive result (B) P. aeruginosa survive result.(C) Sub5-loaded PAA microgel on PCL coupon relative to *S. aureus*. The attachment rate is ~4% for *P. aeruginosa* and less than 0.5% for *S. aureus*.

Conclusions: We successfully deposited PAA microgels on PCL scaffolds and then loaded them with Sub5 AMP. Bacterial challenges indicate that modified PCL scaffolds resist colonization. Those few bacteria able to colonize the modified scaffolds might be the result of uneven microgel coverage. This can be overcome by further engineering the microgel deposition process. Ongoing studies focus on the cytopcompatibility of the modified PCL surfaces.

References:

[1] Xiao, X., Ji, J., Zhao, W., Nangia, S., & Libera, M. (2022). Salt Destabilization of Cationic Colistin Complexation within Polyanionic Microgels. Macromolecules, 55(5), 1736-1746.

[2]Liang, J., Wang, H., & Libera, M. (2019). Biomaterial surfaces self-defensive against bacteria by contact transfer of antimicrobials. Biomaterials, 204, 25-35.

Acknowledgements: This research project was supported by NSF GCR Grant (NSF # 2219014).

DEI: The field of Bioengineering directly benefits from the inclusion of engineers and scientists from various and underrepresented backgrounds. This can be further promoted by funding programs to provide STEM education to economically-challenged regions, and improving access to quality healthcare for people of all background。

Junior Faculty Innovator

High-throughput manufacturing of Hydrogel-Based Microfluidic Devices for Screening Applications

Amir K. Miri

Advanced Biofabrication Lab, Department of Biomedical Engineering, New Jersey Institute of Technology (NJIT), Newark, NJ 07102.

Introduction: Two-dimensional (2D) cell monolayers and 3D cell-based models lack the main features of the native tumor microenvironment (TME), and they cannot recapitulate complex biochemical and biophysical factors in the native tissue. The gold-standard animal models also suffer from ethical issues and human genetic background. Organ-on-a-chip approaches based on microfluidic technology have been introduced for drug screening and studying tumor mechanisms. Microfluidic technology provides easy liquid handling and relevant physiological cues in a controlled environment. The conventional microfluidic fabrication approach is cost ineffective, labor-intensive, complex, and requires additional steps to integrate accessories such as gradient generators for drug components. This study aims to rapidly manufacture cell-laden hydrogel-based microfluidic chips while creating chemical gradients and improving the capacity for anti-cancer screening applications [1, 2].

Methods: The hydrogel-based microfluidic chip consisted of two integrated, 3D bioprinted parts: I) cell-laden gelatin methacryloyl (GelMA) part to create TME, and II) polyethylene-glycol diacrylate (PEGDA) to provide stability and encasement. The GelMA forms the bioreactor core, and it can encapsulate cells. To create the microfluidic chip, we used a digital light processing (DLP) based multi-material 3D printer [1]. The design has eight bioreactors in a circular pattern toward high-capacity screening platforms. We used a human tumor cell line (fibrosarcoma HT1080) to test our design and then varied the bioink concentration to obtain an optimized cellular functionality. Viability analysis applying Cell Proliferation Kit II (XTT) and Lactate Dehydrogenase (LDH) assay for up to three days was performed. We also assessed the stiffness of the cell-laden part. Then, we applied a set of an established drug (Doxorubicin) in the device, and live/dead imaging was used to validate the drug testing.

Results: The bioprinting approach was used to create a microfluidic chip while the metallic connections were used to provide a culture media, as shown in **Fig. 1A**. Our device houses a cell-laden bioreactor strategically within the support structure (up to eight bioreactors) as shown in **Fig. 1C**. The GelMA concentration was between 5% and 7% w/v. Each bioreactor was connected to the main input (single input), and the microchannels were strategically designed to create a set of drug doses by transporting drugs into cell media. This is demonstrated by diluting two different color liquids at the end of the outlet in **Fig. 1B**. Doxorubicin was then introduced in the device at different doses (from 1 to 8 µg/ml) for at 1 hr of exposure to the cell-laden parts. The live/dead assay results are shown in **Fig. 1D**, indicating a higher cell death at the higher dose of DOX.

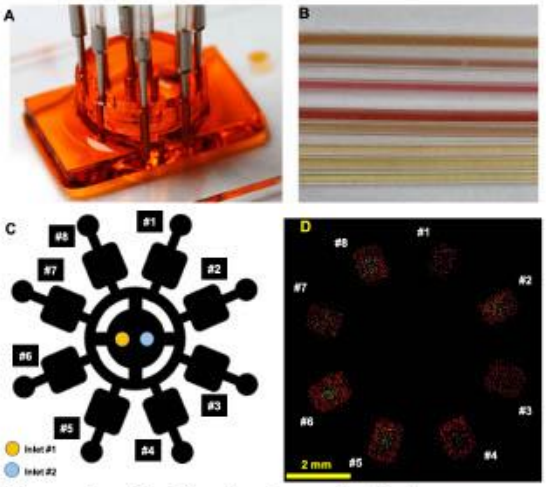

Figure 1: A) Circular dose (gradient) generator microfluidic chip with eight culture chambers, B) Different colors at the outlet tubes, C) Illustration of circular dose (gradient) generator with possible eight culture chamber, and D) Live/dead imaging of eight samples after 1 h of DOX 1 (1 to 8 µg/ml) exposure to eight bioreactors in a single microfluidic chip. (the scale bar is 2 mm).

Conclusions: This study provides a benchmark for creating bioprinted screening chips to test drugs and other biological chemicals against any target tumor cells with a capacity to scale up (to maybe 10-20 doses simultaneously). We can test various cell types and translate them into multi-cellular models upon successfully implementing this work. The key aspect is optimizing the bioink formulation and ensuring the cell-laden part's biological functionality.

References:

[1] Bhusal A., et al., Biofabrication 14.1 (2021): 014103.
[2] Bhusal A., et al., ACS Applied Bio Materials 5.9 (2022): 4480-4492.
[3] Miri A.m et al (US Patent).

Acknowledgments: Dr. Anant Bhusal (he graduated on this project from Rowan University) and Ms. Elvan Dogan (Ph.D. Applicant, NJIT) for contributing to this project.

STEVENS
INSTITUTE OF TECHNOLOGY

Development of a Microfluidic Viscoelastic Hemostatic Assay towards Point-of-care Testing of Coagulopathies

Melikhan Tanyeri
Department of Biomedical Engineering, Duquesne University, Pittsburgh, PA.

Biographical Summary of Applicant: I am a tenure-track assistant professor in the Dept. of Biomedical Engineering at Duquesne University in Pittsburgh. I served as a post-doctoral researcher in Charles Schroeder's group at the Univ. of Illinois at Urbana-Champaign from 2006 to 2012. Subsequently, I held a position as an assistant professor in the Dept. of Electrical and Electronic Engineering at Istanbul Sehir University for three years. Upon returning to the US, I joined Savas Tay's group at the University of Chicago as a research scientist before assuming my current position in 2018. My research interests primarily focus on microfluidics, chemical and biomolecular sensors, and high-resolution imaging. My research group specializes in developing innovative chemical and biological sensor platforms based on micro and nanoscale optofluidic systems.

Clinical Impact and Significance of Research Problem: Rapid and accurate diagnosis of coagulopathies is critical to reducing morbidity and mortality associated with uncontrolled bleeding. Conventional coagulation tests (CCTs) like PT/INR and aPTT provide valuable information but may not fully diagnose complex coagulopathies. Viscoelastic hemostatic assays (VHAs) offer a more integrative evaluation of hemostatic function, mimicking physiological aspects of hemostasis in vitro, but are limited by bulkiness and cost [1]. Implementing portable point-of-care systems for comprehensive blood coagulation profiling could greatly enhance clinical capabilities, personalize treatment, and optimize blood resource management. This advancement holds the potential to mitigate risks associated with hemorrhage and thrombosis, leading to improved patient outcomes. [2].

Innovative Programmatic Approach of Applicant: To address this challenge, we aimed to develop a microfluidic platform capable of performing point-of-care viscoelastic hemostatic assays (μVHA) using minute samples of blood towards real-time in vitro monitoring of whole blood coagulation. To this end, we developed a microfluidic viscometer based on flow-induced deflection of flexible micropillars [3]. The micropillar deflection is optically imaged, quantified, and used to determine the viscosity of the fluid at a given shear rate (**Fig. 1**). We envisioned a platform that measures blood viscosity (clot firmness) as a function of time during clot formation and degradation. This platform generates coagulation curves akin to TEG/TEM traces utilized in diagnosing coagulopathies, facilitating targeted, personalized hemostatic therapies.

Key Findings of Applicant to Date: Our method enables real-time viscosity measurements ranging from 2-100 cP with a sensitivity of 0.5 cP (**Fig. 1c**) using minimal sample volumes (80–400 μL). We measured blood viscosity across different shear rates and recapitulated the shear-thinning behavior (**Fig. 1d**). We further investigated the impact of device geometry on the viscometer performance, enabling us to optimize the sensitivity and dynamic range of viscosity measurements tailored to specific applications [4]. We also performed coagulation experiments with our microfluidic viscometer. Leveraging using machine learning algorithms, we identified three distinct stages of blood coagulation by classifying micropillar deflection as a measure of changing blood viscosity during clot formation [5]. Thus, the μVHA method is ideally suited for real-time detection and monitoring of blood coagulation through viscosity assessments.

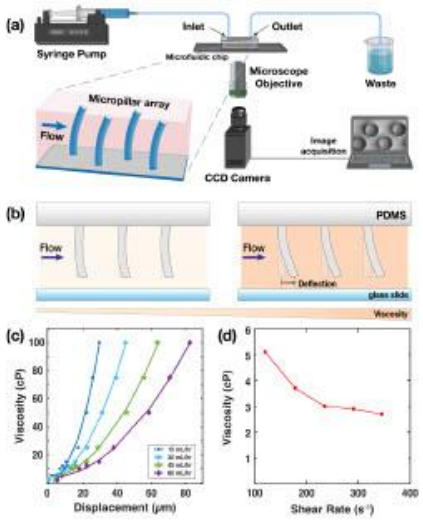

Figure 1: Microfluidic viscometer for coagulation assays. μVHA relies on a microfluidic viscometer which measures blood clot firmness (viscosity) in real-time using flow-induced deflection of flexible micropillars.

Future Goals: We aim to further develop our microfluidic platform to carry out a proof-of-concept demonstration of diagnosing trauma-induced bleeding disorders. Our long-term goal is to integrate an in vitro vascular injury bleeding model into the coagulation sensor. Our group strives towards advancing DEI efforts, especially in expanding the participation of underrepresented groups in STEM fields. To achieve this, we regularly recruit student members from the local Society of Women Engineers (SWE). Further, we plan to recruit high school students from the neighboring Citizen Science Lab.

References

1. Volod, O. et al. *J Clin Med* 11, 860 (2022).
2. Moore, E.E. et al. *Nat Rev Dis Prim.* 7, 30 (2021).
3. Mustafa, A. et al. *Anal. Chim. Acta* 1135, 107-115 (2020).
4. Mustafa et al. *Sensors* 23 (22) 9265 (2023).
5. Mustafa et al. *Sens. Diagn.*, ,2, 1509-1520 (2023).

STEVENS
INSTITUTE OF TECHNOLOGY

Design and Characterization of EPDA Transmembrane Receptors for Engineering Programmable Cell Behavior

Abstract

Over the past three decades synthetic biologists have taken a page from nature's playbook and developed synthetic cell-surface receptors that sense extracellular inputs and convert these signals into user-defined cellular responses. Perhaps one of the most exciting examples of this is the development of CAR (chimeric antigen receptor) T-cell therapy which endows immune cells with the ability to identify and fight cancer. In this seminar, I will first go over different types of synthetic cell-surface receptors with a focus on their clinical applications and limitations. I will then overview how we used a 'design-build-test-learn' approach to develop and characterize the extracellular and intracellular domains of EPDA (Extracellular Peptide-Ligand Dimerization Actuator) cell-surface receptors. Extracellularly, *Stimulatory* and *Inhibitory* EPDA receptors rapidly dimerize with high specificity upon coming in contact with their peptide-ligand counterparts. Intracellularly, dimerized *Stimulatory* EPDA receptors phosphorylate substrates that merge split GFP (green fluorescent protein) halves, and dimerized *Inhibitory* EPDA receptors dephosphorylate substrates leading to GFP separation. Cells programmed with EPDA cell-surface receptors can rapidly and reversibly actuate green fluorescence, and by substituting split GFP with dCas9 the transcription of user-defined genes can be regulated. This synthetic platform enables Mammalian cells to communicate with peptide-ligands and opens exciting avenues of research including the development of 'living' materials and synthetic autocrine signaling for regulating therapeutic outputs during cell therapy.

Bio

Sebastián L. Vega completed two B.S. degrees in Chemical Engineering and in Biomedical Engineering from Carnegie Mellon University in 2006, received his Ph.D. in Chemical & Biochemical Engineering from Rutgers University in 2015, and was a postdoctoral trainee in Bioengineering at the University of Pennsylvania until 2018. Sebastian joined Rowan University as an Assistant Professor of Biomedical Engineering in 2018, and his lab's research focuses on 1) developing tools to improve our understanding of how cells sense and respond to engineered environments and 2) designing tunable materials with applications in cell manufacturing and regenerative medicine. His research has been funded by the NSF, NIH, Camden Health Research Initiative, Cooper Foundation, and New Jersey Health Foundation, and Sebastian is a 2023 NSF CAREER award recipient. As a Chilean native, Sebastian is also passionate about providing students from all backgrounds with the mentorship and guidance he received throughout his life. To inspire high school students to pursue careers in STEM, Sebastian created BEAM (BioEngineering And Me), an undergraduate student-led program that educates high school students about different facets of biology and engineering through modular presentations and activities. Over 50 high school students have participated in *BEAM Hour*, an afterschool club with a local high school, and to-date over 100 students from 12 different states participated in the annual *BEAM Virtual Summer Program*.

STEVENS
INSTITUTE OF TECHNOLOGY

Precise control of cellular motion to prevent chronic disease conditions.

Alexander Buffone, Jr., Ph.D.[1,2]
Assistant Professor of [1]Biomedical Engineering, [2]Chemical and Materials Engineering, New Jersey Institute of Technology

Biographical Summary of Alexander Buffone: Dr. Buffone has been an assistant professor in the department of biomedical engineering at New Jersey Institute of Technology since January of 2022. He also holds appointments in the Chemical and Materials engineering department at NJIT and is a member of the Center for Engineering Mechanobiology (CEMB) and Center for Injury Biomechanics, materials, and medicine (CIBM[3]). Dr. Buffone received both his B.S. and Ph.D. in chemical engineering from SUNY Buffalo. His doctoral research with Dr. Sriram Neelamegham focused on modifying the neutrophil glycocalyx through genetic engineering to alter their migration ability. He was subsequently a postdoctoral fellow in the cellular and molecular biology department at Roswell Park Cancer Institute, where he worked with Dr. Joseph Lau on controlling animal models of systemic inflammation. His most recent position was as a Research Associate at the University of Pennsylvania in the lab of Dr. Daniel Hammer where his research focused on the identifying both which immune cells can utilize and the underlying mechanisms of upstream migration in the vasculature. He also spent a year as a visiting scholar at the University of California, San Francisco in the lab of Dr. Valerie Weaver where he edited the cancer glycocalyx to tune their migration on and interactions with the extracellular matrix.

Clinical Impact and Significance of Research Problem: The **Buffone Cellular Motion Lab** seeks to combat the development of chronic conditions such as cancer, hypertension, atherosclerosis, and others. Since over 50% of adults 55 and older suffer from at least one chronic disease, better understating of the cellular underpinnings (i.e. cellular migration) of these diseases can lead to new advances in their prevention and treatment.

Innovative Programmatic Approach of Applicant: Our research lies at the intersection of Glycobiology, Cell Migration, Mechanobiology, and Engineering. Our lab utilizes a combination of CRISPR genetic engineering, microfluidics, and models of acute inflammation and we study how both cancer and immune cells interact and move in their environment. By disrupting the cell surface, mechanosensitive receptors, and glycocalyx composition, our goal is to fine-tune and precisely control cell migration for therapeutic benefit during disease states. Two of our main research thrusts revolve around: 1) understanding the basics of amoeboid cell upstream migration and how we can tune this mode of motility to our advantage and 2) cellular editing of the mammalian glycocalyx to promote better immune recognition of cancer.

Key Findings of Applicant to Date: During his time as a Ph.D., Postdoc, and current faculty position, three main findings have come from Dr. Buffone's research. First, during his PhD, he was able to character the specific glycosyltransferases involved in sialyl-lewis X synthesis and regulation of selectin binding in human neutrophils (1). Second, his work as a postdoc at Roswell Park and as a visiting scholar at UCSF demonstrated how editing the mammalian glycocalyx controlled mechanical interactions with the extracellular environment (2). Finally, during his postdoc time at UPenn, he was the first to demonstrate that both HSPCs and neutrophils were able to migrate against the direction of shear flow (3). All these findings contribute to ongoing research thrusts of in the Buffone Lab.

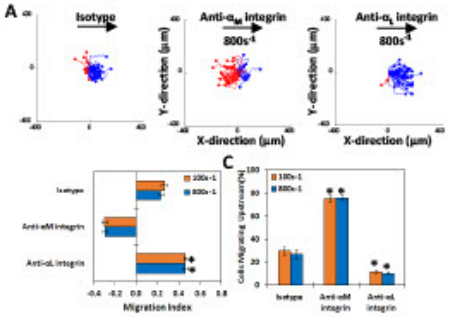

Figure 1. Neutrophils migrate upstream on ICAM-1 once Mac-1 is blocked: (A) cell traces of HL-60 on ICAM-1 under isotype, anti-αM-integrin blocking, or anti-αL-integrin blocking at 800 s^{-1} shear rate at a concentration of 2.5 mg/ml. blue traces indicate downstream migration and red traces indicate upstream migration. (B) HL-60 cell migration as expressed by the MI under isotype, anti-αM-integrin, or anti αL- integrin blocking at 100 and 800 s^{-1} shear rate on ICAM-1. A negative MI indicates migration against the flow, whereas a positive MI indicates migration with the flow. (C) cell (%) traveling upstream under isotype, anti-αL-integrin, or anti-αM-integrin blocking on ICAM-1. HL-60 cells migrate downstream on ICAM-1 whereas blocking the αM-integrin promotes upstream migration. Adapted from (3).

Future Goals: On top of the Buffone's lab's desire to publish groundbreaking science on relieving the development of chronic conditions and establishing a well-funded laboratory at the university (NJIT), state (NJHF, NJCCR) and federal level (NIH, AHA, NSF), the Buffone lab also seeks to make an impact in both teaching and mentoring. We seek to champion and have recruited or are actively recruiting graduate students from a diverse background (Women, African American, LatinX, AAPI, LGBTQIA+, and first gen college) and hope to bring this diversity into the classroom (undergrad and grad) and to the scientific community.

References:

1. BuffoneA *et al.* J Biol Chem. 2013. 288(3):1620-1633.
2. BuffoneA *et al.* J Leuk Biol. 2016. 101(2):459-470.
3. BuffoneA *et al.* Biophys J. 2019. 117(1):1-12.

Acknowledgements: The Buffone Lab acknowledges previous and ongoing support from NJIT startup funds, NIGMS R21-GM133060 and R01 GM143357, CEMB Seed grant subaward 570440, and NJHF grant PC:26-24.

STEVENS
INSTITUTE OF TECHNOLOGY

Universal Prosthetic Socket for Transfemoral Amputees in Underdeveloped Countries

Alyssa Cavella, Alexa Soroka, Andrew Kim, and Nicolas Perez
Department of Biomedical Engineering, Stevens Institute of Technology

1) User Need:

1.a) Use Case:

Transfemoral amputees in underdeveloped countries are in need of an adjustable transfemoral prosthetic socket that is affordable and easily accessible.

1.b) Problem Impact

The current prosthetic socket fitting process includes a complex series of casting and molding, which can take up to six weeks and involves the expertise of specialized personnel. The entire process can cost up to $20,000, including the device, therapies, and refittings, which are necessary for ongoing adjustments. Aforementioned issues are only amplified in underdeveloped countries, with little access to advanced technologies, prosthetic resources and trained professionals.

1.c) Scope (Objective)

The project scope was defined to address the current need for a quick-fitting, cost effective transfemoral prosthesis in underdeveloped areas, rather than creating a high-tech solution that could not be afforded. Project limitations include a simple design and affordable materials.

2) Design Inputs

2.a) Constraints:

Affordability and adjustability are the two major design constraints utilized to classify the device as universal. Cost effective silicone rubber and carbon fiber reinforced thermoplastic were selected. Variations in device size and a tightening mechanism were used to address variations in residual limb geometry and add novelty to the device.

2.b) Requirements:

The device must be made affordable without compromising the mechanical integrity of the device, and effectively allow for ambulation[1]. Material selection must promote a breathable environment to reduce frequency of infection and promote overall comfort[2]. In addition, the socket must work in conjunction with the liner and pylon selected for the prosthetic device.

3) Solution

3.a) Design - Intended Use:

The device contains six panel slots that can accommodate supporting panels based on user need. Each panel can be removed through a release button located on the side of the base of the device. A tightening mechanism located on the outer side of the panel system can be adjusted through a dial to control fine adjustments.

3.b) Build - DEMO

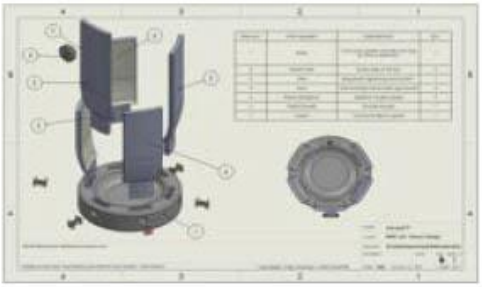

4) Verification Results

4.a) Introduction

The following testing protocol was followed to assess the mechanical response of the device under loading conditions, in order to simulate body weight transferred to the socket during ambulation[3].

4.b) Methods

A finite element analysis (FEA) was performed in Solidworks. Measurements were taken of stress and strain experienced by the device under loading conditions of 500 N in the downward direction, considering that assuming that the individual's total weight was 170 lbs, the femur supports about half of the body's weight, and that the femur experiences 1.75 body weight while walking[4].

4.c) Results

The device experienced stress values of 3.643E03 N/m² as shown in blue below. Unexpectedly, the panels displace from the base, which is accredited to inadequate mating in Solidworks.

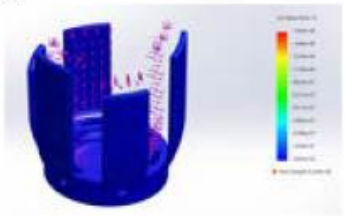

Figure 1. SolidWorks FEA Analysis

5) Conclusion

5.a) Summary:

The results above show that the device distributes load effectively and experiences relatively low stress. The design is expected to be successful in maintaining structural integrity while also addressing the user's need for an adjustable and more universal fitting process. Future testing must be done to ensure that displacement does not impact the device's structure, as shown in the above analysis.

5.b) Revisions:

To increase impact, more diverse panel geometries could be considered in order to easily accommodate a larger population, including those that may not find success with the initial model.

5.c) Impact (Future Version):

Increased personalization will better conform to the specific geometry of the residual limb while considering factors such as muscle mass and advanced trauma to improve user comfort and retention of the device. These revisions will result in a lower number of amputees without prosthetics in underdeveloped areas of the world.

References:

1. Hagberg. Prosthet. Orthot. Int. 2001; 25(3): 186-94.
2. Quiroz, et al. Fact. Med. 2019; 67(1): 117-25.
3. Nat. Center for Health Stat. CDC. 2021.
4. Mu, et al. Jour. Med. Biomech. 2011; 34(2): 73-92.

Acknowledgements: Stevens Institute of Technology (Schafer School of Engineering and Science)

STEVENS
INSTITUTE OF TECHNOLOGY

Knee Extension Device for Post Operative Knee Flexion Contracture

Grace Fukazawa, Brandon Sems, Jalen Bailey, Margaret Gibson.
Stevens Institute of Technology

1) User Need:

1.a) Use Case

Patients with knee flexion contracture suffer pain and stiffness from tendon/ligament stiffness and scar tissue accumulation.[1] Following hands-on training with the Kneesy Does It device, they can continue therapy at home or receive treatment at the clinic.

1.b) Problem Impact

Treating knee flexion contracture typically involves repetitive stretching by physical therapists during sessions. Limited availability and costs often result in patients skipping therapy, impacting compliance and prolonging discomfort or risking further injury.

1.c) Scope (Objective)

The Kneesy Does It device seeks to improve patient compliance in physical therapy by offering a less painful and more convenient experience. By regulating parameters like frequency, force, and heating, it aims to provide consistent and effective therapy, intended as a complement to, not a substitute for, a comprehensive physical therapy regimen.

2) Design Inputs

2.a) Constraints:

Modulating force without influencing frequency (and vice versa), isolating oscillating elements from stationary stable parts, adjustability, heating, and stretching frequency of 0.5 to 2.0 Hz.

2.b) Requirements:

Ease of use, convenience/safety, ensuring the proper amount of force and weight applied to provide effective treatment, preventing further injury.

3) Solution

3.a) Design - Intended Use:

The leg cuffs are attached to the linear actuator by interchangeable elastic bands. The band strength regulates the max applied force and acts as a safety restraint.

3.b) Build - DEMO

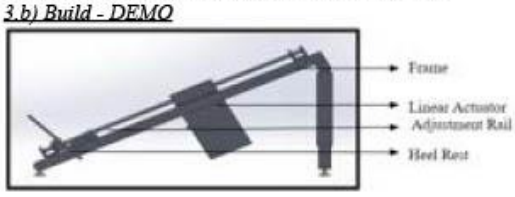

4) Verification Results

4.a) Introduction

Testing confirmed the correlation between increased weight and band strength, validating the predicted spring constant. The data was then used to create a simulink model simulating band behavior.

4.b) Methods

The measurements included the initial and final lengths of the exercise bands when subjected to a 5-pound weight, as well as the analysis of the time for one full cycle during a bounce test. These measurements allowed for the calculation of initial velocity and spring coefficients.

4.c) Results

The information provided mentions that the results were consistent with the group's predictions, showing that as the weight and strength of the exercise bands increased, the spring constant also increased accordingly.

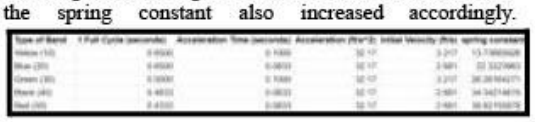

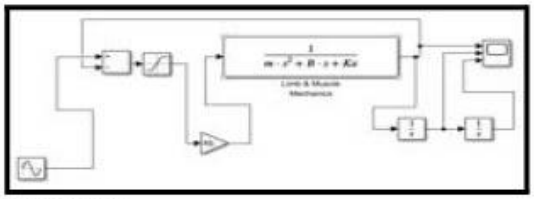

5) Conclusion

5.a) Summary:

The testing methods used were successful in determining the spring constants of the resistance bands and then creating an accurate Simulink model of the resistance band movement. This data will be essential for determining the correct resistance band needed for different patients.

5.b) Revisions:

Revisions for the device design include force and frequency modulation for more precise control, user adjustability to ensure patients understand the adjustments necessary for treatment, and patient safety to decrease potential adverse effects. The Simulink model made after initial testing is a complete model with no revisions needed.

5.c) Impact (Future Version):

Upon implementing these revisions, the device will become more accurate, user-friendly, and safe, which will help to reach the goal of higher patient compliance and an ultimate reduction of patients with knee flexion contracture complications.

References:

1. "Knee Flexion Contracture (Concept ID: C0409355) - MedGen - NCBI." National Center for Biotechnology Information, U.S. National Library of Medicine. Accessed 17 Oct. 2023.
2. Butler, D. L., et al. (2002). Biomechanics of ligaments and tendons. Exercise and Sport Science, 3, 320-335.

Acknowledgements: Special thanks to Joe Caucino, Becky Tucci, Drew Han, Jinho Kim, and Antonia Zaferiou.

Gait 2 Go: Gait Analysis, Anytime & Anywhere

Jade Carter, Shane Corridore, Lukas Cook, Caitlin Mehl
Department of Biomedical and Chemical Engineering, Syracuse University

1) User Need:

1.a) Use Case

Our primary audience is clinicians conducting check-ups or pre-surgery assessments for neuromuscular disorder patients. Gait 2 Go (G2G) enables these professionals to easily collect gait data in their offices by recording videos of a patient walking and uploading them to our system to analyze patient gait.

1.b) Problem Impact

Traditional gait analysis requires access to expensive labs and often lacks insurance coverage. The extensive time and equipment involved pose additional barriers. Current methods can also yield inaccurate results due to the impact of equipment on natural gait patterns.

1.c) Scope (Objective)

G2G overcomes these challenges with a cost-effective, streamlined approach requiring just internet access, two cameras (most smartphones work), and minimal space. This setup significantly reduces reliance on traditional labs, offers quicker results, and is financially feasible for healthcare providers. Our user-friendly platform will be accessible to all healthcare professionals, regardless of their training in gait analysis, ensuring quick and efficient results for both doctors and patients.

2) Design Inputs

2.a) Constraints:

Our program must accomplish two important tasks simultaneously. It must be simple enough to be easily implemented in a clinical setting, and it must also gather accurate gait data. It is challenging to accomplish both of these at once due to the complexity of gait analysis.

2.b) Requirements:

Our system requires minimal equipment and space. The requirements are a well-lit 12 x 15 ft area, two cameras with a minimum frame rate of 60 [1], and internet access. Our goal is to match over 80% accuracy in kinematic results compared to traditional marker-based gait labs while decreasing the calibration time by at least 50%.

3) Solution

3.a) Design - Intended Use:

Our solution is designed to collect accurate gait analysis data without access to a specialized gait lab and the associated equipment. The intended future use is that there will be a platform for clinicians to be able to access our program and upload videos to it. The program will contain instructions on how to set up the cameras and tripods, describe spatial requirements, and output gait analysis graphs. The clinician could annotate the graphs to highlight areas of interest. This accessible platform will bring the technology to spaces that have never been able to use it.

4) Verification Results

4.a) Introduction (i = 1 ... N)

Our control experiment used a gait lab with Vicon cameras to track reflective markers on 16 key body points. The participants walked three strides, allowing the system to capture their gait in a 3D model. This was performed with 4 individuals doing two standard trials and additional "toe walking" and "crouch gait" trials. A gait analysis expert guided this experiment.

4.b) Methods

During the control experiment, two smartphone cameras recorded each individual as they walked in the two planes. Our system will collect kinematic data on these videos so we can compare to the control and see the alignment.

4.c) Results

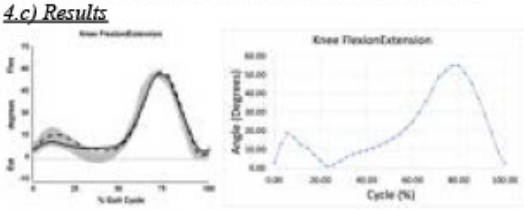

As a proof of concept, we used Tracker video analysis to manually track the positions of the lower limb joints in the frontal and sagittal plane. Joint angles were calculated using vectors and dot products. Examples of a knee flexion-extension graph from our control (left) and from Tracker (right) are shown above. The alignment between the two graphs indicates that our solution is accurate.

5) Conclusion

5.a) Summary:

Our existing results are indicative of the potential success of our project. The alignment of the Tracker data with the example data shows that gait analysis can be done without a specialized lab and equipment. We expect this accuracy to improve with further development. Moving forward, we will be working on streamlining this system by making it completely automated.

5.b) Revisions:

As we work to optimize our system's accuracy and automation, its impact will increase while diminishing time and effort. We plan to establish a functional code file using marker detection or OpenPose, to input videos and output gait analysis graphs. After evaluating each for its effectiveness, we will select one for use in our system.

5.c) Impact (Future Version):

Our solution will decrease a user's need for specialized labs, equipment, or expertise while providing accurate data that furthers patient care. By expanding access to this technology, our project has the potential to enhance patient quality of life, while simplifying clinicians' workflow and reducing cost.

References:

1. Kulkarni V. et al. *JPOSNA*. 2020; 2(3)
2. Martin B. et al. J. Pediatr. Orthop. 2013; 33(4):446-52

Acknowledgements: This work is supported by The Syracuse Office of Undergraduate Research and Creative Engagement (The SOURCE)

Smart Seat Cushion for the Prevention for Pressure Ulcers in Wheelchair Users

Ashlynn Barry, Marie Canencia, Katherine Ohotin, Michelle Wolf
Department of Biomedical Engineering - Stevens Institute of Technology

1) User Need:

1.a) Use Case

Our smart seat cushion with vibration technology is designed to prevent pressure ulcers in wheelchair users by actively redistributing pressure through targeted vibrations. Our solution enhances comfort, preserves mobility, and provides a user-friendly approach to maintaining well-being.

1.b) Problem Impact

In the United States, around 40% of the 3.3 million wheelchair users have an annual incidence of developing a pressure ulcer [1]. These ulcers require constant attention to prevent and treat, creating obstacles to daily life, affecting users and placing a burden on healthcare systems and resources. Existing solutions such as static cushions do not effectively redistribute pressure.

1.c) Scope (Objective)

By incorporating force sensing and vibration technology, our seat cushion senses and redistributes pressure accordingly to actively prevent pressure ulcers.

2) Design Inputs

2.a) Constraints:

Design constraints included ensuring user safety and comfort, meeting portability requirements with constraints on size, weight, and power, compatibility with various wheelchair models, and prioritizing cost-effectiveness in component selection for an affordable yet high-performance solution.

2.b) Requirements:

Our highest priority requirement is to ensure pressure redistribution effectiveness, measured by the reduction in peak pressure points on the user's body. This requirement has a target of at least a 30% decrease in peak pressure to significantly mitigate the risk of pressure ulcers [2].

3) Solution

3.a) Design - Intended Use:

Our innovative smart seat cushion revolutionizes wheelchair comfort and prevents pressure ulcers through integrated vibration technology, dynamically adjusting to user movements. The user-centric interface allows easy customization for a personalized experience. Compatible with various wheelchair models, durable, and prioritizing comfort, it offers a comprehensive solution for effective pressure ulcer prevention.

3.b) Build - DEMO

The cushion will continuously monitor pressure with force sensors and send vibrations through motors every 15 minutes, as clinically recommended [3].

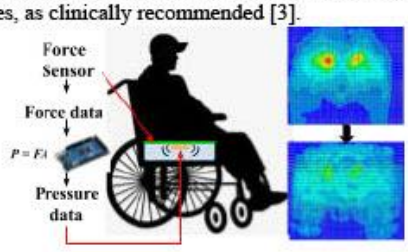

4) Verification Results

4.a) Introduction

Tests must be performed to ensure proper integration and calibration of the force sensors and vibration technology, as well as ensuring the system can accurately and effectively operate over long-term use. It is also necessary to assess the percentage of pressure reduction achieved by our cushion.

4.b) Methods

We aim to monitor the user's pressure data in real time to ensure it is performing effective off-loading [2]. We will also test varying pressures on the cushion to ensure there is proper communication between the force sensors and vibration technology by assessing the response to the weight. The durability of the cushion will also be tested through cyclic loading to ensure the sensors and structure of the cushion can work reliably with prolonged use.

4.c) Results

The results are expected to verify that our solution is durable, performs effective pressure redistribution, and is safe for human use.

5) Conclusion

5.a) Summary:

Without specific testing results, determining the success of the smart seat cushion design in meeting requirements is challenging. While it seems well-conceived for preventing pressure ulcers based on design information, thorough clinical testing is crucial for validation and to address any arising limitations.

5.b) Revisions:

Future testing should evaluate if the smart seat cushion prevents pressure ulcers, meets safety standards, and aligns with specified constraints. To enhance impact, potential revisions may be necessary, including design adjustments based on testing outcomes, refinement of input requirements, overall solution enhancements, and thorough verification of any modifications.

5.c) Impact (Future Version):

This user-friendly solution has the potential to reduce pressure ulcer incidence, alleviating healthcare resource burdens and enhancing overall well-being. It addresses both specific user challenges and the broader societal impact of pressure ulcer management in the United States.

References:

1.Barnes, J. *PubMed*, 1994;2:57-8.
2.Physiopedia. "Wheelchair Skills Training-Pressure Relief."
3.Northwest Regional Spinal Cord Injury System. "Pressure Mapping Assessment for Wheelchair Users."

Acknowledgements: We express our gratitude to Stevens Institute of Technology for its financial support and extend our appreciation to Dr. Peter Popolo for his invaluable guidance throughout the course of this project.

STEVENS
INSTITUTE OF TECHNOLOGY

An *in vitro* Mimic of Bacterial Contamination in the Operating Room

Stephanie Anaya,[1] Dennise Criollo-Quille,[1] Meghan Elder,[1] Axel Johnson,[1] Matthew Libera,[1] and Jordan Katz[2]
Stevens Institute of Technology[1], Orthobond Corp.[2]

1) User Need:

1.a) Use Case

Every year, millions of people in the United States undergo device-implant surgeries where patients face device-infection rates ranging from about 0.1 - 15% or more. In the United States, the annual cost to treat prosthetic joint infections (hips, knees) alone exceeds $1.8 billion dollars.[1] With the economic and personal risks associated with implant technologies, many antimicrobial surfaces have been developed over the past decade. None, however, have been translated to clinical use. A key problem centers on the lack of methods to mimic and assess bacterial surface colonization. We are focusing on the specific problem of bacterial contamination from the atmosphere of a surgical operating room (OR). Our target user needs to test colonization resistance using a method to contaminate a surface with low concentrations of bacteria. A potential user would be a developer of tissue-contacting biomedical devices interested in enhancing their infection resistance, and they would come from academic, clinical, or industrial workplaces.

1.b) Problem Impact

Current contamination methods are based on exposure to bacteria-containing aqueous solutions. However, this method does not mimic a surgical operating room (OR). Thus, there is a need for a new bacterial deposition method. Ideally, this method will become a standard for testing novel antimicrobial surfaces that will help the biomedical-device industry successfully negotiate the FDA regulatory approval process, currently a significant challenge in the area of preventing device infection.

1.c) Scope (Objective) Our objective is to develop a portable aerosolizing system that satisfies the 5 R's (repeatable, reproducible, responsive, rugged, relevant) associated with a standardized test.[2] This device must be able to reproducibly spray small quantities (e.g., hundreds of colony-forming units (CFUs)) onto a surface. The overall aerosolizing system is described schematically by Fig. 1. There are five subsystems. First is the physical enclosure itself. The device must be well sealed and made of noncorrosive and nonabsorbent materials. Second is the specimen holder. This must allow for both vertical positioning as well as rotation. Third is the spray nozzle system. This includes the nozzle, solenoids, and control triggering mechanisms. Fourth is the bacterial suspension system. This includes the bacteria of choice, an autoclavable and shatter-resistant Duran bottle, push-bar regulator, and dual port lid. Lastly, the fifth subsystem comprises electronics. This includes the coding for an Arduino Uno board and a breadboard. To power the solenoids, two different voltages are used, a 14 V spike voltage and a constant 3 V hold voltage, and a third powers the control box at 5 V.

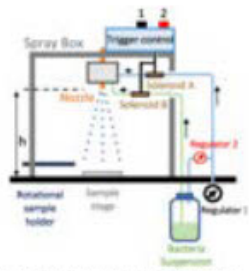

Figure 1: Bacterial Deposition System

2) Design Inputs

2.a) Constraints:

The design challenges center on achieving the 5R's. The system should be capable of producing consistent aerosolizing conditions with minimal variations between experiments, allowing for accurate comparisons and data analysis. Achieving repeatability and reproducibility demands standardized procedures following documented protocols. Responsiveness corresponds to ensuring that the test is sufficiently sensitive to changes in independent variables such as the nature of an antimicrobial coating on a biomaterial surface. Relevance means that testing approach meaningfully relates to real-world clinical settings.

2.b) Requirements:

The spray parameters include the adjustable nozzle-specimen distance, the aerosolizing pressures (e.g., 60 psi from regulator 2 and 10 psi from regulator 1 (see Fig. 1)), the pulse duration (e,g., 2 ms), and the bacterial concentration in the feed solution. The initial design targets are a ~20 µl spray volume with a 0.008" nozzle at 27 cm distance and an aerial density of 100 CFU/cm^2.[3]

3) Solution

3.a) Design - Intended Use:

This aerosolizing system will serve a vital role in the evaluation and testing of different bacteria-resistant coatings. The user will spray a candidate biomaterial with the desired number of bacteria and then assess the antimicrobial properties using standard microbiological culture techniques to assay the number of viable bacteria on the surface.

4) Verification Results

Device performance will be assayed by first spraying controlled bursts of bacteria-free water to determine the spray density and spatial distribution of the spray cone. After establishing baseline system performance, controlled bursts of methicillin-susceptible *S. aureus* will be sprayed directly onto nutrient-infused agar culture plates to quantify the number of viable CFUs and their spatial distribution as a function of the spray time, sample distance from the spray nozzle, and concentration of bacteria in the feed solution.

References:

1. Premkumar, A. et al. Journal of Arthroplasty. 2021; 36(1484-1489). 10.1016/j.arth.2020.12.005
2. Goeres, D. et al. Journal of Microbiological Methods. 2019; 165(105694). 10.1016/j.mimet.2019.105694
3. Zhao, Y. et al. J. Biomed Matls Research: B. 2022;110 (2472-2479). 10.1002/jbm.b.35104

Acknowledgements: We would like to thank Dr. Alex Chou from the Stevens Laboratory for Multi-Scale Imaging and acknowledge funding from an NSF Growing Convergence Research GCR Grant (NSF # 2219014).

Mini-HART: Educational 3D-Printed Humanoid

Kit Kannan[1], Baonghi Trinh[1], Bryant Ortiz[2], Brandon Cook[3], Kiwon Sohn[2]
[1]Biomedical Engineering Program, University of Hartford, West Hartford, Connecticut, 06117
[2]Robotics Engineering Program, University of Hartford, West Hartford, Connecticut, 06117
[3]Electrical Engineering Program, University of Hartford, West Hartford, Connecticut, 06117

1) User Need:

1.a) Use Case

The purpose of this project is to create an accessible and affordable humanoid robot that will be used as an educational tool in the classroom. One that can teach 9-12th grade students several aspects of STEM through its creation and use. These aspects consist of items such as 3-D modeling, design, motor control/mechanics, kinematics, programming, and other related STEM topics. This tool is to be provided to institutions in the form of a kit consisting of all necessary mechanical parts and 3-D printed parts if the institution does not have access to a printer and needs to buy said parts. All provided with instructions to build and program the robot, capable of being understood/created by someone with limited to no prior knowledge.

1.b) Problem Impact

Currently in the market, 3 educational robots have been evaluated in comparison to this humanoid. The existing humanoid robots are either highly expensive and unaffordable by most school systems or does not have high educational options. By creating a project from the ground up and also creating a user guide to teach others to do so, a more cost effective and educational project can be achieved. This would mean teaching students about putting together and coding a robot, and how to build one completely. This would teach them several aspects of STEM and robotics.

1.c) Scope (Objective)

A clear and understandable guide has to be made for this project, following all necessary steps and teaching each aspect that is being worked on. From 3-D printing of the parts to the coding of the humanoid, the scope of this project is to provide 9-12 grade students the beginning to the end product of creating a humanoid robot.

2) Design Inputs

2.a) Constraints:

There are 5 main constraints to factor in for this project. The constraints that are considered for this humanoid are user-friendly interface, cost, safety, and movement. These are all important constraints for this project because there will be human interaction, especially with the students. Due to this, the constraints are evaluated for safety and ease of use, as well as being cost effective for affordability and accessibility.

2.b) Requirements:

The 2 main requirements for this project are for it be affordable and have a full range of motion. This project has to be an educational tool for students, as well as cost effective. Because of this, all programs were opensource or would be free access to students. Since this is intended for children, all the materials are classroom safe, and all parts were made with this intention. The cross-sectional placements of the motors were also considered to provide a wider and smoother range of motion for this humanoid.

3) Solution

3.a) Design - Intended Use:

This humanoid is designed to be used by students therefore safety is a top priority. As such for the completed leg design, fillets of 1.6 mm are done on all open edges leaving only 0.4mm of flat surface on the sides. Leading to parts with no sharp points and safe to be worked on by students.

3.b) Build - DEMO

Currently the lower body design is complete. One leg has also been printed and built successfully to test the design and structure, being able to free stand and balance.

Figure 1. Assembled leg of mini-HART

4) Verification Results

4.a) Introduction (i = 1 ... N)

To test this project, the user guide created will be used to recreate the project from an outside source. As this is something the end user will have to do.

4.b) Methods (i = 1 ... N)

The recreation of this project by the user would be the best test of its success. If a person with no or limited knowledge is able to successful understand all steps and recreate the end product this would mean the project is not only able to be recreated, but the user guide is also doing as intended.

4.c) Results (i = 1 ... N)

A success of this project can be determined by an outside party being able to fully recreate it through the use of the guide. As the goal of the project is to teach students to create a humanoid and learn several STEM aspects.

5) Conclusion

5.a) Summary:

While the project is still in progress, the lower body of the human has been assembled and meets many of the design requirements. PLA was used due to its efficiency and cost.

5.b) Revisions:

The torso and the arms are still a work in progress and will follow the design process of the lower leg. The fillets were revised to be thicker for more of a smooth curve.

5.c) Impact (Future Version):

After completing these revisions, the humanoid will be safe for human use. It will also provide an affordable and accessible STEM and robotics education for those who want to learn more about these fields.

References:1. Velentza, A.-M., Fachantidis, N., & Lefkos, I. 2022. Human-Robot Interaction Methodology: Robot teaching activity. MethodsX, 9, 101866.

Acknowledgements: We would like to thank UHARTs BME, ROBO, and ECE departments for funding this project.

Two-way Thermoresponsive Biliary Stent

Connor Macken, Connor Purcell, Brianna Rodriguez, Maddie Simon, Caroline Snyder.
Brown University School of Engineering.

1) User Need:

1.a) Use Case

The proposed stent will restore flow through the bile duct for patients with benign strictures who are contraindicated for endoscopic retrograde cholangiopancreatography, and normally are candidates for balloon angioplasty and/or drainage catheters.

1.b) Problem Impact

Purcanteously-placed metal and plastic stents are difficult to remove due to the narrow intrahepatic ducts. Patients with intrahepatic strictures often receive external drainage catheters, forcing them to limit mobility [1].

1.c) Scope (Objective)

The proposed thermoresponsive biliary stent can be inserted as a collapsed stent, expand at body temperature, and collapse upon exposure to cold saline, allowing for percutaneous removal.

2) Design Inputs

2.a) Constraints:

The design stent must be capable of reaching diameters between 1 and 8mm, must be stable in a pH range of 6-9 to account for the variable pH of the bile in diseased states [2], and must be deployable against a pressure of 30 cm H_2O in the case of obstructions [3]. Luminal patency is required for at least 6 months, to be evaluated as maintaining the stent's original diameter.

2.b) Requirements:

The stent must re-establish bile flow so that total serum bilirubin values are restored within 10% of the patient's normal concentration. The stent must have a placement and removability success rate of >95%, limit duct injury, and be compatible with current operational standards.

3) Solution

3.a) Design - Intended Use:

Our design exploits the two-way shape memory property of NiTiNOL; it should expand at body temperature and contract upon flushing with cold saline.

3.b) Build - DEMO

The stent can be fabricated using a 10-minute heat treatment at 507C. PTFE coating reduces endothelialization, limiting occlusion. The figure-eight geometry using 37 gauge NiTiNOL allows expansion and contractibility while also offering mechanical support.

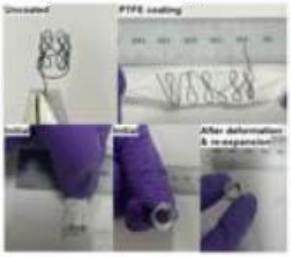

Figure 2. Stent components and shape memory function.

4) Verification Results

4.a) Introduction (i = 1 ... N)

The stent must open to have an inner diameter of 9mm in the 37°C bath and must contact to have an outer diameter of 5 mm when exposed to cold liquid (10°C bath) [4].

4.b) Methods (i = 1 ... N)

After heat-treating the NiTiNOL at 507 C for 10 minutes to fabricate a wire mesh, the stent's shape memory properties were evaluated. The initial stent diameter was measured, and the stent was mechanically deformed to a smaller diameter. The deformed stent was then placed in 37°C water and allowed to expand, after which the re-expansion diameter was measured. ImageJ was used to process pictures and record initial and final diameters.

4.c) Results (i = 1 ... N)

Results verified shape memory of the expanded conformation an stability across a range of temperatures, but did not verify shape memory of contracted conformation.

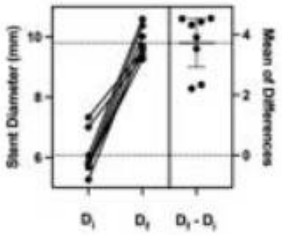

Figure 3. Shape memory of heat-treated stent from various deformed states.

5) Conclusion

5.a) Summary:

The design met dimensional requirements as a 10x scaled version and expansion requirements but needs revision to achieve two-way shape memory.

5.b) Revisions:

Improvements will be made by revising our heat cycling protocol for training the cold-saline responsive conformation. Different mesh geometries will be explored to increase the range of diameter variability. An actual size prototype will also be developed so that testing may give results directly reflecting the final product.

5.c) Impact (Future Version):

The final contractible shape-memory stent will alleviate complications associated with percutaneous treatment of benign biliary stricture, saving time and money for patients and physicians.

References:

1. Fang A. et al. Semin intervent Radiol 2021; 38(03): 291-299
2. Wulkersdorfer B, et al. Antimicrob Agents Chemother. 2017; 61(8)
3. Pitt H, et al. Blumgart's Surgery of the Liver, Biliary Tract and Pancreas, 6th Ed. 2017
4. Couke E, et al. StatPearls. 2022

Acknowledgements: We acknowledge the Brown University School of Engineering for providing a budget for this project as well as Professor Anubhav Tripathi, Professor Lindsay Schneider, Professor Marissa Gray, and Professor Theresa Raimondo for their help throughout the course. This project was performed based on a need identified by Dr. DaeHee Kim and was handed down from Ruth Sullivan, Nathan Ramrakhiani, Juliana Lederman, and Priya Bhanot.

STEVENS
INSTITUTE OF TECHNOLOGY

Selective HIV DNA Enrichment Using Magnetic dCas9

Sophia Bautista[1], Grace Fan[1], Ishika Nevatia[1], Kaleigh Stuart[1], Dr. William Dampier, PhD[2]
[1]Drexel University School of Biomedical Engineering, Science, and Health Systems
[2]Drexel University College of Medicine

1) Need

1.a) Use Case: Our user is Dr. William Dampier and other researchers at Drexel University College of Medicine. Our method would be used to advance HIV research by reducing the time and resources needed to amplify DNA and improve sequencing efficacy. This advancement in research will help in personalizing treatment for those affected with HIV and can help develop a cure that is not a life-long, daily treatment.

1.b) Problem Impact: HIV research is highly important since HIV impacts about 1.2 million Americans [1] and attack's a person's immune system. Some existing solutions that researchers use include silica columns, polymerase chain reaction (PCR), or magnetic beads alone. For example, silica columns may be easy to use to purify DNA but can result in low yields of target materials, leftover impurities in the sample, and potential degradation of the desired material. Therefore a new efficient solution for scientists is needed.

1.c) Scope (Objective): Design a non-toxic method to increase the proportion of target double-stranded DNA by selectively enriching for target strands while leaving the undesired DNA behind within a short time frame.

2) Design Inputs

2a) Constraints: Some of our project specific limitations include the avoidance of toxic material usage and the use of plasmids instead of the HIV DNA. We want to avoid using toxic materials out of the safety of the researcher and the DNA sample. The use of plasmids instead of HIV DNA is due to the limited amount of HIV DNA available. Our availability of our resources are confined to what Dr. Dampier's lab has to offer and the current resources it possesses.

2b) Requirements: Our project specific requirements include the DNA enrichment criteria, procedure time, stability, and modularity. Our DNA enrichment criteria describes the desired concentration of amplified DNA we wish to achieve which is by 10-fold. We wish to make the procedure time more effcient to less than a day to make HIV research. We want the final product to be shelf stable and produce reliable and consistent results over several days. Finally, we need the procedure to be applicable to multiple gRNAs inputs since we cannot just focus on HIV DNA for now. The gRNA selected for this project has been used in previous publications regarding HIV research and can be used on the selected plasmids as a model of HIV [2].

3) Solution

3a) Design - Intended Use

Figure 1: Demonstartes the improved process of amplifying target DNA with the the CRISPR-Cas-9 system inbetween PCR runs.

3b) Build - DEMO

Figure 2: The combined system of magnetic beads and the Cas-9 system with the magnetic holder to attract and separate the magnetic beads from the supernatant.

4) Verification Results

4a) Introduction: We plan to use a DNA sequencer to verify that the final product is indeed our target DNA.We will also confirm the concentration increase of our plasmids through a Qu-bit

4b) Methods: We plan to use a DNA sequencer called the Nanopore to verify the DNA sequence is the right target we enriched and targeted. As a test of our verification method, we mixed different ratios of two different plasmids, plasmid A and plasmid B, in several runs and ran it on the Nanopore to see if it could detect the different types of plasmids

4c) Results: The results did verify that our Nanopore can differentiate between the two plasmids.

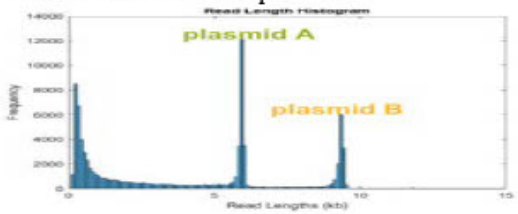

Figure 3: The frequency result of two different plasmids in a sample.

5) Conclusion

5a) Summary: We hope our design will meet all of our criteria of the avoidance of toxic material usage, significantly enriching DNA concentrations, decreasing procedure time to select DNA, and applying modularity to multiple gRNA inputs.

5b) Revisions: Some revisions of our procedure may include the different setting in which the gRNA binds to the target DNA, such as different temperatures or waiting periods. Modularity can also play a big role in furthering our adaptability of our procedure to different viruses or DNA targets

5c) Impact (Future Version): By incorporating our revisions, this procedure could be used for a multitude of research studies and make the procedure more efficient.

References:

1.HIV & AIDS trends and U.S. Statistics Overview. HIV.gov.
2.Sullivan, N. T., Dampier, W., Chung, C. H., Allen, A. G., Atkins, A.. (2019)

Acknowledgements:

We wish to thank the Drexel University College of Medicine for funding a majority of our study, Dr. Dampier for helping us in the lab with the project, and MacKenzie Collins for assisting us in the lab as well and for running some of our experiments when we were unable to.

Improving CRISPR Off-Target Detection Using Transposases

Presenting Ann Abraham, Connor Gazda, Alexis Malamas and Via Wood .
Drexel University School of Biomedical Engineering, Science, and Health Systems, and College of Medicine

1) User Need:

1.a) Use Case - Our users are Dr. William Dampier and other researchers interested in CRISPR innovation. We intend to improve the Genome Wide Unbiased Estimation of Double-Stranded Breaks Enabled by Sequencing (GUIDE-seq) used to assess the safety of Cas9 based gene editing.

1.b) Problem Impact – Cas9 based gene editing techniques are a novel technology for improving human health. It is important to measure the safety of these techniques using an unbiased approach. In this way, potentially harmful therapies can be screened-out early in the process, thus saving time and money. Current implementations of the GUIDE-seq technique require chemical or physical shearing genomic DNA to an appropriate size which are laborious, time-consuming, lossy, and difficult to control. We aim to improve upon these steps in the GUIDE-seq technique, yielding a simpler and faster protocol.

1.c) Scope (Objective) - Our objective is to improve CRISPR's off-target screening procedures by utilizing a new enzyme which boasts a single "cut and paste" step into the GUIDE-seq protocol. In other words, take a 2-step process and turn it to 1 step.

2) Design Inputs

2.a) Constraints: - Current GUIDE-seq procedures utilize Illumina sequencing which requires specific sequences at the ends of each DNA strand. The design is constrained to work within the same existing protocol and thus must use a compatible DNA sequence during the "paste" step. In order to improve upon the current technique our replacement must be faster than 2 hours.

2.b) Requirements: - Our requirements for this project are compatible cut length and produced results should agree with the current technology. Adhering to the MiSeq Illumina sequencer specifications of maximum read length for DNA [3], fragments must be between 100 and 2000 bp with an ideal mean of 300 bp, (R1). After sequencing the number of reads detected at the target sites must exceed the noise level at $p<0.01$ (R2).

3) Solution

3.a) Design - Intended Use: - The transposase enzyme system has a fast "cut and paste" and "copy and paste" functions. EZ-TN5 Transposase is a hyperactive, mutated form of TN5 transposase, a highly efficient enzyme for insertion of an EZ-TN5 Transposon into any target DNA, in vitro. We will be using TN5 transposase to insert a custom DNA sequence.

3.b) Build – DEMO - The main design choice was deciding what TN5 transposase to use that fits our design constraints. Beta Lifescience had a $14.60 price per reaction with a reaction time of 1 hour, fitting our time constraint. Therefore, we chose the Beta Lifescience TN5 enzyme due to it being $14.60 per reaction and fitting our constraint of 1 hour.

4) Verification Results

4.a) Introduction (i = 1) - This test will confirm that the DNA fragments are the ideal size, (R1).

4.b) Methods (i = 1) - The main measurement will be DNA length in bp. CRISPR-tagged DNA will be treated with TN5 at various times and enzyme amounts. This will be tested by utilizing an Agilent 2100 Bioanalyzer, which provides an electropherogram output of the DNA fragment. [2]

4.c) Results (i = 1) - We expect our results to be similar to Figure 1, with peaks of the two ends and a rounded peak around 300 bp. Whichever procedure set-up we that is closest to this we will use in further experiments.

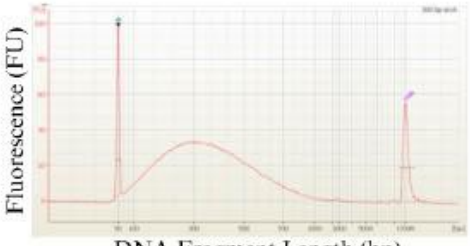

Figure 1. Ideal Bioanalyzer Electropherogram Output [2]

4.a) Introduction (i = 2) – Sequencing the DNA produced after the cut and paste step should produce identical results to those produce by the current shearing methods (R2).

4.b) Methods (i = 2) - We will run the GUIDE-seq procedure with and without TN5 on CRISPR-tagged DNA, and analyze the results from running the fragments through the sequencer. The measurement will be the number of reads that the sequencer identifies that originate from the target site.

4.c) Results (i = 2) - We expect all sites identified by the new method will match the existing method, as both methods have the same end product.

5) Conclusion

5.a) Summary: - The time listed on Beta Lifesience's website proves our hypothesis that the procedure takes one hour. Protocols show that the procedure takes 2 hours.

5.b) Revisions: - The exact time and amount of enzyme need to be confirmed for a regular procedure. Another potential design impact, although unlikely, is the adapter being discovered to be incompatible with the TN5, requiring us to design a new adapter sequence.

5.c) Impact (Future Version): - With these revisions complete, Dr. Dampier will have a high-throughput GUIDE-seq which will accelerate HIV cure research.

References:

1. WHO. (2023). HIV. *Global Health Observatory*. Link
2. Krowczynka. Covaris, inc. Link
3. Apone et al. New England Biolabs. *Feature Articles*. Link
4. Integra. (2023). MIRO CANVAS. Link

STEVENS
INSTITUTE OF TECHNOLOGY

ChromaScan Health - Color Strip Sensing Device

Asmaa Ali, Gisella Guerrero, Hajer Ali, Sachely Antuna, Connie L. Hall, Ph.D.
The College of New Jersey (TCNJ)

1) User Need:

1.a) Use Case

The intended users are elderly and vision-impaired individuals unable to interpret at-home color test strips. The user will input the brand name of the test strip into the device and then place the strip in its designated area in the device. The device will output the stage of the medical condition with any relevant information and store it.

1.b) Problem Impact

This device will impact nearly 3.8 million Americans with chronic kidney disease (CKD) who are primarily older than 65 years.[1] This device will also benefit elderly individuals with illnesses that require monitoring through urinary test strips. The problem statement is a way to address the challenges that elderly and vision-impaired individuals face interpreting at-home color test strips by automating the reading/recording process and simplifying the interpretation of test results. An existing competitive device on the market includes an app for at-home urinalysis tests with a provided kit. This device is only compatible with the company's test strips, and the results might take time, as they are sent to the physician to be interpreted.[2]

1.c) Scope (Objective)

The device must be able to interpret the color of different kinds of test strips and output the resulting medical condition or stage of the condition to the user.

2) Design Inputs

2.a) Constraints:

The device must also follow FDA requirements for sanitation, restricting the way the test strips can be inserted into the device. The device should use the minimal necessary power source because the improper disposal of batteries leads to contamination of air, soil, and water since they are made from lithium.

2.b) Requirements:

ChromaScan Health must take in information from the user as well as communicate the results in a way that visually impaired individuals can do it without needing assistance from someone else. The device must detect the color of the test strips and must be sanitizable because even though it is a noncritical medical device, it will be in contact with the user's urine.

3) Solution

3.a) Design - Intended Use:

ChromaScan Health intends to sense color from urinary test strips from different manufacturers and provide an accurate reading. It is known that the color of the test strip changes based on the concentration of the parameter being measured. The user will place the test strip on a sliding drawer (Figure 1). A color sensor will move along the test strip to identify the color of each specific parameter and process it through an algorithm that will output the information on a touch screen. This drawer mechanism will facilitate the sanitation of the device. The users will also be able to retrieve past results by using a memory card.

3.b) Build - DEMO

The device will be 3D printed with electrically insulative material and built into a rectangular prism. A Nextion 7" TFT touchscreen will be placed on the top. The drawer will be placed in the center. The TCS3200 color sensor will be attached to an Actuonix L12-R linear actuator and positioned over the drawer. The circuitry along with the Arduino Nano® microcontroller will be placed at the bottom part of the device. In addition, the battery and memory card compartment will be located on each side of the device (Figure 1).

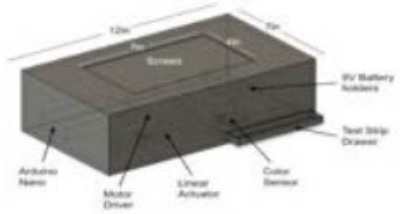

Figure 1. ChromaScan Health device prototype.

4) Verification Results

Different tests will be conducted to verify each specification associated with each design requirement: user input, color detection, output results, user interface, power source, sanitation, electrical safety, and data storage. User input verification will test that the device records information from the user by specifying the exact input on the interface screen, such as the test strip details. The color detection verification will ensure the device senses the colors by comparing it to a color range graph. For the user interface, the font size and type will be tested. The power source test will assess if the device can run 10 readings on one charge. Sanitation will be verified using disinfecting wipes and inspecting for visual residue. For electrical safety, the current leakage will be measured. Lastly, the data storage will be verified by comparing memory size to the number of bytes needed per test strip. Procedures are supported by these standards: IEC 60601, 21 CFR 892, ISO 17664, IEC 62304, OSHA - HCS 1910.

5) Conclusion

ChromaScan Health is currently under development following various design requirements and specifications for user input, color sensing, output results, power source, sanitation, electrical safety, and data storage. After the device is complete, the verification and validation protocols will be conducted to ensure its functionality. Upon the culmination, elderly and visually impaired individuals will benefit themselves by using this assistive technology. ChromaScan Health will provide a user-friendly interface that will automate the reading of colorimetric-based test strips.

References:

1. Kovesdy C. P. KI Suppl. 2022;12(1), 7–11.
2. Yonatan A. 2024. Healthy.io. UTI

Acknowledgements: The School of Engineering at TCNJ for funding this senior design project.

STEVENS
INSTITUTE OF TECHNOLOGY

Developing an Inexpensive Device for Wheelchair Transfer

Justin Chen[1], Rachel Kim[1], Luke Pothen[1], Robert Zika[1], Ghaith J. Androwis, Ph.D.[1,2*]
[1]New Jersey Institute of Technology, Biomedical Engineering department, Newark NJ
[2]Kessler Foundation, Center for Mobility and Rehabilitation Research, West Orange, NJ
(Corresponding author e-mail: ghaith.j.androwis@njit.edu)

1) User Need

1.a) Use Case: Our project targets individuals with physical disabilities, including paralysis, muscular dystrophy, multiple sclerosis, and elderly individuals who may be mobility challenged due to age-related factors. This population has increased from an average of 4.7 per 100 people in 2011 to 7.1 in 2019, and the trend continues to grow[1]. Our proposed device will enable users to effortlessly deploy a manual wheelchair from the trunk of the Tesla Model 3 and transfer it to the driver's side seat.

1.b) Problem Impact: Current transfer methods often require a caregiver's support or the use of costly, complex assistive devices [2]. The average cost of a wheelchair transfer device ranges from $10,000-$20,000, most of which require the use of larger vans [2]. By providing a solution that eliminates the need for expensive equipment or external assistance, we aim to enhance the quality of life(QoL) for individuals with physical limitations and promote inclusivity in transportation accessibility.

1.c) Scope (Objective): Our solution focuses on eliminating the reliance on costly assistive devices or caregiver support, making the process more accessible/affordable.

2) Design Inputs

2.a) Constraints: Our strictest constraints revolve around affordability to be widely accessible, usability for individuals to operate the device independently, and compatibility with the Tesla Model 3 for its autonomous driving capabilities.

2.b) Requirements: Ensuring affordability is paramount, driving us to design a solution that maximizes functionality while staying under the budget of $1000. Simultaneously, seamless integration with the Tesla Model 3 is essential, as many of our users rely on this specific vehicle for transportation because of its autonomous capabilities.

3) Solution

3.a) Design - Intended Use:

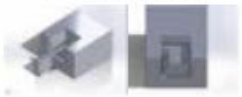

Fig 1: A 3D Model of device.

Our wheelchair device operates in two main phases. In Phase 1, the wheelchair is deployed from the trunk of the vehicle using a platform and rail system. A DC motor powers a threaded rod mechanism to move the wheelchair linearly out of the trunk. Once at the trunk entrance, the platform folds out, allowing the wheelchair to descend to the ground. Phase 2 involves transferring the wheelchair to the driver's seat and back.

3.b) Build - DEMO

Our device is not fully assembled or functioning yet, but we have begun testing on some of the components and the current results show promise.

4) Verification Results

4.a) Introduction: The requirements included in this test were focused on ensuring the compatibility of our wheelchair device with the Tesla Model 3 trunk space and verifying the smooth deployment of the wheelchair from the vehicle. These requirements were supported by the need to validate the design components virtually on Solidworks to ensure functionality.

4.b) Methods: Measurements were taken to assess the fit of the device components within the virtual space of the Tesla Model 3 trunk, ensuring no interference with vehicle structure or operation. The solution was tested by constructing and simulating the platform and rail system in Solidworks, analyzing its movement and interaction with the wheelchair.

4.c) Results: The virtual testing in Solidworks verified that our solution met the requirement of fitting within the given measurements of the Tesla Model 3 trunk space. Initial simulations demonstrated smooth deployment of the wheelchair from the vehicle, indicating that the platform and rail system design is on track for implementation.

5) Conclusion

5.a) Summary: Our design closely follows the requirements set forth by our customers while also keeping in mind the various physical, practical, and economical constraints presented to us. Further mechanical testing will reveal to us if our progress so far has yielded favorable results and will potentially bring to light other concerns to be dealt with.

5.b) Revisions: Testing could have occurred sooner if we had acquired the necessary materials earlier on which would have given us a better idea of what other tests are necessary for different unexpected outcomes. While CAD designs are useful and necessary, we can't neglect trying things out on the electrical side.

5.c) Impact (Future Version): Our device has the potential to become a commonly used product for those who seek to live more free and independent lives due to needing less assistance from another individual. This device will allow these people to travel and complete tasks in their communities more similar to how the general public can.

References:

[1] Q. Nie, L. A. Rice, J. J. Sosnoff, S. Shen, and W. A. Rogers, "Understanding wheelchair use in older adults from the National Health and Aging Trends Study," *Archives of Physical Medicine and Rehabilitation*, 2023.

[2] L. L. Haubert *et al.*, "Car transfer and wheelchair loading techniques in independent drivers with paraplegia," *Frontiers in bioengineering and biotechnology*, vol. 3, p. 139, 2015.

EchoAware: An electronic vision aid with auditory feedback capabilities

Esther O. Adeniji[1,*], Emily A. Baccaglini[1,*], Emma Gutierrez[1,*], Rosalía Minyety[1,*], Caitlyn A. Walker[1,*]
[1]Department of Biomedical Engineering, Columbia University in the City of New York (*all authors contributed equally to this work)

1) User Need:

1.a) Use Case

EchoAware is designed for visually impaired individuals facing challenges navigating various environments due to limited visual acuity, encompassing tasks like crowd navigation, stair identification, and obstacle detection.

1.b) Problem Impact

NuEyesPro smart glasses and Biped's Smart Harness use magnification technology to notify users of obstacles but at a significant expense[1,2]. EchoAware addresses the need for an affordable obstacle alert system for individuals with visual impairments.

1.c) Scope (Objective)

EchoAware uses object and distance detection technology to provide real-time audio and/or haptic feedback to visually impaired users, enhancing safety and independence. The device is customizable via an app to meet individual needs and preferences.

2) Design Inputs

2.a) Constraints:

The device needs a 150° field of view, the average human field of view, to detect objects at least 2 meters ahead based on average reaction times.[3]

2.b) Requirements:

The device must be discreet, provide Bluetooth auditory feedback for obstacle notification, and include an accessible phone app for user personalization.

3) Solution

3.a) Design - Intended Use:

EchoAware is a clippable motion sensor device with LiDAR and camera modules, paired via Bluetooth to a smartphone app, enabling obstacle detection, decision tree analysis, and auditory feedback on hazards (Figure 1).

Figure 1. EchoAware clip-on LiDAR sensor and camera

3.b) Build - DEMO

The device alerts users about obstacles not detected by a primary mobility aid (Figure 2).

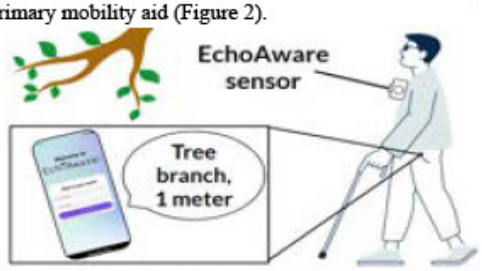

Figure 2. Potential users alerted about overhead objects.

4) Verification Results

4.a) Introduction

The range and accuracy of LiDAR sensors were assessed as well as the performance of the YOLOv5 object detection algorithm. The LiDAR sensor's minimum acceptable lateral range is calculated at 2 meters, with a minimum lateral field of view of 1 meter, based on average human walking speed and reaction time[3]. YOLOv5's performance mandates a minimum classification accuracy of 90% for common objects.

4.b) Methods

Various LiDAR sensors were tested for accuracy in reporting known distances until detection ceased. To evaluate the performance of YOLOv5, images of all known classes were processed, returning the algorithm's classification certainty.

4.c) Results

After testing various LiDAR sensors, we found the best sensor for the needs of this device to be the Arducam IMX219, with an axial range of roughly 4 meters and a 70° field of view. The assessment of YOLOv5 revealed an average 80% certainty and 95% accuracy in identifying current classes, but it requires more training to recognize additional classes relevant to urban environments.

5) Conclusion

5.a) Summary:

The team confirmed LiDAR and YOLOv5 effectively identify and alert users to immediate hazards, affirming their impact on individuals with visual impairment.

5.b) Revisions:

The team will develop a decision tree to prioritize user notifications. Integrating the camera and LiDAR sensor with an app will enable audio and haptic feedback. Continuous user dialogue will ensure needs are met.

5.c) Impact (Future Version):

EchoAware prioritizes object detection, integrates sensory feedback, and engages users continuously to enhance safety and independence. It empowers visually impaired individuals with affordable, personalized navigation assistance utilizing real-time obstacle detection technology, fostering autonomy.

References:

1. "Empowering Your Vision." NuEyes.
2. "Smart Copilot for Blind and Visually Impaired People.", Biped
3. "Outdoor Walking Speeds of Apparently Healthy Adults: A Systematic Review and Meta-analysis", Murtagh EM et al. Sports Med. 2021 Jan.

Acknowledgments: Thank you to Dr. Laura Bozeman, Dr. Rachel Partner, Jeanine Markey, and the Senior Design instructional team from the Department of Biomedical Engineering at Columbia University.

BreatheEZ Respiratory Device (BERD)

Nicholas J. Cavallero, Allen Hong, Nikhil Parab, Sebastian Winter, Brett F. BuSha, PhD
Department of Biomedical Engineering, The College of New Jersey, Ewing, NJ

1) Background:

Chronic obstructive pulmonary disease (COPD) is a progressive respiratory disease resulting in obstructed airflow into and out of the lungs' lower airways. Approximately 15.7 million Americans are diagnosed with moderate to severe COPD, predominantly affecting the adult population. BreatheEZ is designed to help adults over 65 who are experiencing COPD, constituting 12-14% of all COPD cases. Although at-home options exist for spirometry, there are many limitations that impact the user experience and measurements. Often, at home diagnostic spirometry devices can be complex or complicated for these end users over 65 years old. Improper use of spirometers can reduce measurement validity and accessibility to stored data for healthcare professionals. The BreatheEZ respiratory device aims to measure lung function in adult patients with moderate to severe COPD that provides accessible at-home care. The proposed device will calculate forced expiratory volume in one second (FEV_1), forced vital capacity (FVC), and the ratio between both parameters, and provide the user with a method to collect and store their personal information, raw data, and test conclusions.

2) Design Inputs

The BERD must adhere to lung function testing standards set by the American Thoracic Society (ATS) and global regulatory standards. Furthermore, all electronic components must meet medical device electrical and IPX1 standards, ensuring compatibility with electrical standards. Safety measures will include double insulation to prevent electrical shock. With regards to storing and accessing patient data, the device must adhere to HIPAA, HITECH, and other global regulations. ISO23747 standards also specify cleaning and disinfection protocols to encourage clinicians and users to promote health and safety. The device must calculate FEV_1 and FVC using air flow measurements [1]. It must be handheld with a maximum handling circumference of 23.7 cm and length of 9.6 cm [2]. The device must have a secure interface with the patient's mouth and store patient and test data.

3) Solution

The BERD will be handheld with a mouthpiece interface connected to an air filter and a flow divider to equally distribute flow to two flow sensors. At the front of the shell, the mouthpiece and disposable filter can be detached, allowing the user to clean and disinfect the device. The handle will feature storage for batteries and electrical components along with buttons above it to allow the user to start and complete a test. The working prototype design is shown in **Figure 1**.

Figure 1. BERD Prototype

3.b) Build - DEMO

The device has not been constructed yet.

4) Verification Results

4.a) Introduction

The device must be able to calculate spirometry parameters of FEV_1 and FVC from flow rates of up to 550 liters per minute (LPM).

4.b) Methods

Computational fluid dynamic (CFD) simulations were conducted in Ansys Fluent to evaluate the velocity of air flow through a 3-D model of the air splitter with an input flow of approximately 550 liters per minute (LPM).

4.c) Results

The results demonstrate evenly distributed flow through both channels with 274.7 LPM.

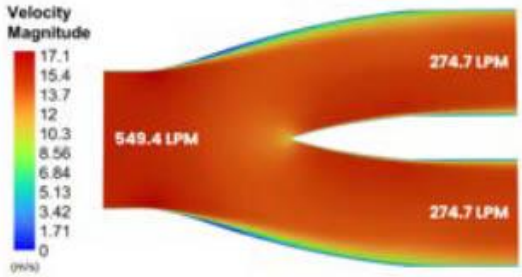

Figure 2. Air splitter CFD velocity simulation results

5) Conclusion

5.a) Summary:

The device has not been fully constructed and requirements are currently undergoing verification testing.

5.b) Revisions:

The group is exploring the implementation of an added adaptive component that will allow the device to be mounted on a table during use, as opposed to being held.

5.c) Impact (Future Version):

Having the ability to mount the device to a table will increase its accessibility to patients that may struggle with holding it.

References:

[1] Mannino DM, et al. 2003;254(6): 540-7 [2] NASA. ANTHROPOMETRY AND BIOMECHANICS, 1(3).

Acknowledgements: Thank you to Joe Zanetti, Brian Wittreich, and Michael Steeil for their guidance on this project. The team would like to thank the TCNJ School of Engineering for funding this project.

STEVENS
INSTITUTE OF TECHNOLOGY

LUMBAR MOVEMENT PREVENTION DEVICE

Mishkat Habib, Alexis Carmine, Annette Jimenez, Jocelin Lai, Sheng Wang, Nathan Hyungsok Choe
The George Washington University

1) User Need:

1.a) Use Case

Our device is designed for individuals with spinal nerve damage, providing real-time alerts through vibrations to warn against potentially harmful lumbar bending or twisting.

1.b) Problem Impact

Current solutions for spinal support, predominantly back braces, fall short in providing an optimal balance between mobility and protection for individuals with spinal nerve damage. These braces can lead to muscle atrophy during long-term hindering daily functionality and quality of life of the user (1). Furthermore, the impracticality of these braces in everyday scenarios leads to inconsistent usage, exposing users to the risk of further injury. The frequency of these complications is significant, as spinal issues are a common health problem, impacting millions (2).

1.c) Scope (Objective)

One objective of this device is to overcome the limitations of traditional back braces by providing a non-restrictive, user-friendly solution.

2) Design Inputs

2.a) Constraints:

To meet the specific needs of our users, the most stringent constraint was designing a device that is both highly sensitive to detect harmful lumbar movements and compact enough to be worn comfortably throughout daily activities. Another limitation was that our team was forced to complete this project under the university's budget and timeline.

2.b) Requirements:

The highest priority requirement for this device is its ability to accurately detect harmful lumbar movements within a threshold of a certain degree of bending or twisting dependent upon the patient (3).

3) Solution

3.a) Design - Intended Use:

This device combines accelerometers, gyroscopes, vibrators, an Arduino Nano, and a nylon sleeve. The accelerometer/gyroscopes detect both linear and angular motion. The vibration motors are compact and lightweight and are effective in alerting users. The sleeve is made of nylon and spandex, to ensure it is breathable, durable, and stretchable. The sleek, comfortable design ensures the device can be worn discreetly tucked in under clothing. The power supply consists of a 5V mini power bank, which is lightweight, portable, and effective.

The device will have adjustable settings for sensitivity, allowing it to be tailored to individual pain thresholds and movement patterns, enhancing its effectiveness across a diverse user range.

Figure 1. Functional Block Diagram

3.b) Build - DEMO

The MPU-6050 and the vibrator are connected to an Arduino Nano, which is programmed with C++ using Arduino IDE. The I2C protocol facilitates communication between the Nano Arduino and the MPU-6050 sensor. A vibration threshold, which can be altered, sets the device's sensitivity. In terms of hardware, three sensors are placed, forming a triangle.

4) Verification Results

4.a) Introduction (i = 1 ... N)

The requirements for this test were that the user should be alerted, with a vibration, from moving further than optimal bending (60°) and twisting (30°) angles [4].

4.b) Methods (i = 1 ... N)

The team tested the device at various sensitivities, on five people, five times, in order to standardize the intended movements. A protractor was used to obtain angle measurements.

4.c) Results (i = 1 ... N)

The Arduino is programmed in terms of the accelerometer value with respect to the vertical, y, direction to generate an output. The values in which the aY directions were equal to 60° and 90° were found experimentally. These values were to program the vibrators not be activated if the aY axis is between 90° and 60° bent forward.

5) Conclusion

5.a) Summary:

The device is successful in vibrating for the bending and twisting motions.

5.b) Revisions:

The team needs to determine how the bending and twisting motions will be changed for specific patients in order to create a more user-centered device.

5.c) Impact (Future Version):

This device will allow patients with nerve damage to stay active without injuring themselves.

References:

1. Kumar D. A. RJPT. 2021; 1(1): 26-28
2. Lee S. et al. Crit Rev Phys Rehabil Med. 2013; 25(3-4):159-172.
3. Knezevic N. et al. Low back pain. 2021; 398: 78–92.
4. Moon, Kee S., et al. "Extraction of Lumbar Spine Motion Using a 3-IMU Wearable Cluster." Sensors, vol. 23, no. 1, Dec. 2022, p. 182.

Acknowledgements: This Project is supported by the biomedical engineering department of the George Washington University.

TrueDose, an Adolescent Medication Adherence iOS Application

Matthew Jester, Skylar Ford, Elle Ferguson, Nicolette Cilenti
University of Pennsylvania

1) User Need:

1.a) Use Case

Medication non-adherence is a pervasive and multifaceted problem in adolescents. Core drivers for non-adherence include a desire for autonomy, a lack of parental support, and a sense of invincibility (S. Foster, personal communication, October 3, 2023). TrueDose aims to increase adherence by connecting patients, parents, and physicians; incorporating positive reinforcement; and promoting patient autonomy.

1.b) Problem Impact

70% of adolescents are non-adherent to their medications, contributing to 50% of treatment failures, 25% of hospitalizations, and 125,000 patient deaths.[1,2] Existing solutions, pill boxes and reminder apps, target forgetfulness, but are limited as they neglect the complex nature of adolescent non-adherence.

1.c) Scope (Objective)

TrueDose aims to increase medication adherence by targeting the core drivers of non-adherence. TrueDose integrates reminder capabilities, a pill identifier, data analytics, and patient incentives to improve adherence by balancing external support with patient autonomy.

2) Design Inputs

2.a) Constraints:

The pill recognition algorithm is constrained to identify pills on a surface through a photo, as there are concerns about images of adolescents' faces being taken or stored. The app is also constrained to assume a patient takes the medication after using TrueDose

2.b) Requirements:

TrueDose must accurately identify various pills, store instances of medication consumption, compute the data into adherence analytics for physician review, and award patients incentives inputted by caretakers upon adherence.

3) Solution

3.a) Design - Intended Use:

Figure 1: TrueDose design outline.

3.b) Build - DEMO

Figure 2: App interfaces and pill recognition UI demo.

4) Verification Results

4.a) Introduction

Testing was conducted to verify the success of the pill recognition algorithm, with the goal of >95% accuracy.

4.b) Methods

Trials were conducted using the ResNet architecture and a comparison was done between ResNet 18 and ResNet 20. Each algorithm was tested on varying numbers of pills, and the accuracy of the model was recorded and plotted.

4.c) Results

The ResNet 18 had higher accuracy with < 10 pills, and both algorithms were at 75% accuracy around 20 pills. Changing the number of levels in future trials led us to use ResNet 18 in our model.

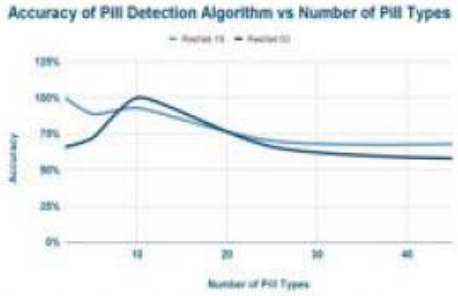

Figure 3: Graph of pill recognition algorithm accuracy.

5) Conclusion

5.a) Summary:

Currently, our design successfully integrates all three interfaces. TrueDose accurately alerts patients based on medication information inputted by the physician and can accurately identify pills (>90%), when <10 pills are included in a regiment.

5.b) Revisions:

The algorithm has seen a high success rate with 10 pills, but an advancement to the algorithm so that it retrains itself for each patient to increase accuracy to 95%. Further advancements may include a calendar feature for physicians to easily track patient adherence.

5.c) Impact (Future Version):

TrueDose aims to improve health outcomes for adolescent patients who must undergo complex medication regimens. We will achieve this by increasing medication adherence through an incentive-based approach that promotes trust between patients, parents, and physicians.

References:

1. DTB. 2016;54:6-9.
2. Kim, J. US Pharm. 2018;43(1)30-34.

Acknowledgements: We gratefully acknowledge the support provided by the University of Pennsylvania throughout the completion of this project. Additionally, we extend our sincere appreciation to the Bioengineering Senior Design faculty for the mentorship and assistance.

ParaVent: An Automatic Resuscitation Device

Megan Crawford, Varsha Thampi, Caroline Kolbusz, Sarah Wein, Robert Kallen, and Ashley Mont
New Jersey Institute of Technology

1) User Need:

1.a) Use Case

Any patient requiring ventilation with evidence of respiratory failure, apnea, or anesthetic induction may use ParaVent (PV). It is meant to replace the bag valve mask (BVM) as a resuscitation device.

1.b) Problem Impact

The standard BVM is a manual device that delivers oxygen to a patient through the compression of a bag. PV performs the same functions while eliminating the need for a clinician to manually operate the device. In addition it has the potential to eliminate human error associated with manually operating the BVM and prevent barotrauma from occurring [1].

1.c) Scope (Objectives)

The goal of PV is to provide ventilation to a patient at a controlled volume and breath rate. PV can operate automatically and manually. This dual use device provides positive pressure to patients who are in need of respiratory assistance. The automatic parts of PV, such as the motor, are reusable, whereas the bag portion is disposable to prevent contamination between patients.

2) Design Inputs

2.a) Constraints

PV must be lightweight and portable for ambulance use and able to deliver a customizable breath rate and tidal volume. The tidal volume varies by patient, so the device outputs a tidal volume range (400 mL - 1000 mL), which is customizable by the clinician [1]. This combination of constraints required the device to be kept as small as possible, while also ensuring that it could hold at least 1000 mL of oxygen.

2.b) Requirements

The device must operate at the appropriate rate of contraction to match the breath rate of the patient, which can range from 12 to 20 breaths each minute. The two highest priority constraints on PV are the breath rate being adjustable between 12-20 bpm and the tidal volume being adjustable between 400 - 1000 mL.

3) Solution

3.a) Design – Intended Use

PV is a two-part system that includes a disposable bag and reusable motorized component shown in Figure 1. Compressions are automated by the motorized component to the clinician's discretion by turning a dial until the desired breath rate is displayed on the LCD screen. The tidal volume is adjusted by sliding a pin that increases or decreases the length of contraction. Oxygen comes into the bag through an inlet valve and goes into the patient's lungs through an outlet valve.

3.b) Build – DEMO

PV is powered by a DC motor, which adjusts speed based on the dial reading set by the clinician. The scotch yoke mechanism moves the compressor up and down as the motor rotates at changing speeds.

Figure 1. ParaVent at full inflation (left) and full compression (right) attached to imitation lung

4) Verification

4.a) Introduction

The main tests performed were a measurement test and a whole system performance test. The measurement test verified the dimensions of the product and the whole system performance test verified the device's functionality and potential for use.

4.b) Methods

Tests included measuring the dimensions ensuring it matched with the device's model and the whole system performance test to verify that the tidal volume and breath rate were adjustable and accurate. In addition, the actual tidal volume output was measured by an anemometer.

4.c) Results

PV passed the measurement test, having accurate dimensions with a small margin of error. The adjustable breath rate input was accurate for each value. The intended tidal volume range was 400 mL - 1000 mL, however the actual range of the device was 100 mL - 500 mL.

5) Conclusion

5.a) Summary

PV is an automatic resuscitation device that provides ventilation without requiring constant clinician monitoring. The adjustable breath rate and tidal volume allow the clinician to decide the appropriate parameters.

5.b) Revisions

Two causes were identified as reasons why the intended tidal volume was not being delivered: 1) a portion of oxygen was leaking from the bag prior to compression and 2) the speed of compression. Improvements to overcome this include recasting the bag and using linear actuators instead of a scotch yoke mechanism.

5.c) Impact (Future Vision)

PV has the ability to greatly impact the medical device industry because it addresses a problem with the current standard of care. Without needing to manually operate a resuscitation device, the clinician is free to perform other operations that can ensure a patient's well-being.

References:

1. Dafilou B. et al. Western Journal of Emergency Medicine. 2020; 21(3): 722–726.

Acknowledgements:

We sincerely thank the BME Department at NJIT and our Senior Capstone Instructors Dr. Joel Schesser, Dr. George Collins, and Dr. Alev Erdi.

STEVENS
INSTITUTE OF TECHNOLOGY

Pulse PairIt: Wireless Vital Monitoring for Neonates

A wireless, non-invasive, and continuous vital monitoring device used to make imminent life-saving decisions

Stephanie Deren, Nina Burden, Alicia Cardoso, Arianna Gehan, Julia Zatyko
Stevens Institute of Technology

1) User Need

400,000 infants per year in the US are admitted to the neonatal intensive care unit (NICU) where medical professionals need to measure the heart rate, oxygen saturation, respiratory rate, and temperature of infants within 1 minute post-birth to determine if medical intervention is necessary.[1] The current method can result in health complications as it requires multiple wired devices which are time-consuming to set up and interfere with the treatment and transportation of the infant. Due to these inconveniences, the Pulse PairIt integrates multiple sensors into a single wireless unit to allow easy placement on the infant to promptly capture vital signs.

2) Design Inputs

Hardware: Neonates can range from 0.5-3.5 kg; the device must be designed for use on varying abdominal sizes.[2] To prevent injuries, such as pressure ulcers, the device can not weigh more than 25 g or be larger than 5 cm in any direction; this limits the sensors that can be used to capture the vitals. Due to the weight and size requirements, a multifunctional sensory system from Arduino was selected.

Software: The data needs to be displayed on a digital system, such as the hospital's existing iPads or computers. The digital interface must be easy to read and quickly display the different vital values. This system has to be easy to set up and connect to the hardware and needs to keep the data secure and private.

3) Solution

The Pulse PairIt is placed on the chest of the infant directly after birth, cleaning of the vernix is not necessary. The device can be secured with a band to ensure there is contact between the neonate and the sensors.

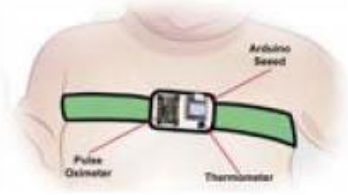

Figure 1. Pulse PairIt Sensor Layout

The device houses a pulse oximeter to measure blood oxygen saturation and heart rate, a microphone to obtain a secondary heart rate measurement using heart sounds, a thermometer, and an accelerometer to measure the rising and falling off the chest. The battery-powered device sends the collected data to a sedentary device through a Bluetooth connection. A novel software is used to analyze and filter the data and display the heart rate, respiratory rate, blood oxygen saturation, and temperature.

4) Verification of Results

To ensure the safety and efficacy of the device, a series of tests were designed to understand the limitations of each component and establish normalized values to account for manufacturing errors in the sensors. The first step was to identify the difference range between the gold standard and device measurements to develop the adjustment factor. Then to test the accuracy of the thermistor, the temperature of the device was recorded and compared to the value of the gold standard once it reached a steady value. Given the data collected, the Pulse PairIt was able to collect data within a minute and yielded a 1.2% margin error compared to the gold standard. The procedure was repeated 3 times for two subjects. An ANOVA Table was used to test the difference in means at a 95% confidence interval. From the ANOVA there was found to be no significant difference between the adjusted value and the gold standard value with a P value of .7888. Based on the developed protocol for the thermistor test, similar tests will be carried out to test and analyze the other components of the Pulse PairIt device.

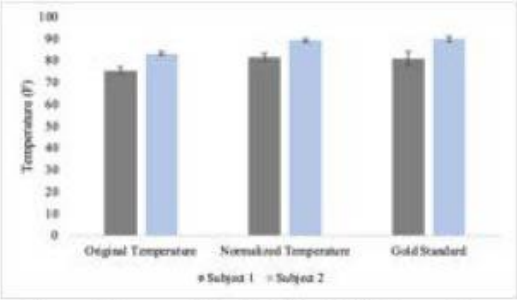

Figure 2. Raw vs Adjusted Pulse PairIt Temperature Measurements Compared to Gold Standard

5) Conclusion

The Pulse PairIt demonstrates the potential to rapidly and accurately measure heart rate, respiratory rate, blood oxygen saturation, and temperature through one wireless device, and will be further verified through ongoing testing. Accuracy will be verified through multiple rounds of rigorous testing. 5 participants will simultaneously have their heart rate, respiratory rate, blood oxygen saturation, and temperature measured with the gold standard techniques and with the Pulse PairIt.

The Pulse PairIt will allow the user to more efficiently and quickly provide the neonate the necessary care and treatment they need based on the vital information the Pulse PairIt provides. With this device, there will be a lower percentage of neonatal deaths as the user will have the critical information they need to treat the neonate.

References

1. Braun D et al, 2020 Jun:1(3) :10.1001
2. Bonner O et al, 2017 Feb;3(1):10.1136

Acknowledgments

Acknowledgments to Stevens Institute of Technology Biomedical Engineering Department for funding and Hackensack Meridian Health for advising

STEVENS
INSTITUTE OF TECHNOLOGY

Erias: A Bluetooth Cardiac Monitoring System for Pediatric Inpatient Use

Angela Song[1], Alexandra Dumas[1], Daphne Nie[1], Georgia Georgostathi[1,2], Samir Maarouf[1].
University of Pennsylvania, School of Engineering and Applied Sciences[1] and College of Arts and Sciences[2]

1) User Need:

1.a) Use Case

Children with chronic heart diseases frequently require continuous monitoring to assess cardiac abnormalities and longitudinal heart health trends. Whilst being monitored in these inpatient settings it is crucial that children are able to move around to play, be held by their parents and use the restroom as part of their developmental milestones.

1.b) Problem Impact

While portable ECG telemetry boxes exist, they must be carried around by the patient. Additionally, wired ECG systems limit patient mobility and can become entangled, causing frustration to clinicians. These factors ultimately reduce the ability to provide continuous cardiac monitoring to children.

1.c) Scope (Objective)

Erias aims to fulfill three main needs: reduce the wires present on pediatric patients for enhanced patient comfort, implement Bluetooth data transmission for improved patient mobility, and integrate arrhythmia detection for streamlined real-time, continuous monitoring of patient conditions.

2) Design Inputs

2.a) Constraints:

Based upon an average child's chest size our clinical mentors recommended maximal device dimensions of 6 cm (diameter) x 2 cm (height). This constraint meant we had to seek out smaller circuitry components, power supplies and back-up data storage micro SD cards which did limit the way we could process and store data on the hardware side of the device.

2.b) Requirements:

We prioritized being able to minimize scale whilst still collecting at least 5 electrophysiological signals.

3) Solution

3.a) Design - Intended Use:

To adhere to the current gold standards utilized in pediatric cardiac intensive care units (CICU), we designed our device to derive 5 leads simultaneously from 5 electrodes. This data is then transmitted to our clinician interface for analysis and signal processing. Our system aims to revolutionize cardiac monitoring by improving patient mobility and comfort and by furthering techniques for accurate cardiac data analysis.

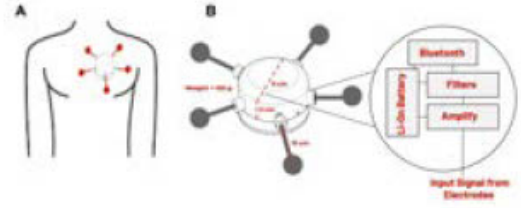

Figure 1. A. Diagram of Erias on chest with extending lead B. Final device schematic with major hardware components.

3.b) Build - DEMO

Our current prototype and physician interface can be seen collecting and transmitting cardiac data in real time (link).

4) Verification Results

4.a) Introduction

For early validation of our device we wanted to be sure our device could collect basic cardiac metrics (heart rate, atrial rate and ventricular rate) and produce results comparable to traditional ECG systems.

4.b) Methods (n=6)

The effectiveness and accuracy of the calculations from our device were performed by comparing with the published parameters associated with an online database (Chapman University & Shaoxing People's Hospital) on patients with normal and abnormal ECG signals as shown in Table 1.

4.c) Results

From our collected signals we were able to successfully measure non-sinus rhythms to a 95% accuracy and we are currently working towards detecting non-sinus cardiac parameters to an accuracy of 55%.

Table 1: Comparison of our Device's Software with Published Data

		Published Parameter Values			Our Algorithm's Values		
Patient	ECG Status	Heart Rate	Atrial Rate	Ventricular Rate	Heart Rate	Atrial Rate	Ventricular Rate
1	Healthy	63	63	63	63.36	63.4	63.36
2	Tachycardia	107	107	107	106.65	106.67	106.65
3	Healthy	71	71	71	70.89	70.91	70.89
4	Tachycardia	113	113	113	113.21	113.25	113.21
5	Healthy	66	66	66	66.11	66.12	66.11
6	Tachycardia	132	132	132	131.85	131.86	131.86

5) Conclusion

5.a) Summary:

Erias can successfully collect electrocardiogram signals from five leads and extract heart, atrial and ventricular rate.

5.b) Revisions:

As we move toward our final product, we hope to shrink the scale of our device so it rests on the chest more easily, explore recharging and backup data storage, expand our backend algorithm to include additional cardiac metrics, and explore software compatibility with Epic. Together these improvements will enable us to create a device that is compact and simple to use for clinicians and nursing staff.

5.c) Impact (Future Version):

Our new compact system will improve the standard of cardiac monitoring by improving pediatric patient mobility and comfort.

References: 1.Mumford, J et al (2023) BJPsych Bulletin, 47(2), 116-116. 2. Wang, L.-H. et al (2019). Sensors, 19(22), 4996. 3. Chen, M.-Y et al (2018). Morbidity and Mortality Weekly Report, 67(38), 1045-1049.

Acknowledgements: We would like to acknowledge Penn's Stephenson Bioengineering Maker Space and the Senior Design teaching staff for their technical support of our project.

DRIPPY: A Gravity Bag Feeding Rate Modulator

Adiva Daniar, Shreya Bathula, Victoria Curry, Gwendolyn Duncan, Annika Eisner
University of Pennsylvania Department of Undergraduate Bioengineering

1) User Need:

1.a) Use Case

500,000 Americans depend on feeding tubes, many relying on gravity bags[1]. Caregivers must monitor feeds to ensure drip rate, controlled by roller clamp tube compression, remains consistent with changes in stomach pressure.

1.b) Problem Impact

Feeds occur ~5x a day for 20-60min; caregivers are instructed to check the drip rate every ~10min, causing strain[2]. A current market option alleviating the need to consistently check rate is a pump. However, pumps are expensive ($500+)[3], complex, and not easily portable.

1.c) Scope (Objective)

In order to address the limitations of existing solutions, an affordable and portable device capable of delivering consistent drip rate is needed.

2) Design Inputs

2.a) Constraints:

The device must be portable (<5lbs and <1L, the size of an average gravity bag) and affordable, which limited the components that could be included. For example, a small, inexpensive motor capable of high precision was required.

2.b) Requirements:

To maintain user workflow of a standard gravity bag, the device should allow the user to set rate by eye and easily interface with standard feeding equipment. The device must accurately detect drip rate to within 20% of true rate to meet or exceed accuracy of a standard gravity bag[4].

3) Solution

3.a) Design - Intended Use:

Rate is calculated using a load cell tracking change over time. Tube compression is adjusted using a servo motor.

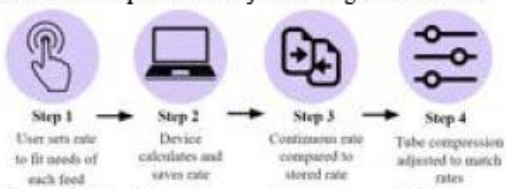

Figure 1. Workflow diagram of use process for Drippy.

3.b) Build - DEMO

Drippy interfaces with a standard gravity bag and IV pole. The gravity bag hangs on a load cell, and the tube inserts into a 3D printed servo motor enclosure. The circuit enclosure and user interface are mounted to the IV pole.

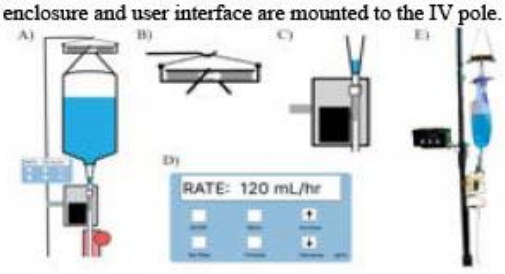

Figure 2. A) Device schematic B) Load cell C) Motor and 3D-printed tube enclosure D) User interface E) Full device

4) Verification Results

4.a) Introduction

Independent and conjoined tests were executed to demonstrate statistical power for both the load cell and servo motor to ensure they met or exceeded the accuracy of the current gold standard.

4.b) Methods

i) 3 trials at 3 rates were executed to verify rate detection, with the calculated rate compared to the measured rate (exact volume released over a 1min testing interval).

ii) Drip rate was detected over 30sec for all servo angles and compared to those measured from 30sec trials at each 5mm increment of the roller clamp (Fig 3).

iii) Over 5 trials, the full system was validated by manually adjusting drip rate while measuring times for the load cell to detect the change and the motor to adjust.

4.c) Results

i) The load cell was found to have a percent error of 17.6%, which is lower than the current caretaker average.

ii) The servo motor was able to cause drip rates along the full range of those of the roller clamp, though the step size was much larger.

iii) The load cell was able to detect a change in rate within 8sec and lead to servo motor correction within 30sec.

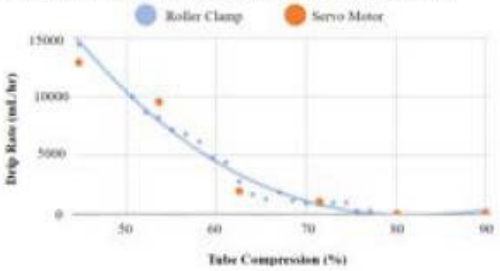

Figure 3. Comparison of drip rate with gravity bag roller clamp and servo motor.

5) Conclusion

5.a) Summary:

User workflow is maintained, weight is <5lbs, volume is <1L, and the 20% accuracy requirement is met. However, tube compression step size of the roller clamp was not maintained with the servo motor.

5.b) Revisions:

To produce more variance in drip rates, a motor with smaller angle changes is needed, and to further increase accuracy, a better load cell filtration algorithm is needed.

5.c) Impact (Future Version):

Drippy will reduce caregiver strain by removing the need to continually monitor and adjust drip rate during gravity bag feeds, allowing caregivers more time to focus on other tasks.

References:

1. Guha, H. et al. PLoS One. 2020; 15(7): e0236644.
2. Bear, DE. et al. Curr Opin Crit Care. 2018;24(4): 256-261.
3. Vitality Medical. 2023. *Feeding Pumps.*
4. Atanda, O. et al. Ther Adv Drug Saf. 2023;14:1-11.

See-Rynge: A Visually Accessible Liquid Measurement Device

Presenting Chiadika Eleh, Isaac Kim, Liam Pharr, Venkatesh Shenoy, Joey Wei
University of Pennsylvania

1) User Need:

1.a) Use Case

Liquid measurement is effortlessly carried out by many in essential daily activities like medication administration and meal preparation. However, for visually impaired individuals, this common practice is challenging due to its strong emphasis on visual ability.

1.b) Problem Impact

This challenge is further exacerbated by the absence of visually accessible liquid measuring devices, forcing impaired individuals to estimate measurements or seek daily assistance. Such actions undermine their autonomy and ability to administer medication for themselves and loved ones.

1.c) Scope (Objective)

In a market bereft of trusted, accurate, and versatile liquid measurement solutions for the visually impaired, See-Rynge stands out by seamlessly integrating automation, precision, and user-friendly technology to create the first true solution to this problem.

2) Design Inputs

2.a) Constraints:

As a device for the visually impaired, See-Rynge required focus on both function (mechanical precision, achieved by a stepper motor) and accessibility (achieved through audio and haptic feedback). From conversations with potential blind users, we also determined that our device needed to be compact, comfortable, and handheld.

2.b) Requirements:

Our primary device requirement is repeated volumetric accuracy. Our acceptable error threshold, based on ISO syringe precision standards, is ±3% of the target volume.

3) Solution

3.a) Design - Intended Use:

See-Rynge is a handheld liquid measurement device for the visually impaired. Our device uses a lightweight stepper motor to draw precise volumes of liquid into a disposable syringe. To accommodate visually impaired users, tactile buttons are used for its user inputs, each of which is associated with an audio cue (shown in Fig. 1). The user may adjust their desired volume via the buttons or an accessible bluetooth-enabled phone application.

3.b) Build - DEMO

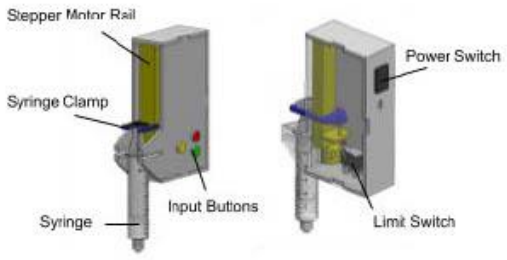

Figure 1: CAD Render of device, with labeled components. Housing is 3D printed PLA.

4) Verification Results

4.a) Introduction (i = 1 ... N)

See-Rynge was subjected to a series of volumetric trials to ensure that it met ISO standards for syringe accuracy, which range from 3% to 5% error depending on nominal and expelled volumes.[1]

4.b) Methods (i = 1 ... N)

To test volumetric error tolerances, See-Rynge was set to intake 5mL of liquid. The intaken liquid was weighed and its true volume calculated using known densities. Repeated trials were conducted to determine the average volumetric error and standard deviation of the device.

4.c) Results (i = 1 ... N)

Figure 2: When set to intake 5 mL of liquid, over 10 trials See-Rynge demonstrated an average volumetric error of 1.05% ± 0.81%, which is within ISO standards for syringe accuracy regardless of nominal and expelled volume.

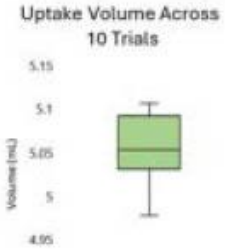

5) Conclusion

5.a) Summary:

See-Rynge successfully achieves both function and accessibility, measuring precise liquid volumes while catering to visually impaired users' needs. At a National Federation of the Blind Keystone Chapter meeting in December 2023, blind users were polled on their need for our device following a hands-on demonstration. 8 of 12 members responded "Very High Need."

5.b) Revisions:

We hope to improve user comfort by making the device smaller and utilizing a more intuitive button layout. We also seek to implement additional app functionality (e.g., common dosage databases) and a rechargeable battery.

5.c) Impact (Future Version):

These revisions will help users apply See-Rynge in a wide range of situations due to greater portability and battery life, granting users autonomy in many areas of life. Users will be able to self-administer medication without risk of overdose, as well as participate in previously inaccessible fields like baking and chemistry.

References:

[1] ISO 7886-1:2017(E). Sterile Hypodermic Syringes for Single Use—Part 1: Syringes for Manual Use. 2nd ed. Geneva, Switzerland: ISO; 2017. [Google Scholar]

Acknowledgements: We would like to thank the University of Pennsylvania Bioengineering Senior Design Program for their funding and guidance. Additionally, we would like to thank the Pennsylvania National Federation of the Blind for their constant support and feedback throughout the development of See-Rynge.

Development of Preeclampsia Wearable Detection Device

Nicholas Forcellati, Dylan Maund, Jana Mucci, & Ursula Oddo-White
Stevens Institute of Technology, Hoboken, NJ

1) User Need

1.a) Use Case

Preeclampsia is one of the leading causes of maternal mortality in the United States, causing over 70,000 annual maternal deaths [1]. Preeclampsia is diagnosed when high blood pressure and one or more of the following arises after 20 weeks of pregnancy: excessive swelling, protein in urine, low blood-platelet count, or neurologic symptoms [2]. MaternaTech aims to design a continuous blood pressure monitoring device for at-home preeclampsia monitoring.

1.b) Problem Impact

The current standard device for monitoring blood pressure, the sphygmomanometer, provides accurate but infrequent readings which limits accurate diagnoses.

1.c) Scope (Objective)

Our solution provides continuous blood pressure monitoring using a small wearable sensor placed near the heart for accurate readings at all times of day. With an easy to use smartphone application, our users will feel confident and in control of their health.

2) Design Inputs

2.a) Constraints

The design specifications for our device include accurate and comfortable sensor placement on the subclavian artery, as well as durable adhesiveness for continuous wear, and low power consumption.

2.a) Requirements

The highest priority requirements for our device are accuracy, size, comfortability, and durability.

3) Solution

3.a) Design - Intended Use:

Our design consists of two main components as shown in Figure 1; the force sensitive resistor (FSR) sensor and the Power & Integration (P&I) center. The FSR sensor will be attached by an OBGYN to the skin since placement is crucial for accurate readings. The P&I center will be detachable to increase comfort and water resistance as well as provide convenient charging. The P&I center will also export the data collected to a mobile application to be viewed by the user and their clinician.

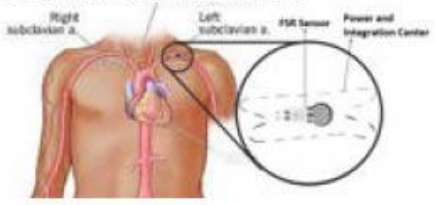

Figure 1. Illustration of Prototype over Subclavian Artery

3.b) Build - DEMO:

MaternaTech is using arterial tonometry to calculate mean arterial pressure. Design testing is currently being completed on the radial artery as shown in Figure 2.

The P&I center is being miniaturized by integrating smaller individual components while working on amplifying the signal without aliasing.

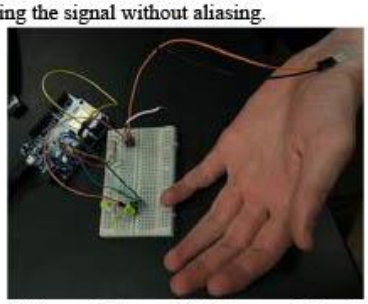

Figure 2. Electrical Setup of FSR Sensor on Radial Artery

4) Verification Results

4.a) Introduction:

Our device's accuracy in calculating a user's mean arterial pressure (MAP) must be tested. A study developed by Meidert proved arterial tonometry for MAP can be accurate within 2 mmHg of the current invasive gold standard, the radial artery catheter [3]. MaternaTech will verify that our measurements fall within this gold standard range.

4.b) Methods:

MAP will be calculated from the diastolic and systolic pressure taken from our device. To ensure accuracy, our measurements will be compared to values generated by a sphygmomanometer. A statistical analysis of the measured values will be conducted using an ANOVA table.

4.c) Results:

Testing has not been conducted yet.

5) Conclusion

5.a) Summary:

The software development of our sensor and mobile application are on track to be integrated in the upcoming weeks. Testing results have not been collected but the team anticipates the device's measurements will successfully fall within the gold standard range.

5.b) Revisions:

After the final development of our first prototype, MaternaTech will explore alternative options for adhesives for improved durability, and alternative hardware to make our product more compact.

5.c) Impact (Future Version):

Through incorporating the above revisions, the accuracy and comfortability of our device will be improved.

References:

[1] Dawson, Erica, et al CDC, 2022
[2] Fox, Rachael, et al. J Clin Med, 2019; 8:10:(1625)
[3] Meidert, A. S., Br J Anaest, 2014, 112:3:(521-528)

Acknowledgements:

We would like to thank Dr. Peter Popolo, Dr. Jennifer Kang-Mieler, and Dr. Ziyi Huang for their guidance and support throughout our design and development process.

STEVENS
INSTITUTE OF TECHNOLOGY

Affordable Cricothyrotomy Training Device

Emma Crowley, Ryan Jaworski, Timothy Lyons, Matthew Manduca, Maeve O'Connell, Christine Aloi, DNP, CRNA, APRN, Susan Freudzon, Ph.D.
Fairfield University

1) User Need:

Cricothyrotomy is a procedure used to establish an airway in emergency situations when the patient's anatomy or medical condition makes it impossible to insert a breathing tube through the mouth. Clinicians who are responsible for airway management must be trained in this procedure, including emergency medicine physicians, anesthesiologists, and nurse anesthetists. The procedure involves making an incision in the cricothyroid membrane just above the trachea (1).

Training is typically performed on a mannequin designed specifically for practicing cricothyrotomies. These mannequins made by companies such as TruCorp cost approximately $1,000 to $2,000 and include a removable trachea piece and artificial skin that must be replaced after multiple uses. Since this mannequin is designed specifically for the cricothyrotomy procedure, airway training programs must also purchase mannequins for procedures that are more commonly performed such as endotracheal intubation, central line placement and more. This project aimed to develop a low cost cricothyrotomy training system with high quality anatomy for use by the Fairfield University Nurse Anesthesia program.

2) Design Inputs

The user needs for the cricothyrotomy trainer were obtained from interviewing two nurse anesthesia faculty members. The faculty members demonstrated the commercially available device and described its limitations and cost challenges. your strictest constraints and how they limited your design choices. The main constrants are that the cost to produce the training system remain under $200. The anatomy of the trachea must be realistic to enable nurses to palpate the cricothyroid membrane, and the material should be somewhat flexible, resembling cartilage. Once the needle is inserted, the nurses must be able to inflate a simulated lung to ensure that the needle was properly inserted into the airway.

3) Solution

The prototype for the cricothyrotomy trainer was made using a combination of 3D printed components and commercially available tubing. The anatomically correct trachea was 3D printed using thermoplastic polyurethane (TPU) to make for a flexible realistic feel similar to cartilage (Figure 1). The model for the trachea is a publically available resource available through the Airway Collaboration (2). Commercial tubing and a bag were used to mimic a functioning lung. The 3D printed trachea was covered with a layer of silicone simulated skin.

4) Verification Results

Feasibility testing was performed using the first revision of the custom 3D printed trachea (Figure 2). Nurse anesthesia students practiced the cricothyrotomy procedure on both the custom assembled trainer as well as a commercially available trainer.

Figure 1 (left). A 3D-printed model showing trachea, thyroid cartilage and an opening representing the cricothyroid membrane where the incision is performed. **Figure 2 (right).** Nurse anesthesia students practicing the cricothyrotomy procedure using the custom device.

Nurse anesthesia students were surveyed and the 3D printed trachea was assembled along with commercially available tubing and artificial skin on a rectangular piece of plywood. The nurse anesthesia students practiced the cricothyrotomy procedure using both a commercially available device as well as the new custom 3D-printed training tool.

The nursing students were able to successfully practice the cricothyrotomy procedure using the custom 3D-printed device. Students were successfully able to palpate the cricothyroid membrane and insert a breathing tube.

5) Conclusion

Based on the feasibility testing of the device, the initial prototype successfully mimics the anatomy of the trachea. The cost of production of the prototype was approximately $100, well under the budget of $200.

Future revisions will require an improved base for the 3D printed trachea to support it and ensure it does not move. Additionaly, improved tubing and bag will be included to better fit inside the trachea and allow for easier puncture by the needle used in cricothyrotomy. These improvements will enhance the training experience for the next airway workshop.

An affordable anatomically correct cricothyrotomy trainer, can help provide enhanced training to healthcare professionals, ensuring proficiency in the essential skill of managing emergency airways.

References:

1. Moll V. Cricothyrotomy. Merck Manual Professional Version. 2023.
2. http://www.airwaycollaboration.org

Acknowledgements: We would like to thank the Fairfield University Hardiman Scholars Fund for funding this project.

Realistic Ultrasound Phantom for Regional Anesthesia Training

Ryan Baker, Emma Crowley, Wilson Kaznoski, Julia Kilroy, Christine Aloi, DNP, CRNA, APRN, Susan Freudzon, Ph.D.
Fairfield University

User Need

This project aims to provide the Nurse Anesthesia Program at the Fairfield University Egan School of Nursing with a brachial plexus ultrasound phantom for regional anesthesia training. The project will become open source and will assist student nurse anesthetists in performing interscalene nerve blocks. However, there are currently no reusable, low-cost ultrasound phantoms for regional anesthesia that exist on the market that accurately simulate anatomy involved in an interscalene nerve block. Existing solutions are often expensive, not durable, or anatomically inaccurate, which can limit accessibility for institutions to purchase the device and users' experience with an accurate training tool. To address this problem, we created a reusable, low-cost ultrasound phantom for regional anesthesia that accurately simulates anatomy involved in an interscalene nerve block.

Design Inputs

The design inputs are based on feedback from faculty and students in the Fairfield University Nurse Anesthesia program. The main design constraint is to keep each device cost below $200 to produce. We aim to produce two ultrasound phantoms that are resistant to deterioration after many uses while maintaining a low-cost budget, which includes selecting low-cost materials. The material should not leave needle tracks upon needle removal and must exhibit a consistency similar human tissue during needle insertion. The material's appearance in ultrasound images must resemble human tissue. Simulated brachial plexus nerves will be located 2-3 cm below the surface of the phantom since needle insertion does not exceed this point. It is critical that the ultrasound image of the brachial plexus is anatomically correct and the needle can be viewed in the image. This will ensure that users can practice an interscalene nerve block procedure properly and effectively.

Solution

The current prototype (Fig. 1) was made with a silicone rubber material that includes a 3-D resin printed brachial plexus nerve (Fig. 2) that can be imaged via ultrasound. The silicone material is designed for needle insertion and manipulation at the proper depth about 2-3 cm below the surface.

Figure 1 (Left). Prototype of the ultrasound phantom.
Figure 2 (Right). CAD model of the resin printed brachial plexus nerve.

Verification Results

Initial verification of the prototype consisted of a feasibility test involving ultrasound imaging of the phantom using the Telemed ArtUs Ultrasound System. Typical ultrasound images of the interscalene brachial plexus (Fig. 3) were referenced to look for the presence of three nerve roots of the brachial plexus (Fig. 4) and the needle on the ultrasound image (Fig. 5) to verify that the materials of the prototype showed accurate brachial plexus anatomy and eliminated needle tracks in the image.

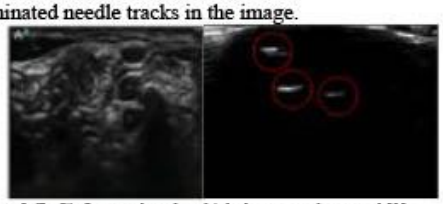

Figure 3 (Left). Interscalene brachial plexus on ultrasound [1].
Figure 4 (Right). Phantom ultrasound image showing the three brachial plexus nerve roots.

Figure 5. Ultrasound image showing the needle inserted near the brachial plexus.

Conclusion

Based on the feasibility test conducted, we conclude that the prototype successfully shows the brachial plexus nerve roots and the needle on ultrasound. The needle was able to be inserted and manipulated within the phantom material, and needle marks were not shown in the ultrasound image. The total cost to produce the prototype was approximately $160, which is below our budget of $200 per phantom.

Future revisions will be made to improve the phantom design. A skin-like material will be added as an outer covering for the phantom to improve realistic feel of the needle insertion. The material of the 3-D printed brachial plexus will be changed to allow for it to show up brighter and clearer on the ultrasound image. Tubing will also be inserted to simulate the local artery. Lastly, the 3-D printed brachial plexus must be secured during the silicone curing process so that it does not move to an anatomically incorrect position. These improvements will allow users to practice on a phantom that accurately simulates interscalene nerve block anatomy both physically and on ultrasound imaging. An anatomically correct phantom will not only help increase the accuracy in which the nerve block is performed but reduce the time it takes to locate important anatomical markers, resulting in improved patient outcomes.

References:

1. P. K. B. C. Raju and D. M. Coventry. Continuing Education in Anaesthesia Critical Care & Pain. 2014;14(4):185–191

Acknowledgements: We would like to thank the Fairfield University Hardiman Scholars Fund for providing the necessary funding for this project.

WoundWatch: Chronic Wound Monitoring System

Amelia Rehrig, Janelle Garcia, Andrew Dzikowski, Hans San-Luis, Morgan Whitlock
Stevens Institute of Technology

1) User Need:

1.a) Use Case

Annually, 9.5 million Type II diabetics in the U.S. will develop chronic wounds, associated with high morbidity and the risk of amputation[1]. The WoundWatch device provides a once a day diagnostic to monitor metrics of a patient's wound health status, alleviating these risks.

1.b) Problem Impact

Current chronic wound treatment consists of excessive physician appointments for visual wound assessment. This method is subjective to the physician's opinion and expertise, creating disparities in care. Research advances in the field have yielded viable monitoring solutions, but most are not currently on the market and are often invasive or expensive.

1.c) Scope

The taxing nature of standard chronic wound care causes high patient non-compliance in completing treatment. WoundWatch allows patients to quantify wound health and bridge the gap between physician visits, which will empower patients to manage their health independently.

2) Design Inputs

2.a) Constraints:

For accessibility to populations vulnerable to chronic wounds, the device must be non-invasive and affordable. Chronic wounds can occur anywhere on the body, therefore, the device must be hand-held and portable for non-hindered application. The device must wirelessly connect and upload data to the user's personal device for processing and output on the companion software.

2.b) Requirements:

This device will include accurate and effective data collection and manipulation to provide daily patient diagnostics. Collected data includes wound pH (unit pH), temperature (°F), and percent SpO_2 (SpO_2%). Patient diagnostics include the daily value of each collected metric and notification of each data metric's trends through the use of targeted messaging and a cumulative plot of the data over the past 30 days.

3) Solution

3.a) Design - Intended Use:

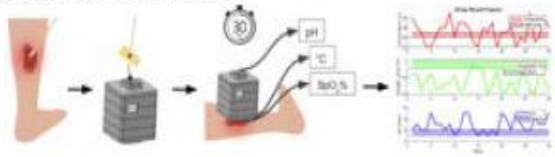

Figure 1. WoundWatch Monitors a Chronic Wound.

The patient swabs their wound with a sterile cotton swab, placing the sample on the pH strip on the device lid for data collection. After closing the lid, the device is pressed against the wound for 30 seconds to record temperature and SpO_2 data. The collected data is sent to the user's personal device, where companion software processes the data for user output, providing messaging about wound health state and a graph depicting wound health trends.

3.b) Build - DEMO

The device features a six layered design, housing the circuitry and sensor components. These layers seamlessly stack to organize the device hardware and form an easy to clean user-friendly product. A protruding compartment from the top layer houses the pH strip and LED sensor for pH strip color detection, which is correlated to a unit pH value by the software. Another compartment protrudes from the bottom layer to house the temperature and SpO_2 sensors, allowing them to directly contact the wound.

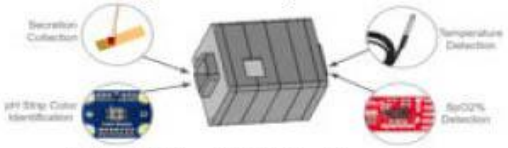

Figure 2. WoundWatch Key Components

4) Verification Results

4.a) Introduction

Efficacy tests will be conducted for the device sensor's measurement ability of temperature, pH and SpO_2.

4.b) Methods

A commercial thermometer, optical pH sensor, and pulse oximeter will collect control data, which will be compared to multiple experimental trials conducted using the device sensors. Statistical analyses, including ANOVA and Tukey Post Hoc, will identify significant differences between control and experimental data.

4.c) Results

Upon completion of efficacy testing, the sensor accuracy is anticipated to follow the standards specified in the respective product manuals. For temperature, an error of ±0.5°C between the range -10°C to 85°C is expected. For pH, an error of ±1 pH unit is expected. For SpO_2, an error of 1.5% (± 0.55%) is expected.

5) Conclusion

5.a) Summary:

The affordable and practical design accurately quantifies chronic wound health status within a minute, omitting the need for frequent physician visits and empowering patients to continuously manage their wound healing.

5.b) Revisions:

To reduce direct contact with open wounds, a deeper penetrating light source for the SpO_2 sensor and an infrared temperature sensor should be used, allowing for better retention of a sterile wound environment. Revisions to the device housing and hardware should be considered to further optimize user experience and device portability.

5.c) Impact (Future Version):

WoundWatch will integrate its data into existing telemedicine systems to reduce patient burden of traveling to physicians and allow for constant feedback from healthcare providers, improving wound healing outcomes.

References:

1. CDC. 2023

Acknowledgements:
Dr. Sally Shady, Dr. Hongjun Wang & Dr. Nicole Fosko

STEVENS
INSTITUTE OF TECHNOLOGY

TESee: A TEE Visualization Simulator

Christian Acuña*, Megha Gopal*, Sean Gull*, Abigail Masri*, George Pittas*, and Dr. Christopher Page
*All presenters contributed equally to this project
Department of Biomedical Engineering, Stony Brook University, 11794.

User Need:

Transesophageal echocardiogram (TEE) allows for planar ultrasound (US) images of the heart to be taken through a probe navigated down the esophagus [1]. Medical students and residents training in this imaging modality experience difficulties due to the technical complexity of adjusting the US head to proper angles for diagnostically relevant images. TEE simulator training has been shown to result in higher skill level and post-training test scores, making it an integral aspect of training curricula [1]. Existing TEE training simulators, including augmented reality and computer-based models, suffer from high cost and limited portability [2]. This creates a potential disparity in training access between well-funded medical centers and those with smaller budgets while also hindering skill development and procedural competency. The ethical imperative for accurate and safe medical procedures underscores the need to improve training through accessible and realistic simulation technology.

Our TESee device aims to address existing limitations in TEE simulator cost, software overhead, and portability by replacing the US probe head with a laser, allowing visualization of the relationship between the probe angle and imaging plane.

Design Inputs

The TESee device contains a TEE probe with a controllable laser head, a heart model, and a phantom of the esophagus for the device to move through. The strictest design constraints are the need for a transparent heart model, budget and size. The 3D printed heart model must be transparent to best visualize the laser imaging plane while minimizing reflection and diffraction of the light. The laser used also must be strong enough to properly penetrate through the heart while small enough to fit down the esophagus. Most importantly, it is of utmost priority that the material cost of the TESee device is minimized and portability of the device is maintained.

Solution

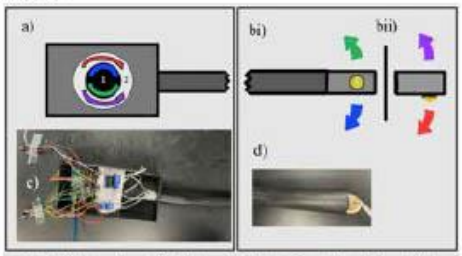

Fig 1. Probe schematic (a-b) and prototype (c-d). Knob 1 controls medial/lateral movement of the probe (bi) and Knob 2 controls anterior/posterior movement (bii).

Our Laser-Tipped TEE probe replaces the ultrasound tip with a line laser (Fig 1b/1d) such that the anatomic plane is visibly highlighted. The movement control mimics an actual TEE probe, ensuring users can replicate placement and movement of the probe with the knobs (Fig 1a/b) for specific views. Note that the control box has been opened to view the interior mechanism (Fig 1c).

Verification Results

The proposed design was tested at transducer angles between 0° and 140° at the upper-esophageal, mid-esophageal, and transgastric levels to ensure the incident laser illuminated the proper anatomic plane as per ASE Guidelines (Fig 2a-c) [3]. Photographs of laser penetration at each angle were taken along the sagittal (Fig 2di) and transverse (Fig 2dii) planes to ensure proper light propagation through the heart model over n=5 insertion and retraction cycles of the TEE probe in the esophagus.

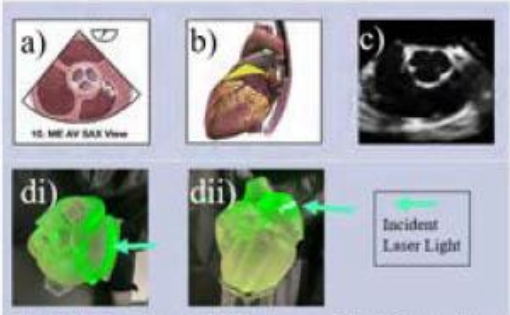

Fig 2. Mid-esophageal TEE views at 25°– 45° transducer angle, visualized with an a) illustrated imaging plane, b) drawn 3D model, c) 2D TEE image, and d) printed transparent heart with incident laser light. [3]

Conclusion

Our design successfully allows accurate user visualization of the relationship between probe angle and anatomical plane illumination without the need of a computer or US, thus decreasing product cost in comparison to competitors. Further avenues of development in this design will include increasing the transparency of the heart to allow for increased anatomical plane visualization as well as having experienced clinicians providing feedback for model accuracy, ease of use, and fidelity to in vivo conditions. Ultimately, with our product, users can be confident that they will gain an understanding of correct probe placement and angle necessary to take anatomically accurate and diagnostically relevant US images during clinical TEEs.

References

1. Jujo S et al. *J. Soc Sim Healthcare* 2021.
2. Benson M et al. *Echocardiography* 1995.
3. Hahn R. et al. *J Am Soc Echocardiogr* 2013.

Acknowledgements: We would like to thank Dr. Christopher Page, who aided in the development and discussion of the product, serving as our clinical mentor. All funds for this project were given through the Stony Brook Biomedical Engineering Department as per the budget allocated for the Senior Design class curriculum.

STEVENS
INSTITUTE OF TECHNOLOGY

Case-Based Reasoning to Aid in Clinical Decision Support of Traumatic Brain Injury

Ethan Moyer[1,2], Gabriella Grym[1,2], Ali Youssef[1], Tony Okeke[1], Caroline Vitkovitsky[1], Ed Kim[1], Dmitriy Petrov[3]
[1] Drexel University, [2] Moberg Analytics, [3] Penn Presbyterian Medical Center

1) User Need:

1.a) Use Case Neurosurgeons play a vital role in effective treatment planning of traumatic brain injury (TBI). Despite their extensive expertise, these specialists face challenges due to the heterogeneity and lack of understanding of TBI. One such challenge is deciding whether the benefits of surgery outweigh the risks.

1.b) Problem Impact Physicians often use medical records, clinical guidelines, and personal experience for deciding if a patient needs surgery. These sources, however, are not always actionable. Clinical guidelines especially, fall short, being mainly consensus-based rather than evidence-based. Individual physician experience is limited, with some trauma centers seeing only one to three cases per month. This lack of decision support contributes to the 80,000 out of 1.5 million annual TBI cases in the US that lead to permanent disability and the 50,000 that result in death [1].

1.c) Scope (Objective) This project aims to address these limitations by building a data-driven system that delivers actionable and adaptable clinical decision support for the management of moderate to severe TBI.

2) Design Inputs

2.a) Constraints Dataset - Our model will be trained and tested on the medical record, imaging, and waveform data of the 2206 patients of the TRACK-TBI dataset.

2.b) Requirements Predictive Accuracy - To match or exceed clinician proficiency, we will leverage a subset of the TRACK-TBI data for testing. Dr. Petrov (neurosurgeon, Penn Presbyterian Medical Center) will aid in identifying clinically relevant features and intermediate endpoints for our algorithm. Our aim is an AUC of at least 0.8085[2].

3) Solution

3.a) Design - Intended Use Our solution will leverage case-based reasoning (CBR) to store and retrieve similar past patient cases, offering clinicians valuable decision support. Subsequently, new cases will be looped back into the case library for continuous growth.

3.b) Build - DEMO

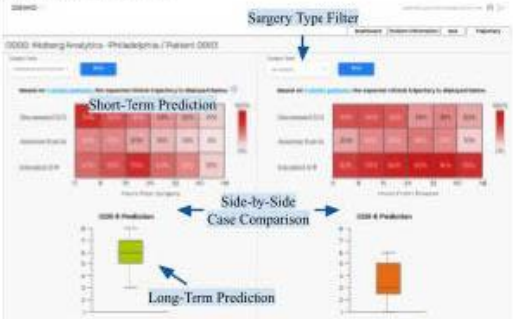

4) Verification Results

4.a) Introduction Our verification focused on the Predictive Accuracy requirement, critical for assessing the system's capability in clinical decision-making for TBI treatment. Our approach involved predicting patient trajectories - based on the decision to do surgery, and the surgery the patient will undergo - using machine learning models and the TRACK-TBI dataset.

4.b) Methods Three machine learning models—Decision Tree (DT), Random Forest (RF), and XGBoost (XGB)—were used to evaluate the system's accuracy. The models were trained using a dataset of 2206 patients from TRACK-TBI, with 24 features such as patient age and ward location; these were identified based on their correlation with the need for surgery. The models' performances were assessed using AUC of the ROC curves and F1-scores, reflecting their discriminative ability and precision-recall balance, respectively.

4.c) Results The RF model exhibited superior predictive accuracy, with an AUC (0.83) higher than our target benchmark of 0.8085. These results affirm that our system, particularly through the RF model, successfully meets the Predictive Accuracy requirement, validating its potential as a reliable, data-driven decision-support tool in TBI treatment. See figure below for detailed ROC curves illustrating each model's performance metrics.

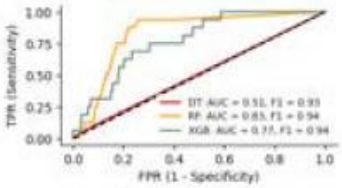

5) Conclusion

5.a) Summary The RF model surpassed the AUC benchmark of 0.8085, meeting our requirement. A limitation in verification testing includes reliance on the specific TRACK-TBI dataset, which may not generalize to broader TBI patient populations. Further, the complexity of TBI's heterogeneity poses ongoing challenges for any predictive model.

5.b) Revisions To enhance the solution's impact, several revisions are recommended. Firstly, expanding the dataset could improve the model's generalizability and robustness. Secondly, integrating additional clinical parameters might refine predictive accuracy. Finally, iterative testing and feedback from neurointensivists will refine the solution's clinical relevance.

5.c) Impact (Future Version) Our solution leverages past patient data to individualize care through actionable clinical decision support. If successful, our approach aligns with calls from researchers and institutions for a more precise, patient-centric approach to TBI treatment.

References:

1. Center for Disease Control and Prevention. 2016
2. Farzaneh N. Npj Digital Medicine. 2021;4:78.

Acknowledgements: We extend our gratitude to Moberg Analytics for their expert guidance and resources, which were invaluable to the success of this project.

STEVENS
INSTITUTE OF TECHNOLOGY

Advanced Optical Probe for Early Detection for Pediatric Hemorrhagic Shock

Emma Goodrow, Tasmia Hasan, Joshua Andrews, Jess Schable
Drexel University

1) Need

1.a) Use Case

Hemorrhagic shock (HS) is a critical condition that results from significant blood loss due mainly to a traumatic event. With over 60,000 deaths per year, traumatic injury is the leading cause of death in children and adolescents. Rapidly detecting HS can benefit clinicians to take proper care, and it can increase the survival rate of pediatric patients (newborn to 18 years) and thus reduce the death rate from HS in the public.

1.b) Problem Impact

Cerebral Blood Flow (CBF) is crucial for brain function and viability, assessed through techniques like laser doppler flowmetry (which is invasive), transcranial doppler (which assesses only major arteries), magnetic resonance imaging (which lacks portability), and diffuse correlation spectroscopy (DCS). Standard probe sizes also do not accommodate for pediatric measurements. These limitations, especially in cases like suspected HS, where symptoms are subtle and pediatric diagnosis is challenging, delay timely care, with broader implications for public health.

1.c) Scope (Objective)

This project focusses on DCS systems and the objective is to develop a prototype probe for clinical use of DCS in the pediatric population.

2) Design Inputs

2a) Constraints

The biggest constraint is to ensure the DCS housing probe accommodates pediatric head circumference measurements. Other constraints include the availability of the 3.0mm (~0.12 in) 45-90-45 uncoated prism, testing the optical measurements using phantom models, and assembling the optical measurement system.

2b) Requirements

The design's primary requirement involves the photon detector count, aiming for a maximum count of [1000kHz] from the nearest source-detector separation (1cm) within the allotted measurement time. The device must maintain precise source-detector separations at specified distances (10, 15, 20, & 25mm) for enabling light penetration into the tissue at different depths and aligning with the existing optical measurement system.

3) Solution

3a) Design - Intended Use

This probe housing design integrates patient comfort and optic fiber precision, enabling the use of DCS measurements as a crucial biomarker during monitoring and treatment. Its versatility and portability seamlessly integrate into the healthcare continuum, offering valuable insights and supporting early benchmark readings for the timely detection of HS.

3b) Build - DEMO

Currently, our design is in the preliminary stage of being developed and printed. Design prototypes are being designed to meet the desired requirements.

4) Verification Results

4a) Introduction (1)

Source Detector Spacing - This verification test is most related to our light penetration precision requirement which specifies the specific distances between source detectors.

4b) Methods (1)

This test aims to validate the structural integrity and precision of the source detector spacing, ensuring that the measurements align closely with the specified distances. A calibrated caliper will be utilized to measure the distances between the source detector holes incorporated into the probe housing. The precision of these measurements leads to the functionality of the device, necessitating a rigorous approach to minimize any margin for error. To test the functionality of the new probe, we will conduct an occlusion test first and compare with existing lab prototypes by inducing ischemic occlusion and pressure-cuff release, i.e., manipulate blood flow changes.

4c) Results (1)

This verification test has not yet been completed.

4a) Introduction (2)

Light Leakage - This verification test relates most closely to our photon detector count as well as the penetration precision requirements. To produce accurate measurements, photons should not leak from the sides of the probe housing.

4b) Methods (2)

This test enables qualitative assessment of potential light leakage by visually identifying any undesired illumination and pinpointing its specific location. To precisely quantify light leakage, we reference a study that employs filters to measure and analyze the extent of luminous escape, contributing to the robustness of our experimental methodology in assessing probe housing performance.

4c) Results (2)

This verification test has not yet been completed.

5) Conclusion

5a) Summary

Design would be considered a success if the verification tests are passed.

5b) Revisions

Several revisions have been made to our need and design inputs. Additional fine-tuning may be required based on testing results.

5c) Impact (Future Version)

If successful, this design will be the first pre-clinical prototype to detect HS in pediatric populations.

References:

1. *Erin M. Buckley, et. Al, "Diffuse correlation spectroscopy for measurement of cerebral blood flow: future prospects," Neurophoton. 1(1) 011009 (20 June 2014) https://doi.org/10.1117/1.NPh.1.1.011009*
2. *Zhu B, et. Al Reduction of excitation light leakage to improve near-infrared fluorescence imaging for tissue surface and deep tissue imaging. Med Phys. 2010 Nov;37(11):5961-70. doi: 10.1118/1.3497153. PMID: 21158309; PMCID: PMC2988832.*

Acknowledgements:

We would like to acknowledge Dr. Kurtulus Izzetoglu and his ICONS Lab as well as Randolph Sinahon.

STEVENS
INSTITUTE OF TECHNOLOGY

Triple C+: An Adaptive Neck Orthotic

Colin Babick, Roxana Gomez, Shaila Cuellar, Brenna Henderson.
Syracuse University College of Engineering and Computer Sciences.

1) User Need:

1.a) Use Case

Our users consist of patients who suffer from neurodegenerative diseases with the complication of dropped head syndrome (DHS). DHS leads to neck muscle weakness, causing increased difficulty in performing the activities of daily living, and is negatively associated with survival time in this patient demographic [2]. Our goal for this device is to offer a neck orthotic that improves patient's comfort, safety, and quality of life.

1.b) Problem Impact

Over 50 million Americans annually are affected by neurodegenerative disorders, with over 1 billion people worldwide impacted. 1-3% of those patients suffer from dropped head syndrome [1], equating to over 1.5 million Americans affected annually and 30 million individuals around the world.

1.c) Scope (Objective)

Limitations of our solution involve this diverse patient population. With adaptability and adjustability at the forefront of our design use cases, we must create a design that meets the needs of all patients but is not lacking in user comfortability, comfort, and safety.

2) Design Inputs

2.a) Constraints:

In developing the neck orthotic design, the team faced challenges in highlighting all established requirements—comfort, adaptability, and support—without compromising any feature. Despite the existence of many devices similar to ours, they typically forgo one aspect. Our objective was to create a design that delivers on all fronts.

2.b) Requirements:

Our highest priority requirements are comfort, support, and adaptability. The target audience might not have complete use of their limbs and are wheelchair-bound but can still move their jaw, or vice versa. This is currently compromised by current neck brace designs which will lack one aspect or another. With our design, we hope to adapt to these requirements fully and have removable parts to compensate where support and comfort are needed simultaneously. This is to be done through an innovative chin rest with an adaptable platform, as well as a head support component that can also be tailored to the individual's needs.

3) Solution

This figure depicts the latch mechanism we intend on using for the chin rest that allows it to be moved up and down to cater to the needs of the individual. Included above is also a sketch of the intended design which can be better visualized through these images of our low fidelity prototype.

4) Verification Results

4.a) Introduction (i = 1 ... N)

The device will eventually go through testing to ensure its comfortability, its safety, and that it improves the patient's quality of life. Testing will look at a user's range of motion and comfort using a variety of sensors and equipment.

4.b) Methods (i = 1 ... N) TALK ABOUT DESIGN PROCESS AND MATERIALS

To test and verify our device, we will compare a subject's range of motion with Triple C+, without any orthotic device, and with a common device in the market. The measurements will be the distance that a subject can turn their head to the left and right as well as how far the head can tip in either direction. A goniometer will be used to measure angles and head positions that can be achieved in different devices. Similarly, we will use a digital tracker to compare possible jaw movement with Triple C+, without any orthotic device, and with a common device in the market. This will indicate if Triple C+ allows patients to speak and eat comfortably. An additional test of importance is the pressure distribution of the head weight while a patient wears Triple C+. A pressure distribution map will be created using an array of pressure sensors placed on the brace. Likewise, thermal imaging cameras will be used to create heat distribution maps to ensure Triple C+ does not create hot spots or sores on a patient.

4.c) Results (i = 1 ... N)

Testing has not yet occurred, but the desired results will indicate that the device is a new and upgraded solution for patients with Dropped Head Syndrome. First, anticipated results of the range of motion test will show that the Triple C+ allows a patient to turn and tilt their head farther to the left and right than current solutions and with no brace. Additionally, the attainable jaw movement, and therefore the ability to eat and speak, will be greater when wearing Triple C+ versus the other conditions. Lastly, we anticipate that the pressure and heat distribution maps will not show any area that bears the most weight and therefore experiences the most pressure.

5) Conclusion

5.a) Summary:

Although testing has yet to occur as we wait for materials to arrive to begin prototyping, we aim to adhere to all regulations without violating the constraint guidelines. With this, we'll be able to successfully execute our design idea.

5.b) Revisions:

To ensure we have an impactful project, we have instilled a secondary design plan in place. Once we begin prototyping, we will also have another version of our design just in case our primary one is not feasible. Need be, we will tailor regulations, verifications, and constraints accordingly if the back-up design needs to be used instead.

5.c) Impact (Future Version):

We hope that the changes made will not negatively impact the user experience. Our goal is to adhere to the same functionality of the device that was initially established.

References:

1. Dropped Head Syndrome associated with Motor Neurone Disease. Physiopedia. Accessed October 15, 2023. https://www.physio-pedia.com/Dropped_Head_Syndrome_associated_with_Motor_Neurone_Disease
2. Gourie-Devi M, Nalini A, Sandhya S. Early or late appearance of "dropped head syndrome" in amyotrophic lateral sclerosis. *J Neurol Neurosurg Psychiatry*. 2003;74(5):683-686. doi:10.1136/jnnp.74.5.683
3. Pancani S, Tindale W, Shaw PJ, McDermott CJ, Mazzà C. An Objective Functional Characterisation of Head Movement Impairment in Individuals with Neck Muscle Weakness Due to Amyotrophic Lateral Sclerosis. *PLoS One*. 2017;12(1):e0169019. doi:10.1371/journal.pone.0169019

Acknowledgements: Dr. Douglas Yung and SOURCE Funding, Syracuse University.

Humeral Rod with a Suture Tab

Avo Elebyijan, Hans Elijah Hugo, Colton Prentzel, Emad Sawaged
New Jersey Institute of Technology

1) User Need:

1.a) Use Case

The Humeral Rod with a Suture Tab was developed in partnership with orthopedic surgeon Dr. Michael Levy and addresses proximal and shaft fractures and rotator cuff attachment while meeting the current standard of care. The user needs include stabilizing the humeral fracture, attachment to the rotator cuff ligaments, preventing axial rotation of the humerus, and having a low-profile contour to the humeral head. These tasks are essential for achieving successful surgical outcomes and promoting patient recovery.

1.b) Problem Impact

The current standard of care procedure has separate procedures to address hard and soft tissue stabilization, prolonging surgical times and increasing the risk of complications. The inadequacies in current solutions, including insufficient support for both tissue types and lack of precision in measurement and positioning, contribute to higher healthcare costs and broader burdens on healthcare systems.

1.c) Scope

The proposed solution aims to address key limitations in existing humeral fracture repair procedures. By providing comprehensive support for hard and soft tissues, and compatibility with standard operating room equipment and techniques, the Humeral Rod with Suture Tab seeks to enhance surgical outcomes and patient experiences. These objectives align with the project's scope, ensuring effective resolution of challenges faced by orthopedic surgeons.

2) Design Inputs

2.a) Constraints:

The most critical constraint revolved around maintaining compatibility with established surgical procedures and equipment used in humeral fracture repair. This constraint also includes materials choice based on biocompatibility and manufacturability. In addition, the suture tab needs to contour over the humerus head and have a low-profile under the skin. We prioritized ensuring seamless integration with existing surgical protocols and instruments, ensuring usability and effectiveness in real-world surgical settings.

2.b) Requirements:

The Humeral rod must have a length of 180mm and have a locking mechanism on the top of the rod for suture tab attachment. The rod must also have 3 threaded holes for the cortical screws. The Suture tab must contour to the humeral head and protrude not more than 20mm from the center of the rod. The Cortical screws must have size M3.5x0.6 and have a total length of 40mm. The locking bolt must have size M5x0.8 size and have a total length of 12mm. The rod, suture tab, cortical screws, and must be fabricated in Ti-6Al-4V. The associated instruments such as the reamer, awl, and drill guide must be fabricated in stainless steel. These dimensions ensure that the devices fit into each other, are biocompatible with the human body, and meet current standard of care.

3) Solution

The design was intended to be used for procedures regarding proximal and shaft humeral fractures along with rotator cuff repair. The main feature is a suture tab with an associated locking mechanism to the humeral rod which allows easy repair of the rotator cuff. This allows surgeons to fixate humeral fractures and secure rotator cuff in one procedure. This serves to reduce total surgical time and expedite the healing process.

The humeral nail is designed for implantation down the shaft of the proximal humerus. Three cortical screws on three different axes affix the bone to the rod, thereby providing stability for effective healing. The nail is press-fit into the bone, allowing for relative ease in implantation, while providing sufficient stability and ease of removal.

Figure 1: Rod Implant and Suture Tab

4) Verification Results

Our focus is on verifying whether the fabrication meets the dimensions requirements for our humeral rod implant. Verification of dimension requirements will be conducted by measuring dimensions of the fabricated device using a caliper and measuring tape. Furthermore, bending tests for the humeral rod and pull-out tests for the suture tab will be conducted. For the pull-out test, we will attach the suture tab to the rod and steadily apply a tensile load until it's pulled out. In the bending test, we'll place the rod on supports and gradually apply a load to measure its stiffness and strength. Currently, results are pending.

5) Conclusion

5.a) Summary:

To meet our objective, continuous feedback was collected from a physician to refine the design until the user needs were met. Verification of the design will be conducted to confirm that the final output aligns with the requirements. Additional verification will be conducted to test the strength of the devices. With this, we can submit our designs to our user, ready for commercialization if desired.

References:

1. M. S. Levy. 2018: 10074342

STEVENS
INSTITUTE OF TECHNOLOGY

Wearable Device for Lee Silverman Voice Treatment-BIG Therapy Amplitude Training

Sam Kim, Timothy Luu, Anix Binu
Drexel University, DrExcel Health

1) User Need:

1.a) Use Case: Around 10 million Patients suffering from Parkinson's Disease are often prescribed Lee Silverman Voice Treatment-BIG Therapy (LSVT-BIG), but it is only available in a clinical setting. Patients unable to attend therapy sessions need a remote option with instruction and feedback available that would typically come from practitioners.

1.b) Problem Impact: Existing solutions implementing LSVT-BIG pose difficulties in producing precise and accurate results. The usage of contemporary technology may complicate the older demographic that is targeted.

1.c) Scope (Objective): The team aims to develop a simple device that can guide movements related to LSVT-BIG Therapy, providing users with instruction and feedback regarding the quality of their movements. The team aims to address limitations related to restricted accessibility and improve the accuracy of the feedback system.

2) Design Inputs:

2.a) Constraints: The device requires a comfortable user experience regarding physical design, clear feedback, and cost. As the product targets those with limited movements and provides necessary LSVT-BIG therapy, the device must be easily wearable, affordable, and technological but easily usable and manageable by the user themselves.

2.b) Requirements: The product will measure (1) range of motion of patient (providing angular measurements), (2) velocity of the movement (measuring linear velocity), and (3) real-time feedback (conveying the data to the user and their respective clinicians).

3) Solution:

3.a) Design - Intended Use: The team's solution is successful. With the Arduino being able to track the patient's movement. The interpretation of the data and recommendations will be given in real-time. Data of the movements are stored for further post-processing as desired by the clinician.

3.b) Build - DEMO: The video presents a demonstration of one of our team members using the arduino board to monitor arm movement.
https://youtu.be/G2toKv7OtTw

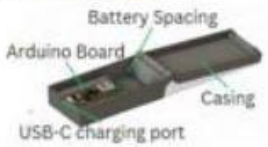

Figure 1. CAD Model of the Prototype

The motherboard is kept inside the casing with the device sitting on the patient's wrist stabilized with two straps.

4) Verification Results:

4.a) Introduction: In the verification test, the team aims to see if the range of motion recorded by the Arduino is precise and accurate. Using a set of tests, the team will measure if the device produces exact readings on subject movements.

4.b) Methods: The test will include a predetermined range of motion produced by a test subject where the motion is captured from the subject flexing their shoulders in a semi-circular motion. The design will be attached to the arm of the object, and with MATLAB, the data then will be produced over a 30 second interval. There will be multiple trials done to validate the results.

4.c) Results: The MATLAB code that the project runs utilizes accelerometer and gyroscope data in real time. This information will be relayed to the patients to correct patient movement during therapy. As shown in Figure 2, the linear acceleration and angular velocity over time is measured. With x, y, and z axis angular velocity and linear acceleration measured, these values will later be integrated to determine position. The team also highlighted an area on the desired target range for subject movement.

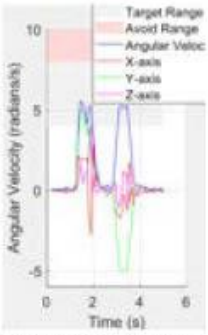

Figure 2a. Real-time Angular Velocity of Two Repetition of Shoulder flexion

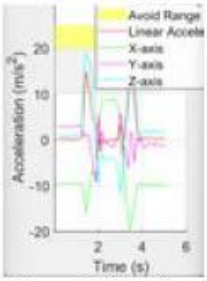

Figure 2a. Real-time Acceleration of Two Repetition of Shoulder flexion

5) Conclusion:

5.a) Summary: The design is deemed successful with the data producing exact measurements and with correct pinpoint of arm location through proper integration during the test trial. With proper translation of these measurements, the information will be relayed to the patient as well as therapists for therapeutic assessments.

5.b) Revisions: The team will look for replacements on Arduino boards as the current version is powered through a USB-C cable. The team will research motherboards that can be powered with a miniature, lightweight battery.

5.c) Impact (Future Version): As the work purely focuses on arm movements at the moment, the team hopes to implement this design on the entire body functions. With this goal, the device will be able to track the specific patient body movements, allowing a complete LSVT-BIG therapy in a remote setting.

References:

1. Mirelman A. et al. Arm swing as prodromal marker. 2016;31(10):1527-1534.
2. Warmerdam E. et al. Quantification of Arm Swing during Walking Healthy & Parkinson's Patients. 2020;20(20):5963.

Acknowledgements: As the team partnered with DrExcel Health under the advisory team of Dr. Anh-Thu Vu and Dr. Robert Hand, the team acknowledges their funding provided by DrExcel Health for this project. Moreover, the team also acknowledges Drexel University Biomedical Engineering Department for Dr. Jaimie Dougherty's supervision.

STEVENS
INSTITUTE OF TECHNOLOGY

Designing a 3-D Heart Model for In-Vitro Testing of Bioadhesive Cardiac Interventions

Sai Chamarthi[1], Nina Li[1], Joanne Liu[1], Finja Scholz[1], Ruhul Abid, M.D., Ph.D.[2]
[1]Center for Biomedical Engineering, Brown University
[2]Division of Cardiothoracic Surgery, Cardiovascular Research Center, Rhode Island Hospital

1) User Need: Researchers developing cardiac surface interventions (e.g. cardiac patches) lack reliable methods for conducting in-vitro validation of their product's attachment mechanism, long biodegradability, therapeutic drug diffusivity, and product safety/efficacy. Early preclinical studies are necessary to assess the utility of their designs to ensure meeting of FDA performance standards prior to clinical trials[1]. Current in-vitro testing methods rely on animal models and tissue-engineered alternatives. The former permits access to a complex physiological environment but creates huge resource and ethical burdens[2]. Additionally, long-term studies are limited due to tissue degradation. The latter overcomes some previously mentioned limitation but provides an oversimplification of heart physiology unsuitable for studies[1,2]. As such, the proposed solution provides an alternative to current in-vitro testing of cardiac surface therapeutics by allowing for cost-efficient, accessible, long-term adhesion and degradation studies.

2) Design Inputs: Physiological factors constrain the model to mimic the in vivo environment, heart surface characterization, and tissue mechanical properties.

To preserve reliability of testing results outputted by the proposed solution to researchers, biological and mechanical similarity of the model to human hearts remains the utmost priority. Based on previous literature, these values include ensuring a surface pH of 7.1 - 7.2, temperature of 37°C, apex-base deflection of around 6 mm, surface thickness of <13.5 mm, and non-cytotoxicity[3,4,5]. Additionally, the friction coefficient of the heart surface will be necessary to model.

3) Solution:

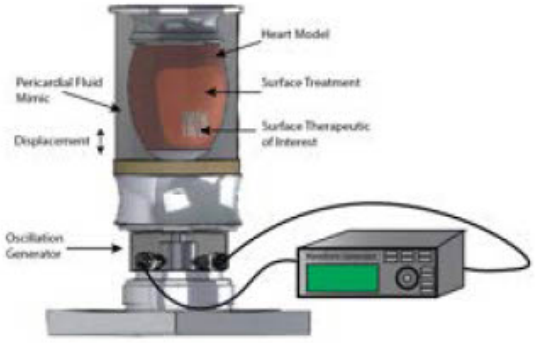

The Heart Model will be coupled with an image processing algorithm to measure therapeutic adhesion over time. It will be placed in an incubator to maintain desired temperatures.

4) Verification Results:

Surface Friction Coefficient

The applied force needed to cause the "slip" of the pig heart on a developed cardiac patch was recorded and averaged from 3 different trials, and used to calculate the approximate static friction coefficient for the developed heart model to match. The same experiment was repeated on the designed silicone heart surface before and after surface treatments.

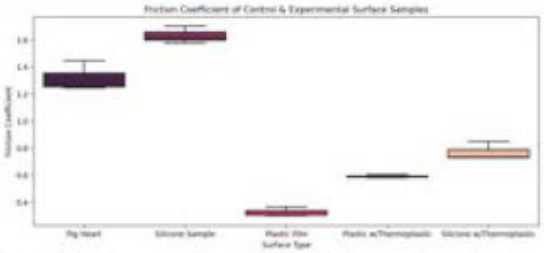

Fig 1. Friction coefficient of control and experimental surface samples.

Deflection of Heart Under Heart Contraction

The deflection, measured from the apex to base of the model heart, was recorded when a Frederiksen Vibration Generator no. 218 connected to a waveform generator set to 1 Hz and maximum amplitude was applied to the developed heart model. Iterations of the heart model structure and mechanical properties allowed for cyclic contraction of 4 mm at 60 bpm. The necessary force applied on the heart model to deflect it to target values is approximately 3.1 N.

Fig 2. Compressive displacement of heart model (mm) vs applied force (N).

5) Conclusion: The design is successful in relying on non-living materials (i.e. animal models or cells) to reproduce the heart surface environment and beating mechanism of the heart, reducing pre-clinical trial costs, and increasing accessibility of cardiac surface treatment testing. In doing so there are notable approximations made to a true epicardial surface and environment, and additional parameters listed in design requirements will need to be tested and optimized.

Further work is required to optimize the surface treatment of the model to better reflect epicardial properties. Increased model accuracy with more precise calibrations to replicate the in-vivo environment will allow access to reliable adhesion and longevity testing of prototypical cardiac surface therapeutics. This may reduce the cost of research and development for these devices and accelerate the timeline to patient access.

References:

1. Abdelsayed G. et al. Applications in Engineering Science. 2022;12:100115.
2. Mathur, A. et al. Advanced drug delivery reviews. 2016;96;203-213.
3. Shechter G, Resar JR, McVeigh ER. IEEE Trans Med Imaging. 2006;25(3):369-75.
4. Meenakshi, K. et al. Indian Heart Journal. 2016;68(3);336-341.
5. Prokopovich, P. et al. Acta Biomaterialia. 2010;6(10);4052-4059

Acknowledgements: We would like to thank the Brown University School of Engineering and ENGN 1931L Profs. Tripathi, Schneider, Gray, and Raimondo for their support and funding through the course.

STEVENS
INSTITUTE OF TECHNOLOGY

Development of a Myoelectric Controlled Shoulder Orthotic for Persons with UE Impairment

Prajit Dhuri[1], Alysabeth Gaito[1], Juan Ramirez[1], Ghaith J. Androwis, Ph.D.[1,2*]
[1]New Jersey Institute of Technology, Biomedical Engineering department, Newark NJ
[2]Kessler Foundation, Center for Mobility and Rehabilitation Research, West Orange, NJ
(Corresponding author e-mail: ghaith.j.androwis@njit.edu)

1) User Need:

1a) Use Case

The leading cause of disabilities in the United States stems from strokes, a common neurological condition that affects 795,000 people each year[2]. Approximately 80% of stroke patients experience some degree of upper extremity (UE) impairments[1]. The intricately crafted design of the M.A.X. system caters to individuals with mobility lost in the upper region by offering a myoelectric-controlled shoulder orthotic. The functionality of the device has been tailored to address the challenges that post-stroke patients encounter with activities of daily living (ADL) and improve their quality of life (QoL).

1b) Problem Impact

Few cost-effective devices on the market consist of electrical and mechanical capabilities to enhance arm motion. However, these devices can be bulky and limit the mobility of the patient. In addition, not many orthotic devices provide a smartphone application that receives recorded data on muscle movement to aid researchers in evaluating the patients' progress[2]. Effective research can lead to better tools for patients and a faster recovery.

1c) Scope (Objective)

The aim of our developed shoulder orthotic M.A.X. is to offer a wearable, lightweight option that can be customized to the patient. The design must be actuated using an electrical mechanism and controlled using muscle feedback.

2) Design Inputs

2a) Constraints:

The load limitation to weigh less than 5 pounds narrows the selection of materials. The model is composed of TPU and carbon fiber polycarbonate as lightweight options to maintain strength and flexibility. Nylon-breathable mesh blended fabric is incorporated with the printed components to create a body support.

2b) Requirements:

The facilitation of motor control via an EMG sensor(s) is intended to repair the loss of UE function by performing the task the patient wants to execute from recorded muscle data.

3) Solution

3a) Design - Intended Use:

Shoulder abduction and adduction is restored to patients with UE impairments by employing an actuation provider: a Dynamixel XH430-V210-R servo motor connected to a 4:1 gearbox. A nylon cord is drawn from the gearbox to a cuff, a part of the exoskeleton, at the triceps brachii to facilitate the actuation. The progress of the patient is collected from the Myoware 1.0 EMG and flex sensor data by an Arduino UNO R3 to ensure proper motion and is displayed on a mobile application via Bluetooth.

3b) Build - DEMO

The full assembly of the M.A.X. is not complete or functioning currently. The synthetic material serves as the connection between different components and the body.

4) Verification Results

4a) Introduction:

The EMG signal from the latissimus dorsi and the deltoid must produce a waveform that can indicate between shoulder abduction and shoulder adduction.

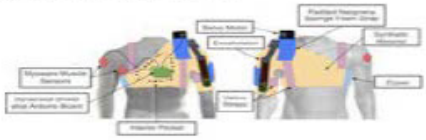

Figure 1. 3D model of the M.A.X.

4b) Methods:

EMG data sensed from the latissimus dorsi and the deltoid are initially processed through filtering and rectification, followed by extracting an envelope for each sensor's output. These EMG envelopes' amplitudes are then compared to predetermined thresholds to determine the patient's desired movement. Our algorithms evaluate the changes in these incoming signals to dictate the CCW or CW rotation that will lift or lower the arm.

4c) Results)

There was a peak in the EMG waveform every time the subject lifted their arm in shoulder abduction.

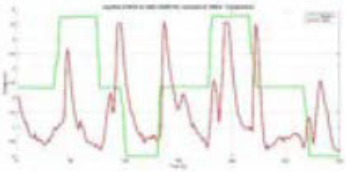

Figure 2. Demonstration of the EMG signal recorded

5) Conclusion

5a) Summary:

Tests with the EMG sensor have shown promising results for future efforts. The product is too early in development for success or failure to be determined.

5b) Revisions:

The current device is only capable of movements along the frontal plane, whereas loss in shoulder mobility can affect the shoulder's entire range of motion. The device is only limited to a single joint and can not provide aid to mobility below the elbow joint. Many UE impairments can consist of more dexterous movements.

5c) Impact (Future Version):

The M.A.X. has the potential to make an impact on the manufacturing of shoulder orthotics for people with disabilities. This is evident as the designed orthotic could be used to enhance the ability of a person with an UE impairment to complete ADL tasks effectively.

References:

1. Ingram L. A. et al. American Physiological Society. 2021; 3(131):949-965.
2. Sions, J. M. et al. HHS. 2012; 3(35):155-161.

STEVENS
INSTITUTE OF TECHNOLOGY

Cardiopulmonary Resuscitation (CPR) Assistive Device For Cardiac Arrest (CA) Patients

Hadeel Abdul-Rehman, Lauren Bazay, Erica Bonheur, Lizzy Caso, Ijeoma Obi, Carol Xu
Columbia University, School of Engineering and Applied Sciences, Department of Biomedical Engineering

1) User Need:

1.a) Use Case: Over 356,000 U.S. out-of-hospital cardiac arrests (OHCA) occur per year, and immediate CPR increases survival rate[1]. Risk factors for cardiac arrest (CA), which results in sudden unresponsiveness[2] include lifestyle and genetics, where older adults, men, and Black individuals are disproportionately affected[3]. Mitigating barriers to effective CPR is key, and by targeting laypeople this device aims to reduce deaths from OHCAs.

1.b) Problem Impact: Compression-only CPR simplifies bystander intervention but may compromise oxygen delivery, impacting its effectiveness over prolonged periods despite increasing intervention rates[4]. AEDs significantly enhance survival, guiding shock delivery to restore heart rhythm, yet their effectiveness is contingent on timely deployment[5]. The Beaty provides live feedback, but functionality issues limit emergency use[6]. The LUCAS device provides automated compressions, but its high price limits its accessibility to trained medical professionals[7].

1.c) Scope (Objective): The solution must simplify CPR, making it less physically taxing and more intuitive for untrained users, adaptable to all body types, portable for broad access, and cost-effective for widespread use.

2) Design Inputs

2.a) Constraints: This device must allow users to deliver effective CPR with a rate of 100-120 beats per minute (bpm) and a depth of 5cm[4]. Its design must be intuitive and simple for ease of use in high-stress situations and have a low-cost, portable design for widespread use. Durability is also key, to ensure longevity and compliance with health standards.

2.b)Requirements: (1) address the aforementioned constraints, (2) ensure stability to prevent slipping, (3) deliver consistent compressions, (4) distribute force evenly, and (5) maintain normal forces while accommodating different body sizes.

3) Solution

3.a) Design - Intended Use: Our device consists of a linear actuator for force generation controlled by an Arduino and a lever system to amplify and deliver the force to the patient. The linear actuator can deliver optimal compression forces. The lever system allows adjustment of forces based on patients' body types and the appropriate compression rate.

3.b) Build - DEMO: A lever system with a movable fulcrum allows for efficient force delivery. By moving the fulcrum, we can adjust force delivery as well as position based on patients' body size. A platform at the end of the rod delivers force to patients, and pivots at each end of the device ensure normal force delivery.

4) Verification Results

4.a) Introduction (i = 1 ... N)

Compression Force & Rate: Must achieve a compression rate of 100-120 bpm, depth of 5cm, and force of 500N. *Stability*: Must be able to stand firm on the ground and prevent disruptions. *Maintaining Normal Forces*: Must transfer force to the patient. Forces must be normal to all surfaces at contact points. *Adjustability in Force Magnification/Attenuation*: Must be adjustable to either magnify or attenuate forces without dismantling and rebuilding the device for proper force and rate delivery.

4.b) Methods (i = 1 ... N)

Measuring Forces: A CPR layperson, and a CPR trained individual, attempted compressions on a load cell over a period of thirty seconds at 110 bpm. *Fulcrum Position*: Using the leverage principle, we found that the rod had to be placed 20.55 cm away from the linear actuator to produce a downward force of 500 N.

4.c) Results (i = 1 ... N)

Measuring Forces: The CPR lay person was able to reach the required compression force (100-120 lbs) once over a 20 s period. The trained individual was able to reach this force, albeit inconsistently [Fig. 1]. Since neither a CPR lay person nor a person with CPR training were able to reach and maintain necessary compression forces, this experiment reaffirmed the need for a device to ease the physical aspect of providing effective CPR.

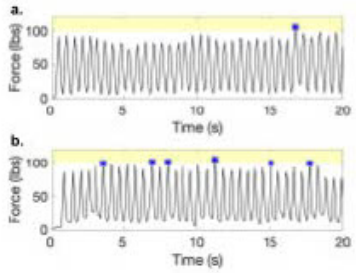

Figure 1. (a) CPR force on load cell by CPR layperson. (b) CPR force on a load cell by a CPR-trained person. Yellow bar indicates required force for effective CPR.

5) Conclusion

5.a) Summary: Our device applies manipulatable force by repositioning the fulcrum. Pivots on the ends of the lever ensure normal and stable compression. Hence, the device satisfies our current functional requirements.

5.b) Revisions: In our next prototype, we plan to use more durable materials to improve device strength and explore other force generation methods. We will also reduce the device size, add feedback mechanisms to measure compression depth, and implement adjustability to account for different body sizes.

5.c) Impact (Future Version): These revisions will allow our device to aid bystanders in performing life-saving interventions to prevent death by CA. Having an automated device on hand will expedite response time to improve survival rates in CA.

Acknowledgements: We would like to thank our professor, Dr. Lauren Heckelman, as well as the Columbia BME faculty who are supporting our work.

References: 1. Centers for Disease Control and Prevention. Cardiac arrest. CDC. 2023. 2. American Heart Association. What is cardiac arrest? Heart.org. 2023. 3. US Department of Health and Human Services. Causes and risk factors. NHLBI. 2023. 4. Geddes LA, et al. Chest Compression Force of Trained and Untrained CPR Rescuers. Cardiovasc Eng. 2007;7(2):47-50. 5. Hammet E. Cardiac arrests - How to Perform CPR and Use an AED. First Aid for Life. n.d. 6. Beaty. "About Us". 2023. 7. CPRSavers and First Aid Supply. LUCAS 3.1: Chest Compression System. 2023.

STEVENS
INSTITUTE OF TECHNOLOGY

A Device to Quantify Non-Nutritive Infant Sucking Force

Peter DiPietro, Carsi Kim, Christopher Moore, Giuseppina Than, Ashley Valenton.
Department of Biomedical Engineering, Stony Brook University.

1) User Need:

1.a) Use Case

Users include any provider who cares for infant subgroups with critical health conditions. Infants must demonstrate non-nutritive sucking (NNS) behavior, referring to when an infant sucks without receiving nutrients, that can be monitored and analyzed by the user.

1.b) Problem Impact

Due to limitations in current solutions and techniques (e.g. the gloved finger technique[1] and other smart pacifiers[2]) such as ease-of-use, safety, accuracy, automation, and monitoring time, providers are unable to perform a reliable and quantitative assessment of infant NNS force. These inconsistencies limit the quality of infant healthcare in the NICU, leading to increased hospital costs and poor diagnostics.

1.c) Scope (Objective)

Our smart pacifier allows users to quantitatively, instead of subjectively, measure the NNS force of an infant and receive the recorded data through Bluetooth to a smartphone app. This addresses the limitations of current techniques' ease of use, safety, and accuracy.

2) Design Inputs

2.a) Constraints:

The constraints in our device include accurate quantification of NNS, infant-safe materials, and accessible data collection. Accuracy limits what characteristic we choose to identify NNS. The device must follow similar safety constraints as currently approved infant devices. The device is marketed towards clinicians; therefore data should be easily accessible via tablet or smartphone.

2.b) Requirements:

Quantifiability of sucking force and data acquisition is our device's main requirement. NNS studies show that infant sucking qualities of strength and frequency proved strong indicators of infant health[3]. The device measures intraoral pressure (mmHg), which is defined as the negative suction, created when the palate and tongue separate[5].

3) Solution

3.a) Design - Intended Use:

Our device, PaciMetrics, features 3D-printed housing for electronics and wireless charging to fit a Philips Soothie pacifier including a circuit board with a microcontroller, air pressure sensor, and battery management, and an app for displaying NNS pressure data.

Figure 1. *PaciMetrics workflow illustration.*

3.b) Build - DEMO

To use the device, the infant will suck on the pacifier. Then, the air pressure sensor will take measurements of intraoral pressure, and the microcontroller will send the measurements to the smartphone app.

Figure 2. *CAD-designed casing and electronics.*

4) Verification Results

4.a) Introduction

A syringe was used to prove that the air pressure sensor is functional and can measure and record data in the expected ranges for NNS (max of 10 mmHg[4]).

4.b) Methods

Air pressure measurements were taken with a testing apparatus consisting of a syringe and hardware from our first pressure measurement prototype.

4.c) Results

As a result of pulling on the plunger, a drastic pressure drop is seen. Releasing the plunger brings the pressure back to the baseline atmospheric pressure. Small amounts of leakage explain measurements above the baseline.

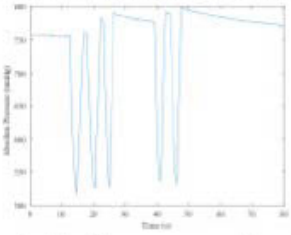

Figure 3. *Absolute pressure vs. Time data.*

5) Conclusion

5.a) Summary:

Our device successfully measured and displayed simulated NNS data. We were able to receive accurate burst measurements of suck using alternate methods instead of traditional pressure measurement methods. Limitations include the inability to test with infants.

5.b) Revisions:

Verification testing of an added pump instead of a syringe will be used. NNS assessment should be conducted with infants instead of the testing apparatus to address accuracy issues.

5.c) Impact (Future Version):

Obtaining actual infant data using our device will allow us to continue improving our design after taking into account inconsistencies (i.e. infant movement, infant chewing, etc.) caused by data collection. Our device could then be implemented into hospitals and healthcare facilities for providers to use during infant care.

References:

1. Chantal L. et al, Springer. 2001; 16:58-67
2. Akbarzadeh S. et al, IEE. 2022; 69(7):2370-2378
3. Pickler RH. et al, PMC. 2006; 20(2):157-162
4. Nascimento MD. et al, ACR. 2019; 24:e2191
5. Akbarzadeh S. et al, IEE. 2022; 69(7)

Acknowledgements:

We would like to thank Dr. Helmut Strey, Dr. Annie Rohan, and Daniel Pardo.

STEVENS
INSTITUTE OF TECHNOLOGY

Lower Extremity Joint Loading Deficits During Dynamic Single Limb Loading Tasks in Individuals Following Anterior Cruciate Ligament Reconstruction: A Retrospective Motion Analysis Study

Monica Padykula, Evan Bouchard, and Dr. Kristamarie Pratt
University of Hartford, CETA, and ENHP

1) User Need

1. a) Use Case: Anterior Cruciate Ligament Reconstruction (ACLR) and postoperative rehabilitation continue to be a multidisciplinary focus in both research and clinical environments as approximately 1 in 3,500 people tear their ACL [1]. This study can inform individuals who have had ACLR surgery and rehabilitation specialists about the motion at the hip, knee, and ankle in the sagittal, frontal, and transverse planes in athletes who have undergone ACLR during a series of single-limb loading tasks (SLL).

1. b) Problem Impact: Current post-ACLR functional tests include an evaluation of an individual's ability to perform non-compensated functional movements including the use of evidence-based testing: range of motion, digital hand-dynamometry, symmetrical strength, gait symmetry, balance, Functional Movement Screening, and Y-Balance Screening. SLL is not widely used due to a lack of evidence-based data. This motion analysis study investigates variations of the SLL task since recent studies have shown that despite reduced loading demands during a forward SLL, individuals post-ACLR display deficiencies in knee dynamics during both SLL and running, indicating a challenge in dynamically accommodating forces at the knee during the transition to running in rehabilitation [2].

1. c) Scope (Objective): To investigate the mechanics of forward, 90°, and 180° SLL tasks in the ankle, knee, and hip joints of both the uninvolved (non-ACLR limb) and involved (ACLR) limbs using raw biomechanical data, Cortex™ and Visual3D™ to quantify these dynamic tasks and ultimately integrate into rehabilitation practices.

2) Design Inputs

2. a) Constraints: This study does not have a control group. Additional constraints in this study include different sports played, method of injury, post-injury timeline, and functional testing results.

2. b) Requirements: Participants were individuals with primary unilateral ACL reconstruction using either bone-patellar-tendon-bone (BTB) autograft or allograft. Testing took place at The Center for Musculoskeletal Health Bone and Joint Institute Motion Lab Hartford Healthcare Rehabilitation Network from 2020-2022, thus making it a retrospective study. A total of 43 reflective markers were placed on participants. Kinematic data and ground reaction force data were collected using a marker-based, 12-camera motion capturing system at 250Hz and force plates at 1000Hz. The participants were instructed to stand on both feet on a single force platform in front of a target. The tape was placed on the ground on an adjacent force platform as a target. The distance from the target was normalized to each individual as a distance equal to the length of their tibia. Participants were asked to leap forward to the target location onto a single limb, to lower as far as they could, and then return to the start position. For the forward SLL, participants faced the positive Y-direction. For the 90º turn SLL, participants faced the positive X-direction, and for the 180º turn SLL, participants faced the negative Y-direction.

Despite the change in starting position for each task, testing the hypotheses requires a similar set of testing protocols and they do not differ from one another.

3) Solution

3. a) Hypotheses 1. During the forward SLL task, there will be a greater peak knee flexion angle than in the 90° turn SLL task and 180° turn SLL task.

2. In all 3 tasks when compared to the uninvolved limb, the involved limb will exhibit less knee power absorption and smaller vertical ground reaction force.

3. When compared to the uninvolved limb, the involved limb will exhibit more plantarflexion and inversion at the ankle. It is anticipated that these differences will be greater during the 90° turn and 180° turn than the forward SLL task.

4) Verification Results

4. a) Introduction: Data collection files were properly obtained and trials without greater trochanter markers were removed due to the inability to determine hip joint center.

4. b) Methods: The following steps were employed to ensure data quality to extract accurate results:

1. Review the data collected and organize it appropriately. Record issues.
2. Troubleshoot data accordingly via Cortex™ and Visual3D™.
3. Identify the deceleration phase; initial contact to maximal knee flexion.
4. Run a report via Visual3D™ to display graphical representations of inverse kinematics.
5. Apply MANOVA to compare differences in the variables of interest between involved and uninvolved limbs during the different SLL tasks.

4. c) Results: Currently, no results are available as trials are still being validated and corrected. It is anticipated to have preliminary results by the presentation date. Results will include joint kinematics, kinetics, and statistical analysis to apply to the hypotheses created for further discussion.

5) Conclusion:

5. a) Summary: The summary will include major findings and trends from results and the hypotheses proposed will be examined within the context of the study's outcomes.

5. b) Revisions/Future Impact: Revisions include adding a control group and improving data collection procedures to enhance quality, for example having the participants land on the same force plate. Future impact would improve the reliability and validity.

References:

1. Kaeding CC, Léger-St-Jean B, Magnussen RA. Injuries. 2017;36(1):1-8.
2. Pratt, K. A., & Sigward, S. M. Reconstruction. 2017;47(6): 411–419.

Acknowledgments: Thank you to Hartford Healthcare Bone and Joint Institute and the University of Hartford-CETA and ENHP.

STEVENS
INSTITUTE OF TECHNOLOGY

RhythmRehab: A Programmable Exoskeleton Glove for Personalized Hand Therapy

Osama Eltoum[1,*], Ian Huang[1,*], Rohin Patel[1,*], Danyal Sheikh[1,*], Zetian Zhang[1,*]
[1]Department of Biomedical Engineering, Columbia University (*All authors contributed equally to this project)

1) User Need:

1.a) Use Case: Cardiovascular and cerebrovascular diseases often lead to severe patient outcomes, such as stroke, paralysis, and loss of limb motor functions, resulting in significant pain and involuntary movements [1]. These conditions compromise patients' independence, necessitating lifestyle adjustments and reliance on caregivers [2]. Rehabilitation is critical for restoring neural plasticity and motor functions. In response, we developed RhythmRehab, targeting patients with impaired hand functions to enhance hand dexterity and achieve personalized treatment goals. We aim to improve patients' ability to perform daily activities and boost their quality of life.

1.b) Problem Impact: Rehabilitation devices, including the Amadeo Robotic Arm and RAPAEL Smart Glove, play a crucial role in enhancing hand therapy by offering movement facilitation, resistance, support, and feedback. Despite their benefits, these high-quality devices are often unaffordable for many, creating a gap in access to effective hand therapy. Low-cost alternatives often lack customization, sensory feedback, and progress tracking, which can demotivate patients and delay recovery. The economic burden of advanced therapy devices not only strains households but also exacerbates disparities within the healthcare system, impacting the overall quality of medical care and recovery outcomes.

1.c) Scope (Objective): Our solution aims to address the key challenges of high cost and lack of customization on low-cost devices. By bridging the gap in the current market, we seek to make our products more financially accessible while improving customization with features such as progress tracking and sensory feedback.

2) Design Inputs

2.a) Constraints: Our design was constrained by a budget of $500 and the need for the rehabilitation device to be customizable to fit individual users' hands. This steered us towards selecting cost-effective materials and leveraging institutional resources that were provided free of charge.

2.b) Requirements: We envision our glove to place minimal weight on patients' hands while maintaining flexibility at each joint. The design should not interfere with rehabilitation activities when worn by patients.

3) Solution

3.a) Design - Intended Use:
Our solution is a remotely controlled exoskeleton device integrated into a glove for patient rehabilitation. It supports various tasks across different difficulty levels, aiming to reduce patient dependence on the device for daily activities over time.

3.b) Build – DEMO: Our design is inspired by the conveyor belt system, which is powered by a DC motor to bend and retract each joint **(Figure 1)**. An L298N H-Bridge powers the DC motor with an Arduino to control direction and speed.

4) Verification Results

4.a) Introduction: The primary objective was to assess the functionality and performance of the rehabilitation glove, specifically focusing on its capability to facilitate flexion and extension movements in finger joints.

4.b) Methods: We employed a finger goniometer to measure the degree of flexion and extension for proximal interphalangeal and metacarpophalangeal joints following AMA guides and compared with the normal range of biomechanical motions documented in the studies [3].

4.c) Results: Our conveyor belt-driven device successfully facilitated flexion and extension, closely mirroring the natural range of motion expected in human fingers. Achieving 61 degrees of movement, our design fell within the normal ranges reported for both flexion and extension at the two joints [4].

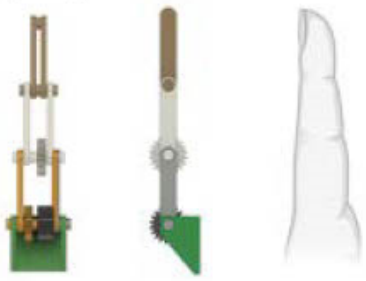

Figure 1. Design Prototype. Mechanical components (gears and conveyor belts) are aligned with finger joints.

5) Conclusion

5.a) Summary: Our initial prototype enables flexion and extension for a range of normal joint motions; the device is 3D printed and easy to manufacture at low cost; however, the size and weight of the device prevent prolonged usage.

5.b) Revisions: To enhance rehabilitation, we aim to extend the glove's functionality to include the distal interphalangeal joint, and streamline its design for better ergonomics. Additionally, we will develop an app featuring exercises of varying difficulties for patients to complete, further supporting their recovery process.

5.c) Impact (Future Version): The enhanced RhythmRehab glove is designed for patients with stroke and neurological disorders, aiming to efficiently restore hand dexterity. It offers cost-effective, high-quality rehabilitation with personalized therapy options, enhancing recovery and alleviating the economic impact on households.

References:

1. Bonini-Rocha. et al. *Hand Ther*. 2022; 36(3):693-705
2. Kabir. et al. *Micromachines (Basel)*. 2020;13(7):1033
3. Talmage. et al. *Guides Newsletter*. 2015; 20(3):3–5
4. Hume. et al., *J Hand Surg Am*. 1990;15(2):240-3

Acknowledgments: We thank Columbia University Biomedical Engineering for their support.

Transtibial Amputee Prosthetic for Bionic Monofin

Author Names: Jessica Baggett, Melissa Le, Soham Patel, Hannah Teson
Drexel University

1) Need

1.a) Use Case: In the U.S., there are about one million people living with lower limb amputations (29% transtibial) [1,2]. A form of recreational swimming is monofinning, which attaches both feet to a single large fin to propel. Amphi Americas has developed a bionic monofin called the Amphi Anhinga which has a propeller providing additional propulsion [3]. It is not accessible to transtibial amputees.

1.b) Problem Impact: Currently, there are no existing solutions that allow amputees to monofin. All water prosthetics are exclusively for traditional swimming. Transtibial amputees cannot use the Amphi Anhinga, so the impact of the problem is very high. Since monofinning is a recreational activity that is not done on a daily basis, the frequency of the problem is low.

1.c) Scope (Objective): **The objective is a prosthetic device for singular transtibial amputees to swim with Amphi Anhinga. Features are (1) withstand marine environments and (2) swimming forces, (3) articulating ankle, (4) generate biomechanically symmetrical forces, and (5) compatible with the Amphi Anhinga.**

2) Design Inputs

2a) Constraints: There are several zones on the residual limb that are sensitive to pressure. To not cause discomfort or pain, the largest amount of force placed on the residual limb must not occur on pressure sensitive areas of the fibula or tibia [4]. The device must also withstand the torque and torsion forces that occur while monofinning. The device's materials should have a shear modulus above that of the fibula, which is 1.923 GPa [5].

2b) Requirements: It must not move more than 6mm translationally when experiencing drag forces of 24 N, to prevent removal due to drag. The 6mm allowance was determined from literature to be the average slippage between standing prostheses and skin without irritation [6]. During use, it should not move 6mm in any direction when experiencing rotational moments of 40 N*m [7]. The moment value was found through computational simulation from the Swimming Human Model (SWUM).

3) Solution

3a) Design - Intended Use: **A diagram of the intended use can be found in Figure 1. The solution provides adjustability in key areas including the foot length, ankle angle, pylon length, and residual limb attachment. The residual limb is kept in place via a shuttle lock graded to handle required forces which utilizes a pin sleeve to prevent translation movement and secured with velcro straps to stop rotation. All parts are made from marine-grade materials making it suitable for the intended environment.**

3b) Build - DEMO: The device is currently being built and is not yet complete.

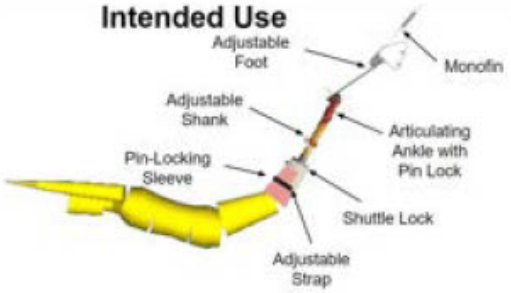

Figure 1: Intended Use of Proposed Solution

4) Verification Results

4a) Introduction Test 1: Testing will be on the translational security of the device.

4b) Methods Test 1: Once fully assembled, weight will be added to the bottom of the device to simulate the swimming drag force. The solution will pass if the device does not move more than 6mm from its original position on the residual limb after weight is applied.

4c) Introduction Test 2: Testing will be on the rotational security of the device.

4d) Methods Test 2: Once fully assembled, force will be applied perpendicular to the device to simulate the moments experienced during swimming. The solution will pass if the device does not move more than 6 mm from its original position on the residual limb after weight is applied.

4c) Results: **All test results are pending.**

5) Conclusion

5a) Summary: As tests have yet to be conducted, we are unsure if the design is successful, but the design would be considered successful if 5 of 6 tests were passed.

5b) Revisions: Revisions are to be made once verification testing is conducted.

5c) Impact (Future Version): If successful, the device will allow transtibial amputees to enjoy the mental and physical benefits of monofinning. This prosthetic creates an avenue for a new type of universal fit prosthetics, which has a potential to decrease costs for users.

References:

[1] Sanders J.E. et al, J Rehab Res Dev. 2011; 48(8)949-986; [2] Murray C. et al Dis & Rehab. 2023;1-20; [3] Amphi Americas. 2023 [4] Edelstein J.E. et al, Low Limb Pros. 2010; [5] Sadeghi S. et al. J Biomech, 2019; 83:190-196; [6] Commean P.K. et al,Med & Rehab, 1997;78(5):476-485; [7] Nakashima M. et al. J Biomech & Eng. 2010,4:408-420

Acknowledgements:

Special thanks to Dr. Marek Swoboda of Drexel University, Michal Swoboda of Amphi Americas, Dr. Chad Duncan of Salus University, and Dr. Motomu Nakashima of Tokyo Institute of Technology.

STEVENS
INSTITUTE OF TECHNOLOGY

UNIVERSAL HITCH ATTACHMENT FOR STROLLERS

Alexa Warren, Bailey Erickson, Christopher Iuliucci, Marvin Moreno, Joshua Perry, Anna Sasse, Dr. Erik Brewer

Rowan University

1) User Need:

1.a) Use Case

Mike Nelson is a United States Army veteran who sustained life-changing injuries during his service that caused him to lose his vision. With the loss of his vision, Mr. Nelson experiences difficulties transporting his five children in their strollers, as the strollers impede the use of his white cane for navigation.

1.b) Problem Impact

No current solutions exist for this specific issue. Alternatives found through interviews with specialists include using a wagon or baby carrier instead of a stroller or pulling a stroller backward. However, these options do not consider Mr. Nelson's children's safety, his preferences, or the design requirements he expressed.

1.c) Scope (Objective)

Mr. Nelson needs an attachment that can attach to any stroller universally, includes a breaking mechanism, is light enough to carry, can be stored, and allows the users to be comfortable and not impede on any usability of a stroller.

2) Design Inputs

2.a) Constraints:

This design requires portability, compatibility, and doorway-friendly size (<35 inches), prioritizing passenger comfort and safety for the veteran with specific needs. The design incorporates insights from occupational therapists and mobility specialists, where we must maintain forward alignment and not impede on the arc width of Mr. Nelson's white cane. (180° left to right of his body)

2.b) Requirements:

The requirements provided by Mr. Nelson are a need for a brake, compactable for storage purposes, and compatible with varying stroller and cart models while still being able to attach/detach independently.

3) Solution

3.a) Design - Intended Use:

This design allows all varieties of strollers to attach to our device by either extending or compressing the platform and securing with straps to prevent movement. In the case of keeping the device in a stationary position, locking in wheels can be applied.

3.b) Build - DEMO

Figure 1. SOLIDWORKS Prototype with Stroller Attached

4) Verification Results

4.a) Introduction

Requirements in this design included safety locks to prevent unnecessary rolling, must be able to universally applicable to any stroller, and must withhold weight for the stroller and children in the stroller without breaking.

4.b) Methods

Measurements along the extended platforms were measured from smallest to longest and were tested for weight load with a maximum weight of 100 lbs to abide by ASTM standard *6.2.2 - A stroller shall support a static load of 100 lb. [1]*. To prevent unnecessary rolling, we will abide by ASTM standard *6.1.1 - A parking brake shall be provided on the unit [1]* and ensure that the wheel cannot roll on 60-grit sandpaper when locked.

4.c) Results

This project is still underway, but the prototype is currently in production. Our current SOLIDWORKS prototype was approved by Mr. Nelson, and we hope the built prototype meets his approval too.

5) Conclusion

5.a) Summary:

After a thorough analysis of the specified criteria and adherence to design constraints, Mr. Nelson has provided his authorization for the advancement to the prototyping phase based on our finalized design specifications. This milestone signifies an initial triumph within the project lifecycle, notwithstanding its incomplete state, as the team progresses toward fulfilling its expectations.

5.b) Revisions/ Impact:

We would like to eliminate the boxiness of the platform and condense the overall length of the device so that it is not so difficult to make turns with. We would also like to ensure that the device is as low to the ground as possible to avoid the stroller sitting on a large degree of incline when strapped on top of the platform and putting the child at risk. We would also like to incorporate a safety braking mechanism rather than a twist lock mechanism.

References:

1. ASTM International. (2021). Standard consumer safety performance specification for carriages and strollers (ASTM F833-21). Retrieved from ASTM International website: https://www.astm.org/f0833-21.html

Acknowledgements: We acknowledge Quality of Life + for sponsoring this project. We also extend our gratitude to Mike Mulligan of Blind on the Move, Ally Futty, Barry Hulce, Jen Kaldenberg, and Darick Wright from the University of Massachusetts - Boston, and Melanie Amadoro of Rowan University for their time, skills, and knowledge, which have contributed to the success of this project.

STEVENS
INSTITUTE OF TECHNOLOGY

Electrical Stimulation Device

Arslan Hashmi, Riya Kalbag, Aisha Khan, Selma Shifa, Dr. Jonathan M. Grasman
New Jersey Institute of Technology

1) User Need:

1.a) Use Case

Users of the electrical stimulation device (ESD) include tissue engineers, researchers, and healthcare workers. The purpose of this product is to electrically stimulate tissue constructs in 24-well plates. Tailored for tissue engineering research, our device is designed for *in vitro* applications such as drug screening, disease modeling, and the formation of constructs for critically sized tissue defects.

1.b) Problem Impact

Existing solutions on the market are costly and only offer bulk electrical stimulation to tissue constructs in 24-well plates. The high cost of competitor devices makes research less accessible to underfunded facilities. Additionally, current devices are limited by stimulating an entire well plate with a single set of parameters (voltage, frequency, duty cycle).

1.c) Scope (Objective)

The ESD must offer a modular and cost-effective (<$500) alternative to competitors. Modularity, defined as the ability to stimulate specific rows within a well plate, is a novel concept on the market. Addressing these limitations is the main goal of our project, as they satisfy user needs and provide an advantage against products in the market.

2) Design Inputs

2.a) Constraints:

The ESD must fit within a 24-well plate without impeding the lid from closing to maintain sterility and basic cell culture techniques must be possible with the device present in the well plate. To achieve this, the dimensions of the device must be no larger than 85 mm x 127 mm and the height of the device without electrodes must be ≤1.5 mm. Additionally, the device must successfully operate in incubation conditions (humidity, 37℃, and 5% CO_2) without accumulating moisture and corrosion or experiencing any loss of function.

2.b) Requirements:

The ESD must provide modular and tunable electrical stimulation. Additionally, since this device interfaces with cells, it must be cytocompatible and sterilizable. The highest priority requirements of this product are that it must electrically stimulate tissue constructs without obstructing construct visibility within the well plate or compromising sterility during the operation of the device.

3) Solution

3.a) Design - Intended Use:

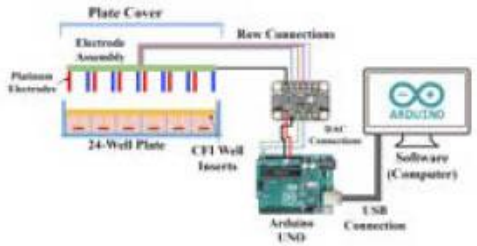

Figure 1. Overview of the Electrical Stimulation Device.

The ESD contains two main components: the electrode assembly and the control system (**Fig 1**). The electrode assembly incorporates a printed circuit board (PCB) with platinum wire electrodes, enabling it to fit seamlessly beneath the plate cover and meet the height constraint. The PCB features openings along its length to allow operators to perform basic cell culture maintenance. A hydrophobic silicone coating is applied on the top of PCB to prevent moisture formation and corrosion, allowing the device to withstand incubation conditions. Lastly, the PCB incorporates independent row connections linked to the control system, consisting of an Arduino UNO connected to an MCP4728 digital-to-analog converter (DAC). Through the Arduino script, users can select preferred parameters, including rows to stimulate, voltage, frequency, duty cycle, and duration of stimulation.

3.b) Build - DEMO

Figure 2. PCB Prototype.

The PCB was fabricated with stainless steel electrodes as a prototype for testing and evaluation purposes. The independent row connections (colored wires) allow the control system (**Fig 1**) to stimulate user selected rows.

4) Verification Results

4.a) Introduction (i = 1 ... N)

Verification testing for the ESD includes assessment of the quality of the stimulation signal, a user-demo to perform cell culture maintenance with the device present, and an evaluation of device cytotoxicity [1].

4.b) Methods (i = 1 ... N)

For stimulation signal assessment, an oscilloscope is used to evaluate whether the stimulation signal matches the desired electrical parameter inputs and whether the signal deteriorates across rows in the well plate. For cytotoxicity assessment, live tissue constructs are stimulated and tissue viability is measured through imaging.

4.c) Results (i = 1 ... N)

Testing is currently ongoing. User tests involving inputting parameters into the Arduino script have been successful. Results of voltage testing indicate minimal voltage drops across rows in a well plate, although the maximum voltage supplied is 4.74 V (Table 1).

Table 1. Voltage Drop Across a Row with DMEM

Input Voltage	Well 1	Well 6
1 V	1.04 ± 0.00	1.04 ± 0.00
2 V	2.04 ± 0.05	2.02 ± 0.04
3 V	3.02 ± 0.04	3.04 ± 0.00
4 V	4.00 ± 0.00	4.00 ± 0.00
5 V	4.74 ± 0.08	4.68 ± 0.08

5) Conclusion

5.a) Summary:

Although testing is ongoing, the ESD has successfully met the low-profile requirement by fitting underneath the well plate cover and does not experience a voltage drop across rows of wells. Frequency and duty cycle testing are pending and results will be updated when the next stage of testing is completed.

5.b) Revisions:

In order for our solution to increase its impact, testing different electrode materials may be required to assess which material performs best (corrosion resistance, conductivity, and strength). Additionally, modifying the code to allow for rows to be stimulated with different voltage/frequency requirements would make this device completely modular.

5.c) Impact (Future Version):

An ideal electrode material will maximize the device's lifetime. Additionally, achieving complete modularity will greatly increase the number of tissue engineering research applications for the ESD.

References:

1. Tandon N. et al. Nat Protoc. 2009;4(2): 155–173.

Acknowledgements:

We would like to acknowledge Sydnee Sicherer and the TIMM lab for their contributions, as well as funding from the NIH (R21-AR079708) and startup funds from NJIT.

STEVENS
INSTITUTE OF TECHNOLOGY

A Hydrogel-Based Artificial Corneal Implant To Improve Outcomes of Patients With Corneal Blindness

Author Names: Daniel Habboush[1], Victoria Le[1], Natalie Lau[1], Maria Jose Garcia[1]
[1]Drexel University, Philadelphia, PA

1) Need

1.a) Use Case

The stakeholders involved are ophthalmologists, who treat corneal blindness patients with implantation. These clinicians aim to perform minimally invasive surgeries with implants that are biocompatible with low probability of extrusion, perforation, and infection. Lack of donor corneas and failed implants lead to high-risk surgeries that require keratoprosthesis such as the Boston Kpro, the standard of care.

1.b) Problem Impact

Existing solutions include the Boston Keratoprosthesis (Boston KPro), Modified osteo-odonto Keratoprosthesis (MOOKP), and AlphaCor. While the Boston KPro has a relatively simple procedure with good cosmetics, it is highly invasive with a high risk of complications and indefinite need for post-operative care. The Boston KPro also requires a donor cornea, which may not be readily available [1]. The MOOKP, on the other hand, does not require a donor cornea and has very high success rates. However, the drawbacks include procedural expense, complexity, and availability, with the final result having bad cosmetics [2]. The final existing solution, AlphaCor, has a relatively simple design and good cosmetics, but has permeability issues and limited diffusion of nutrients and is no longer used clinically [3].

1.c) Scope (Objective)

Based on the need and existing solutions for high-risk corneal implantation, the overall objective for our solution is to design a proof of concept, hydrogel-based keratoprosthesis device for high-risk patients ineligible for corneal transplants that improves on existing solutions by increasing implant permeability while maintaining a natural aesthetic.

2) Design Inputs

2a) Constraints

The first constraint (C1), is a project budget of $300, which must cover all expenses pertaining to the project, which limits the complexity of the project and testing of requirements, thus leading into the second constraint (C2), resources. Fabrication and testing of the hydrogel will be constrained to the lab resources provided by the project advisory team and Drexel University. Any other resource outside of the ones available may impact C1. The third constraint (C3) is time, as the project must be completed within 9 months. The fourth constraint (C4) is hydrogel size; as this device is intended for use in the eye, the device is constrained by the dimensions of the cornea.

2b) Requirements

The first requirement (R1) is that the device must have a shear modulus similar to or better than the existing AlphaCor implant to ensure rigidity (10-200 kPa) [1]. The second requirement (R2) is cell viability (0.57-0.69% cell damage), which ensures the device maintains epithelial cell growth [2]. The third requirement (R3), hydrophilicity (10° Contact Angle), ensures the device maintains a certain moisture content to promote diffusion [3]. The fourth requirement (R4), diffusivity (3.1 ± 1x10-8 cm2/s), requires the device to diffuse nutrients [4]. The last requirement (R5) is transparency (>92%), which ensures adequate visibility through the device [5].

3) Solution

3a) Design - Intended Use

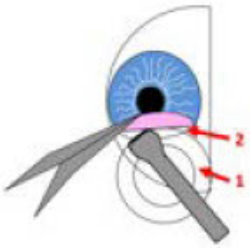

Implant (1) will be inserted under the lamellar pocket (2), a similar procedure as AlphaCor, a less invasive and complex procedure compared to Boston KPro. Material choices such as using sulfonated PEG with HEMA, supports epithelial cell growth and emulates corneal properties, like rigidity, which are ideal for proper implant integration and function.

3b) Build - DEMO

Results Pending-Proof of Concept.

4) Verification Results

Results Pending.

5) Conclusion

5a) Summary

A successful hydrogel will have demonstrated adequate diffusivity, cell viability, transparency, and shear modulus, thus indicating a successful proof of concept for a corneal implant.

5b) Revisions

Pending the results of verification testing, revisions can be made regarding the composition of the hydrogel to change the properties accordingly.

5c) Impact (Future Version)

A successful solution would yield hydrogel based KPros with fewer complications related to biointegration, diffusivity, and hydrophilicity. Additionally, the aesthetics will vastly improve over the KPro leading to a better quality of life for patients who receive the procedure. Globally, this procedure and device will allow for more high-risk patients suffering from corneal blindness to see, as this device does not require a donor cornea. Maximization of diffusivity and biointegration reduces the risk of complications and infection, which ties into the idea of patients needing less follow-up care and lifetime treatments, which is also important in eliminating the need for replacements that are wasteful and detrimental to the environment.

References:

1. Avadhanam VS et al. Clin Ophthalmol 2015; 9,697-720
2. Tan A. et al. Ocular Surface. 2012; 10:15-25
3. Myung D. et al. Biotech. Progress. 2008;24(3):735–741
4. Formisano N et al. Mechanical. 2021; 10, 2100972
5. Means T. L. et al., Archives of Ophthalmology. 1995
6. Jeong S. Kim HW. ScienceDirect. 2023
7. R. A. Charalel et al. Ophthalmic research. 2012;48(1),50–55.
8. Musgrave CS. et al. Contact. 2019; 12(2), 261.

Acknowledgments:

We would like to thank our advisory team: Dr. Catherine von Reyn, Associate Professor at Drexel University School of Biomedical Engineering (Primary Advisor); Dr. Christopher Rodell, Assistant Professor at Drexel University School of Biomedical Engineering (Mentor/Primary Consultant); Dr. Jaimie Dougherty, Associate Teaching Professor at Drexel University School of Biomedical Engineering (Design Instructor), Dr. Zeba Syed, Ophthalmologist at the Wills Eye Institute (User/Mentor); and Jay Bhatt, Librarian, Engineering (Mentor/Consultant).

STEVENS
INSTITUTE OF TECHNOLOGY

Development of Hydrogel-Based Artificial Meniscus with Self-healing Properties

Ed Delphonse, Feiyan O'Rourke, Solaleh Miar*.
Biomedical Engineering Program, University of Hartford, West Hartford, Connecticut, 06117

1) User Need:

1.a) Use Case

Approximately 850,000 cases of meniscus tears occur annually in the United States. An implant that mimics the natural form and function could revolutionize treatment for those with such injuries. Through this project, we aimed to bridge existing gaps in meniscus repair and enhance available treatment options. Ultimately, our goal was to improve the lives of individuals grappling with meniscal injuries, whether recent tears or long-standing issues due to wear and tear.

1.b) Problem Impact

Individuals experience limited mobility, persistent discomfort, and reduced quality of life due to these limitations, while the public faces higher healthcare expenses and increased morbidity rates. Addressing these challenges through enhanced medical practices and technological advancements is essential to mitigate the impact of meniscus injuries on individuals and society.

1.c) Scope (Objective)

The main goal of this project was to design a hydrogel-based meniscus with self-healing properties, which has the potential to be customized based on the patient's native meniscus shape and size.

2) Design Inputs

2.a) Constraints:

Our method addressed significant restrictions to meet the demands of users with meniscus injuries. To prevent adverse immune reactions, biocompatibility had to be ensured; infections had to be prevented by sterilization; size and shape of the meniscus and mechanical characteristics are required to mimic natural function; and implant integrity is required over time. Our design sought to provide meniscus injury patients with safe and efficient treatment alternatives by addressing these limitations.

2.b) Requirements:

A hydrogel-based implant with self-healing properties was designed to mimic the native mechanical characteristics of the meniscus.

3) Solution

3.a) Design – Intended Use:

The implant is designed to replace the natural meniscus and is personalized for each user using customized 3D-printed molds. Polyvinyl Alcohol (PVA) as a biocompatible biomaterial provides similar modular characteristics to the native tissue. The mechanical properties will be matched with the native tissue, and self-healing properties make the design suitable for real-time applications and a solution for recurring tearing in the meniscus.

4) Verification Results

4.a) Introduction

Understanding how PVA hydrogel responds to swelling and degradation over time was crucial. The swelling and degradation test predicted the material's stability. Additionally, the self-healing capability test provided valuable insights into the material's potential to repair itself, enhancing its durability and functionality.

4.b) Methods

PVA hydrogels were prepared by dissolving PVA powder in deionized water followed by one freeze-thaw cycle at -20ºC over 24 hours. Swelling and degradation tests were conducted in Phosphate Buffer Solution (PBS) at 37ºC and continued to reach the equilibrium (n=6). To understand the PVA self-healing properties, two different dyed PVA samples were cut, attached to each other, and kept at 37ºC to observe the healing process.

4.c) Results

Figures 1 (A and B) show the swelling and degradation behavior of the PVA hydrogels (10,15 and 20% w:w), respectively. Both swelling and degradation reached equilibrium during the observation period. According to the results, PVA hydrogel reaches swelling equilibrium after 8 days. The self-healing result shown in Figure 2 reveals the dye diffusion into the undyed cut, and self-healing was observed in the last first 24 hours.

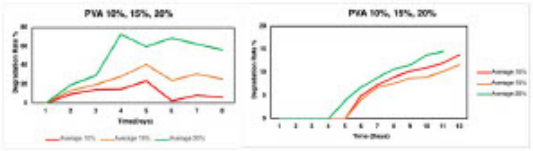

Figure 1. PVA hydrogel Swelling and Degradation Behavior (A) Swelling of PVA

Figure 2. Customized hydrogel-based meniscus implant and self healing Daily Progression

5) Conclusion

5.a) Summary:

The customized design of meniscus implants based on PVA hydrogel was achieved with potential self-healing properties. The swelling and degradation behavior of PVA hydrogel was also evaluated over time.

5.b) Revisions:

Further investigation into the impact of Sodium Sulphate on the swelling, degradation, and self-healing properties will be required. The mechanical characterization will be conducted to evaluate Young's modulus of the samples compared to human meniscus mechanical properties.

5.c) Impact (Future Version):

Once the project is completed, the design will provide a successful prototype of an artificial meniscus implant with self-healing properties.

References:

1. E. Luvsannyam, et al., Cureus, vol. 14, no. 5, Article ID e25121,

STEVENS
INSTITUTE OF TECHNOLOGY

Convolution Neural Network (CNN) for Nonpalpable Breast Lesion Localization

[1]Lara Aklouk, [1]Ishitaa Gupta, [1]Karolina Palac, [1]Rachel Rowey, [1]Marissa Gray, [1]Theresa Raimondo, [1]Anubhav Tripathi, [1]Lindsay Schnieder, [2]Jennifer Fieber, [1]Akshit Chhabra, [1]Brown University Center for Biomedical Engineering, Providence, RI. [2]College of Medicine, UF, Gainesville, FL

1) User Need: Women face a 1 in 8 chance of developing breast cancer in their lifetime. Nonpalpable breast masses, common in early stages of cancer, have a 20-30% chance of becoming cancerous, necessitating effective removal and localization methods[1]. Existing methods like wire localization, SAVISCOUT, and MagSeed have drawbacks like a lack of real-time feedback, preoperative procedures, patient discomfort, and incomplete margin assessment[2]. IOUS provides real-time guidance but involves a steep learning curve and ineffective margin analysis. These limitations affect surgical accuracy, potentially leading to incomplete removal of cancerous tissue and increased healthcare costs. An AI-based algorithmic approach allows surgeons to leverage A-scan ultrasound wave data analysis to visually and audibly guide them during IOUS procedures, mitigating the steep learning curve and ultimately benefiting patients and healthcare institutions.

2) Design Inputs: Our design must detect tumors smaller than 1cm and locate lesions up to 11cm deep, exceeding the 6cm limit of current solutions. An ultrasound provides metrics associated with tissue interface depths in the tissue, which our algorithm uses to determine tumor size (mm) and depth (mm) within a mean average percent error (MAPE) of 0.5%. This method improves margin analysis, reduces IOUS reoperation rates from 7%, and mitigates additional reoperation costs and inconveniences. Our solution aims to keep procedure duration under an hour to maintain efficiency. These metrics ensure the solution meets clinical needs, reducing patient discomfort and surgical time.

3) Solution: In our solution, a CNN, a type of artificial neural network that uses backpropagation to learn spatial hierarchies for image classification and object recognition [3], will be trained using ultrasound signals simulated on breast tumor models created with Abaqus. This training will focus on teaching the CNN to identify specific tumor parameters—depth, size, and margins—utilizing finite element analysis (FEA). Our AI model will then be tested

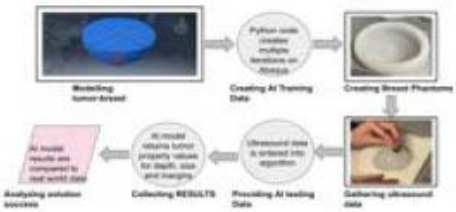

Figure 1. Demonstration of solution in practice

on data from a handheld ultrasound that allows for the detection of the same parameters for agarose breast phantoms containing a stiffer agarose tumor. Our novel use of FEA techniques integrated with AI modeling makes our solution the first of its kind in breast cancer localization. **Figure 1** displays our solution.

4) Verification Results: Testing our algorithm entails evaluating its capacity to precisely localize nonpalpable lesions, accurately predict tumor size and depth within breast tissue. This assessment must cover diverse scenarios of agarose samples. Crucially, it involves developing molds to replicate tumor characteristics accurately, ensuring the generation of realistic phantoms and the precision of actual values used in testing. Statistical analyses, including Mean Percent Error, Mean Absolute Error (MAE), and Root Mean Squared Error (RMSE), will be conducted to quantify disparities between predicted and actual values of simulations. We have synthesized a 1:100 agarose:DI-water breast phantom with a known radius of 8 cm. Embedded inside was a 2:100 agarose:DI-water tumor with a known diameter of 1 cm and depth of 4 cm. Scanning this breast phantom yielded the ultrasound data in **Figure 2.** The first peak, indicated by the blue gate, was measured at 34.97 mm and the second peak, indicated by the red gate, was measured at 42.94 mm. From these measurements, the parameters in **Table 1** were calculated.

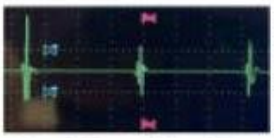

Figure 2. Ultrasound data for breast phantom with tumor.

Table 1:

	Measured Value	Actual Value	% Error
Tumor Size (mm)	7.97	10.00	20.3%
Tumor Depth (mm)	38.96	40.00	2.6%
Breast Phantom Depth (mm)	69.77	80.00	12.8%

Tumor size is calculated by subtracting the 2 relevant peak depths. Tumor depth, relative to the center of the tumor, is calculated by adding tumor radius to the first peak depth. Percent error is calculated using the following equation: $\frac{|measured - actual|}{actual} \times 100\%$.

5) Conclusion: Our results successfully show proof of concept. Ultrasound data provides our algorithm with parameters for lesion localization and accurate tumor depth determination, and the parameters fall within acceptable ranges considering IOUS limitations. The algorithm, based on a previous project, demonstrates a close correlation between predictions and actual values for estimating size and allows expansion of the model to include depth. Extensive testing with diverse breast-tumor parameters will verify results. Our non-invasive solution integrates with existing tools, offering clinicians an efficient means of enhancing depth limitations and margin analysis accuracy. By providing accurate tumor properties, it holds promise in reducing reoperation rates and improving patient outcomes and its compatibility with existing IOUS technology ensures cost-effectiveness.

References:

[1]Wen et al. (2020). https://doi.org/10.1097/MD.00000000
[2]Garzotto et al. (2021). https://doi.org/10.1016/j.breast.20
[3]Yamashita et al. (2018). https://doi.org/10.1007/s13244-0

Improved Test Fixture for Implantable Pulse Generator Magnetic Resonance Imaging Testing

Ethan Roy[1], Riley Franzo[1], Michael J. Rust[1], Neal Peterson[2].
Western New England University[1], Boston Scientific[2]

1) User Need:

1.a) Use Case

Millions of patients worldwide currently have Implantable Pulse Generators (IPGs) to treat various heart conditions, with the global market size being valued at approximately 4.5 billion dollars as of 2022 [1]. One of the driving factors for this growth is the introduction of Magnetic Resonance Imaging (MRI)-conditionally safe IPGs. MRI scans function by using multiple electromagnetic fields, which can cause an IPG to malfunction, creating potential danger for patients.

1.b) Problem Impact

Due to this risk, patients with IPGs were historically denied access to MRI technology. With the advent of MRI-conditionally safe IPGs, patients will be able to receive the imaging they need, though these devices must conform to standards outlining requirements and test protocols. Current testing systems are able to verify the safety of MRI-conditionally safe IPGs, but are often designed with only one type of IPG in mind. A refinement to this process to allow the testing of multiple IPG types would pose value to millions around the world who would benefit from an MRI-conditionally safe IPG.

1.c) Scope (Objective)

The goal of this project is to redesign a current mono-device testing process both in terms of software and hardware. This includes the updating and debugging of LabVIEW code, as well as the design and production of a new printed circuit board (PCB) to enable compatability with multiple IPG types.

2) Design Inputs

After having multiple meetings with customers to determine user needs, it was decided that the new PCB will be designed so as to not exceed a size of 36.5 x 32.5 cm, with all components housed on a single board. The new testing fixture must also be compatible with 3 varying models of IPGs, each with a different number of electrodes to collect data from. These constraints will ensure a significantly reduced footprint compared to the current testing setup, saving valuable laboratory space. The new testing fixture must also adhere to ANSI PC76:2021 standards for the testing of active implantable medical devices [2].

3) Solution

This board is designed with the user in mind, creating a less complicated test fixture allowing for a simpler, automated process. Using individual, modular headers that can be swapped in-and-out easily for each of the different IPG types allows for a universal board, in turn helping to create a smaller PCB footprint. Figure 1 shows a CAD model of this proposed design.

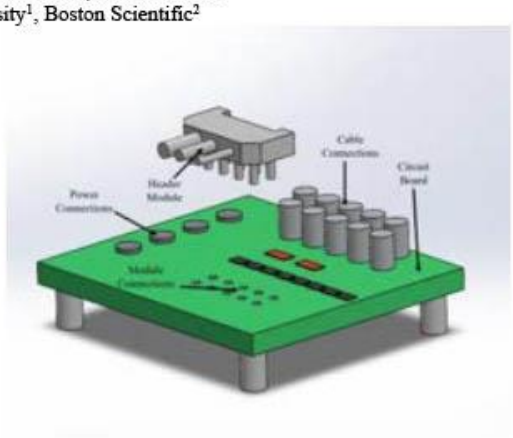

Figure 1. An exploded view of the proposed modular PCB (36.5cm x 32.5cm x 8cm) to replace the current test fixture's circuit board.

4) Verification Results

4.a) Introduction

Verification of the proposed testing process will be conducted through several tests to ensure the fixture meets the designated user needs. These tests include dimensional, performance, and signal analysis.

4.b) Methods

Dimensional analysis of the testing fixture will be performed by measuring the width and length of the PCB using calipers. Measurements will be conducted by two different operators to confirm accuracy. Performance testing will be performed by connecting different types of IPGs to the test fixture, and running the accompanying LabVIEW code 3 times. The results will be compared to those obtained from the existing test fixture to ensure performance equivalence. Signal analysis will be performed using an oscilloscope attached to the PCB while a test is being run, allowing the user to monitor if the correct charge injections are being applied to the IPG per ANSI PC76:2021 standards [2].

5) Conclusion

If successful, this new testing fixture would save potential customers time, money, and resources that may currently be spent on IPG testing. These savings would allow medical device companies to divert focus and resources to more projects that have the potential to change patient's lives. An expedited and more flexible testing process would also present opportunities for companies to more easily convert newer devices to become MRI-conditionally safe, providing the opportunity for a better quality-of-life to millions of patients.

References:

1. J.A. Puette, R. Malek, M.B. Ellison, "Pacemaker," *StatPearls [Internet]*, Jan. 2023. Pacemaker - StatPearls - NCBI Bookshelf (nih.gov)
2. *Active Impantable Medical Devices*, ANSI/AAMI PC76:2021, 2021.

HeraHealth: Revolutionizing Postpartum Care through an Innovative Blood Loss Monitoring Application

Sophia Mains, Lauren Smith, Aya Zaatreh, and Sally Shady
Stevens Institute of Technology

1) User Need:

1.a) Use Case

HeraHealth is an innovative medical application that addresses postpartum hemorrhage (PPH) by enabling women to accurately quantify their blood loss. In the hospital, women use HeraHealth to upload images of their maternal pads after use, enabling the image processing algorithm to calculate blood loss volume. Patients receive real-time metrics, and healthcare professionals are notified if blood loss approaches the 500mL hemorrhage threshold [1].

1.b) Problem Impact

PPH poses a critical threat to women's health, impacting 1 in every 6 women giving birth and accounting for over 20% of all maternal fatalities worldwide. Current technology emphasizes quantifying blood loss during delivery, neglecting the crucial first 24 hours postpartum, leading to late detection and intervention [1].

1.c) Scope (Objective)

HeraHealth is the first application to address the limitations of existing solutions by targeting this 24 hour time period. The project's scope includes providing accurate and real-time blood loss monitoring through a MatLab-based algorithm and user interface (UI), ensuring prompt identification for expedited intervention.

2) Design Inputs

2.a) Constraints:

The capabilities of HeraHealth are limited by the quality of the image uploaded by the user. Factors such as image lighting (>500 Lux) and pixel value (>8 megapixels) determine the ability for the image processing algorithm to accurately determine a blood volume output.

2.b) Requirements:

Current methods rely on physician visual estimation during delivery, resulting in a 25 to 89% error rate and volume underestimation [2]. HeraHealth's greatest priority is developing user-friendly medical imaging technology that most accurately calculates blood volume within each maternal pad, clarifying patient health status without purchase of additional medical equipment.

3) Solution

3.a) Design - Intended Use:

The HeraHealth UI incorporates image upload which provides real-time blood loss metrics. At the PPH threshold, the UI notifies the clinician contact. Additionally, HeraHealth includes comprehensible information about postpartum health, empowering and educating women to manage their well-being.

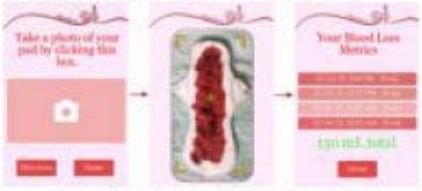

Figure 1: HeraHealth User Interface

3.b) Prototype

Upon UI image capture, the HTML file is transferred to the compatible MatLab algorithm. The 2D image is reconstructed into individual pixels that are processed within the medical image processing technology. Based on corresponding index values, different levels of saturation are used to calculate the blood volume quantity in milliliters for each pad file.

4) Verification Results

4.a) Introduction

MatLab analysis was utilized in order to validate the blood volume calculation algorithm.

4.b) Methods

The team used three pad images, acquired from web-based sources, containing gradually increasing blood quantities that were inputted into the MatLab algorithm and outputted a volume quantity.

4.c) Results

Figure 2 validates the algorithm; as the blood volume visually increases, so does the subsequent blood volume quantity. Further testing will be conducted with quantified blood samples and ANOVA statistical analysis.

Figure 2: Blood Volume Calculations [3]

5) Conclusion

5.a) Summary:

The image processing algorithm verified the increasing trend of blood loss in the tested pad images.

5.b) Revisions:

The software will be further verified through experimentation to ensure that the blood volume output is equal to the amount of blood added to the pad. The team will then be able to garner physician support to integrate HeraHealth into hospital systems.

5.c) Impact (Future Version):

By addressing disparities in medical care and enabling earlier detection of PPH, HeraHealth contributes to the broader goal of reducing maternal mortality. This algorithm has the potential to track blood loss related conditions such as PCOS, menopause, and endometriosis, empowering women to take control of their health.

References:

1. World Health Organization. ISBN: 978 92 4 008180 2.
2. Lertbunnaphong, Tripop. 2016;10:11622
3. Australian Birth Stories. *Implantation Bleeding.*

Acknowledgements: The team thanks Dr. Lance Bruck and Jersey City Medical Center for guidance.

STEVENS
INSTITUTE OF TECHNOLOGY

Inguinal Lymph Node Window Chamber with Channels

Jack Tangstrom, Mackenzie Graham, Hanna Pasqualini, Alexandra Shevtsova.
West Virginia University Biomedical Engineering.

1) User Need:

1.a) Use Case

Intravital imaging of the inguinal lymph node is used in preclinical studies to observe the progression of cancer and immune response as the lymphatic system destroys malignant cells over time. The focus of this project was to construct an inguinal lymph node window chamber with a backing that lasts up to three weeks in mice and addresses issues with intravital imaging quality.

1.b) Problem Impact

Existing chambers aren't designed for the inguinal region. They are in out-of-reach areas, like the abdomen (Ritsma) or on dorsal skin (Liu), where they can be bulky without interfering with movement and don't need to hide sutures since the mice can't reach them. These issues must be considered for inguinal imaging, so the chamber doesn't shift during the experiment. Additionally, the material must be durable so the mice can not chew through it. Currently, the silicon-secured glass coverslip being used creates bubbles resulting in poor image quality. Due to insufficient longevity, there is an inability to collect meaningful data related to disease progression, and the issues with image quality mean any collected intravital imaging is unusable due to artifacts.

1.c) Scope (Objective)

The backing must be made from a durable, autoclavable, and lightweight material that protects the sutures and is capable of keeping the window chamber in place for up to three weeks. The window chamber must allow for high-quality intravital imaging.

2) Design Inputs

2.a) Constraints:

The material must be durable to withstand damage from mice, autoclavable because of its surgical use, reusable, and lightweight to not hinder the mobility of the mice. A retaining ring must hold the glass coverslip in place to prevent bubbles from impeding intravital imaging quality.

2.b) Requirements:

The backing design must be able to be 3D printed with a thickness of less than 1 mm. It must withstand temperatures up to 120℃ to be autoclavable. The design must keep the window chamber in place for 14-21 days. The window chamber must have a retaining ring with a lip wide enough to allow a glass coverslip with a 1.2 cm diameter to snap into place. The design must be reusable and be able to be implemented with a mix of both continuous stitching and single stitches.

3) Solution

3.a) Design - Intended Use:

Both the backing and window chamber have eight evenly spaced suture holes that are connected to the two adjacent holes and to the edge by channels that cut partially through the device. These channels are meant to house sutures, which limits access to increase the longevity of the implant. In the window chamber, a retaining ring is meant to hold a glass coverslip to prevent bubbles that interfere with imaging quality. This design was 3D-printed using surgical guide resin (Figure 1).

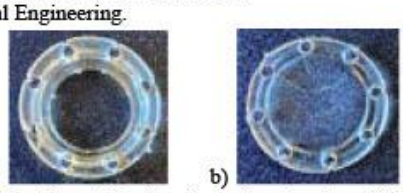

a) b)

Figure 1. Channel Design a) window chamber, b) backing

3.b) Build - DEMO

The window chamber and backing both have eight evenly spaced suture holes. The window chamber is secured using a purse suture. The backing is connected to the window chamber using sutures passing through the suture holes. The pressure from the backing encloses the lymph node in the window chamber for intravital imaging.

4) Verification Results

4.a) Introduction

The window chamber must stay in place for up to three weeks while allowing for optimal intravital imaging while not impeding quality of life.

4.b) Methods

The design was implanted and the client gave feedback on longevity, durability, and imaging quality regarding the window chamber and backing design.

4.c) Results

The chamber was implanted and lasted one day. The surgical guide resin, chosen for its autoclavability and biocompatibility, was not durable enough to withstand mouse attacks and could not support the structure of the channels. The backing did not hinder movement but also did not result in usable images. A new steel iteration of the design aims to eliminate these problems.

5) Conclusion

5.a) Summary:

The window chamber was unsuccessful since it only lasted a day due to the inadequate material chosen. The sutures escaped the channels, causing the window to migrate as it loosened. Imaging could not be conducted since the coverslip wasn't able to stay in place as well. These issues will be addressed by the modified design.

5.b) Revisions:

The revisions that will be incorporated are the change in material to steel and scaling up the design to ease the process of 3D printing. This will hinder the mouse's movement, but solves durability and biocompatibility and lets the channels be utilized as intended.

5.c) Impact (Future Version):

With the revisions, long-term imaging of a mouse's inguinal lymph node is possible. This allows for the accurate study of the progression of various diseases.

References:

1. Liu TW. et al. PMC. 2021;10:499.
2. Ritsma L. et al. Science. 2012;4:145

Acknowledgement: Supported in part by the Department of Defense Peer Reviewed Cancer Research Program Career Development award (W81XWH-10-1-0203) and National Institute of Health National Institute of General Medical Sciences CoBRE award (P20GM121322).

STEVENS
INSTITUTE OF TECHNOLOGY

SmartRise Patient Lift

Sera Lukens, Anthony DiStefano, Ryan Sesera, Connie L. Hall, PhD
The College of New Jersey

1) Background:

There are numerous medical devices which are assistive for disabled individuals and improve their quality of life. In particular, for adults who are wheelchair-bound. These patients with limited mobility may utilize a patient lift, which transfers them between a wheelchair and a bed or vice-versa. Patient lifts are common in hospitals, but less common in the home. Home lifts present different challenges in terms of space, ease of operation and safety.

1.a) Problem Impact

Full body floor-based lifts are generally safe within home environments, yet due to the factors noted above that are related to the typical household environment, operators face challenges in operating with ease and safety[1]. In addition to caregiver injury, the patient faces several safety risks. During a lift, a chair or bed with limited control of the process, patients often report a free-falling sensation. This may create feelings of unease, potentially causing the individual to move or grasp the device leading to instability such as an offset center of mass, which can cause the lift to tip over and fall.

1.b) Problem Statement

This project aims to design a device that is a way to address patient safety in home-based lifts for wheelchair-bound adults. The device will incorporate sensors designed to maximize safety during a lift.

1.c) Objective

Based on repetitive issues of patient unease and injury to assisting caregivers, this project seeks to provide additional safety and security to wheelchair-bound adults through the integration of sensors. These additional sensors will monitor patient position and weight, and ensure secure attachment of accessories. Visual and audio alarms will alert the patient and caregiver when an unsafe condition is detected. This will allow for any injury risk to be immediately recognized and prevented. The use of a remote control will allow for increased patient independence, requiring minimal caregiver support.

2) Design Inputs.

2.a) Requirements:

Device will lift 400 lbs to meet a variety of user needs. This was chosen due to this meeting the 95% percentile[2]. The device will have audio and visual safety alerts. The alert sound will be 15dB above ambient noise with the main frequency spectrum between 500 hz and 1500 hz, and alternate tones/intermittent tones. The light alert will have an intensity of at least 75 candela. Both values are based on ISO 7731:2003, and OSHA 29 CFR 1910.165.

3) Solution

3.a) Design - Intended Use:

The intended design is depicted above. There will be sensor systems placed strategically to meet user needs. Weight sensors will be integrated into the curved arm structure to ensure that the weight of the patient does not exceed 400 pounds upon loading. Position sensors will be integrated into the base of the model, in order to provide accurate data on the location of the device. This will prevent incidences of collision with household objects.

4) Verification Results

4.a) Introduction

The requirements included in this test were the weight limit of 400 lbs.

4.b) Methods

A Solidworks™ model was made and analysis was done under the max load of 400 lbs. for displacement and stress under the expected materials used.

4.c) Results

The tested stress of the project was under the yield stress of the material at max load expected by the project.

Figure 1. Solidworks™ analysis of Stress

5) Conclusion

5.a) Summary:

The device design has been completed in addition to successful preliminary structural analyses. Prototype construction will be followed by full verification and validation testing.

References:

1. Nourollahi, M., Afshari, D., & Dianat, I. (2018). Awkward trunk postures and their relationship with low back pain in hospital nurses. Work (Reading, Mass.), 59(3), 317–323. https://doi.org/10.3233/WOR-182683

2. Series 3, Number 46 January 2021 - Centers for Disease Control And ..." Vital and Health Statistics, CDC, www.cdc.gov/nchs/data/series/sr_03/sr03-046-508.pdf. Accessed 20 Sept. 2023

Acknowledgements: Thank you to Lindsay Dunn who was present during meetings and offered opinions.

STEVENS
INSTITUTE OF TECHNOLOGY

PolypStop: Improved Hemoclip to Enhance Post-Polypectomy Procedure Outcomes

Luke Zibbell, Ryan John, Amanda Mavricos, Cara McMahon, Dylan Woodward.
Stevens Institute of Technology

1) User Need:

1. a) Use Case

The users of the device are gastroenterologists who perform polypectomies to remove cancerous or precancerous polyps during colonoscopies. Following the removal of a polyp up to 20mm in size, the physician can apply a clip to prevent bleeding at the resection site.

1. b) Problem Impact

Each year, over 15 million colonoscopies are performed in the US as colorectal cancer screenings. Polypectomies are performed during the colonoscopy to remove polyps that are cancerous or have the potential to become cancerous. Delayed post-polypectomy bleeding (DPPB) affects up to 1.2%[1] of individuals undergoing a polypectomy, with a heightened risk of 6.2%[1] for those with larger polyps. Current solutions such as hemoclips are geared towards smaller polyps while over-the-scope clips are invasive and extend procedure durations.

1. c) Scope (Objective)

Our device, PolypStop, offers a novel solution that leverages cutting-edge technologies to reduce DPPB for larger polyps and further enhances patient outcomes, reduces hospital readmissions, and reduces healthcare costs for patients and healthcare providers.

2) Design Inputs

2. a) Constraints:

The colonoscope houses a 2mm working channel through which hemoclips are administered, limiting the size of the clip. Since the clip will be used in an invasive procedure, the clip must be biocompatible. The clip must also be able to retract back through the working channel after deployment as a safety precaution.

2.b) Requirements:

The device must be able to close polyp resection sites up to 20mm in diameter. It must withstand the 1-3N strength of current clips[2] and must be able to withstand the 1.7N peristaltic force in the gastrointestinal environment[2].

3) Solution

3. a) Design - Intended Use:

PolypStop is intended for use by gastroenterologists during colonoscopies to induce hemostasis for polyp resection sites up to 20mm in diameter. The clip is intended to be a sterile device consisting of a pre-loaded,
single-use endoscopic device. The device is administered through the working channel of the colonoscope should any polyps need to be removed. Once the wound site heals, the clip detaches and passes naturally.

3. b) Build - DEMO

The PolypStop hemoclip consists of three main components: the cylindrical housing, four claws, and the internal mechanism. The clip will be made of titanium for its mechanical integrity and biocompatibility. Regarding deployment, the clip is designed to be adaptable to current delivery systems for increased market acceptance.

Figure 1: Open Clip

Figure 2: Closed Clip

4) Verification Results

4. a) Introduction (i = 1 ... N)

The grip strength of the clip will be tested with an Instron to confirm that the design will be able to function as intended while withstanding the internal forces of the colon. The clip must be able to withstand a 3N force[2] from the instron to pass. Additionally, a finite element analysis (FEA) was performed to evaluate the structural integrity as it pertains to mechanical failure. For this test, the clip had a prescribed displacement of 0.25 mm for the claws and the stress and yield strength were determined.

4. b) Methods (i = 1 ... N)

The Instron will be used to test the grip strength and will operate at 0.5mm/min. To determine grip strength, the clip will be applied to silicone imitating the skin and pulled off by the Instron. Statistical analyses will include a comparison of the test results with the clips currently on the market. The FEA assessed mechanical failure with the clip fixed in the open position and a prescribed displacement of 0.25 mm on each claw.

4. c) Results (i = 1 ... N)

FEA testing revealed that the clip has a yield strength of $3.7*10^8 N/m^2$ and maximum stress of $1.25*10^{11} N/m^2$, which means that the clip can withstand the gastrointestinal environment as these forces are magnitudes higher than those generated by the large intestine. Instron testing has yet to be conducted.

Figure 3: FEA Set-Up

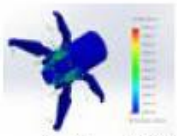

Figure 4: Stress FEA Results

5) Conclusion

5. a) Summary:

The current prototype has the potential to improve patient outcomes following polypectomies. It features four claws to increase the area grasped, unlike current hemoclips which only have two. Instron test data has yet to be collected, but the team anticipates the device will yield results similar to clips currently on the market.

5. b) Revisions:

If we were to expand upon the current design, we would make the clip smaller. Ideally, the clip will need to be 2mm in diameter to fit through the working channel.

5. c) Impact (Future Version):

PolypStop offers a novel solution to reduce DPPB for larger polyps, further enhances patient outcomes, reduces hospital readmissions, and reduces healthcare costs. We envision a future where post-polypectomy bleeding is a rarity, enabling safer and more cost-effective procedures for all patients.

References:

1. Oliver B. et al. Clin & Exp Gastro. 2021; 14: 477-492.
2. Daram S. et al. Surg Endoscopy. 2013; 27: 1521-1529.

Acknowledgments:

We would like to thank Dr. Herman Morchel, Dr. Ligrestie, Dr. Shady, and Dr. Nicole Fosko, for all their support throughout the project.

VITAFLOW - Future of Heart Preservation

Jimin Jung, Nigel Newby, Spencer Tuohy, Tyler McGoldrick
University of Pennsylvania

User Need

Historically, the limited availability of hearts for donation has created a large supply-demand disparity. Recently, advances enabling the usage of "donation after circulatory determination of death" (DCD) hearts, rather than just "donation after brain death" (DBD), show promise in significantly increasing the supply of available organs. Ischemia, or heart damage, limits the distance across which donor hearts can be transported. Ischemia reduces the total available donor hearts, as such engineering a preventative measure to address ischemia is a clear need. To reduce ex vivo heart damage, perfusion is necessary to provide nutrients to the heart during transport and reduce ischemia. With only two platforms achieving clinical success in ex-vivo heart preservation, and high price points of $20,000 - $80,000 per use, there is a clear need for a disruptive, effective, and affordable technology within this field to address the persisting supply-demand gap. Our proposed solution, VITAFLOW, seeks to integrate successful techniques and technologies from ex-vivo preservation and perfusion theory, maintaining efficacy, monitoring, and patient outcomes while drastically reducing costs using sub-normothermic temperature.

Design Inputs

Some of Vitaflow's strictest constraints and requirements are cost of design, temperature regulation, sterility, supply chain issues, and portability. We designed our own parts instead of buying existing solutions and the outcome of our own design efforts allowed us to attain greater user affordability. To address sterility, we plan to incorporate UV light and design our organ transport device for one time use to reduce contamination. For portability, we plan to make a compact carrying structure with wheels and handles to facilitate easy transportation of the donor heart.

Solution

Figure 1. *3D rendering of VITAFLOW*

Our solution contains an oxygenator, , a central heart chamber which will house the donor organ, a temperature regulator module, a pump, sensors, a touch screen, and an ArduinTo. Our engineered solution addresses our problem. We have developed a system that continuously perfuses and oxygenates normothermic blood through a donor heart. The system is intended to provide an optimal environment for heart preservation. We have real-time sensor data of Sp02, Pressure, pH, and temperature which feed information back into an Arduino microcontroller to regulate the system's environment based on set parameters of the user on the touchscreen.

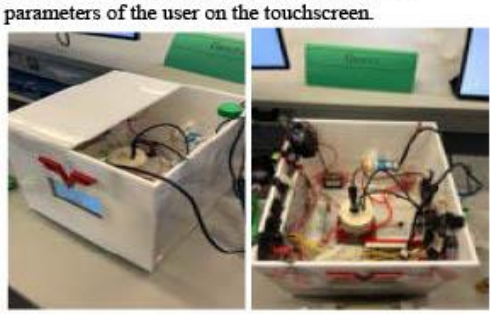

Figure 2. *Minimal Viable Product of VITAFLOW*

The minimum viable product contained a pump, pH sensor and temperature sensors, an oxygenator, a central chamber, a heating and cooling module, and an Arduino with a touchscreen.

Verification of Results

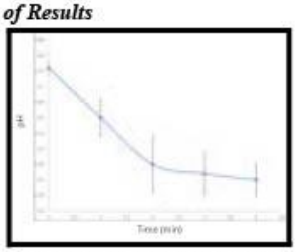

Figure 3. *Time and pH graph for CO2 gas exchange*

Measuring pH showed an initial reading that CO2 could be effectively perfused into our system which indicates effective gas exchange. We used bicarbonate to show that if there was gas exchange pH would be lowered (Figure 3).

Conclusion

We have been able to meet our requirements without violating our constraintIs. By fabricating most of our own parts and creating a functioning system that successfully changes the purfusing fluid, we are optimistic about our product design. Potential revisions include automatic injections potential nutrients into the perfusing blood to further decrease ischemic damage and prolong viability. Prolonged viability of donor hearts would contribute to closing the supply demand disparity. Furthermore, our low-cost transport device could potentially expand supply to lower-income parts of the world.

Acknowledgements:

Ayyaz Ali, MD, PhD, Erin Berlew, PhD, Dave Meaney, PhD, Dayo Adewole, PhD, Melanie Hilman, MSE

References:

Alomari, Mohammad et al. doi:10.7759/cureus.26281,
Bryner, Benjamin S et al. doi:10.1016/j.xjon.2021.04.020,
"Heart Disease"
Facts."www.cdc.gov/heartdisease/facts.htm.

Multi-Purpose Adaptor to Improve Hands-Free Storage for Patients with Retinitis Pigmentosa

Anish Aitha, Aaveg Mishra, Darshan Patel, Sukethram Sivakumar
Primary Advisor: Dr. Sriram Balasubramanian | Drexel University

1) Need

1.a) Use Case

Dr. Sriram Balasubramanian, an associate professor of Biomedical Engineering, suffers from Retinitis Pigmentosa (RP), which affects his peripheral and night vision. Due to the condition, Dr. Balasubramanian has to use a mobility cane in daily activities. Dr. Balasubramanian expressed a need to temporarily store the cane (without folding it) in situations requiring both hands and for a way to attach a flashlight to the cane in poor lighting.

1.b) Problem Impact

Existing solutions do not provide a way to temporarily store the cane without folding and unfolding it. The lack of a product that allows the user to store the cane temporarily and can hold any hand-held flashlight poses a threat to the user's safety. Users can potentially lose their canes or fall while attempting to look for it. Such limitations also contribute to the lower quality of life experienced - in context to limitations within daily living activities.

1.c) Scope (Objective)

The objective is to develop a universal mobility cane adaptor for hands-free storage and flashlight attachment.

2) Design Inputs

2a) Constraints

Designing such a solution is limited by time, budget, resources, policies, and weight constraints. Given such constraints, the design should be simplistic and accessible. Policies guide our design to follow good manufacturing and FDA principles. A major constraint of weight limits the materials that can be used within this design. To reduce any potential stress on the user - the center of gravity of the can should not deviate significantly from its original position.

2b) Requirements

During construction and delivery of the solution, the highest priority requirement is that the adaptor make the body and the arms alike as low profile as possible. From empirical findings, the total diameter of the cane (with adaptor) should see less than a 100% increase in the diameter. The adapter must also attach to a range of cane diameters (9.5 - 12.7mm) to ensure its universal nature. Lastly, the clip must be able to grasp onto clothing and hang on restroom stall doors, allowing for hands-free storage. Such components should have a clasp force greater than 7 newtons.

3) Solution

The team's solution is a 3D-printed ABS adaptor that can snap onto a cane. It includes two arms free to rotate out and clasp onto an object when compressed with a rubber band. Such a design allows for an easily replicable and convenient solution. With the arms, users can attach their mobility canes to articles of clothing, handbags, etc. The arms (gray) also include a notch to allow the user to hang the cane over bathroom stall doors.

The base (yellow) features multiple hooks on either side, allowing the user to fasten a flashlight along the back using rubber bands. The entire design is low profile and unobstructed to using the mobility cane. The solution will be printed in ABS plastic for flexibility compared to PLA filament.

Figure 1: 3-Dimensional Rendering of Proposed Design

4) Verification Results

4a) Introduction

The verification tests aim to verify the adaptor meets the requirements for maximum diameter increase, grasping ability, and ability to hold a flashlight.

4b) Methods

High-precision calipers will be used to measure diameter, which will be compared to the diameter of the cane without the adaptor. Force measurements will be obtained empirically using different rubber bands. The absolute force the arms can produce, as well as the minimum force necessary for the assembly to support itself on clothing, will be found through compression tests. Statistical tests will be employed to determine if statistical significance is met.

4c) Results

The results are expected to indicate success if all user objectives and established requirements are satisfied. The attachment should be able to attach to one's clothing and a surface while having a flashlight holder. Furthermore, there should be less than a 100% increase in total diameter and greater than 7 N in clasp force.

5) Conclusion

5a) Summary

The design has been successfully implemented in online modeling software. Verification tests will indicate success/failure based on the real 3D-printed adaptor.

5b) Revisions

The need for the product may be altered based on other patients with RP or associated ocular diseases and if they face similar problems as Dr. Balasubramanian. Design inputs, solution, and verification do not change as the concept of the solution is what helps meet the need. To increase the impact, there would need to be an increase in the need of users with similar conditions.

5c) Impact (Future Version)

Upon completion and proper verification of the device, the user can temporarily store their cane to free their hands. Their daily lives would be easier because the user could keep their cane with them while using both hands freely. Such a low-profile and accessible solution to a daily issue would profoundly impact the user's life.

Dilate: Enhancing Lactation with Adjustable Flange and Integrated Heating

Giuliana Cascarano, Eva Soler Cruz, Neha Narayan, Alexa Schlotter, Laura Torre
Columbia University Biomedical Engineering Department

1) User Need:

Breastfeeding is one of the most effective ways to ensure a child's health by providing nutrients and strengthening the immune system. However, 60% of lactating parents have issues breastfeeding, which has led to the use of breast pumps to facilitate milk expression.

Current breast pumping solutions are insufficient in addressing the challenges faced while breastfeeding. The correct flange fit around the nipple is crucial, as incorrect fit can result in conditions like mastitis, trauma, nipple wounds, low milk supply or oversupply, thrush, and blocked milk ducts, leading parents to use formula.

Conventional breast pumps often only come with flanges in a limited range of sizes [1]. Additionally, having to figure out one's flange size and change flange sizes while pumping is inefficient and uncomfortable. Therefore, there is a need to have an adjustable flange that fits properly on the nipple, allowing for maximization of milk letdown. In addition, warming the surface of the breast tissue increases the amount of milk during a pumping session [2], helps treat breast engorgement [3], and helps mitigate blocked ducts [4]. However, most breast-warming compresses are sold separately from the pump. Therefore, there is a need for a warming element that is incorporated into the breast shield, allowing for warming of the breast during a pumping session.

2) Design Inputs

Anatomical and practical constraints must be considered. First-degree burns occur at 42°C, so any heating element attached to the electric breast pump needs to remain below that threshold temperature. Our project has a budget of $500, so any purchases related to the design must remain under that limit. The flange should be 4mm greater than the nipple, allowing for 2mm of clearance around the nipple on all sides to maximize milk letdown. Additionally, to maximize milk letdown, the breast tissue should be warmed to 39°C.

3) Solution

Our design should provide an improved pumping experience. Users would be able to dynamically adjust the flange during their pumping session, allowing for maximization of milk letdown. The adjustable flange and integrated heating will improve user comfort.

We developed an adjustable mechanism that actively changes the diameter of the flange. A flange insert was created out of silicone, in the shape shown in Figure 1. This insert creates a gap between the wall and the flange, where air can be pumped in and vacuumed out. Pumping of air will allow for the flange to dynamically change size.

Figure 1. Flange insert

Our first prototype also includes an integrated heating element in the breast shield. The heating element will also have a safety shutoff to ensure that the heat threshold is not reached.

4) Verification Results

Adjustable breast flange

Three differently sized nipple phantoms were made by 3D printing molds and casting with medical grade silicone. The nipples were pierced with a 20 G syringe to mimic milk ducts, allowing for fluid letdown. The breast pump pulled water from a beaker, through the nipple and into a collection bottle. Different nipple size/flange size combinations were tested over a 5-minute pumping session.

For each of the nipple sizes, the recommended size flange allowed for the largest fluid output (a flange 4 mm greater in diameter than the nipple).

	20 mm nipple	24 mm nipple	28 mm nipple
24 mm flange	1	0.554	0
28 mm flange	0.943	1	0.672
32 mm flange	0.554	0.947	1

Figure 2. Results of flange fit vs. milk letdown experiment (normalized to correct size flange)

Heating

Medical grade silicone pucks were placed between a hot plate and a breast phantom and monitored with a thermometer for surface temperature starting at 25℃ (room temperature) to 40℃ to capture the temperature found to be beneficial (39℃).

The findings demonstrate that medical-grade silicone effectively conducts heat at temperatures that positively influence a pumping session (39°C) and to reach steady state in less than 25 minutes.

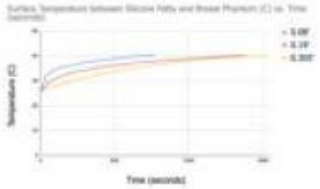

Figure 3. Line Graph of Measured Temperatures for Varying Silicone Thicknesses Over Time

5) Conclusion

We have shown that the correct flange fit can increase milk supply and that silicone is an effective heat conductor. We have also developed an adjustable mechanism that allows for dynamic change in flange diameter and a heating element on the breast shield. Going forward, we would like to integrate our dilation mechanism and heating elements into a single flange. This device would have the ability to increase milk supply and comfort for parents who are breast pumping.

References:

1. M. M. School. Lactation Foundation.
2. Yiğit F, et al. Breastfeed Med. 2012;7(6):487-488.
3. Zakarija-Grkovic I, et al. Cochrane Database.2020;9(9).
4. Boi W. Intl. Journal of Nursing Studies.

Acknowledgements: We would like to thank Dr. Lauren Heckelman and Joe Viola for their support of our project

STEVENS
INSTITUTE OF TECHNOLOGY

BiRed Imaging: Breast Cancer Screening Table

Mathieu Barthelemy, Dominic Clinch, Jonathan Ngo, Alyssa Shelburne
Department of Biomedical and Chemical Engineering, Syracuse University

1) User Need:

1.a) Use Case

The BiRed Ergonomic Breast Cancer Imaging Table prioritizes patient comfort and accessibility whilst optimizing screening accuracy and efficiency. Our user-centric design paired with infrared imaging provides a non-invasive breast cancer screening experience, promoting early detection and regular screenings.

1.b) Problem Impact

In pursuit of improved breast cancer detection, it is imperative to address the margin of error associated with current methods. Mammography, while prevalent, is prone to issues such as overdiagnosis, false positives, anxiety, and radiation injuries. The American Cancer Society states that about half of the women who get annual mammograms over a 10-year period will receive at least one false-positive.[3] We are committed to mitigating the number of false-positives, emphasizing the ergonomics and the modernization of the non-invasive scanning mechanisms.

1.c) Scope (Objective)

The breast cancer screening table solution must include support for a 400lbs+ weight load, adaptability for diverse body shapes, and precise positioning for accurate medical imaging; ensuring safety, comfort, and effective screenings.

2) Design Inputs

2.a) Constraints:

The primary constraints for the breast cancer imaging table involve space limitations, weight capacity, regulatory compliance, and budget considerations. It must fit compactly into medical imaging rooms, support a diverse range of patient weights and sizes, adhere to healthcare regulations as a class 2 medical device, and be cost-effective to avoid financial strain on hospitals and patients.

3) Solution

3.a) Design - Intended Use:

The alpha prototype features a foldable design, accessibility enhancements, steps and handlebars, contoured edges for user comfort, interchangeable hole size, and a headrest for added support and positioning.

3.b) Build – CAD Model

Figure 1

4) Verification Results

4.a) Introduction

Our primary focus is to assess the weight capacity, pressure distribution, and overall comfort of the BiRed breast cancer screening table.

4.b) Methods

To confirm a weight capacity of 400 lbs or more, we will conduct controlled load tests using mannequins and sand, making sure to adhere to industry standards and guidelines. Additionally, pressure mapping analysis will be employed utilizing Velostat and Arduino to identify potential discomfort areas during use, and to assess ergonomics quantitatively. We will gauge subjective user experience using a Likert scale (1 to 4) to rate comfort level, which will provide valuable insights into the table's usability and patient satisfaction.

4.c) Results

Anticipated results for the weight capacity verification are reinforced by the structural integrity of our CAD design and data from the stress analysis function. Successful completion of load tests will affirm the table's ability to support at least 400 lbs. Pressure mapping analysis is expected to reveal an even distribution across the table surface, minimizing discomfort points and validating the optimal ergonomic design. Utilizing the Likert scale, we anticipate receiving favorable comfort ratings, confirming the overall usability and patient satisfaction with the BiRed design.

5) Conclusion

5.a) Summary:

The CAD prototype for the breast cancer imaging table will showcase the successful implementation of our ideas to improve both patient comfort and camera functionality. Success hinges on the translation to a physical, full-scale prototype, with proper verification testing.

5.b) Revisions:

Regularly updating a user specification chart is crucial for refining the breast cancer screening table. The chart guides targeted design revisions for continuous improvement, enhancing inclusion for all patients.

5.c) Impact (Future Version):

The goal is to enhance the patient's experience and reduce healthcare expenses associated with invasive procedures Our design will increase early detection, allowing for timely interventions and avoidance of false positives. By achieving these goals, this project contributes to saving lives and making a significant impact in the fight against breast cancer.

References:

1. American Cancer Society. (2022). Limitations of mammograms. https://www.cancer.org/cancer/types/breast-cancer.
2. Mambou, S. J., et al. (2018); 18(9), 9.
3. Gardezi, S. J. S., et al. (2019; 21(7), e14464.

Acknowledgements:
Special thanks to BiRed Imaging for their invaluable contributions to this research.

NOMASOUND: LED BASED PHOTOACOUSTIC DEVICE FOR MELANOMA SCREENING

David Bendis, Matthew Feroz, Tyler Jacklitsch, Cesar Noguera Saigua
Department of Biomedical Engineering, Stevens Institute of Technology

1) User Need:

1.a) Use Case

The users of Nomasound will be providers and their staff who screen patients for Melanoma. The disease makes up 75% of all skin cancer deaths [1], and cases have increased by 320% since 1975 [2]. Early detection can be life saving. If diagnosed before the tumor has spread, the affected tissue can be removed with an 80% success rate [3]. However, if the melanoma metastasizes the response rate to treatment falls to 5–20%, with a 10 year survival rate of only 10% [4].

1.b) Problem Impact

Current screening methods often involve a provider looking over the suspected cancer area by eye or small microscope (dermoscopy). However, this only has a 30% accuracy rate for non-dermatologists and an 80% accuracy rate for dermatologists [5]. More accurate diagnostic methods are invasive (biopsy) or technically complicated and expensive (OTC) [5]. These limitations compound, leading to patients with Melanoma being undiagnosed [5]. Since early detection is paramount to survival these missed diagnostics can be deadly.

1.c) Scope (Objective)

Nomasound is designed to universally attach to and integrate with the existing hardware and software of current ultrasound devices. By enhancing the imaging capabilities of the ultrasound device with high powered LEDs, a quality image with biomarkers (hemoglobin deoxygenation) will be produced. This noninvasive enhanced imaging modality will allow dermatologists and other providers the ability to more accurately screen for melanoma, ultimately saving lives.

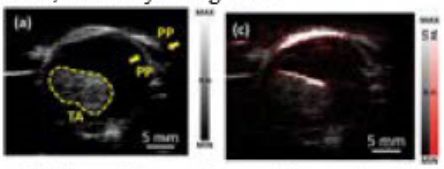

Figure 1: Ultrasound image vs ultrasound image overlayed with LED based photoacoustic imaging [7]

2) Design Inputs

2.a) Constraints:

The strictest constraints of the device's design were the grip shape, the specific intensity of the high powered LEDs and ensuring the universal capability of the device.

2.b) Requirements:

The highest priority requirement is ensuring the device's effectiveness at screening melanoma.

3) Solution

3.a) Design - Intended Use:

The proposed design solution incorporates high-powered LEDs in an array that will be shone into the skin while performing an ultrasound screening. The signal received from usage will be two parts one ultrasound and one photoacoustic then combined in real time to produce an enhanced photoacoustic image. The device is activated using a power switch on an attached microcontroller and will be powered through an attached power supply. The team's selection of LEDs with a pulse width of 35 ns and wavelength of 850 nm were the most critical part of this device due their innate ability to produce a photoacoustic image within penetrated tissue.

3.b) Build -DEMO

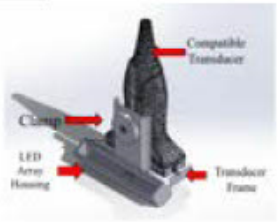

Figure 2: Nomasound Prototype Version 2

4) Verification Results

4.a) Introduction

The team will test the efficiency of the device by performing an ultrasound mimicking signaling test [6]. This will include two mediums, an ultrasound and an oscillator to capture test data.

4.b) Methods

To test the efficacy of the device, the team will use LEDs to pulse light at a thin material within the substrate and record if a photoacoustic effect was created, which will be shown on an oscillator as a interrupted signal.

4.c) Results

Testing has not yet been but will be conducted at Weill Cornell Imaging at New York-Presbyterian with Dr. Jeffrey Ketterling.

5) Conclusion

5.a) Summary:

The team is confident that Nomasound will be able to create the photoacoustic effect with LEDs while universally fitting all ultrasounds. Testing has not been conducted, but the team is confident with future results.

5.b) Revisions:

Utilization of high powered lasers would produce higher quality photoacoustic images. However, lasers are dangerous and expensive.

5.c) Impact (Future Version):

Nomasound is to be used as an early screening device for melanoma. If screened early, patients and physicians will be able to create an efficient treatment plan earlier, significantly improving life expectancy and saving lives.

References:

1. Davis LE. et al. Cancer Biol Ther. 2019;20(11):1366-1379
2. Saginala K. et al. Med Sci (Basel). 2021;9(4):63
3. Melanoma of the Skin. National Cancer Institute. Bethesda, MD
4. Liu Y. et al. Mol Cell Pharmacol. 2014;6(3):228
5. Bakos RM. et al. Am J Clin Dermatol. 2018;19:3-14.
6. Joanna Brunker. Scientific Report. 2016.
7. Yunhao Zhu et al. Sensors 2020.

STEVENS
INSTITUTE OF TECHNOLOGY

A Novel Rapid Delivery Device For Intravenous Adenosine Administration

Evrim E. Ozcan[1], Venkatsai Bellala[1], Albert Q. Wu[1], Christopher J. Shin[1], Tobias Meng-Saccoccio[1], Paul Ogan[1], Patrick Lee, PharmD[2], Sakina Sojar, MD[2]
[1]Department of Engineering, Brown University, Providence, RI, [2]Department of Emergency Medicine, Warren Alpert Medical School of Brown University, Providence, RI

1) User Need:

1.a) Use Case

In the emergency department and other acute care settings, certain critical, life-saving medications require rapid administration with high dosing accuracy. One such medication is adenosine, which is used in the treatment of supraventricular tachycardia (SVT). SVT is a common, life-threatening arrhythmia in infants and children (prevalence between $\frac{1}{250}$ and $\frac{1}{1{,}000}$), that can lead to cardiogenic shock and heart failure if not treated promptly and adequately[1]. The current standard of care involves intravenous delivery through a three way stopcock. Given that multiple, manual steps are required, there exists significant potential for errors that may delay successful adenosine administration.

1.b) Problem Impact

In addition to the potential for error, the current standard of care is highly inefficient: it often requires two clinical providers to operate and a residual volume of adenosine remains within the stopcock, which then never reaches the site of action. Previous literature has quantified this residual volume as being approximately 0.05 ml[2]. We have used this volume loss to solve for the percentage of a standard 0.1mg/kg body weight dose of adenosine that is not delivered to the patient, given the standard adenosine vial concentration of 6 mg/2 mL.

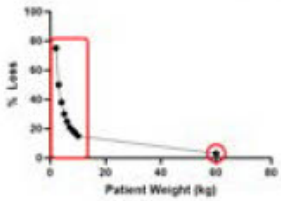

Figure 1. Adenosine Loss Based on Patient Weight

Combined with a slightly higher prevalence in pediatrics (the general population prevalence is 2.25/1000[3]) and a disproportionately higher percent drug loss, an improved delivery method is required to avoid underdosing consequences: such as greater progression to risky interventions like electric cardioversion if SVT is unable to be terminated with adenosine. Inability to terminate SVT with a second dose was found in 15% of cases in one study on children under the age of 18, with increasing likelihood at younger ages[4].

1.c) Scope

Our novel device addresses all limitations, in that it is intuitive, can be operated by one individual, and has a residual drug loss of <0.0125 mL following saline flush.

2) Design Inputs:

2. Constraints and Requirements

Our strictest constraints involved limiting operation to <2 clinical providers, reducing residual drug loss to <0.0125mL, reducing manufacturing cost <$2.83, and maintaining standard syringe ejection velocity. The manufacturing cost ceiling was calculated by the total cost of the current standard of care: two syringes and one three way stopcock. This way hospitals can be reimbursed under existing CMS codes for adenosine administration. The system must have <0.0125 mL residual volume, since the smallest SVT patients, low birth weight infants (2.5 kg), require a 0.25 mg adenosine dose. This would maintain <5% medication loss for the smallest patient doses. Finally the velocity constraint was set given the adenosine half life of 0.6-1.5 seconds in the bloodstream, and hence speed of delivery must at least match current delivery standards [5].

3) Solution:

3.a) Design - Intended Use:

Our solution is intended to be used by one clinician. This will greatly simplify workflow and reduce time to administration.

3.b) Build - DEMO

The novel device takes the standard stopcock, saline syringe, and adenosine syringe, and combines them into one system. We currently have a working prototype, but are unable to disclose CAD models or images as we are in the process of filing for a provisional patent. Our design complies with ISO standards for similar devices, again we cannot disclose the specific type of device.

4) Verification Results

4.a) Introduction

Ultraviolet-visible spectroscopy was performed to validate lower than 0.0125 mL residual volume and compare delivery profiles against the three-way stopcock.

4.b) Methods

Figure 2. Customized testing apparatus for UV-Vis kinetics studies.

4.c) Results

Results are currently being analyzed in MATLAB, and can be disclosed and presented upon patent-pending.

References:
[1] Chu PY. et al. Early Hum Dev. 2015;91(6):345-350. [2] Weberding NT. et al. Ann Emerg Med. 2018;71(2):220-224. [3] Kotadia ID. et al. Clinical Medicine. 2020;20(1):43-47. [4] Lewis J. et al. J Pediatr. 2017;181:177-182.e2. [5] Reiss AB. et al. Amer J Card Drugs. 2019;19(5):499-464

Acknowledgements: This study was funded by the Rothberg Catalyzer Fund and Hazeltine Grant, Brown University. The authors would like to thank Professors Anubhav Tripathi, Lindsay Schneider, Marissa Gray, Theresa Raimondo, Daniel Harris, Roberto Zenit, and Zachary Saleeba for their support.

SOLaware: Personalized UV exposure quantification device for UV-sensitive population

Stella Park[1], Suheyla Tozan[1], Ivan Rivera[1], Vanshika Siriram[1], Ethan Romano[1], Xinze Tan[1]
[1]Department of Biomedical Engineering, Columbia University

1) User Need:

1.a) Use Case

Ultraviolet radiation overexposure can lead to a variety of complications and, in more serious circumstances, disease such as melanoma and immune suppression[1]. Particularly vulnerable are photosensitive groups such as patients with autoimmune diseases[2]. In order to prevent further progression of photosensitive conditions, there is a medical need for a device that can monitor UV exposure real-time.

2) Design Inputs

2.a) Constraints:

For a typical user to conveniently carry around a device that quantifies the UV exposure on a daily basis, the device must be (1) wearable, (2) small enough, and (3) secure in its attachment to the parts of the body and be easily exposed to UV-light. Prior arts that tackle UV quanitification has failed to design their device to be easly wearable or securely attached[3]. This is concerning since populations susceptible to large UV exposure may lose their motivations to wear such device if they are prone to be lost.

2.b) Requirements:

For a device to provide meaningful UV quanitifcation for UV-sensitive patient population, the quantification should be personalized and the readout should be easy to comprehend[6]. The weather forecast UV index is not sufficient for UV quantification since it encompasses such a broader region[7] and does not reflect personal activities. Therefore, a personalized UV-readout unit would be familiar[7] and be beneficial[6].

3) Solution

3.a) Design - Intended Use:

SOLaware, the wearable UV quantification device, is designed to be attachable to any part of the body including on clothing and skin. Our design incorporates a secure case containing the sensor and can be placed into a brace-let or, with a adhesive, can be attached onto fabric. The readout of the data is to exported to a mobile app, where it incorporates an innovative metric of personal UV meas-urement for people of all skin tones and pre-existing con-ditions.

3.b) Build - DEMO

Figure 1B and 1A show the initial prototype. The circuit consists of a UV sensor, Arduino Nano with Bluetooth, and a micro-SD card reader for temporary data storage.

Figure 1. (A) Proposed app-based User Graphic Interface (B) Physical construction and wiring of prototype (C) 3D render of intended future product

4) Verification Results

4.a) Introduction and Methods

The primary requirement was to be able to quantify UV accurately and be able to relay this information in numerical terms to an external processing unit. Firstly, the sensor must be able to determine variations in UV intensity rather than just recognize the presence of UV[6]; such measurements will be critical for the determination of an individual's UV exposure in reference to health metrics. As outlined before, the final readout should be in UV index[7]. To test if the sensor was able to detect changes of UV exposure outdoor, we composed our sensor circuit and conducted the measurement outside. The measurement was conducted for 10 minutes, and for the first 5 minutes, the device was in the shade to see if it accurately reflects the subtle change in UV exposure. Three sensors were tested in order to compare its sensitivity, and the readout was converted to UV index.

4.b) Results

The sensor measurement readout converted to UV index confirmed that each sensor is capable of quantifying UV accurately and be able to provide easily readable and exportable data. However, we have also confirmed a need to calibrate each sensor in order for its readout to be relatable.

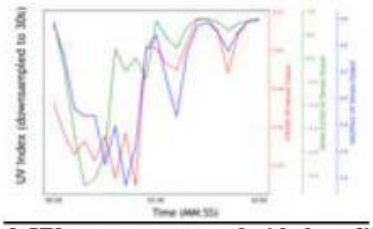

Figure 2. UV exposure measured with three different sensor outdoor, measured 11/24/2023 for 10 minutes. For the first 5 minutes, the sensors were in shade.

5) Conclusion

5.a) Summary:

The current prototype demonstrated it is confirming the most important functional requirement of the design, to provide an accurate measurement of UV and exportable data.

5.b) Revisions:

Our experiment also shows a room for improvement: for the final design, SOLaware will replace the raspberry pi and miniaturize the whole circuit into 2x2 inch dimention by using a printed circuit board with only a microprocessor, battery, and the UV sensor. We also are in the active process of designing a waterproof attachable case.

References:

1. D'Orazio J. et al. Int J Mol Sci. 2013; 14(6): 12222-48
2. Murphy GM. et al. J Photochem Photobiol B. 2001; 64(2-3):93-8.
3. Ceres P. Wired. 2018 (News article)
4. Clover. MacRumors. 2019 (News article)
5. Heo SY. et al. Sci. Transl .Med. 2018; 10(470): eaau1663
6. Huang X. et al. Ann Biomed Eng. 2021;49(3)
7. Moshammer H. et al. Int. J. Environ. Res. Public Health. 2016;(13):1041.

STEVENS
INSTITUTE OF TECHNOLOGY

Modified Vacuum-Assisted Male External Catheter System

Annamarie Piccirillo (Team Leader), Katerina Pratsinakis, Ryan LaPare, Zachary Steffens
Advisor: Dr. Wagner
Department of Biomedical Engineering, The College of New Jersey

1) Introduction and problem statement

The device improves urinary collection for hospitalized males with incontinence or limited mobility, benefiting patients and clinicians by minimizing attachment site irritation, urine leakage, and easing the burden on nursing staff.[1,2] Current male external catheters present challenges for clinicians, including urine leakage, canister overflow, house vacuum misuse, continuous patient exposure to vacuum, and limited urinalysis options. Leakage leads to skin irritation and inaccurate output measurement, while overflow necessitates staff cleanup. Improper house vacuum settings can cause complications, and continuous application irritates the attachment site.[3,4] Addressing these complications and offering viable urinalysis options in external catheters enhances overall system function and improved nursing staff efficiency in collecting daily samples.

2) Design inputs and constraints

Justified design inputs per 21CFR820.30 were developed. The device must maintain a secure attachment, efficiently collect urine outputs, accommodate male anatomical variations, and facilitate accessible urine sample collection.[5,6] Timely warnings for canister capacity are essential to prevent canister overflow of biohazardous material.[7] Regulation of negative pressure based on urination cycles with proper house vacuum settings ensures device functionality and safety for patient use.[8] The device must be compatible with standard hospital vacuum systems. In addition, user comfort and minimal device noise production are paramount for extended device use. Safety requirements demand fail-safe operations regarding the vacuum and adherence to electrical standards.

3) Design solution

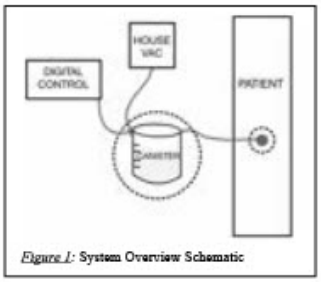

Figure 1: System Overview Schematic

The final design encompasses an novel condom attachment site intended to be placed on a patient. Fabricated in silicone by casting from a 3D-printed mold, the tip features a collection chamber designed to resist collapse when subjected to vacuum. A temperature sensor, embedded in the collection chamber silicone wall, will detect urination cycles and regulate a solenoid valve to apply vacuum for a clinically relevant period to assist collecting urine output in a canister. The tip collection chamber contains one-way check valves to modulate vacuum level while preventing urine leakage. Load sensors monitor the canister's volumetric contents and trigger an alert, auditory or visual, to staff when full. Additional information, such as urine output rate and canister volume, is displayed on an LCD. A separate urinalysis mode, activated at any point during use, allows convenient urine sampling by diverting urine flow with a pinch solenoid. Final features include a moisture trap to protect house vacuum and a 2000ml collection canister.

4) Initial testing results

Figure 2: Temperature as a function of time evaluated at different depths in silicone, modeled as a semi-infinite system. Model validity was demonstrated for depths of up to 3.79 mm. This relationship will be used to determine the temperature sensor depth in the silicone collection chamber wall.

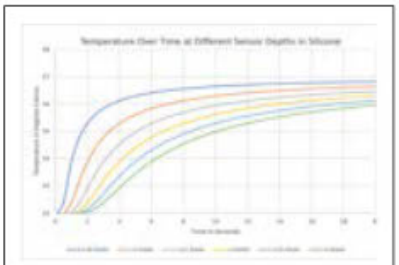
Figure 2: Thermal profile of attachment site using semi-infinite model.

Figure 3: The temperature sensor calibration curve represents a mathematical relationship between voltage output and temperature to establish precise and accurate temperature measurements.

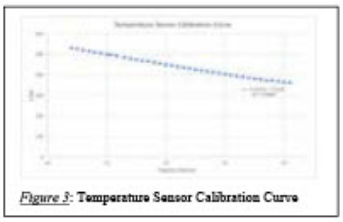
Figure 3: Temperature Sensor Calibration Curve

Figure 4: FSR calibration curve established a relationship between weight and voltage output, where the density of urine will be utilized to calculate approximate volume.

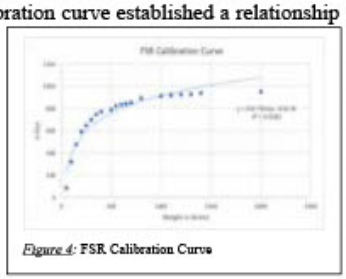
Figure 4: FSR Calibration Curve

5) Integration and verification/ validation testing

The testing above, along with developed fabrication processes and an arduio-driven control system, will be used to integrate selected parts in a final prototype. Verification tests will include size testing and displacement force testing using anatomical models, flow stream testing to simulate urine flow rate range, load cell testing for canister fluid level accuracy across design range, and assessment of the alarm and urine detection systems. Additional tests include auditory alarm decibel range, thermistor accuracy, solenoid air leakage, pressure gauge detection of negative pressure, electrical safety leakage current, and moisture trap efficiency. Clinical nursing staff will be used for functional validation testing.

References: [1] Junqueira JB et al. Rev Lat Am Enfermagem, e2970, 2018. [2] Schnalle, J.F. et al. Int Urogynecol J4, 89–94, 1993. [3] Saint S, et al., J Hosp Med, 14:E1-E4, 2019. [4] Sinha AK, et al. J Surg Case Rep, (10):rjy275, 2018. [5] Van Mastrigt, et al. Indian Journal of Urology, 25(1), 2009, 99–104, [6] Mayo Clinic Staff. Urinalysis, Mayo Foundation for Medical Education and Research. 2023 [7] NIOSH. Guidelines for Protecting the Safety and Health of Health Care Workers, Publication No. 88-119. 2014 [8] NFPA 99. Health Care Facilities Code. 2024

Adaptable Acoustic Startle Response Device (AASRD)

Rai, Isha; Karp, Max; Caswell, Sean
New Jersey Institute of Technology

1) User Need:

1.a) Use Case

The AASRD is marketed toward users conducting animal testing on rodent models and need a cheap, adaptable device that can test the acoustic startle response of a variety of rodent models.

1.b) Problem Impact

Existing devices that fulfill this need are far more expensive and are suited to only one rodent model, lacking the adaptability that many researchers require. The acoustic startle is a monumental test following brain trauma in animal models. The data can be used to test diagnostics and treatments that may be translated to human models [1].

1.c) Scope (Objective)

In order to meet the user's needs, the device must be adaptable, low-cost, and run from one centralized software, selected to be LabVIEW.

2) Design Inputs

2.a) Constraints:

Using a single centralized software was the main constraint. This minimized electrical components used in the designs to a DAQCard, accelerometer, amplifier, and speakers. The design requirement included adaptability to different-sized rodent models. The sound-attenuating chamber had to be large enough to accommodate enclosures for mice, rats, and ferrets.

2.b) Requirements:

Adaptability between different animal models was of the highest priority. The user conducts research on a variety of animal models. Adaptability also keeps the user cost low; the need for multiple devices is negated. The device would need to accurately output sounds determined by user inputs of frequency (Hz) and volume (dB) to offer customizability to the device and experimentation.

3) Solution

3.a) Design - Intended Use:

The product is designed to be used in a laboratory setting to test auditory reflexes in a variety of rodent models, with the device being unique in its ability to accommodate different rodent models and be highly adaptable to different input frequencies and decibel levels at the user's discretion.

3.b) Build - DEMO

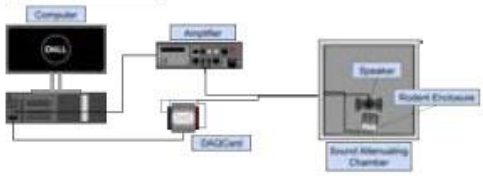

Figure 1. Full AASRD setup

The solution shows an easy-to-use AASRD that allows the animal enclosures to be swapped with sizes ideal for other models, keeping functionality across species.

4) Verification Results

4.a) Introduction

The speakers must output sound with specific frequency and decibel levels matching user inputs, measured with frequency and decibel meters. The accelerometer must detect the motion of the rodent enclosure, displaying it on a LabVIEW graph with the magnitude of acceleration.

4.b) Methods

Monitors for frequency and decibel levels will be used to analyze the sound output generated by user inputs three times, with a t-test done to verify no significance between the values. An initial test will be done to verify the accelerometer's ability to detect motion three times by graphing the magnitude of acceleration and conducting a t-test between max magnitude of acceleration and resting values. After individual testing, the full device will be tested to ensure sound output and motion recording align properly with respect to time. Testing of functionality will initially be conducted using a mouse toy to simulate movement without requiring the use of a live animal.

4.c) Results

Testing supports the device's viability; the acceleration is detected and plotted in LabVIEW. The program produces target decibel and frequency values through speakers.

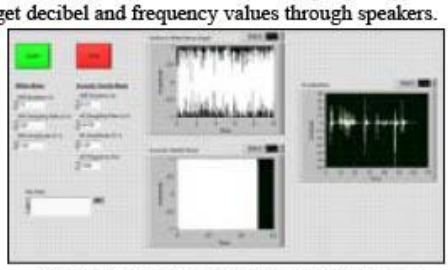

Figure 2. LabView Front Panel Showing Test Results

5) Conclusion

5.a) Summary:

The design is projected to be successful. Motion has been detected and sound has been outputted and altered using inputted values. The preliminary software testing and electrical component testing have been successful, but final confirmation will be defined following complete construction and subsequent animal testing. Final construction and testing have been delayed by a change in amplifier and a delay in the arrival of ordered parts.

5.b) Revisions:

Future steps to increase impact would be testing and implementation to obtain user reviews. A future addition may be including a shock plate on the base to test for conditioning along with the acoustic reflex.

5.c) Impact (Future Version):

Developing a deeper understanding of an auditory acoustic startle response will heavily influence the development of diagnostic techniques. Testing of potential treatments can be completed on different species of rodent models in a single device, increasing the reliability of results prior to human testing.

References:

1. Clark A.L. Front in Neurol. 9: 873

Acknowledgements: Dr. Bryan J. Pfister, Dr. Joel Schesser

STEVENS
INSTITUTE OF TECHNOLOGY

Plume Evacuation Device For Blepharoplasty

Noah Reilly, Mitchell Gray, Chris Thiagarajah, and Robert Gettens
Western New England University

1) User Need

This project aims to develop an apparatus to remove the carcinogenic plume created during electrosurgical blepharoplasty. The current standard procedure requires operating room nurses to hold a vacuum tube above the electrosurgical area for as long as one hour per procedure and up to five procedures per day (Figure 1).

Figure 1: The current set-up used in operating rooms, where nurses need to hold the surgical vacuum tube during surgery.

A new design will more efficiently remove the plume and allow nurses to focus on more urgent tasks in the operating room. Current solutions include electrosurgical pen attachments [1]. Electrosurgical pen attachments are expensive one-time-use items costing upwards of $150 per surgery and negatively impact surgical ergonomics, lowering precision and stability.

2) Design Inputs

This apparatus must interface with standard medical vacuum tubing such as the Buffalo PlumeSafe TURBO [2].
The device must conform to three main standards, Colorado State Bill 19-041 requiring the removal of hazardous plumes, Airbase-5635 requires particulates to be removed in the operating room, and ASTM-F431-21 ensuring that the attachments developed do not interfere with airflow.
A traceability matrix was developed to link user needs with product specifications and verification/validation testing. Design inputs include 1) surgical area access (non-interference), 2) surgical plume evacuation, 3) fire safety, 4) skin contact biocompatibility, 5) set-up time, 6) surgical space utilization, and 7) part and maintenance sustainability.

3) Solution

As stated the plume evacuation device interfaces with standard surgical vacuum systems. Each prototype (Figure 2) has a different base attachment, either via the surgical table (Figures 2A, and 2C) or via contact with the patient (Figures 2B, and 2D). Each prototype is tailored to accurately collect the dangerous plumes that occur during the cauterization of the blephara.

Figure 2: Design concepts created to fit the design criteria, A) manifold which connects to a segmental tube, B) laboratory goggle based manifold concept, C) wrap around suction system, and D) above eye suction system.

4) Verification & Results

Airflow testing was conducted to compare the suction performance of each concept vs. control (Buffalo PlumeSafe TURBO) using an anemometer measuring airflow at the surgical site. An ANOVA was used to determine differences amongst the experimental groups with Post Hoc t-tests comparing each group to control.
An ANOVA determined that the average airflow for the concepts generated (Figure 3) were significantly different. The Manifold concept had 35% less suction than the Control (Buffalo PlumeSafe TURBO) (Post Hoc t-test, $p<0.05$). The Goggles concept had 29% less suction than the Control (Buffalo PlumeSafe TURBO) (Post Hoc t-test, $p<0.05$). The Dual Suction concept had 37% less suction than the Control (Buffalo PlumeSafe TURBO) (Post Hoc t-test, $p<0.05$). The Top Suction concept had 12% less suction than the Control (Buffalo PlumeSafe TURBO) (Post Hoc t-test, $p<0.05$).

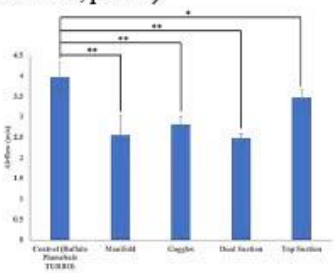

Figure 3: The average airflow in m/s for each design with Post Hoc t-test ($p<0.05$). Significant difference between control and the new designs found.

5) Conclusion

5. a) Summary:

The developed designs were found to have some significant differences in airflow compared to the original concept. The Top Suction design was the most similar to the original concept with only a 12% difference in airflow through the vacuum.

5. b) Revisions:

Revisions will be made to the Top Suction concept to decrease the difference in airflow and develop an integration system to either the patient (mask design) or surgical table. Continued prototypes will be developed to test different materials the attachment could be made out of as well.

5. c) Impact (Future Version):

Future versions of the developed devices will go through particulate testing to ensure that hazardous plumes can be removed from the surgical area.

References:

1. Cordero I. Community Eye Health. 2015; 28(89): 15-16
2. Buffalo Filter Catelog. 1991; 3

Acknowledgments: We would like to thank Timothy Shannon for his help with consulting on the development of the different concept prototypes.

Assistive Cannulation Device for Home Hemodialysis

Adel Alnatour, Tina Liu, Julian Michaud, Feven Naba, Eloy Sanchez, Harry Xiao
Columbia University Biomedical Engineering

1) User Need:

1.a) Use Case

Home hemodialysis (HD) holds many benefits over in center dialysis, but only 14% of patients who need hemodialysis choose HD (USRDS, 2023). HD requires patients to self cannulate their arteriovenous fistula (AVF), but many patients report a fear of needles and lack of manual dexterity, leading to the underutilization of HD. The need for extensive training, the burden on the care partner, and the fear of adverse events pose further barriers (Gromko, 2013).

1.b) Problem Impact

Our device aims to reduce fear and difficulty of self cannulation. Thus, we hope to help patients transition from in center to HD, saving them 64% in cost (Cureus, 2021). On a broader scale, we hope to render HD more accessible for all patients who need dialysis.

1.c) Scope (Objective)

The key limitations to address are the dexterity required to cannulate and the fear of needles. Our device must act as a comfortable platform for patients to self-cannulate with minimal fine motor function.

2) Design Inputs

2.a) Constraints:

The device must insert the needle consistently to a set depth to avoid bleeding and tissue damage. The device must also be comfortably operable using one hand.

2.b) Requirements:

The vertical needle displacement should reach 9mm, which would place it within the center of the standard AVF (Oliver, 2018), and should be inserted at a 30˚angle (Brouwer, 2011). The insertion velocity should be high to avoid unintended tissue damage (Heverly, 2005). The needle should be secured to the patient after insertion.

3) Solution

3.a) Design - Intended Use:

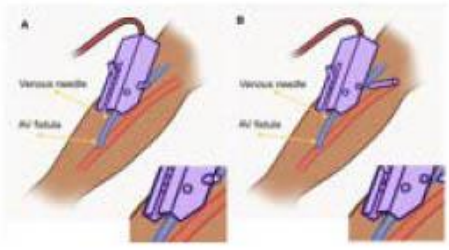

Figure 1. Original sketch of our device sitting at a 30° angle against the patient's arm. In step (A), the needle is loaded by compressing a spring. In step (B), the spring is released and needle inserted.

3.b) Build - DEMO

Our initial prototype utilizes a ballpoint pen ink cartridge as a makeshift needle (Figure 2). The slanted platform provides the 30° insertion angle, and the spring provides the necessary force. This prototype is a proof of concept, showing that the needle is inserted at an appropriate distance and angle.

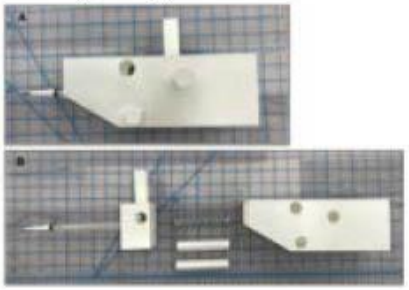

Figure 2. Each square is 12.7 x 12.7 mm. (A) Assembled prototype. (B) Disassembled prototype showing all parts.

4) Verification Results

4.a) Introduction

We evaluated the insertion depth and velocity of our device. Our prototype has two depth settings (2.5mm and 4.8mm) that were tested separately.

4.b) Methods (n = 5)

"Needle" (ink cartridge) travel distance and speed were recorded. Video analysis was conducted to extract velocity data of needle tip.

4.c) Results

Parameter	2.5mm depth	4.8mm depth
Velocity (mm/s)	51.6 ± 6.4	123 ± 54
Depth (mm)	2.5 ± 0.3	4.8 ± 0.3

Table 1. Velocity and needle depth of initial prototype

5) Conclusion

5.a) Summary:

Our design successfully inserted a needle to a desired depth consistently while maintaining a 30° insertion angle. It has maintained a high velocity, which will prevent tissue deformation that can lead to damage.

5.b) Revisions:

This prototype is not yet operable with one hand and does not detach from the needle. The design is currently being improved for needle delivery and detachment through compliant mechanisms.

5.c) Impact (Future Version):

This product will provide an accessible path to HD, saving resources for patients and healthcare providers.

References:
1. Gromko L DPCEC (website)
2. USRDS Annual Data REport. 2023:2
3. Jha CM Cureus. 2021;13(10):e18549
4. Oliver M. J Am Soc Nephrol. 2018;29(11): 2607-2609
5. Brouwer D. Nephrol. Dial. Transplant. 2011:40(10) 434-443
6. Heverly M. IEEE Int. Conf. 2005:1646-1651
7. Kobayashi Y. Med. Eng. Phys. 2012:35(5): 684-689

Acknowledgements: We would like to thank our senior design instructors Dr. Lauren Heckelman, Joe Viola, Mira Roosth, Parth Gami, and consulting physicians Dr. Sean Kalloo and Dr. John Ross.

STEVENS
INSTITUTE OF TECHNOLOGY

NG-LOOP: Nasogastric (Tube) Lightweight Observation and Oversight Product

Dahin Song, Jeffrey Huang, Suh Kyung Yoon, Katherine Han
University of Pennsylvania

1) User Need:

1.a) Use Case: Nasogastric (NG) tube dislodgement occurs when the tip of the tube is displaced from the stomach. There is no automated monitoring system, forcing caregivers (parents, physicians, and nurses) to manually inspect for dislodgement every four hours[1].

1.b) Problem Impact: Infant patients face a disproportionate vulnerability with a 60% of infant patients experience dislodgement, which can result in severe pneumonia[2]. Existing solutions have largely failed to address this issue. Internal bridles (AMT bridle and CORGRIP) loop a rigid tube through the nasal cavity and around the nasal septum to prevent dislodgement[4]. However, the AMT bridle was recalled during clinical trials because it tore thorugh a patient's nasal septum and became wedged between the tear. Evidently, this invasive approach is unsuitable for infant patients due their delicate nasal epithelia.

1.c) Scope: Management of NG tube dislodgement be effective detection and prevention, and have a user-friendly, non-invasive setup approach.

2) Design Inputs

2.a) Constraints: The device itself must be lightweight, biocompatible, stiff without being brittle, compatible with the sensor of choice, and should maximize both comfort and aesthetics while maintaining its functionality. These constraints limit the materials and the design of the device.

2.b) Requirements: The feedback function must dispatch rapid alerts (>1 sec) to the relevant persons in the event of tube dislodgement, and reliability (feedback responses are activated 100% of the time) under various conditions.

3) Solution

3.a) Design - Intended Use: As per the specified requirements, NG-LOOP has the unique capacity to prevent and detect tube dislodgement, and engage appropriate feedback responses using a simple and non-invasive approach. The external bridle clips securely onto the NG tube, providing physical stabilization to prevent dislodgement. The magnetic sensor system detects tube dislodgement in the event of external bridle failure. Upon dislodgement, small magnets secured to the NG tube inside the nostril are brought into proximity of the sensor, triggering a dual feedback mechanism. An SMS alert is promptly dispatched to the caregiver's phone and simultaneously, the feeding pump is automatically halted to prevent inadvertent aspiration of feed into the lungs.

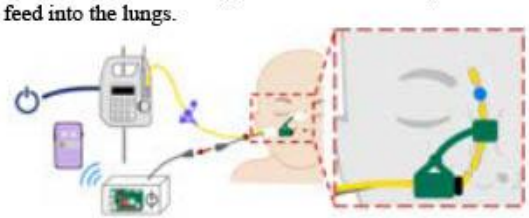

3.b) Build – DEMO: The bridle was 3D printed using Accura 25, a material that passes all requirements. DRV5055 linear hall effect sensor was housed by the clip and connected to a Raspberry Pi 4 microcontroller. 3x2-mm round neodymium magnets were attached to a6 Fr 22' NG tube with medical-grade waterproof polyurethane tape at the dislodgement length.

4) Verification Results

4.a) Introduction

The external bridle must be able to withstand at least 160 kPa while being lightweight[4]. Ideally, the sensor-feedback system has a 100% sensitivity and 100% specificity rate.

4.b) Methods (i = 20)

The bridle was tested by measuring displacement when varying weights were dropped onto the NG tube. The performance of the magnetic sensor system was tested by measuring the voltage change at differing magnet displacement. Furthermore, NG tube dislodgement was simulated by pulling on the NG tube with tweezers immediately outside the nare. Successful tube dislodgement detection and successful feedback mechanism triggering in the event of dislodgement dietection were. For both studies, displacement was measured as length of tubing that has exited the nostril from its original state; tube dislodgement was defined as 5 cm displacement.

4.c) Results (i = 20)

The average displacement without the bridle was 11.4 cm, and with the bridle, it was 2.3 cm. Paired t-test between the bridle and no bridle conditions yielded a p-value of 0.00004, indicating a significant decrease in displacement with the bridle (**Figure 1a**). The sensor achieves significant voltage dropoff past ~6 mm displacement from sensor, allowing for specific detection of dislodgement (**Figure 1b**). The feedback system demonstrated a 90% sensitivity and 100% specificity rate, with both feedback mechanisms being activated in 100% of trials where the threshold was met.

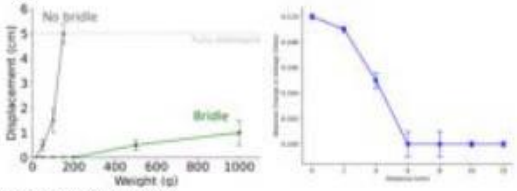

Figure 1 (a and b)

5) Conclusion

5.a) Summary: The external bridle and magnetic system of NG-LOOP consistently prevented and accurately detected dislodgement with prompt feedback responses.

5.b) Revisions: Areas in need of further improvement include the consistency of tube dislodgement detection and the ease of application of the NG-LOOP. Changing the design of the bridle could allow better bridle functionality.

5.c) Impact (Future Version): Making the external bridle easier to apply would invite more patients to use the device and increase the aesthetics of the device, increasing comfort and visual acceptance. Improving the consistency of detection would increase NG-LOOP's efficacy of detecting dislodgement.

References:

1. Rushing, J. 2005. Nursing 35(5)
2. Quandt, D et al. JPGN. 2009. 48(5)
3. Powers, J. Crit Care Nurse. 2019. 39 (4): 61–63.
4. Upshaw, MB. Dev Sci. 2016. 19(2): 195–207.

Acknowledgements: We would like to thank our senior design professors, our project manager, and Penn's Stephenson Foundation Bio-MakerSpace.

Lab-On-A-Chip Migration Assay for Scientific Research

Matthew Steneri, Shelby Edwards & Devina Jaiswal Ph.D.
Biomedical Engineering, Western New England University, Springfield, MA

User Need

Cell migration assay is commonly used to assess cellular response to cytokines and drug molecules [1]. Researchers such as oncologists, pharmaceutical scientists and tissue engineers use conventional techniques to monitor cell movement in reaction change in its microenvironment [2]. This assay is conventionally conducted using trans wells consisting of a semi-permeable membrane placed in a standard cell culture well plate (Fig. 1A). Even though the technology has been helpful in producing meaningful results, it has limitations such as expensive disposable trans-wells, lack of in-house technology for in-depth migration assay and limited application. There is a need in the market for a high throughput, cost effective device that have functional flexibility.

Design Inputs

Based on the customer discovery, five design inputs were conceptualized. (1) The device needs to be optically transparent for compatibility with microscopes. (2) The device needs to be compatible with a commercially available plate reader. (3) The device must be able to run a migration assay and support 3D cell culture, (4) The device needs to have multiple inlets to deliver reagents such as drugs, cytokines, cancer cells, and circulating media, (5) It also needs outlets for sample collection.

Innovative Solution

In consideration with the design inputs and to mimic the current technology on a microfluidic platform, a 12-well three-layer chip was designed and fabricated (Fig. 1B). The bottom layer is a cell culture chamber appropriate for 2D and 3D cell culture with a constant supply of nutrients connected to the inlets and outlets. The top layer mimics a trans well that can house reagents such as cytokines and drugs. These reagents can filter through the semipermeable membrane (Fig 1B, green layer) and interact with the cells. The results from this assay can be obtained in three ways: (1) the device can be directly read in a plate reader, (2) cellular movement can be monitored in real time under a microscope and (3) the secreted proteins can be collected at the outlets of each well for further analysis.

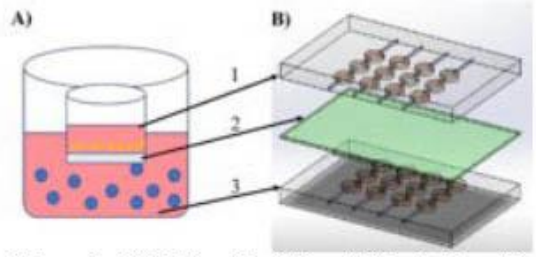

Figure 1: Cell Migration Microfluidic Device. (A) Conventional cell migration assay using trans wells were mimicked on a (B) microfluidic platform with three distinct layers. (1) Cytokines holding layer is directly connected to a (2) semipermeable membrane which allows diffusion of chemical messengers into the (3) cell holding layer.

Verification & Validation

The design of this device followed engineering standards, particularly ISO 22916 [3], which outlines the universal measurements for connections and sizes of chips, making this device compatible with regular laboratory equipment and connectors. The fabrication and adhesion of the three layers was critical for the success of this device. Using guidelines from the Microfluidics Association, leakage tests were conducted. Test resin chips were bonded to various materials using four adhesives. This created four cases: 1. resin to resin using resin in its fluid state as the bonding agent, 2. glass to resin using Loctite Glass Glue, 3. PMMA (Poly-Methyl Meth Acrylate) to resin using Loctite Super glue, and 4. glass to resin using Loctite Super Glue. Blue color water (5 ml) was pumped through the chip using a syringe pump at a rate of 0.07 µL/min. The experiment was recorded using a video camera for qualitative analysis of leaks from the chip due to adhesive failure. Based on the results, the best bonding was resin and resin bonded with resin as seen in Fig 2A with no leaks. Other cases showed minor to major leaks as indicated in Fig. 2C and D (arrows).

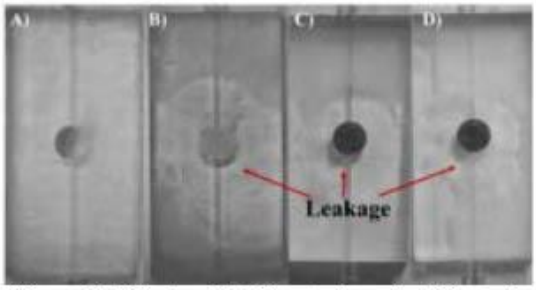

Figure 2: Adhesion Test. Four test samples (A) case 1, (B) case 2, (C) case 3 and (D) case 4 were tested with fluid at 0.07 µL/min. Case 1 showed no leaks and will be used for further testing.

Conclusion

In conclusion, a microfluidic high throughput migration assay chip was successfully designed and fabricated. The bonding of the three layers was tested and the combination of resin and resin bonded by the resin showed no leaks and this design will be further tested for functionality.

References:

1. Kramer, N., Walzl, A., Unger, Cet al, 2013, *Mutation Research/Reviews in Mutation Res.*, *752*(1), 10-24.
2. Eccles, S. A., Box, C., & Court, W. (2005). *Biotechnology annual rev.*, *11*, 391-421.
3. Microfluidic Devices, ISO 22916:2022.
4. H. Heeren, M. Davies, et al. Jun 2022.

GripSense System: Quantifying Stroke-Related Hand Function

Alexandra Stibler, Amanda Dias, Michelle Foong, Cory Sahanas, Advisor: Dr. Brett BuSha
The College of New Jersey (TCNJ)

1) User Need: Over 700,000 people experience a stroke in the United States per year.[1] Those affected may experience a loss of joint ROM, poor dexterity, and reduced grip control leading to loss of autonomy in routine tasks and decreased quality of life. 80% of this population requires hand therapy.[2] Current interventions exist to encourage practice of therapy exercises (*MusicGlove®*) and assist in grasping motions (*SaeboGlove®*), but do not quantify and record physical measurements of grip control. GripSense is being developed to record hand function progression during therapy exercises in patients demonstrating stroke-related hand impairment by offering a device that is capable of calculating and documenting force and ROM of the fingers to assist patients and providers. This way, not only do medical professionals receive detailed information of their patients' current state to better personalize treatment plans, but tracking patient progress with quantifiable data enhances outcomes by recognizing recovery achievements.[4]

2) Design Inputs: Prominent requirements applied to this project are the device's ability to calculate grip force through the fingertips (0-30N)[5], ROM of the PIP and MCP joints (70-200°)[6], and comfortability. The first two requirements provide quantifiable data that medical professionals can use to assess patients' abilities over time. This affects user needs as they are not limited to subjective forms of measurement, but instead have quantifiable data to describe their physical capabilities more accurately. The comfortability of the device directly affects the user's needs to allow the patient to freely use their hand without interference from the form of the device. Factors such as material selection, size, and weight all need to be considered to remain within this requirement.

3) Solution: A digital model of the pronated (a) and supinated (b) views of the intended GripSense design solution is provided. Force sensitive resistors (green circular structures) will be sewn into the glove to determine stroke patients' changes in force production. Rotational potentiometers (cylindrical gray structures) and flex sensors (black components) will be employed to calculate the PIP and MCP joint angles. All electrical wires will be fed through a wrist component to increase organization of wires. These wires will terminate in an armband potion which houses the microprocessors and batteries required for device power.

4) Verification Results: Verification testing protocols are currently being developed and applied to verify required dimensions, function of the force sensors, flex sensors, and batteries. Currently, the verification of the rotational potentiometers (RP) has been performed.

4.a) Methods: The generation of a calibration curve revealed a conversion factor of 4.759, resulting in an equal relationship (R^2>0.99) of sensor output to true angle values. Once calibrated, a range of angular displacements

(a) (b)

varying from 70° to 200° were applied to the RP across trials (n = 3) to verify that this range was met.

4.b) Results: The acceptance criteria for RP verification is no statistical significance from the controlled angle of bending through paired one-sample two-tailed t tests (α=0.05) at each measured interval. The RP met this input requirement by passing verification testing. Simulated sample data (Figure 1) was able to be recorded to represent expected GripSense data upon prototype construction.

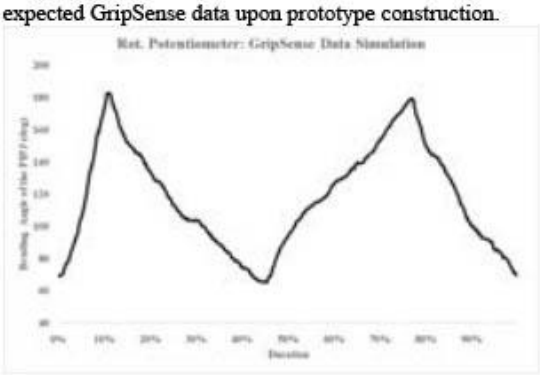

Figure 1. Flexion and extension of the index finger PIPJ.

5) Conclusion

The construction of the prototype has not been completed and further verification testing is currently in progress.

References:

1. Friedman, N., et al. Retraining assessing hand movement. J NeuroEng and Rehabil. 11, 76(2014).
2. Kandaswamy, D., et al. (2018). Quantitative Assessment Hand Dystonia. J Move Dis., 11(1), 35–44.
3. Eschmann, H., et al.(2019). Thumb and finger movement reduced after stroke. PloS one, 14(6).
4. Conrad, F. G., et al.(2010). Impact progress indicators on task completion. Interacting computers, 22(5), 417–427.
5. Zatsiorsky, V. M., et al. (2002). Force and torque production. I Biomech. Biolo cybernet, 87(1), 50–57.
6. Carpinella, I., et al. (2011). Multi-finger coordination. J NeuroEng and Rehab., 8, 19.

Acknowledgements: We would like to thank TCNJ's School of Engineering for funding this project and the BME Department for their guidance.

Portable Breathalyzer for Monitoring Diabetes

Kenneth Kwong, Sadie Smith, Molly Sullivan, Michael J. Rust
Western New England University

1) User Need

1.a) User Case:

Patients with diabetes need a painless method of managing their condition because the current blood glucose testing methods are painful, which leads to decreased compliance.

1.b) Problem Impact:

As reported by the International Diabetes Federation in 2021, an estimated 537 million adults around the world have diabetes [1]. This number is projected to continue rising to over a billion cases by 2050 [1]. Standard blood glucose meters (BGMs) are hand-held devices that use a drop of blood acquired from a finger prick to track glucose levels with a test strip [2]. A lack of patient compliance with this testing can happen because of the pain associated with finger pricking multiple times a day. Continuous glucose meters (CGMs) are a more recent development; however, they are invasive and expensive, also limiting patient compliance.

1.c) Objective and Scope:

The objective is to create a device that can read the acetone level in someone's breath, which is correlated with blood glucose, using an integrated sensor system that works with a user-friendly display. It aims to be a cost-effective device that will be able to give an accurate reading for acetone. If successful, this device would provide a painless method for patients with diabetes to monitor their condition, thus replacing the standard glucose meter.

2) Design Inputs

The highest priority requirement is the device's ease of use so a user can conduct the test by themselves. It must have a maximum size of 12 x 6 x 2 cm and a maximum weight of 0.25 kg [3]. This is so the device remains portable for the user to test throughout their daily life. The device also needs to be accurate and precise in addition to being able to measure and differentiate between the following physiologically relavent acetone ranges: 1-2 ppm which is a healthy range that represents basal level ketosis, 2-75 ppm which is another healthy range for those participating in diets that effect their ketone levels, and 75-1250 ppm which is associated with diabetic ketoacidosis [4].

3) Solution

As shown in Figure 1, the device is designed to take a sample of breath from a user and measure the acetone levels using a gas sensor. The output is displayed on the device to show if the amount of acetone detected is within a normal or unhealthy range for the patient. The form factor of the device is a hand-held slim cylinder with room for a user-friendly display.

4) Verification Testing

4.a) Functional Prototype:

The functional prototype consists of an air quality sensor that detects acetone, an air flow sensor, and a user-friendly interface display. The system is controlled via an Arduino microcontroller board with associated code.

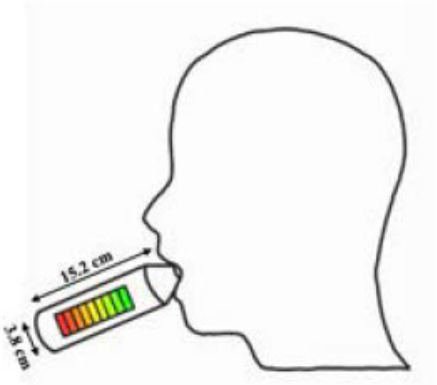

Figure 1. Conceptual diagram of the acetone breathalyzer for diabetes monitoring. Patients breathe into hand-held device and a reading is displayed on the user interface.

4.b) Verification and Validation Testing:

To ensure the right device is being built the right way, multiple verification and validation tests will be completed. A calibration test will be performed with the acetone sensor to ensure functionality as well as to verify detection of concentrations within the physiologically relevant range. Another test will calibrate the air flow sensor to ensure functionality and accurate readings. Finally, different acetone vapor levels of low, medium, and high concentrations will be developed and tested using a separate calibrated sensor. This will simulate a variety of patient breath samples.

5) Conclusion

If the portable breathalyzer is successful, patients with diabetes will have a painless, non-invasive device for monitoring their condition. This may lead to better compliance with treatment regimes, thus improving patient outcomes. As such, there could also be reduced load on healthcare professionals, as patients with diabetes would be able to maintain their condition better during their daily lives. Additionally, there is a large potential global market for a consumer product that can help screen and monitor diabetes.

References:

1. "Diabetes around the world in 2021," *International Diabetes Federation*, 2022.

2. W. Ong, et al. "Barriers and facilitators to self-monitoring of blood glucose in people with type 2 diabetes using insulin: a qualitative study." *Patient preference and adherence,* vol. 8, Feb. 2014.

3. BACtrack S80 breathalyzer user manual, KHN Solutions Inc., San Francisco, CA, U.S., 2016, p. 11.

4. J. Anderson, "Measuring breath acetone for monitoring fat loss: Review." *Obesity (Silver Spring)*, vol. 23, no. 12, pp. 2327-2334, 2015.

WOVEN: Wearable Onesie for Vitals and Ease of Nursing

Karly Terlevich, Eric Nawrocki, Chaitanya Karimanasseri, Ambika Gaur
University of Pennsylvania

1) User Need:

1.a) Use Case: WOVEN targets improved neonatal care efficiency and safety in NICU and PICU settings, catering to nurses, parents, and infants. WOVEN's integration of sensors into a wearable onesie simplifies monitoring, eliminating wire clutter and enhancing accessibility for care. This innovation improves the visual and emotional environment for parents while reducing the risk of injuries associated with traditional monitoring methods.

1.b) Problem Impact: WOVEN reduces wire entanglement, infant injuries, and caregiver stress. Integrating heart rate, SpO2, and temperature sensors into a single wearable device eliminates multiple wires, potentially reducing nurse workloads and hospital costs.

1.c) Scope (Objective): WOVEN addresses wire entanglement and monitoring inefficiencies by prioritizing safety, streamlining monitoring, and enhancing care experience.

2) Design Inputs

2.a) Constraints: Design constraints include integrating multiple sensors into a single wearable without compromising sensor accuracy or patient comfort. Feedback from healthcare professionals influenced design choices, emphasizing ease of use and effective monitoring.

2.b) Requirements: Key requirements were sensor accuracy within accepted ranges, ease of use through design features like snap buttons and Velcro, and a software system for data tracking. These requirements support the primary goal of improving neonatal care efficiency.

3) Solution

3.a) Design - Intended Use: At the core of this solution is a sensor band located at the onesie's foot, essential for monitoring heart rate, SpO2, and temperature. This is complemented by a nurse-driven onesie featuring innovative elements such as snap buttons and Velcro closures for easy dressing and medical access, including G-Tube and IV insertion flaps, as well as heel prick openings. Furthermore, the onesie allows the top half to be fully removable, enabling vital skin-to-skin contact between parents and infants while preserving the monitoring setup's integrity.

3.b) Build – DEMO: The WOVEN has a compact and user-friendly sensor band with an easy-removal connector. Integration with existing hospital technology is a priority, ensuring seamless incorporation into the neonatal care ecosystem without workflow disruption.

4) Verification Results

4.a) Introduction: In validating WOVEN's vital sign measurements, methods ensured accuracy. WOVEN's sensors were compared with hospital standards, using a finger pulse oximeter for HR and SpO2, an infrared temperature sensor for temperature, and manual counting for RR. Readings were collected over one minute using both methods for each vital sign. Statistical analysis, including mean average percent error (MAPE) calculation and Bland-Altman analysis, assessed accuracy and systematic bias.

4.b) Methods (i = 1 ... N): In validation, WOVEN's vital sign measurements were compared with hospital standards using a finger pulse oximeter for HR and SpO2, an infrared temperature sensor for temperature, and manual counting for RR. Statistical analysis, including mean average percent error and Bland-Altman analysis, confirmed accuracy and reliability. No systematic bias was detected for HR, SpO2, and RR, but a temperature discrepancy prompted algorithmic modification, ensuring confidence in WOVEN's performance for vital sign monitoring.

4.c) Results: WOVEN's sensor data were all within a 10% deviation from standard care devices, indicating a high level of accuracy. Temperature measurements displayed a systematic bias attributed to sensor circuitry heat, necessitating algorithmic adjustments for accurate readings.

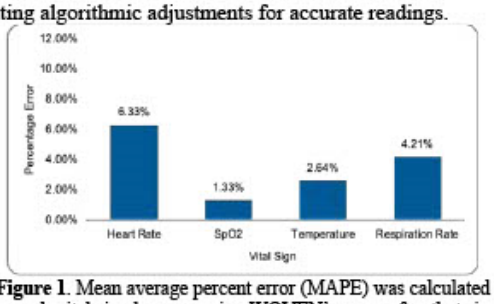

Figure 1. Mean average percent error (MAPE) was calculated for each vital sign by comparing WOVEN's sensor for that sign against its hospital standard of care [12].

5) Conclusion

5.a) Summary: WOVEN has successfully met many of its design requirements, particularly in vital sign monitoring accuracy. Despite challenges with temperature measurements, corrections are underway, illustrating the project's adaptability and commitment to improvement.

5.b) Revisions: Necessary revisions include refining the temperature sensor's accuracy and enhancing the user interface based on feedback. WOVEN is currently in the process of collecting data and feedback from nurses and parents to identify additional areas for improvement as well as time WOVEN against the standard of care.

5.c) Impact (Future Version): WOVEN will better align with user needs, enhancing its effectiveness in neonatal care. WOVEN's focus on real-world feedback underscores the potential to improve care quality and operational efficiency, benefiting both individual experiences and broader societal outcomes.

References:

1. Pineda R, et al. J Perinatol. 2023;43:796-805.
2. Debelić I, et al. Int J Environ Res Public Health. 2022;19(18):11450.
3. Bonner O, et al. BMJ Innov. 2017;3(1):12-18.
4. Janiszewski Goodin H, et al. J Pediatr Nurs. 2012;27(6):725-733.
5. Xu S. MIT Solve. 2021.
6. Sibel Health, Inc. Clinical Care. 2023.
7. Boundy EO, et al. Pediatrics. 2016;137(1).
8. Malhi S. Washington Post. 2023, June 7.
9. Saltzmann AM, et al. Adv Neonatal Care. 2021;22(3):261–269.
10. Logan G, et al. Pediatr Crit Care Med. 2020;21(11):941–948.
11. Nelson BW, Allen NB. JMIR Mhealth Uhealth. 2019;7(3):e10828.

PadIAD Incontinence Intervention

Integrated Detection and Alerting Wet pad for Incontinence Associated Dermatitis Intervention

Malik Thomas, Nick Taylor, Gian Cuchapin, Ana Utrilla Benito, Jules Ciniello, Daniel Bardin.
Duquesne University of the Holy Spirit.

1) User Need:

1.a) Use Case

IAD (Incontinence Associated Dermatitis) is a form of dermatitis caused by irritants that develop from chronic exposure to urine or liquid feces that affects an estimated 13 million Americans annually. In a clinical setting, IAD can, depending on the severity of incontinence, lead to immediately life-threatening conditions or even death. Health care professionals (HCP) must identify when patients soil wet pads and change pads on a consistent basis to avoid over-exposure to moisture. They must also make effective use of time and not be hindered by having to check pads consistently. Bed-ridden patients, generally 65 and older, must have their incontinence absorbed to lessen infection risk and be able to feel that their incontinence will be monitored and taken care of in a timely manner.

1.b) Problem Impact

Absorbency pads are the ideal intervention in preventing IAD because they promote airflow and do not alter the feel of the hospital bed [1]. While these pads help prevent IAD, they rely on timely changes by healthcare providers (HCPs) who lack effective detection methods. Many patients sit on soiled pads for prolonged time periods because they cannot identify that their pad is soiled. This presents HCP with a dilemma: squander time checking pads too frequently or check pads seldom and risk development of infection. Other interventions utilize sensors built into hospital bed padding; these beds require staff training and do not automate the incontinence care process, making them too expensive for hospitals to utilize on a large scale.

1.c) Scope (Objective)

Our device will enable HCP to identify soiled wet pads in an efficient and straightforward way before over-exposure to urine and feces.

2) Design Inputs

2.a) Constraints:

The strictest constraints, stemming from our user needs, are the size of a standard hospital bed (36"-by-80"), minimum absorption (250mL), and affordability (less than $15/pad). These factors influenced our decision to base our design off of pre-existing wet pads being they meet these requirements as a standard. Our theoretical device cost influenced the amount of sensors we used in the pads.

2.b) Requirements:

The highest priority requirements are comfortability, proper bed and patient fit, moisture detection and absorption, HCP notification, affordability, and ease of use. These requirements will ensure we meet our user needs as they will offer a well-fitted device that does not inconvenience patients. The device must also alert in such a way that does not contribute to alarm fatigue.

3) Solution

3.a) Design - Intended Use:

The device will consist of hydrosensors enveloped in a standard wet pad [Fig. 1] and an alerting LED device that attaches to the bed. The sensors will turn the LED orange and activate a timer countdown when they detect moisture amounts that meet the activation threshold. Skin breakdown occurs in as little as 2 hours; this time is decreased significantly when skin is in contact with urine [2]. Thus, the time will count up from the time of activation to 1.5 hours and turn the LED red to signal overexposure. The core of the device will emit data wirelessly to wristbands to alert nurses at time of overexposure via vibration or be integrated with hospital alerting infrastructure to relay the alert.

3.b) Build – DEMO

The device and its components can be seen in Figure1.

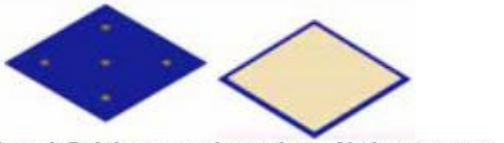

Figure 1: Pad, deconstructed as two layers (black squares represent hydrosensors, white part is absorbent layer).

4) Verification Results

4.a) Introduction

Requirements included in testing will be bed fit, absorption, detection, and alertion. The pad must fit onto a standard hospital bed, absorb 250ml, trigger threshold ranges, properly light LEDs and relay incontinence info to a display.

4.b) Methods

Material dimensional analysis, absorption in mL, time to orange LED activation, and time to red LED activation will be measured. We will also measure the moisture signaling threshold.

4.c) Results

Our verification procedures will ensure that our device meets requirements by confirming successful absorption, detection, alertion, and fit. Criteria will be checked off on a performance assessment sheet.

5) Conclusion

5.a) Summary:

The device will conclusively be successful when it passes all verification testing. A comprehensive evaluation of the cost associated with the device will be conducted to ensure it is financially viable.

5.b) Impact:

This device will enable HCP to care for patients with incontinence and reduce incontinence associated diseases substantially, with percentage reduction increasing exponentially with use rate increases.

References:

1. Banharak S. et al. 14,2983-3004.
2. Shaked E, Gefen A. 1:9.

Acknowledgements: This work relied on Duquesne University's Biomedical Engineering department funding. Dr. Leda Kloudas' and Dr. Yvonne Weideman's guideance and design input were critical in assessing user needs and design inputs.

STEVENS
INSTITUTE OF TECHNOLOGY

Optoband: Demonstrating Feasibility of Optomyography for Active Prosthetics

Nicholas Volpe, Luis Paulino, Oluwaseun Abiona, Jongsang Son
New Jersey Institute of Technology

1) User Need:

1.a) Use Case

The assumed user has had a limb amputation and needs an active prosthetic to perform the daily functions and needs. The user is assumed to be in middle class or lower, and does not have access to high end medical treatment.

1.b) Problem Impact

Current solutions for muscular sensing in active prosthetics (e.g., EMG and MMG) have proven to be expensive and unreliable for daily use. According to the World Health Organization, 9 out of 10 people who need active prosthetics do not have access due to the technology being too expensive [1]. In addition to cost, current technologies are prone to interference; in particular, EMG is sensitive to hair, sweat, and electromagnetic interference, while MMG is sensitive to vibrations that are not caused by the muscle responsible for the movement.

1.c) Scope (Objective)

Our solution must address the cost and noise issue with current technologies. The sensor array must be low cost enough to be accessible to a far larger crowd and should be easier to equip than current solutions while providing comparable functionality.

2) Design Inputs

2.a) Constraints:

The main constraint was cost, which needed to be as low as possible, effectively placing a limit on the cost of materials. Also, limited amount of data lowered the complexity of hand gestures that could be trained into the network, while also decreasing the accuracy of simpler ones.

2.b) Requirements:

Since the solution needs to be worn while in use, the weight should be as low as possible. The power consumption had to be reasonably low to allow for portable implementations of the solution which would require an embedded battery.

3) Solution

3.a) Design - Intended Use:

The solution is designed to be worn like an armband around the forearm area. Therefore, the optical sensors needed to collect data were placed around a circumference, connected by an elastic material that allows expansion to fit slightly larger forearm sizes.

3.b) Build - DEMO

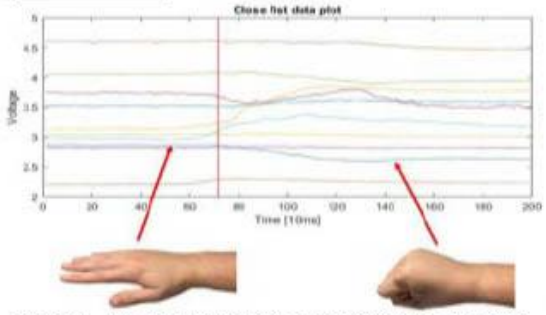

Figure 1. A representative data collected during close fist.

4) Verification Results

4.a) Introduction:

To verify our results, our solution needed to be tested by collecting data on hand gestures and analyzing them in real time to check the reliability and accuracy of the solution. Therefore, testing methods were developed for this purpose.

4.b) Methods:

Hand gesture data was collected using optical sensors, which was then used to train a bidirectional long short-term memory (Bi-LSTM)-based network for hand gesture recognition. A graphical user interface application was developed to predict hand gestures from the trained model and incoming new optical sensor data.

4.c) Results:

After testing was completed, we verified that it is promising to recognize hand gestures based on optomyography, while being cheaper than alternatives. Our prototype had a total cost of around $43 (US dollars).

Figure 2. An example of using Optoband and graphical user interface application developed for hand gesture recognition.

5) Conclusion

5.a) Summary:

The prototype was able to reliably recognize some gestures, although not very complex ones, while being a fraction of the cost of the average EMG or MMG device. Therefore, we believe the design was successful to demonstrate the feasibility.

5.b) Revisions:

With an approved IRB request, the number of test subjects can be expanded, and a more reliable model can be trained. Furthermore, our BiLSTM-based model only works for specific hand gestures. Pivoting to a sequence-to-sequence model, along with developing a proper dataset collecting environment, will allow for the next generation of this method to fully go under way. Implementing the model weights into a phone app would enable the sensor array to be fully portable, assuming the user has a smart phone.

5.c) Impact (Future Version):

Revising the solution with the suggested improvements will help it provide more accurate prediction of hand movements for the user, while also making the solution more convenient and easier to use.

References:

1. WHO standards for prosthetics and orthotics. Geneva: World Health Organization; 2017. License: CC BY-NC-SA 3.0 IGO
2. H. H. Muhammed. R. Jammalamadaka. IBIOMED. 2016;6(26):972-1018

STEVENS
INSTITUTE OF TECHNOLOGY

Portable Impedance Breast Imaging Device (P.I.B.I.)

Carly Ward, Elizabeth Su, Isabelle Lewis, Mia-Marie Fields
Syracuse University, College of Engineering and Computer Science

1) User Need:

1.a) Use Case

The target demographic of P.I.B.I. are those at high risk of developing breast cancer in resource-limited areas, where 60% of deaths [are] due to breast cancer. The aim of P.I.B.I. is to encourage early detection and treatment of breast cancer. Users would wear the device over one breast and follow color-coded instructions to differentiate between tissue densities.

1.b) Problem Impact

Portable breast cancer detection devices face challenges such as high costs, power supply issues, and the need for specialized training, making them less viable in resource-limited settings. P.I.B.I. is a cost-effective, user-friendly breast cancer screening that operates without steady power, promising reliable use in under-resourced areas.

1.c) Scope (Objective)

P.I.B.I addresses the lack of medical training and resource limitations by utilizing Electrical Impedance Tomography (EIT), which illustrates signal results in distinct color codes. The device will be powered by batteries and include lightweight, cost-effective, and stretchable fabric that will fit all breast sizes. The easy-to-use color codes of EIT have high specificity, reducing the likelihood of false positives, as EIT signals can process the different resistances of fat and fibroglandular tissue.

2) Design Inputs

2.a) Constraints:

The impedance detection system must frame the breast and the body for accurate reading. It must be one size fits all and the user instructions need to be understandable universally for more accessibility. Additionally, the meticulous orientation of the electrodes is crucial to allow the electrical signal to pass through the breast tissue. We selected specific electrodes and orientations to improve clarity.

2.b) Requirements:

The wearable vest includes the surface electrode breast lining, a handheld Arduino portable EIT device, a battery powered energy source, and instructions section. Users will put on the wrap and adjust to cover the breast surface area. Once powered on, the device generates an impedance map showing the breast density based on a specific threshold.

3) Solution

3.a) Design - Intended Use:

P.I.B.I. is designed to be a wearable wrap consisting of 16 electrodes in a multi-ring pattern that interface with the breast. This is connected to an Arduino microprocessor to calculate impedance. One electrode inputs a known voltage and current of 1mA and 5V. The remaining 15 electrodes then record the resulting voltage in different areas on the breast. Using the recorded voltage and known current, the impedance can be calculated in each section of the breast. This impedance data is then used to determine the density of the breast, and create an impedance map visualizing the density in the breast.

4) Verification Results

4.a) Introduction

By using an agar and fat model, certain sections of the artificial breast can be given different concentrations of denser materials, increasing its impedance. The anticipated results will show the compositions in different areas of the breast, with examples shown below illustrating how a tumor, circled in red, can hide beneath dense tissues. The impedance map will show the areas of the artificial breast that have a different compostition than the rest of the breast to correlate BI-RADS scale for tissue density, successfully illustrating a higher risk of developing breast cancer.

Breasts that are (A) fatty or (B) scattered, are "not dense" breasts. Breasts that are (C) heterogeneously dense or (D) extremely dense, are "dense" breasts.

4.b) Initial Results:

Our experiments have proved the effectiveness of using EIT technology to determine areas of different density. We could reliably distinguish between a gradient of densities corresponding to the BI-RADS tissue density scale.

5) Conclusion

5.a) Summary:

Our device has been successful in the uniqueness and innovation of the design due to its portability and user friendly features. The impedance results from testing on phantom breasts will provide insight into modifications that need to be made before beta prototyping a design that will be implemented on a human model, but it is limited by the variations from phantoms to living tissues.

5.b) Revisions:

As the work progresses, revisions in inputs and solutions will be made in order to create an accessible and working device. The product must include inclusive directions that will be made in accordance with all possible regions of impact. Testing procedures will be altered as the phantom model progresses to more complex materials and eventually human breast tissue.

5.c) Impact (Future Version):

The users of P.I.B.I. will be able operate the medical device on their own, with whatever level of privacy and discretion they desire. It will impact those at risk of developing breast cancer who also have limited access to medical care and face gender based discrimination. This product can help to reduce the stigma surrounding breast cancer and eventually lead to a decrease in late stage diagnoses and mortality rates in resource limited regions.

References:

1. M. T. Islam. et al. Sci Rep. 2019;9(1):15491-15504.
2. DenseBreast-info. DenseBreast-info, Inc..2024;1
3. M. T. Islam. et al. IEEE Access. 2018;6:78587-78597
4. M. J. Yaffe. Breast Cancer Res. 2008;10(3):209-219

Acknowledgements: Supported by The SOURCE at Syracuse University, Dr. Douglas Yung and our clients: Jennifer A. Harvey, M.D. and Nebojsa Duric, Ph.D.

Dual Linear-Rail Parallel Suture Sampler

Roberto Duran Brea, Nicholas Wilken, Chris Cybart, Saleem Ibrahim, Robert Gettens
Western New England University

1) User Need:

This project aims to create a programmable and automated process allowing the creation of 100s to 1000s of suture samples reducing the manual cutting strain on engineers or technicians, who would otherwise have to create samples by hand. This automation will assist in accelerating many types of design processes by lowering time commitments of employees and reducing manual labor efforts. [1]

Engineers and technicians in the medical device industry currently create suture samples manually, by pulling suture material from spools and extending until the desired length. This task is carried out hundreds of times for each type of suture product in development. Due to the strenuous and repetitive nature of the process, and time required for sample creation, this limits the ability of engineers and technicians to complete other tasks. In turn, this limits the time for wound management innovation.

2) Design Inputs

The device must adhere to guidelines that meet our user's needs. The device must create suture samples at a rate similar to that of an engineer or technician, must procude sample lengths rangling from 6'' to 36'', and create samples that pass standard USP testing procedures 43-NF38 [4]. These needs are created to free the device user to complete other facets of their employed roles. Companies such as Sonderegger, who makes the Fibapic suture cutting machine [2], and LiveAutomation have individualized dedicated approaches to meet the needs of medical textile manufacturing customers [3].

3) Solution

The design team developed a dual linear-rail parallel sampler. This concept relies on two parallel cutters on respective linear rails. Each gantry is powered by a NEMA 23 stepper motor with a maximum speed of 1500 rpm at 200 steps per revolution. At max speed, the gantry travels at 10 inches per second. A motor slider rides on a guiding rail using the rotation of the ball screw rod, to travel linearly. The motor slider moves over one inch every 2 ½ revolutions based on the threads in the ball screw rod. An electric motor is mounted onto the slider. A motor grip adapter is attached to the servo motor. This grip adapter attaches to the motor through its rotation knob. Each linear rail has 40 inches of travel. The system will be controlled using a microcontroller with a Graphical User Interface (GUI).

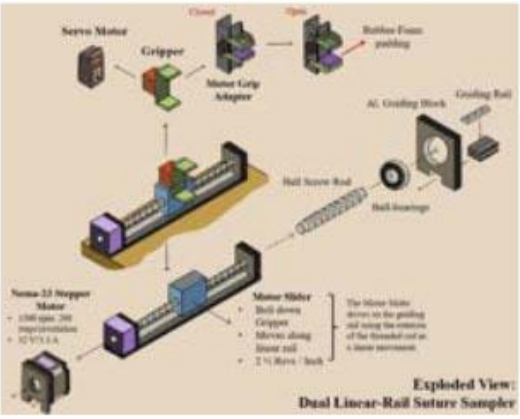

Figure 1. Dual Linear-Rail Parallel Sampler. Two mirrored linear rail gantries each with a gripper to grab sutures and travel left or right. Run by a Nema 23 stepper motor.

4) Verification Results

Testing for this machine will be conducted at a future date. This will include characterizing the distance traveled along a linear rail due to step count of a NEMA 23 stepper motor. The speed of the motor will also be characterized in terms of revolutions per minute (RPM). Seprately, the gripping system must be able to grab and cut suture samples. This requires finding the proper durometer for the gripping system to have proper strength without deforming material.

Respectively for characterizing distance and speed, this will involve digital measurement of distance via a controller module along with hand-made measurements with a distance measuring tool. These will be made running between multiple cutting distances to look for accuracy and precision of steps along the linear-rail.

5) Conclusion

The Dual Linear-Rail Parallel Suture Sampler will allow wound management engineers to produce necessary suture samples for product investigation using complex Design Of Experiment (DOE) techniques. The final design will be thoroughly verified to ensure compliance of the device with standard testing protocols.

References:

1. "The rise of automation in manufacturing," Plex, by Rockwell Automation, https://www.plex.com/platform/manufacturing-automation/rise-automation-manufacturing (accessed Dec. 10, 2023).
2. S. E. AG, "Suture cutting machine: Fibapic," heat tipping and suture cutting machines, https://www.suturecutter.com/ (accessed Dec. 10, 2023).
3. "Custom Automation Systems, equipment, machines: Live automation ma," Live Automation, https://liveautomation.com/products-services/custom-automation-equipment/ (accessed Dec. 10, 2023).
4. "Surgical Sutures-Performance Criteria for Safety and Performance Based Pathway," USP 43-NF38, United States Pharmacopeia, Washington, D.C., USA, Nov. 1, 2019.

FlexFlow™ NOVEL 3 WAY STOPCOCK DESIGN

Andrew Willwerth, Katherine Sheire, Emma Hagenaars, Amy Vu, Valentina Grether, Sree C. G. Venkata, Mridvika Shah.
Brown University School of Engineering

1) User Need

Use Case: Supraventricular tachycardia (SVT) is characterized by irregularly fast or erratic heart beats. Extreme SVT episodes require treatment by medical professionals, accounting for about 50,000 emergency department (ED) visits annually. Additionally, about 25% of SVT ED visits will lead to long-term hospitalization [1]. The primary treatment for SVT is adenosine, which causes temporary and complete AV node blockade. The standard practice of adenosine administration is pushing the drug bolus through an IV line followed by a saline flush, using two syringes connected by a 3-way stopcock.

Problem Impact: Current stopcock designs are primarily limited by counterintuitive labeling. Specifically, the central control valve design highlights the "OFF" switch, focusing the process of opening a given pathway around the closure of another ("To open Path A, I must close Path B"). This is unclear and increases cognitive load in a high stress environment, thus increasing administration error rate. Moreover, the design is limited in both control and accuracy. A lack of indicators or haptic feedback to inform the user when the openings are properly aligned leads to impaired fluid flow in some cases.

Scope: Our solution will address the labeling, usability, and error rate associated with the current standard of care. Our design increase usability by changing key features, shape, and markings. This will make it an easy to use product with low error rate.

2) Design Inputs

There are multiple constraints to the design. Currently available stopcocks are inexpensive and used for a range of applications. Our design must be simple and cheap to manufacture to compete with industry standards. Due to sterility concerns, the device should be single-use. Lastly, the device should be compatible with standard IV equipment, adhering to ISO standard 80369-7:2021 and integrating with existing equipment without additional adapters. There are multiple quantitative requirements defining a successful device. Assembly of the setup must be possible within 17 seconds. The process should be intuitive to providers (<10% error). Drug delivery from syringe to port should be accomplished within 15 seconds to compete with current standards. Finally, the device must be manufactured at less than $1.11 per stopcock.

3) Solution

The pivoting IV line nozzle is the major design element that creates a clear visual and tactile confirmation to healthcare providers. When turned, the FlexFlow creates a 180-degree angle (shown in Figures 1 & 2) to quickly confirm which line is open, reinforced by a large arrow to show direction. The pivoting IV line also has a hard stop when fluid lines are open, ensuring precise alignment. The FlexFlow can be adopted without workflow disruption in hospital and clinic operations due to its low manufacturing cost and compatibility with existing medical tools (i.e. IV lines and syringes).

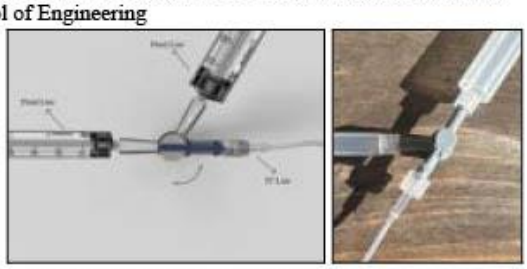

Fig. 1 & 2: FlexFlow rendering and prototype setups

4) Verification Results

Our testing will evaluate the previously listed design criteria including both assembly and drug delivery times, overall drug administration error rate, and first time use error rate. We will test the design with licensed emergency room nurses to evaluate effectiveness across the primary provider profile. During testing we will also collect user feedback to further optimize usability.

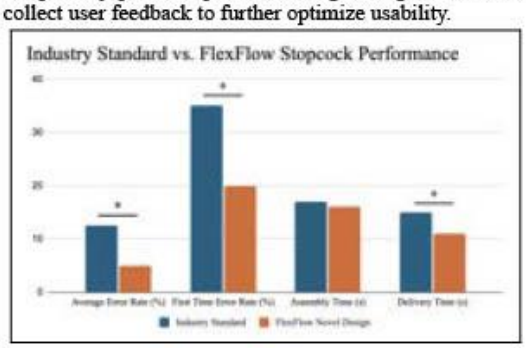

Fig. 3: Standard vs. FlexFlow Performance (Theoretical)

5) Conclusion

The FlexFlow stopcock will be successful if and when the device meets requirements without violating constraints. Thus, the design will have rapid assembly and delivery, a low error rate, and a low cost while being easy to manufacture, single-use and disposable, and standard IV compatible. The FlexFlow will meet stakeholder needs of patients, providers, hospitals, and payers. Future design revisions include adding haptic feedback upon precise alignment and adding ISO-compliant Leur ports. Extensive testing with ER nurses will provide useful input on FlexFlow usability and performance, informing future revisions and ensuring FlexFlow effectively serves user needs. FlexFlow reduces error rates and ensures rapid drug delivery. An arrow clearly indicates the open path and a haptic cue confirms precise alignment, overcoming potential impaired fluid flow. The novel FlexFlow will increase usability and decrease error rate of commonly used stopcocks, thus improving the outcomes for countless affected patients and providers.

References:

1. Khurshid S. Circ Arrhythm Electrophys. 2018;11(7)

Acknowledgements: Dr. John Triedman, Dr. Elizabeth Blume, Dr. Anubhav Tripathi, Dr. Marissa Gray

ParkinPlay: Affordable and Accessible Monitoring of Parkinson's Symptoms Outside of the Clinic

Keondre Herbert[1,*], Kiana Mohammadian[1,*], Kosisochukwu Ugorji[1,*], Aunika Zheng[1,*]
[1]Columbia University in the City of New York, Department of Biomedical Engineering, [*]authors contributed equally

1) User Need

The current gold standard for monitoring symptoms of Parkinson's disease (PD) is the MDS-UPDRS test [1]. This test, limited by the subjectivity of the physician and administered only 2-3 times a year, offers a costly and time-consuming snapshot of a disease that fluctuates daily. ParkinPlay satisfies the need for a more objective and comprehensive method of frequent monitoring of PD symptoms outside of the clinic. Our users include early-to middle-stage PD patients receiving treatment and their caregivers. We target patients seeking daily monitoring of their symptoms and lifestyle. We also serve patients whose doctors request more frequent symptom reports to assess treatment efficacy and track progression into the later stages of PD. ParkinPlay surpasses existing solutions for monitoring PD by providing tracking of both motor (e.g., gait and tremor) and non-motor (e.g., mood and sleep) symptoms and lessening the burden on caregivers.

2) Design Inputs

PD primarily affects an elderly demographic, often impairing fine motor control and overall mobility. To respect the physical limitations of our users, our wearable solution is designed to be easy to put on. Additionally, we prioritize an unobtrusive design for user comfort; the device's size is restricted so it can easily be hidden under clothes. To avoid the hassle of frequent charging and ensure uninterrupted monitoring, a long battery life is a key requirement. Considering the technological challenges an elderly population may face, our application is user-friendly with simplified features and navigation.

3) Solution Design: Intended Use and Build

ParkinPlay consists of a mobile application and a wearable sensor **(Figure 1)**. The MPU6050 inertial measurement unit (IMU) sensor, connected to an Arduino Nano, is attached above the ankle via a velcro band to measure gait instability, quantified from angular velocities. Users complete activities and track their symptoms in the app. Activities include a finger-tapping game measuring bradykinesia (slowness of movement), a spiral-drawing task measuring tremor, and patient questionnaires for non-motor symptoms. Patients can also log medication times, deep brain stimulation adjustments, diet, and other lifestyle changes. Users can easily view and share summaries of symptom changes with their physicians. Results can guide adjustments in treatment and enhance understanding of how lifestyle changes improve symptom progression.

4) Verification Results

4.a) Introduction (1 and 2)

Since we did not have access to PD data, we performed a **(1)** simulated gait instability analysis to identify whether the built-in sensor and application could distinguish between different motion perturbations and **(2)** a test of spiral tracing accuracy using an iPad.

4.b) Methods (1 and 2)

(1) Swing time and cadence were measured using 3 conditions: normal, post-spinning dizziness, and blindfolded dizziness in 3 subjects walking straight for 10 seconds. **(2)** 13 participants traced a square Archimedean spiral with either hand [2]. Accuracy was quantified with a k-nearest neighbor algorithm in MATLAB.

Figure 1. a. Application layout for symptom tracking and monitoring. **b.** Ankle sensor for measuring gait instability.

4.c) Results (1 and 2)

(1) Experimental normal gait was similar to published gait cycle data in angular displacement. Blindfolded dizzy cadence was significantly higher than normal literature values (179 vs 100 steps/min, $p<0.05$), as confirmed by one-way ANOVA and post-hoc Holm-Sidak t-tests [3]. **(2)** Distance measurements between drawn and template spirals were significantly higher for non-dominant versus dominant hands via a paired t-test ($p<0.05$).

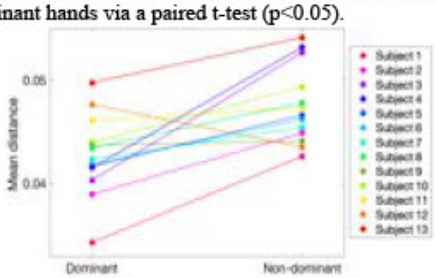

Figure 2. A difference was observed in the mean distance between the square spiral template and the drawings using dominant vs. non-dominant hands ($p<0.05$).

5) Conclusion

Both the gait sensor and spiral analysis were effective in detecting differences between normal and abnormal movement patterns. As these simulation methods are not representative of actual PD symptoms, we plan to validate our results with PD patient data. Besides spiral analysis, we will include additional activity monitoring tasks and logging features in our app. With these improvements, our solution will help PD patients and their physicians manage the condition more autonomously and effectively.

References: [1] Sotirakis[+] (2023). *NPJ Parkinson's Dis.* [2] Galli[+] (2014). *J Appl Biomater Funct Mater.* [3] Gujarati[+] (2019). *ICCCNT.*

Acknowledgements: We thank Columbia University Biomedical Engineering for their guidance and support.

STEVENS
INSTITUTE OF TECHNOLOGY

AirEase BiPAP Mask

Grace Palahnuk, Mario Rezkalla, Nathaniel Safar, Steve Vazquez, Dr. Xuefeng Wei
Department of Biomedical Engineering, The College of New Jersey, Ewing, NJ

1) Introduction:

1.a) Use Case:

Non-invasive ventilation masks are used across a variety of applications to deliver pressurized air to the upper airways as an alternative to tracheal intubation. Bilevel positive airway pressure (BiPAP) machines switch between an inhalation pressure and a lower exhalation pressure to ensure proper ventilation for patients in acute and chronic respiratory failures.[1,2]

1.b) Problem Impact:

Consistent use of current masks for prolonged therapies can result in pressure ulceration on the facial skin and may lead to sinus cavity complications. To mitigate the risk of pressure ulcerations for patients who require mask use for 6-8 hours, a new active BiPAP mask is designed to redistribute pressure when certain thresholds are exceeded during use. This new design will address the pressure related injuries caused by long term use of oronasal masks and improve the quality of noninvasive ventilation treatments for patients in home and hospital settings.

1.c) Scope:

The design solution must address pressure ulceration that may occur during long term therapy uses while not interfering with current ventilation processes. The limitations addressed are understanding how pressure is distributed on the face when the mask is secured to a patient.

2) Design Inputs

2.a) Constraints:

The usage and functionality of the device must follow the medical device standard ISO 13485. This device must follow electrical safety standards outlined in IEC 60601-1-12 and adhere to the disinfection standard ISO 17664-1. The device must be built and verified within a budget of $500. The device must be compatible with standard size conventions of oronasal masks currently on the market (small, medium, large).

2.b) Requirements:

The device must be able to measure the pressure applied by the mask onto the nose bridge, cheeks, and chin within a range of 10-100 mmHg.[3] Active adjustments of the mask must be made when pressure exceeds 30 ± 0.5 mmHg for longer than 1 hour to reduce application pressure to 25 ± 0.5 mmHg.[4] With this integrated adjustment technology, the device must allow for normal airflow functionality via a proper seal of the noninvasive ventilation mask. The noise generated by the device must be dampened to not awaken a patient during sleep.

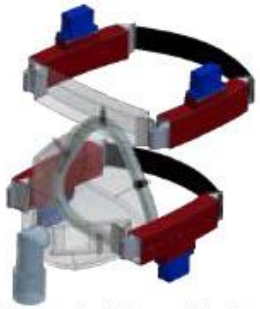

Figure 1: CAD model of actively adjusting mask

3) Solution

3.a) Design:

The AirEase BiPAP Mask will utilize 4 force-sensitive resistors placed directly onto the mask in contact with the skin to measure pressure. Four 9 gram continuous servo motors, integrated into the straps of the mask, are implemented to actively adjust on the patient's face when a pressure of 30 ± 0.5 mmHg is detected at the four desired locations.

3.b) Build:

The device has not been fully built at this time.

4) Verification Results

4.a) Introduction:

Requirements related to active adjustment and pressure sensing capabilities will be verified through testing of the mask under known conditions.

4.b) Methods:

Using a mechanical testing frame, pressure will be applied to each location within the mask to ensure measurement of pressure between 10 to 100 mmHg within 95% accuracy. Using a similar methodology, pressure exceeding 30 mmHg will be applied to the sensors for longer than an hour to verify that the strap adjustment is initiated and terminated when pressure is reduced to 25 mmHg. The weight and sound of the device are to be verified by measuring the mass of the finished mask and the decibel level during strap adjustments.

4.c) Results:

The device has not been fully built, and therefore, results have not been generated at this time.

5) Conclusion

5.a) Summary:

The verification testing is limited in only observing the sensor and motor activity under the circumstance of a constant applied pressure over time and will not consider possible fluctuations of pressure during use. Additionally, another limitation is that the device's performance will not be evaluated on the face of a patient at this stage.

5.b) Revisions:

As the device has not been built yet, current revisions are unknown. However, it is anticipated that any such revisions will be geared towards reducing pressure ulceration via monitoring the applied pressure and allowing for patient comfort through the design.

5.c) Impact:

The device is aimed to reduce the amount of pressure related injuries caused by noninvasive ventilation masks specifically when used for long term purposes. This promotes patient safety and comfort in using these masks.

References:

1. Mansukani MP. Exp Rev Med Dev. 2014;11:283-294.
2. Worsley PR. Med Dev. 2016;9:409-417.
3. Brill AK. ERJ Open Research. 2018;4:2012-2017.
4. Agrawal K. Indian J Plast Surg. 2012;45:244-54.

STEVENS
INSTITUTE OF TECHNOLOGY

Skin Tone Sensitive Pulse Oximeter

James Dolan, Victor Guzman, Chase Miller, Juwon Park, Dr. Xuefeng Wei.
Department of Biomedical Engineering, The College of New Jersey.

1) User Need:

1.a) Use Case

This device is designed to accurately measure blood oxygen saturation for patients of various skin tones. To do this, patients will follow prompts given by the device in order to have their skin tones recognized and then their blood oxygen saturation levels determined while incorporating their skin tones.

1.b) Problem Impact

Due to the use of light waves penetrating the skin, a patient's skin tone will have an impact on how much light can pass through the skin. Current pulse oximeters are designed based on a patient with pale skin and how easily his/her skin allows light to pass through. Because of this, patients with darker skin tones continuously receive up to 4% higher SpO_2 readings[1].

1.c) Scope (Objective)

This device is a way to address variance in blood oxygen saturation readings through photoplethysmography pulse oximetry caused by varying skin tones.

2) Design Inputs

2.a) Constraints:

One of the main constraints of the device was distinguishing the range of skin tones that the device was required to detect. This was to make sure that all of the skin tones are correctly accounted for in the process of measurement calibration. This limited the design choice, because the device required a subjective standard of skin tone ranges. This eliminated the option to allow the users to distinguish the skin tones, as the subjectivity may be affected in this design choice.

2.b) Requirements:

The device must be able to measure the light energy ratio from the patient, distinguish between different skin tones, and incorporate skin tone into blood oxygen saturation level calculation.

3) Solution

3.a) Design - Intended Use:

The device utilizes the SparkFun Triad Spectroscopy Sensor on the finger in order to quantify the patient's skin tone. From here, the patient places the finger on the photodiode sensor, a SparkFun Pulse Oximeter and Heart Rate Sensor. Information from both sensors is then sent to an Arduino Nano RP2040 in order to calculate blood oxygen saturation based on data collected from both sensors.

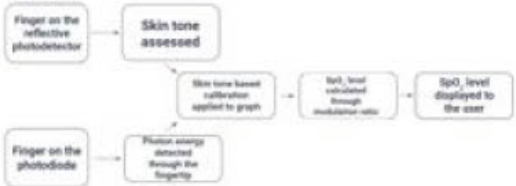

Figure 1. Workflow illustration demonstrating device function.

3.b) Build - DEMO

The device is not fully built at this time.

4) Verification Results

4.a) Introduction

The test results would verify that the device must be able to measure the light energy ratio from the patient, distinguish between different skin tones, and incorporate skin tone into blood oxygen saturation level calculation.

4.b) Methods

Diffraction grating will be used to verify that the red light is 685±65 nm. Infrared light will not be able to be verified due to budget constraints therefore the manufacturer specification sheet describing the light as 890±110 nm will be trusted[2]. Paint samples with given RGB values will be used to verify that the spectral sensor has been calibrated to measure color correctly. Baseline SpO_2 levels for a pale-skinned subject will be recorded. To artificially adjust SpO_2 levels, the subject will hold breath for 60 seconds. Model skin layers of varying skin tones will be placed above the subject. Recordings will then be taken for each model's skin tone.

4.c) Results

Data has not been collected yet.

5) Conclusion

5.a) Summary:

It is premature to conclude the success of the design as it has not gone through full development as well as testing.

5.b) Revisions:

In the future, different sensors could be tested and compared to find a potential alternative to the current design solution. Furthermore, the number of skin tone groups could be increased to allow for increased accuracy.

5.c) Impact (Future Version):

If these revisions were to be implemented, the accuracy of the pulse oximeter would increase. This would allow for an easier diagnosis of pathological conditions by the users, regardless of their skin tone.

References:

1. Cabanas, Ana M et al. Sensors. 2022;22(9):3402.
2. Edward D. Chan, et al. Respiratory Medicine. 2013;107(6):789-99.

Acknowledgements: Thank you to The College of New Jersey's Engineering Department for funding this project and the professors for their continued support.

STEVENS
INSTITUTE OF TECHNOLOGY

The Lip and Palate Prosthetic Interface

Serena Carson, Ryan Lim, Ravikiran Ramjee, Andrea Urdaneta, Camilla Whitesel
University of Pennsylvania

1) User Need:

One in 1,600 infants are born with cleft lip and/or palate (CLP) annually in the U.S. CLP occurs when orofacial tissue improperly fuses together during gestation, resulting in openings/clefts.[1] Infants with CLP are unable to create a seal, resulting in improper feeding and poor weight gain.

A concern of CLP in infants is feeding, with CLP infants often unable to breastfeed or traditionally bottle feed.[2] CLP infants are unable to create the pressure necessary for breastfeeding (4 psi) and cannot create a true seal around the tip of a bottle. CLP causes nasal regurgitation and swallowing of air during feeding, reducing weight gain compared to non-CLP infants. To treat CLP, reconstructive surgeries can be performed once infants meet certain biomarker thresholds, including age and weight. However, CLP infants are consistently below the 50th percentile for weight up to 5 months of age, which can delay surgery.[3]

Current solutions seek to improve feeding for CLP infants but are inconsistent and ineffective. LAPPI is a set of two products to occlude clefts and help create suction allowing CLP infants to bottle-feed or breastfeed.

2) Design Inputs

The lip and palate covers are not designed for specific cleft openings or manifestations but can be adjusted in size to fit most presentations of CLP in infants. LAPPI's palate cover design intentionally covers a large portion of the palate to account for most defects. This design choice reflects LAPPI's goal of accessibility where caregivers can use it for most infants within a certain size range.

LAPPI for bottles includes a one-way valve to reduce backflow while LAPPI for breastfeeding has an open bottom to allow mandible movement. LAPPI's material will be food-grade silicone allowing for sterilization.

3) Solution

LAPPI for bottle-feeding includes a one-way valve reducing backflow while LAPPI for breastfeeding has an open bottom to allow unrestricted mandible movement.

Figure 1: (A) LAPPI for bottle (B) LAPPI for breastfeeding

Figure 2: LAPPI interfacing with breastshield on model

4) Verification Results (n=5, error bars st. dev)

To test LAPPI for bottle-feeding, an air compressor was used to create pressure in a standard baby bottle to indirectly create the pressure difference in the oral phase of feeding. To test LAPPI's efficacy with breastfeeding, a testing setup with a breast model and a syringe pump was made to replicate the pulsatile movement of milk through the breast duct.

The CLP model had two pathways for fluid travel: one representing retained liquid through the esophagus and another representing fluid lost to regurgitation/leakage.

Trials using LAPPI had significantly higher fluid retention, demonstrating the devices' efficacy in occluding the CLP.

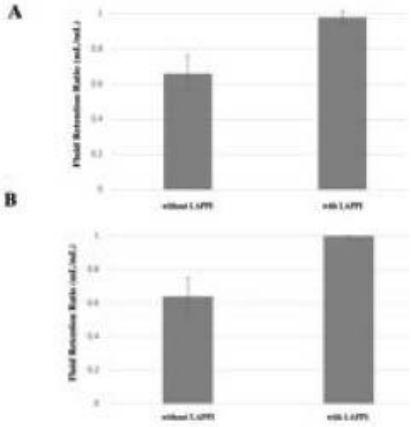

Figure 3. (A) LAPPI for bottle-feeding fluid retention (B) LAPPI for breastfeeding fluid retention

5) Conclusion

Preliminary testing of the LAPPI MVP demonstrated an increase in fluid retention by over 35%. The LAPPI solution will relieve caregivers of the burden of implementing specific CLP feeding techniques as well as increasing feeding efficiency. This will enable reconstructive surgery with minimal delay, alleviating CLP for infants.

The lip cover on LAPPI for breastfeeding will be adjusted to allow more mandible movement and the product will be made out of food-grade silicone.

LAPPI can be evaluated with a pressure regulator added to ensure constant, consistent pressure difference simulating that in oral feeding. These evaluations can be done on LAPPI's final product with the one-way valve and FDA approved materials.

References:

1. Kosowski,, T. R., et al. Seminars in Plastic Surgery. 2012;26(4):124-169.
2. Bessell, A. Cochrane Library. 2011;2.
3. Da Silva Freitas, Renato, et al. Plastic Surgery International. 2012;1-4.

Acknowledgements: We thank the University of Pennsylvania Education Commons for providing the CLP infant head model and 3D printing services. We thank the Children's Hospital of Philadelphia (CHOP) for providing pacifiers and as a source for CLP clinicians and caregivers.

Sustainable Prosthetic Socket Design

Connor Fallon, Julia Lescarbeau, Brendon Mersincavage, Andrea Kwaczala
Western New England University

1) User Need:

1.a) Use Case: People with limb differences need a rapid process to create prosthetic sockets as the traditional method takes weeks for device delivery and typically requires several fitting appointments to ensure a proper fit and alignment. Amputation due to war-related injuries is a growing problem worldwide with over 50,000 amputees since the start of the Ukraine-Russia war. Many of these new amputees are still waiting for prosthetic care since medical facilities have been destroyed and therei s a shortage of certified prosthetists. We have developed a sustainable method to produce prosthetic sockets onsite without the need for a manufacturing facility. Users of this product are transtibial amputees in developing and redeveloping countries like Ukraine who do not have access to state of the art prosthetic facilities and clinical care. The users need a sustainable and affordable process to make custom-fit prosthetic sockets on site without manufacturing equipment.

1.b) Problem Impact: Current manufacturing processes involve several different methods that make it challenging for developing and redeveloping countries to implement: outsourced manufacturing, expensive equipment, and multiple fitting appointments, etc. However, within these countries only 5-15% of people in need of prosthetic care have access to devices due to lack of onsite prosthetists, reduced material availability and high costs for equipment in facilities [1]. It typically can take between 3 weeks to 3 months from the first clinical appointment to receive a prosthetic device and costs between $3,000-$120,000 which might not be covered by insurance [2].

1.c) Scope (Objective): The proposed solution includes sustainable materials that are locally sourced from targeted developing and redeveloping countries, to avoid shipping and transportation barriers. The process proposed is intuitive and comes with instructions so that it can be constructed onsite by a user or caregiver and still provide a comfortable load-bearing socket.

2) Design Inputs

2.a) Constraints: The design must use sustainable materials that are readily available in developing and redeveloping countries. The design must be manufactured in less than a week for rapid delivery.

2.b) Requirements: The design must be manufactured to be a custom-fit for the user. It must function like current prosthetic sockets: able to be load-bearing and support the weight of a human, be durable to last for at least 5-years, and must attach to standard metal components that connect to the prosthetic leg on the distal end of the device.

3) Solution

3.a) Design - Intended Use: The socket is intended to be used by transtibial amputees while the construction process is intended to be done by anyone using intuitive instructions. The final solution will be made using widely accessible materials to help increase availability of technology and decrease the production and delivery time.

3.b) Build – DEMO:

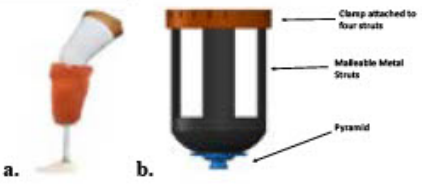

Figure 1. *Prosthetic Socket Designs. A.) Rapid Socket B.) Strut Design. A pyramid located on the bottom for a universal change for various pylons, clamp located at the top to help tighten the socket to the residual limb allowing flexibility to the amputee.*

4) Verification Plans

4.a) Introduction: In order to verify that the prosthetic socket will meet design specifications, Finite Element Analysis and mechanical testing will be performed.

4.b) Methods: The team will use Finite Element Analysis on a SolidWorks model of a prosthetic socket to identify appropriate materials that can sustain loads during use. Material properties of resin-infused materials such as carbon fiber, recycled materials, etc. will identify material properties of the composites. A dynamic Instron test of the prosthetic leg with socket prototypes will be conducted to determine optimal structural design and thickness of the socket. The final socket design must withstand a dynamic load test similar to the support of a 300 pound person.

4.c) Results: Once a prototype has been created that can meet the verification criteria, the rapid process of device construction will be validated using untrained users.

5) Conclusion

5.a) Summary: Over the course of the semester, the team will finalize the socket design, while still following the constraints and requirements, and produce a prosthetic socket that can implemented by a transtibial amputee.

5.b) Revisions: Currently, there are several verification and validation steps that need to be completed. While the design inputs and overall concepts are complete, prototypes need to be produced in triplicates for materials testing and Instron testing and FEA analysis will confirm the design's functionality.

5.c) Impact: Finding a solution to a global health crisis will allow amputees to gain access to proper prosthetic care. If successful, this change in manufacturing practice could revolutionize the way people access care, and make it more accessible to this population of people. It has the potential to improve the quality of life for those with limb differences and give them better mobility that utilizes an affordable service delivery model.

References:

1. Abbady H., Klinkenberg E., Moel L., et al, Prosthetics and orthotics international. February 2022.
2. Zepeda E. Primecare Orthotics & Prosthetics. April 2023.

Acknowledgements: We want to thank Hanger Clinic and Shriner's Childrens Hospital for support on this project.

STEVENS
INSTITUTE OF TECHNOLOGY

Design of Balloon Dilator Pressure Testing Apparatus and Balloon Dilator Machine Testing

Elyse Gathy, Mathew Dougherty, and Andrea Kwaczala[1].
Department of Biomedical Engineering, Westen New England University, Springfield, MA

1) User Need:

1.a) Use Case: Endoscopic balloon dilators serve as an alternative to surgery when there is a stricture in the gastrointestinal (GI) tract. The balloons are used to dilate the closed regions of the digestive tract. The design team's Project Sponsor, Hobbs Medical, manufactures these endoscopic balloons but their process is inefficient, and they need to transition to an automated manufacturing machine. The current process is labor and time intensive. Manufacturing operators at Hobbs Medical need a way to make balloon dilators quickly that still meet FDA standards. Hobbs Medical needs a fast, reliable process to make balloon dilators of consistent size and physical properties.

1.b) Problem Impact: The current balloon manufacturing process at Hobbs requires significant time that is labor intensive with repetitive motions. This can lead to Cumulative Trauma Disorder (CTD) in operators. Furthermore, the lack of automation requires operators to constantly input each setting on the machine which can cause stress and anxiety for the operators and produces human error.

1.c) Scope (Objective): The aim of this project is to configure the optimal operating settings and design a process to manufacture high-quality balloon dilators.

2) Design Inputs:

2.a) Constraints: The balloons must be manufactured by the heat molding machine on site at Hobbs Medical. The balloons must be made from ELVAX 3165, an ethylene vinyl acetate copolymer. All balloon components must maintain pressure when inflated to 35 PSI for 30 seconds. The balloon region must have a length of 8 ± 1.0 cm and expand to 20 ± 1.0 mm, specified on each component's engineering drawing.

2.b) Requirements: To determine the optimal settings (e.g. mold temperature, inflation time, inflation pressure, material stretch distance) required to produce quality balloons, a design of experiments was utilized. The design of experiments helped to isolate the various parameters in the machine's settings that alter performance of the final balloon. When not appropriately defined, poor quality balloons are generated (e.g. reduced soak – heat time creates inconsistent inflation region along the length). For quality testing, a balloon pressure testing apparatus was designed to ensure proper balloon function.

3) Solution:

3.a) Design - Intended Use: The pressure testing apparatus was used to rapidly test dozens of balloons produced by the design of experiments. Additionally, a quality rating system was used to determine the output quality of each balloon manufactured. The final manufacturing recipe along with a Standard Operating Procedure will be delivered to Hobbs Medical at the conclusion of the project.

4) Verification Results:

4.a) Testing and Setup: To determine the optimal settings, Verification & Validation testing was performed. Engineering standard ISO 10555 for inflation and deflation characteristics of balloon catheters. Balloon quality via visual inspection and measurements with vernier calipers will be assessed.

4.b) Methods: The design of experiments will determine the machine settings by statistical analysis of quality for each setting with samples n=5/group. The team will also assess the time it takes to produce the balloons and opportunities to reduce manufacturing time without compromising balloon quality. Quality testing measurements will be taken of the individual balloons when inflated, including length, width, thickness, pressure, and time at pressure. Gage R&R analysis will determine operator and machine error.

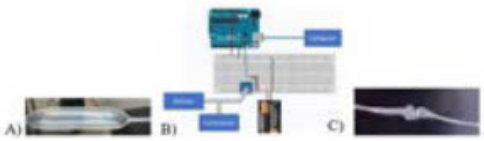

Figure 1. Experimental setup of DOE for Balloon Dilators. A) Example balloon dilator. B) Fritzing diagram of the pressure testing apparatus used to test balloon function. C) Example failed balloon dilator.

4.c) Results: Individual samples of balloons at each setting have been produced, and the team is currently at scale-up to manufacture batches of balloons at varying qualities. All balloons will be visually inspected, and the pressure tested. The conclusions of this design project will provide insight into the optimal operating settings to produce quality balloon dilators.

5) Conclusion:

5.a) Summary: The team is currently collecting samples for the design of experiments and will utilize their own apparatus for pressure testing. In working directly with Quality Engineers, it is possible to create a measurement system to assess the outcome measures of the balloon manufacturing process. This project has allowed the incorporation of design into a real-world manufacturing environment with interaction with operators, quality engineers and designers.

5.b) Revisions: The success of this DOE will result in transition to a new balloon manufacturing process in a medical device company. In order to be adopted, the machine must reduce the number of operator tasks and automate the process to improve the workflow. These are set by the specifications governed by the Trace Matrix which is guiding the overall project.

5.c) Impact: In conclusion, the design of experiments will help bring us closer to creating balloons on the new machine. The testing apparatus will characterize the balloons along with quality inspections. The new machine will provide operators at Hobbs Medical with a simple are reliable process on the new machine that requires less labor.

Acknowledgements: We would like to thank our sponsors at Hobbs Medical for their guidance, with a special thanks to Gio Santucci.

Design and Fabrication of Microfluidic Chip Integration Platform

Emily Kowal, Mica Van Iderstine and Dr. Devina Jaiswal
Biomedical Engineering, Western New England University, Springfield, MA, USA

1) User Need:

By 2032, the global oncology market is expected to surpass $470 billion [1]. The oncology market includes the amount of money spent on development, production and selling of cancer drugs and treatments. A large contributor to the exorbitant market is cellular based cancer research. Traditionally, this research is done in labs using expensive equipment as well as high volumes of chemicals, cells and other necessary biologics [2]. Costly research techniques translate into the price of cancer treatment for the patients. In fact, the average cancer patient and their families are responsible for paying over $2500 out of pocket, after insurance, every month to treat their disease [3]. This number is unattainable for many working-class people, making cancer treatment inaccessible for them.

One possible way of lowering research costs is implementing microfluidic chips into cancer laboratories. Microfluidic chips are miniaturized platforms capable of running cellular experiments at a smaller scale than traditional techniques [4]. With these chips, lower volumes of expensive media, cells and other biologics will be required for experimental procedures. This will decrease the overall cost of research [5]. Unfortunately, microfluidic chips are not widely used in the research setting due to their complicated set-ups and susceptibility to air bubble occlusions.

Cancer researchers need an intuitive, versatile, and reusable microfluidic chip integration platform. This platform will increase the use of microfluidic devices in the research space, hence decreasing the volume of biologics used causing a decrease in the cost of research and ultimately increasing the accessibility of cell-based cancer treatments.

2) Design Inputs

An integration platform was designed using the criteria determined after interviewing researchers from National Institute of Health and performing research on the difficulties associated with the use of microfluidic chips (figure 1). The platform must: (a) be capable of running high throughput cellular experiments, (b) prevent the incorporation of air bubble occlusions into the microfluidic system, (c) fit into an incubator and withstand standard incubator conditions for a prolonged period of time, (d) primarily be made of reusable and sterilizable parts, (e) allow for the user to change the inlet and outlet vials throughout the experiment without having to directly interact with the microfluidic chip, (f) be intuitive for use and easily handled, and (g) be able to fit and work with microfluidic chips of different functions

3) Solution

The early focus of the design ideation was to produce platforms that would allow airtight connections between the microfluidic device and the integration platform. The computer aided design (CAD) prototype of this design can be seen in Fig. 1. Our current concept design is to have a system in which the microfluidic chip is inserted into piece 1, meeting the inlet connection on the side of the chip and locking into place with press-fit O-rings. Piece 2, then slides in after the microfluidic chip and locks the chip into place, with O-rings at each chip output, securing the airtight connections of the chip and the integration platform. This design would then be stacked on top of itself four times, to meet the high throughput demand of our customers.

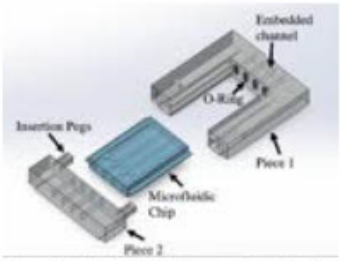

Figure 1: Microfluidic chip holding device:CAD rendering of one level of the integration platform in an exploded view with labels indicitacting cruical components of the platform design.

Figure 2: Early stage physical prototype of microfluidic chip holding device: This prototype was 3D printed and includes a sample resin printed microfluidic chip.

4) Verification Results

To verify the functionality of the device, a test microfluidic chip will be connected to the platform. Cell suspension and media will be fed to the chip through the inlets of the device. The test will be performed for five days and repeated thrice to get robust results. A peristaltic pump will be used to circulate the media to keep the cell healthy during the test. The device will be monitored for air occlusions and sterility throughout the experiment. A successful test would include no air occlusions in the system, healthy cells as well have as no leakage of liquid biologics between the various connection points. A live-dead test will measure cell survivability with device use.

5) Conclusion

In conclusion, a prototype microfluidic platform was successfully designed and fabricated. The design went through two iterations to secure water tight connections. In future, the platform will be comprensively tested for durability and its applicability in a research laboratory. This work has the potential of decreasing the cost of research and thereby reducing the downstream cost of cancer treatment.

6) References

1. Vantage Market Research. 2022
2. Prec. Res. 2023;1467
3. Iragorri N. et al. Current Oncology. 2021
4. Regmi S. et al. MDPI. 2022;12.
5. Nguyen H. et al. MDPI. 2018

STEVENS
INSTITUTE OF TECHNOLOGY

Novel ASO Treatment for Voltage-Gated Sodium Channel Nav 1.5 Metastasis in TNBC

Cassidy Ho, Isabel Hansmann Cañas, Hannah Kang, Harrison Wilson
Tufts University

1) User Need:

1.a) Use Case

Triple Negative Breast Cancer (TNBC) is the most aggressive form of breast cancer, with the worst prognosis and limited treatments. Metastatic TNBC (mTNBC), when tumor cells disseminate throughout the body, occurs in 30% of TNBC patients, decreasing 5-year survival rates from 65% to 11%[1].

1.b) Problem Impact

Established targeted treatments are unavailable for mTNBC patients because they lack human epidermal growth factor receptor 2, and progesterone and estrogen receptors. Median overall survival on chemotherapy is 12-18 months for mTNBC patients and immunotherapy is only available to patients with specific protein expression criteria[2].

1.c) Scope (Objective)

Electrochemical gradients maintained by Na^+ channels are capable of promoting cell invasion, which is critical for metastasis[3,4]. The SCN5A gene, encoding for the Na^+ channel Nav1.5, is alternatively spliced into mutually exclusive isoforms at pre-mRNA exon 5: neonatal (5N) and adult (5A). High 5N in mTNBC tumors is associated with increased invasiveness[5]. This project aims to modulate the alternative splicing of SCN5A to induce exclusive expression of the less invasive 5A isoform.

2) Design Inputs:

2.a) Constraints

Constraints include developing a treatment that targets the specific Nav1.5 channel without affecting similar SCNXA genes. Requirements include increased specific binding affinity, nuclease resistance, and biocompatibility.

2.b) Requirements

During alternative splicing, the design must target exon 5N's splice site to prevent the cell's splicing machinery from binding. This will allow for an exclusion of 5N and an inclusion of 5A expression.

3) Solution:

3.a) Design - Intended Use

Antisense oligonucleotides (ASOs) are short sequences capable of specific binding to target mRNA. When composed of complementary RNA bases to exon 5N, ASOs provide specific binding to block the splicing machinery from binding to 5N **(Figure 1)**. This process excludes exon 5N and includes exon 5A in modified mRNA, resulting in healthy production of Na^+ channels to reduce invasiveness.

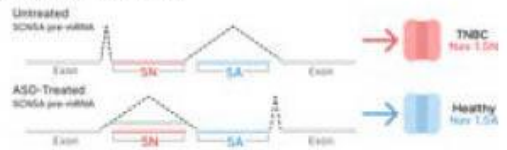

***Figure 1:** Model of ASO interaction with 5N exon and associated splicing pattern.*

3.b) Build - DEMO

ASOs were designed with a backbone and sugar modification to fit the constraints above while inducing the sole expression of 5A. With 5N complementary bases, these may reduce invasion and function as a novel treatment for mTNBC.

4) Verification Results:

4.1) Introduction

Five ASOs were used to treat four TNBC cell lines. Gel electrophoresis after enzyme digestion was used to determine ASO success through an increased 5A/5N ratio.

4.b) Methods

TNBC cell lines (MDA-MB-231, HST579TS, SUM159, and BT-549) were treated with ASOs. After rt-PCR, an mRNA band intensity shift was expected from exon 5N to 5A after digestion with restriction enzymes SACI (5N) and BSNI (5A). This was quantified using ImageJ software.

4.c) Results

***Figure 2:** 5N/5A expression in MB-231 samples*

5) Conclusion

5.a) Summary:

The first ASO transfection shows a moderate increase in 5A/5N where 5A values increased from 2% in untreated MDA-MB-231 cells to 27.3% when treated with our most efficient ASO design, ASO 3 **(Figure 2)**.

5.b) Revisions:

A higher ASO dose may yield a larger increase in 5A/5N. We will further evaluate ASO efficiency by subjecting treated TNBC cells to in vitro cell shape analysis and tumor matrix adhesion assays for invasion evaluation.

5.c) Impact (Future Version):

With performed revisions, the aim is to develop and identify a highly functional ASO which successfully switches expression from exon 5N to 5A. If administered to patients, this design may become a broadly-applicable, yet targeted novel treatment for mTNBC.

References:

1 Almansour, N. M. *Front. Mol. Biosci.* 9, 836417 (2022) **2** Huppert, L. A. *et al. Ther. Adv. Med. Oncol.* 14, 17588359221086916 (2022) **3** Han, Y. *et al. Am. J. Cancer Res.* 10, 727–742 (2020) **4** Winstead, E. (2022) **5** Leslie, T. K. *et al. J. Physiol.* 601, 1543–1553 (2023)

Acknowledgements: Oudin Laboratory, NIH Grant A470001-NIH230